Holistic Framework for Design and Optimization of Electric Aircraft Propulsion Systems

Zur Erlangung des akademischen Grades eines

DOKTORS DER INGENIEURWISSENSCHAFTEN (Dr.-Ing.)

von der KIT-Fakultät
für Elektrotechnik und Informationstechnik des
Karlsruher Instituts für Technologie (KIT)
angenommene

Dissertation

von
M.Sc. Stefan Biser
geboren in Freyung

Tag der mündlichen Prüfung: 11.09.2025

Referent: Prof. Dr.-Ing. Mathias Noe
Korreferent: Prof. Christopher Gerada
(University of Nottingham)

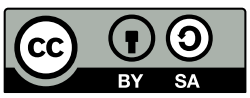

Acknowledgement

This thesis was written over the past seven years in collaboration with the Electrical Division of Rolls-Royce Deutschland GmbH & Co KG (formerly the eAircraft department of Siemens AG) and the Institute for Technical Physics (ITEP) at Karlsruhe Institute of Technology (KIT). I am deeply grateful for the opportunity to conduct my research in such a stimulating industrial and academic environment. A doctoral thesis is not written alone, it is carried forward by mentors, colleagues, and those who believe in you even when you hesitate. I would like to take this opportunity to thank all those who have accompanied me on this journey.

I would like to express my sincere appreciation to Dr. Mykhaylo Filipenko for his mentoring during my initial year, and to Dr. Martin Boll, who was always approachable and willing to engage, whether it was to discuss a technical question or explore an off-topic idea. His support and positive perspective significantly contributed to the quality of this work.

I am especially grateful to Prof. Dr.-Ing. Mathias Noe for his role as my doctoral supervisor. His continuous trust throughout this long journey, constructive guidance, and technical insight were instrumental in the successful completion of this work. I highly appreciate his thoughtful comments and feedback, which helped elevate the scientific quality of this thesis.

I also thank Prof. Chris Gerada for serving as the second referee, for his interest in my research, and for his valuable feedback.

My heartfelt thanks go to all my colleagues and collaborators for countless fruitful technical discussions. In particular, I would like to acknowledge Dr. Benjamin Cheong, Andreas Mayr, Dr.-Ing. Bastian Lehner, Dr.-Ing. Daniel Prokein, Dr.-Ing. Andreas Reeh, Dr.-Ing. Tobias Schumm, Dr.-Ing. Lars Kühn, Dr.-Ing. Matthias Corduan, Dr. William Hunter, Anton Rudenko, Daniel Merz, Dr.-Ing. Yang Zhang, Dr. Thomas Gleixner, Dr. Marc Leßmann, Dr.-Ing. Nikolai Herzog, Sunil Shreedharan, Matthias Manig, Dr.-Ing. Guido Wortmann, Dr. Florian Schulz, Dr.-Ing. Marco Ambrosi, Dr.-Ing. Johannes Bauer, Mabroor Ahmed, Patrick Sowinski, Manzar Lodhi, Alexander Zakrzewski, and Philipp Weber. Your ideas, openness, and encouragement have made a lasting difference.

I am particularly thankful to Markus Christmann, Max Scheulen, Matheu Parr, and once more to Dr. Martin Boll for fostering my professional development and giving me the opportunity to grow within the company. When Rolls-Royce decided to close the Electrical business, I was fortunate to have the support of Frik-Jan Kruger, Dr. Akin Keskin, and Dr. Steve Mountain, who ensured that I could complete my thesis despite the organisational changes. I am grateful to Dr. Keskin and Dr. Mountain for their thoughtful review and valuable feedback on the manuscript.

Finally, I would like to thank my family for their unwavering support and for making this journey possible. Your belief in me has meant everything. Most of all, I am deeply grateful to my wife, Sandra. Your love, patience, and understanding have been my anchor, providing me with the strength and inspiration to persevere until the end. Throughout these years, you and our little son have been the lighthouse in my life, soon to shine even a little brighter.

Abstract

The decarbonization of aviation has become an urgent priority amid growing concerns about the environmental impact of global air travel. In this context, hybrid and fully electric propulsion systems offer a promising alternative to conventional gas turbine engines, particularly in light of recent advances in battery technology and the broader electrification of aircraft systems. However, the design of electric aircraft requires a highly integrated, system level approach due to stringent mass and performance constraints that are not adequately captured by traditional evaluation metrics.

This thesis presents a modular, physics based framework for the conceptual design and optimization of electric propulsion systems. The proposed models explicitly incorporate key physical domains, including electrical, electromagnetic, thermal, thermodynamic, and structural aspects. These models are formulated using analytical expressions that reflect essential component behaviors and design constraints, while remaining computationally efficient. The framework enables consistent sizing and performance estimation of all major propulsion components, including electric machines, power converters, gear transmission units, electrical cables, thermal management equipment such as heat exchangers, pumps and pipes, and battery packs. Its modular structure supports both individual subsystem analysis and fully integrated propulsion system studies.

To identify optimal propulsion architectures, a set of multi objective optimization algorithms is evaluated using a test case. The NSGA-II algorithm emerges as the most suitable method due to its robust convergence, its ability to handle discrete and continuous parameters, and its performance under multiple constraints. A penalty factor method is developed to guide design selection from the resulting Pareto fronts by combining primary objectives such as mass and losses with additional system level penalties, including efficiency reductions and aerodynamic drag.

The framework is applied in a comparative study of electric propulsion topologies and configurations for a reference aircraft with vertical take off and landing capability. The study is based on the mission profile and layout of a aircraft vehicle similar to Joby's S4 technology demonstrator. Examined configurations include direct drive and geared topologies, air cooled and liquid cooled variants, local and central cooling systems, and different thermal operating limits. The analysis identifies a liquid cooled direct drive solution with elevated machine temperature limits and a local cooling system as the most effective option. A specific design proposal is then developed for this configuration, supported by numerical validation through finite element analysis of critical subsystems.

This work contributes a scalable methodology for early stage design space exploration and system integration of electric propulsion systems. While developed for aerospace applications, the approach is readily transferable to other sectors such as ground transportation and marine propulsion. As the aviation sector advances toward environmentally sustainable technologies, frameworks such as the one proposed in this thesis will play a central role in managing the complex design challenges associated with electric flight.

Zusammenfassung

Die Dekarbonisierung der Luftfahrt ist angesichts der zunehmenden Umweltauswirkungen des globalen Luftverkehrs zu einem vorrangigen Ziel geworden. Hybride und vollelektrische Antriebssysteme gelten dabei als vielversprechende Alternative zu konventionellen Gasturbinen, insbesondere im Hinblick auf Fortschritte in der Batterietechnologie und die zunehmende Elektrifizierung von Flugzeugsystemen. Die Auslegung elektrischer Flugzeugarchitekturen erfordert jedoch einen stärker integrierten, systemorientierten Ansatz, da die im Vergleich zu Gasturbinen geringere Leistungsdichte zu restriktiven Anforderungen an Gewicht und Leistung führt, die klassische Bewertungsmetriken nicht adäquat erfassen.
Diese Arbeit präsentiert eine modulare, physikalisch-motivierte Methode zur konzeptionellen Auslegung und Optimierung elektrischer Antriebssysteme. Die Modelle integrieren verschiedene Disziplinen, darunter elektrische, elektromagnetische, thermische, thermodynamische und strukturelle Aspekte. Sie basieren auf analytischen Gleichungen, die das wesentliche physikalische Verhalten akkurat abbilden, ohne die rechnerische Effizienz zu beeinträchtigen. Die Methode ermöglicht eine konsistente Analyse und Dimensionierung aller Hauptkomponenten eines elektrischen Antriebsstrangs, einschließlich elektrischer Maschine, Leistungselektronik, Getriebe, Kabel, thermischer Systeme und Batteriespeicher. Die modulare Struktur erlaubt sowohl Subsystemanalysen als auch komplexe Systemstudien.
Zur Identifizierung optimaler Antriebsarchitekturen wird eine Reihe multikriterieller Optimierungsalgorithmen anhand eines Testfalls evaluiert. Der NSGA-II Algorithmus erweist sich als geeignetste Methode aufgrund robuster Konvergenzeigenschaften und ihrer Fähigkeit, eine Vielzahl diskreter und kontinuierlicher Variablen sowie Randbedingungen effizient zu verarbeiten. Ein Straffaktorverfahren ermöglicht die Auswahl geeigneter Designs aus den entstehenden Pareto-Fronten, wobei Masse und Verluste des Antriebsstrangs mit einem Strafwert kombiniert werden, der die Zunahme der Batteriemasse infolge niedrigerer Wirkungsgrade und zusätzlichen aerodynamischen Widerstand berücksichtigt.
In einer vergleichenden Studie werden verschiedene elektrische Antriebstopologien auf ein Referenzflugzeug mit senkrechter Start- und Landefähigkeit angewendet, wobei Konfigurationen mit unterschiedlicher Anzahl an Propellern betrachtet werden. Die Studie basiert auf dem Missionsprofil und der Auslegung eines Demonstrators, der dem Technologieträger S4 von Joby Aviation ähnelt. Untersucht werden unter anderem Direktantriebe und Antriebe mit Getriebe, luft- und flüssigkeitsgekühlte Varianten, Konzepte mit lokalem oder zentralem Kühlsystem sowie unterschiedliche thermische Betriebsgrenzen der Maschine. Die Analyse identifiziert eine flüssigkeitsgekühlte Direktantriebskonfiguration mit erhöhten Temperaturgrenzen und lokalem Kühlsystem in der Konfiguration mit zehn Propellern als effektivste Lösung. Für diese wird ein spezifischer Entwurf sowie dessen Leistungsdaten präsentiert, wobei kritische Subsysteme durch Finite-Elemente-Analysen validiert werden.
Diese Arbeit leistet einen Beitrag zu einer skalierbaren Methodik für die Analyse des Designraums elektrischer Antriebssysteme in frühen Entwicklungsphasen. Obwohl ursprünglich für die Luftfahrt konzipiert, ist der Ansatz auch auf den Automobil- und Schiffsverkehr übertragbar. Angesichts des Wandels der Luftfahrt hin zu umweltverträglicheren Technologien werden Methoden wie die hier vorgestellte eine zentrale Rolle bei der Bewältigung interdisziplinärer Herausforderungen elektrischer Flugantriebe spielen.

Table of Contents

1 Introduction

Emissions by Aviation

As can be seen in Figure 1.1, the total share of aviation in global CO_2 emissions rose only slightly, ranging between $2.0-2.8\,\%$ over the last 40 years, while the absolute emissions roughly doubled, resulting in a total of $1.04\,\mathrm{Gt\,CO_2\,yr^{-1}}$ in 2019, including both passenger and freight volume [1].

The Covid-19 pandemic hit the world, and especially the aircraft industry, in an unprecedented way, reducing the total number of domestic flights by 38 % and international flights by as much as 66 % in 2020 due to national lockdowns and closed borders [2]. Since then, air traffic has recovered to pre-pandemic levels, and emissions are expected to exceed them in 2025 [3].

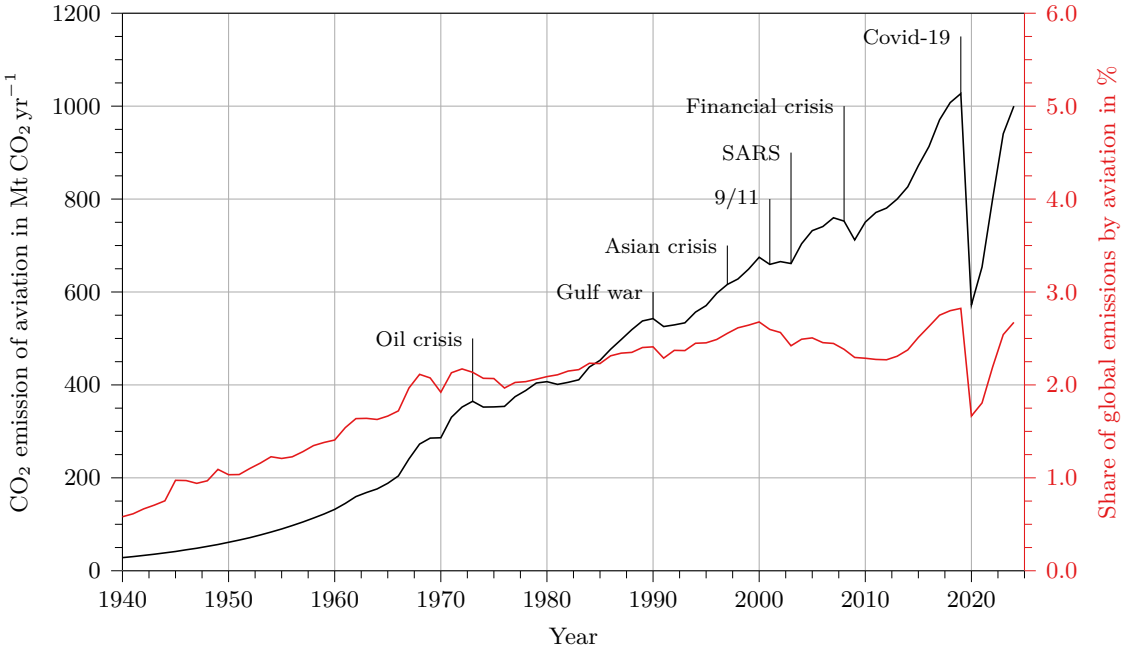

Figure 1.1: Total CO_2 emissions of aviation and its share of global CO_2 emissions as a function of the year. Crises affecting air travel are marked at their beginnings. Adapted from Lee et al. [1] and extended with data from the International Council on Clean Transportation [4], Bergero et al. [5], and the International Energy Agency [3].

Emissions generated by burning kerosene are about 3160 g of carbon dioxide (CO_2), 13.3 g of nitrogen oxide (NO_x), 1 g of sulphur oxide (SO_x), and 1230 g of water (H_2O) per kilogram of fuel at cruise altitude for a typical long-haul flight [6]. Their global warming potential is even higher because these emissions are produced at altitudes between $8-13\,\mathrm{km}$ [7].

In the past, aviation has seen an improvement in fuel burn efficiency of nearly 3.0 % on a year-to-year basis over the last two decades, reaching as low as $115\,\mathrm{g\,CO_2}$ per revenue passenger kilometer (RPK) in 2024, as shown in Figure 1.2. These large improvements are outweighed by a steady increase in revenue passenger kilometers of about 5.5 % per year, resulting in an overall net increase in CO_2 emissions from aviation of 2.5 % per year, as also shown in Figure 1.1. Interestingly, the Covid-19 pandemic worsened fuel efficiency and led to a temporary increase in emissions afterward, mainly due to lower passenger

loads and less efficient flight patterns.

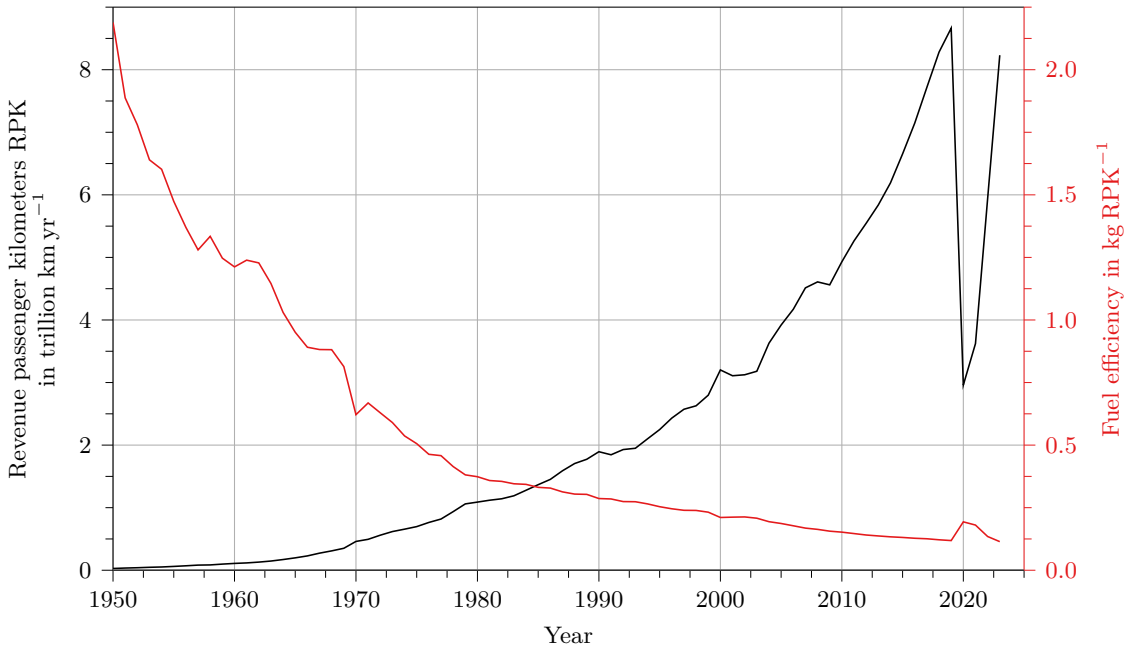

Figure 1.2: Revenue passenger kilometers (RPK) and fuel efficiency as a function of year. Adapted from Lee et al. [1].

Besides the absolute amount of emissions, the distribution of passenger aircraft CO_2 by aircraft class and flight distance is of high importance to analyse the current status and define effective measures to mitigate them in the future.

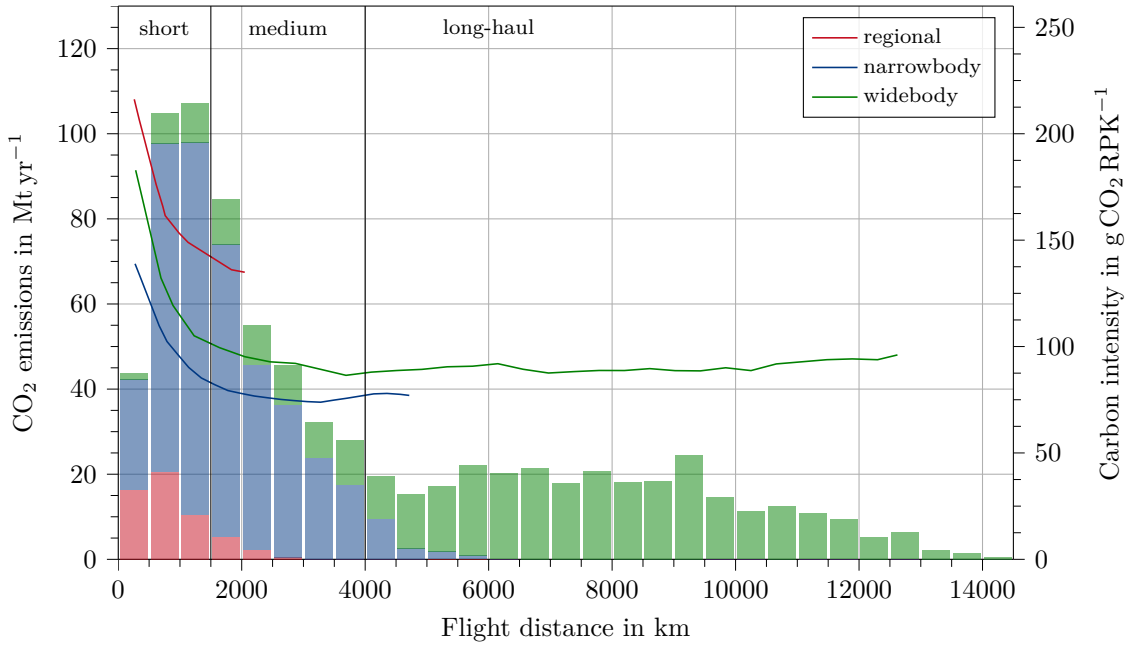

Figure 1.3: Share of passenger CO_2 emissions by aircraft class and carbon intensity as a function of mission length. Adapted from [4].

Figure 1.3 shows that approximately one third of passenger CO_2 is emitted per distance group. Long-haul flights with mission lengths greater than 4000 km, served by widebody (multi-aisle) aircraft such as the Airbus A350 or Boeing 777, emit as much CO_2 as medium-length flights between 1500 – 4000 km and short-haul flights up to 1500 km, served by

narrowbody (single-aisle) aircraft such as the Airbus A320neo and Boeing 737, as well as small regional airliners.
A more detailed analysis reveals that regional flights with less than 1000 km account for approximately 20 % of total CO_2 emissions, while medium- and long-haul flights cover the rest. However, the carbon intensity for such short flights is about $160\,\mathrm{g\,RPK^{-1}}$ on average, with low values of $140\,\mathrm{g\,CO_2\,RPK^{-1}}$ for narrowbody aircraft such as the Airbus A320neo and up to $220\,\mathrm{g\,CO_2\,RPK^{-1}}$ for regional aircraft such as the ATR72-600 and De Havilland Dash 8-400. Their higher carbon intensity results from extra fuel needed for the disadvantageous take-off to cruise phase, and from generally less fuel-efficient regional aircraft. The data indicate that there is both a large need and high potential to reduce emissions, especially on regional and short-haul flights where no alternative modes of transportation, such as rail, are available.

Passenger and Emission Forecast

Before the Covid-19 pandemic, Airbus [8] estimated an annual passenger growth of about 4.3 %. Since the end of the pandemic, lockdowns and general travel restrictions are no longer a factor.
With passenger numbers now recovering to pre-pandemic levels as predicted, this will lead to increasing CO_2 emissions unless adequate measures to mitigate them are taken. This concern is highlighted by the International Energy Agency, which identifies aviation along with heavy trucks and shipping as one of the transportation modes in a sustainable development scenario that will contribute most to direct emissions of CO_2 from fossil fuel consumption in 2070 [9].
These sectors are regarded as particularly difficult to decarbonize due to a variety of reasons, primarily their high specific energy and power demands, which cannot easily be substituted. In aviation, other factors also come into play. The typical lifetime of an aircraft, around 25 years, leads to a very slow fleet turnover, meaning that old technology remains in service for an extended period. Secondly, the development costs of a new aircraft, such as the Airbus A350 or Boeing 777, range from $5-15$ bn$ for a new design, with slightly lower costs for a redesign such as the Airbus A320neo, making manufacturers very risk-averse when it comes to radically new designs [10].

Emission Targets and Possible Solutions

All major aircraft and aviation agencies, including the National Aeronautics and Space Administration [11, 12], the International Civil Aviation Organization [13, 14], the Aviation Transport Action Group [15], and the European Commission's Flightpath 2050 [16], have presented ambitious plans to reduce greenhouse gas emissions in the aircraft sector by up to 75 % in terms of reduced fuel burn, and 90 % in NO_x emissions by 2050.
Such substantial emission reductions require equally significant technological advances. Currently, three major technology areas are under investigation. The first possibility involves Sustainable Aviation Fuels, which can serve as a drop-in replacement for kerosene, as their gravimetric and volumetric energy densities are not a limiting factor compared to batteries or hydrogen fuels. These synthetic fuels are either produced from biological resources (biomass, sewage) or synthetic sources (hydrogen and CO_2), making them a net-zero decarbonization option [17]. Currently, there are seven certified pathways, including the hydrotreating of oil-based and Fischer-Tropsch synthesis of renewable feedstocks [18]. Recent projections estimate a maximum production capacity of $3.4\,\mathrm{Mt\,yr^{-1}}$ by 2030, which would contribute to 5.5 % of projected jet fuel demand [19].
Hydrogen fuels represent a second method for reducing emissions and can be used either as a drop-in fuel for combustion or as a true zero-emission alternative in fuel cells. While the complexity of both solutions is high, hydrogen combustion would not require any novel engines or electrical systems, only some minor modifications to the aircraft architecture. In

contrast, fuel cells would require a complete redesign of both the aircraft and its electrical systems [20]. Hydrogen has the potential to reduce net carbon emissions significantly, as its gravimetric energy density is about three times that of conventional jet fuel. However, hydrogen also requires four to five times the volume to store the same energy. Another advantage of hydrogen is its short refuelling times and fast turnaround [20].
The necessary reduction in fuel consumption has also led to increased interest in partly or fully electrified aircraft to replace conventional gas turbines [21, 22], making hybrid-electric propulsion systems the third alternative. These systems range from parallel-hybrid to series-hybrid solutions, to all-electric battery or fuel-cell-only systems, in order of increasing emission reduction potential. A key advantage of hybrid-electric propulsion is that it does not necessarily require the establishment of a hydrogen supply chain [20].
It is expected that all-electric drivetrains will be suitable for small aircraft with short ranges, assuming batteries can overcome the critical gravimetric energy density challenges. Sustainable fuels are expected to be used for long-haul aircraft, due to the volumetric and gravimetric energy densities required. For the medium-range market, hydrogen and (hybrid-) electric propulsion systems are likely to compete with each other [20].
This work will focus on all-electric propulsion systems, particularly in the context of short-haul, small aircraft with flight distances of up to 1000 km. These aircraft contribute around 20 % of aviation emissions and are by far the most carbon-intensive aircraft in operation today. The potential of all-electric systems to offer a sustainable solution is driven by the evolving battery technologies and the increasing demand for emissions-free aviation.

1.1 Hybrid- and All-Electric Power Train Configurations for Aircraft

Power trains with two or more controllable and distinct energy sources, such as kerosene, batteries, solar, or fuel cells, are defined as hybrid-electric systems. They can furthermore utilize mechanical transmission devices such as gearboxes, electrical motors and generators, and various kinds of power electronics such as inverters, rectifiers, and circuit breakers [23]. Due to the large number of possible architectures of hybrid-electric power trains, only specific types of architectures will be investigated.
As already outlined previously, electrification of aviation is seen as one possibility to reduce carbon dioxide emissions. While hybrid- and all-electric ground-based vehicles have managed to make it to large-scale mass production, especially within the automotive sector with more than 2.1 million units sold in 2019 [24], electrification of aircraft is still in its infancy. Efforts have been made to replace heavy hydraulic and inefficient pneumatic subsystems, e.g., air-conditioning packs and wing anti-ice systems, with electrical ones to save weight and reduce lifecycle costs. By applying bleedless electrical systems, Boeing claims to improve fuel efficiency by about 3 % on its latest Boeing 787 with a total of 1 MW of power installed [25]. This approach is called More Electric Aircraft (MEA) [26]. Even in fully electric aircraft, where all onboard subsystems are electrical and only a mechanical power off-take is used to drive the fan or propeller, the expected gain in fuel efficiency remains insufficient to meet ambitious emission reduction targets [26].
Therefore, a turn towards electrification of the propulsive drive train is the next logical step to further reduce emissions. Five general such configurations are shown in Figure 1.4. The first topology to be discussed is a full turbo-electric configuration given in Figure 1.4a. One sole energy source, in this example fossil kerosene, is fed to a gas turbine which converts chemical into mechanical energy powering an electric generator to finally convert the energy into electrical one. An Electric Power Distribution System (EPDS) is responsible

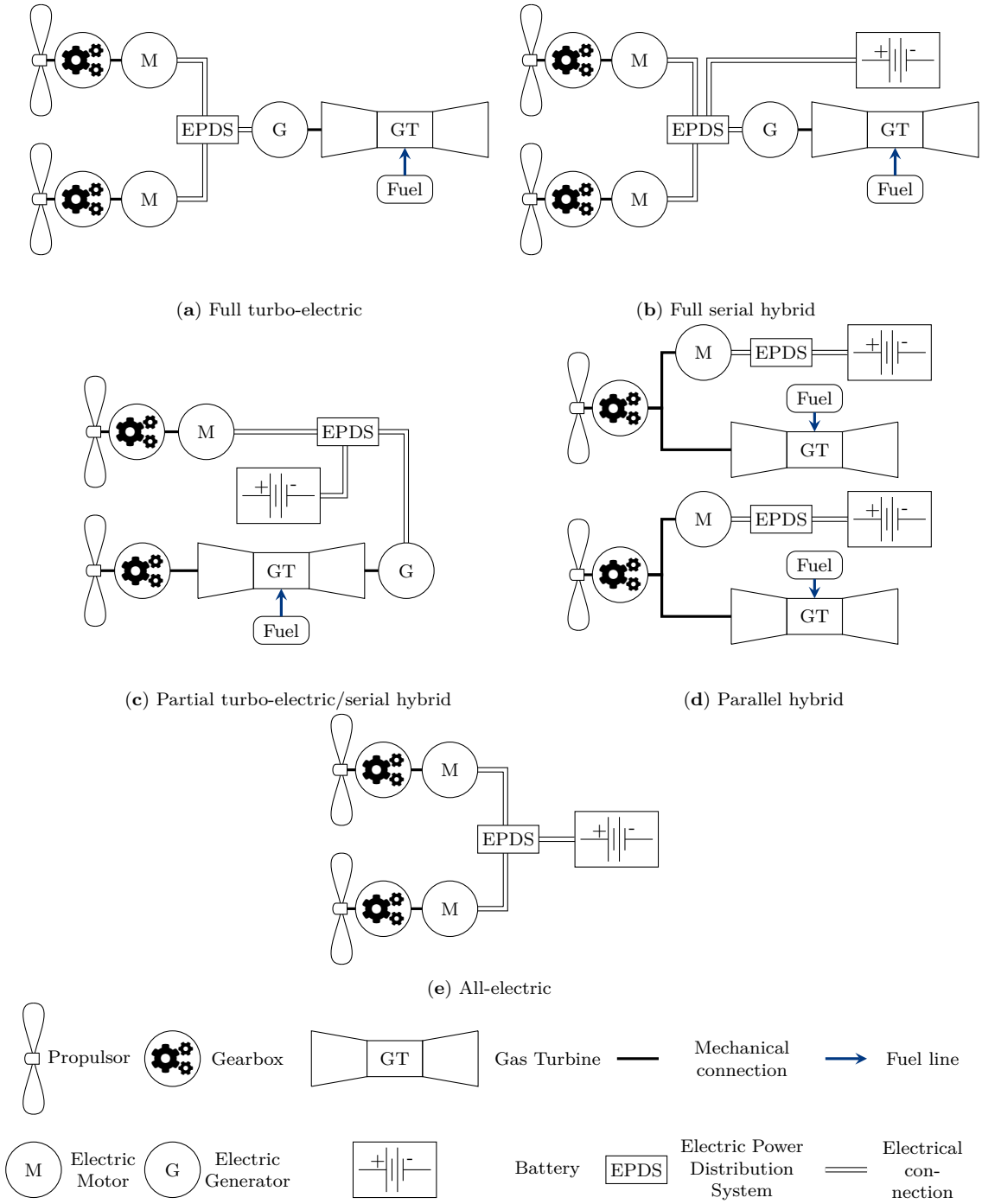

Figure 1.4: Various kinds of hybrid-electric power trains ranging from full-turbo electric via serial and parallel hybrids to all-electric configurations.

for transferring the electrical energy from the generation to the consumer side. Depending on the chosen voltage type of electrical transmission, the EPDS can consist of AC-DC rectifiers, cables, switches and circuit breakers, and DC-AC inverters. The propulsive side of the drive train is composed of electric motors converting electrical energy to mechanical one. Depending on requirements, a gearbox to transform torque and rotational speed may be placed between the motor and the propulsor, e.g., a fan or propeller, to generate thrust. With regards to the given definition of hybrid-electric drive trains, full turbo-electric configurations actually do not meet the requirement of a second energy source. However, this configuration has been proposed by several studies, especially for use in medium and long-haul flights for larger aircraft [27–31] but also for regional aircraft with

moderate power requirements [32, 33].
When a second source of energy, e.g., a battery, is added to the system, a full serial hybrid configuration can be realized (see Figure 1.4b). Both a generator driven by a gas turbine as well as the battery feed into a common power distribution system. Both turbo-electric and serial-hybrid configurations result in a total mechanical decoupling of power generation and consumption and offer large flexibility to operate both sources at their most optimal efficiency. This comes at the cost of sizing the electrical system for the total propulsive power, thus the higher efficiencies of the electric drive train must compensate for the extra losses generated by it [34].
A partial turbo-electric system refers to a configuration in which the majority of gas turbine power is transmitted mechanically to a propulsor, while only a fraction is converted into electrical power to drive an additional propulsor via an electric motor [35, 36]. This can be extended to a partial serial hybrid system if the electric transmission line is backed up by a second energy source (see Figure 1.4c).
Another variant is generated if both generation paths are combined mechanically at the propulsor input shaft, with both of them delivering mechanical power simultaneously. This gives a parallel hybrid layout. In contrast to a serial hybrid, the mechanical decoupling is not present anymore and the advantage of efficiency-optimal components is lost, but for that the electrical system can be sized freely with respect to the total propulsive power, i.e., the electric path assists the gas turbine, e.g., as a booster for take-off [37] (see Figure 1.4d).
The last discussed configuration is an all-electric or universally-electric drive train where a battery or a fuel cell is the sole source of electric energy. If a battery is used, high inner efficiencies of the total power train larger than 90 % are achievable, but this results in a larger mass due to the currently low power and energy density of available battery cells. Several studies consider energy densities about 500 kW h to reach mission lengths around 1000 – 1500 km [38, 39]. Thus, all-electric configurations will be limited to small and short-range (regional) aircraft only in the near future.
To mathematically classify the degree of hybridization, Lorenz et al. [40] proposed two independent metrics. The first quantifies the share of the total installed propulsive power that is provided by electrical means. This is referred to as the degree of power hybridization and is denoted by H_P, which is defined as follows:

$$H_\mathrm{P} = \frac{P_\mathrm{elec}}{P_\mathrm{tot}} = \frac{P_\mathrm{elec}}{P_\mathrm{conv} + P_\mathrm{elec}}, \tag{1.1}$$

where P_elec represents the total electric propulsive power installed, P_conv refers to the propulsive power provided by conventional gas turbines, and P_tot is the sum of both. A value of H_P equal to zero corresponds to a fully conventional system, while a value of one indicates that all propulsion power is supplied by electric motors. In cases where hybrid systems include a battery, it has been shown that these can be sized such that their power capacity does not limit system performance [41]. However, this does not mean that the specific energy of the battery can be chosen independently of its specific power, since both the total energy and total power must be accounted for in system design.
To address the energy aspect, Lorenz et al. [40] introduced a second metric known as the degree of energy hybridization, denoted by H_E. This metric describes the fraction of energy stored in electrical form relative to the total available energy:

$$H_\mathrm{E} = \frac{E_\mathrm{elec}}{E_\mathrm{tot}} = \frac{E_\mathrm{elec}}{E_\mathrm{conv} + E_\mathrm{elec}}. \tag{1.2}$$

Here, E_elec is the amount of energy stored electrically, E_conv is the energy stored in conventional sources such as kerosene, and E_tot is the sum of both. A value of H_E equal to zero indicates that only conventional energy sources are used, whereas a value of one means all

energy is stored electrically. These two metrics provide a consistent framework for classifying a wide range of propulsion system configurations, from conventional to fully electric and hybrid concepts. However, Vratny [37] pointed out that the combination of H_P and H_E does not allow a clear distinction between certain architectures such as parallel and partial serial hybrids, even though these offer significant design flexibility. An overview of how different configurations map to these two metrics is provided in Table 1.1.

Table 1.1: Parameter settings for various (hybrid-) electric configurations

Configuration	**Degree of Power Hybridization H_P**	**Degree of Energy Hybridization H_E**
Conventional	0	0
Full Turbo-Electric	1	0
Partial Turbo-Electric	$0 < H_P < 1$	0
Serial Hybrid	1	$0 < H_E < 1$
Parallel Hybrid	$0 < H_P < 1$	$0 < H_E < 1$
Partial Serial Hybrid	$0 < H_P < 1$	$0 < H_E < 1$
All-Electric	1	1

Examplary hybrid-electric aircraft presented in several studies by various manufacturers and institutions are shown in Figure 1.5 as a function of the degree of power and energy hybridization.

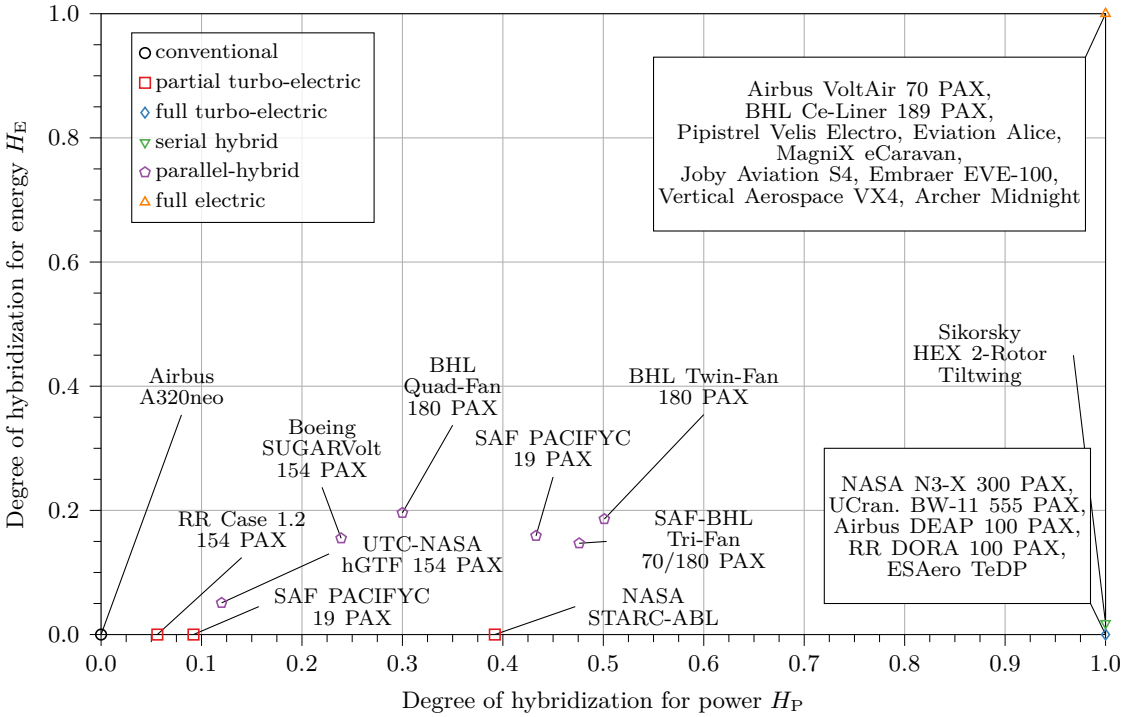

Figure 1.5: Example hybrid-electric aircraft studies by various manufacturers as a function of the degree of hybridization of power H_P and energy H_E. Adapted from [42].

Partial and full turbo-electric as well as parallel-hybrid propulsion architectures have remained confined to conceptual studies, with no known full-scale prototypes built to date. These configurations, typically proposed for larger aircraft, face significant challenges in system integration and energy storage, which have so far precluded hardware realization. For serial-hybrid concepts, Sikorsky announced that a technology demonstrator of its HEX 2-Rotor Tiltwing is under construction [43]. This indicates initial progress in hardware realization within this drivetrain class.

Fully electric propulsion has achieved the highest level of technological maturity to date. While long-range fully electric aircraft remain at the conceptual level, several regional aircraft have advanced to the prototype stage. Pipistrel's Velis Electro is the first fully electric plane that has received full type certification from EASA, demonstrating regulatory acceptance for small electric aircraft [44]. Other platforms, such as the Eviation Alice and MagniX eCaravan, have completed maiden flights [45, 46]. A large number of electric vertical take-off and landing aircraft have also entered extensive test flight campaigns. These include Joby, Archer, and Vertical. However, none of them have yet achieved full type certification [47].
The data suggest that electrification of aviation is currently most viable for small and regional aircraft using fully electric architectures. Battery energy and power densities are sufficient to enable commercially relevant performance in this segment. In contrast, drive-train architectures targeting larger aircraft face prohibitive development and operational costs. Consequently, they are currently at the conceptual stage.

1.2 Current Design and Optimization Methods for Electric Propulsion Systems

Depending on the drive train topology, architecture, and mission profile, requirements can be derived to size the electric components accordingly. In a review article, Sahoo et al. [48] summarized various sizing tools used for the multidisciplinary design of hybrid-electric aircraft and their drive trains.
For conventional aircraft, the Top Level Aircraft Requirements (TLAR) define the operational envelope and thereby guide the sizing of the aircraft and propulsion system to provide sufficient thrust to overcome drag. The trade-off among the three major disciplines, namely aerodynamics, structure, and propulsion, is typically achieved via correlation-based scaling laws. However, this approach is not directly applicable to (hybrid-) electric aircraft due to the fundamentally different energy source characteristics, such as the fixed weight of batteries and the variable weight of fuel. Moreover, performance depends on mission time and varies with the selected degree of power and energy hybridization. A key difference lies in the integration of electrical and thermal systems, which significantly influence the design of the propulsion train and must therefore be considered in the sizing process [48].
Current electric system sizing methods are reviewed with a focus on electric aircraft. From a technical perspective, two key factors influence the feasibility and performance of a design: the overall mass of the electric propulsion system m_{EPS}, defined as the sum of the component masses m_{comp}

$$m_{\mathrm{EPS}} = \sum_i m_{\mathrm{comp,i}}, \tag{1.3}$$

and its total efficiency η_{EPS}, computed as the product of the component efficiencies η_{comp}

$$\eta_{\mathrm{EPS}} = \prod_i \eta_{\mathrm{comp,i}}. \tag{1.4}$$

Preliminary sizing therefore consists of estimating or computing the masses and efficiencies of the individual components. The most straightforward approach to derive these metrics is to use specific power densities, or power-to-weight ratios, $PTW_{\mathrm{comp,i}}$, and specific efficiencies $eta_{\mathrm{comp,i}}$. The component masses are then estimated from the power requirements $P_{\mathrm{comp,i}}$ using

$$m_{\mathrm{comp,i}} = \frac{P_{\mathrm{comp,i}}}{PTW_{\mathrm{comp,i}}}, \tag{1.5}$$

and the total mass and efficiency follow from Equations (1.3) and (1.4). This method has been applied in studies of turboelectric and all-electric systems [27, 39, 49, 50] as well as hybrid-electric configurations [51–55]. While enhancements exist, such as for all-electric aircraft [56], they often rely on fixed parameter settings. Batteries have received more refined treatment in some studies [57], but other components are still treated using high-level parameterizations for both all-electric [57] and hybrid-electric architectures [58]. Similar methodologies have been adopted in the automotive sector [59, 60], but with limited component modeling and often lacking the fidelity required for aircraft applications. A key drawback of these methods is that they typically rely on a single design point, which limits the ability to capture variations in power, rotational speed, voltage, and other parameters.

Stückl [38] was among the first to develop physically derived models for electric motors, switches, and power transmission lines, with all correlations accounting for the transmitted power. Aigner et al. [61] integrated this approach into the MICADO preliminary aircraft design software, which has been updated over time [62, 63]. However, the software remains tailored to conventional aircraft and only recently began incorporating hybrid-electric drive train development, without exploring component-level modeling in depth.

Significant progress has been made by researchers at the Visionary Concepts Division of Bauhaus Luftfahrt [33, 38, 39, 53], with Vratny et al. [37, 64, 65] introducing a holistic framework for the design of hybrid-electric drive trains. This framework features analytical, physically derived models for individual components, coupled through key physical properties. For example, the sizing of the battery pack is based on a cell arrangement defined by voltage characteristics as a function of state of charge (SOC), which is used not only to calculate the battery's weight and efficiency, but also to define the output voltage for power electronics and distribution system design. Key parameters throughout the system include power, voltage, and rotational speed, while additional parameters are considered as needed. However, they did not implement multi-objective optimization algorithms to explore optimal component parametrizations.

Holdstock and Bryant [66] presented a method for automotive drivetrains that models the performance of gearboxes, electric motors, and power electronics. Each component includes multiple design options, such as topology and geometry, and results are correlated through physical laws, enabling broad design space explorations. Nevertheless, optimization techniques were not applied, and batteries were excluded. Additionally, the software was not designed to meet the stringent requirements of electrified aircraft.

Mester et al. [60] proposed a system-level optimization methodology and concluded that simultaneously modeling all electric components yields better results than sequential evaluation. Hadbi et al. [67] introduced the Extended Pareto Front Method, which conducts subsystem-level optimizations and combines their results to determine optimal system-level performance in an aircraft context.

1.3 A Modelling Framework for Electric Propulsion System Design and Optimization

While very high-fidelity toolchains, including coupled simulations across disciplines such as electromagnetics, structural mechanics, and thermal analysis, certainly exist for the design and optimization of individual components like electric motors, only high-level methodologies and loosely connected frameworks are available for the design and optimization of entire drive trains during the preliminary design phase, particularly in applications with stringent mass and efficiency requirements such as in the aviation industry.

Sahoo et al. [48] provide an extensive overview of current research activities in electric aircraft development. Their review identifies several gaps and inconsistencies currently encountered by airframers, including:

- the lack of electrical system design tools capable of optimising aircraft and electric system performance concurrently across different missions and aircraft configurations
- reliance on projected future technology levels
- subsystem-level assessments that consider only limited disciplinary interactions
- weight and performance estimations of electrical systems performed by conceptual aircraft designers without sufficient understanding of the interdisciplinary interactions and resulting trade-offs

Figure 1.6 visualizes the competing interests present at different stages of the design process. It is based on a typical V-shaped development process for aircraft, which includes the design of the electric subsystem and its components on the left side, proceeding from top to bottom, and their verification on the right side, progressing in the opposite direction.

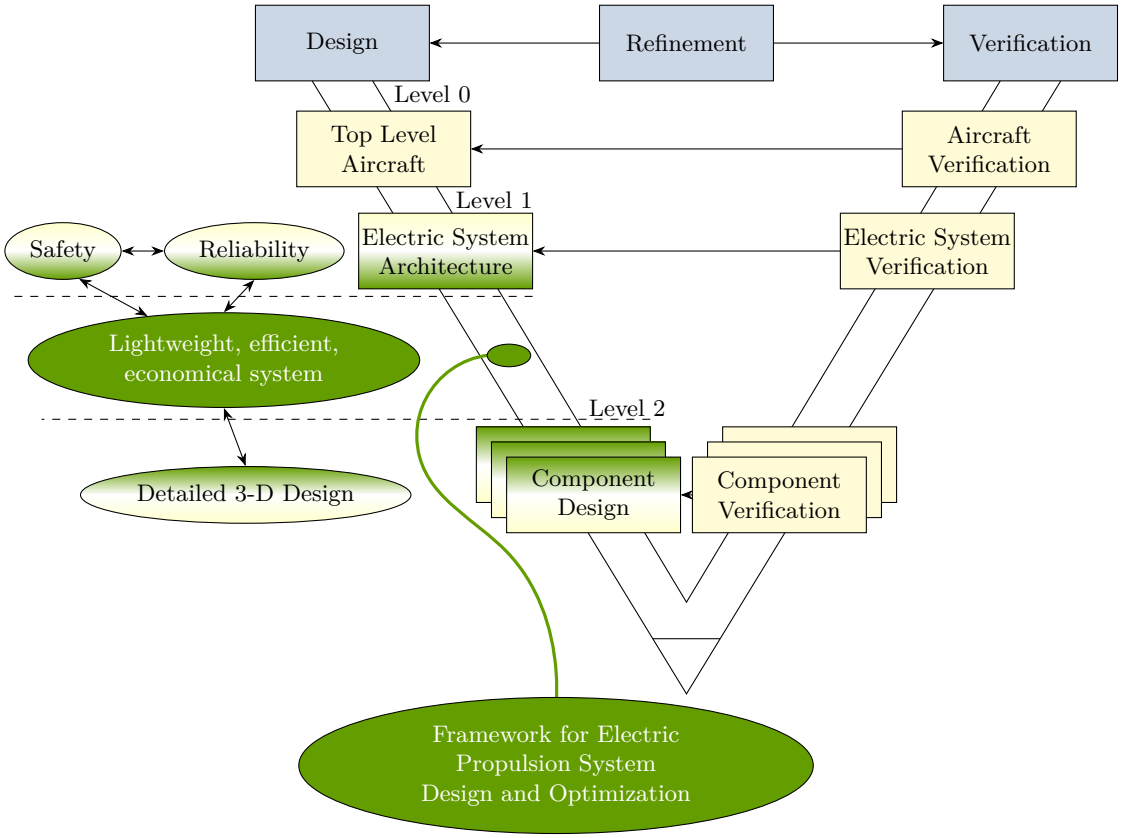

Figure 1.6: Typical V-shaped development process (adapted from [68, 69]). The development process is divided into a design phase, with increasing level of detail from top to bottom, and a verification phase, with increasing system size from bottom to top. The ellipses on the left indicate typical trade-off properties during the design phase. The green ellipse highlights the focus of this thesis, namely the development and application of a framework for electric propulsion system design and optimization.

The top level aircraft requirements defined during the aircraft design process are used to derive requirements for the electric system architecture. At this stage, the system architect must define a system layout that accommodates safety and reliability constraints alongside other design objectives such as weight, efficiency, and cost. In contrast, component designers are responsible for creating detailed three-dimensional designs to verify the feasibility

of the proposed concept. It is challenging to make fundamental architectural decisions that optimise system weight, efficiency, and cost without a comprehensive understanding of interdisciplinary interactions at the electric system level and without accounting for feedback effects on the overall aircraft design.
Recognising the need for a holistic design and optimization framework for hybrid-electric propulsion systems situated between architecture and component-level design, the central idea of this thesis is to develop a software tool that enables comprehensive design space exploration and optimization. The aim is to support the integration of components and disciplines into a coherent system with manageable computational requirements on standard workstations. This is intended to accelerate preliminary design phases and provide accurate starting points for subsequent component design activities.

1.4 Thesis Outline

This thesis presents a comprehensive approach to the design and optimization of electric propulsion systems for aircraft. Chapter 1 introduces the motivation behind the research, emphasizing the urgent need for cleaner alternatives in aviation due to the environmental impact of global air travel. It discusses the challenges of integrating electric propulsion systems, focusing on mass, efficiency, and operational constraints specific to aircraft. The chapter outlines the thesis objectives, particularly the development of a modular, physics-based framework for early-stage design and optimization. An extensive review of the state-of-the-art in electric propulsion systems for aviation is provided, identifying limitations in current methods and highlighting the need for multidisciplinary approaches in early design stages, particularly in integrating propulsion systems with airframe designs. The chapter also surveys existing optimization methods and their applicability to electric propulsion systems.
In Chapter 2, a detailed description of the models developed for key subsystems of the electric propulsion system will be provided. These include electric machines, power electronics, gearboxes, cables, cooling systems, and batteries for energy storage. The chapter explains the modular, physics-based approach used to model these components, ensuring their behaviors and constraints are captured realistically and efficiently. These models form the foundation for system-level integration and optimization, enabling early-stage design exploration.
Chapter 3 explores various optimization algorithms and their applicability to electric propulsion systems. The chapter presents the results of evaluating different algorithms on a representative case study involving a DC cable, with the aim of identifying the most suitable optimization strategy in terms of convergence behavior, accuracy, and computational efficiency.
In Chapter 4, the framework developed in earlier chapters will be applied to optimize the electric propulsion system of an electric vertical take-off and landing aircraft. The reference aircraft and mission will first be defined, followed by a performance point analysis to determine the power unit requirements under various flight conditions. Several propulsion system architectures will be developed, incorporating different cooling methods, temperature limits, and mechanical configurations. A multi-criteria optimization approach will be used to minimize both weight and power losses, ultimately identifying the optimal propulsion system configuration.
Chapter 5 provides a summary of the work and its key findings. Additionally, an outlook on future developments to enhance the framework will be presented.

2 Drive Train Components Modelling

This chapter presents the component-level models that form the foundation of the modular, physics-based framework developed in this thesis. Each section introduces one key subsystem of the electric propulsion drivetrain: electric machines, gearboxes, power electronics, transmission cables, thermal management systems, and batteries. The modelling approach focuses on combining computational efficiency with sufficient fidelity for early-stage design and system-level integration.

2.1 Electric Machines

Electric machines are used in drivetrain architectures as motors to drive propulsors and as generators to convert mechanical power into electricity, for example, at the shaft of a gas turbine. As stated by Cao et al. [70], various types of electric machines are suitable for aircraft applications, but the Permanent Magnet Synchronous Machine (PMSM) is considered the most promising due to its high power density and efficiency across a wide speed range, as well as its low torque ripple and reduced acoustic noise compared to induction or reluctance machines. However, permanent magnet synchronous machines exhibit drawbacks, such as higher costs due to rare-earth materials and increased complexity in fault management, particularly under short-circuit, since the magnets continuously produce a magnetic field that cannot be switched off [70]. Given the critical importance of low mass in aerospace applications, numerous publications have demonstrated fault-tolerant permanent magnet synchronous drive designs [71, 72] and corresponding control strategies [73]. Figure 2.1 illustrates the scope of the developed electric machine model.

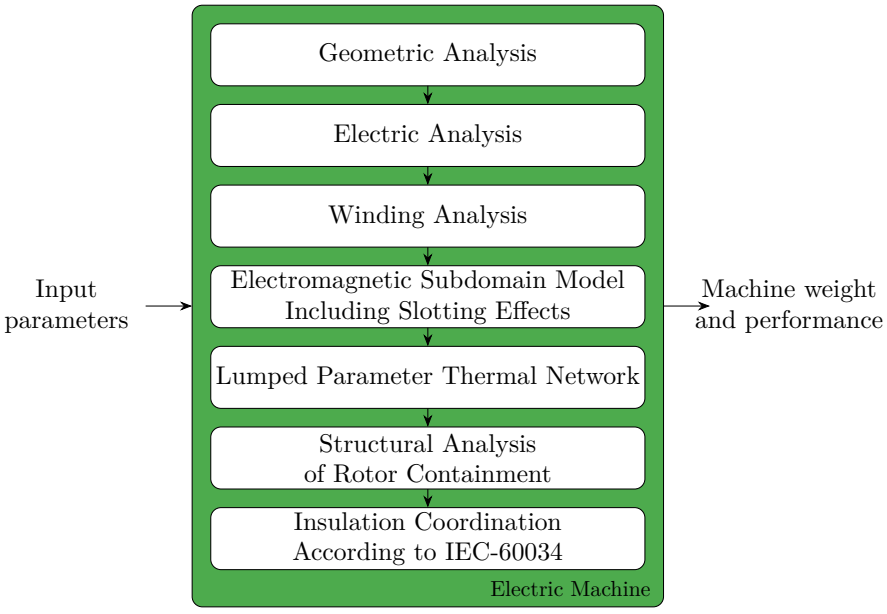

Figure 2.1: Overall setup and included disciplines of electric machine modelling

It begins with basic geometric and electrical analysis, followed by a more detailed study of winding design and electromagnetic behavior using a subdomain model to determine airgap flux densities, including slotting effects. This phase is central to calculating performance parameters such as mechanical power and efficiency. The resulting losses are then used to evaluate the temperature distribution of the machine, which is essential for avoiding hot spots and demagnetization. The evaluation concludes with a structural analysis of rotor containment and an assessment of safety factors against insulation breakdown due to high voltages.
Although permanent magnet synchronous machines with surface-mounted magnets offer limited field-weakening capability, their uniform rotor geometry enables analytical electromagnetic modelling and makes them a suitable baseline for machine design studies. As Cheong [74] highlights, fast and straightforward models are required for optimization purposes. This section improves the model proposed by Cheong [74], extending it to include additional electromagnetic and thermal considerations, as well as structural mechanics and insulation coordination.

2.1.1 Geometric Modelling of Permanent Magnet Synchronous Machines

A basic geometric model is selected to provide a fully parameterized cross-section of the rotor and stator components of a surface-mounted permanent magnet synchronous machine, as shown in Figure 2.2.

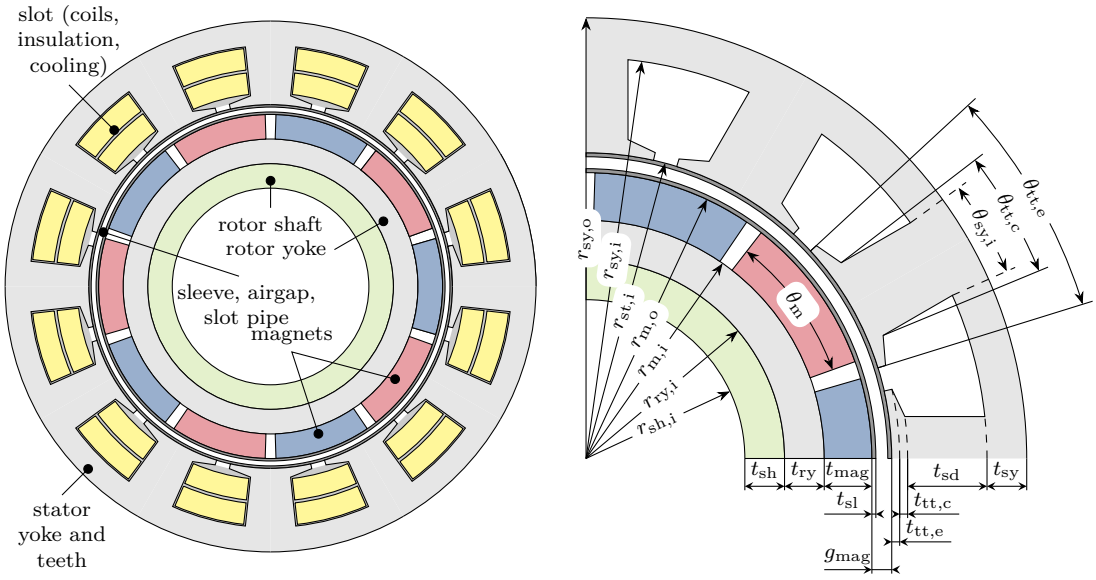

(**a**) General structural layout of rotor and stator (**b**) Detailed radial cross-section

Figure 2.2: Cross-sectional view of a surface permanent magnet synchronous machine showing the active parts. Slot-specific details such as winding layout or insulation coordination will be discussed in more detail later.

The rotor consists of a structural shaft with inner radius $r_{\mathrm{sh,i}}$, a magnetic rotor yoke of thickness t_{ry}, surface-mounted magnets aligned in north-south direction with thickness t_{mag}, and a retaining sleeve. The remaining radii are derived from the specified thicknesses. The rotor has p pole pairs, hence the pole pitch τ_{p} is defined as

$$\tau_{\mathrm{p}} = \frac{\pi}{p} \tag{2.1}$$

and the magnet segment width as

$$\theta_{\mathrm{m}} = \alpha_{\mathrm{p}}\,\tau_{\mathrm{p}} \tag{2.2}$$

where α_{p} denotes the pole width to pole pitch ratio.
The mechanical airgap g_{mech} separates the rotor from the stator. The retaining sleeve with thickness t_{sl} ensures the magnets are mechanically retained, preventing radial detachment, while the slot pipe with thickness t_{sp} seals the stator slots against the airgap, enabling direct slot cooling. Both components contribute to the magnetic airgap g_{mag} from an electromagnetic perspective. If no direct liquid cooling is used, the slot pipe is omitted.
The electromagnetic stator teeth and yoke are enclosed by a structural housing, which is not depicted in Figure 2.2. The tooth tip is characterized by the inner radius $r_{\mathrm{st,i}}$, the edge and center thicknesses $t_{\mathrm{tt,e}}$ and $t_{\mathrm{tt,c}}$, and the edge and center angular widths $\theta_{\mathrm{tt,e}}$ and $\theta_{\mathrm{tt,c}}$. For ease of use in optimization, angular dimensions are expressed relative to the slot pitch

$$\tau_{\mathrm{s}} = \frac{2\,\pi}{Q_{\mathrm{S}}}, \tag{2.3}$$

where Q_{S} denotes the total number of stator slots. The angular quantities are given by

$$\theta_{\mathrm{tt,e}} = \beta_{\mathrm{tt,e}}\,\tau_{\mathrm{s}} \tag{2.4}$$
$$\theta_{\mathrm{tt,c}} = \beta_{\mathrm{tt,c}}\,\tau_{\mathrm{s}} \tag{2.5}$$
$$\theta_{\mathrm{sy,i}} = \beta_{\mathrm{sy,i}}\,\tau_{\mathrm{s}} \tag{2.6}$$

where $\beta_{\mathrm{tt,e}}$, $\beta_{\mathrm{tt,c}}$ and $\beta_{\mathrm{sy,i}}$ represent the respective angle-to-slot pitch ratios for the tooth tip edge, center, and inner stator yoke.
To define the axial parameters, Figure 2.3 shows the axial cross-section of the machine.

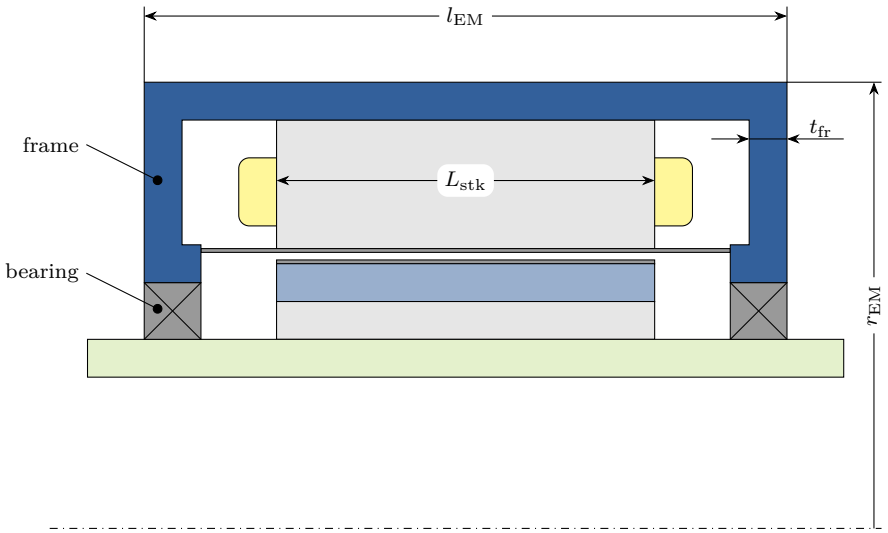

Figure 2.3: Axial cross-section of a surface permanent magnet synchronous machine including passive parts.

In addition to the overall dimensions, including passive parts such as the rotor shaft and machine frame, the main design variable in axial direction is the active stack length L_{stk}. The figure also illustrates the physical separation between the end-winding space and the rotor, implemented via a dedicated slot pipe. This allows the application of direct slot cooling. Bearings are integrated into the stator frame. The total machine radius r_{EM} and length l_{EM} therefore include both active and passive components required for mechanical and thermal functionality.
Table 2.1 presents an exemplary parameterization of an electric machine, which will be used throughout Section 2.1 to illustrate results from the various analysis steps.

Table 2.1: Exemplary electric machine design design to visualize and validate the analysis steps (taken from [75])

Parameter	Symbol	Value	Unit
Number of stator slots	Q_S	12	-
Number of pole pairs	p	5	-
Number of phases	m_ph	3	-
Phase current	I_S	15	A
Number of turns	N_t	36	-
Outer shaft radius	$r_\mathrm{sh,o}$	0.0356	m
Rotor yoke thickness	t_ry	0.0474	m
Magnet thickness	t_mag	0.006	m
Magnet pole width to pole pitch ratio	α_p	0.75	-
Sleeve thickness	t_sl	0.5	m
Airgap thickness	g_mech	0.0005	m
Thickness of tooth tip edge	$t_\mathrm{tt,e}$	0.002	m
Tooth tip edge to slot pitch ratio	$\beta_\mathrm{tt,e}$	0.9193	-
Thickness of tooth tip center	$t_\mathrm{tt,c}$	0.0005	m
Tooth tip center to slot pitch ratio	$\beta_\mathrm{tt,c}$	0.664	-
Slot depth	t_sd	0.0367	m
Stator tooth width to slot pitch ratio	$\beta_\mathrm{sy,i}$	0.4742	-
Stator yoke thickness	t_sy	0.0258	m
Stack length	L_stk	0.12	m

2.1.2 Electrical Analysis

The currents and voltages of a symmetrical three-phase AC system in the *uvw*-system (according to [76]) are transformed into a *dq* representation using a Park transformation [77]. This converts the three-phase system into a linear time-invariant system, enabling simplified analysis of electrical quantities. Figure 2.4 shows the current and voltage components along the direct and quadrature axes. The voltage leads the current by an angle φ_PF as the machine behaves as an inductive load.

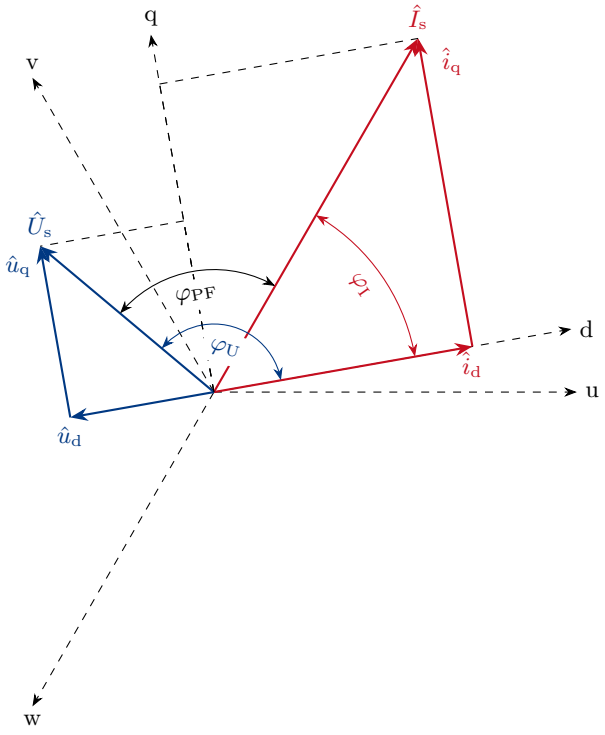

Figure 2.4: Voltages and currents in the *dq* reference frame

Using the peak stator convention, $\hat{i}_\mathrm{d}$ and $\hat{i}_\mathrm{q}$ are the peak currents on the direct and quadrature axes respectively. These components add up to the peak source current $\hat{I}_\mathrm{s}$, which is identical to the peak phase current $I_\mathrm{AC,Ph,pk}$ of the AC system for wye-connected phases:

$$I_\mathrm{s} = \sqrt{\frac{\hat{i}_\mathrm{d}^2 + \hat{i}_\mathrm{q}^2}{2}}. \tag{2.7}$$

A similar formulation applies to the voltage components. The angles between the current and voltage vectors and the d-axis define the electrical lead angle and thus the machine's power factor $\cos\varphi_\mathrm{PF}$:

$$\varphi_\mathrm{I} = \arctan2\left(\hat{i}_\mathrm{q}, \hat{i}_\mathrm{d}\right) \tag{2.8}$$

$$\varphi_\mathrm{U} = \arctan2\left(\hat{u}_\mathrm{q}, \hat{u}_\mathrm{d}\right) \tag{2.9}$$

$$\varphi_\mathrm{PF} = \varphi_\mathrm{U} - \varphi_\mathrm{I} \tag{2.10}$$

The instantaneous phase currents in the symmetrical three-phase system at a rotor position ωt are then given by:

$$i_\mathrm{u} = \hat{I}_\mathrm{s}\,\cos(\omega t + \varphi_\mathrm{I}) \tag{2.11}$$

$$i_\mathrm{v} = \hat{I}_\mathrm{s}\,\cos(\omega t + \varphi_\mathrm{I} - \frac{2\,\pi}{3}) \tag{2.12}$$

$$i_\mathrm{w} = \hat{I}_\mathrm{s}\,\cos(\omega t + \varphi_\mathrm{I} - \frac{4\,\pi}{3}) \tag{2.13}$$

2.1.3 Winding Configuration

The pole-slot combination (Q_S, p) of an m_ph-phase electric machine strongly influences the feasible winding layout and the achievable fundamental winding factor k_w1. A valid winding scheme and a high k_w1 cannot be guaranteed for every combination. Therefore, a general mathematical formulation of the winding layout is essential for fully automated machine design.
Several publications address key aspects of automated winding layout synthesis [78–81]. These works build on the fundamentals introduced by Sequenz [82, 83] and Richter [84], who employed the star-of-slots method to classify and construct winding layouts.
Figure 2.5 illustrates the workflow used to derive the winding layout. It reflects an implementation of the general formulation by Caruso et al. [78]. Based on the winding parameters defined in Table 2.1, the coil pitch, machine periodicity, and number of wound coils per phase are used to assess the general feasibility of the winding in Section 2.1.3.1. If a valid layout is found, the winding is mathematically defined in the winding distribution table, and the associated winding factors are computed.

2.1.3.1 General Feasibility

The throw or pitch y_p of a coil, defined as the number of slots spanned by a coil around the circumference, is typically chosen to cover a maximum of

$$y_\mathrm{p} = \left\lfloor \frac{Q_\mathrm{S}}{2\,p} \right\rfloor \geq 1. \tag{2.14}$$

A necessary condition for winding feasibility is that the number of slots is an integer multiple of the number of phases, i.e. $Q_\mathrm{S}/2p \in \mathbb{N}$. If this condition is met, the following parameters can be calculated: the machine periodicity t_wdg, the number of wound coils per

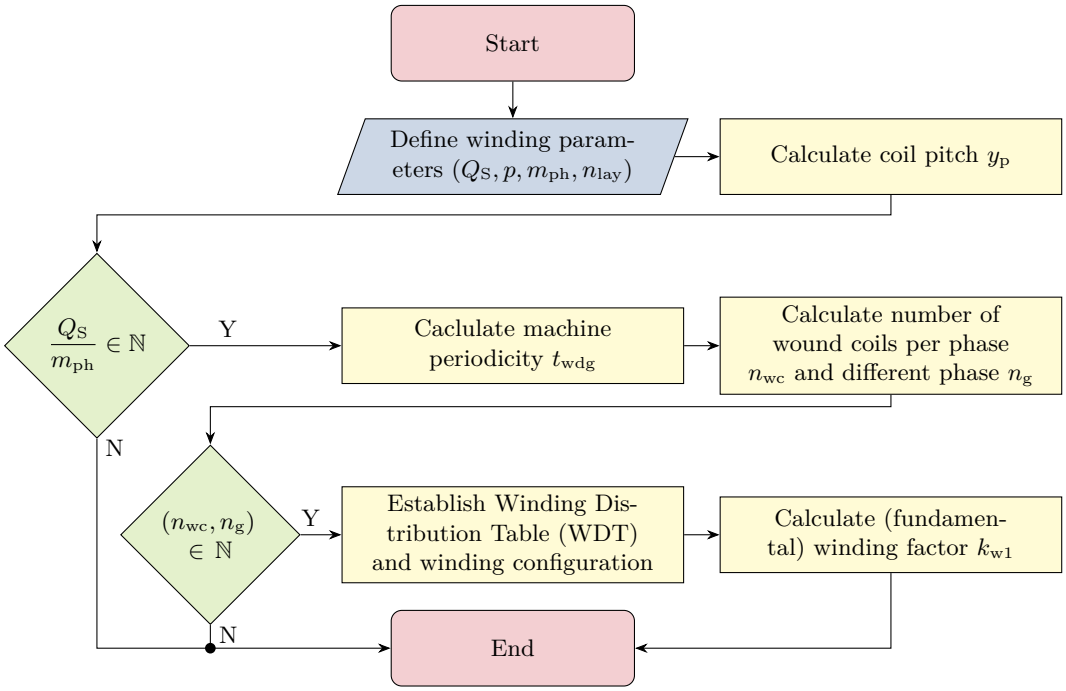

Figure 2.5: Description of workflow to compute the winding distribution table and (fundamental) winding factors for an arbitrary pole-slot combination

phase n_{wc}, and the number of wound coils assigned to different phases within one periodic segment n_g:

$$t_{wdg} = \gcd(Q_S, p) \tag{2.15}$$

$$n_{wc} = n_{wdg,lay} \frac{Q_S - n_{es}}{2\,m} \tag{2.16}$$

$$n_g = \begin{cases} n_{wdg,lay} \dfrac{Q_S}{2\,m_{ph}\,t_{wdg}} & \text{if } m_{ph} \text{ is even} \\ \dfrac{Q_S}{2\,m_{ph}\,t_{wdg}} & \text{if } m_{ph} \text{ is odd} \end{cases} \tag{2.17}$$

Here, $n_{wdg,lay}$ denotes the number of winding layers per slot, and n_{es} is the number of empty slots (also referred to as dead coils), given by

$$n_{es} = \left\lfloor Q_S - 2\,m_{ph} \frac{\lfloor N_c \rfloor}{n_{wdg,lay}} \right\rfloor . \tag{2.18}$$

A symmetrical and balanced winding layout is considered feasible only if both n_{wc} and n_g are positive integers and no dead coils. Other winding types are not considered within the scope of this thesis.

2.1.3.2 Winding Distribution Table

Once the feasibility conditions are met, a procedure to construct the full winding distribution table is applied. This begins by initializing an empty matrix of dimensions $(m_{ph}, {}^{Q_S}/_{m_{ph}})$. The integers from 1 to Q_S are then inserted in ascending order, such that the i-th number is placed in the cell at position $((1 + i\,p) \bmod Q_S)$ of the matrix.
If a targeted cell is already occupied, the next free adjacent cell is used. This procedure continues until all Q_S positions are filled.
Next, the matrix is split vertically into two equal submatrices. The right-hand submatrix is shifted upwards by ξ rows and its entries are assigned a minus sign to represent the

negative coil sides. The row shift ξ is given by

$$\xi = \begin{cases} \frac{m_{\mathrm{ph}}}{2} - 1 & \text{if } m_{\mathrm{ph}} \text{ is even} \\ \frac{m_{\mathrm{ph}} - 1}{2} & \text{if } m_{\mathrm{ph}} \text{ is odd.} \end{cases} \tag{2.19}$$

Finally, the missing "go" and "return" coil sides are appended by adding the coil pitch y_{p} with the appropriate sign, depending on the winding layer and direction. This completes the winding distribution table for a multi-layer winding.
Table 2.2 shows the described procedure applied to the example machine defined in Table 2.1. This example assumes no empty slots and uses a coil pitch of $y_{\mathrm{p}} = 1$.

Table 2.2: Exemplary procedure to derive the winding distribution table for a two-layer, three phase machine with $Q_{\mathrm{S}} = 12$ slots and $p = 5$ pole pairs. The rows represent phases u, v, and w, which are color-coded as blue, green, and red, respectively.

1	6	11	4		1	6	-7	-12		1	-2	6	-7	-7	8	-12	1
9	2	7	12	⇒	9	2	-3	-8	⇒	9	-10	2	-3	-3	4	-8	9
5	10	3	8		5	10	-11	-4		5	-6	10	-11	-11	12	-4	5

2.1.3.3 Winding Factor Calculation

The winding factors k_{w} and its fundamental k_{w1} are calculated using the per-unit electromotive force (EMF) phasors for each winding element [85], defined as

$$\vec{E}_i = e^{j \frac{\pi p}{Q_{\mathrm{S}}} \mathrm{WDT}(i)}. \tag{2.20}$$

Building on the general formulation by Caruso et al. [78] and applying Euler's formula, the expression for the winding factor of the ν-th harmonic simplifies for balanced and symmetrical windings to

$$\begin{aligned} k_{\mathrm{w},\nu} &= \frac{\left| \sum_{i=1}^{2\,p\,q\,n_{\mathrm{lay,wdg}}} \vec{E}_{i,\nu} \right|}{2\,p\,q\,n_{\mathrm{lay,wdg}}} \\ &= \frac{1}{2\,p\,q\,n_{\mathrm{lay,wdg}}} \sqrt{\left(\sum_i C_{\nu,i} \right)^2 + \left(\sum_i S_{\nu,i} \right)^2} \end{aligned} \tag{2.21}$$

where

$$C_{\nu,i} = \mathrm{sgn}(\mathrm{WDT}(i)) \cos\left(2\,\pi\,p\,\nu \frac{|\mathrm{WDT}(i)|}{Q_{\mathrm{S}}} \right) \tag{2.22}$$

$$S_{\nu,i} = \mathrm{sgn}(\mathrm{WDT}(i)) \sin\left(2\,\pi\,p\,\nu \frac{|\mathrm{WDT}(i)|}{Q_{\mathrm{S}}} \right) \tag{2.23}$$

are the in-phase and quadrature components of the EMF phasors, and

$$q = \frac{Q_{\mathrm{S}}}{2\,p\,m_{\mathrm{ph}}} \tag{2.24}$$

is the number of slots per pole per phase.
Figure 2.6 illustrates the amplitude of the winding factors for phase U of the example introduced in Table 2.1. Due to the symmetrical and balanced configuration, all phases exhibit identical winding factors. The resulting spectrum shows a significant presence of spatial harmonics, which is characteristic of fractional-slot windings.

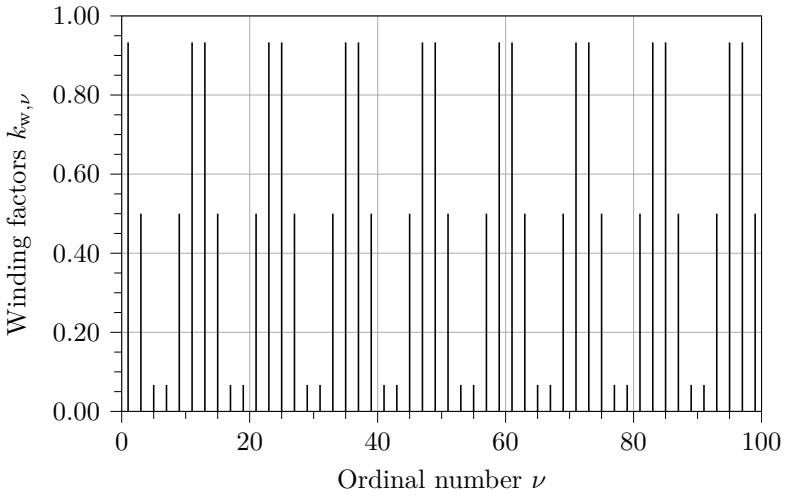

Figure 2.6: Spectral analysis of the winding factor for a three-phase, two-layer fractional-slot winding with $Q_S = 12$ and $p = 5$. A rich spatial harmonic content is observed.

The pitch factor $k_{p,\nu}$ is defined as

$$k_{p,\nu} = \frac{n\pi}{2} \sin\left(np\frac{\tau_c}{2}\right) \tag{2.25}$$

and the distribution factor $k_{d,\nu}$ is obtained from the relation

$$k_{w,\nu} = k_{d,\nu}\, k_{p,\nu}. \tag{2.26}$$

2.1.3.4 Magnetomotive Force Calculation

To evaluate the influence of armature reaction on machine performance, the magnetomotive force (MMF) generated by the winding system must be determined. The MMF of each phase is defined as

$$\mathrm{MMF}_{u/v/w} = \int_{\alpha=0}^{2\,\pi} \Theta_{u/v/w}\, d\alpha \tag{2.27}$$

with

$$\Theta_{u/v/w} = N_t\, i_{u/v/w} \tag{2.28}$$

representing the ampere-turns per slot for each phase. This formulation is aligned with the base winding function concept described by Farshadnia et al. [86], where $N_t\, i_{u/v/w} = 1$ is used to represent the per-unit MMF per phase.
The resulting distribution is shown in Figure 2.7a. By summing the contributions of all phases, the total magnetomotive force distribution is obtained, as illustrated in Figure 2.7b. This magnetomotive force waveform is then analyzed using a Discrete Fourier Transform (DFT) to assess its harmonic content, as shown in Figure 2.7c. For clarity, only harmonics contributing more than 1 % of the fundamental are included. This threshold also explains the visible slot-to-slot oscillations in the spectrum. The spectral analysis shows that, for the given slot-pole combination, the fundamental magnetomotive force component is relatively low. However, significant harmonics, particularly the 7^{th}, 17^{th}, and 19^{th}, are present. Such analysis is a critical step in the design process, enabling early-stage elimination of unsuitable winding configurations based on low fundamental winding factors or excessive harmonic content, without requiring full design completion.

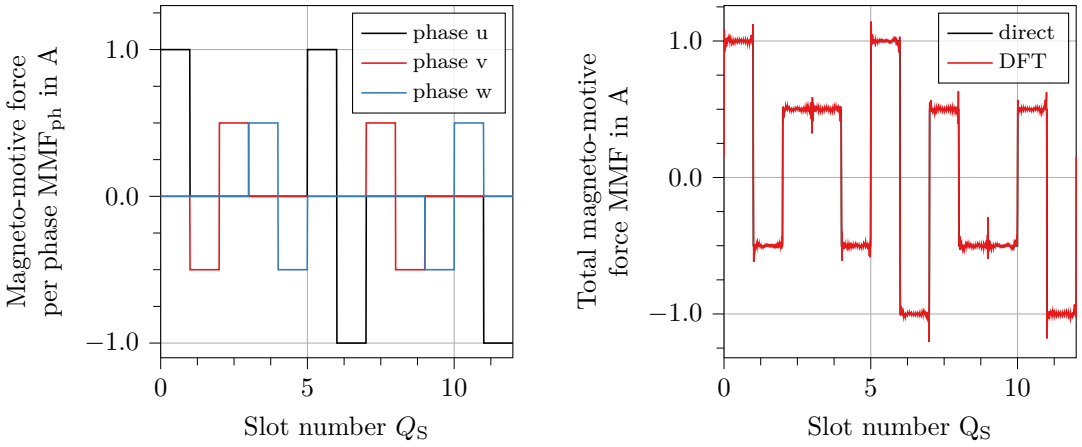

(**a**) Magnetomotive force per phase

(**b**) Total magnetomotive force

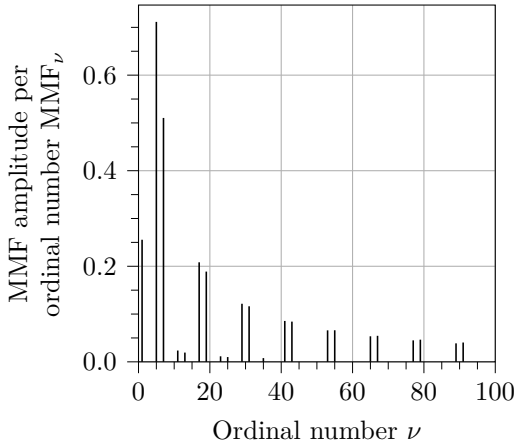

(**c**) Spectral analysis of the total magnetomotive force

Figure 2.7: Full winding analysis of the total magnetomotive force for a three-phase, two-layer fractional slot winding with $Q_S = 12$ and $p = 5$.

2.1.4 Subdomain-Based Electromagnetic Analysis of the Magnetic Field Distribution

Detailed knowledge of the magnetic field distribution within the airgap of an electric machine is essential for evaluating its electromagnetic performance. To enable efficient system-level performance evaluation, a subdomain model based on the work of Wu et al. [87, 88] is employed, as it is significantly less computationally intensive than Finite Element (FE) simulations and remains suitable for modelling the machine under both no-load and armature reaction conditions. The field prediction accuracy of this method surpasses that of a combined approach using a simpler subdomain model [89–93] together with a complex permeance function [94, 95], particularly for fractional slot windings and machines with deep or semi-closed slots.

Figure 2.8 shows the flowchart of the tasks carried out during the electromagnetic analysis in the following subsections. The parametrization of the machine from Table 2.1 is first used as input for the improved subdomain model, which directly calculates the magnetic field distribution throughout the machine, including slot openings and teeth effects. This approach provides the airgap and magnet flux densities both at open-circuit and under armature load conditions, without the need for complex permeance functions. The resulting magnetic vector potential is then used to derive the stator tooth and yoke flux densities, allowing the calculation of the associated iron losses. Furthermore, the no-load

airgap flux density enables the calculation of the back electromotive force, while the flux densities associated with the armature reaction allow the determination of the machine inductances.

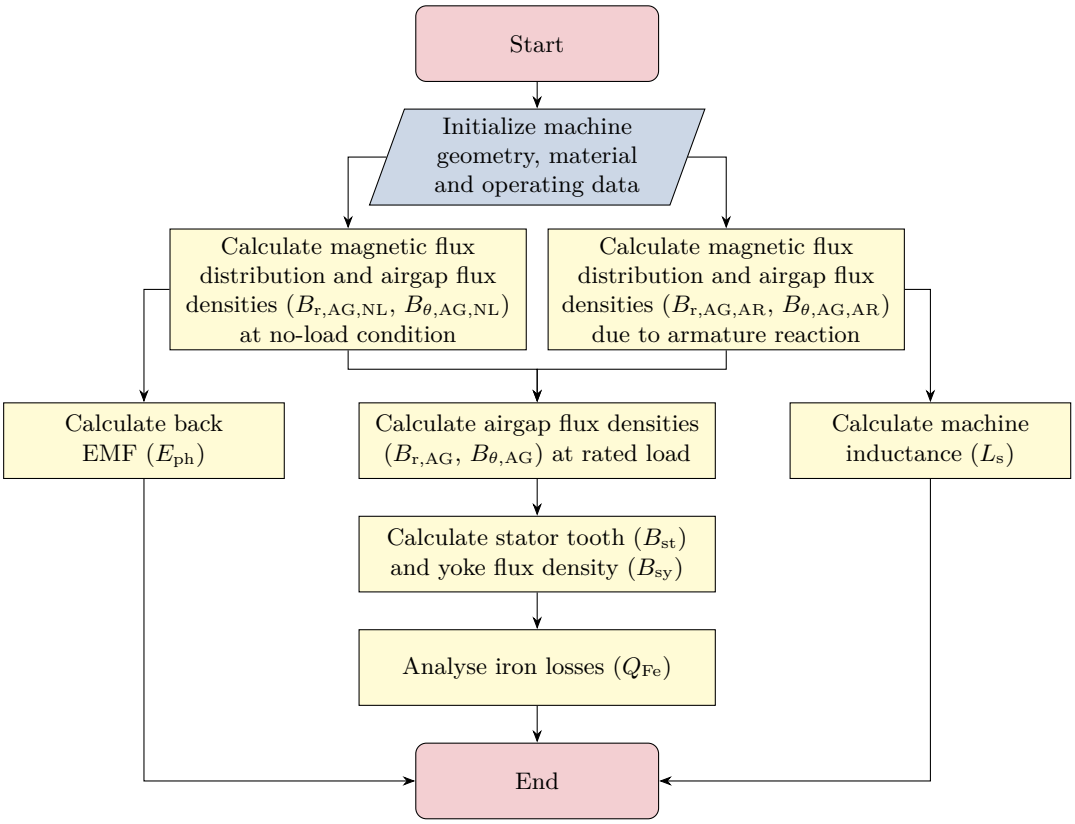

Figure 2.8: Description of workflow to analyse the electromagnetics of the machine

The subdomain method analytically solves Maxwell's equations in different regions of the electric machine geometry. Each subdomain, such as the rotor magnets, airgap, slots, slot openings, and stator teeth, is treated individually [87, 88].
To enable an analytical solution of the differential equations, the following assumptions are made:

- The demagnetization characteristic of the magnets is linear,
- end effects are neglected, resulting in a purely two-dimensional evaluation,
- the stator and rotor back iron are assumed to have infinite magnetic permeability.

The governing equation for the magnetic vector potential A_z in each subdomain is given by the Poisson equation, which accounts for both conduction currents and magnetization effects:

$$\nabla^2 A_z = -\mu_0 \left(J_z + \nabla \times \vec{M} \right) \tag{2.29}$$

where J_z is the conduction current density in the z-direction and $\vec{M}$ is the magnetization vector representing the permanent magnets. Depending on the region, one or both terms may vanish, simplifying the equation to either a Laplace or Poisson form. The solution is obtained by enforcing continuity of the tangential component of the magnetic field H_Θ and the normal component of the magnetic flux density B_r across the subdomain boundaries. The general solution can be expressed as the sum of the homogeneous and particular parts:

$$A_z(r,\theta) = A_h(r,\theta) + A_p(r,\theta) \tag{2.30}$$

where the homogeneous solution in polar coordinates is given by

$$A_{\mathrm{h}}(r,\theta) = \sum_{k=0}^{\infty} \left(A_k\, r^k + B_k\, r^{-k} \right) \cos(k\theta) + \sum_{k=0}^{\infty} \left(C_k\, r^k + D_k\, r^{-k} \right) \sin(k\theta) \tag{2.31}$$

with constants A_k, B_k, C_k, and D_k determined from the boundary conditions. The particular solution A_{p} depends on the specific source terms and satisfies the inhomogeneous Poisson equation within each subdomain.
The magnetic flux density components in the radial B_{r} and tangential direction B_θ are obtained from the magnetic vector potential A_{z} as

$$B_{\mathrm{r}}(r,\theta) = \frac{1}{r}\frac{\partial A_{\mathrm{z}}}{\partial \theta}, \tag{2.32}$$

$$B_\theta(r,\theta) = -\frac{\partial A_{\mathrm{z}}}{\partial r}. \tag{2.33}$$

The magnetic field strength components are then calculated as

$$H_{\mathrm{r}}(r,\theta) = \frac{1}{\mu_{\mathrm{r}}} \left(\frac{B_{\mathrm{r}}(r,\theta)}{\mu_0} - M_{\mathrm{r}}(r,\theta) \right), \tag{2.34}$$

$$H_\theta(r,\theta) = \frac{1}{\mu_{\mathrm{r}}} \left(\frac{B_\theta(r,\theta)}{\mu_0} - M_\theta(r,\theta) \right), \tag{2.35}$$

where μ_{r} is the relative permeability, and M_{r} and M_θ are the radial and tangential components of the magnetization vector.
The subdomain method is applied to both the open-circuit and armature reaction conditions to retrieve the field distribution for rated conditions via superposition.

2.1.4.1 Open-Circuit Condition

The open-circuit or no-load condition describes the operation of the electric machine without armature current, where magnetization is solely provided by the permanent magnets. Under these conditions, the magnetization terms are the exclusive sources in the Poisson equation and form the particular solution of the governing equation.
As shown in Figure 2.9, the domain is split into four regions: magnets, air-gap, slot openings, and slots. The rotor and stator iron are assumed infinitely permeable and are not modeled explicitly.

Particular Solution Due to Magnet Magnetization
While Equation (2.31) provides the general solution for the air-gap, slot openings, and slots, in the magnet region the vector potential must satisfy [96]

$$\frac{\partial^2 A_{\mathrm{z1}}}{\partial r^2} + \frac{1}{r}\frac{\partial A_{\mathrm{z1}}}{\partial r} + \frac{1}{r^2}\frac{\partial A_{\mathrm{z1}}}{\partial \theta^2} = \frac{\mu_0}{r}\left(M_\theta - \frac{\partial M_{\mathrm{r}}}{\partial \theta} \right). \tag{2.36}$$

The radial and circumferential components of the magnetization can be expressed as [97]:

$$M_{\mathrm{r}} = \sum_{k=1,3,5,\ldots}^{\infty} M_{\mathrm{rck}}\, \cos(k\,\theta) + M_{\mathrm{rsk}}\, \sin(k\,\theta) \tag{2.37}$$

$$M_\theta = \sum_{k=1,3,5,\ldots}^{\infty} M_{\theta\mathrm{ck}}\, \cos(k\,\theta) + M_{\theta\mathrm{sk}}\, \sin(k\,\theta) \tag{2.38}$$

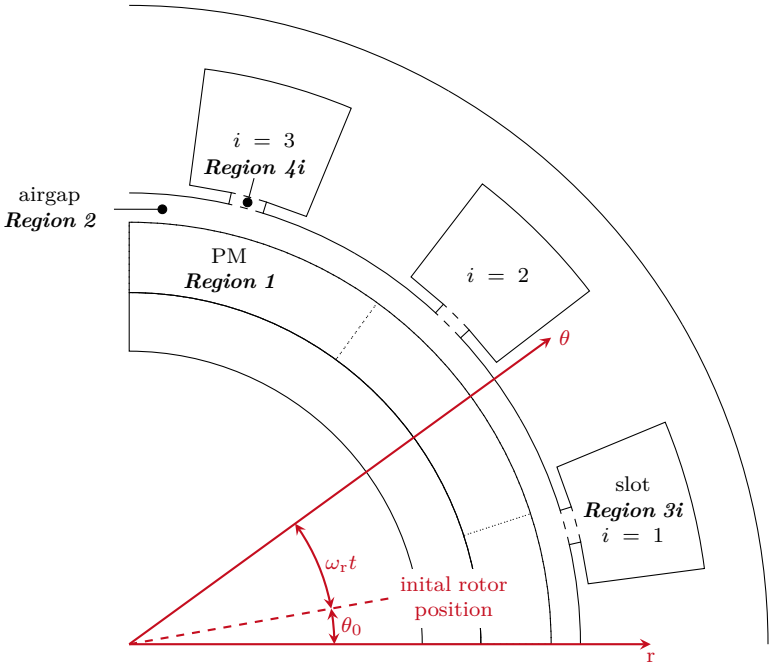

Figure 2.9: Subdomain regions for open-circuit (no-load) condition. Adapted from [87].

$$M_{\mathrm{rck}} = M_{\mathrm{rk}} \cos(k\omega_r t + k\theta_0) \tag{2.39}$$
$$M_{\mathrm{rsk}} = M_{\mathrm{rk}} \sin(k\omega_r t + k\theta_0) \tag{2.40}$$
$$M_{\theta\mathrm{ck}} = -M_{\theta\mathrm{k}} \sin(k\omega_r t + k\theta_0) \tag{2.41}$$
$$M_{\theta\mathrm{sk}} = M_{\theta\mathrm{k}} \cos(k\omega_r t + k\theta_0) \tag{2.42}$$

In the case of radial magnetization, the magnetization vectors are defined as [87]

$$M_{\mathrm{rk}} = \frac{4\,p\,B_{\mathrm{r}}}{k\,\pi\,\mu_0} \sin\left(\frac{k\,\pi\,\alpha_{\mathrm{p}}}{2p}\right) \tag{2.43}$$
$$M_{\theta\mathrm{k}} = 0 \tag{2.44}$$

where B_{r} is the remanent induction, and α_{p} is the pole coverage of the magnet. Magnetization vectors for more complex arrangements can be found in [87] for parallel magnetization and in [98, 99] for Halbach arrangements, including generalized configurations.
Finally, the particular solution for the magnet domain is found as [87]

$$A_{\mathrm{p}} = \mu_0\, r \sum_{k}^{\infty} \frac{1}{k^2 - 1} \left[(M_{\theta\mathrm{ck}} - k\,M_{\mathrm{rsk}}) \cos(k\,\theta) + (M_{\theta\mathrm{sk}} - k\,M_{\mathrm{rck}}) \sin(k\,\theta)\right]. \tag{2.45}$$

Interface and Boundary Conditions

To determine the coefficients of the homogeneous solution, boundary and interface conditions are applied, as summarized in Table 2.3. These conditions can be grouped into two categories: boundary conditions that ensure the magnetic flux enters or leaves ferromagnetic materials normally, and interface conditions that enforce the continuity of tangential magnetic field components and the magnetic vector potential. Specifically, at the magnet-airgap interface, the normal component of the magnetic flux density and the tangential component of the magnetic field intensity must be continuous to satisfy electromagnetic boundary conditions in the presence of magnetization. At other interfaces, such as airgap-slot opening and slot regions, the continuity of the tangential component of the magnetic flux density and of the magnetic vector potential is imposed to ensure a physically consistent solution across regions of different permeabilities without intrinsic

magnetization.

Table 2.3: Boundary and interface conditions for open-circuit condition

Interface	Conditions
Rotor yoke surface	$H_{1\theta}(r = r_{\mathrm{m,i}}) = \frac{1}{\mu_0\,\mu_\mathrm{r}} B_{1\theta}(r = r_{\mathrm{m,i}}) - \frac{1}{\mu_0\,\mu_\mathrm{r}} M_\theta = 0$
Magnet - airgap	$B_{1\mathrm{r}}(r = r_{\mathrm{m,o}}) = B_{2r}(r = r_{\mathrm{m,o}})$ $H_{1\theta}(r = r_{\mathrm{m,o}}) = H_{2\theta}(r = r_{\mathrm{m,o}})$
Airgap - slot opening	$B_{2\theta}(r = r_{\mathrm{st,i}}) = \begin{cases} B_{4i\theta}(r = r_{\mathrm{st,i}}) & \theta_i - \frac{b_{\mathrm{oa}}}{2} \leq \theta \leq \theta_i + \frac{b_{\mathrm{oa}}}{2} \\ 0 & else \end{cases}$ $A_{\mathrm{z}2}(r = r_{\mathrm{st,i}}) = \begin{cases} A_{\mathrm{z}3i}(r = r_{\mathrm{st,i}}) & \theta_i - \frac{b_{\mathrm{oa}}}{2} \leq \theta \leq \theta_i + \frac{b_{\mathrm{oa}}}{2} \\ 0 & else \end{cases}$
Slot opening - slot	$B_{4i\theta}(r = r_{\mathrm{tt,c}}) = \begin{cases} B_{3i\theta}(r = r_{\mathrm{tt,c}}) & \theta_i - \frac{b_{\mathrm{oa}}}{2} \leq \theta \leq \theta_i + \frac{b_{\mathrm{oa}}}{2} \\ 0 & else \end{cases}$ $A_{\mathrm{z}4i}(r = r_{\mathrm{tt,c}}) = \begin{cases} A_{\mathrm{z}3i}(r = r_{\mathrm{st,i}}) & \theta_i - \frac{b_{\mathrm{oa}}}{2} \leq \theta \leq \theta_i + \frac{b_{\mathrm{oa}}}{2} \\ 0 & else \end{cases}$
Slot bottom	$B_{4i\theta}(r = r_{\mathrm{sy,i}}) = 0 \quad \text{for} \quad \left(\theta_i - \frac{b_{\mathrm{sa}}}{2} \leq \theta \leq \theta_i + \frac{b_{\mathrm{sa}}}{2}\right)$

With these boundary and interface conditions, a linear system of equations can be established and solved for the integration constants of the general solution. The resulting expressions can then be used, for example, to calculate the magnetic flux densities in the airgap. The detailed calculation steps are provided in [87].

Back Electromotive Force

The rotation of the magnets induces a voltage called the back electromotive force (EMF), which, according to Lenz's law, opposes the applied voltage and reduces the current flowing in the coils [100]. The sinusoidal distribution of the windings in the stator produces a sinusoidal back electromotive force. Together with the inherently sinusoidal nature of three-phase AC currents, this results in a nearly constant torque with very low torque ripple, as well as high efficiency and low noise. The back electromotive force per phase e_{ph} can be calculated based on Faraday's law [101]. Using the relationship between electrical angle and time, the back EMF can be expressed as [102]

$$e_{\mathrm{ph}}(t) = -\omega_{\mathrm{el}} \frac{d\Psi_{\mathrm{ph}}(\theta)}{d\theta} \tag{2.46}$$

where Ψ_{ph} is the flux linkage per phase and ω_{el} is the electrical angular speed. As the magnetic vector potential within the slots is known, the flux linkage of a single coil side Ψ_{i} located in the i-th slot can be calculated by applying Stokes' integral theorem [102]

$$\Psi_{\mathrm{i}} = \frac{L_{\mathrm{stk}}\, N_{\mathrm{t}}}{A_{\mathrm{slot}}} \int_{\theta_i - \frac{b_{\mathrm{sa}}}{2}}^{\theta_i + \frac{b_{\mathrm{sa}}}{2}} \int_{r_{\mathrm{tt,c}}}^{r_{\mathrm{sy,i}}} A_{\mathrm{z3i}}(r, \theta)\, r\, dr\, d\theta \tag{2.47}$$

with L_{stk} being the stack length, N_{t} the number of turns per coil, and A_{slot} the slot area. The total flux linkage per phase can then be retrieved by the summation of all flux linkages of a certain phase

$$\Psi_{\mathrm{ph}} = \sum_{i \in \mathrm{ph}} S_{\mathrm{w}}(i) \Psi_{\mathrm{i}}, \tag{2.48}$$

where $S_{\mathrm{w}}(i)$ represents the winding distribution matrix and Ψ_{i} is the flux linkage for the i-th coil side.

2.1.4.2 Armature Reaction

For armature reaction, the only active source term in the Poisson equation is the current density within the slots. This allows for a simplified magnetic field domain compared to the open-circuit case. As shown in Figure 2.10, the domain is now divided into three regions: the airgap including magnets, the slot openings, and the slots.

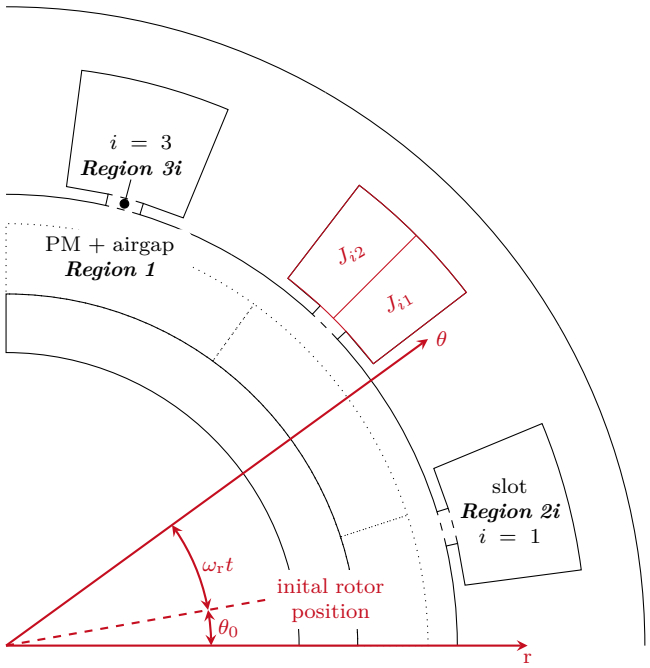

Figure 2.10: Subdomain regions for armature reaction condition. Adapted from [88].

Particular Solution Due to Armature Current Density

While Equation (2.31) is again a valid general solution for the air-gap including the magnets as well as the slot openings, the vector potential in the slot must satisfy [88]

$$\frac{\partial^2 A_{z2}}{\partial r^2} + \frac{1}{r}\frac{\partial A_{z2}}{\partial r} + \frac{1}{r^2}\frac{\partial A_{z2}}{\partial \theta^2} = -\mu_0 J_z \tag{2.49}$$

with J_z being the current density distribution within the slot. Assuming a uniform distribution of the current density within the coils, the current density in the i-th slot for a non-overlapping winding as shown in Figure 2.10 is stated as [88]

$$J = J_{i0} + \sum_n J_{in}\left[\frac{n\,\pi}{b_{sa}}\left(\theta + \frac{b_{sa}}{2} - \theta_i\right)\right] \tag{2.50}$$

for $\theta_i - \frac{b_{sa}}{2} \leq \theta \leq \theta_i + \frac{b_{sa}}{2}$, where

$$J_{i0} = \frac{J_{i1} + J_{i2}}{2} \tag{2.51}$$

$$J_{in} = \frac{2}{n\,\pi}\left(J_{i1} - J_{i2}\right)\sin\left(\frac{n\,\pi}{2}\right) \tag{2.52}$$

with n being the n-th harmonic in the slot.
Thus, the particular solution of the magnetic vector potential within the slot can be written as [88]

$$A_p = -\frac{\mu_0}{4} J_{i0} r^2 + \sum_n \frac{\mu_0 J_{in}}{E_n^2 - 4} r^2 \cos\left(E_n \theta\right) \tag{2.53}$$

with E_n being defined as

$$E_n = \frac{n\,\pi}{b_{\mathrm{sa}}}. \tag{2.54}$$

The interface and boundary conditions are similar to those provided for the open-circuit condition in Table 2.3, except for the naming of the subdomains. Once applied, the integration constants can be retrieved, and all other parameters, such as vector potentials or flux densities, can be explicitly calculated.

Energy Stored in Winding Coils

The magnetic energy W stored in the winding due to the armature-reaction and without magnet magnetization is defined as [103]

$$W = \frac{1}{2} L_{\mathrm{stk}} \sum_{i}^{Q} \int_{\theta_i - \frac{b_{\mathrm{sa}}}{2}}^{\theta_i + \frac{b_{\mathrm{sa}}}{2}} \int_{r_{\mathrm{tt,c}}}^{r_{\mathrm{sy,i}}} A_{\mathrm{z2i}}\, J_{\mathrm{z}}\, r\, dr\, d\theta, \tag{2.55}$$

where the integrand $A_{\mathrm{z2i}}\, J_{\mathrm{z}}\, r$ quantifies the local energy density within each stator slot, as a function of the applied current. This expression can be used to determine the winding inductances, as discussed in Section 2.1.4.5.

2.1.4.3 Rated Load Conditions

At rated load conditions, characteristics such as the total magnetic vector potential or the flux densities within the different domains of the machine can be calculated by superposition of the previously determined no-load and armature current conditions. This approach allows, for example, the direct computation of the radial and tangential flux density components within the airgap based on the individual contributions from the permanent magnets and the current-carrying windings.

$$B_{\mathrm{r,AG}} = B_{\mathrm{2r,NL}} + B_{\mathrm{1r,AR}} \tag{2.56}$$

$$B_{\theta,\mathrm{AG}} = B_{2\theta,\mathrm{NL}} + B_{1\theta,\mathrm{AR}} \tag{2.57}$$

Figure 2.11 shows the airgap flux densities at rated load for both the radial and tangential component evaluated at the mean airgap radius. While the radial component is mainly driven by the flux caused by the permanent magnets the tangential component is dominated by the contribution of the current-carrying windings. To validate the model the results from the analytical calculation are compared with finite element results.

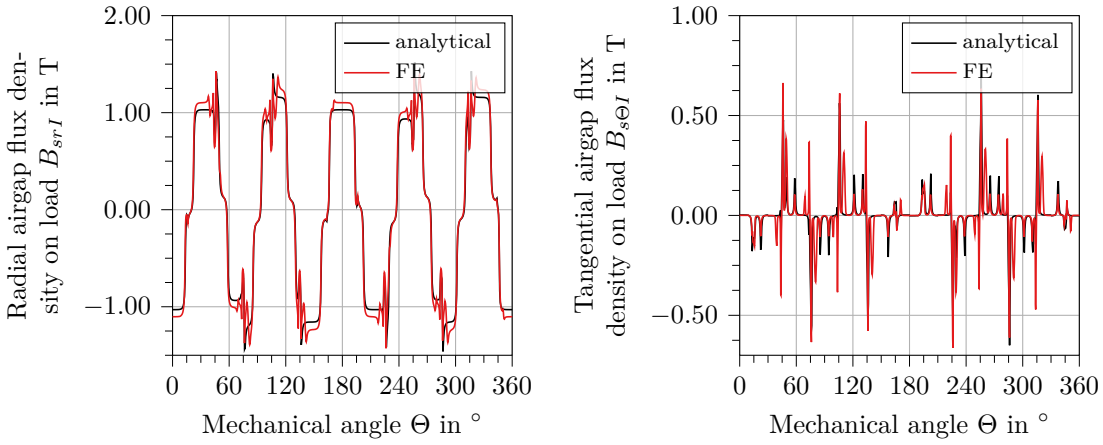

(**a**) Radial direction

(**b**) Tangential direction

Figure 2.11: Airgap flux density at rated load conditions in a three-phase electric machine with $Q_{\mathrm{S}} = 12$ and $p = 5$ taking into account slotting effects.

The radial and tangential airgap flux densities in Figures 2.11a and 2.11b show very good agreement in overall shape and peak positions. However, some peak values deviate by up to 20 %. These differences can be attributed to the analytical method's assumptions made in Section 2.1.4, mainly due to neglecting saturation.

Electromagnetic torque
Rated load conditions are also used to retrieve the electromagnetic torque T of the machine by using the Maxwell stress tensor

$$T = \frac{L_{\mathrm{stk}} R^2}{\mu_0} \int_0^{2\pi} B_{2\mathrm{r}}\, B_{2\theta}\, d\theta \tag{2.58}$$

where R is the mean airgap radius.

2.1.4.4 Flux and Flux Densities in Rotor and Stator Back Iron and Teeth

While the magnet and airgap region are of highest interest to determine the magnetic field distribution for torque production the flux densities of rotor back iron, stator teeth and stator back iron are necessary to avoid magnetic saturation during the machine design. Due to the low permeability of the permanent magnets and thus a relatively large effective airgap of surface mounted permanent magnet synchronous machines, the rotor core flux is mainly driven by the flux produced by the magnets. To caculate the flux density in the rotor core B_{ry}, it is assumed that the flux through the rotor yoke surface under one magnet pole splits equally and mainly flows tangentially to the adjacent pole. This can be calculated using Stokes' theorem and using the difference of the magnetic vector potential at two points [104–106]

$$B_{\mathrm{ry}} = \frac{A_{\mathrm{z1}}(r = r_{\mathrm{m,i}}, \theta = \frac{\theta_{\mathrm{m}}}{2}) - A_{\mathrm{z1}}(r = r_{\mathrm{m,i}}, \theta = 0)}{k_{\mathrm{sf}}\, t_{\mathrm{ry}}}, \tag{2.59}$$

where k_{sf} is the staple factor of the iron sheets. In case of the stator the armature reaction contributes significantly to the flux $\Phi_{\mathrm{st,i}}$ entering the i-th teeth. Therefore, the rated-load conditions from Equation (2.57) are used. Again Stokes' theorem is used to calculate the stator flux density at the mean tooth radius by evaluating the vector potential at the tooth sides

$$B_{\mathrm{st,i}} = \frac{A_{\mathrm{z3i}}(r = \frac{r_{\mathrm{tt,c}} + r_{\mathrm{sy,i}}}{2}, \theta = \theta_{i+1} - \frac{b_{\mathrm{sa}}}{2}) - A_{\mathrm{z3i}}(r = \frac{r_{\mathrm{tt,c}} + r_{\mathrm{sy,i}}}{2}, \theta = \theta_i + \frac{b_{\mathrm{sa}}}{2})}{k_{\mathrm{sf}}\, w_{\mathrm{st}}}, \tag{2.60}$$

For the stator yoke, the vector potential at the slot bottom and outside the stator yoke is used, assuming all the flux goes through the stator yoke

$$B_{\mathrm{sy,i}} = \frac{A_{\mathrm{z3i}}(r = r_{\mathrm{sy,i}}, \theta = \theta_i) - 0)}{k_{\mathrm{sf}}\, w_{\mathrm{sy}}}, \tag{2.61}$$

Figure 2.12 shows the flux density in the stator teeth comparing the analytical results with those obtained via Finite Element analysis.
The flux densities in the stator teeth in Figure 2.12 show that the averaged stator tooth flux densities closely match the Finite Element results, indicating that in this example the iron parts do not saturate.

2.1.4.5 Machine Inductances

The main flux Φ_{m} across the airgap creating a flux-linkage Ψ_{m} allows the conversion of electrical into mechanical energy. However, a second portion which does not cross the

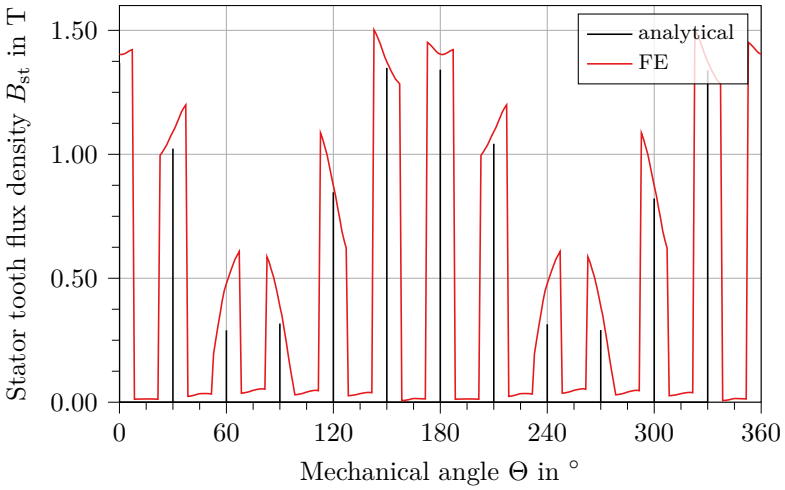

Figure 2.12: Comparison of analytical and FE results for the stator tooth flux density of an electric three-phase machine with $Q_S = 12$ and $p = 5$.

airgap called the leakage flux Φ_σ does not contribute to this energy conversion, but its flux-linkage Ψ_σ is part of the total flux-linkage of the winding. Due to the flux leakage either more magnetic material or a higher magnetizing current is necessary compared to the ideal case. The synchronous inductance L_s is thus the sum of the magnetizing inductance L_m and the leakage inductance L_σ which correspond to the flux-linkages [104, 107, 108].

$$L_s = L_m + L_\sigma \tag{2.62}$$

Magnetizing Inductance

The magnetizing inductance of a phase L_m from the winding can be split into the self-inductance L_{ms} and the mutual inductances L_{mm} due to the flux from the other phases

$$L_m = L_{ms} + L_{mm}. \tag{2.63}$$

The calculation follows an energy-based approach [103] using Equation (2.55)

$$L_{ms} = \frac{2W_u}{I_u^2} \tag{2.64}$$

$$L_{mm} = \frac{W_{uv} - W_u - W_v}{I_u\, I_v}, \tag{2.65}$$

where W_u, W_v and W_{uv} are the magnetic energies due to the armature reaction, when the phase currents I_u only, I_v only, and both I_u and I_v are applied.

Leakage Inductance

Leakage inductance can become significant in fractional-slot concentrated windings [108] and can be written as

$$L_\sigma = L_{slot} + L_{tt} + L_{ew} + L_\delta \tag{2.66}$$

with L_{slot} being the slot, L_{tt} the tooth tip, L_{ew} the end winding and L_δ the air gap leakage inductance. In the following, all parts except the slot leakage will be neglected. The slot leakage permeances Λ_1, Λ_2 and Λ_{12} represent the influence of the slot dimensions. For semiclosed, trapezoidal slots as shown in Figure 2.2 the direct solution of the Poisson's equation for a double layer winding delivers [109]

$$\Lambda_1 = \mu_0\, L_{stk} \left(\sum_{k=1}^{N} \left(\frac{\Delta s_k}{w_{m,k}} \left(S_1\, K_1(\alpha_k) \; + \bar{S}_1\, K_0(\alpha_k) \right) \right) + \frac{\Delta h_{sg}}{w_a} \right) \tag{2.67}$$

$$\Lambda_2 = \mu_0 L_{\mathrm{stk}} \left(\sum_{k=1}^{N} \left(\frac{\Delta s_{\mathrm{k}}}{w_{\mathrm{m,k}}} \bar{S_1} \left(S_2 K_1(\alpha_{\mathrm{k}}) + \bar{S_2} K_0(\alpha_{\mathrm{k}}) \right) \right) + \frac{\Delta h_{\mathrm{sg}}}{w_{\mathrm{a}}} \right) \tag{2.68}$$

$$\Lambda_{12} = \mu_0 L_{\mathrm{stk}} \left(\sum_{k=1}^{N} \left(\frac{\Delta s_{\mathrm{k}}}{w_{\mathrm{m,k}}} \bar{S_1} \left(S_2 K_{\mathrm{M}}(\alpha_{\mathrm{k}}) + \bar{S_2} K_0(\alpha_{\mathrm{k}}) \right) \right) + \frac{\Delta h_{\mathrm{sg}}}{w_{\mathrm{a}}} \right) \tag{2.69}$$

where the boolean functions S_1 and S_2 describe the position of a discretized trapezoidal layer with respect to the other layers, $w_{\mathrm{m,k}}$ the mean width, α_{k} the inclination, Δh_{k} the radial height and Δs_{k} the edge length of those layers. The parameters K_0, K_1 and K_M describe the inclination coefficients for non-parallel slot walls

$$K_0(\alpha) = \frac{1}{2\alpha} \log\left(\frac{1+\alpha}{1-\alpha}\right) \tag{2.70}$$

$$K_1(\alpha) = \frac{1}{16\alpha^2} \left(\frac{(\alpha-1)^4}{2\alpha} \log\left(\frac{1+\alpha}{1-\alpha}\right) - \alpha^2 + 4\alpha - 1 \right) \tag{2.71}$$

$$K_M(\alpha) = \frac{1}{4\alpha} \left(1 - \frac{(\alpha-1)^2}{2\alpha} \ln\left(\frac{1+\alpha}{1-\alpha}\right) \right) \tag{2.72}$$

and the geometrical permeance factor $\Delta h_{\mathrm{sg}}/w_{\mathrm{a}}$ as

$$\frac{\Delta h_{\mathrm{sg}}}{w_{\mathrm{a}}} = \frac{\xi_{\mathrm{a}}}{2} - \frac{2\xi_{\mathrm{a}} \arctan(\xi_{\mathrm{a}}) - \ln(\xi_{\mathrm{a}}^2 + 1) + 2\ln 2}{2\pi} \tag{2.73}$$

with

$$\xi_{\mathrm{a}} = \frac{2 g_{\mathrm{mag}}}{w_{\mathrm{sy,i}}}. \tag{2.74}$$

The self and mutual slot leakage inductance is then

$$L_{\sigma 1} = \left(\frac{N_{\mathrm{t1}}}{n_{\mathrm{par}}} \right)^2 \Lambda_1 \tag{2.75}$$

$$L_{\sigma 2} = \left(\frac{N_{\mathrm{t2}}}{n_{\mathrm{par}}} \right)^2 \Lambda_2 \tag{2.76}$$

$$L_{\sigma 12} = \left(\frac{N_{\mathrm{t1}}}{n_{\mathrm{par}}} \right) \left(\frac{N_{\mathrm{t2}}}{n_{\mathrm{par}}} \right) \Lambda_1 \tag{2.77}$$

and results in the phase leakage inductance [107]

$$L_{\sigma \mathrm{ph}} = 2p \left(q \left(L_{\sigma 1} + L_{\sigma 2} + 2L_{\sigma 12} \right) - \left| \frac{Q_{\mathrm{S}}}{2p} - y_{\mathrm{p}} \right| L_{\sigma 12} \right) \tag{2.78}$$

which allows the calculation of the machine inductances.

2.1.4.6 Losses and Efficiency

The available shaft torque is reduced due to various loss mechanisms, which can be categorized into three main groups [104]:

- Resistive losses in the stator winding, Q_{Cu} (commonly known as copper losses),
- Iron losses in the rotor yoke, stator teeth and yoke Q_{Fe}, as well as losses in the magnets
- Mechanical losses, such as bearing losses and windage losses .

This analysis focuses on the resistive and iron losses. Bearing losses are not considered as their share is small and calculation needs knowledge about the applied bearing forces [104]. Windage losses are generally small, and calculation requires knowledge of surface finishes not available at the pre-design stage [110]. While magnet losses influence rotor heating, their calculation is quite complex, and they can be limited by axial and circumferential segmentation [111].
The total losses can therefore be expressed as

$$Q_{\mathrm{EM}} = Q_{\mathrm{Cu}} + Q_{\mathrm{Fe}}. \tag{2.79}$$

This results in the efficiency of the machine being calculated as

$$\eta_{\mathrm{EM}} = 1 - \frac{|Q_{\mathrm{EM}}|}{|P_{\mathrm{in}}|}. \tag{2.80}$$

Resistive Losses

In high power density machines, resistive losses can represent a significant portion of the total losses. These Ohmic and additional AC losses in the winding are given by

$$Q_{\mathrm{Cu}} = m_{\mathrm{ph}}\, R_{\mathrm{AC}}\, \hat{I}_{\mathrm{s}}^2 \tag{2.81}$$

where R_{AC} is the overall resistance of the winding, including AC effects such as proximity and skin losses. It is defined as

$$R_{\mathrm{AC}} = k_{\mathrm{AC}}\, \frac{2\, N_{\mathrm{ts}}}{n_{\mathrm{par}}}\, L_{\mathrm{stk}}\, \frac{\rho_{\mathrm{el}}}{\frac{k_{\mathrm{slot}}\, A_{\mathrm{slot}}}{N_{\mathrm{t}}}}. \tag{2.82}$$

Here, k_{AC} is the loss increase factor due to AC effects, and ρ_{el} is the electrical resistivity of the conductor material.

Iron Losses

Iron losses in the rotor and stator cores can significantly impact the machine's efficiency, especially at higher operating frequencies. These losses can be divided into hysteresis, eddy current, and excess losses. For low computational effort with reasonable accuracy, a modified Steinmetz model as proposed by Ionel et al. [112], which is also available in Motor-CAD, is used. The specific iron losses, p_{Fe}, are expressed as

$$p_{\mathrm{Fe}} = p_{\mathrm{hyst}} + p_{\mathrm{eddy}} \tag{2.83}$$

$$= K_{\mathrm{hyst}}\, f_{\mathrm{el}}\, \hat{B}^{\alpha+\beta\,\hat{B}} + 2\pi^2\, K_{\mathrm{eddy}}\, f_{\mathrm{el}}^2\, \hat{B}^2. \tag{2.84}$$

Here, K_{hyst} and K_{eddy} are material-dependent coefficients representing hysteresis and eddy current losses, respectively. They capture the influence of the magnetic material's properties on the loss behavior as a function of frequency f_{el} and peak flux density $\hat{B}$. The total iron losses are then calculated by

$$Q_{\mathrm{Fe}} = p_{\mathrm{Fe}}\, m_{\mathrm{Fe}}, \tag{2.85}$$

where m_{Fe} is the mass of the iron core.

2.1.5 Structural Analysis of Rotor Containment

Electric machines are subject to different types of loads that influence their mechanical stability and behaviour, such as

- static loads, i.e., loads resulting from gravitational forces or static pressures,
- centrifugal loads, i.e., loads resulting from rotation around a defined axis, and
- thermal loads, i.e., loads resulting from temperature differences in various parts of the machine.

A component of particular interest during the design of an electric machine is the magnet retention sleeve, as it directly impacts the necessary airgap and thus the electromagnetic performance. Therefore, the sleeve will be modelled together with the magnets, yoke, and shaft as a multi-layer system of thick-walled cylinders with a radial interference fit.
The calculation of such a multi-layer system and its practical application have been described by several researchers [113–116]. Particularly, the work of Chen et al. [116] is of great interest, as it also covers segmented magnets with non-magnetic pole fillers and their effect on the stress distribution.
Figure 2.13 shows a sketch of an n-layered interference fit of thick-walled cylinders.

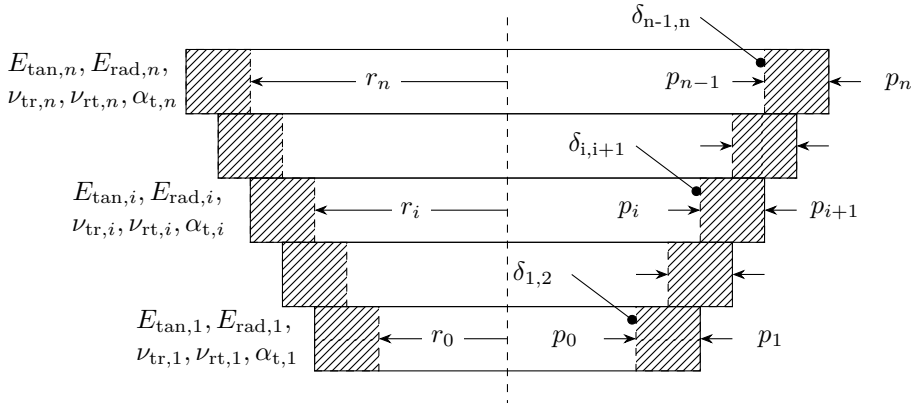

Figure 2.13: Sketch of an n-layered interference fit of thick-walled cylinders, showing the material and geometrical properties on the left side, and interferences and pressures between the layers on the right.

The interference vector $\underline{\delta} = [\delta_1, \ldots, \delta_{n-1}]$ results from the displacement of the concentric cylinders due to the applied loads, i.e., static pressure, centrifugal force, and thermal expansion. To calculate the contact pressures $\underline{p}$ at the interference sections, the following system must be solved:

$$\underline{\delta} = \underline{\delta}_{\text{stat}} + \underline{\delta}_{\text{rot}} + \underline{\delta}_{\text{Q}} = \mathbf{A} \cdot \underline{p} + \underline{G} \cdot \omega^2 + \underline{Q}, \tag{2.86}$$

where

- $\mathbf{A}$ is the stiffness matrix against static pressure,
- $\underline{G}$ is the stiffness vector against centrifugal force,
- $\underline{Q}$ is the stiffness vector against thermal loads,
- ω is the angular velocity of the shrink-fit system, and
- $\underline{p}$ contains the internal, external, and contact pressures between layers.

To calculate the contact pressures, the displacement terms at the contact surfaces must be determined for the i-th cylinder, which has an inner radius r_{in}, an outer radius r_{out}, an inner pressure p_{in}, and an outer pressure p_{out}, under the influence of an angular velocity ω and a temperature difference $\Delta T = T_i - T_{\text{ref}}$, where $T_{\text{ref}} = 20\,^{\circ}\text{C}$. The interference δ_i

at the i-th contact surface must equal the radial displacement $u_{i+1,\,r=r_{\text{in}}}$ of the $(i+1)$-th section at its inner surface minus the radial displacement $u_{i,\,r=r_{\text{out}}}$ of the i-th section at its outer surface:

$$\delta_i = u_{i+1,\,r=r_{\text{in}}} - u_{i,\,r=r_{\text{out}}}. \tag{2.87}$$

The principle of superposition allows the total displacement of the i-th cylinder to be expressed as the sum of the displacements due to static pressure, centrifugal forces, and thermal loads:

$$u_i = u_{\text{stat}} + u_{\text{rot}} + u_{\text{Q}}. \tag{2.88}$$

Thus, the specific displacement terms must be derived individually. This is achieved by solving the governing differential equations for both closed hollow cylinders representing the shaft, yoke, and sleeve, and hollow cylinder segments representing the magnets.
This information is sufficient to calculate the matrices and vectors in Equation (2.86) and thus determine the contact pressures for a given vector of interferences at the contact surfaces.

2.1.5.1 Thick-Walled Cylinder Disks with Orthotropic Material Properties

As very high-strength carbon fiber reinforced plastics are of great interest for retention sleeve manufacturing, the solution must account for orthotropic material parameters while remaining consistent with the isotropic case. To derive formulae for the displacement, the equilibrium differential equation must be solved in combination with the geometric and constitutive equations.
Figure 2.14 shows the forces acting on a cylinder segment used to derive the governing equation.

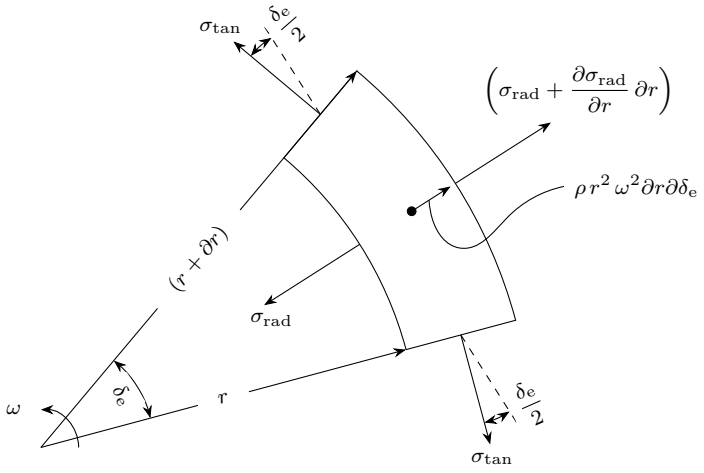

Figure 2.14: Finite element of a closed cylinder ring showing the forces acting on it, including body forces due to centrifugal loads.

According to Cheng et al. [117], the equations for an annular cylinder are:

- the governing equilibrium equation,

$$\frac{\partial \sigma_{\text{rad}}}{\partial r} + \frac{\sigma_{\text{rad}} - \sigma_{\text{tan}}}{r} + \rho r \omega^2 = 0, \tag{2.89}$$

- the constitutive material equations,

$$\epsilon_{\text{rad}} = \frac{\sigma_{\text{rad}}}{E_{\text{rad}}} - \frac{\nu_{\text{tr}}}{E_{\text{tan}}}\,\sigma_{\text{tan}}, \tag{2.90}$$

$$\epsilon_{\text{tan}} = \frac{\sigma_{\text{tan}}}{E_{\text{tan}}} - \frac{\nu_{\text{rt}}}{E_{\text{rad}}}\,\sigma_{\text{rad}}, \tag{2.91}$$

- and the geometric equations,

$$\epsilon_{\text{rad}} = \frac{\partial u_{\text{rad}}}{\partial r} + \alpha_{\text{T}}\,T(r), \tag{2.92}$$

$$\epsilon_{\text{tan}} = \frac{u_{\text{rad}}}{r} + \alpha_{\text{T}}\,T(r), \tag{2.93}$$

here σ_{rad} and σ_{tan} are the radial and tangential stresses, ϵ_{rad} and ϵ_{tan} the corresponding strains, E_{rad} and E_{tan} the radial and tangential Young's moduli, and ν_{rt} and ν_{tr} the Poisson's ratios representing transverse strain responses, with ν_{rt} being the Poisson's ratio for strain in the tangential direction due to radial stress, while ν_{tr} is the Poisson's ratio for strain in the radial direction due to tangential stress. Furthermore, α_{T} is the thermal expansion coefficient, and $T(r)$ is the temperature distribution within the cylinder. A detailed explanation is given by Chen and Zhu [115].
Equations (2.89) to (2.93) can be combined and solved for the radial displacement in a cylindrical disk with orthotropic material properties ($E_{\text{tan}} \neq E_{\text{rad}}$, $\nu_{\text{tr}} \neq \nu_{\text{rt}}$). It must be noted that this is a complex task, as the combination of the above equations results in an Euler-type, inhomogeneous, second-order ordinary differential equation. For the sake of solvability, the equation is solved twice, once without centrifugal forces and once without temperature gradients, and the results are then superimposed. Chen et al. [116] have shown that the results differ only slightly from those derived using a fully coupled model.

Radial Displacement
The radial displacement for a complete orthotropic material can be written as given by Chen and Zhu [115]:

$$k = \sqrt{\frac{E_{\text{tan}}}{E_{\text{rad}}}} \tag{2.94}$$

$$\beta = \frac{r_{\text{in}}}{r_{\text{out}}} \tag{2.95}$$

$$\begin{aligned} u_{\text{rad}}(r) = {} & \left(\frac{k}{E_{\text{tan}}} - \frac{\nu_{\text{tr}}}{E_{\text{rad}}}\right) C_1 r^k + \left(\frac{k}{E_{\text{tan}}} + \frac{\nu_{\text{tr}}}{E_{\text{rad}}}\right) C_2 r^{-k} \\ & + \left(\frac{3}{E_{\text{tan}}} - \frac{\nu_{\text{tr}}}{E_{\text{rad}}}\right) \frac{\rho\omega^2(3+\nu_{\text{tr}})r^3}{k^2-9} + \frac{\rho\omega^2 r^3}{E_{\text{tan}}} + \alpha_{\text{T}}\,\Delta T\, r. \end{aligned} \tag{2.96}$$

For a hollow cylinder, the integration constants C_1 and C_2 can be determined using the following boundary conditions [115]:

$$\sigma_{\text{rad}}(r = r_{\text{in}}) = -p_{\text{in}} \tag{2.97}$$

$$\sigma_{\text{rad}}(r = r_{\text{out}}) = -p_{\text{out}}. \tag{2.98}$$

The resulting expressions for the integration constants are

$$C_1 = \frac{p_{\text{in}} - \beta^{-k-1} p_{\text{out}}}{r_{\text{out}}^{k-1}(\beta^{-k-1} - \beta^{k-1})} - \frac{\rho\omega^2 r_{\text{out}}^2 (3+\nu_{\text{tr}})(1-\beta^{3+k})}{r_{\text{out}}^{k-1}(k^2-9)(1-\beta^{2k})} \tag{2.99}$$

$$C_2 = \frac{-p_{\text{in}} + \beta^{k-1} p_{\text{out}}}{r_{\text{out}}^{-k-1}(\beta^{-k-1} - \beta^{k-1})} + \frac{\rho\omega^2 r_{\text{out}}^2 (3-\nu_{\text{tr}})(1-\beta^{3-k})}{r_{\text{out}}^{-k-1}(k^2-9)(1-\beta^{-2k})}. \tag{2.100}$$

For a solid cylinder, the integration constants can be found in Chen and Zhu [115].

Stresses in Radial and Tangential Direction
The radial and tangential stresses in an orthotropic cylinder are given by [115]

$$\sigma_{\mathrm{rad}}(r) = C_1\, r^{k-1} - C_2\, r^{-k-1} \; + \frac{\rho\,\omega^2\,(3+\nu_{\mathrm{tr}})\,r^2}{k^2-9} \tag{2.101}$$

$$\sigma_{\mathrm{tan}}(r) = k\,C_1\, r^{k-1} + k\,C_2\, r^{-k-1} \; + \frac{3\,\rho\,\omega^2\,(3+\nu_{\mathrm{tr}})\,r^2}{k^2-9} \; + \rho\,\omega^2\,r^2 \tag{2.102}$$

2.1.5.2 Ring of Segmented Magnets with Orthotropic Material Properties

The constitutive and geometric equations for segmented magnets are identical to Equations (2.90) to (2.93). Since the magnets do not form a closed cylinder and they are theoretically unable to transfer forces at their tangential boundaries, the governing equation lacks a term for tangential stresses [117].

$$\frac{\partial \sigma_{\mathrm{rad}}}{\partial r} + \frac{\sigma_{\mathrm{rad}}}{r} + \rho r \omega^2 = 0 \tag{2.103}$$

Radial Displacement of Segmented Magnets
This results in [115]

$$\begin{aligned} u_{\mathrm{rad},r=R} = {} & \frac{1-\nu_{\mathrm{tr}}}{E_{\mathrm{tan}}} \frac{r_{\mathrm{in}}^2 p_{\mathrm{in}} - r_{\mathrm{out}}^2 p_{\mathrm{out}}}{r_{\mathrm{out}}^2 - r_{\mathrm{in}}^2} R \; + \frac{1+\nu_{\mathrm{tr}}}{E_{\mathrm{tan}}} \frac{r_{\mathrm{in}}^2 r_{\mathrm{out}}^2 (p_{\mathrm{in}} - p_{\mathrm{out}})}{r_{\mathrm{out}}^2 - r_{\mathrm{in}}^2} \frac{1}{R} \\ & - \frac{\rho\omega^2 (R^2 - r_{\mathrm{in}}^2)(R + r_{\mathrm{in}})}{E_{\mathrm{tan}} R^2 (r_{\mathrm{out}}^2 - r_{\mathrm{in}}^2)} \; \Big(r_{\mathrm{in}}^2 (R^2 + r_{\mathrm{out}}^2 + \nu_{\mathrm{tr}}(r_{\mathrm{out}}^2 - R^2)) \\ & \qquad - r_{\mathrm{out}}^2 (R^2 + r_{\mathrm{in}}^2 - \nu_{\mathrm{tr}}(R^2 - r_{\mathrm{in}}^2)) \Big) \\ & + \frac{\rho\omega^2}{4E_{\mathrm{tan}}} \left(\frac{R^3}{3} + \frac{r_{\mathrm{in}} R^2}{2} - r_{\mathrm{in}}^2 R \; + r_{\mathrm{in}}^3 \left(-\ln R + \frac{1}{6} + \ln r_{\mathrm{in}} \right) \right) \\ & + \left(\frac{(1-\nu_{\mathrm{tr}})R}{r_{\mathrm{in}}^2} + \frac{1+\nu_{\mathrm{tr}}}{R} \right) \; \frac{r_{\mathrm{in}}^2}{2}\, \alpha_{\mathrm{T}}\, \Delta T \\ & + (1+\nu_{\mathrm{tr}}) \frac{R^2 - r_{\mathrm{in}}^2}{2R}\, \alpha_{\mathrm{T}}\, \Delta T \end{aligned} \tag{2.104}$$

Stresses in Radial and Tangential Direction of Segmented Magnets
The tangential stress in a ring of segmented magnets is calculated as [115]

$$\begin{aligned} \sigma_{\mathrm{tan}}(r) = {} & \frac{r_{\mathrm{in}}^2 p_{\mathrm{in}} - r_{\mathrm{out}}^2 p_{\mathrm{out}}}{r_{\mathrm{out}}^2 - r_{\mathrm{in}}^2} \; + \frac{r_{\mathrm{in}}^2 r_{\mathrm{out}}^2 (p_{\mathrm{in}} - p_{\mathrm{out}})}{r_{\mathrm{out}}^2 - r_{\mathrm{in}}^2} \frac{1}{R^2} \; + \frac{\rho\omega^2 (r_{\mathrm{out}} + r_{\mathrm{in}}) r_{\mathrm{out}}}{4} \left(1 + \frac{r_{\mathrm{in}}^2}{R^2} \right) \\ & - \frac{\rho\omega^2}{4(1-\nu_{\mathrm{tr}}^2)} \left(\frac{R^3}{3} + \frac{r_{\mathrm{in}} R^2}{2} - r_{\mathrm{in}}^2 R \; + r_{\mathrm{in}}^3 \left(-\ln R + \frac{1}{6} + \ln r_{\mathrm{in}} \right) \right. \\ & \qquad \left. + \nu_{\mathrm{tr}} \left(R^2 + r_{\mathrm{in}} R - r_{\mathrm{in}}^2 - \frac{r_{\mathrm{in}}^3}{R} \right) \right) \end{aligned} \tag{2.105}$$

2.1.5.3 Definition of Failure Criterion and Design Criteria

The von Mises equivalent stress model is selected for ductile materials, including steels such as Inconel 718 for the sleeves and, to some extent, magnet materials. The von Mises equivalent stress σ_{vMises} is calculated as

$$\sigma_{\mathrm{vMises}} = \sqrt{0.5\,((\sigma_{\mathrm{rad}} - \sigma_{\mathrm{tan}})^2 + \sigma_{\mathrm{rad}}^2 + \sigma_{\mathrm{tan}}^2)}. \tag{2.106}$$

For materials such as carbon fiber reinforced plastics, the equivalent stress model is not applicable. Instead, the maximum tangential strain criterion is used:

$$\epsilon_{\tan} = \frac{\sigma_{\tan}}{E_{\tan}}. \tag{2.107}$$

During operation, several load cases occur, which are summarized in Table 2.4.

Table 2.4: Exemplary load cases for the evaluation of the retention sleeve stresses, considering different operational speeds relative to nominal, constant temperature throughout the rotor, and whether torque needs to be transferred.

Case	$\omega/\omega_{\text{nom}}$	ΔT	Load Transfer	Description
1	0	0	yes	Standstill with full torque for analysis of pre-tension.
2	1.1	110	yes	Design torque at 10 % overspeed at operating temperature.
3	1.2	110	no	Rotor burst test at 20 % overspeed at operating temperature.
4	1.1	-75	yes	Design torque at 10 % overspeed at cold start.
5	1.2	-75	no	Rotor burst test at 20 % overspeed at cold start.

If a certain torque must be transferred during operation, the contact pressure p_{c} for each load case must exceed the average shear stress $\tau_{\text{avg},i}$ in the i-th section, assuming a friction coefficient of $f_c = 0.10$. This requirement can be relaxed if the magnet carrier transmits torque not solely via friction, but also via form fit.
Additionally, a minimum contact pressure $p_{\text{min},i} = 10\,\text{Pa}$ must be ensured to prevent lift-off of the magnets under any condition. Lastly, the maximum occurring von Mises stress $\sigma_{\text{vMises},i,\text{max}}$ in each layer must not exceed the corresponding yield strength. These criteria are summarized as:

$$p_{\text{c,load},i} \geq \frac{\tau_{\text{avg},i}}{f_{\text{c}}} \tag{2.108}$$

$$p_{\text{c,noload},i} \geq p_{\text{min}} \tag{2.109}$$

$$\sigma_{\text{vMises},i,\text{max}} \leq \sigma_{\text{y},i} \tag{2.110}$$

By applying these load cases and design constraints, the suitability of the rotor containment can be evaluated.

2.1.6 Lumped Parameter Thermal Network

A thorough evaluation of the thermal behaviour of an electric machine is essential to prove the feasibility of a design. Thermal network methods are therefore applied to obtain temperature distributions. Figure 2.15 shows a workflow diagram illustrating the process of thermal analysis for electric machines.
The thermal analysis is an iterative process, as convective thermal resistances such as between the frame and ambient air or between a fluid and a solid depend on local temperatures. Furthermore, material properties are temperature-dependent, further necessitating an iterative approach. This is carried out using a Newton-Raphson technique.
In Sections 2.1.6.1 and 2.1.6.2, the general thermal transport phenomena and the concept of nodalization are explained, which are used to solve the thermal network. Section 2.1.6.3 describes how thermal resistances are calculated for various cases, and Section 2.1.6.4 details the construction of the thermal networks for the components. These are required to set up the local resistance matrices, transform them into a global system, and map the boundary conditions, such as ambient and coolant temperatures, as well as electromagnetic and mechanical losses.

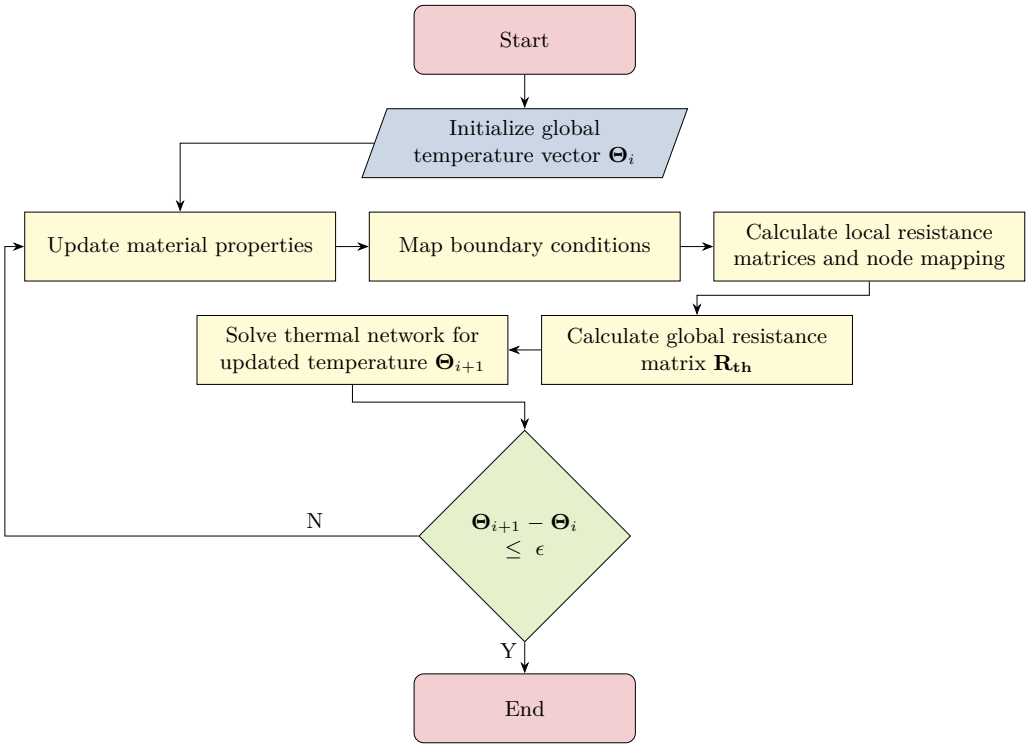

Figure 2.15: Workflow diagram illustrating the process of the thermal analysis of an electric machine using Lumped Parameter Thermal Networks (LPTN) to determine temperature distributions and heat fluxes among nodes.

2.1.6.1 Theory of Thermal Transport Phenomena

Generic Partial Differential Equation of Thermal Transport

The transport equation [118] in a continuum can be written as

$$\frac{\partial(\rho\Phi)}{\partial t} + \nabla \cdot (\rho\Phi\mathbf{u}) = \nabla \cdot (\Gamma\nabla\Phi) + S_\Phi \tag{2.111}$$

where ρ is the density, Φ is a scalar or vector property, Γ is the appropriate diffusion coefficient, and S_Φ is a source term. The equation consists of:

- a transient term, $\frac{\partial(\rho\Phi)}{\partial t}$, which accounts for the accumulation of Φ in the control volume;
- a convection term, $\nabla \cdot (\rho\Phi\mathbf{u})$, which accounts for the transport of Φ due to the velocity field;
- a diffusion term, $\nabla \cdot (\Gamma\nabla\Phi)$, which accounts for the transport of Φ due to its spatial gradients; and
- a source term, S_Φ, which accounts for sources or sinks that generate or deplete Φ.

Any additional terms that cannot be cast into convection or diffusion are included in the source term.

Heat Transfer Mechanisms

Three primary mechanisms of heat transfer exist [119]. Conduction refers to the transfer of energy between molecules within a medium. It is a linear process that occurs in solids, fluids, and gases, and is the only mode of heat transfer in solids. The heat transfer by conduction is described by:

$$Q = \frac{1}{R_{\text{th}}}(T_i - T_j) \tag{2.112}$$

where Q is the heat flow, R_{th} is the thermal resistance of the control volume, and T_i, T_j are the temperatures at its boundaries.
Convection occurs in fluids and gases due to the movement of molecules. Unlike conduction, where heat is transferred through molecular vibration and interaction, convection enhances heat transfer through the bulk motion of fluid. This process intermixes molecules with different energy levels, increasing the rate of heat exchange. Similar to conduction, the mechanism is linear and also described by Equation (2.112).
Radiation is the third mechanism of heat transfer, where energy is emitted in the form of electromagnetic waves. The intensity of radiation depends on emissivity, surface area, and strongly on temperature, following Stefan-Boltzmann's law. The net radiative heat transfer between two surfaces is

$$Q = \sigma_{\text{SB}}\, \varepsilon_{\text{eff}}\, A\, (T_i^4 - T_j^4), \tag{2.113}$$

where σ_{SB} is the Stefan-Boltzmann constant, and ε_{eff} is the effective emissivity factor accounting for surface properties and geometry. According to [120], radiation effects in electric machines are generally negligible compared to conduction and convection, and are therefore disregarded in further calculations.

2.1.6.2 Concept of Nodalization

A thermal resistance network model is employed to solve Equation (2.111) because it requires less computational effort than Computational Fluid Dynamics and Finite Element Methods, making it suitable for pre-design applications. The main limitation is that temperatures can only be evaluated at pre-defined points. The fundamentals of lumped parameter thermal networks are discussed in [120–124].
To construct a circuit model with a finite number of elements, simplifications are inevitable. Nodalization refers to dividing an object into sub-elements, where each element or junction is represented by one or a few nodes. Lumped parameter modelling approximates the thermal properties of a body with manageable quantities such as average temperature, volume, and thermal mass.
Although nodal division can be performed arbitrarily, it must meet certain criteria, such as ensuring accurate temperature prediction and preserving computational simplicity.
The steady-state thermal behaviour can be modelled by analogy to electrical systems, using a network of thermal resistances, heat flows, and temperature sources [121]. The conductance matrix $\mathbf{G}$ of a system with $(n+1)$ nodes is given by:

$$\mathbf{G} = \begin{pmatrix} \sum_{i=1}^{n} \frac{1}{R_{1,i}} & \frac{-1}{R_{1,2}} & \cdots & \frac{-1}{R_{1,n}} \\ \frac{-1}{R_{2,1}} & \sum_{i=1}^{n} \frac{1}{R_{2,i}} & \cdots & \frac{-1}{R_{2,n}} \\ \vdots & \vdots & \ddots & \vdots \\ \frac{-1}{R_{n,1}} & \frac{-1}{R_{n,2}} & \cdots & \sum_{i=1}^{n} \frac{1}{R_{n,i}} \end{pmatrix} \tag{2.114}$$

The heat injection vector $\mathbf{Q}$ is defined as:

$$\mathbf{Q} = \begin{pmatrix} Q_1 \\ Q_2 \\ \vdots \\ Q_n \end{pmatrix} \tag{2.115}$$

and the corresponding temperature vector $\boldsymbol{\Theta}$ as:

$$\boldsymbol{\Theta} = \begin{pmatrix} \Theta_1 \\ \Theta_2 \\ \vdots \\ \Theta_n \end{pmatrix}. \tag{2.116}$$

The temperature distribution can then be solved using:

$$\boldsymbol{\Theta} = \mathbf{G}^{-1}\mathbf{Q} \tag{2.117}$$

Although building an accurate thermal network model requires validation against Finite Element models or experimental data, the resulting model allows for rapid evaluation of parameter variations. This computational efficiency is critical for enabling large-scale design space exploration.

2.1.6.3 Thermal Resistance Calculation of Electric Machine Components

This section addresses the various convective and conductive thermal resistances that occur within an electric machine.

2.1.6.3.1 Conductive Resistances

The thermal resistance of a solid is calculated with respect to the direction of heat flow as

$$R_{\mathrm{th}} = \frac{1}{G} = \int_0^L \frac{1}{\lambda\, A\, l_{\mathrm{path}}}\, \mathrm{d}l_{\mathrm{path}} \tag{2.118}$$

where λ denotes the thermal conductivity, L the distance between the two thermal nodes, and A the cross-sectional area. This formulation allows the cross-sectional area to vary along the integration path [125]. The following discusses different geometrical configurations.
For a flat plate, the thermal resistance is given by [125]

$$R_{\mathrm{th}} = \frac{L}{\lambda\, A} \tag{2.119}$$

The case of a hollow cylinder is generalised to allow the calculation of thermal resistance for cylindrical segments with radially varying angular spans.

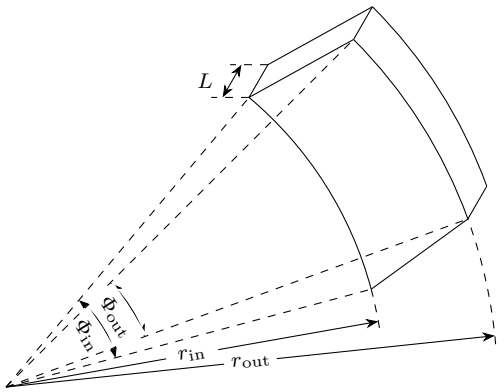

Figure 2.16: Hollow cylinder segment with linearly varying angles along the radius.

If the angular span varies linearly along the radius according to

$$\Theta(r) = \theta_{\mathrm{in}} - \frac{\theta_{\mathrm{in}} - \theta_{\mathrm{out}}}{r_{\mathrm{out}} - r_{\mathrm{in}}}(r - r_{\mathrm{in}}) = a\,r + b \tag{2.120}$$

the resulting thermal resistance in radial direction is [122]

$$R_{\mathrm{cseg,rad}} = \frac{1}{\lambda\,l\,b} \ln\left(\frac{r_{\mathrm{out}}}{r_{\mathrm{in}}} \frac{a\,r_{\mathrm{in}} + b}{a\,r_{\mathrm{out}} + b}\right) \tag{2.121}$$

For the circumferential direction, the general formulation for a flat plate (2.119) can be applied using

$$L_{\mathrm{char}} = r_{\mathrm{in}}\,\theta_{\mathrm{in}} \tag{2.122}$$

as the characteristic path length and

$$h = \frac{r_{\mathrm{in}}\,\theta_{\mathrm{in}} + r_{\mathrm{out}}\,\theta_{\mathrm{out}}}{2} \frac{r_{\mathrm{out}} - r_{\mathrm{in}}}{r_{\mathrm{in}}\,\theta_{\mathrm{in}}} \tag{2.123}$$

as the mean radial thickness associated with the cross-sectional area [122].

Thermal Resistance of Stator Slot and Windings

Modelling the thermal resistance of the stator slot and windings is challenging due to several interacting phenomena:

- The presence of slot insulation between the stator iron and copper windings significantly contributes to the thermal resistance between the teeth and the slot. This insulation layer often contains small air pockets that reduce its effective thermal conductivity.
- The winding region exhibits an inhomogeneous composition, comprising copper conductors coated with impregnation material, as well as voids or filler media such as air or grease between strands. While thermal conductivity is relatively high along the axial direction due to the copper, it is considerably lower in the radial direction, where low-conductivity materials dominate.
- Heat generation within the windings is spatially distributed and typically non-uniform, which complicates the thermal modelling.
- The complex geometry of the slot leads to non-trivial heat flow paths, as temperature gradients occur at varying radial positions. This contrasts with components like magnets, where radial heat flow can be assumed more straightforwardly.

In a first step, a model is developed to determine the effective thermal conductivities within the stator slot. Figure 2.17 illustrates the considered slot geometry, which adopts a double-layer, vertical winding arrangement. Solid, flat conductors with width w_{cond} and height h_{cond} are individually insulated by a wire insulation of thickness $t_{\mathrm{wire,ins}}$. These insulated wires are stacked with a separation distance t_{sep}, which is filled with impregnation material. The slot itself includes a slot liner of thickness $t_{\mathrm{slot,ins}}$, and the void between the two winding layers is reserved for phase insulation. In the case of a direct slot-cooled configuration, this void is used as a cooling channel.
Each winding layer is represented by two vertically stacked cuboidal elements, following the approach of Wrobel and Mellor [126]. On the right-hand side of Figure 2.17, an enlarged view of one such cuboid is shown, defined by its width w_{cube} and height h_{cube}.

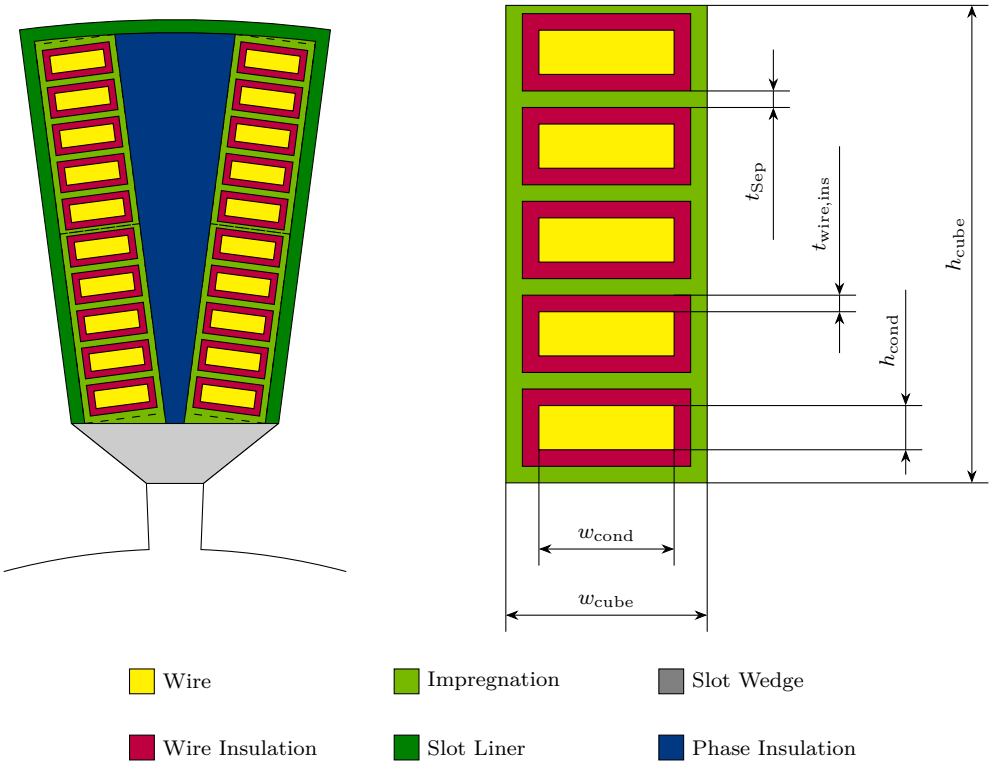

Figure 2.17: Double-layer winding arrangement in slot and definition of cuboidal elements

The effective thermal conductivities in radial λ_{rad}, tangential λ_{tan}, and axial direction λ_{ax} are then calculated using the dimensions provided in Figure 2.17 as

$$\lambda_{\mathrm{rad}} = \frac{\frac{h_{\mathrm{cond}}}{2} + t_{\mathrm{wire,ins}} + \frac{t_{\mathrm{sep}}}{2}}{\frac{h_{\mathrm{cond}}}{2\,\lambda_{\mathrm{cond}}} + \frac{t_{\mathrm{wire,ins}}}{\lambda_{\mathrm{wire,ins}}} + \frac{t_{\mathrm{sep}}}{2\,\lambda_{\mathrm{impreg}}}} \tag{2.124}$$

$$\lambda_{\mathrm{tan}} = \frac{\frac{w_{\mathrm{cond}}}{2} + t_{\mathrm{wire,ins}} + \frac{t_{\mathrm{sep}}}{2}}{\frac{w_{\mathrm{cond}}}{2\,\lambda_{\mathrm{cond}}} + \frac{t_{\mathrm{wire,ins}}}{\lambda_{\mathrm{wire,ins}}} + \frac{t_{\mathrm{sep}}}{2\,\lambda_{\mathrm{impreg}}}} \tag{2.125}$$

$$\lambda_{\mathrm{ax}} = \frac{\lambda_{\mathrm{cond}} A_{\mathrm{cond}} + \lambda_{\mathrm{wire,ins}} A_{\mathrm{wire,ins}} + \lambda_{\mathrm{impreg}} A_{\mathrm{impreg}}}{A_{\mathrm{cube}}} \tag{2.126}$$

The areas A_{cond}, $A_{\mathrm{wire,ins}}$, A_{impreg}, and A_{cube} represent the cross-sectional regions of the cuboidal element occupied by the copper conductors, the wire insulation, the impregnation resin, and the entire cuboid, respectively. The thermal conductivities λ_{cond}, $\lambda_{\mathrm{wire,ins}}$, and $\lambda_{\mathrm{impreg}}$ denote the heat conduction capabilities of the respective materials. As evident from the structure of Equation (2.126), the radial and tangential components are modelled as a series connection of the respective thermal resistances, whereas the axial direction is represented by an area-weighted average of the individual material conductivities, corresponding to a parallel thermal path. While litz wires offer advantages at high frequencies, modelling their effective thermal conductivity remains challenging and is largely based on empirical models [127–129] supported by application-specific validation through measurements [130]. For this reason, they are not considered in the present work.
The second step involves modelling the thermal resistance of the slot as a whole. This approach, initially introduced by Soderberg [131] and later formalised by Kylander [121], was extended by Wrobel and Mellor [126] to account for three-dimensional effects. In this method, the complex geometry of the stator slot is transformed into an equivalent rectangular domain to facilitate the analysis of heat flow.
For two-dimensional heat conduction, the analytical solution derived by Soderberg [131]

forms the basis of the model. The corresponding node configuration is illustrated in Figure 2.18, where internal heat generation is also considered.

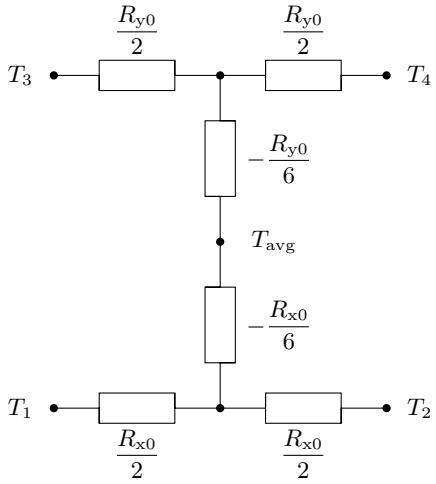

Figure 2.18: Node configuration for two-dimensional heat flow with internal heat source, adapted from [121]

The equivalent thermal resistances in the tangential and radial directions are calculated as follows [126]:

$$R_{x0} = \frac{w_{cube}}{4\,\lambda_{tan}\,h_{cube}\,L_{stk}\,Q_s} \tag{2.127}$$

$$R_{y0} = \frac{h_{cube}}{4\,\lambda_{rad}\,w_{cube}\,L_{stk}\,Q_s} \tag{2.128}$$

These expressions form the basis for determining the thermal network parameters used in the lumped parameter thermal model of the stator slot region.

2.1.6.3.2 Convective Resistances

The second type of resistance in electric machines is convective resistance. It primarily occurs at the rotor and stator surfaces, but also within the airgap and at the interfaces between cooling channel walls and the cooling fluid, such as in direct slot or water jacket cooling configurations. The thermal resistance of a solid surface in contact with a fluid or gas is expressed as

$$R_{th} = \frac{1}{G} = \frac{1}{\alpha_{conv}\,A} \tag{2.129}$$

where α_{conv} is the heat transfer coefficient and A is the surface area of the solid in contact with the fluid [125]. Empirical correlations exist for common cases, linking the so-called Nusselt number to the heat transfer coefficient in the form

$$\alpha_{conv} = \frac{Nu\,\lambda}{L_{char}} \tag{2.130}$$

where Nu is the Nusselt number, λ the thermal conductivity, and L_{char} the characteristic length scale of the specific problem. The following sections introduce several types of convective resistances.

Thermal Resistance at Outer Surface of Static Cylinder

At the outer surface of a cylinder, two types of convection may occur: natural convection driven by gravity acting on a fluid or gas, and forced convection. In both cases, fluid

properties are evaluated at the mean temperature T_m,

$$T_\mathrm{m} = \frac{T_\mathrm{w} + T_\mathrm{amb}}{2} \tag{2.131}$$

where T_w is the wall temperature and T_amb the ambient temperature, defined as sufficiently far from the wall. For natural convection, the Nusselt correlation is given in [125], based on equations developed by Churchill and Chu [132], Staton et al. [133]:

$$Gr = \frac{g\, r_\mathrm{out}^3}{8\,\nu^2}\,\beta\,(T_\mathrm{w} - T_\mathrm{amb}) \tag{2.132}$$

$$Ra = Gr\,Pr \tag{2.133}$$

where g is the gravitational acceleration, r_out the outer radius of the cylinder, β the thermal expansion coefficient, Gr the Grashof number, Pr the Prandtl number, and Ra the Rayleigh number. The Nusselt number is then calculated as

$$Nu = \left(0.60 + 0.387\,Ra^{\frac{1}{6}}\left(1 + \left(\frac{0.559}{Pr}\right)^{\frac{9}{16}}\right)^{\frac{-8}{27}}\right)^2 \tag{2.134}$$

The characteristic length for this case is the cylinder diameter,

$$L_\mathrm{char} = 2\,r_\mathrm{sy,o} \tag{2.135}$$

which is used in Equation (2.130) to determine the heat transfer coefficient.
For forced convection, a cross-flow perpendicular to the cylinder axis is assumed [125], based on Gnielinski [134]. Mixed convection, where natural convection is superimposed on forced convection as proposed by [132], is not considered here. The characteristic length is taken as half the perimeter:

$$L_\mathrm{char} = r_\mathrm{sy,o}\,\pi \tag{2.136}$$

The corresponding Reynolds number is given by

$$Re = \frac{r_\mathrm{sy,o}\,\pi\,v}{\nu} \tag{2.137}$$

where v is the fluid flow velocity. The Nusselt number for forced convection is then computed as

$$Nu_\mathrm{L} = 0.664\,Re^{\frac{1}{2}}\,Pr^{\frac{1}{3}} \tag{2.138}$$

$$Nu_\mathrm{T} = \frac{0.037\,Re^{0.8}\,Pr}{1 + 2.443\,Re^{-0.1}\left(Pr^{\frac{2}{3}} - 1.0\right)} \tag{2.139}$$

$$Nu = 0.3 + \sqrt{Nu_\mathrm{L}^2 + Nu_\mathrm{T}^2} \tag{2.140}$$

As in the natural convection case, the heat transfer coefficient can be calculated using Equation (2.130).

Thermal Resistance in Rotor-Stator Airgap

The flow in the rotor-stator airgap is modeled as Taylor-Couette flow following the approach described by Nerg et al. [120]. This model assumes that the airgap fully encircles the rotor. The characteristic length of the problem is defined as twice the mechanical airgap, g_mech.
Given an axial flow velocity v_ax and a rotational airgap velocity v_rad, an effective velocity

v_{eff} can be computed as

$$v_{\mathrm{eff}} = \sqrt{v_{\mathrm{ax}}^2 + \left(\frac{v_{\mathrm{rad}}}{2}\right)^2} \tag{2.141}$$

This allows the calculation of the axial and effective Reynolds numbers:

$$Re_{\mathrm{ax}} = \frac{2\, v_{\mathrm{ax}}\, g_{\mathrm{mech}}}{\nu} \tag{2.142}$$

$$Re_{\mathrm{eff}} = \frac{2\, v_{\mathrm{eff}}\, g_{\mathrm{mech}}}{\nu} \tag{2.143}$$

The Taylor number, characterising the influence of rotational effects in the annular flow, is given by

$$Ta = \frac{g_{\mathrm{mech}}\, v_{\mathrm{rad}}}{\nu} \sqrt{\frac{g_{\mathrm{mech}}}{r_{\mathrm{sl,o}}}} \tag{2.144}$$

Detailed correlations for the Nusselt number in the rotor-stator airgap are provided by Chong [135] as functions of Reynolds and Taylor numbers and the thermophysical properties of air. These expressions, which are not reproduced here due to their length, are used in this work as given for the relevant flow regimes defined by Kaye and Elgar [136].

Thermal Resistance of a Rectangular Cooling Channel

Another geometry of interest is the rectangular cooling channel, which is perfused by a cooling liquid. In electric machines, such slots are commonly used to implement direct slot cooling or water jacket cooling channels. For the case of a constant heat flux density $Q = \text{const.}$, the Nusselt number can be calculated for different flow regimes. The hydraulic diameter r_{h} of a rectangular slot is defined as

$$r_{\mathrm{h}} = \frac{h_{\mathrm{cc}}\, w_{\mathrm{cc}}}{h_{\mathrm{cc}} + w_{\mathrm{cc}}}, \tag{2.145}$$

where h_{cc} and w_{cc} are the height and width of the cooling channel, respectively.
In the case of laminar flow ($Re < 2300$), the Nusselt number can be calculated as in [137, 138]:

$$\begin{aligned} Nu_{\mathrm{L}} = 8.235 \Bigg(& 1 - 2.0421 \left(\frac{h_{\mathrm{cc}}}{w_{\mathrm{cc}}}\right)^{-1} + 3.0853 \left(\frac{h_{\mathrm{cc}}}{w_{\mathrm{cc}}}\right)^{-2} \\ & -2.4675 \left(\frac{h_{\mathrm{cc}}}{w_{\mathrm{cc}}}\right)^{-3} + 1.0578 \left(\frac{h_{\mathrm{cc}}}{w_{\mathrm{cc}}}\right)^{-4} - 0.1861 \left(\frac{h_{\mathrm{cc}}}{w_{\mathrm{cc}}}\right)^{-5} \Bigg) \\ & + 2 \cdot \frac{0.065\, \frac{d_{\mathrm{h}}}{L}\, Re\, Pr}{1 + 0.04 \left(\frac{d_{\mathrm{h}}}{L}\, Re\, Pr\right)^{2/3}} \end{aligned} \tag{2.146}$$

If the flow is turbulent ($Re > 10^4$), the Nusselt number can be calculated using the correlation from [125] based on [134]:

$$\zeta = (0.79 \log Re - 1.64)^{-2} \tag{2.147}$$

$$Nu_{\mathrm{T}} = \frac{\frac{\zeta}{8}\, (Re - 1000)\, Pr}{1 + 12.7 \sqrt{\frac{\zeta}{8}} \left(Pr^{\frac{2}{3}} - 1\right)} \left[1 + \left(\frac{2\, r_{\mathrm{h}}}{l_{\mathrm{ax}}}\right)^{\frac{2}{3}}\right] \tag{2.148}$$

Transient flow represents a transition between laminar and turbulent regimes. The Nusselt numbers at the boundaries are denoted as $Nu_{\mathrm{L},2300}$, corresponding to the laminar value at a Reynolds number of 2300, and $Nu_{\mathrm{T},10^4}$, corresponding to the turbulent value at a

Reynolds number of 10^4. The Nusselt number in the transitional regime is then given by

$$\gamma = \frac{Re - 2300}{10^4 - 2300} \tag{2.149}$$

$$Nu = (1 - \gamma)\, Nu_{\mathrm{L},2300} + \gamma\, Nu_{\mathrm{T},10^4}. \tag{2.150}$$

Knowing the heat transfer coefficient enables calculation of temperature profiles, e.g., from windings to the fluid in cooling channels. The pressure drop along such a channel is an important parameter as it is the sizing element of a pump which drives the fluid. Pressure loss coefficients for different geometries will be listed. In general, the pressure loss Δp can be calculated as

$$\Delta p = \zeta\, l_{\mathrm{ax}}\, \rho\, \frac{v^2}{4\, r_{\mathrm{h}}} \tag{2.151}$$

where ζ is the pressure loss coefficient. The pressure loss coefficients inside a rectangular slot can be calculated according to [125]:

$$\zeta = \begin{cases} \dfrac{64}{Re}\,\varphi & Re < 2300 \\ 0.3164\, Re^{\frac{-1}{4}} & 2300 < Re < 10^5 \\ (1.8 \log Re - 1.5)^{-2} & 10^5 < Re < 10^6 \\ (1.819 \log Re - 1.64)^{-2} & Re > 10^6 \end{cases} \tag{2.152}$$

with φ defined as a coefficient to take into account the non-circular form of the rectangular slots for laminar flow [125].

Thermal Resistance of End Space

Heat transfer from the end-winding into the void between the end-shields and the frame, as well as toward the slot pipe or rotor depending on the motor topology, is among the most difficult to predict. A literature review by Staton et al. [133] proposes the following empirical correlation:

$$h = k_1 \left(1 + k_2\, v^{k_3}\right) \tag{2.153}$$

where h is the heat transfer coefficient, v the local fluid velocity, and k_1, k_2, and k_3 are curve-fit coefficients. The first term accounts for natural convection, while the second represents the contribution of forced convection. Throughout this thesis, the values proposed by Schubert [139] are adopted ($k_1 = 15$, $k_2 = 0.4$, and $k_3 = 0.9$). If a stator sleeve is used, heat transfer around the end-windings and within the housing and endcap is limited to natural convection, which corresponds to setting k_2 to zero.

2.1.6.4 Lumped Parameter Thermal Network of the Machine

Two cooling topologies are considered for the electric machine: an indirect jacket-cooled design and a direct slot-cooled variant. In the jacket-cooled configuration, rectangular axial cooling channels are integrated into the housing. The slot-cooled configuration, in contrast, utilizes the space reserved for the phase divider, as illustrated in Figure 2.17. While the jacket-cooled design can be air- or liquid-cooled and is easier to manufacture, the slot-cooled approach enables improved heat transfer directly at the primary sources of loss, i.e., copper and iron losses, by providing a significantly shorter thermal path and thus enable higher power densities at similar thermal limits.
From a thermal modelling perspective, both topologies are structurally similar. Figure 2.19 presents the general lumped parameter thermal network, which is valid for both configurations. The specific differences introduced by each cooling approach are illustrated in Figure 2.20.

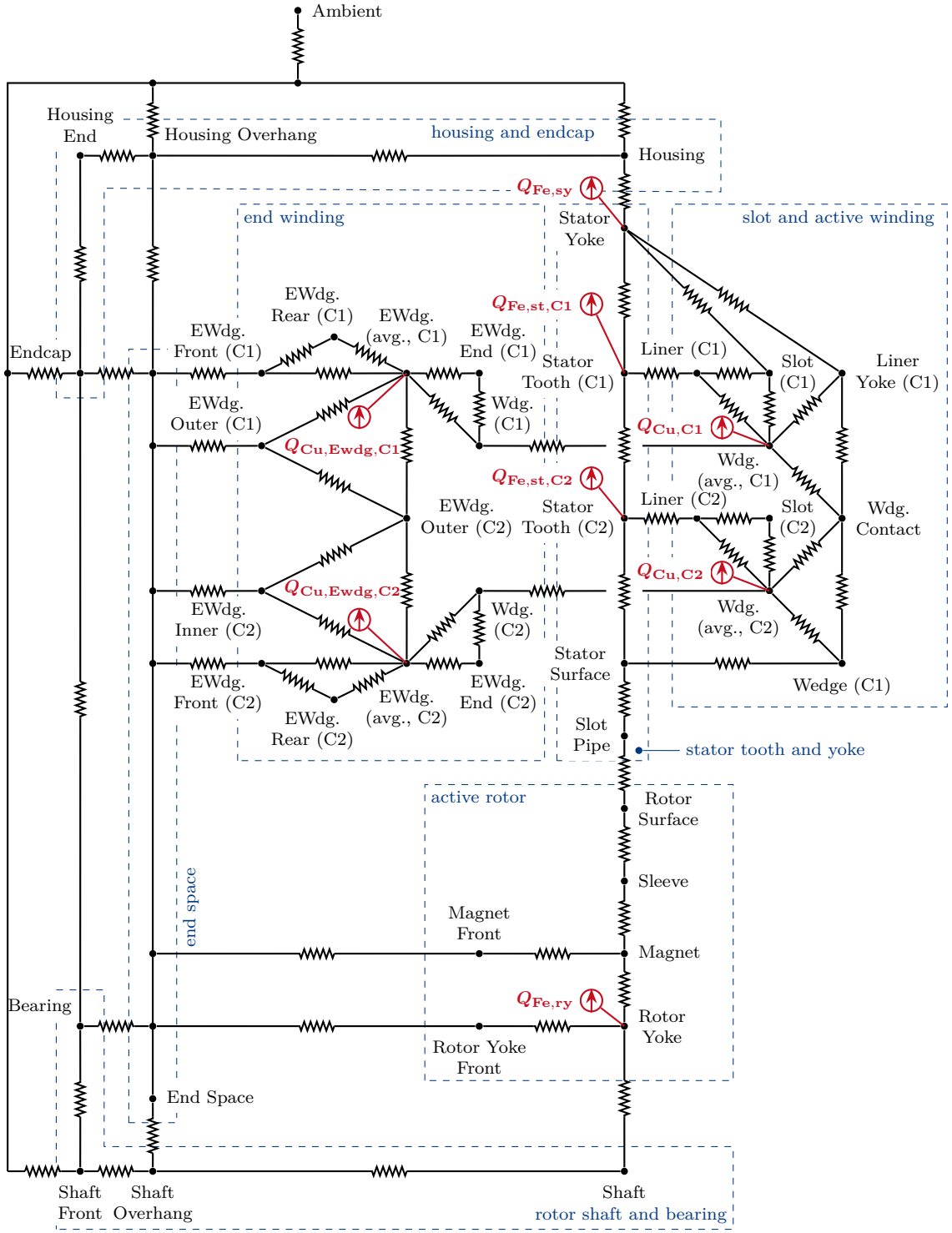

Figure 2.19: Lumped parameter thermal network of the entire electric machine including temperature nodes, thermal resistances, and injected losses. For clarity and due to symmetry, only the active and front sections are shown. The complete list of temperature nodes and resistances can be found in Chapter A.

Both topologies use a detailed thermal network comprising approximately 65 temperature nodes and 120 thermal resistances. The network captures radial, tangential, and axial heat fluxes, including dissipation into the end space. A quasi-3D formulation is employed based on rotational and axial symmetry, enabling efficient yet spatially resolved heat flow estimation. Its structure follows the modelling principles described in the Motor-CAD manual [140].

The thermal resistances of the rotor, the stator tooth and yoke, and structural components such as the housing and end caps are calculated using Equations (2.119) to (2.123). The winding is modelled as two stacked cuboids, as shown in Figure 2.17, with C1 representing the outer and C2 the inner region. The resistances of the active slot and end-winding regions are obtained using the methods presented in Equations (2.126) and (2.128). Convective resistances, including those in the airgap, cooling channels, and end space, are derived from the equations discussed in Paragraph 2.1.6.3.2.
The copper and iron losses retrieved from Section 2.1.4.6 are distributed volumetrically across the active and end-winding regions, as well as between the inner and outer parts of the stator tooth and yoke, in accordance with the segmented cuboid model.
The difference between the two cooling topologies is visualized in Figure 2.20, which shows the additional resistance networks complementing the common network presented in Figure 2.19.

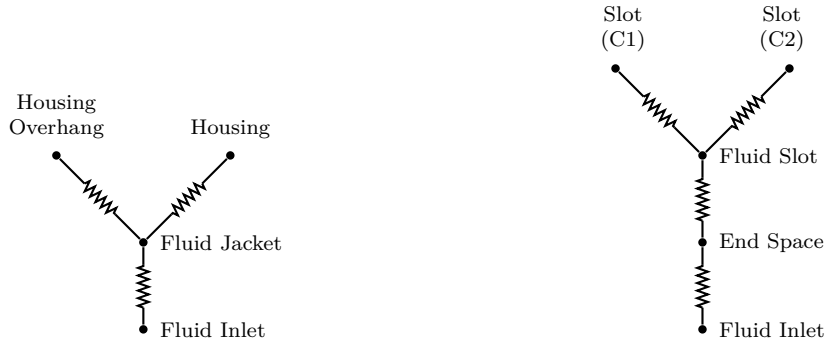

(**a**) Jacket cooling

(**b**) Slot cooling

Figure 2.20: Lumped parameter thermal network addendums for jacket- and slot-cooled variants complementing the common network described in Figure 2.19. The complete list of resistances can be found in Chapter A.

For jacket-cooled variants, heat flows from the housing and housing overhang into the fluid jacket. Consequently, losses generated in the winding and iron components must conduct through the stator teeth and yoke before dissipation. In contrast, the direct slot-cooled variant introduces cooling fluid into the endspace before it enters the cooling channels located in the phase divider region, where the network is directly connected to the slot nodes. This topology enables more efficient heat extraction directly at the source.
The ambient and fluid inlet nodes have fixed temperatures, imposing Dirichlet boundary conditions. Nodes with loss sources are treated as Neumann boundary conditions. Once all thermal resistances are computed, the temperature distribution is obtained by solving Equation (2.117).

2.1.7 Insulation Coordination according to IEC-60664

Insulation breakdown can lead to hazardous failures that are not tolerable in aerospace applications [141]. The insulation material is affected by electrical, mechanical, thermal, and environmental stresses [142, 143], which can result in short circuits between damaged stator windings [144]. A thorough evaluation of insulation strength is therefore essential during pre-design, as the insulation thickness is a major contributor to the high thermal resistance from the slot to the stator teeth due to its low thermal conductivity, typically around $\lambda_{\mathrm{ins}} = 0.25\,\mathrm{W\,m^{-1}\,K^{-1}}$ [141]. As a result, research projects aim to increase the thermal conductivity of these materials. While current insulation systems are primarily based on mica-epoxy organics, nanocomposite polymers with fillers such as aluminium

oxide or aluminium nitride can increase torque and current density by more than 15 % due to an improved thermal conductivity of up to $\lambda_{\text{ins}} = 0.7\,\text{W}\,\text{m}^{-1}\,\text{K}^{-1}$ [141].
Recent efforts have been made to raise the DC link voltage above 1 kV to reduce cable weight for power transmission. However, the insulation breakdown strength is influenced by elevated internal temperatures [145], reduced air pressure at high altitudes [146] (see Paschen's law [147]), and high $\text{d}V/\text{d}t$ pulses from pulse width modulated (PWM) signals [146, 148–151]. These signals are also affected by the cable length, which may cause reflections due to an impedance mismatch between the motor and the cable [141].

2.1.7.1 Pulse Shapes at Machine Terminal

According to IEC 60034 [76], the signal at the inverter output is not an ideal rectangular pulse but typically exhibits an overshoot after rapidly rising from zero before reaching the DC link voltage (see Figure 2.21).

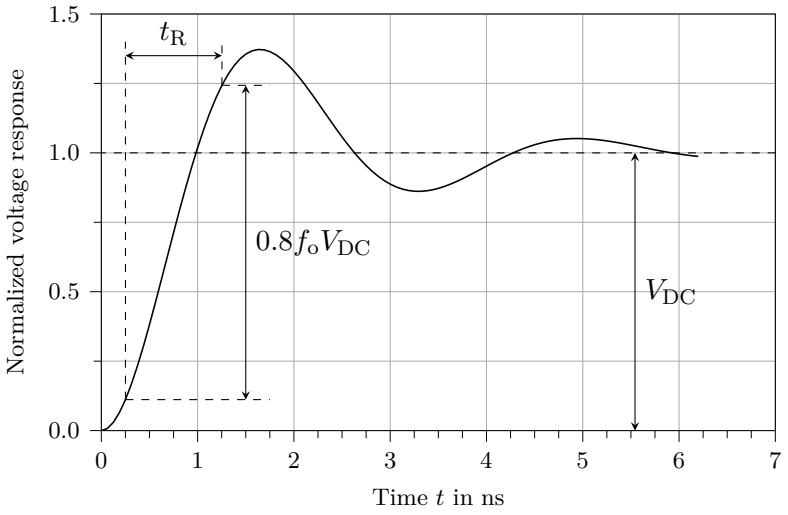

Figure 2.21: Qualitative impulse signal with overshoot at the inverter output

The peak voltage, signal rise time t_{r}, and slew rate $\text{d}V/\text{d}t$ are key parameters in insulation coordination. If not measured, the overshoot factor is taken as $f_{\text{o}} = 1.1$. The signal rise time is defined as the time required for the signal to rise from 10 % to 90 % of the peak voltage [76], given by

$$t_{\text{r}} = \frac{0.8\, f_{\text{o}}\, V_{\text{DC}}}{\text{d}V/\text{d}t}. \tag{2.154}$$

In addition to overshoot, signal reflections may occur along the inverter-machine connection, depending on cable length and impedance mismatch. The critical cable length L_{crit} at which full reflection occurs is

$$L_{\text{crit}} = \frac{t_{\text{r}}\, v_{\text{p}}}{2}, \tag{2.155}$$

where v_{p} is the wave propagation velocity, which depends on the cable's inductance and capacitance per unit length. A typical value of $v_{\text{p}} = 150\,\text{m}\,\mu\text{s}^{-1}$ is used when specific data are unavailable.
Based on the actual cable length L_{Cab}, the reflection factor r is defined in IEC 60034 [76] as

$$r = \begin{cases} 0.0 & L_{\text{Cab}} \leq \dfrac{L_{\text{crit}}}{10} \\ 0.25 & \dfrac{L_{\text{crit}}}{10} < L_{\text{Cab}} < \dfrac{2L_{\text{crit}}}{3} \\ 1.0 & L_{\text{Cab}} \geq L_{\text{crit}}, \end{cases} \tag{2.156}$$

resulting in a total overshoot factor

$$f_\mathrm{t} = (1 + r)\, f_\mathrm{o}. \tag{2.157}$$

For a given number of inverter levels n_Inv and simultaneous switching events n_o, the switching voltage V_s becomes

$$V_\mathrm{s} = \frac{V_\mathrm{DC}}{(n_\mathrm{Inv} - 1)}\, n_\mathrm{o}, \tag{2.158}$$

leading to the total overshoot voltage at the machine terminal

$$V_\mathrm{o} = (f_\mathrm{t} - 1)\, V_\mathrm{s} \tag{2.159}$$

and the expected maximum voltage stress during normal operation

$$V_\mathrm{r} = V_\mathrm{DC} + V_\mathrm{o}. \tag{2.160}$$

2.1.7.2 Type and Acceptance Test Voltages

The insulation is validated against type and acceptance criteria. According to IEC 60034 [76], the type test voltage V_type is defined as

$$V_\mathrm{type} = \begin{cases} 2\, V_\mathrm{r} & \text{phase-phase} \\ 1.4\, V_\mathrm{r} & \text{phase-neutral, phase-ground} \\ 0.7\, V_\mathrm{r}\, f_\mathrm{w} & \text{turn-turn} \end{cases} \tag{2.161}$$

and the acceptance test voltage V_acc as

$$V_\mathrm{acc} = \begin{cases} 2\,(V_\mathrm{r} + \sqrt{2}\,1000) & \text{phase-phase} \\ 2\,(1.4\, V_\mathrm{r} + \sqrt{2}\,1000) & \text{phase-neutral, phase-ground} \\ \dfrac{1.4\, V_\mathrm{r} + \sqrt{2}\,1000}{N_\mathrm{c}} & \text{turn-turn} \end{cases} \tag{2.162}$$

where f_w accounts for non-uniform voltage distribution in the winding and is calculated by

$$f_\mathrm{w} = \frac{0.9}{e^{\frac{0.05}{3.95}}\, \ln\left(\frac{4.0}{9.0}\right)}\, e^{\frac{t_\mathrm{r}}{3.95}}\, \ln\left(\frac{4.0}{9.0}\right). \tag{2.163}$$

2.1.7.3 Breakdown Voltages and Safety Factors

The insulation thickness t_ins and the material's dielectric strength ε_r determine the system's breakdown voltage

$$V_\mathrm{b} = t_\mathrm{ins}\, \varepsilon_\mathrm{r} \tag{2.164}$$

and the insulation safety factor

$$SF_\mathrm{ins} = \frac{V_\mathrm{b}}{\max(V_\mathrm{type}, V_\mathrm{acc})}. \tag{2.165}$$

For rotating electric machines, safety factors of 1.5 – 2.0 are typically required [76].

2.1.8 Short Summary

This section presents the analytical and physical modelling of permanent magnet synchronous machines. It defines the machine geometry and investigates the electromagnetic behaviour, including a detailed analysis of the winding configuration, magnetic field and flux density distributions, inductances, and loss mechanisms under operating conditions. Structural integrity is evaluated using analytical stress models that incorporate orthotropic material properties of the rotor components. Thermal behaviour is assessed through a complex lumped parameter thermal network, allowing estimation of the internal temperature distribution. Insulation coordination is established in accordance with IEC-60664, ensuring compliance with electrical safety requirements. The models are structured to balance accuracy and computational efficiency, facilitating early-stage design iterations. Analytical results are validated where appropriate against reference solutions and showed good agreement.

2.2 Power Transmission Gearboxes

Gearboxes convert torque and speed to meet specific application requirements. Typically, power is transmitted from a high-speed, low-torque electric machine to a low-speed, high-torque propeller. As previously discussed, the mass of electric machines decreases significantly with increasing speed due to the corresponding reduction in torque requirements. Consequently, a trade-off exists between torque-dense direct-drive configurations and high-speed machines coupled with a reduction gearbox.
Ideally, the transmission system would be supported by a modeling tool as comprehensive as the one developed for the electric machine. However, gearbox design is highly application-specific and depends on boundary conditions governed by kinematic constraints, mechanical strength, manufacturability, and other practical factors [152–154].
The standard works of Radzevich [155] and Niemann et al. [156], Niemann and Winter [157] describe the gearbox design process and its key components, including:

- the gearset for torque and speed conversion,
- shafts to support and transmit torque,
- bearings to carry loads and maintain alignment,
- a lubrication system for gear meshing,
- and a housing to enclose and support all components.

Various configurations exist for defining gearsets. In aerospace applications, spur and helical gears are typically used in stepped or planetary arrangements. Gearset performance depends on both macrogeometry and microgeometry, which influence load-bearing capacity and mechanical efficiency [154–157]. Over the years, extensive design experience has been consolidated into international standards, most notably ISO 6336 [158–161] and AGMA 2001 [162]. These standards are widely used for gearset optimization, often in combination with genetic algorithms and other heuristic methods [152, 163–168].
However, these guidelines focus primarily on gear tooth design and do not fully account for the geometry of supporting structures such as web thickness or rim shape. The design of shafts, bearings, and housings is highly case-specific and depends on the applied load conditions. These components significantly contribute to overall gearbox mass and are not easily described by first-principles analytical models. For the purposes of this work, a generalized empirical estimation method is adopted to predict gearbox mass and efficiency as functions of power, speed, and gear ratio across a wide design space.
To estimate gearbox mass and efficiency, the number of gear stages N_{st} must be determined if the total gear ratio exceeds the maximum permissible ratio per stage. In [169, 170], a random search optimization method was proposed to distribute the overall gear ratio among the individual stages. The authors concluded that the most mass-efficient configurations followed a harmonic progression of gear ratios. Although this approach offers high flexibility, it increases complexity, especially when the number of stages is not fixed in advance. To simplify the approach, a geometric progression with a constant ratio per stage is employed, which has been shown to yield near-optimal efficiency and low weight [171].
The overall gearbox ratio i_{GB} is defined as

$$i_{\mathrm{GB}} = \frac{n_{\mathrm{EM}}}{n_{\mathrm{Prop}}} = \frac{T_{\mathrm{Prop}}}{T_{\mathrm{EM}}} \tag{2.166}$$

where n_{EM} and n_{Prop} are the rotational speeds of the electric machine and propeller, respectively, and T_{EM}, T_{Prop} are the corresponding torques.

The required number of stages is then given by

$$N_{\mathrm{st}} = \left\lceil \frac{\ln i_{\mathrm{GB}}}{\ln i_{\mathrm{st,max}}} \right\rceil \tag{2.167}$$

where $i_{\mathrm{st,max}}$ is the maximum allowable gear ratio per stage, set to six. The constant gear ratio per stage is then computed as

$$i_{\mathrm{st}} = (i_{\mathrm{GB}})^{1/N_{\mathrm{st}}}. \tag{2.168}$$

2.2.1 Mass

The total gearbox mass m_{GB} is computed as the sum of the individual stage masses $m_{\mathrm{st,i}}$, that is,

$$m_{\mathrm{GB}} = \sum_{i}^{N_{\mathrm{st}}} m_{\mathrm{st,i}}. \tag{2.169}$$

The mass of each gearbox stage is estimated using a heuristic method originally developed by NASA engineers from empirical data on aircraft gearboxes. This correlation includes the mass of the lubrication system and has been slightly adapted in this work to incorporate the efficiency of the respective stage as well as convert it to metric units:

$$\begin{aligned} m_{\mathrm{st,i}} &= 0.45359237 \cdot 72 \cdot K_{\mathrm{GB}} \\ &= 0.45359237 \cdot 72 \cdot \left(\frac{P_{\mathrm{st,i}}}{746 \cdot \eta_{\mathrm{st,i}}} \right)^{0.76} \cdot \frac{(i_{\mathrm{st,i}} \cdot n_{\mathrm{st,i}})^{0.13}}{n_{\mathrm{st,i}}^{0.89}} \end{aligned} \tag{2.170}$$

where $P_{\mathrm{st,i}}$, $n_{\mathrm{st,i}}$, and $i_{\mathrm{st,i}}$ denote the input power, speed, and gear ratio of the ith stage, respectively.

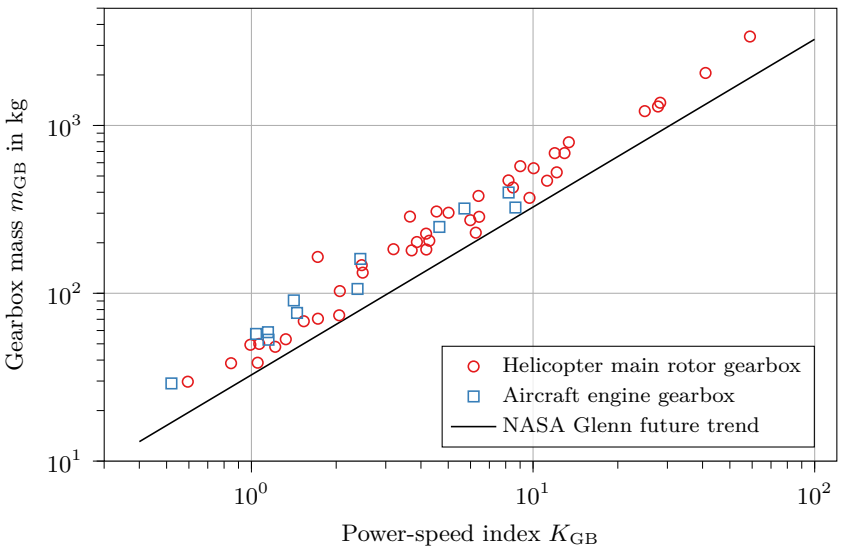

Figure 2.22: Gearbox mass versus power-speed index (see Equation (2.170)) for various helicopter and aircraft gearboxes, including continuous correlation. Adapted from [172].

Figure 2.22 shows an adapted version of the NASA market study, illustrating the correlation for a range of helicopter and aircraft gearboxes. Evaluating Equation (2.170) on a per-stage basis rather than for the entire gearbox allows the decreasing torque and thus lower mass of higher-speed stages to be captured more accurately.

2.2.2 Efficiency

The total gearbox efficiency η_{GB} is calculated as the product of the individual stage efficiencies $\eta_{\mathrm{st,i}}$:

$$\eta_{\mathrm{GB}} = \prod_{i}^{N_{\mathrm{st}}} \eta_{\mathrm{st,i}}. \tag{2.171}$$

Unlike gearbox mass, no simple and generalized correlation for efficiency is available in the literature. To address this gap, a heuristic estimation method is developed.
The approach proposed by Zakrzewski [173] is adopted to conduct a parameter study. Only planetary gearsets with three to six planet gears are considered. These configurations are compact, coaxial with the shaft, and offer high efficiency with minimal aerodynamic drag. The fan or propeller speed n_{Prop} is varied in the range $1000 - 3000\,\mathrm{min}^{-1}$, under the assumption that higher speeds are unlikely in practical applications. Similarly, the electric machine speed n_{EM} is varied within $2000 - 15\,000\,\mathrm{min}^{-1}$. The mechanical shaft power delivered to the propeller $P_{\mathrm{Prop,mech}}$ is varied over $100 - 1000\,\mathrm{kW}$, covering the majority of relevant design scenarios. The gear ratio i_{GB} is varied within the range from 2 to 5. Ratios below two typically do not yield sufficient electric machine mass reduction to justify the additional gearbox losses, while ratios above five tend to produce impractical face geometries.
The resulting finite element data has been statistically evaluated to derive a continuous approximation of stage efficiencies. Several two-dimensional fit functions were tested separately for each gear ratio, including quadratic, cubic, and exponential ones. The optimal fitting parameters were derived by means of a least-squares approximation, and the coefficient of determination R^2, also called goodness of fit, was used to assess the quality of the approximation:

$$R^2 = 1 - \frac{\sum_i (y_i - f_i)^2}{\sum_i (y_i - \bar{y})^2} \tag{2.172}$$

where the numerator describes the residual sum of squares and the denominator the total sum of squares, with y_i being the actual, f_i the predicted, and $\bar{y}$ the mean of the actual data.
The two-dimensional quadratic fit function yielded the best performance across all gear ratios:

$$f_{\mathrm{2D,quad}}(x, y) = (a\,x^2 + b\,x + c)\,(d\,y^2 + e\,y + f) + g \tag{2.173}$$

The corresponding fitting parameters and R^2 values are summarized in Table 2.5.

Table 2.5: Fitting parameters for two-dimensional quadratic fit of gearbox efficiency by gear ratio based on data from [173]

Parameter	**Gear ratio i_{st}**		
	2	**3**	**4**
a	-6.54E-17	-6.22E-14	-8.71E-14
b	8.34E-10	8.09E-07	1.09E-06
c	6.43E-02	-3.15E+03	-1.61E+02
d	-5.30E-10	1.10E-14	1.60E-12
e	-1.24E-06	1.73E-10	3.21E-10
f	1.66E+00	1.67E-03	1.45E-03
g	8.85E-01	6.27E+00	1.22E+00
R^2	0.9775	0.9850	0.9981

The 2D quadratic approximation achieves high correlation with the simulation data for all gear ratios, with R^2 values ranging from 0.9775 to 0.9981. With only seven parameters per gear ratio, the model remains computationally efficient. The parameter signs and

magnitudes produce a realistic surface shape, ensuring efficiency values remain below one and follow expected trends.
Figure 2.23 shows the contour plot of gearbox efficiency against input power and speed for a fixed gear ratio of three, based on the two-dimensional quadratic fit. The efficiency increases with higher shaft power and decreases with higher propeller speed. This trend is consistent across all other gearbox ratios.

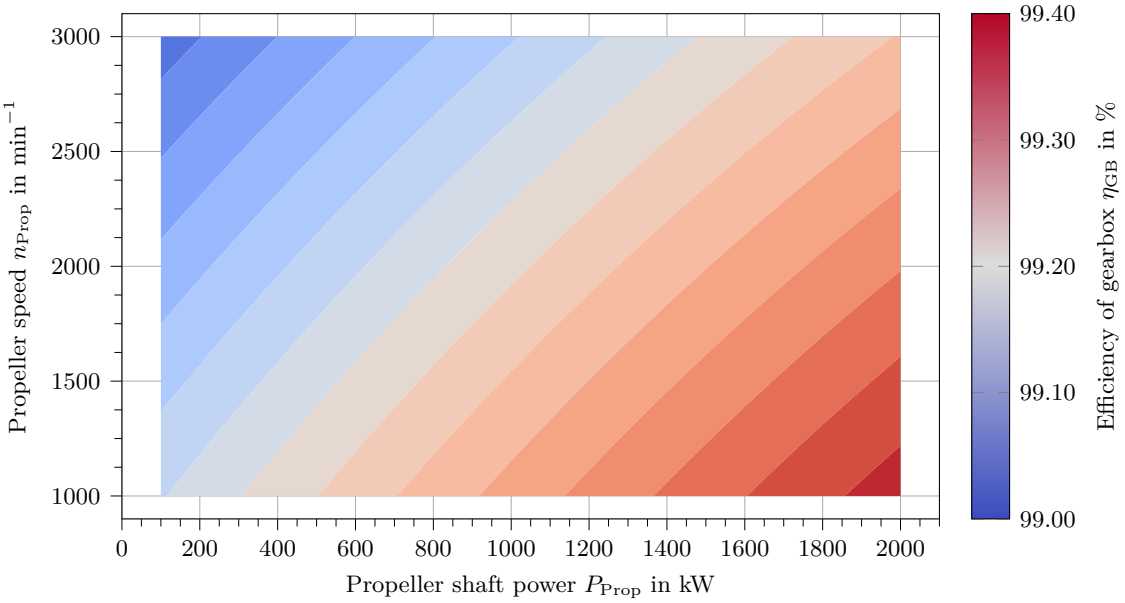

Figure 2.23: Contour plot of gearbox efficiency against input power and speed for a fixed gear ratio of $i_{\mathrm{GB}} = 3$, using the 2D quadratic fit with the optimal parameter set from Table 2.5.

2.2.3 Short Summary

An analytical tool has been developed to estimate the mass and efficiency of power transmission gearboxes based on basic design assumptions. While this method provides a useful starting point for system-level assessments, it lacks the physical depth and resolution of more advanced component models. Future work should focus on incorporating detailed physical modeling to improve accuracy and confidence in the results, as well as enhance consistency and comparability across component evaluations. The foundational work by Anderson et al. [174], Otten et al. [175] offers valuable guidance for further development.

2.3 Power Electronics

Solid-state semiconductors, such as Insulated Gate Bipolar Transistors (IGBTs) and Metal-Oxide-Semiconductor Field Effect Transistors (MOSFETs), have a wide range of applications [176]. Four types of electric power conversion can be distinguished [177], as shown in Figure 2.24, with almost all typically present in automotive and aerospace drivetrains.

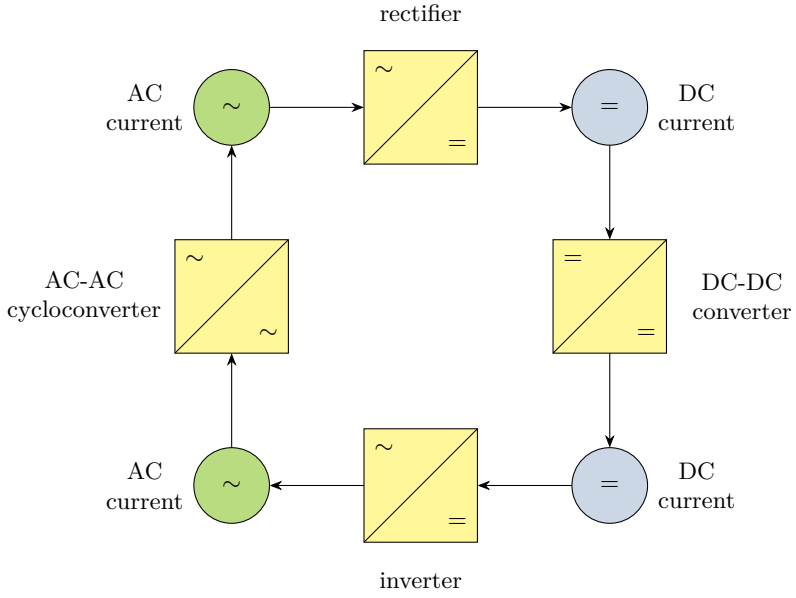

Figure 2.24: Classification of power electronics converters

Electric aerospace drivetrains employ DC-DC converters, for instance in combination with batteries, to stabilize voltage levels. This is necessary as battery voltage decreases with state of charge. DC-DC converters are also used to supply low-voltage systems for control and communication from a high-voltage bus. Additionally, DC-AC inverters convert DC power into three-phase AC to drive electric machines, while rectifiers perform the inverse operation, for example in generator applications. Since most mobile power distribution systems are based on DC, AC-AC cycloconverters are rarely used in automotive and aerospace applications.
Every power converter uses semiconductor devices such as switches and diodes to facilitate energy conversion [176, 177]. Figure 2.25 illustrates the schematic of an *n*-*p*-*n* field-effect transistor.

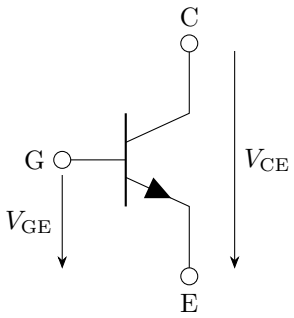

Figure 2.25: Schematics of a transistor

The device is normally off. When a positive voltage is applied to the gate (G), and the gate-emitter voltage V_{GE} exceeds the threshold while being less than the collector-emitter voltage V_{CE}, electrons are emitted from the emitter (E), flow through a narrow *n*-channel in

the p-region, and are collected at the collector (C), establishing current flow. The channel width, and therefore the current and collector-emitter resistance, is modulated by the gate voltage. If a negative gate-emitter voltage is applied, conduction stops [178]. The maximum allowable collector-emitter voltage V_{CES} is known as the blocking voltage. Common discrete voltage levels used in power applications include 600 V, 1200 V, and 1700 V [179].
The development of switchable devices such as MOSFETs and IGBTs has enabled a broader range of electric drivetrain applications due to their low losses and compact form factor. More recently, wide bandgap semiconductors such as Silicon-Carbide (SiC) and Gallium-Nitride (GaN) have enabled highly power-dense and efficient converters, particularly suited for high switching frequencies [180].
The following sections provide analytical models and design considerations for DC-AC inverters, AC-DC rectifiers, and DC-DC converters. Wintrich et al. [179] offers a comprehensive overview of power semiconductor applications.

2.3.1 DC-AC Inverters and AC-DC Rectifiers

DC-AC inverters and AC-DC rectifiers are among the most critical components in an electric drivetrain, as they are required in several drivetrain architectures shown in Figure 1.4. In this investigation, only DC-AC inverters are analyzed in detail. Since only bidirectional topologies are considered, AC-DC rectifiers exhibit similar characteristics in terms of mass and efficiency and therefore do not require separate modelling. A power inverter comprises several functional parts that must be considered in the design process, as illustrated in Figure 2.26.

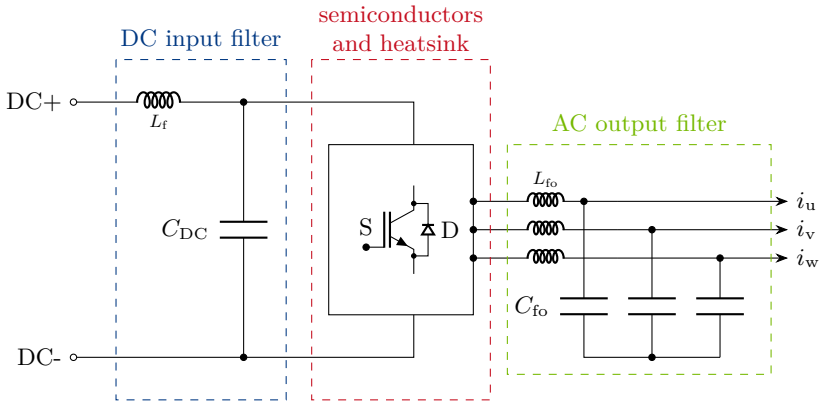

Figure 2.26: Voltage source inverter with DC input filter, the active part consisting of semiconductors and heatsink, and an AC output filter. The control unit with gate drivers, busbars, and connectors, as well as the housing, are not shown.

A DC source is connected to a DC input filter, typically of LC type, to limit voltage and current ripple at the inverter input. The active part of the inverter, comprising semiconductors and a heatsink, generates a sinusoidal three-phase AC current. The inverter output is connected to a filter to attenuate harmonics. Components such as the control unit, gate drivers, busbars, connectors, and the housing are omitted in the figure but are considered in the analysis.
The following sections address different voltage source inverter topologies, the electrothermal analysis of semiconductor power modules in combination with a heatsink, and the design of DC-link capacitors for voltage ripple mitigation. Additionally, gate driver boards, busbars, power connectors, and housing design are considered. In battery-powered systems, a dedicated DC input filter is typically unnecessary, as the battery provides a stable DC voltage with inherently low ripple due to its low output impedance. The primary purpose

of AC output filters is to reduce overvoltages caused by impedance mismatches between motor and cable [181]. The critical cable length, given in Equation (2.155), is typically above 2 m, even for high voltage slew rates up to $^{\mathrm{d}V}/_{\mathrm{d}t} = 50\,000\,\mathrm{V\,\mu s^{-1}}$ [182]. Therefore, AC output filters can be neglected in aerospace applications, provided the power inverters are installed in close proximity to the electric machines.

2.3.1.1 Topologies of Voltage Source Inverters

Adjustable-speed drives are controlled by voltage waveforms. For three-phase AC systems, voltage source inverters are used to provide sinusoidal AC signals with controllable magnitude, frequency, and phase [176]. Among the various available inverter and rectifier topologies, the two-level (2L) inverter is the most widely employed due to its simplicity, low weight, and cost. For applications requiring higher switching frequencies, a transition to wide-bandgap devices such as SiC MOSFETs or GaN transistors is possible, albeit at increased cost. Numerous alternative topologies have also been proposed and investigated [183, 184].
In addition to the standard two-level topology, this thesis considers two three-level topologies: the three-level neutral-point clamped (3LNPC) and the three-level T-type neutral-point clamped (3LTNPC) inverter [183–186]. The primary motivations for employing higher-level topologies are improved efficiency at elevated switching frequencies and the ability to operate at higher voltages without requiring series-connected semiconductors. An additional benefit is the potential reduction in the size of passive components such as filters, owing to the lower harmonic content of the output voltage. However, these advantages come at the cost of increased complexity and a higher number of semiconductor devices, which generally lead to increased system cost and weight [184, 187–189].

2L inverter

Figure 2.27 shows the standard 2L inverter topology for a three-phase system, with an input voltage V_{DC} on the DC side and the three output voltages $v_{\mathrm{u,v,w}}$ on the AC side, connected to a load, e.g., an electric machine [183, 184, 190].

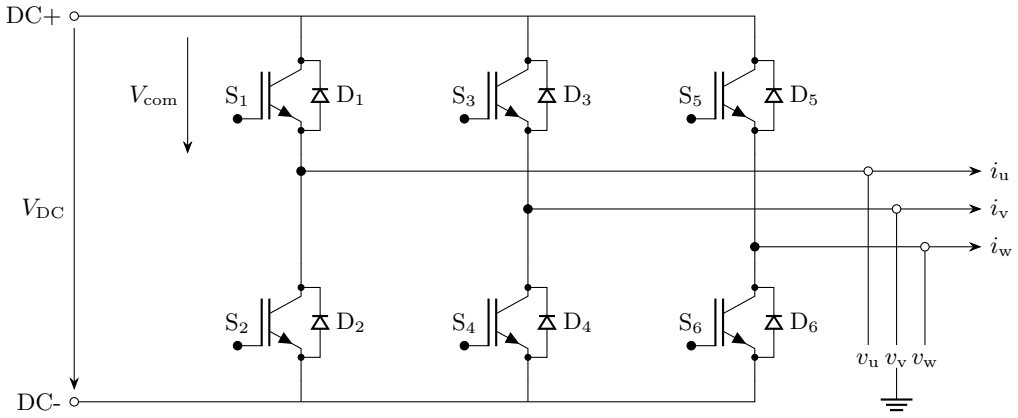

Figure 2.27: Schematics of a 2L inverter connected to a DC source and an AC load

The inverter consists of three phase legs, each comprising a pair of semiconductor switches configured as a half-bridge. Each switch is formed by an actively controlled transistor switch(S), typically an IGBT or MOSFET, in parallel with a freewheeling diode (D). The six switches yield eight (2^3) possible switching states, since the switches S_1 and S_2, S_3 and S_4, and S_5 and S_6 operate in complementary pairs. These eight states include six active output voltage states and two zero-voltage states [184, 190].
Table 2.6 lists the two active switching states of a single phase and the corresponding output voltages.

Table 2.6: Allowable switching states of a 2L inverter

switch state	S_1	S_2	v_u
1	1	0	$+\frac{V_{DC}}{2}$
2	0	1	$-\frac{V_{DC}}{2}$

If both switches are off ($S_1 = S_2 = 0$), no output voltage is generated. Both switches must not be on simultaneously ($S_1 = S_2 = 1$), as this would create a short circuit between DC+ and DC-. Thus, only one of the switches can be on at any given time, while the other is off, resulting in two valid states per phase. In the 2L topology, all semiconductor devices are subjected to the full DC-link voltage V_{DC} in their blocking state. Since each switch transitions under this voltage, it defines the commutating voltage:

$$V_{com} = V_{DC} \tag{2.174}$$

as illustrated in Figure 2.27 [183].
Figure 2.28 shows the current paths and commutation states for one half-bridge. When the output voltage and current are both positive, switch S_1 conducts. If the current reverses, diode D_1 conducts (Figure 2.28a). Depending on the sign of the output power gradient, the commutation is termed forced (capacitive) if the gradient is negative, or natural (inductive) otherwise. The figure also marks the locations where switching losses occur.

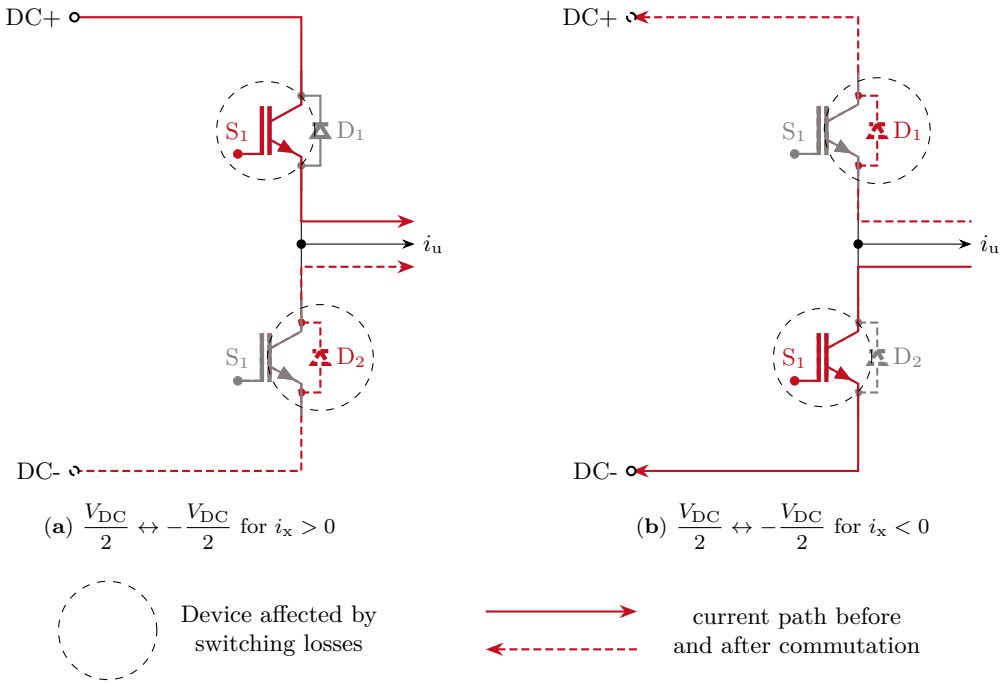

Figure 2.28: Possible commutations of 2L inverters. Solid red lines indicate current paths before commutation; dashed red lines show the paths after commutation. Dashed circles mark locations of switching losses.

3LNPC inverter

A Three-Level Neutral Point Clamped (3LNPC) inverter is one of the multi-level topologies considered in this thesis. Figure 2.29a shows one phase leg of a 3LNPC inverter.
This topology comprises four transistor-diode pairs and two additional clamping diodes connected to the neutral point. Compared to the two-level inverter, it doubles the number of semiconductor devices. The DC link is split into two halves, requiring voltage balancing,

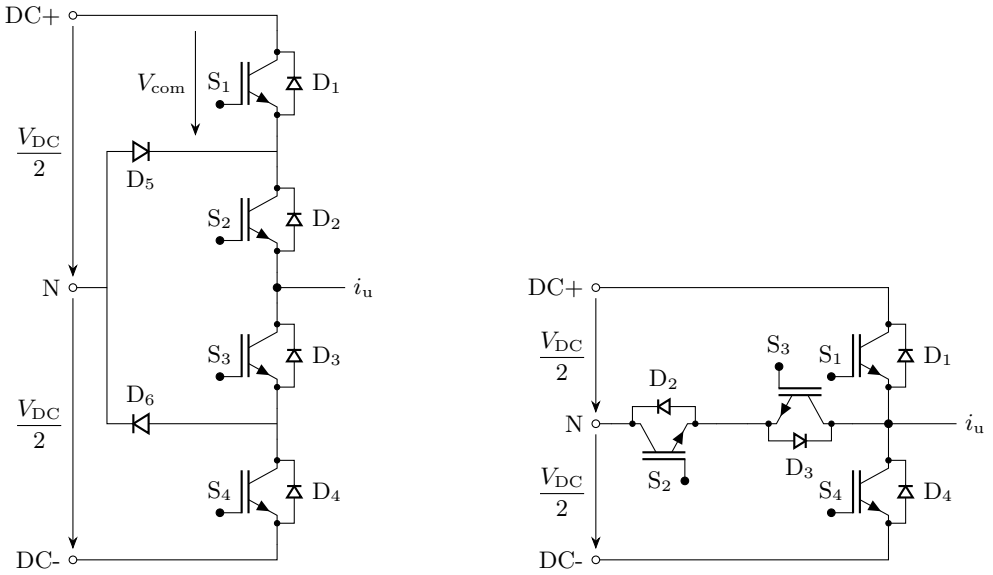

(**a**) 3LNPC (**b**) 3LTNPC

Figure 2.29: Schematics of a single phase leg of different three-level inverter topologies

but this also reduces the commutating voltage to

$$V_{\text{com}} = \frac{V_{\text{DC}}}{2}. \tag{2.175}$$

Permissible switching states include all switches off, only S_2 or S_3 on, or any two adjacent switches on, as shown in Table 2.7. Certain states are destructive and must be strictly avoided: if three adjacent switches are on, a short circuit of the upper or lower half of the DC link occurs. If three non-adjacent switches are on, the full DC link voltage may be applied to either S_2 or S_3 [189].

Table 2.7: Allowable switching states of a 3LNPC inverter

switch state	$\mathbf{S_1}$	$\mathbf{S_2}$	$\mathbf{S_3}$	$\mathbf{S_4}$	$\mathbf{v}_{\text{u}}$
1	1	1	0	0	$+\frac{V_{\text{DC}}}{2}$
2	0	1	0	0	$+\frac{V_{\text{DC}}}{2}$
3	0	1	1	0	0
4	0	0	1	0	$-\frac{V_{\text{DC}}}{2}$
5	0	0	1	1	$-\frac{V_{\text{DC}}}{2}$

3LTNPC inverter

Another option is the Three-Level T-Type Neutral Point Clamped (3LTNPC) inverter, illustrated in Figure 2.29b. In contrast to the 3LNPC topology, this configuration does not require additional clamping diodes. Instead, the outer switches S_1 and S_4 must block and commutate the full DC link voltage, whereas the inner switches S_2 and S_3 operate at half the DC link voltage:

$$V_{\text{com}} = \begin{cases} \frac{V_{\text{DC}}}{2} & \text{S}_2, \text{S}_3 \\ V_{\text{DC}} & \text{S}_1, \text{S}_4. \end{cases} \tag{2.176}$$

All switching states are allowed except for combinations where two non-adjacent switches are turned on simultaneously. Such configurations result in a short circuit of either the

upper or lower half of the DC link, or a direct short between DC+ and DC- [189], as summarized in Table 2.8.

Table 2.8: Allowable switching states of a 3LTNPC inverter

switch state	$\mathbf{S_1}$	$\mathbf{S_2}$	$\mathbf{S_3}$	$\mathbf{S_4}$	$\mathbf{v_u}$
1	1	0	0	0	$+\frac{V_{\mathrm{DC}}}{2}$
2	1	1	0	0	$+\frac{V_{\mathrm{DC}}}{2}$
3	0	1	0	0	0
4	0	1	1	0	0
5	0	0	1	0	$-\frac{V_{\mathrm{DC}}}{2}$
6	0	0	1	1	$-\frac{V_{\mathrm{DC}}}{2}$
7	0	0	0	1	$-\frac{V_{\mathrm{DC}}}{2}$

2.3.1.2 Modulation Strategies

To realize the switching states described in Section 2.3.1.1, the transistors must be switched on and off at the correct instants. This technique is known as modulation [191–193]. Today, modulation is predominantly achieved using pulse width modulation methods. A key parameter in this context is the modulation index m_{a},

$$m_{\mathrm{a}} = \frac{\hat{V}_{1,\mathrm{ph}}}{\left(\frac{V_{\mathrm{DC}}}{2}\right)} \tag{2.177}$$

defined as the ratio of the amplitude of the fundamental phase voltage at the inverter output to half the DC link voltage. It characterizes the voltage utilization of the inverter output signal [192].

Carrier-Based Sinusoidal Pulse Width Modulation

Carrier-based pulse width modulation schemes, such as sinusoidal pulse width modulation, use a sinusoidal reference voltage v_{ref} that is compared against a high-frequency triangular carrier signal v_{c}. The carrier signal operates at a switching frequency f_{sw}, which is related to the fundamental electrical frequency f_{el} by the frequency ratio m_{f}:

$$f_{\mathrm{sw}} = m_{\mathrm{f}}\, f_{\mathrm{el}}. \tag{2.178}$$

In the case of a two-level inverter, the switching states $\mathrm{S_u}$, $\mathrm{S_v}$, and $\mathrm{S_w}$ for the three phase legs are defined as

$$v_{\mathrm{ref}} \begin{cases} > v_{\mathrm{c}} & \mathrm{S_x} = 1 \\ < v_{\mathrm{c}} & \mathrm{S_x} = 0. \end{cases} \tag{2.179}$$

Based on the switching functions, the corresponding pole voltages v_{un}, v_{vn}, and v_{wn} are calculated as

$$v_{\mathrm{xn}} = \left(\mathrm{S_x} - \frac{1}{2}\right) V_{\mathrm{DC}} \tag{2.180}$$

while the neutral point voltage v_{sn} in a wye-connected circuit is given by the average of the three pole voltages:

$$v_{\mathrm{sn}} = \frac{V_{\mathrm{DC}}}{3}\left(\mathrm{S_u} + \mathrm{S_v} + \mathrm{S_w} - \frac{3}{2}\right). \tag{2.181}$$

The top half of Figure 2.30 illustrates one period of an exemplary sinusoidal reference signal and a triangular carrier signal.

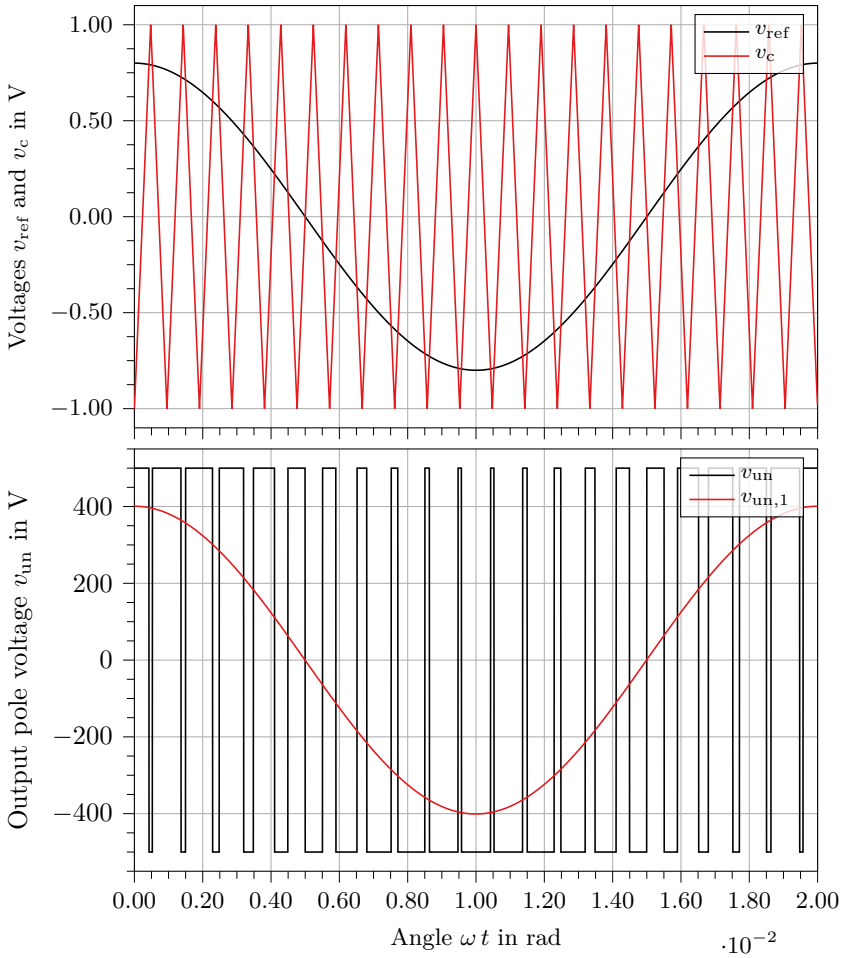

Figure 2.30: Pulse width modulation. (top) Sinusoidal reference signal v_{ref} ($m_a = 0.8$) and triangular carrier signal v_c ($m_f = 21$); (bottom) output pole voltage v_{un} and its fundamental component $v_{un,1}$ for phase U. A DC link voltage $V_{DC} = 1000\,\mathrm{V}$ is employed.

The bottom half of Figure 2.30 shows the resulting pole voltage v_{un} and its fundamental component $v_{un,1}$, which again is a sinusoidal waveform. Its amplitude is 800 V, consistent with the specified modulation index and DC link voltage.
The phase voltages v_{us}, v_{vs}, and v_{ws} can be derived from the switching functions as follows:

$$v_{us} = \frac{V_{DC}}{3}\,(2S_u - S_v - S_w) \tag{2.182}$$

$$v_{vs} = \frac{V_{DC}}{3}\,(-S_u + 2S_v - S_w) \tag{2.183}$$

$$v_{ws} = \frac{V_{DC}}{3}\,(-S_u - S_v + 2S_w) \tag{2.184}$$

Space Vector Modulation

In contrast to carrier based Pulse Width Modulation, where the reference signals are modulated individually, Space Vector Modulation (SVM) employs a single reference vector in the complex plane. The advantages of space vector modulation include a higher achievable fundamental output voltage, approximately 15.5 % greater than that of sinusoidal Pulse Width Modulation, as well as reduced harmonic distortion, lower torque ripple, and decreased switching losses [192–194].
The eight switching states introduced in Section 2.3.1.1 correspond to six active output voltage vectors $\overrightarrow{V}_1$ to $\overrightarrow{V}_6$, each having a length $|V|$ of $^2/_3\,V_{DC}$, and two zero voltage vectors $\overrightarrow{V}_0$ and $\overrightarrow{V}_7$ in the dq-frame, as illustrated in Figure 2.31a.

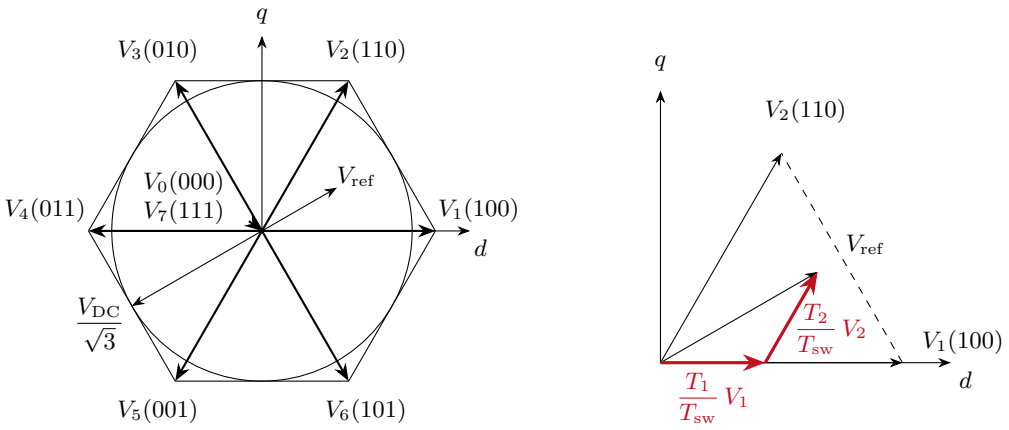

(**a**) Space vector hexagon

(**b**) Modulation process for voltage generation

Figure 2.31: Space vector modulation principles according to [192]

The output vectors form a hexagon, within which the reference voltage vector must remain. Consequently, the maximum achievable reference voltage and modulation index are given as

$$|V_{\text{ref}}|_{\max} = \frac{V_{\text{DC}}}{\sqrt{3}}, \tag{2.185}$$

$$m_{\text{a,max}} = \frac{2}{\sqrt{3}}. \tag{2.186}$$

The reference vector is synthesized by time-weighted application of the two adjacent active vectors and the zero vectors, based on the volt-second balancing principle over a switching period T_{sw} [192, 193]. The required on-time durations are determined from

$$\int_0^{T_{\text{sw}}} V_{\text{ref}}\,\mathrm{d}t = \int_0^{T_1} V_{\text{n}}\,\mathrm{d}t + \int_{T_1}^{T_1+T_2} V_{n+1}\,\mathrm{d}t + \int_{T_1+T_2}^{T_{\text{sw}}} V_{0,7}\,\mathrm{d}t. \tag{2.187}$$

Assuming constant V_{DC} during the switching period, the reference vector can be decomposed into two components aligned with the adjacent output vectors. If the vector lies within the first sector, as shown in Figure 2.31b, the corresponding on-times are given by [192]

$$T_1 = \frac{\sqrt{3}}{2}\, m_{\text{a}}\, \sin\left(\frac{\pi}{3} - \omega t\right) T_{\text{sw}}, \tag{2.188}$$

$$T_2 = \frac{\sqrt{3}}{2}\, m_{\text{a}}\, \sin(\omega t)\, T_{\text{sw}}, \tag{2.189}$$

$$T_{0,7} = T_{\text{sw}} - T_1 - T_2. \tag{2.190}$$

The on-times for the remaining sectors can be derived analogously. The relative on-times, such as $\delta_{(100)}$, denote the ratio of individual on-times to the total switching period.
A key advantage of space vector modulation is the flexibility in distributing the vectors within the switching period without altering their average. The most commonly used sequence for switching transitions is

$$V_0(000) \rightarrow V_1(100) \rightarrow V_2(110) \rightarrow V_7(111) \rightarrow V_2(110) \rightarrow V_1(100) \rightarrow V_0(000), \tag{2.191}$$

which minimizes switching losses, as only one transistor toggles at each transition. Figure 2.32 shows the pole and phase voltages for one electrical period under space vector modulation, revealing the characteristic double-hump shape.

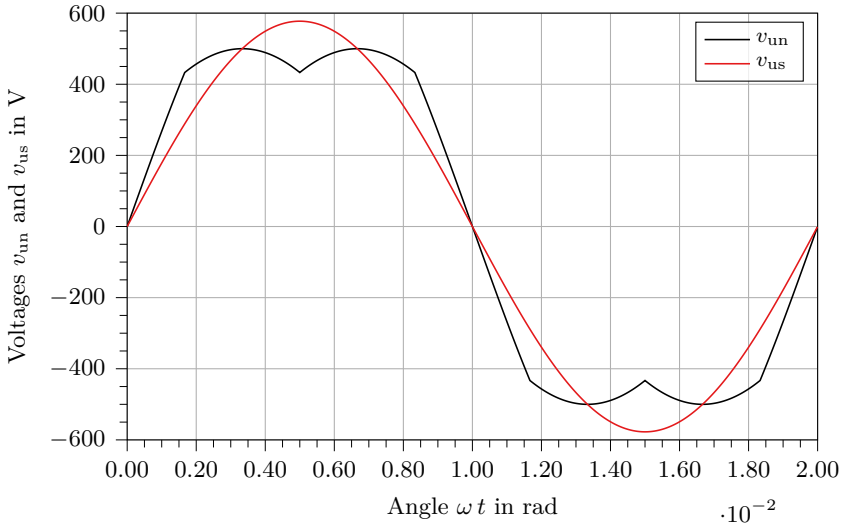

Figure 2.32: Output pole and phase voltage of phase u for SVM with $V_{\mathrm{DC}} = 1000\,\mathrm{V}$, $m_{\mathrm{a}} = \frac{2}{\sqrt{3}}$, and $m_{\mathrm{f}} = 21$.

For ease of implementation and reduced computational effort, space vector modulation can also be translated into an equivalent carrier-based pulse width modulation scheme. In this approach, the sinusoidal reference is modified by adding a common-mode signal, and a center-aligned triangular carrier is used [194–198].

2.3.1.3 Electro-Thermal Performance of Semiconductor Modules

2.3.1.3.1 Voltage and Current Rating

The maximum operating collector-emitter voltage V_{CE} is typically equal to the commutation voltage in most topologies, with some exceptions such as switches S_1 and S_4 in a 3LTNPC. Semiconductors must therefore be selected such that their collector-emitter voltage remains below or equal to their blocking voltage. If the required commutation voltage exceeds the blocking capability, several devices can be connected in series to accommodate the higher voltage. However, the practical utilization of the rated blocking voltage, and thus the device's reliability, depends on the applied DC link voltage, the junction temperature T_{j} of the semiconductor, and the operating altitude h, due to the exponentially increased exposure to cosmic radiation at higher altitudes [199–202]. Cosmic radiation may lead to single-event burnout failures when a high-energy particle strikes the semiconductor. The failure rate is measured in Failures In Time (FIT), where one Failure In Time corresponds to one failure per 10^9 h.
Manufacturers such as ABB Power Grids Switzerland Ltd. [201] and Semikron International GmbH [203] define the Failure In Time rate λ_{FIT} per switch as

$$\lambda_{\mathrm{FIT}}(V_{\mathrm{DC}}, T_{\mathrm{j}}, h) = C_3 \exp\left(\frac{C_2}{C_2 - V_{\mathrm{DC}}}\right) \exp\left(\frac{25 - T_{\mathrm{j}}}{47.6}\right) \exp\left(\frac{1 - \left(1 - \frac{h}{44300}\right)^{5.26}}{0.143}\right) \tag{2.192}$$

with C_1, C_2, and C_3 being device-specific parameters.
A 2L inverter comprising six modules operating at a DC Link voltage V_{DC} of 1200 V and an altitude of 6000 m would statistically experience one failure within 19 years ($1/\lambda_{\mathrm{FIT}}$). If a longer or shorter lifetime is required, the failure rate must be adjusted accordingly.

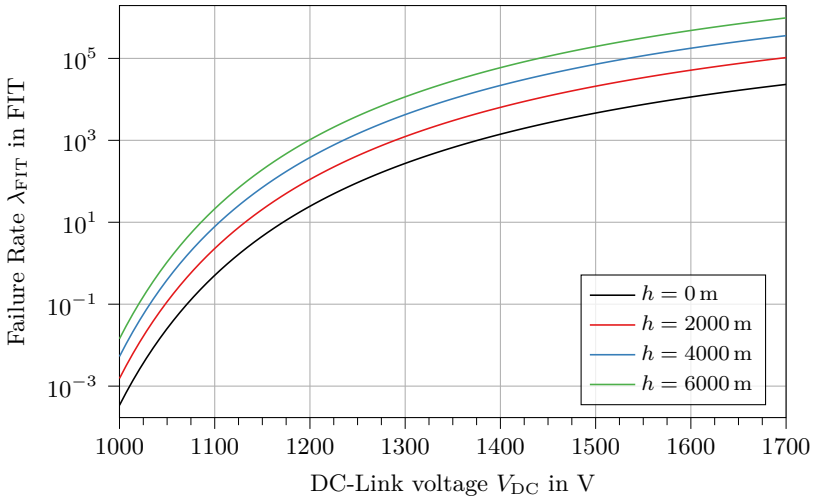

Figure 2.33: Failure In Time rate of a 1700 V IGBT module (ABB 5SNG 0225R170300) for varying DC-link voltages and altitudes above sea level at a junction temperature of $T_{\mathrm{j}} = 125\,^{\circ}\mathrm{C}$. The fit parameters are $C_1 = 773\,\mathrm{V}$, $C_2 = 5422\,\mathrm{V}$, and $C_3 = 1.15 \times 10^8$ FIT according to [201].

Figure 2.33 shows that an increase in DC-link voltage leads to an exponential increase in the failure rate. Conversely, increasing the junction temperature decreases the failure rate exponentially, while increasing altitude leads to an exponential rise in the failure rate [201, 203]. Recent studies indicate that SiC-based semiconductors offer improved robustness compared to their Si counterparts [200]. For practical design, the allowable utilization

$$z = \frac{V_{\mathrm{CE}}}{V_{\mathrm{CES}}} \tag{2.193}$$

is thus set to 60 % for Si and 75 % for SiC chips.
Regarding current ratings, the power losses generated during operation determine the semiconductor's operating temperature, which must remain within the limits specified by the manufacturer. Current ratings are typically provided for pre-assembled components such as half-bridges. If a higher current is required, either multiple devices must be paralleled or a higher-rated product must be selected.

2.3.1.3.2 Linearization of Semiconductor Characteristics

Manufacturers provide datasheets, such as in [204], containing the necessary information for the transistor and diode properties. A linearization around the reference point is employed to enable analytical calculations, as losses are dependent on the operating point. Figure 2.34 shows the transistor and diode output characteristics, as well as the loss characteristics, versus the collector current.
Figure 2.34a shows the current flowing through the collector I_{C} versus the collector-emitter saturation voltage $V_{\mathrm{CE,sat}}$ at a certain reference temperature (in this case, $T_{\mathrm{ref}} = 125\,^{\circ}\mathrm{C}$). The dashed line represents the linearization around the reference point for the transistor:

$$V_{\mathrm{CE}}(T_{\mathrm{j}}) = V_{\mathrm{CE,0}}(T_{\mathrm{j}}) + r_{\mathrm{on,T}}(T_{\mathrm{j}})\, I_{\mathrm{C}} \tag{2.194}$$

where $V_{\mathrm{CE,0}}$ is the threshold voltage and $r_{\mathrm{on,T}}$ is the on-state resistance of the transistor. Both the threshold voltage and the on-state resistance depend on temperature. Therefore, two thermal coefficients, $\alpha_{V_{\mathrm{CE,0}}}$ and $\alpha_{r_{\mathrm{on,T}}}$, are calculated from two reference temperatures, usually $T_{\mathrm{ref1}} = 25\,^{\circ}\mathrm{C}$ and $T_{\mathrm{ref2}} = 125\,^{\circ}\mathrm{C}$:

$$\alpha_{V_{\mathrm{CE,0}}} = \frac{V_{\mathrm{CE,0}}(T_{\mathrm{ref2}}) - V_{\mathrm{CE,0}}(T_{\mathrm{ref1}})}{T_{\mathrm{ref2}} - T_{\mathrm{ref1}}} \tag{2.195}$$

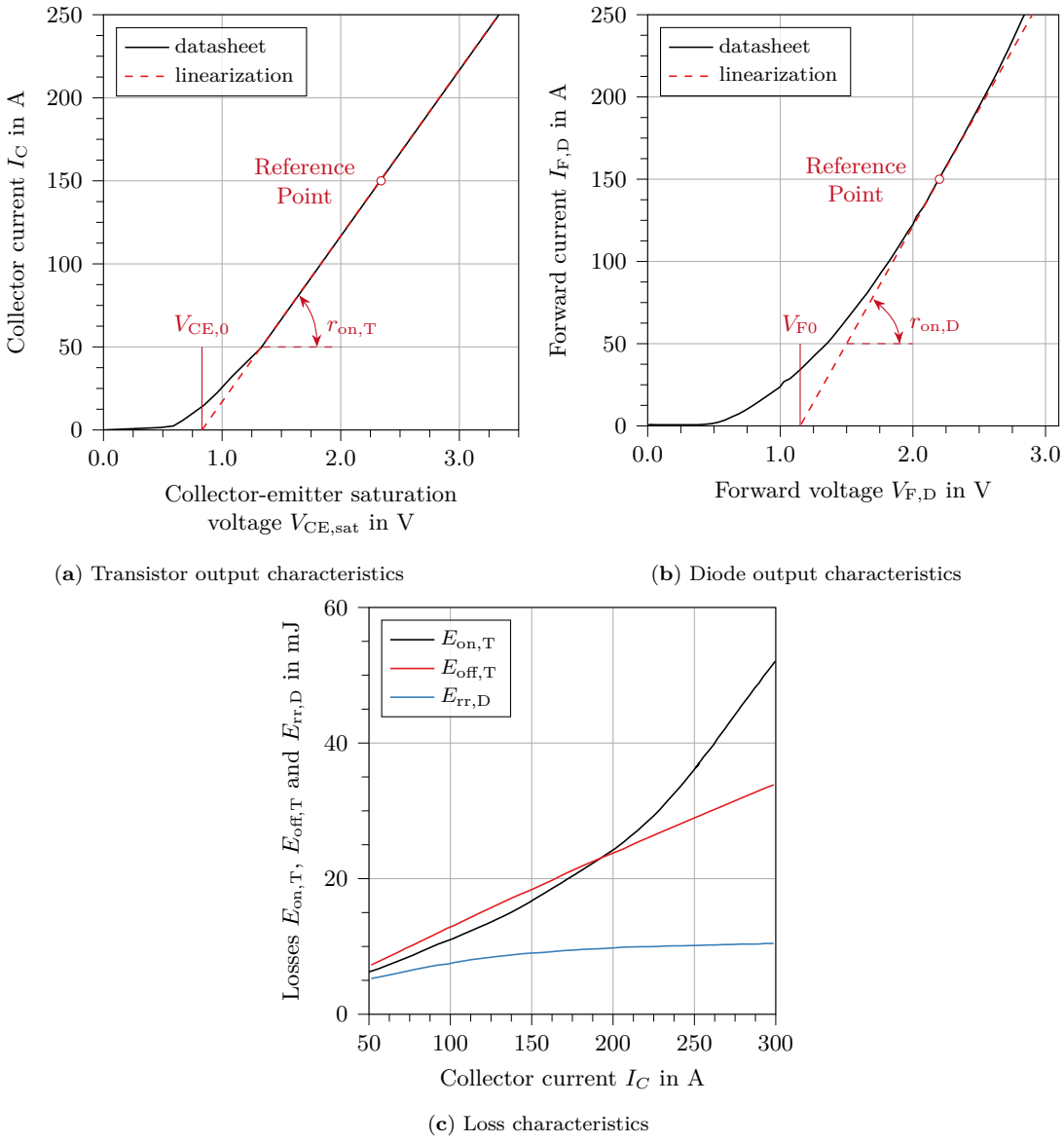

(**a**) Transistor output characteristics

(**b**) Diode output characteristics

(**c**) Loss characteristics

Figure 2.34: Output and loss characteristics of a Semikron SEMiX151GB12E4 module rated for $V_{CES} = 1200\,\text{V}$ and $I_C = 150\,\text{A}$, including a linearization around the reference point. Data from [204]

$$\alpha_{r_{on,T}} = \frac{r_{on,T}(T_{ref2}) - r_{on,T}(T_{ref1})}{T_{ref2} - T_{ref1}}. \tag{2.196}$$

These coefficients can now be used to define current- and temperature-dependent expressions for the threshold voltage, on-state resistance, and collector-emitter voltage of the transistor as:

$$V_{CE,0}(T_j) = V_{CE,0}(T_{ref1}) + \alpha_{V_{CE,0}}\,(T_j - T_{ref1}) \tag{2.197}$$

$$r_{on,T}(T_j) = r_{on,T}(T_{ref1}) + \alpha_{r_{on,T}}\,(T_j - T_{ref1}) \tag{2.198}$$

$$V_{CE}(I_C, T_j) = V_{CE,0}(T_{ref1}) + (\alpha_{V_{CE,0}} + \alpha_{r_{on,T}}\,I_C)\,(T_j - T_{ref1}). \tag{2.199}$$

The same procedure can be applied to derive the linearized characteristics for the diode using the data provided in Figure 2.34b. To calculate the switching losses, manufacturers provide data such as those shown in Figure 2.34c, which depicts the loss energies: $E_{on,T}$ for switching on the transistor, $E_{off,T}$ for switching off, and $E_{rr,D}$ for reverse recovery (switching off) of the diode.

2.3.1.3.3 Power Loss Calculation

Losses of power electronic devices such as transistors and diodes can be distinguished depending on static and dynamic, i.e. switching, states within a switching cycle. Conduction losses Q_{con} are the most important type of static losses, while switching losses occur during switch-on $Q_{\mathrm{sw,on}}$ and switch-off $Q_{\mathrm{sw,off}}$ processes. Each of these states is prone to energy dissipation, which leads to heating of the semiconductors and to the total power loss of the inverter. Figure 2.35 shows the different types of losses. Losses marked red will be covered in this analysis, as blocking and driving losses are negligible [179].

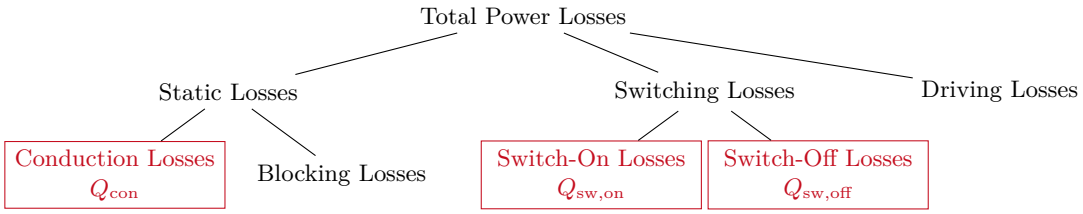

Figure 2.35: Loss components of semiconductors according to [179]

While all three components contribute to the total loss in transistors, given by

$$Q_{\mathrm{tot,T}} = Q_{\mathrm{con,T}} + Q_{\mathrm{sw,on,T}} + Q_{\mathrm{sw,off,T}}, \tag{2.200}$$

switch-on losses can be neglected for fast-switching diodes. Therefore, the total loss in a diode is given by

$$Q_{\mathrm{tot,D}} = Q_{\mathrm{con,D}} + Q_{\mathrm{sw,off,D}}. \tag{2.201}$$

Here, the subscripts T and D refer to the transistor and diode, respectively.
The conducting and switching losses of a 2L inverter can be calculated analytically from [179], assuming that the deadtimes of switches and diodes are negligible, the junction temperatures are temporarily constant, and the switching frequency is much higher than the fundamental output frequency. The losses of a transistor are given by

$$Q_{\mathrm{con,T}} = \left(\frac{1}{2\pi} + \frac{m_{\mathrm{a}}\,\cos\varphi_{\mathrm{PF}}}{8}\right) V_{\mathrm{CE,0}}\,\hat{I}_{\mathrm{u}} \; + \left(\frac{1}{8} + \frac{m_{\mathrm{a}}\,\cos\varphi_{\mathrm{PF}}}{3\pi}\right) r_{\mathrm{con,T}}\,\hat{I}_{\mathrm{u}}^2 \tag{2.202}$$

$$Q_{\mathrm{sw,T}} = f_{\mathrm{sw}}\,(E_{\mathrm{on,T}} + E_{\mathrm{off,T}})\frac{\sqrt{2}}{\pi}\left(\frac{I_{\mathrm{u}}}{I_{\mathrm{ref}}}\right)^{K_{\mathrm{I,T}}} \left(\frac{V_{\mathrm{com}}}{V_{\mathrm{ref}}}\right)^{K_{\mathrm{V,T}}} (1 + \alpha_{\mathrm{E,T}}\,(T_{\mathrm{j,T}} - T_{\mathrm{ref}})) \tag{2.203}$$

while the losses of the antiparallel diode are defined as

$$Q_{\mathrm{con,D}} = \left(\frac{1}{2\pi} - \frac{m_{\mathrm{a}}\,\cos\varphi_{\mathrm{PF}}}{8}\right) V_{\mathrm{F,0}}\,\hat{I}_{\mathrm{u}} \; + \left(\frac{1}{8} - \frac{m_{\mathrm{a}}\,\cos\varphi_{\mathrm{PF}}}{3\pi}\right) r_{\mathrm{con,D}}\,\hat{I}_{\mathrm{u}}^2 \tag{2.204}$$

$$Q_{\mathrm{sw,D}} = f_{\mathrm{sw}}\,E_{\mathrm{rr,D}}\frac{\sqrt{2}}{\pi}\left(\frac{I_{\mathrm{u}}}{I_{\mathrm{ref}}}\right)^{K_{\mathrm{I,D}}} \left(\frac{V_{\mathrm{com}}}{V_{\mathrm{ref}}}\right)^{K_{\mathrm{V,D}}} (1 + \alpha_{\mathrm{E,D}}\,(T_{\mathrm{j,D}} - T_{\mathrm{ref}})) \tag{2.205}$$

where $E_{\mathrm{on,T}}$, $E_{\mathrm{off,T}}$, $E_{\mathrm{rr,D}}$, $V_{\mathrm{CE,0}}$, $V_{\mathrm{F,0}}$, $r_{\mathrm{on,T}}$ and $r_{\mathrm{on,D}}$ are datasheet values, e.g., from [204], for a reference point V_{ref}, I_{ref} and T_{ref} and operating parameters I_{u}, V_{com} and $T_{\mathrm{j,T}}$ or $T_{\mathrm{j,D}}$ respectively. It is important to note that the losses are temperature dependent, thus an interactive approach for the thermal and loss analysis has to be chosen. The exponents which describe the current and voltage dependency of the switching losses and the coefficients which show the temperature dependency of the switching losses are also given by manufacturers and usually are $K_{\mathrm{I,T}} = 1.0$, $K_{\mathrm{I,D}} = 0.6$, $K_{\mathrm{V,T}} = 1.3$, $K_{\mathrm{V,D}} = 0.6$, $\alpha_{\mathrm{E,T}} = 0.003\,\mathrm{K}^{-1}$ and $\alpha_{\mathrm{E,D}} = 0.006\,\mathrm{K}^{-1}$ [189]. Loss calculation for other topologies is based on [183, 189, 205, 206].

Finally, the total semiconductor losses within a 2L topology are given by

$$Q_{\mathrm{SC}} = 6\left(Q_{\mathrm{con,T}} + Q_{\mathrm{con,D}} + Q_{\mathrm{sw,T}} + Q_{\mathrm{sw,D}}\right) \tag{2.206}$$

2.3.1.3.4 Lumped Parameter Network Model of Semiconductor Modules

The switches and diodes in power electronics are very intense and concentrated sources of heat, thus they have to be cooled sufficiently to avoid overheating and destruction. Therefore, heat sinks, either air or liquid cooled, are applied to facilitate good heat transfer to a cooling medium. As heat sinks usually consist of thermally good conducting materials such as aluminum or copper, their weight fraction is significant and has to be assessed. As mentioned in the previous paragraph, the temperature distribution and the losses can only be calculated iteratively as they rely on each other. Therefore, a lumped parameter thermal network for the heat path from the semiconductor junctions to a heat sink is established in Figure 2.36.

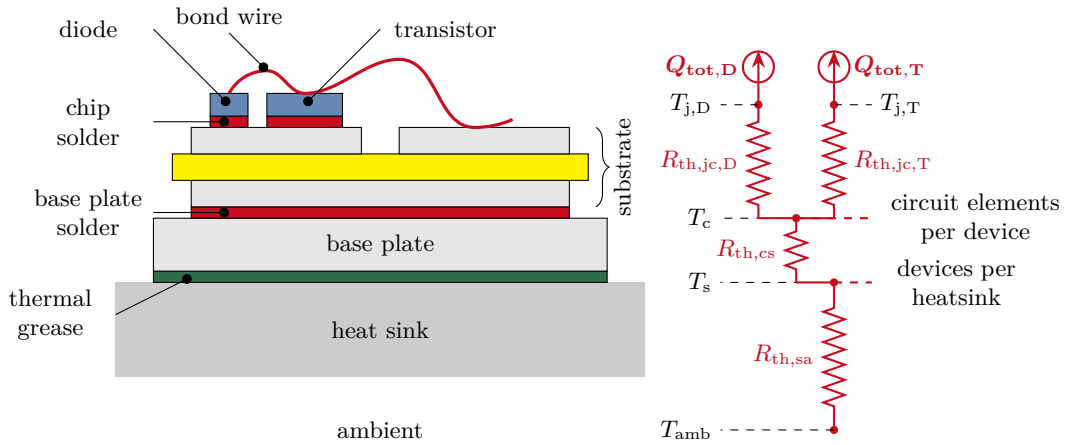

Figure 2.36: Structural layout and thermal resistance network of a semiconductor module with transistor and antiparallel diode [179]

Within pre-configured semiconductor modules, usually a number of switches (IGBTs, MOSFETs) and the corresponding antiparallel diodes are integrated in parallel. They are connected via a bond wire and soldered onto a substrate consisting of two copper layers separated by a ceramic such as alumina (Al_2O_3) or aluminum nitride (AlN) acting as a dielectric. The substrate is soldered onto a base plate which can be directly mounted onto a heatsink. Thermal grease is used to enhance the heat distribution [179]. Both liquid and air-cooled applications can be used. The theory to calculate the corresponding thermal resistances from sink to ambient $R_{\mathrm{th,sa}}$ is explained in Section 2.5. The thermal resistance from junction to case $R_{\mathrm{th,jc,T}}$ and $R_{\mathrm{th,jc,D}}$ as well as from case to sink $R_{\mathrm{th,cs}}$ are usually provided in the manufacturer's datasheet. Newer generations of modules come without base plate to reduce the thermal resistance and improve heat flow and thus performance [179].
Several assumptions are made to ease the calculation of the temperature distribution. The steady-state temperatures at ambient T_{amb}, heat sink T_{s}, case T_{c} and the junctions $T_{\mathrm{j,T}}$ and $T_{\mathrm{j,D}}$ are considered constant independent of the number of devices per heatsink and circuit elements per device, even though the cooling method will result in spatially differing temperatures. Furthermore, the total losses of the semiconductors are distributed to the heat sink while direct convection and radiation from the chip to the ambient is neglected. Thus, the case temperature is calculated as

$$T_{\mathrm{c}} = T_{\mathrm{s}} + R_{\mathrm{th,cs}}\left(Q_{\mathrm{tot,T}} + Q_{\mathrm{tot,D}}\right) \tag{2.207}$$

while the junction temperatures are defined as

$$T_{\mathrm{j,T}} = T_{\mathrm{s}} + R_{\mathrm{th,jc,T}}\, Q_{\mathrm{tot,T}} \tag{2.208}$$

$$T_{\mathrm{j,D}} = T_{\mathrm{s}} + R_{\mathrm{th,jc,D}}\, Q_{\mathrm{tot,D}}. \tag{2.209}$$

2.3.1.4 Gate Driver and Control Board Design

The control board is a microprocessor which is responsible for generating the pulse width modulation signals for modulation and executing the logic processes to control the machine's dynamic behaviour. The control unit furthermore hosts position and current sensors [207, 208]. The gate driver then links the semiconductor modules with the control board [209].
Selecting the right gate driver is crucial for the correct functioning of the inverter. In the following, the selection rules for the gate driver are stated [209]. The gate driver must be able to supply the required gate charge Q_{G} specified in the data sheet. The output power of the driver is then

$$P_{\mathrm{GD}} = Q_{\mathrm{G}}\,(V_{\mathrm{G,on}} - V_{\mathrm{G,off}})\, f_{\mathrm{sw}} \tag{2.210}$$

with $V_{\mathrm{G,on}}$ and $V_{\mathrm{G,off}}$ being the turn-on and turn-off gate voltage. The driver has to be able to supply both the average gate current $I_{\mathrm{G,avg}}$

$$I_{\mathrm{G,avg}} = Q_{\mathrm{G}}\, f_{\mathrm{sw}} \tag{2.211}$$

and the peak gate current $I_{\mathrm{G,pk}}$

$$I_{\mathrm{G,pk}} = \frac{V_{\mathrm{G,on}} - V_{\mathrm{G,off}}}{R_{\mathrm{G}} + R_{\mathrm{G,int}}} \tag{2.212}$$

where R_{G} and $R_{\mathrm{G,int}}$ are the external and internal gate resistances specified in the manufacturer datasheet.
A database with commercially available gate driver units has been established mainly from Semikron's SKYPER series [209]. These gate drivers have two channels able to provide the power signals for two switches, thus three units are necessary for a 2L inverter.
The size and weight of the control board are assumed to be ⅔ of the accumulated gate driver mass and size, because the design of the controller board is a difficult task depending on the required logic functions to implement.

2.3.1.5 DC Link Capacitor Design for Voltage Ripple Limitation

A DC-Link capacitor is introduced in the intermediate circuit at the bus between a rectifier on the grid side and the inverter on the load side to balance the instantaneous currents at the grid and load side. According to Kolar and Round [210], the main functions of the DC-Link capacitor are to compensate for the difference between the power required at the inverter switch side and the DC input from the grid, to reduce the current harmonics with pulse frequency to the grid, and to protect the inverter from too high peak voltages from the grid side. The capacitors have to be dimensioned such that the current can be carried from a thermal point of view and that a maximum voltage ripple at the DC Link is not violated [183, 210, 211]. Figure 2.37 shows the general modelling of the intermediate DC-Link circuit in the case of a two- and three-level inverter.

2.3.1.5.1 DC Link Current Characteristics

To evaluate the performance of the DC Link capacitor, the current i_{C}

$$i_{\mathrm{C}} = i_{\mathrm{DC,L}} - i_{\mathrm{DC,S}} \tag{2.213}$$

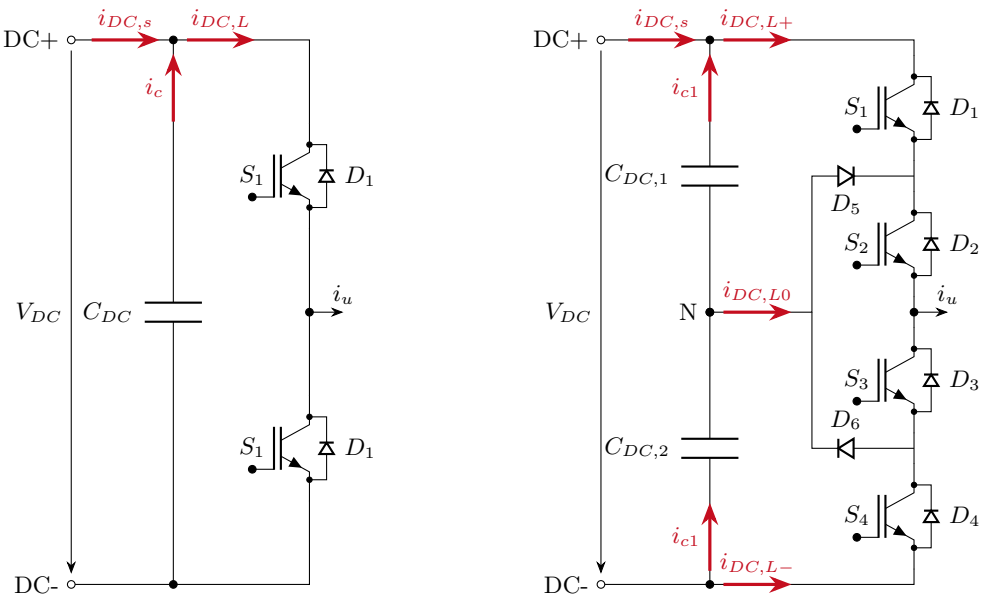

(**a**) 2L (**b**) 3LNPC

Figure 2.37: Schematics of the intermediate DC link circuit [210]

has to be calculated depending on the source current $i_{\mathrm{DC,S}}$ and load current $i_{\mathrm{DC,L}}$. This procedure is outlined briefly in the following paragraphs and follows [210].

Mean Inverter Input Current

Assuming a purely sinusoidal shape of the inverter output currents similar to Equation (2.13) and with the inverter input current $i_{\mathrm{DC,L}}$ being defined by the switching states as

$$i_{\mathrm{DC,L}} = \mathrm{S_u}\, i_{\mathrm{u}}(\omega\, t) \;+ \mathrm{S_v}\, i_{\mathrm{v}}(\omega\, t) \;+ \mathrm{S_w}\, i_{\mathrm{w}}(\omega\, t) \tag{2.214}$$

the average inverter input current $i_{\mathrm{DC,L,avg}}$ related to a pulse period is identical to the mean value of the inverter input current $I_{\mathrm{DC,L,avg}}$ related to the fundamental of the output voltage. For the example space vector from Figure 2.31b, this leads to

$$\begin{aligned} i_{\mathrm{DC,L,avg}} = I_{\mathrm{DC,L,avg}} &= \frac{1}{T_{\mathrm{sw}}} \int_0^{T_{\mathrm{sw}}} i_{\mathrm{DC,L}}\, \mathrm{d}t \\ &= \delta_{(100)}\, i_{\mathrm{u}}(\omega\, t) - \delta_{(110)}\, i_{\mathrm{w}}(\omega\, t) \\ &= \frac{3}{4}\, \hat{I}_{\mathrm{s}}\, m_{\mathrm{a}}\, \cos\varphi_{\mathrm{PF}}. \end{aligned} \tag{2.215}$$

RMS Inverter Input Current

In analogy to Equation (2.215), the RMS value of the inverter input current $i_{\mathrm{DC,L,rms}}$ is defined as

$$\begin{aligned} i^2_{\mathrm{DC,L,rms}} &= \frac{1}{T_{\mathrm{sw}}} \int_0^{T_{\mathrm{sw}}} i^2_{\mathrm{DC,L}}\, \mathrm{d}t \\ &= \delta_{(100)}\, i^2_{\mathrm{u}}(\omega\, t) - \delta_{(110)}\, i^2_{\mathrm{w}}(\omega\, t) \end{aligned} \tag{2.216}$$

resulting in a global RMS value $I_{\mathrm{DC,L,rms}}$ of the inverter input

$$I^2_{\mathrm{DC,L,rms}} = \frac{3}{\pi} \int_0^{\frac{\pi}{3}} i^2_{\mathrm{DC,L,rms}}\, \mathrm{d}t \tag{2.217}$$

$$I_{\mathrm{DC,L,rms}} = I_{\mathrm{s}} \sqrt{\frac{2\sqrt{3}}{\pi}\, m_{\mathrm{a}} \left(\frac{1}{4} + \cos^2\varphi_{\mathrm{PF}}\right)} \tag{2.218}$$

DC Link Capacitor RMS Current Ripple

All currents can be divided into a fundamental and the harmonic contents. As the fundamentals of source and load current are identical during quasi-stationary operation, the global RMS current ripple $i_{\mathrm{C,rms}}$ of the DC Link capacitor is derived [210] as

$$I_{\mathrm{C,rms}} = \sqrt{\frac{3}{\pi}\int_0^{\frac{\pi}{3}} i_{\mathrm{C}}^2 \,\mathrm{d}t} = \sqrt{I_{\mathrm{DC,L,rms}}^2 - I_{\mathrm{DC,L,avg}}^2} \tag{2.219}$$

$$= I_{\mathrm{s}} \sqrt{2\, m_{\mathrm{a}} \left(\frac{\sqrt{3}}{4\pi} + \cos^2 \varphi_{\mathrm{PF}} \left(\frac{\sqrt{3}}{\pi} - \frac{9}{16} m_{\mathrm{a}} \right) \right)}. \tag{2.220}$$

The influence of the harmonics of the source side is neglected as it is much lower than that of the load side [183]. In addition, it has been proven that the correlation also holds true for three-level architectures [188, 212]. Figure 2.38 shows the normalized DC Link capacitor RMS current ripple with respect to the inverter output phase current for varying modulation degrees and power factors. It can be seen that the current ripple has a quadratic form. The higher the power factor is, the higher the absolute peak value of the current ripple and the lower the corresponding modulation degree where the peak is located.

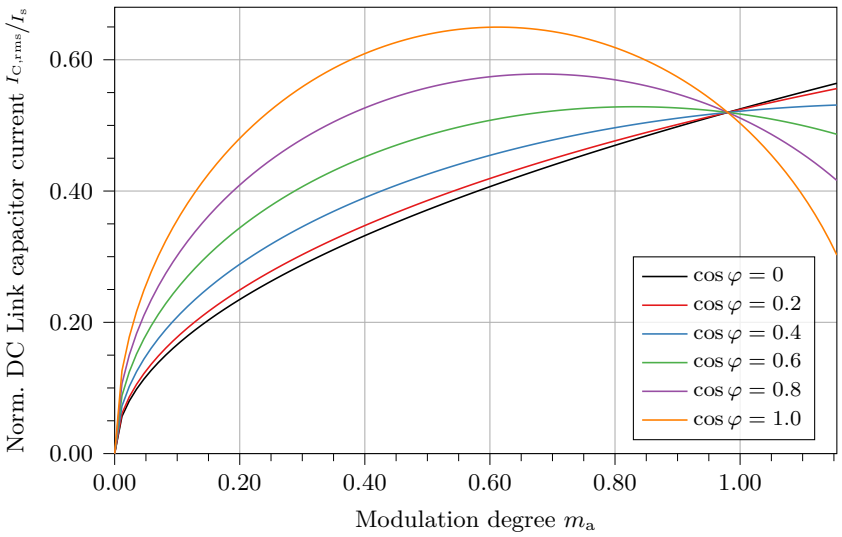

Figure 2.38: Normalized DC link capacitor RMS ripple current for varying modulation degree and power factors based on Equation (2.220)

2.3.1.5.2 DC Link Voltage Ripple

As outlined in Section 2.3.1.5, the second aspect that determines the performance of the DC Link capacitor is the voltage ripple. Similarly to the current, the voltage can be divided into a DC average component and high-frequency harmonics,

$$v(t) = V_{\mathrm{DC,avg}} + \Delta V(t). \tag{2.221}$$

Usually, a maximum allowable peak-to-peak voltage ripple $\Delta V_{\mathrm{pp,DC}}$ is defined as the difference between the maximum and minimum value during a switching period. When the current component at the switching frequency $\Delta i_{\mathrm{DC,L}}$ is defined as

$$\Delta i_{\mathrm{DC,L}} = i_{\mathrm{DC,L}} - i_{\mathrm{DC,L,avg}}, \tag{2.222}$$

then the peak-to-peak voltage ripple is given by

$$\Delta V_{\mathrm{pp,DC}} = \left| \frac{1}{C_{\mathrm{DC}}} \int_0^{t_{\mathrm{pp}}} \Delta i_{\mathrm{DC,L}} \mathrm{d}t \right| \approx \frac{1}{C_{\mathrm{DC}}} |\Delta I_{\mathrm{DC,L}}\, t_{\mathrm{pp}}, \tag{2.223}$$

assuming the high-frequency harmonic current remains constant over the switching period. The voltage ripple calculation is studied extensively in [213, 214] and can be reduced to the first sector of the space vector diagram. Evaluating different cases depending on the value of $i_{\mathrm{DC,L,avg}}$ leads to

$$\Delta V_{\mathrm{pp,DC}} = \frac{\hat{I}_{\mathrm{s}}\, T_{\mathrm{sw}}}{C_{\mathrm{DC}}} r_{\mathrm{pp,DC}}(m_{\mathrm{a}}, \varphi_{\mathrm{PF}}, \omega t), \tag{2.224}$$

where

$$r_{\mathrm{pp,DC}} = \max\left(r_{\mathrm{pp}}^{\mathrm{A}}, r_{\mathrm{pp}}^{\mathrm{B}}\right) \tag{2.225}$$

with

$$r_{\mathrm{pp}}^{\mathrm{A}} = \frac{3}{8} m_{\mathrm{a}} \cos\varphi_{\mathrm{PF}} \left(1 - \frac{\sqrt{3}\, m_{\mathrm{a}}}{2} \sin\left(\frac{\pi}{3} + \omega t\right)\right) \tag{2.226}$$

$$\begin{aligned} r_{\mathrm{pp}}^{\mathrm{B}} = \frac{3}{8} m_{\mathrm{a}} \Bigg| & \cos\varphi_{\mathrm{PF}} \left(1 - \frac{\sqrt{3}\, m_{\mathrm{a}}}{2} \sin\left(\frac{\pi}{3} + \omega t\right)\right) \\ & + \frac{4}{\sqrt{3}} \sin\left(\frac{\pi}{2} - \omega t\right) \left(\frac{3}{4} m_{\mathrm{a}} \cos\varphi_{\mathrm{PF}} - \cos(\omega t - \varphi_{\mathrm{PF}})\right) \Bigg| \end{aligned} \tag{2.227}$$

representing the normalized peak-to-peak ripple amplitudes. Figure 2.39 shows the DC Link capacitor peak-to-peak ripple voltage amplitude within the first sector of the space vector diagram for two different phase angles φ_{PF} and various modulation indices ranging from $m_{\mathrm{a}} = 0.5 - 2/\sqrt{3}$.

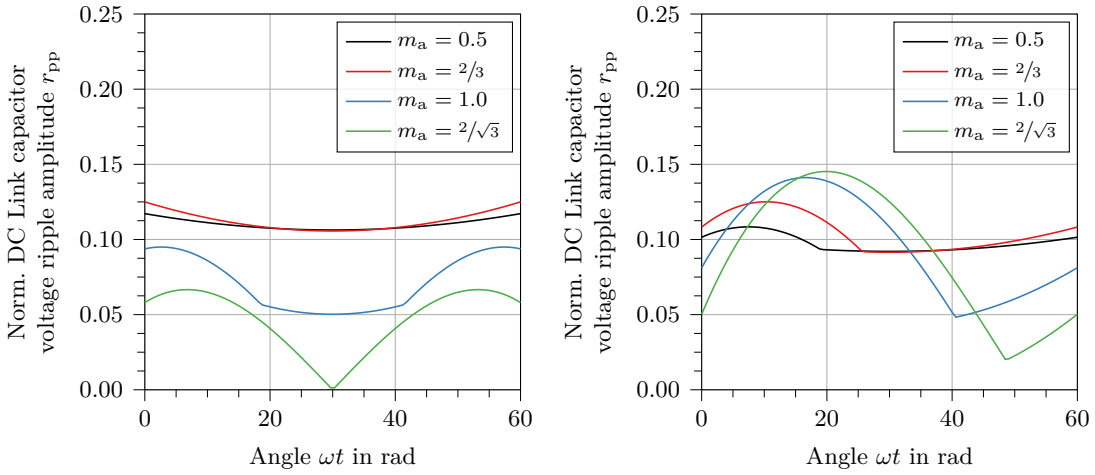

(**a**) $\varphi_{\mathrm{PF}} = 0°$ (**b**) $\varphi_{\mathrm{PF}} = 50°$

Figure 2.39: Normalized peak-to-peak voltage ripple amplitude r_{pp} for different modulation indices and phase angles within one sector of the space vector diagram

Within one period, the normalized voltage ripple amplitude varies between 0 and 0.25. The maximum value within a period increases with both phase angle and modulation index (see Figure 2.40).
Using Equation (2.224), the required capacitance of the DC Link C_{DC} can be calculated for a specified peak-to-peak voltage ripple amplitude. For similar normalized ripple amplitudes

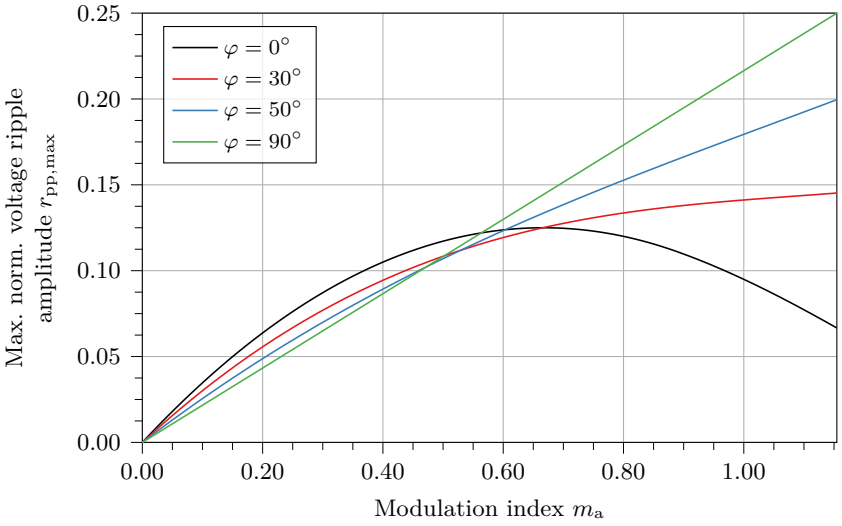

Figure 2.40: Maximum normalized DC link capacitor peak-to-peak voltage ripple amplitude $r_{\mathrm{pp,max}}$ for varying modulation index $m_{\mathrm{a}} = 0.5 - 2/\sqrt{3}$ and different phase angles $\varphi_{\mathrm{PF}} = 0 - 90°$

as shown in [214], it can be concluded that the required DC Link capacitance in the case of a two-level inverter is equal to the individual capacitances of the split capacitors in a three-level inverter, i.e., $C_{\mathrm{DC}} = C_{\mathrm{DC,1}} = C_{\mathrm{DC,2}}$. Therefore, the total capacitance in a three-level inverter is halved compared to that of a two-level inverter.

2.3.1.5.3 Losses and Thermal Analysis

The RMS ripple current causes losses within the capacitor Q_{Cap} according to

$$Q_{\mathrm{Cap}} = R_{\mathrm{ESR}}\, I_{\mathrm{C,rms}}^2 \tag{2.228}$$

with R_{ESR} being the equivalent series resistance of the capacitor, as specified by the manufacturer. As these losses are Joule losses, they cause heating of the capacitor [215, 216]. The core temperature $T_{\mathrm{c,Cap}}$, which is equivalent to the operating temperature, can thus be calculated as

$$T_{\mathrm{c,Cap}} = T_{\mathrm{amb}} + (R_{\mathrm{th,cc}} + R_{\mathrm{th,ca}})\, Q_{\mathrm{Cap}} \tag{2.229}$$

where $R_{\mathrm{th,cc}}$ and $R_{\mathrm{th,ca}}$ are the core-to-case and case-to-ambient thermal resistances, respectively, as specified in datasheets. Maximum allowable core temperatures are typically around $T_{\mathrm{c,Cap}} = 105\,°\mathrm{C}$ [215, 216].

2.3.1.5.4 Physical Capacitor Model

In DC Link applications, either aluminum electrolytic capacitors, metallized film capacitors, or multi-layer ceramic capacitors are used [217, 218]. Ceramic capacitors are not commercially available for the evaluated power classes and are therefore not considered in this study. Electrolytic capacitors have high capacitance and low cost, making them a suitable choice for many applications. However, they exhibit inferior characteristics in terms of RMS current rating, temperature sensitivity and resistance, available power rating, and lifetime when compared to metallized film capacitors [218]. Both types require a parallel arrangement of multiple individual capacitors to meet the required RMS current or capacitance, leading to a tradeoff in terms of volume and mass.
Different modelling methods such as database approaches or empirical correlations can be employed [74, 219, 220]. This thesis uses the database approach with capacitor data from various manufacturers [221–223], as it offers higher accuracy compared to empirical correlations, which are typically limited to a fixed capacitor type or manufacturer series.

The drawback of the database method is its higher effort, as all possible combinations that meet the requirements in terms of voltage, RMS ripple current, and capacitance must be evaluated to identify the configuration with minimum mass and volume.

2.3.1.6 Bus Bar Design

The connection of the semiconductor modules to the DC link via the capacitors, as well as to the AC output, is realized by laminated busbars. These busbars play an important role not only with respect to weight, but also from an electromagnetic perspective. A low-inductance design is preferable to limit voltage overshoot, reduce inverter switching losses, and mitigate the effects of electromagnetic interference [224]. The focus in this work is on the additional weight introduced by the busbars.
In [224], different busbar application possibilities for power converters are presented. As none of them offers a clear advantage in terms of weight reduction, and since busbar design is also driven by structural integration, one representative type is chosen for reference. Figure 2.41a shows the selected layout of the power electronic components and the associated busbar structure, while Figure 2.41b illustrates the cross section of two possible internal configurations of the busbar, one with open and one with sealed edges. The second option is preferred, as it provides better protection against arcing, although it is the more costly solution.

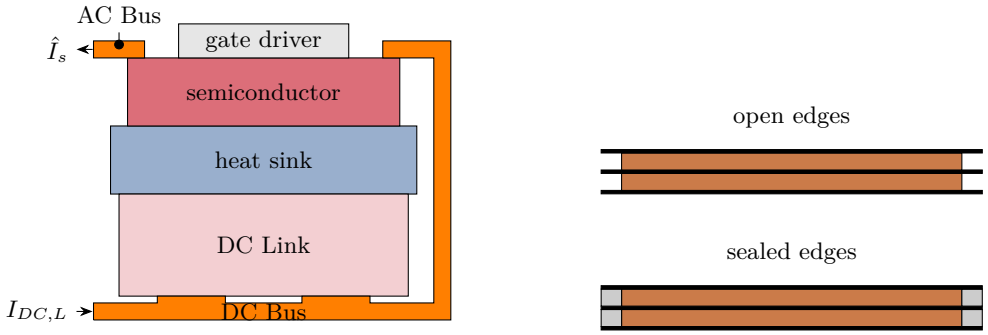

(**a**) Arrangement of power electronic components and associated busbar structure

(**b**) Schematics of the cross section of two different types of laminated busbars with two poles

Figure 2.41: Laminated busbar and its application within a power converter

The design of the busbar follows several rules. Firstly, the required insulation thickness $t_{\mathrm{ins,bb}}$ is determined using Equation (2.165), considering only phase-to-phase and phase-to-ground distances. The conductor cross section is determined at the terminals of the power modules, with a terminal width w_{bb} typically specified in manufacturers' datasheets. Two conditions for the conductor thickness must be fulfilled [224]. To avoid a detailed thermal analysis and safely limit the temperature rise due to Joule losses to approximately 30 K, the current density in the conductor cross section $J_{\mathrm{bb,RMS}}$ should be limited to

$$J_{\mathrm{bb,RMS}} = \frac{I_{\mathrm{RMS}}}{A_{\mathrm{bb}}} = \frac{I_{\mathrm{RMS}}}{w_{\mathrm{bb}}\, t_{\mathrm{bb}}} \leq 5\,\mathrm{A\,mm^{-2}}. \tag{2.230}$$

Additionally, the conductor thickness t_{bb} should be at least twice the penetration depth δ_{skin} of the AC currents, due to the skin effect, to ensure maximum utilization of the conducting area. The skin depth for a rectangular conductor is calculated as

$$\delta_{\mathrm{skin}} = \frac{1}{\sqrt{\pi\, f_{\mathrm{sw}}\, \sigma_{\mathrm{el}}\, \mu_0}} \left(1 - e^{-t_{\mathrm{bb}} \sqrt{\pi\, f_{\mathrm{sw}}\, \sigma_{\mathrm{el}}\, \mu_0}}\right) \tag{2.231}$$

where σ_{el} is the electrical conductivity of the conductor material.

2.3.1.7 Structural Housing and Power Connectors

The final step in the design and evaluation of an inverter is the development of its structural housing and the connection of power cables at both the input and output.
For estimating the weight of the power connectors on the DC and AC sides, the correlation for female sockets provided in Section 2.4.2 is used. The use of pluggable connectors enables straightforward integration and facilitates maintenance, particularly during testing.
The structural housing follows the inverter layout shown in Figure 2.41a and is represented as a simple cuboid enclosing the system, with an average wall thickness $t_{c,Inv}$ set to a generic value of 2 mm. This value represents the minimum typical thickness for a cast casing [225]. Aluminum is the most commonly used material, although alternatives such as magnesia or fiber-reinforced materials have also been explored [226].

2.3.2 DC-DC Converters for Batteries and Fuel Cells

In addition to inverters and rectifiers, high-voltage, high-power DC-DC converters are employed in various electric drivetrain architectures. In a fully battery-electric drivetrain, a DC-DC converter can be used to stabilize the DC Link voltage at a consistently high level, close to the open-circuit voltage of a fully charged battery, in order to match the rated voltage of the inverter and motor system. As a result, maximum current levels are reduced compared to an unstabilized system. This allows components such as power cables and power electronics to be dimensioned smaller, due to lower conduction losses and improved efficiency at reduced current levels. In the case of a bidirectional topology, additional benefits include energy recovery during deceleration and regenerative braking [177, 227, 228].
In hybrid systems with two or more electrical energy sources, a DC-DC converter is essential to interface sources with differing voltage characteristics, such as fuel cells and batteries. Moreover, it enables controlled power flow between the energy sources and the load [227, 228].
Similar to inverters, DC-DC converters consist of several functional subsystems that must be considered during the design process, as illustrated in Figure 2.42.

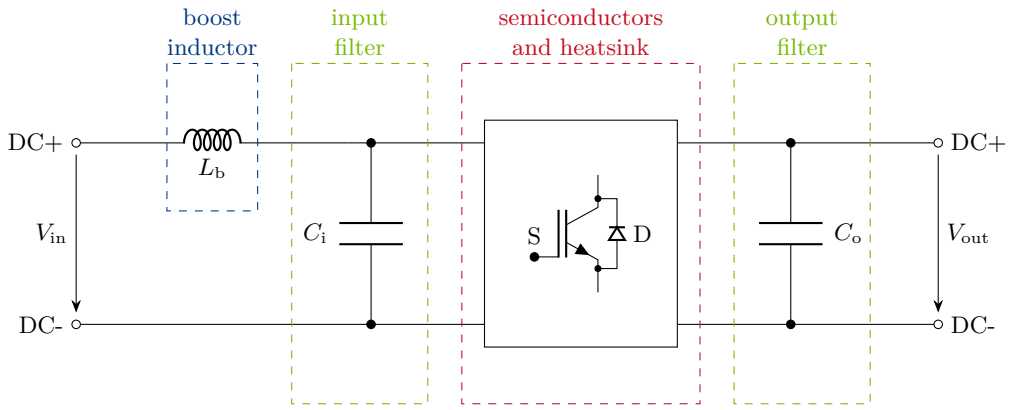

Figure 2.42: DC-DC converter with boost inductor, the active part consisting of semiconductors and heatsink, and capacitive input and output filters. The control unit with gate drivers, busbars and connectors, as well as the housing, are not shown.

The general layout is similar to that of an inverter described in Figure 2.26. The main distinction lies in the fact that a DC-DC converter performs voltage conversion between two DC levels rather than between DC and AC.

2.3.2.1 Topologies of Converters

DC-DC converters can be classified as either isolated or non-isolated power supplies. An isolated converter provides galvanic isolation between the input and output sides, thereby preventing direct current flow. This is typically achieved using a transformer. In contrast, non-isolated converters, also referred to as transformerless, operate using a single electrical circuit without galvanic separation [229, 230].
Non-isolated topologies offer several advantages. Isolated converters require bulky transformers, whereas non-isolated ones use only inductors. Additionally, non-isolated converters operate at higher switching frequencies, which leads to smaller magnetic components and capacitors, thereby reducing both volume and cost. The higher frequency also results in lower losses and improved transient performance and efficiency [229, 230]. Since weight and efficiency are two key objectives in aerospace drivetrains, only non-isolated designs are considered in this thesis.
The two fundamental non-isolated converter topologies are the buck and boost types. The buck converter, also known as a step-down converter, produces an output voltage lower than its input voltage. In contrast, the boost converter, or step-up converter, increases the input voltage to a higher output level [177, 229, 230]. Figure 2.43 illustrates the schematics of these two topologies.

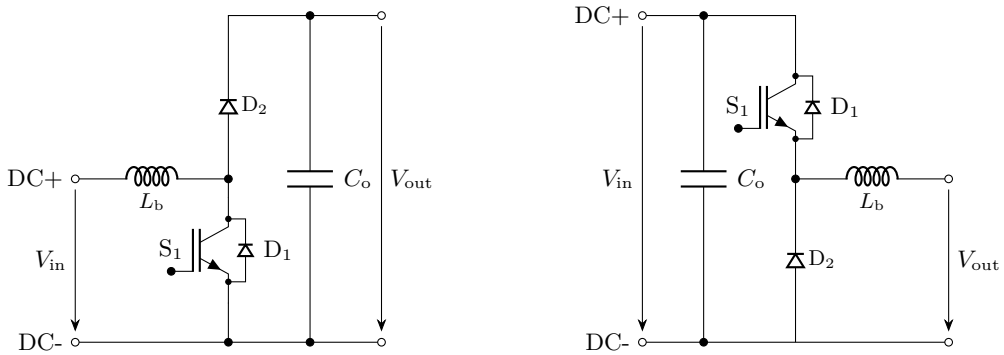

(**a**) Boost (**b**) Buck

Figure 2.43: Schematics of different non-isolated DC-DC converters [177]

As mentioned at the beginning of Section 2.3.2, the overall system benefits from lower current levels. Therefore, this thesis focuses on the boost topology.

2.3.2.2 Electrical Analysis of Boost Converters

Figure 2.44 shows the steady-state waveforms of inductor current and voltage. The boost converter operates in two distinct states:
When switch S_1 is on, current flows through the boost inductor L_b, storing energy in its magnetic field. The inductor voltage V_L equals the input voltage V_{in}, and the inductor current I_L increases linearly from $I_{L,min}$ to $I_{L,max}$. During this interval, the output capacitor C_o supplies the output voltage V_{out} to the load [176, 177].
When switch S_1 is off, the stored energy in the inductor drives a current that supplies the load and charges the output capacitor. The voltage across the switch V_s equals the output voltage, and the inductor voltage adjusts such that its average value over one switching cycle is zero. During this phase, the inductor current decreases linearly over the same range as in the on-state [176, 177].
The current ripple ΔI_L depends on the boost inductance. As long as the minimum inductor current remains above zero, the average inductor current $I_{L,avg}$ equals the input current, and the converter operates in continuous conduction mode (CCM). The ripple

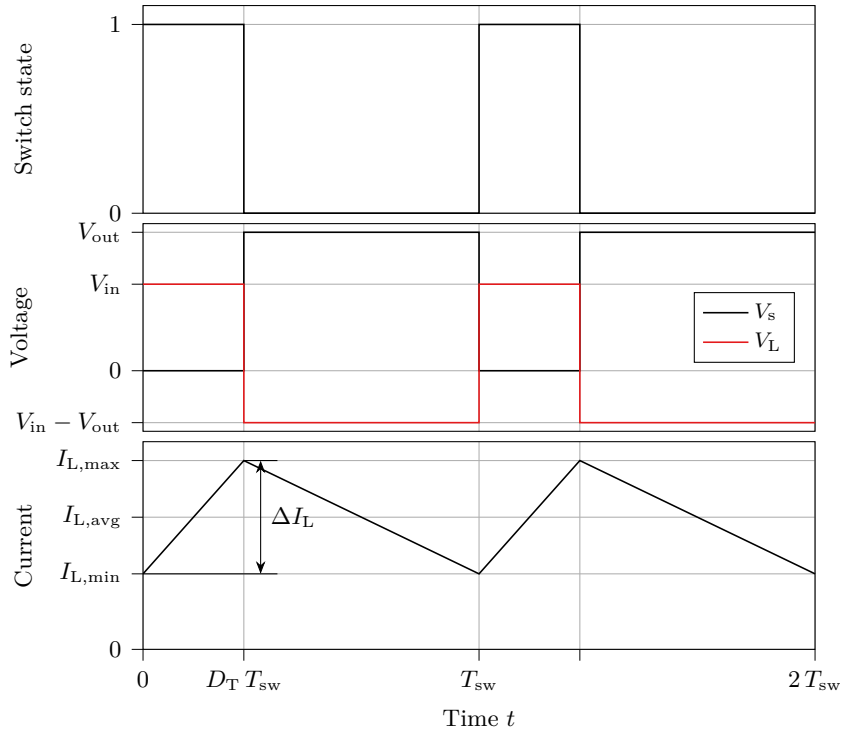

Figure 2.44: Waveforms of boost inductors, adapted from [176, 177] (top) switch state (middle) switching V_s and inductor voltage V_L (bottom) inductor current I_L

increases as the inductance decreases. When the minimum inductor current reaches zero, a third operational interval arises where the inductor current is zero. In this discontinuous conduction mode (DCM), the average inductor current exceeds the input current, as energy conservation holds for the full switching cycle [176, 177]. Continuous conduction mode is generally preferred whenever feasible.
Assuming an ideal, lossless converter, the power balance yields

$$I_{out} = \frac{V_{in}}{V_{out}}\, I_{in} \tag{2.232}$$

where I_{in} and I_{out} denote the DC currents at the converter's input and output, respectively. The duty cycle of the transistor D_T is defined as the ratio of the switch's on-time to the switching period T_{sw}, while the diode's duty cycle D_D is the ratio of the off-time to T_{sw}. In continuous conduction mode, the duty cycles are given by [177, 231]

$$D_{T,CCM} = 1 - \frac{V_{in}}{V_{out}} \tag{2.233}$$

$$D_{D,CCM} = \frac{V_{in}}{V_{out}}. \tag{2.234}$$

In discontinuous conduction mode, the duty cycles differ [177, 231]:

$$D_{T,DCM} = \sqrt{2\,L_b\; f_{sw}\,\frac{I_{out}}{V_{in}}\left(\frac{V_{out}}{V_{in}} - 1\right)} \tag{2.235}$$

$$D_{D,DCM} = \sqrt{2\,L_b\; f_{sw}\,\frac{I_{out}}{V_{out} - V_{in}}} \tag{2.236}$$

It is evident that in continuous conduction mode, the duty cycles depend only on the input and output voltages, and their sum equals one. In discontinuous conduction mode,

where $D_{\mathrm{T,DCM}} < D_{\mathrm{T,CCM}}$, the output current, switching frequency, and boost inductance influence the duty cycles, and their sum is less than one.

2.3.2.3 Boost Inductor Design for Current Ripple Limitation

The boost inductance L_b determines the current ripple and the operating mode of the DC-DC converter. Various inductor shapes with toroidal cores or cores shaped like a "U" or an "E" are available. The toroidal core is selected due to its advantages over other geometries. Its closed magnetic path confines the magnetic field within the core, enabling higher magnetic field strength and inductance than open geometries. It also emits less electromagnetic interference due to reduced leakage flux. Furthermore, it enables efficient energy transfer, allowing for smaller and lighter designs [232, 233].
The calculation of the winding is described in detail in Section 2.4.1, including analysis of insulation and the electro-thermal performance of the wires.

2.3.2.3.1 Geometric Layout

Figure 2.45 shows the geometry of a toroidal inductor with a rectangular cross-section. The core is wound with N_t turns, evenly distributed along the circumference. The current I_L flowing through the winding generates a magnetic field B_ind within the core.

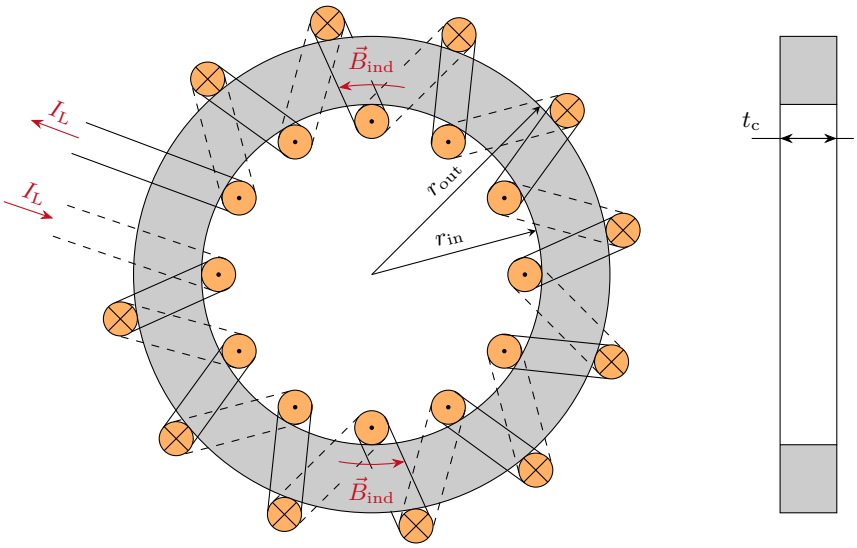

Figure 2.45: Front (left) and side view (right) of a toroidal boost inductor

2.3.2.3.2 Electromagnetic Analysis

Applying Ampere's law, the magnetic field inside the toroid is given by [234]

$$B_\mathrm{ind} = \frac{\mu_0 \, \mu_\mathrm{eff} \, N_\mathrm{t} \, \hat{I}_\mathrm{L}}{2 \, \pi \, r_\mathrm{m}} \tag{2.237}$$

where $\hat{I}_\mathrm{L}$ is the maximum inductor current, defined as

$$\hat{I}_\mathrm{L} = I_\mathrm{in} + \frac{\Delta I_\mathrm{L}}{2} \tag{2.238}$$

and the current ripple is given by [177]

$$\Delta I_\mathrm{L} = \frac{D_\mathrm{T} \, V_\mathrm{in}}{L_\mathrm{b} \, f_\mathrm{sw}}. \tag{2.239}$$

The magnetic flux per turn, Φ, is obtained by integrating the magnetic field over the core cross-section [234]:

$$\Phi = \int B_{\mathrm{ind}} \mathrm{d}A = \frac{\mu_0 \, \mu_{\mathrm{eff}} \, \hat{I}_{\mathrm{L}} \, t_{\mathrm{c}}}{2 \, \pi} \, \ln\left(\frac{r_{\mathrm{out}}}{r_{\mathrm{in}}}\right) \tag{2.240}$$

which leads to the inductance L_{b} by definition [234]:

$$L_{\mathrm{b}} = \frac{N_{\mathrm{t}} \, \Phi}{\hat{I}_{\mathrm{L}}} = \frac{\mu_0 \, \mu_{\mathrm{eff}} \, N_{\mathrm{t}}^2 \, t_{\mathrm{c}}}{2 \, \pi} \, \ln\left(\frac{r_{\mathrm{out}}}{r_{\mathrm{in}}}\right) \tag{2.241}$$

Equation (2.239) shows that the inductance must be sufficiently large to limit the current ripple. For a given core geometry, the inductance can only be tuned by adjusting the number of turns or the effective permeability, as seen in Equation (2.241). This can be achieved by selecting a different core material or introducing air gaps. However, these modifications also affect the flux density in the core, as described by Equation (2.237). The design is therefore constrained by the material's saturation induction, the number of turns that can be physically accommodated, and the required inductance.

2.3.2.4 Electro-Thermal Performance of Semiconductor Modules

The calculation of semiconductor losses and resulting temperatures is based on the models established in Section 2.3.1.3. The only difference lies in the computation of transistor and diode losses, which must account for the specific shapes of the voltage and current waveforms in the DC-DC converter. The linearization of semiconductor behavior and the thermal network models introduced in Paragraphs 2.3.1.3.1, 2.3.1.3.2 and 2.3.1.3.4 remain unchanged. In a conventional half-bridge boost converter, as shown in Figure 2.43a, each leg includes a pair of transistors and diodes. The conduction losses are calculated using the RMS current:

$$Q_{\mathrm{con,T1}} = D_{\mathrm{T}} \, V_{\mathrm{CE}}(I_{\mathrm{RMS}}, T_{\mathrm{j,T}}) \, I_{\mathrm{RMS}} \tag{2.242}$$

$$Q_{\mathrm{con,D2}} = D_{\mathrm{D}} \, V_{\mathrm{F}}(I_{\mathrm{RMS}}, T_{\mathrm{j,D}}) \, I_{\mathrm{RMS}} \tag{2.243}$$

The conduction losses of the second transistor and diode are zero.
Switching losses for the transistor must be divided into switch-on and switch-off contributions due to the nature of the current waveforms shown in Figure 2.44:

$$Q_{\mathrm{sw,on,T1}} = f_{\mathrm{sw}} \, E_{\mathrm{on,T}} \left(\frac{I_{\mathrm{L,min}}}{I_{\mathrm{ref}}}\right)^{K_{\mathrm{I,T}}} \left(\frac{V_{\mathrm{com}}}{V_{\mathrm{ref}}}\right)^{K_{\mathrm{V,T}}} (1 + \alpha_{\mathrm{E,T}} \, (T_{\mathrm{j,T}} - T_{\mathrm{ref}})) \tag{2.244}$$

$$Q_{\mathrm{sw,off,T1}} = f_{\mathrm{sw}} \, E_{\mathrm{off,T}} \left(\frac{I_{\mathrm{L,max}}}{I_{\mathrm{ref}}}\right)^{K_{\mathrm{I,T}}} \left(\frac{V_{\mathrm{com}}}{V_{\mathrm{ref}}}\right)^{K_{\mathrm{V,T}}} (1 + \alpha_{\mathrm{E,T}} \, (T_{\mathrm{j,T}} - T_{\mathrm{ref}})) \tag{2.245}$$

$$Q_{\mathrm{sw,D2}} = f_{\mathrm{sw}} \, E_{\mathrm{rr,D}} \left(\frac{I_{\mathrm{L,min}}}{I_{\mathrm{ref}}}\right)^{K_{\mathrm{I,D}}} \left(\frac{V_{\mathrm{com}}}{V_{\mathrm{ref}}}\right)^{K_{\mathrm{V,D}}} (1 + \alpha_{\mathrm{E,D}} \, (T_{\mathrm{j,D}} - T_{\mathrm{ref}})) \tag{2.246}$$

With MOSFETs becoming increasingly popular, their low on-state resistance allows for the implementation of synchronous boost converters using two actively switching devices. This results in higher efficiency. The total semiconductor losses are therefore given by:

$$Q_{\mathrm{SC}} = Q_{\mathrm{con,T1}} + Q_{\mathrm{con,D2}} + Q_{\mathrm{sw,on,T1}} + Q_{\mathrm{sw,off,T1}} + Q_{\mathrm{sw,D2}}. \tag{2.247}$$

2.3.2.5 Filter Capacitors

Filter capacitors are essential components in DC-DC boost converters. Their primary functions are to stabilise voltage levels and attenuate current and voltage ripples at both the input and output terminals. The input capacitor primarily absorbs high-frequency

current variations caused by the switching operation, while the output capacitor maintains a steady output voltage by buffering the energy delivered to the load. Both capacitors also influence the converter's electromagnetic interference performance. Accurate sizing and thermal evaluation are necessary to ensure long-term reliability and compliance with electrical specifications [231, 235]. To evaluate capacitor operating performance, including current and voltage utilisation, power losses and temperatures, the voltage ripple and RMS current must be determined. Once known, the physical capacitor model developed in Paragraph 2.3.1.5.4 can be applied accordingly.

2.3.2.5.1 Input Capacitor

The input capacitor stabilises the input voltage and absorbs current pulses drawn by the switching action of the power stage. The voltage ripple across the capacitor is given by [235]:

$$\Delta V_{\mathrm{in}} = \frac{(D_{\mathrm{T}} + D_{\mathrm{D}})\,(I_{\mathrm{L,max}} - I_{\mathrm{in}})^2}{2\,\Delta I_{\mathrm{L}}\,C_{\mathrm{i}}\,f_{\mathrm{sw}}}. \tag{2.248}$$

The RMS current through the input capacitor is calculated as:

$$I_{\mathrm{C,in,RMS}} = \sqrt{I_{\mathrm{L,RMS}}^2 - I_{\mathrm{in}}^2}. \tag{2.249}$$

2.3.2.5.2 Output Capacitor

The output capacitor smooths the output voltage and supplies the load during each switching cycle. Its voltage ripple depends on both the capacitance and the equivalent series resistance R_{ESR} [231]. Depending on the inductor value, the output voltage ripple is calculated as [235]:

$$\Delta V_{\mathrm{out}} = \begin{cases} \left(\dfrac{I_{\mathrm{L,max}} + I_{\mathrm{L,min}} - 2I_{\mathrm{out}}}{2\,f_{\mathrm{sw}}\,C_{\mathrm{o}}} + R_{\mathrm{ESR}}\,I_{\mathrm{out}}\right), & \text{if } L \geq \dfrac{V_{\mathrm{in}}}{2\,I_{\mathrm{in}}\,f_{\mathrm{sw}}} \\ \left(\dfrac{D_{\mathrm{T}}\,(I_{\mathrm{L,max}} - I_{\mathrm{out}})^2}{2\,\Delta I_{\mathrm{L}}\,C_{\mathrm{o}}\,f_{\mathrm{sw}}} + R_{\mathrm{ESR}}\,I_{\mathrm{out}}\right), & \text{otherwise} \end{cases} \tag{2.250}$$

The RMS current through the output capacitor is given by:

$$I_{\mathrm{C,out,RMS}} = \sqrt{\left(\frac{I_{\mathrm{L,min}}^2 + I_{\mathrm{L,min}} \cdot I_{\mathrm{L,max}} + I_{\mathrm{L,max}}^2}{3}\right) D_{\mathrm{T}} - I_{\mathrm{out}}^2}. \tag{2.251}$$

2.3.3 Short Summary

This section establishes a detailed analytical foundation for designing power electronic systems, covering both DC-AC inverters and DC-DC converters. It introduces common topologies and control strategies while addressing key electro-thermal considerations for semiconductor devices. Emphasis is placed on the interplay between electrical performance and thermal management, including gate driver design, DC link capacitors, bus bar layout, and cooling integration. Structural elements such as housing and power connector configuration are also considered. This unified treatment ensures component compatibility and delivers consistent input data for holistic propulsion system modelling and optimization.

2.4 Power Distribution

Power distribution is an essential part of any drivetrain, connecting various electrical components such as electric machines and converters through three-phase AC cables, and linking the battery to the inverter input via DC cables. This section presents a model of the cables and their auxiliaries, including male and female connectors, to enable a system-level sensitivity analysis of mass and efficiency.

2.4.1 Power Cables

The DC and AC power cables are modeled as cylindrical conductors made of either aluminum or copper, with an insulation layer surrounding them and exposure to ambient conditions. For the assumed voltage levels, shielding sheaths and additional protective layers are not considered, as their impact on mass and efficiency is negligible. Figure 2.46 shows the geometrical layout of the modeled cable.

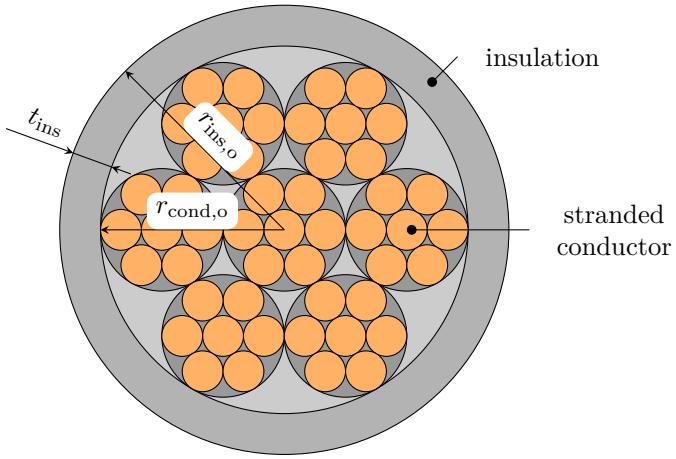

Figure 2.46: Schematic view of a multi-stranded, concentric, and unshielded cable

The following subsections present the geometric and electro-thermal analysis of these cables, with the insulation thickness assessed using the methodology outlined in Section 2.1.7.

2.4.1.1 Geometrical Model of Conduction Layer

The conductor consists of finely stranded wires, also referred to as Litz wires, which are used to reduce skin and proximity losses and to improve manufacturability and handling, for example by reducing the bending radius. The physical structure typically features a concentric multi-layer arrangement of single wires twisted along the longitudinal axis [236]. An analytical description of the temperature distribution in such layers is not feasible. Therefore, the model complexity is reduced by using a homogenized structure with an equivalent fill factor to calculate the thermal resistance, as already applied for machine windings in Section 2.1.6.3.

Equivalent Fill Factor of Stranded Wires

Aerospace-grade power distribution cables from Glenair's TurboFlex Series 96 [237] were analyzed to determine the conductor fill factor k_{cond} as a function of conductor diameter. Figure 2.47 shows the original data and the corresponding piecewise linear fit. With increasing outer conductor radius, the achievable fill factor decreases linearly within distinct sections. These steps correspond to discrete changes in the stranding layout. A lower fill factor leads to a higher thermal resistance and thus inferior heat dissipation characteristics.

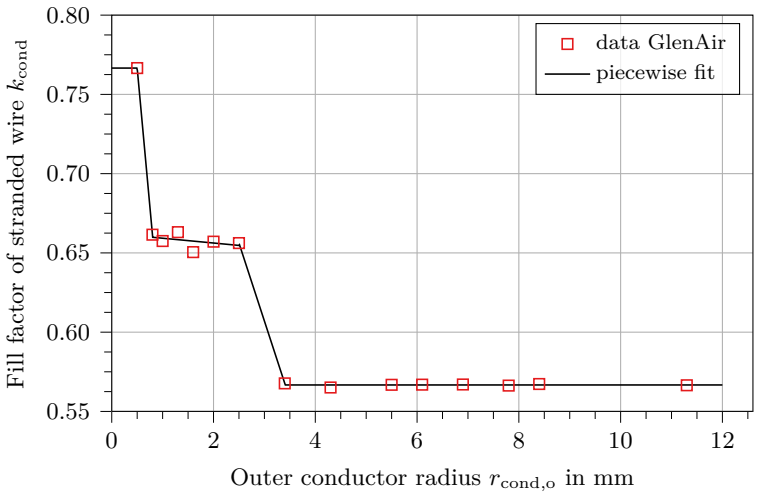

Figure 2.47: Fill factor k_{cond} versus outer conductor radius r_{cond} for Glenair TurboFlex Series 96 [237]

Stranding Factor

The mass and electrical resistance of the conductor increase due to stranding and laying, i.e., twisting the wires of each layer around a central axis. The standards ASTM B231 and B8 [238, 239] define standard layouts for concentric stranding and provide corresponding calculation methods. Since the exact layout is unknown in this case, the stranding factor m_{strand}, which accounts for this mass and resistance increase, is derived from datasheet values shown in Figure 2.48 and fitted by a piecewise linear function. The stranding factor varies between approximately eight and 13 %, depending on the conductor radius.

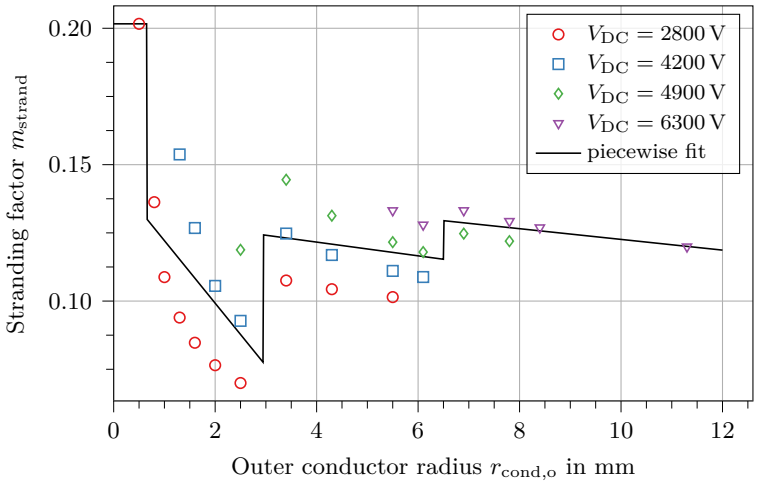

Figure 2.48: Stranding factor m_{strand} versus conductor radius r_{cond} for Glenair TurboFlex Series 96 [237]

Weight of Stranded Cable in Mounted Condition

The total mass of the cable is given by:

$$\begin{aligned} m_{\text{Cab}} &= m_{\text{cond}} + m_{\text{ins}} \\ &= (1 + k_{\text{mount}}) \left(m_{\text{strand}}\, k_{\text{cond}}\, r_{\text{cond,o}}^2\, \pi\, L_{\text{Cab}}\, \rho_{\text{cond}} \right. \\ &\qquad \left. + (r_{\text{ins,o}}^2 - r_{\text{cond,o}}^2)\, \pi\, L_{\text{Cab}}\, \rho_{\text{ins}} \right) \end{aligned} \tag{2.252}$$

where ρ_{cond} and ρ_{ins} are the material densities of the conductor and insulation, respectively. The parameter k_{mount} accounts for additional mounting-related mass, typically ranging from 30 – 50 %.

2.4.1.2 Electro-Thermal Analysis of Multi-Stranded Wires

Under operational load, a cable heats up due to Joule losses in the conductor and dielectric losses in the insulation. The ability of a conductor to carry a specific current is referred to as ampacity and represents one of the most critical design parameters for power cables. Studies on achievable ampacities have been conducted extensively, particularly for underground and subsea power grids [240–243], and are summarized in IEC 60287-1 [244]. The calculation of ampacity includes the determination of losses in the various cable layers followed by a temperature evaluation.

2.4.1.2.1 Joule and Dielectric Losses

The losses in a power cable can be divided into conduction (Joule) losses occurring in the conductive sections, and dielectric losses occurring in the insulation. For insulation materials such as paper (up to 6 kV) and cross-linked polyethylene (up to 60 kV), dielectric losses are negligible [245]. Voltage levels in aircraft applications typically remain below these thresholds, particularly in light of Paschen's law [147].
Therefore, the proposed model considers only Joule losses. The resistance of a cable under DC current, R_{DC}, is given by

$$R_{\mathrm{DC}} = \frac{m_{\mathrm{strand}}\, L_{\mathrm{Cab}}\, \rho_{\mathrm{cond}}}{k_{\mathrm{cond}}\, r_{\mathrm{cond,o}}^{2}\, \pi} \tag{2.253}$$

where ρ_{cond} is the electrical resistivity of the conductor. For AC currents, additional frequency-dependent losses occur due to the skin and proximity effects. The corresponding AC resistance R_{AC} has been studied by numerous researchers [240, 241, 246, 247], with many models based on the exact solution by Dowell [248] or simplified versions such as those in IEC 60287 [244]. It has been shown that for electrical fundamental frequencies below 5 – 10 kHz, the increase in resistance due to AC effects remains small [249–251].
Since the detailed geometry of the conductor is not specified, the additional losses attributed to the AC resistance are expressed using a loss factor k_{AC}, set to 0.1. The total power losses in the cable are then defined as

$$Q_{\mathrm{Cab}} = (1 + k_{\mathrm{AC}})\, R_{\mathrm{DC}}\, I^{2} \tag{2.254}$$

where the current I represents either the DC current I_{DC} or the AC RMS current $I_{\mathrm{AC,rms}}$.

2.4.1.2.2 Radial Temperature Distribution

The cable is modelled as an infinitely long, cylindrically symmetric system, reducing the temperature distribution to a one-dimensional radial profile. End-effects can be safely neglected when the ratio of cable length to conductor radius exceeds 1000 [241, 246, 252]. Although this may not hold for very short AC connections between closely integrated machines and power converters, the effect on the overall system remains negligible. Temperatures at the boundaries of adjacent layers must be continuous. Temperature-dependent material properties are evaluated at the mean temperature within each layer. A simplified cross-section with key parameters and boundary conditions is shown in Figure 2.49.
Under steady-state conditions, the radial heat equation becomes

$$\frac{1}{r}\,\frac{\partial}{\partial r}\left(r\,\frac{\partial T(r)}{\partial r}\right) + \frac{\dot{q}_{\mathrm{v}}}{\lambda(T)} = 0 \tag{2.255}$$

where $\dot{q}_{\mathrm{v}}$ denotes the specific volumetric heat generation rate in the layer. By separation

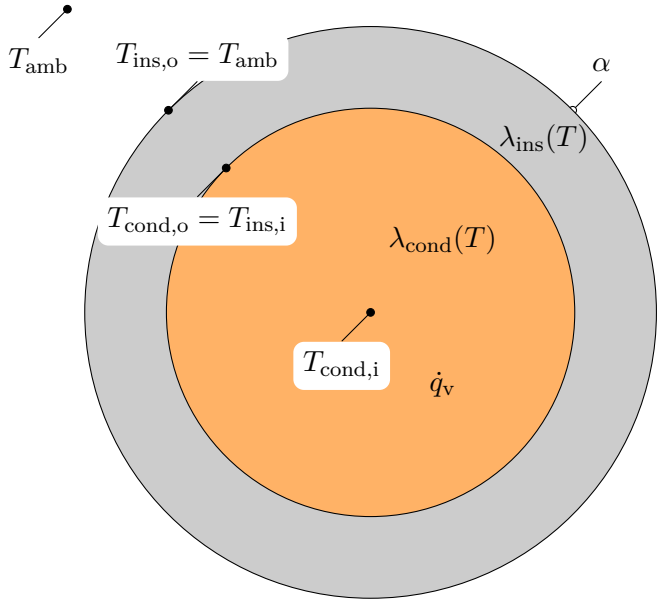

Figure 2.49: Simplified two-dimensional cross-section of cable for thermal model showing the relevant temperature nodes, volumetric loss sources, and temperature-dependent material properties.

of variables and integrating twice, the general solution is

$$T(r) = -\frac{\dot{q}_{\text{v}}}{4\,\lambda}\,r^2 + C_1\,\ln(r) + C_2 \tag{2.256}$$

with C_1 and C_2 as integration constants.

Insulation Wall Temperature

The first step in evaluating the cable's temperature profile is to determine the convective heat transfer coefficient α at the outer surface of the insulation layer. All power cables are assumed to be naturally air-cooled, since forced air cooling is rarely available at all installation sites, and implementing a liquid cooling system would require considerable effort for routing, insulation, coolant selection, and ensuring availability across operating conditions.

Heat transfer occurs via both convection and radiation. However, due to uncertainty in the installation environment, radiation is omitted to avoid overly optimistic thermal predictions. With a known loss value Q_{Cab} generated in the conductor, the specific volumetric loss density $\dot{q}_{\text{v}}$ is calculated as

$$\dot{q}_{\text{v}} = \frac{Q_{\text{Cab}}}{V_{\text{cond}}} = \frac{Q_{\text{Cab}}}{r_{\text{cond,o}}^2\,\pi\,L_{\text{cab}}}. \tag{2.257}$$

The convective heat transfer coefficient is calculated using Equations (2.130), (2.131) and (2.133) to (2.135), and the outer insulation temperature is determined by

$$T_{\text{ins,o}} = T_{\text{amb}} + \frac{\dot{q}_{\text{v}}\,r_{\text{cond,o}}^2}{2\,r_{\text{ins,o}}\,\alpha_{\text{Cab}}}. \tag{2.258}$$

Temperature Profile Inside Insulation Layer

Two boundary conditions are needed to solve Equation (2.255) for the hollow cylindrical insulation layer:

$$T(r = r_{\text{ins,i}}) = T_{\text{ins,i}} \tag{2.259}$$

$$T(r = r_{\text{ins,o}}) = T_{\text{ins,o}}. \tag{2.260}$$

Using these conditions and Equation (2.258), the temperature profile becomes

$$T_{\mathrm{ins}}(r) = T_{\mathrm{ins,o}} + \frac{\dot{q}_{\mathrm{v}}\, r_{\mathrm{cond,o}}^2}{2\,\lambda_{\mathrm{ins}}}\, \ln\left(\frac{r_{\mathrm{ins,o}}}{r}\right) \tag{2.261}$$

which exhibits a logarithmic temperature gradient in the radial direction.

Temperature Profile Inside Stranded Conductor

The temperature profile inside the conductor is derived using a Neumann boundary condition at the center and a Dirichlet condition at the outer conductor radius:

$$\left.\frac{\mathrm{d}T}{\mathrm{d}r}\right|_{r=0} = 0 \tag{2.262}$$

$$T(r = r_{\mathrm{cond,o}}) = T_{\mathrm{cond,o}}. \tag{2.263}$$

The resulting specific solution for the temperature distribution in a solid cylinder with uniform internal heat generation is

$$T_{\mathrm{cond}}(r) = T_{\mathrm{cond,o}} + \frac{\dot{q}_{\mathrm{v}}\, r_{\mathrm{cond,o}}^2}{4\lambda_{\mathrm{cond}}} \left(1 - \frac{r^2}{r_{\mathrm{cond,o}}^2}\right). \tag{2.264}$$

This yields a parabolic (quadratic) temperature distribution symmetric about the center axis of the conductor. The complete temperature profile across the conductor and insulation, including a schematic extension into the ambient, is shown in Figure 2.50. The dimensions of the conductor and insulation are exaggerated to clearly illustrate the thermal gradients. It is evident that, even for large conductors, most of the temperature drop occurs between the cable surface and the surrounding air. This effect becomes more pronounced for smaller conductors operating at higher current levels.

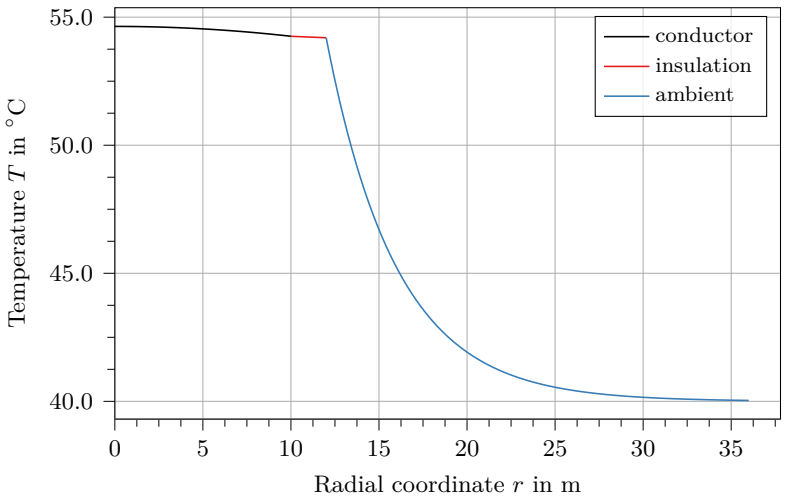

Figure 2.50: Analytical temperature distribution with quadratic profile in the conductor, logarithmic profile in the insulation, and an exponential decay (schematic only) into the ambient for a DC cable made of copper with $r_{\mathrm{cond,o}} = 10\,\mathrm{mm}$ insulated with a Duralectric™ layer of $t_{\mathrm{ins}} = 2\,\mathrm{mm}$, operating at $V_{\mathrm{DC}} = 2000\,\mathrm{V}$ and $I_{\mathrm{cond}} = 300\,\mathrm{A}$ in an ambient temperature of $T_{\mathrm{amb}} = 40\,^{\circ}\mathrm{C}$.

Derating for Elevated Ambient Temperatures

Cable nominal ratings are typically specified for an ambient temperature of $T_{\mathrm{amb}} = 40\,^{\circ}\mathrm{C}$. In aerospace applications, ambient or operating temperatures can be significantly higher. Standard designs may assume $50\,^{\circ}\mathrm{C}$ ambient, but temperatures above $100\,^{\circ}\mathrm{C}$ are common when cables are installed near hot gas turbines in hybrid-electric configurations. It is

therefore necessary to determine the ampacity derating for a given cable design under elevated ambient conditions. Figure 2.51 shows the normalized ampacity $I_{\max}/I_{\max,40\,^\circ\mathrm{C}}$ as a function of ambient temperature between 40 and 260 °C for a generic cable with a maximum permissible conductor temperature of $T_{\max} = 260\,^\circ\mathrm{C}$.

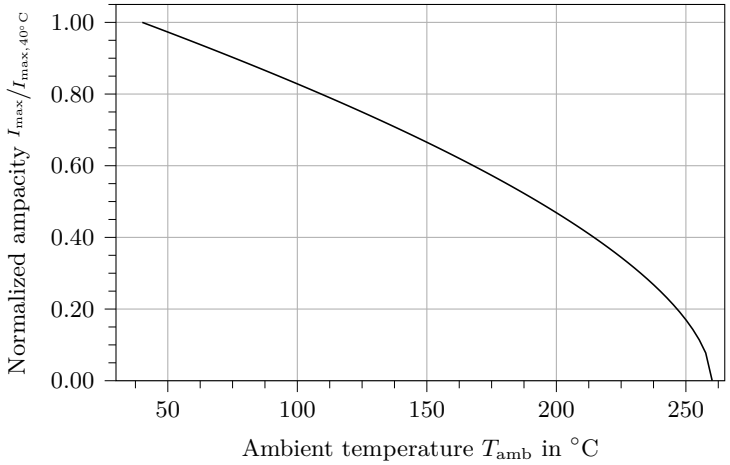

Figure 2.51: Normalized ampacity $I_{\max}/I_{\max,40\,^\circ\mathrm{C}}$ versus ambient temperature T_{amb} for a generic cable design with a maximum allowed conductor temperature of $T_{\max} = 260\,^\circ\mathrm{C}$.

The current-carrying capacity decreases quadratically with rising ambient temperature, reaching zero when the ambient equals the maximum allowable conductor temperature.

2.4.2 Connectors at Cable Terminals

At the terminals of a cable pole, an appropriate method must be provided to connect it to another cable or device. Common solutions include soldered joints, crimped lugs, and removable plug-and-socket systems comprising a male plug and a female receptacle. Power connectors from GlenAir Inc. [253] have been evaluated with respect to their weight as a function of ampacity. Figure 2.52 shows the weight of a single plug or receptacle (assumed equal) for varying conductor current levels.

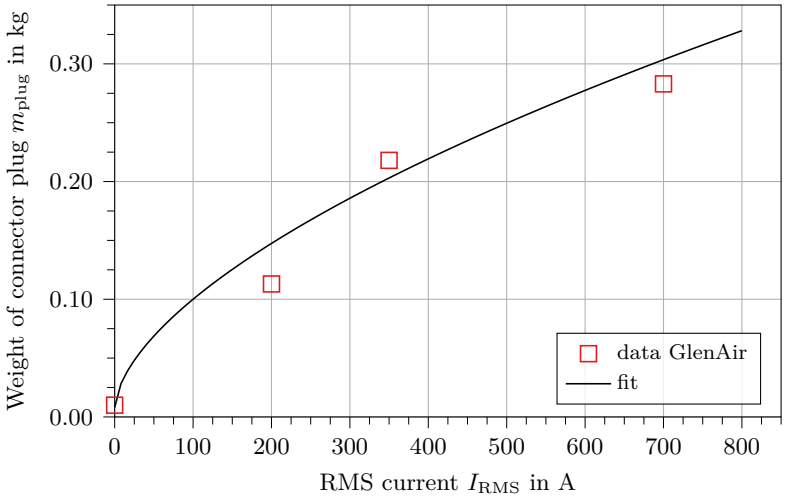

Figure 2.52: Approximated weight of a single connector plug or receptacle, fitted with an exponential function based on measured data of PowerTrip 970 connectors from GlenAir Inc. [253], as a function of conductor current.

Although a quadratic fit yields a higher coefficient of determination for the available data points, the exponential fit was chosen as it increases monotonically and avoids unrealistic behaviour when extrapolated beyond the measured current range.

2.4.3 Short Summary

A model for power distribution elements, including DC and AC cables as well as connectors, has been introduced with a focus on the electro-thermal behaviour of the cable. Off-the-shelf components from GlenAir Inc. [237, 253] are used as benchmarks and show very good agreement with the proposed physical models. As an example, the size and specific weight of cables are compared for copper and aluminum conductors operating at a fixed DC link voltage (see Figure 2.53).

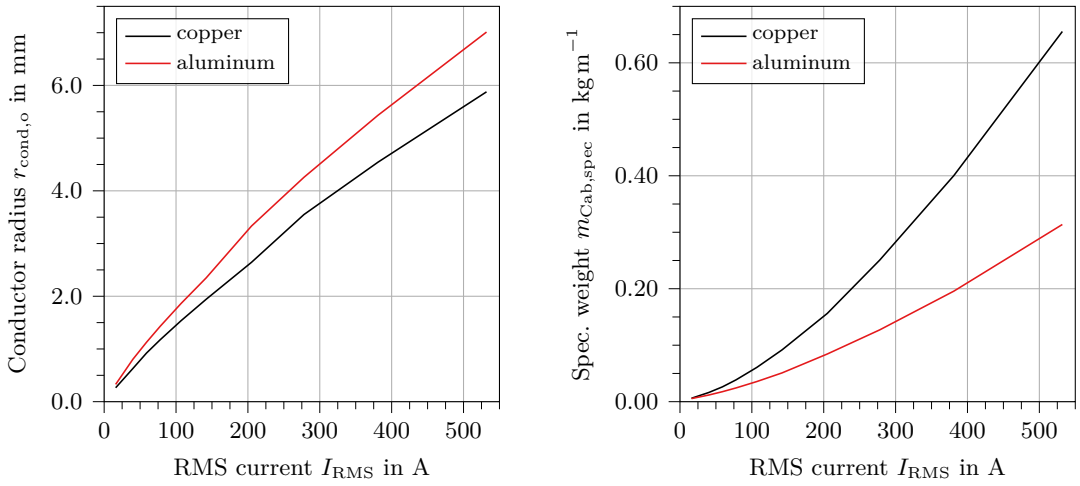

(**a**) Size

(**b**) Weight

Figure 2.53: Comparison of copper and aluminum as conductor materials in terms of cable size and specific weight

The required conductor radius $r_{\mathrm{cond,o}}$ increases logarithmically and is approximately 30 % larger for aluminum than for copper, which is consistent with aluminum's electrical resistivity being roughly 63 % higher. Conversely, the lower specific mass $m_{\mathrm{Cab,spec}}$ of aluminum cables results from its density being only about one third that of copper. The model enables detailed exploration of such trade-offs and naturally accounts for secondary effects such as surface area for cooling and temperature-dependent material properties.

2.5 Thermal Management System

The thermal management system consists of a heat exchanger that transfers heat from one fluid (or gas) to another, a pump that drives the fluid against pressure losses through the cooling circuit, and piping that guides the fluid. Auxiliaries, such as valves, are accounted for as a fraction of the total tubing mass only [254]. The primary task of the thermal management system is to dissipate heat generated by all electric components, ensuring each operates within its specified thermal limits. Owing to their broad applicability, both liquid and gaseous cooling systems are considered, with particular focus on compact heat exchangers. These enable high thermal loads at low mass and are therefore especially well suited for aircraft applications [254, 255].
This section presents the modelling of all relevant components of the thermal management system based on the required heat dissipation and the system's operating conditions, namely temperature and pressure drop within the cooling loop.

2.5.1 Compact Heat Exchangers

A heat exchanger is a device that transfers thermal energy between two or more fluids operating at different temperature levels, commonly referred to as the hot and cold streams. Heat exchangers are typically classified by their flow arrangement: parallel-flow, where both fluids move in the same direction; counterflow, where they flow in opposite directions; and cross-flow, where the fluids move perpendicularly to each other [256].
Compact heat exchangers are designed to achieve high heat transfer surface area per unit volume. These devices employ dense arrays of finned tubes or plates and are particularly effective when at least one of the fluids is a gas, which typically has a low convection coefficient. According to [256], compact heat exchangers exhibit surface densities β_{HX} exceeding $400\,\mathrm{m^2\,m^{-3}}$. Offset strip and louvered fin geometries are especially well suited for such applications. A computational model as shown in Figure 2.54 is used to evaluate the thermodynamic performance of such exchangers and is supported by extensive research [254, 256, 257].
For a specified heat exchanger, the model evaluates the outlet temperatures and pressures. The required input parameters include:

- definition of heat exchanger type and overall dimensions,
- complete specification of the hot and cold surfaces, including surface geometry and material selection (see 2.5.1.1),
- fluid properties, mass flow rates, and inlet conditions (temperature and pressure).

The surface types and their thermal characteristics are discussed in Section 2.5.1.1, while the geometrical properties are defined in Section 2.5.1.2. The outlet conditions are then computed iteratively by evaluating thermodynamic properties and pressure losses until convergence is achieved, as described in Section 2.5.1.3.

2.5.1.1 Surface Types of Plate Fin Heat Exchangers

Heat exchangers typically consist of hot and cold sides, each featuring a heat transfer surface separated by plates. Various surface types are used in heat exchangers, including plain, wavy, louvered, and offset strip fins. A visual example of an offset strip fin heat exchanger is shown in Figure 2.55.
The heat exchanger is composed of N_{p} hot passages and $(N_{\mathrm{p}}+1)$ cold passages, alternating in the vertical (L_3) direction. Figure 2.56 shows a section of a plate fin heat exchanger

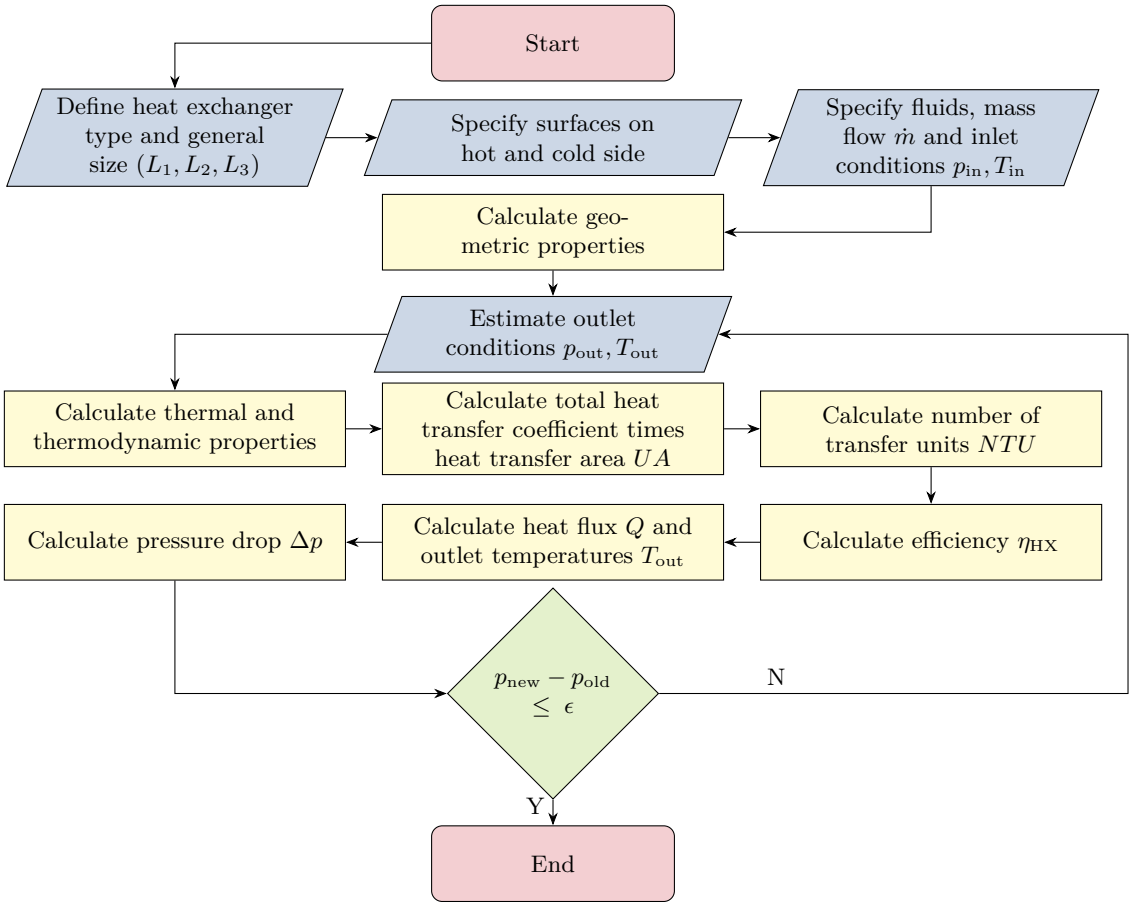

Figure 2.54: Workflow for computing the thermodynamic performance of heat exchangers, including outlet temperatures and pressures based on specified inputs

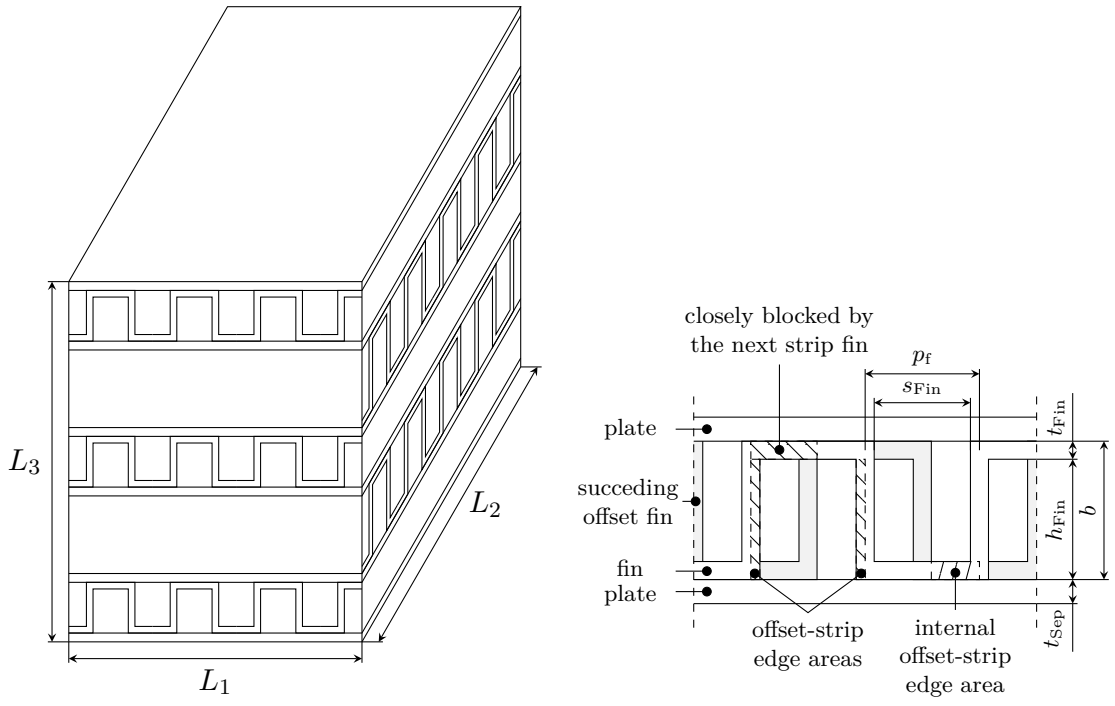

(**a**) Overall layout of plate fin heat exchanger with offset strip fins

(**b**) Schematic of an offset strip fin geometry

Figure 2.55: Overall structure of a plate fin heat exchanger with offset strip fins and the detailed geometric schematic of the fins

with offset strip fins, where the fluids enter the heat exchanger perpendicularly to each other in a cross-flow configuration. This cross-flow arrangement maximizes the temperature difference between the hot and cold fluids, providing the highest performance for the layout. The color-shaded area qualitatively represents the decreasing temperature of the hot fluid along the flow direction, with the temperature change reversed for the cold side.

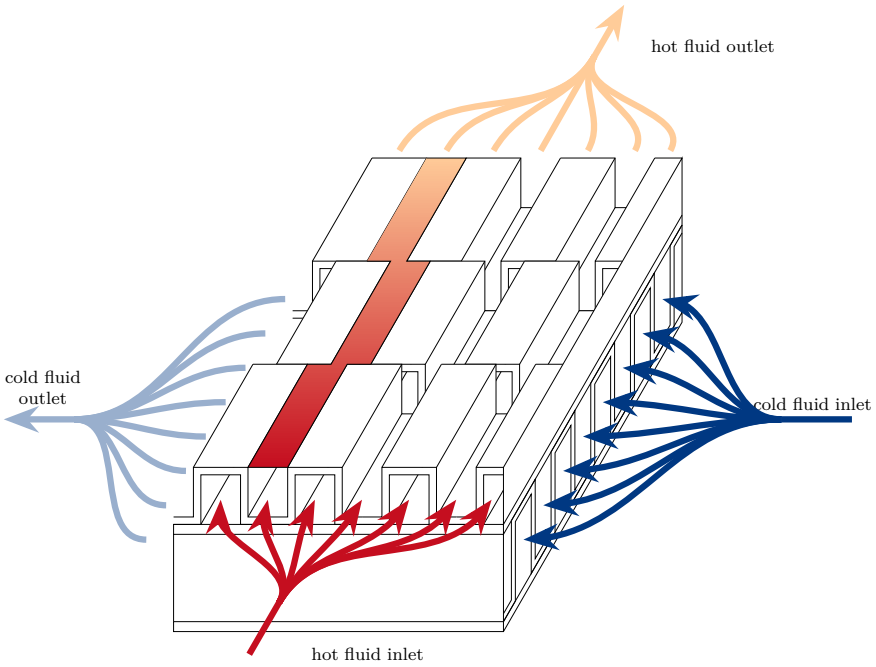

Figure 2.56: Section of a plate fin heat exchanger with offset strip fins. The cross-flow arrangement is chosen to provide the highest performance for the given layout. The color-shaded area qualitatively represents the decreasing temperature of the hot fluid along the flow direction.

For offset strip fins, a comprehensive description of the heat transfer surfaces requires the specification of the following parameters (as shown in Figures 2.55 and 2.56):

- Offset strip fins:
  - Fin thickness, t_{fin}
  - Plate spacing, b_{fin} (together with t_{fin}, this defines the channel height, h_{fin})
  - Fin pitch, p_{fin} (together with t_{fin}, this defines the lateral channel width, s_{fin})
  - Length of fins in the flow direction, l_{fin}
- Other fin types (e.g., wavy, louvered, plain, or custom):
  - All of the above parameters, plus
  - Hydraulic radius of the fluid passage, r_{h}
  - Surface area density, β_{HX}
  - Fin-to-total area ratio, A_{ft}

The number of parameters required to fully specify other types of heat exchangers is larger than for offset strip fins, due to the lack of generalized correlations for geometrically describing these surfaces.

2.5.1.2 Geometrical Definition

A variety of specific geometric parameters can be calculated for the evaluation of compact heat exchangers. Explicit analytical formulas for offset strip fin geometries are provided

by Manglik and Bergles [258], while general formulas for various types of heat exchangers can be found in [254, 257]. These equations have been modified to account for different thicknesses of separation plates, t_{sep}, and end plates at the top and bottom of the heat exchanger, t_{end}.
First, the hydraulic diameter d_{h} of the surface is calculated. The more general formulation is applicable to all types of surfaces, while the second formula is specifically for offset strip fins.

$$\begin{aligned} d_{\mathrm{h}} &= \frac{4\,A_{\mathrm{c}}\,l_{\mathrm{FP}}}{A_{\mathrm{t}}} \\ &= \frac{4\,s_{\mathrm{fin}}\,h_{\mathrm{fin}}\,l_{\mathrm{fin}}}{(2\,(s_{\mathrm{fin}}\,l_{\mathrm{fin}} + h_{\mathrm{fin}}\,l_{\mathrm{fin}} + t_{\mathrm{fin}}\,h_{\mathrm{fin}}) + t_{\mathrm{fin}}\,s_{\mathrm{fin}})} \end{aligned} \tag{2.265}$$

where l_{FP} is the length of the flow path in one direction, and A_{c} and A_{t} represent the free-flow and total heat transfer surface areas, respectively.
The heat exchanger consists of N_{p} hot passages and $(N_{\mathrm{p}} + 1)$ cold passages to minimize heat loss to the ambient. The top and bottom passages are assumed to be cold fluid passages. The total number of passages, L_3, is given by

$$L_3 = N_{\mathrm{p}}\,b_{\mathrm{fin},1} + (N_{\mathrm{p}} + 1)\,b_{\mathrm{fin},2} + 2\,N_{\mathrm{p}}\,t_{\mathrm{sep}} + 2\,t_{\mathrm{end}} \tag{2.266}$$

Solving for N_{p} yields

$$N_{\mathrm{p}} = \frac{L_3 - b_2 - 2\,t_{\mathrm{end}}}{b_1 + b_2 + 2\,t_{\mathrm{sep}}} \tag{2.267}$$

where L_3 is the total active height. This can be used to calculate the number of fins n_{f} on each side:

$$n_{\mathrm{fin},1} = \frac{L_1}{p_{\mathrm{fin},1}}\,N_{\mathrm{p}} \tag{2.268}$$

$$n_{\mathrm{fin},2} = \frac{L_2}{p_{\mathrm{fin},2}}\,(N_{\mathrm{p}} + 1) \tag{2.269}$$

and the number of offset fins, n_{off}:

$$n_{\mathrm{off}} = \frac{l_{\mathrm{FP}}}{l_{\mathrm{fin}}} \tag{2.270}$$

where the fin pitch p_{fin} is the inverse of the fin density.
The total primary area A_{p} (in this case, on the hot side) consists of the total plate areas, passage side wall areas, and the passage front and back wall areas, minus the fin base areas. It is defined as

$$A_{\mathrm{p,h}} = \begin{cases} 2\,L_1\,L_2\,N_{\mathrm{p}} - 2\,t_{\mathrm{fin}}\,L_2\,n_{\mathrm{fin},1} + 2\,b_{\mathrm{h}}\,L_2\,N_{\mathrm{p}} \\ +2\,(b_{\mathrm{c}} + 2\,t_{\mathrm{sep}})\,L_1\,(N_{\mathrm{p}} + 1) \\ +4\,(t_{\mathrm{end}} - t_{\mathrm{sep}})\,L_1 & \text{offset strip fins} \\ A_{\mathrm{t,h}} - A_{\mathrm{f,h}} & \text{for all other types.} \end{cases} \tag{2.271}$$

The total fin area A_{f} consists of the fin area and offset-strip edge areas, and is calculated using the fin-to-total area ratio, A_{ft}:

$$A_{\mathrm{f}} = \begin{cases} 2\,(b - t_{\mathrm{fin}})\,l_{\mathrm{FP}}\,n_{\mathrm{fin}} + 2\,(b - t_{\mathrm{fin}})\,t_{\mathrm{sep}}\,n_{\mathrm{off}}\,n_{\mathrm{fin}} \\ +(p_{\mathrm{fin}} - t_{\mathrm{fin}})\,t_{\mathrm{fin}}\,(n_{\mathrm{off}} - 1)\,n_{\mathrm{fin}} \\ +2\,p_{\mathrm{fin}}\,t_{\mathrm{fin}}\,n_{\mathrm{f}} & \text{offset strip fins} \\ A_{\mathrm{ft}}\,A_{\mathrm{t}} & \text{for all other types.} \end{cases} \tag{2.272}$$

The total heat transfer area A_t is then given by

$$A_\mathrm{t} = \begin{cases} A_\mathrm{p} + A_\mathrm{f} & \text{offset strip fins} \\ \beta_\mathrm{HX}\, V & \text{for all other types.} \end{cases} \tag{2.273}$$

where β_HX is the surface area density and V is the volume of the respective side. The free-flow (cross-sectional) area A_c is obtained by

$$A_\mathrm{c} = \begin{cases} (b_\mathrm{fin} - t_\mathrm{fin})\,(p_\mathrm{fin} - t_\mathrm{fin})\,n_\mathrm{fin} & \text{offset strip fins} \\ \dfrac{d_\mathrm{h}\, A_\mathrm{t}}{4\, l_\mathrm{FP}} & \text{for all other types.} \end{cases} \tag{2.274}$$

The frontal area A_fr, where the fluid enters, is defined by

$$A_\mathrm{fr} = L\, L_3 \tag{2.275}$$

and the porosity σ_HX of the surface is computed as

$$\sigma_\mathrm{HX} = \beta_\mathrm{HX}\, L_3. \tag{2.276}$$

2.5.1.3 Thermo- and Fluid Dynamics

In addition to geometric considerations, thermodynamic and fluid dynamic calculations are crucial for the design of heat exchangers. Specifically, compact air-liquid heat exchangers are of particular interest for aircraft applications, as they dissipate heat losses to the ambient both while on the ground and in flight.

Mass Velocities and Reynolds Numbers

The mass velocity G and Reynolds number Re on both the hot and cold sides of the heat exchanger can be calculated as:

$$G = \frac{\dot{m}}{A_\mathrm{c}} \tag{2.277}$$

and

$$Re = \frac{G \cdot d_\mathrm{h}}{\mu} \tag{2.278}$$

where $\dot{m}$ is the mass flow rate and μ is the dynamic viscosity of the fluid.

Chilton-Colburn and Fanning Friction Factors of Surfaces

For accurate heat exchanger rating and sizing, it is essential to have a clear understanding of both heat transfer and friction flow characteristics. The heat transfer characteristics are defined by the Chilton-Colburn factor j, while the pressure drop is related to the Fanning friction factor f [256].

Analytical equations for offset strip fin geometries, taking into account the surface's geometric properties, are provided by Manglik and Bergles [258]. For many other surface types, tabulated data can be found in [254, 256].

Using the following dimensionless parameters:

$$\begin{aligned} \alpha &= \frac{s_\mathrm{fin}}{h_\mathrm{fin}} \\ \delta &= \frac{t_\mathrm{fin}}{l_\mathrm{fin}} \\ \gamma &= \frac{t_\mathrm{fin}}{s_\mathrm{fin}} \end{aligned} \tag{2.279}$$

the Chilton-Colburn factor j_{fin} and Fanning friction factor f_{fin} for an offset strip fin are given by:

$$j_{\text{fin}} = 0.6522\, Re^{-0.5403}\, \alpha^{-0.1541}\, \delta^{0.1499}\, \gamma^{-0.0678} \left(1 + 5.269 \times 10^{-5}\, Re^{1.340}\, \alpha^{-0.504}\, \delta^{0.456}\, \gamma^{-1.055}\right)^{0.1} \tag{2.280}$$

$$f_{\text{fin}} = 9.6243\, Re^{-0.7422}\, \alpha^{-0.1856}\, \delta^{0.3053}\, \gamma^{-0.2659} \left(1 + 7.699 \times 10^{-8}\, Re^{4.429}\, \alpha^{0.920}\, \delta^{3.767}\, \gamma^{0.236}\right)^{0.1} \tag{2.281}$$

Figure 2.57 shows a comparison of the correlations developed by Manglik and Bergles [258] and experimental data from [254] for a 1/8-19.86 strip fin.

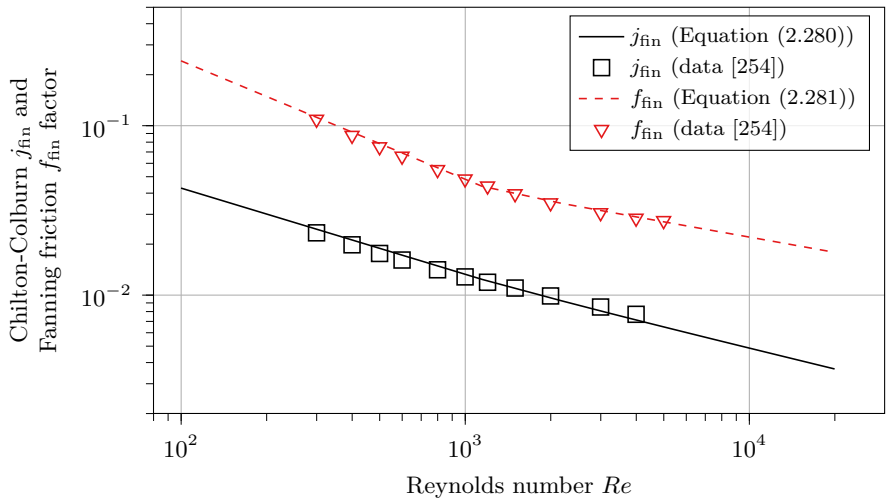

Figure 2.57: Chilton-Colburn j_{fin} and Fanning friction f_{fin} factors for 1/8-19.86 strip fin. Comparison of correlations developed by [258] and experimental data from [254].

Overall Fin Efficiency of Surfaces

When extended surfaces, such as offset strip fins, are used, the temperature effectiveness is reduced due to temperature gradients along the fins extending into the fluid [254]. For fins extending from wall to wall, the corrected fin length l_{c} is given by

$$l_{\text{c}} = \frac{b_{\text{fin}}}{2} - t_{\text{fin}} \tag{2.282}$$

The fin effectiveness parameter m_{fin} and the fin surface efficiency η_{fin} are defined by Gardner [259] as follows:

$$m_{\text{fin}} = \sqrt{\frac{2\,h}{\lambda\, t_{\text{fin}}} \left(1 + \frac{t_{\text{fin}}}{l_{\text{fin}}}\right)} \tag{2.283}$$

$$\eta_{\text{fin}} = \frac{\tanh(m_{\text{fin}}\, l_{\text{c}})}{m_{\text{fin}}\, l_{\text{c}}} \tag{2.284}$$

where h is the heat transfer coefficient and λ is the thermal conductivity of the fin material. Finally, the overall fin surface efficiency η_{o} can be computed as

$$\eta_{\text{o}} = 1 - A_{\text{ft}}\,(1 - \eta_{\text{fin}}) \tag{2.285}$$

Heat Transfer Coefficients of Surfaces

The heat transfer coefficients h for each surface side in terms of Chilton-Colburn j_{fin} and Fanning friction f_{fin} factors are calculated using the Prandtl number Pr:

$$h = \frac{j_{\text{fin}}\, G\, c_{\text{p}}}{Pr^{\frac{2}{3}}} \tag{2.286}$$

The overall heat transfer coefficient times the heat transfer area UA of the heat exchanger is the sum of the thermal wall resistance $R_{\text{th,sep}}$:

$$R_{\text{th,sep}} = \frac{t_{\text{sep}}}{\lambda_{\text{sep}}\, A_{\text{w}}} \tag{2.287}$$

and the heat transfer times area for the hot or cold side:

$$UA_{\text{h/c}} = \frac{1}{\eta_{\text{o}}\, h\, A_{\text{t}}} \tag{2.288}$$

This leads to the following relation:

$$UA = \frac{1}{UA_{\text{h}} + R_{\text{th,sep}} + UA_{\text{c}}} \tag{2.289}$$

ε-NTU Method

When the heat transfer rate or outlet temperatures are unknown, the log mean temperature difference method requires numerous iterations. In 1955, Kays and London [254] developed the ε-NTU method to eliminate the need for a large number of iterations. This method requires the calculation of the heat capacity rate C, which is the product of mass flow rate and specific heat. The minimum and maximum transfer rates, C_{min} and C_{max}, as well as the heat capacity ratio C_{r}, are defined as

$$C = \dot{m}\, c_{\text{p}} \tag{2.290}$$

$$C_{\text{min}} = \min(C_{\text{c}}, C_{\text{h}}) \tag{2.291}$$

$$C_{\text{max}} = \max(C_{\text{c}}, C_{\text{h}}) \tag{2.292}$$

$$C_{\text{r}} = \frac{C_{\text{min}}}{C_{\text{max}}} \tag{2.293}$$

where c_{p} is the specific heat capacity of the fluid. The heat exchanger effectiveness ε_{HX} is then given by

$$\varepsilon_{\text{HX}} = \frac{Q}{Q_{\text{max}}} \tag{2.294}$$

and the number of transfer units NTU is defined by

$$NTU = \frac{UA}{C_{\text{min}}} \tag{2.295}$$

Kays and London [254] developed several correlations for different types of flow arrangements, for which the effectiveness can be calculated directly. For parallel flow (i.e., both fluids enter the heat exchanger on the same side and exit on the other), the correlations are as follows:

$$\varepsilon_{\text{HX}} = \frac{1 - e^{-NTU(1+C_{\text{r}})}}{1 + C_{\text{r}}} \tag{2.296}$$

$$NTU = \frac{1}{1 + C_{\text{r}}}\, \ln(1 - \varepsilon(1 + C_{\text{r}})) \tag{2.297}$$

For counterflow (i.e., the fluids enter the heat exchanger from opposite sides), the correlations are as follows:

$$\varepsilon_{\mathrm{HX}} = \frac{1 - e^{-NTU(1-C_\mathrm{r})}}{1 - C_\mathrm{r}\, e^{-NTU(1-C_\mathrm{r})}} \tag{2.298}$$

$$NTU = \frac{1}{1 - C_\mathrm{r}} \cdot \ln\left(\frac{1 - \varepsilon C_\mathrm{r}}{1 - \varepsilon}\right) \tag{2.299}$$

For a cross-flow heat exchanger (i.e., the fluids enter the heat exchanger perpendicular to each other) where both fluids are unmixed, the following correlations are derived:

$$\varepsilon_{\mathrm{HX}} = 1 - e^{\frac{1}{C_\mathrm{r}} NTU^{0.22(e^{-C_\mathrm{r}}\, NTU^{0.78} - 1)}} \tag{2.300}$$

$$NTU = -\ln\left(1 + \frac{1}{C_\mathrm{r}} \ln(1 - \varepsilon C_\mathrm{r})\right) \tag{2.301}$$

Calculation of Outlet Temperatures

Based on the ε-NTU correlations, the outlet temperatures on the hot ($T_{\mathrm{out,h}}$) and cold ($T_{\mathrm{out,c}}$) sides can be derived as follows:

$$T_{\mathrm{out,h}} = T_{\mathrm{in,h}} - \varepsilon_{\mathrm{HX}} \frac{C_{\min}}{C_\mathrm{h}} (T_{\mathrm{in,h}} - T_{\mathrm{in,c}}) \tag{2.302}$$

$$T_{\mathrm{out,c}} = T_{\mathrm{in,c}} + \varepsilon_{\mathrm{HX}} \frac{C_{\min}}{C_\mathrm{c}} (T_{\mathrm{in,h}} - T_{\mathrm{in,c}}) \tag{2.303}$$

Pressure Drop

Calculating the pressure drop Δp along the flow path length L of one side of the heat exchanger includes not only core losses, but also entry losses due to contraction effects K_c and exit losses due to expansion effects K_e as well as losses from flow acceleration. The entrance and exit losses are considered for higher accuracy [254].

$$\begin{aligned} \Delta p = \frac{G^2}{2\rho_\mathrm{i}} \Bigg[& \left(1 - \sigma_{\mathrm{HX}}^2 + K_\mathrm{c}\right) + 2\left(\frac{\rho_\mathrm{i}}{\rho_\mathrm{o}} - 1\right) \\ & + \frac{4\, f_{\mathrm{fin}}\, L}{r_\mathrm{h}} \left(\frac{\rho_\mathrm{i}}{\rho_\mathrm{m}}\right) - \left(1 - \sigma_{\mathrm{HX}}^2 - K_\mathrm{e}\right) \frac{\rho_\mathrm{i}}{\rho_\mathrm{o}} \Bigg] \end{aligned} \tag{2.304}$$

Contraction and Expansion Coefficients

The jet contraction ratio for a tube-to-square geometry $C_{\mathrm{c,tube}}$ is given by [254]

$$C_{\mathrm{c,tube}} = 4.374\, 10^{-4} e^{6.737\sqrt{\sigma_{\mathrm{HX}}}} + 0.621 \tag{2.305}$$

while the friction factor f_d used for the calculation is deduced as

$$f_\mathrm{d} = \begin{cases} 0.049\, Re^{-0.2} & Re \geq 2300 \\ \dfrac{16}{Re} & \text{otherwise} \end{cases} \tag{2.306}$$

The velocity-distribution coefficient for circular tubes $K_{d,tube}$ can be then defined as and converted to a correlation for square tubes [254]

$$K_{\mathrm{d,tube}} = \begin{cases} 1.09068\,(4f_\mathrm{d}) + 0.05884\,\sqrt{4f_\mathrm{d}} + 1 & Re \geq 2300 \\ 1.33 & \text{otherwise} \end{cases} \tag{2.307}$$

$$K_{\mathrm{d,square}} = \begin{cases} 1 + 1.17\,(K_{\mathrm{d,tube}} - 1) & Re \geq 2300 \\ 1.39 & \text{otherwise} \end{cases} \tag{2.308}$$

Finally, the contraction coefficient (entry loss coefficient) $K_{\mathrm{c,square}}$ and expansion coefficient (exit loss coefficient) $K_{\mathrm{e,square}}$ can be calculated as [254]

$$K_{\mathrm{c,square}} = \frac{1 - 2C_{\mathrm{c,tube}} + C_{\mathrm{c,tube}}^2(2K_{\mathrm{d,square}} - 1)}{C_{\mathrm{c,tube}}^2} \tag{2.309}$$

$$K_{\mathrm{e,square}} = 1 - 2K_{\mathrm{d,square}}\sigma_{\mathrm{HX}} + \sigma_{\mathrm{HX}}^2 \tag{2.310}$$

The parameters K_{c} and K_{e} for each fluid are determined by the porosity of the surface arrangement and the Reynolds number which is assumed to be fully turbulent ($Re \geq 10^7$) because of the frequent boundary layer interruptions due to the fins [254].

2.5.2 Heat Sinks with Rectangular Fins

Power semiconductors require heat sinks to dissipate thermal energy to the environment. To accommodate both air- and liquid-cooled configurations, a base plate with rectangular fins, as illustrated in Figure 2.58, is used to evaluate the cooling potential under given operating conditions. Arrays of rectangular fins offer high heat transfer performance, ease of manufacture, low cost, and the advantage of analytical tractability for both thermal and hydraulic evaluations. These features are particularly valuable during the pre-design stage.

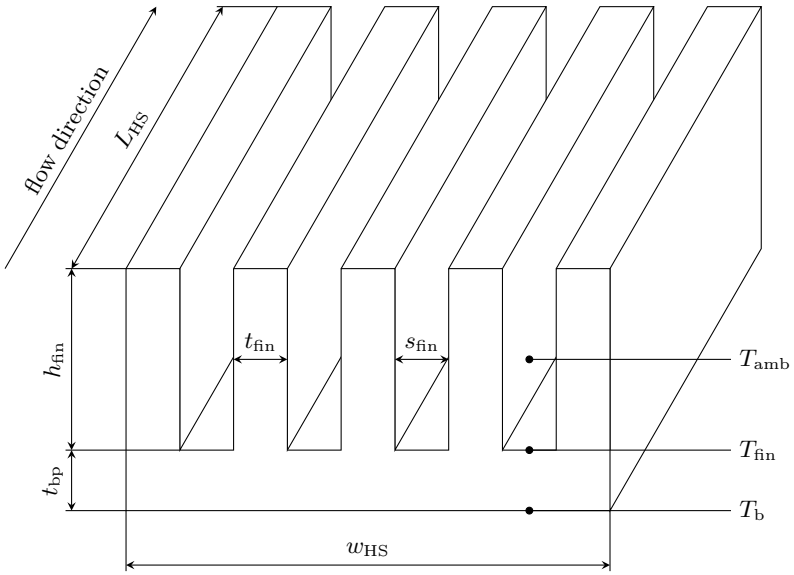

Figure 2.58: Schematic geometry of a plate with longitudinal, rectangular fins used as a heat sink, for example in power semiconductor applications. The model shows key geometric parameters, nodes used for temperature evaluation, and the direction of forced convection. The model also remains valid for natural convection scenarios.

In general, the calculation process used to derive the temperature distribution and pressure drop under forced convection is similar to the approach outlined in Figure 2.54. The main difference is that the fin surface temperature T_{fin} must be determined iteratively. The relevant models are presented in the following.

2.5.2.1 Geometrical Properties of Rectangular Fins

The overall size of the heat sink is defined by its length L_{HS} and width w_{HS}. The heat source is located at the bottom, with the base temperature T_{b}, and is separated from the fins by the baseplate of thickness t_{bp}.
The primary area of the base A_{p}, the wetted fin area A_{f}, and the area contributing to radiative heat emission A_{d}, which includes all surfaces except the base plate surface where the heat source is applied, are the most relevant geometric parameters for thermodynamic evaluation.

$$A_{\mathrm{p}} = L\, t_{\mathrm{fin}}\, (N_{\mathrm{fin}} - 1) \tag{2.311}$$

$$A_{\mathrm{f}} = L\, (2\, h_{\mathrm{fin}} + t_{\mathrm{fin}})\, N_{\mathrm{fin}} \tag{2.312}$$

$$A_{\mathrm{d}} = (L\, t_{\mathrm{fin}} + 2\, h_{\mathrm{fin}}\, t_{\mathrm{fin}})\; N_{\mathrm{fin}} + 2\, h_{\mathrm{fin}}\, L + 2\, t_{\mathrm{BP}}\, (L + w) \tag{2.313}$$

2.5.2.2 Thermo- and Fluid Dynamics

To derive the surface temperature of the fins and the pressure drop along the flow axis, heat transfer characteristics for convection and radiation under both natural and forced conditions are required. Fin efficiency is also an important factor.

2.5.2.2.1 Heat Transfer Through U-Shaped Channels

The U-shaped channels are subject to natural or forced convection and, in the case of air cooling, to radiation. For liquid-cooled configurations, convective heat transfer is typically at least an order of magnitude greater than for air, allowing radiation to be neglected.

Natural Convection
For natural convection, the heat transfer coefficient is calculated using the Elenbaas number El [260], which is based on the Rayleigh number Ra (see Equations (2.131) and (2.133)) and the corresponding characteristic length L_{char}:

$$El = Ra\, \frac{L_{\mathrm{char}}}{L} \tag{2.314}$$

$$L_{\mathrm{char}} = \frac{2\, h_{\mathrm{fin}}\, s_{\mathrm{fin}}}{2\, h_{\mathrm{fin}} + s_{\mathrm{fin}}} \tag{2.315}$$

The Nusselt number is then calculated as

$$Nu = \frac{El}{\Psi_{\mathrm{B}}} \left(1 - e^{-\Psi_{\mathrm{B}} \left(\frac{0.5}{El}\right)^{0.75}}\right) \tag{2.316}$$

using Bilitzky's geometrical coefficient Ψ_{B} [261], based on prior work [262]. It is defined as

$$\Psi_{\mathrm{B}} = \frac{24 \left(1 - 0.483\, e^{-0.17/a}\right)}{\left(1 + \frac{a}{2}\right) \left(1 + (1 - e^{-0.83\, a}) \left(9.14 \sqrt{a}\, e^{-B} - 0.61\right)\right)^3} \tag{2.317}$$

$$a = \frac{s_{\mathrm{fin}}}{h_{\mathrm{fin}}} \tag{2.318}$$

$$B = 1.25 \left(1 + \frac{s_{\mathrm{fin}}}{2\, h_{\mathrm{fin}}}\right) \tag{2.319}$$

where a and B are helper coefficients. Equation (2.319) is a fit of experimental data [263] and carries a standard error of estimate. The heat transfer coefficient is then determined using Equation (2.130).

Forced Convection

For forced convection, a composite model based on the Churchill-Usagi correlation [264] was proposed in [265] to account for both developing and fully developed flows within the channels:

$$Nu = \left(\frac{1}{\left(0.5\,\frac{s_{\mathrm{fin}}}{L}\,Re\,Pr\right)^3} + \frac{1}{\left(0.664\,\sqrt{\frac{s_{\mathrm{fin}}}{L}\,Re}\,Pr^{1/3}\sqrt{1+3.65\,\sqrt{\frac{L}{s_{\mathrm{fin}}\,Re}}}\right)^3} \right)^{-1/3}. \tag{2.320}$$

Figure 2.59 shows that for a typical design, a maximum heat transfer coefficient is achieved at a specific number of fins. Natural cooling is more effective at low air velocities (up to $0.3\,\mathrm{m\,s^{-1}}$). To ensure sufficient heat transfer, especially under forced conditions, the flow velocity should be high enough to induce turbulence. The inclination of the profile also has a significant impact on natural convection [266].

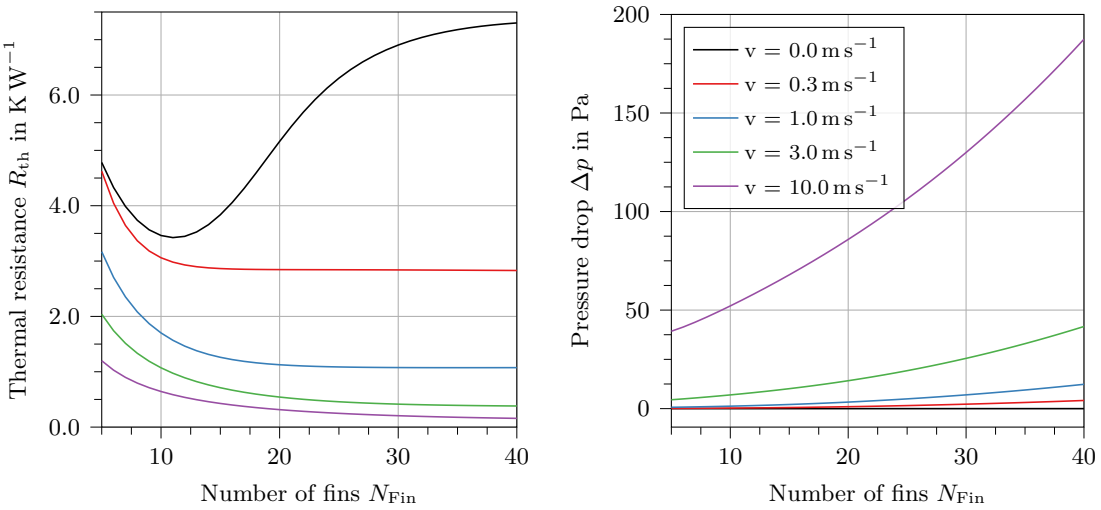

(**a**) Thermal resistance

(**b**) Pressure drop

Figure 2.59: Influence of fin number on an otherwise unchanged geometric profile with rectangular fins for air stream velocities ranging $v = 0.0 - 10.0\,\mathrm{m\,s^{-1}}$.

The chart shows that thermal resistance decreases with an increasing number of fins, while the pressure drop increases exponentially. The benefit of increasing air velocity diminishes with higher values: an order-of-magnitude increase in velocity reduces thermal resistance by only about two-thirds. The pressure drop, however, increases sharply with both velocity and fin number.

Radiation

In air-cooled equipment with rectangular fins on a base plate, radiative heat transfer can be non-negligible. The total radiative heat transfer $Q_{\mathrm{tot,rad}}$ is calculated as [267]

$$Q_{\mathrm{tot,rad}} = (N_{\mathrm{fin}} - 1)\,Q_{\mathrm{ch,rad}} + A_{\mathrm{d}}\,\sigma_{\mathrm{SB}}\,\varepsilon\,(T_{\mathrm{fin}}^4 - T_{\mathrm{amb}}^4) \tag{2.321}$$

where $Q_{\mathrm{ch,rad}}$ is the radiation from a single U-shaped channel, defined as

$$Q_{\mathrm{ch,rad}} = \frac{\sigma_{\mathrm{SB}}\,(s_{\mathrm{fin}} + 2\,h_{\mathrm{fin}})\,L\,(T_{\mathrm{fin}}^4 - T_{\mathrm{amb}}^4)}{\frac{1-\varepsilon}{\varepsilon} + \frac{1}{F_{\mathrm{s\text{-}surr}}}}. \tag{2.322}$$

The channel view factor $F_{\text{s-surr}}$, describing the radiative exchange with the surroundings, is approximated with less than 5 % deviation as

$$F_{\text{s-surr}} = 1 - \frac{2\,\bar{H}\,(\sqrt{1+\bar{L}^2}-1)}{2\,\bar{H}\,\bar{L} + (\sqrt{1+\bar{L}^2}-1)} \tag{2.323}$$

$$\bar{H} = \frac{h_{\text{fin}}}{s_{\text{fin}}} \tag{2.324}$$

$$\bar{L} = \frac{L}{s_{\text{fin}}} \tag{2.325}$$

with $\bar{H}$ and $\bar{L}$ being the normalized fin height and length. The corresponding radiation heat transfer coefficient α_{rad} is

$$\alpha_{\text{rad}} = \frac{Q_{\text{tot,rad}}}{(A_{\text{p}} + A_{\text{f}})\,(T_{\text{fin}} - T_{\text{amb}})}. \tag{2.326}$$

The total heat transfer coefficient is then the sum of the convection and radiation components. In liquid-cooled heat sinks, convection dominates and radiation is negligible. In air-cooled applications, radiation can contribute up to 25 % of the total heat transfer [268].

2.5.2.2.2 Temperature Distribution

With the previously determined geometric properties and heat transfer coefficients, the thermal resistance from the fins to the ambient $R_{\text{th,fa}}$ can be determined as

$$R_{\text{th,fa}} = \frac{1}{\alpha_{\text{tot}}\,(A_{\text{p}} + \eta_{\text{fin}}\,A_{\text{f}})} \tag{2.327}$$

to calculate the surface temperature of the fins T_{fin}:

$$T_{\text{fin}} = T_{\text{amb}} + R_{\text{th,fa}}\,Q. \tag{2.328}$$

The fin efficiency η_{fin} is derived using Equations (2.282) and (2.284). In the case of trapezoidal fins, a more general solution is required and can be found by employing Bessel functions of the first and second kind as shown in [269].
The temperature at the heat sink base T_{b} is similarly calculated as

$$T_{\text{b}} = T_{\text{f}} + (R_{\text{th,b}} + R_{\text{th,sp}})\,Q \tag{2.329}$$

where the thermal resistance of the base $R_{\text{th,b}}$ is computed using Equation (2.119), and the resistance due to heat spreading $R_{\text{th,sp}}$ must be considered if the ratio ϵ of loss source area A_1 to base surface area A_2 is less than 90 %. For a loss source with constant heat flux and adiabatic conditions on the emitting surface, the spreading resistance can be estimated according to [270, 271]:

$$R_{\text{th,sp}} = \frac{1.08076 - 1.41042\epsilon + 0.26604\epsilon^3 - 0.00016\epsilon^5 + 0.058266\epsilon^7}{4\,\lambda\sqrt{A_1}}. \tag{2.330}$$

For power electronics applications, where multiple loss sources (e.g., semiconductors) are often mounted on a single heat sink, the accuracy of this solution can be further improved by considering the eccentricity of the loss source, as demonstrated in [272].

2.5.2.2.3 Pressure Loss Characteristics

Besides thermal performance, the pressure drop characteristics along the fin length are also critical, as they define a penalty on the system performance related to fan or pump power consumption. Several models, similar to Equation (2.304), for calculating the pressure drop have been proposed [273–276]. These account for entrance and exit effects, as well as core losses, using the apparent friction factor f_{app}:

$$\Delta p = \left(K_{\mathrm{c}} + 2\, f_{\mathrm{app}} \frac{L_{\mathrm{HX}}}{s_{\mathrm{fin}}} + K_{\mathrm{e}} \right) \rho_{\mathrm{m}} \frac{v^2}{2} \tag{2.331}$$

Entrance and Exit Effects

Losses due to sudden contraction at the entrance K_{c} and sudden expansion at the exit K_{e} are evaluated as

$$K_{\mathrm{c}} = 0.42 \left(1 - \sigma^2 \right) \tag{2.332}$$

$$K_{\mathrm{e}} = \left(1 - \sigma^2 \right)^2 \tag{2.333}$$

$$\sigma = 1 - \frac{N_{\mathrm{fin}}\, t_{\mathrm{fin}}}{w_{\mathrm{HX}}}. \tag{2.334}$$

Sudden contraction and expansion represent worst-case conditions, but as the detailed installation is unknown during preliminary design, this approach is regarded as the most general.

Core Friction

The dominant portion of the pressure loss is due to friction in the core section, represented by the apparent friction factor f_{app}. This factor is modeled as a composite function using the Churchill–Usagi method [264], as developed in [275, 277]. For a rectangular channel, it is defined as

$$f_{\mathrm{app}} = \frac{1}{Re} \sqrt{ \left(3.44 \sqrt{\frac{2\, s_{\mathrm{fin}}\, Re}{L_{\mathrm{HX}}}} \right)^2 + \left(f_{\mathrm{fd}}\, Re \right)^2 } \tag{2.335}$$

with the Reynolds number determined using the hydraulic diameter of the channel. The friction factor for fully developed flow f_{fd} is then a function of the channel's aspect ratio:

$$\begin{aligned} f_{\mathrm{fd}}\, Re = 24 - 32.527 \left(\frac{s_{\mathrm{fin}}}{h_{\mathrm{fin}}} \right) + 46.721 \left(\frac{s_{\mathrm{fin}}}{h_{\mathrm{fin}}} \right)^2 - 40.829 \left(\frac{s_{\mathrm{fin}}}{h_{\mathrm{fin}}} \right)^3 \\ + 22.954 \left(\frac{s_{\mathrm{fin}}}{h_{\mathrm{fin}}} \right)^4 - 6.089 \left(\frac{s_{\mathrm{fin}}}{h_{\mathrm{fin}}} \right)^5. \end{aligned} \tag{2.336}$$

2.5.3 Auxiliaries

The thermal management system also includes auxiliary components such as pipes for fluid transport, pumps for circulation, filters to remove particles, and valves to regulate or redirect flow. In this work, only pipes and pumps are considered. The number and placement of filters and valves depend heavily on the specific integration within the aircraft and are therefore difficult to define at this early design stage.

2.5.3.1 Pumps

A scaling law for the pump mass m_{pump} with respect to the volume flow is derived from a set of certified products by manufacturers such as Cascon [278], Barber-Nichols [279],

and a combination of engine-driven pumps from Parker Hannifin [280] with motors from Woodward [281].
A quadratic fit function

$$f_{1D,quad}(x) = a\,x^2 + b\,x + c \tag{2.337}$$

was chosen to model the data. In addition to yielding a good match in terms of coefficient of determination R^2 and visual agreement, particularly in the lower volume flow range relevant for liquid-cooled propulsion systems, the quadratic shape is also supported by physical reasoning. Assuming the pump geometry scales roughly like a cylinder, its volume and thus mass can be expected to increase approximately with the square of the volumetric flow rate.
Figure 2.60 shows the manufacturer data and the resulting quadratic fit. The coefficients of the quadratic pump mass model were obtained through regression as $a = -3.10 \times 10^5$, $b = 6.13 \times 10^3$, and $c = 4.07 \times 10^{-1}$.

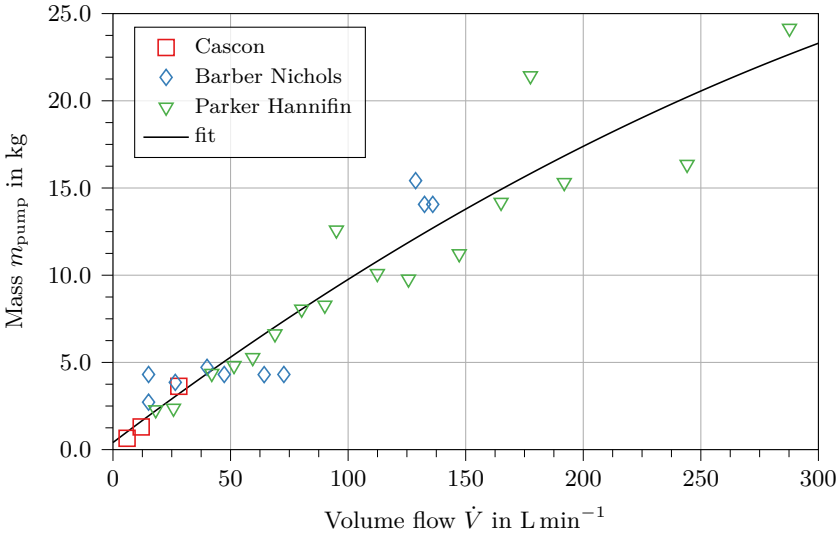

Figure 2.60: Mass of pump as a function of volume flow using a quadratic fit to manufacturer data from [278–281]

2.5.3.2 Pipes

Pipes are used to build a network for fluid transport between the liquid-cooled components, such as electric machines and power electronics, and accessories including pumps, heat exchangers, and filters. Depending on the type of cooling architecture selected, their mass contribution can be significant. Pipes are considered as hollow cylinders completely filled with fluid. Consequently, both their mechanical integrity under internal fluid pressure and the pressure drop along their length must be evaluated to assess the system's performance. Heat loss to the environment is neglected, as it would be beneficial to the cooling system but is relatively minor and subject to high uncertainty at the pre-design stage.

2.5.3.2.1 Structural Mechanics

The fluid exerts an internal pressure p_{int} on the inner radius r_{in} of the pipe, causing tangential and radial stresses in the cylindrical wall. These can be calculated using Equations (2.100) to (2.102), neglecting centrifugal forces. The von Mises equivalent stress model from Equation (2.106) is again used to evaluate a safety factor against yield, which should be greater than five to provide sufficient margin for pressure shocks. Additionally, a minimum wall thickness of 1 mm is imposed due to manufacturing constraints.

2.5.3.2.2 Thermodynamics

A pressure drop occurs along both straight pipe sections and bends, which must be accounted for in the thermal management system sizing. The pressure drop in a straight pipe of length L is given by the Darcy-Weisbach equation [282, 283]

$$\Delta p = f_{\mathrm{D}} \frac{\rho}{2} \frac{v^2}{2\, r_{\mathrm{in}}} L, \tag{2.338}$$

where f_{D} is the Darcy friction factor. This factor depends on the flow regime and fluid properties and is determined in the following sections.

Laminar Flow

At low fluid velocities, the Reynolds number is small, and laminar flow can be assumed. For $Re \leq 2000$, the Darcy friction factor follows a linear relation with Reynolds number, described by Hagen-Poiseuille's law [284, 285]:

$$f_{\mathrm{D}} = \frac{64}{Re}. \tag{2.339}$$

Turbulent Flow

As the Reynolds number exceeds the critical threshold, the flow becomes unstable and turbulent, characterized by vortex formation. This regime is described by the Colebrook-White equation [286, 287]:

$$\frac{1}{\sqrt{f_{\mathrm{D}}}} = -2 \log\left(\frac{2.51}{Re\sqrt{f_{\mathrm{D}}}} + \frac{k}{3.71}\right), \tag{2.340}$$

where k is the relative roughness of the inner pipe surface, representing the ratio of surface protrusion to diameter. Typical values for k range from 0 to 0.1. Although this equation is accurate, its transcendental nature requires iterative solutions. To avoid iterative solving, several explicit approximations have been proposed. In a recent review [288], the formulation by Vatankhah [289] was identified as the most accurate, with a mean relative error below 0.01 %. The first continued-fraction approximation is given by:

$$\frac{1}{\sqrt{f_{\mathrm{D}}}} = 0.8686 \ln\left(\frac{0.3984\, Re}{(0.8686\, s)^{\frac{s}{s+\lambda_1}}}\right), \tag{2.341}$$

with the coefficients

$$s = 0.12363\, Re\, k + \ln\left(0.3984\, Re\right), \tag{2.342}$$

$$\lambda_1 = 1 + \frac{1}{\frac{1+s}{0.5\, \ln(0.8686\, s)} - \frac{1+4\, s}{3\,(1+s)}}. \tag{2.343}$$

Pressure Loss in Bends

In addition to straight pipe sections, bends, elbows, junctions, and valves are required to maintain appropriate pressure levels across system components. These features can introduce significant additional pressure losses. For example, a 90° elbow bend can cause a pressure drop equivalent to that of 30 to 50 pipe diameters of straight section [290].
The pressure drop in curved sections is calculated similarly to Equation (2.338), but with a modified friction factor $f_{\mathrm{D,c}}$ for curved geometries. According to the review by Spedding

et al. [291], for laminar flow the correlation by White [292] is the most accurate:

$$f_{\mathrm{D,c}} = \frac{1}{1 - \left(1 - \left(\frac{11.6}{De}\right)^{0.45}\right)^{1/0.45}} f_{\mathrm{D}}, \tag{2.344}$$

using the Dean number De defined as

$$De = Re \sqrt{\frac{r_{\mathrm{in}}}{r_{\mathrm{bend}}}}. \tag{2.345}$$

For turbulent flow, the correlation proposed by Itō [293] is recommended:

$$f_{\mathrm{D,c}} = \left(0.029 + 0.304 \left(Re \frac{r_{\mathrm{in}}}{r_{\mathrm{bend}}}\right)^2\right)^{-0.25} \sqrt{\frac{r}{r_{\mathrm{bend}}}}. \tag{2.346}$$

The length of an elbow bend is defined as the arc length of its centerline, given by

$$L = \frac{r_{\mathrm{bend}}\,\pi}{2}. \tag{2.347}$$

2.5.4 Short Summary

Models for key elements of the thermal management system, including compact heat exchangers, heat sinks, and auxiliaries such as piping and pumps, have been introduced. These models enable the estimation of both thermal and fluid-dynamic performance under relevant operating conditions. By allowing the derivation of pressure losses within each component, the models improve pre-design accuracy and reduce dependence on external assumptions. Parametric geometric descriptions capture the influence of fin structure and fluid path on heat transfer efficiency and required pumping power. This facilitates a systematic comparison of cooling strategies across drivetrain components and supports integrated system-level thermal management.

2.6 Batteries as Electric Storage System

Full-electric drive trains rely on batteries as their primary energy source. Among various options, lithium-ion batteries have been identified as the most suitable choice due to their high energy and power density compared to lead-acid or nickel-metal hydride alternatives [294–296]. This section therefore focuses exclusively on lithium-ion cells, as other technologies with potentially superior performance characteristics, such as lithium-air, are not yet available for mass production [297]. Once such technologies become commercially viable, they can be evaluated using the same methodology introduced in the following.
In contrast to all other component models discussed so far, the performance evaluation of a battery pack involves two major challenges. First, the battery current and voltage are not known a priori, as the mission profile can be highly dynamic due to alternating hover and cruise phases. Second, the characteristics of the cells themselves depend on their current state of charge, temperature, and instantaneous load current. As a result, battery performance evaluation requires a sufficiently small time step on the order of seconds to obtain a convergent solution [298, 299]. While all other components can be sized using steady-state conditions, the transient behavior of cell voltage and temperature along the mission profile must be captured to determine whether a given battery design is viable.
Figure 2.61 provides an overview of the main aspects addressed in the design process of an electric storage system.

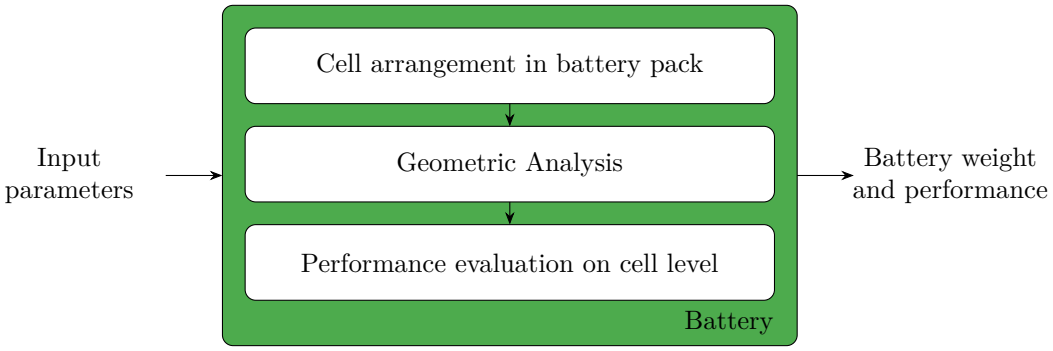

Figure 2.61: Overall setup and included disciplines of battery modelling

The section begins with a discussion of the arrangement of individual cells within the battery pack to derive pack-level characteristics, followed by a brief overview of the geometric properties of the system. The main part of the section focuses on the performance evaluation of a single cell, taking into account its electrical behavior, mission-dependent state of charge, and electro-thermal response. Specifying cell data in a generalised format enables comparisons between different commercially available options.

2.6.1 Cell Arrangement in Battery Pack

A single cell typically delivers a cell voltage V_{cell} of around 3.7 V. To achieve the required battery voltage V_{Bat}, power P_{Bat}, and capacity E_{Bat}, a series connection of n_{s} cells is made, with n_{p} such strings connected in parallel, as shown in Figure 2.62.
The overall battery pack characteristics are thus:

$$V_{\mathrm{Bat}} = n_{\mathrm{s}}\, V_{\mathrm{cell}} \tag{2.348}$$

$$I_{\mathrm{Bat}} = n_{\mathrm{p}}\, I_{\mathrm{cell}} \tag{2.349}$$

$$P_{\mathrm{Bat}} = n_{\mathrm{s}}\, n_{\mathrm{p}}\, V_{\mathrm{cell}}\, I_{\mathrm{cell}} \tag{2.350}$$

$$E_{\mathrm{Bat}} = n_{\mathrm{p}}\, E_{\mathrm{cell}}. \tag{2.351}$$

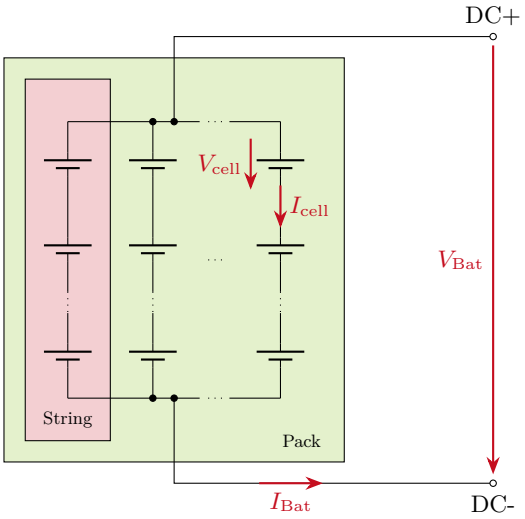

Figure 2.62: Electrical setup of a battery pack with n_{s} cells connected in series and n_{p} such strings in parallel.

Throughout this chapter, a generic battery pack consisting of 180 NCR18650GA cells [300] in series and 50 in parallel will be evaluated. The power profile of the battery pack and its energy capacity usage are shown in Figure 2.63.

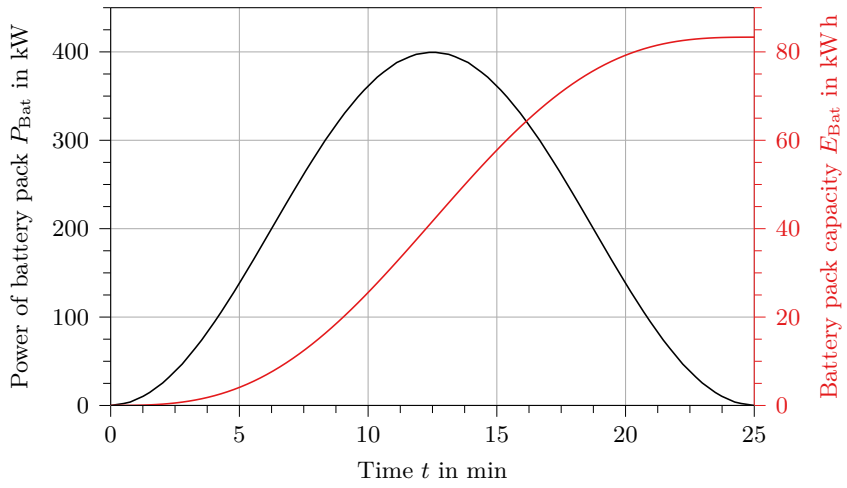

Figure 2.63: Power profile P_{Bat} and used capacity E_{Bat} over time for a generic battery pack.

While the cells are the most critical components of the pack, other elements, such as the battery management system, thermal management system, electrical components (e.g., switches, fuses, connections), and housing, are essential for reliable operation [301]. These components are challenging to model from a physics-based perspective in the preliminary design phase. Therefore, additional weight and volume at the battery pack level are estimated using cell-to-pack penalty factors $k_{\text{m,cell}}$ for mass and $k_{\text{v,cell}}$ for volume, as follows:

$$m_{\text{Bat}} = (1 + k_{\text{m,cell}})\, n_{\text{s}}\, n_{\text{p}}\, m_{\text{cell}} \tag{2.352}$$

$$V_{\text{Bat}} = (1 + k_{\text{v,cell}})\, n_{\text{s}}\, n_{\text{p}}\, V_{\text{cell}} \tag{2.353}$$

where m_{cell} and V_{cell} represent the mass and volume of a single cell. Based on values from [302], the penalty factors are optimistically estimated as $k_{\text{m,cell}} = 0.3$ and $k_{\text{v,cell}} = 1.0$, implying a 30 % increase in mass at the pack level compared to the cell level and a doubling of volume.

2.6.2 Performance Evaluation on Cell Level

Assuming the battery management system functions correctly, the mission load is evenly distributed among all cells. To accurately simulate a single cell's behaviour, its voltage V_{cell}, current I_{cell}, state of charge, and temperature T_{cell} must be known, as these parameters govern the cell's performance characteristics [303].
The evaluation procedure is illustrated in Figure 2.64.

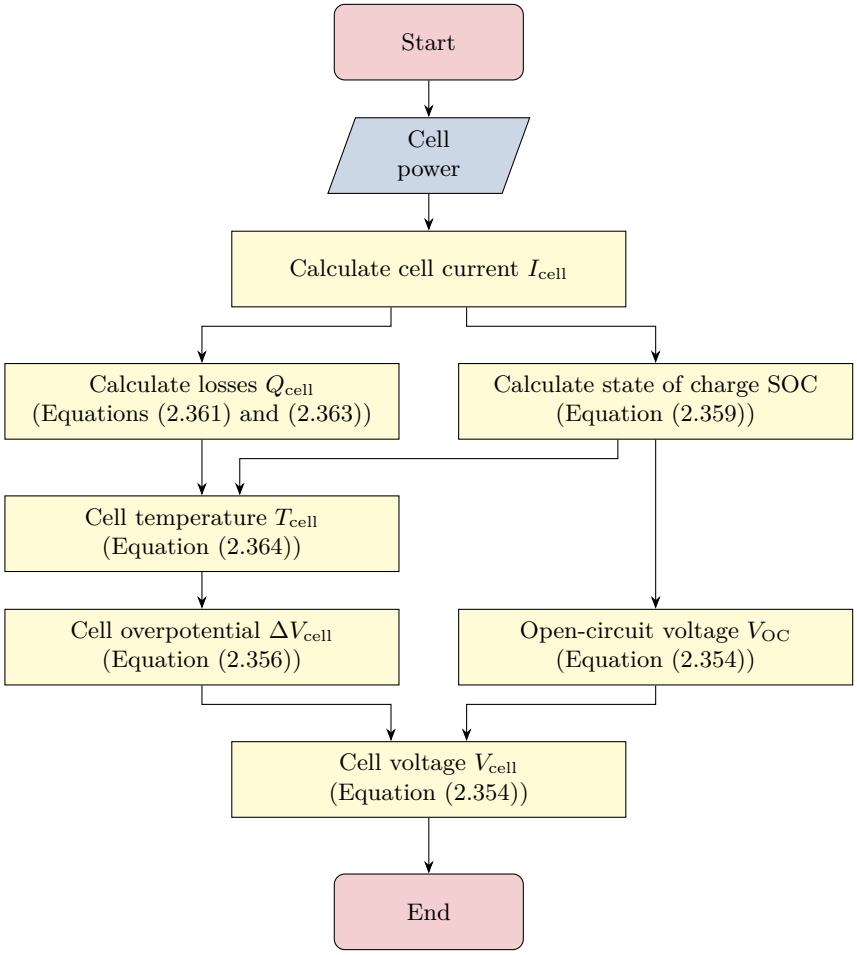

Figure 2.64: Flowchart visualizing the calculation procedure for the performance evaluation of a single battery cell.

Starting from a given power requirement on cell level and initial values for all relevant parameters, the computation begins with evaluating the cell current I_{cell}, followed by updating the state of charge SOC. This, in combination with the current, yields the cell temperature T_{cell} as well as the open-circuit voltage V_{OC} and the overpotential ΔV_{cell}. The models used in each step are detailed below.

2.6.2.1 Cell Characteristics

To establish the methodology, the widely used 18650 cell format is considered. Specifically, Panasonic's NCR18650GA cell [300] is chosen. General parameters are listed in Table 2.9. Beyond these general specifications, discharge voltage curves are of primary interest. The cell voltage depends on the state of charge, C-rate C_{cell}, and cell temperature:

$$V_{\text{cell}} = f(\text{SOC}, C_{\text{cell}}, T_{\text{cell}}). \tag{2.354}$$

Table 2.9: General cell data of Panasonic's NCR18650GA (taken from [300])

Parameter	Symbol	Value	Unit
Nominal voltage	$V_{\text{cell,nom}}$	3.6	V
Nominal capacity	$E_{\text{cell,max}}$	12060	A s
Operating temperature window	T_{cell}	$-20-60$	°C
Cell emmissivity	$\varepsilon_{\text{cell}}$	0.65	-
Cell radius	r_{cell}	9.25	mm
Cell height	h_{cell}	65.3	mm
Cell mass	m_{cell}	48.0	g

The C-rate is defined as the ratio of current to maximum energy capacity:

$$C_{\text{cell}} = \frac{I_{\text{cell}}}{E_{\text{cell,max}}}. \tag{2.355}$$

In the special case $C_{\text{cell}} = 0$, the resulting voltage is the open-circuit voltage V_{OC}.
Figure 2.65 shows discharge curves for various C-rates under constant temperature conditions ($T_{\text{cell}} = 25\,°\text{C}$).

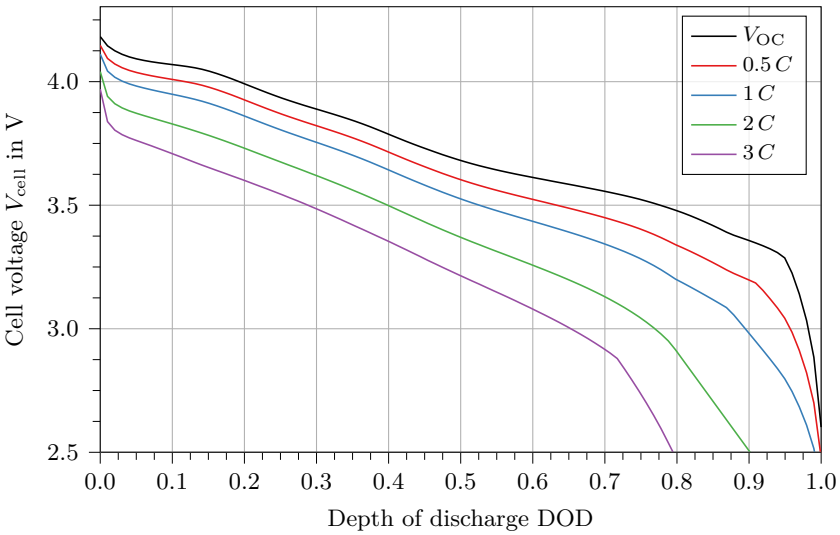

Figure 2.65: Discharge curves of NCR18650GA at different C-rates and constant temperature $T_{\text{cell}} = 25\,°\text{C}$.

Even under open-circuit conditions, voltage drops during discharge due to three main effects: the Ohmic drop from current flow, activation polarization from reaction kinetics, and concentration polarization from mass transport resistance [304].
The overpotential ΔV_{cell} is defined as the difference between open-circuit voltage and the actual voltage:

$$\begin{aligned}\Delta V_{\text{cell}}(\text{SOC}, C_{\text{cell}}, T_{\text{cell}}) &= V_{\text{OC}}(\text{SOC}) - V_{\text{cell}}(\text{SOC}, C_{\text{cell}}, T_{\text{cell}}) \\ &= V_{\text{OC}}(\text{SOC}) - V_{\text{cell}}(\text{SOC}, C_{\text{cell}}, T_{\text{cell}} = 25\,°\text{C}) \\ &\quad + \Delta V_{\text{cell,corr}}(T_{\text{cell}})\end{aligned} \tag{2.356}$$

where $\Delta V_{\text{cell,corr}}(T_{\text{cell}})$ accounts for temperature deviations from the nominal curve:

$$\Delta V_{\text{cell,corr}}(T_{\text{cell}}) = \Delta V_{\text{cell}}(T_{\text{cell}}) - \Delta V_{\text{cell}}(25\,°\text{C}) \tag{2.357}$$

The resulting correction is shown in Figure 2.66.
As temperature increases above 25 °C, the voltage drop decreases due to enhanced reaction kinetics. However, the impact of temperature becomes significant near the operational

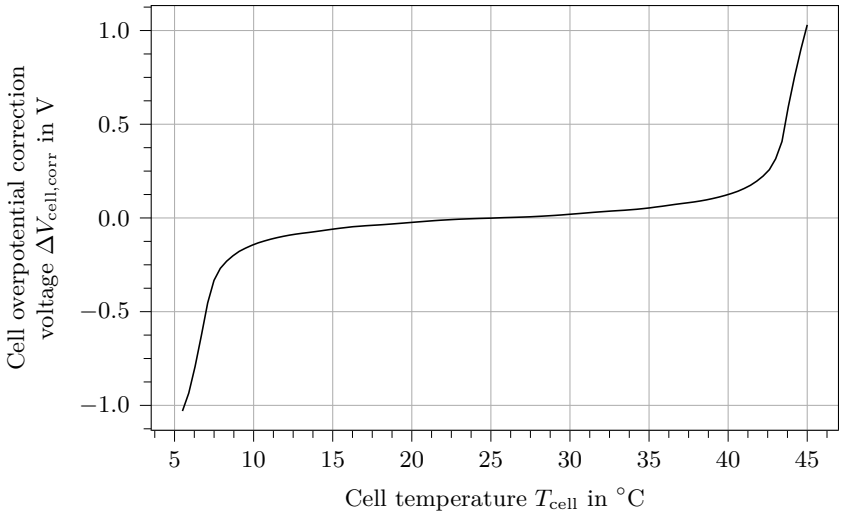

Figure 2.66: Overpotential correction function $\Delta V_{\text{cell,corr}}(T_{\text{cell}})$ of NCR18650GA for varying temperatures.

boundaries defined in Table 2.9, reinforcing the need for an electrothermal model. This will be addressed in Section 2.6.2.3.
Figure 2.67 shows the open-circuit voltage, actual cell voltage, and overpotential during the mission profile introduced in Figure 2.63. The effects of state of charge, discharge rate, and temperature are reflected in the voltage trends.

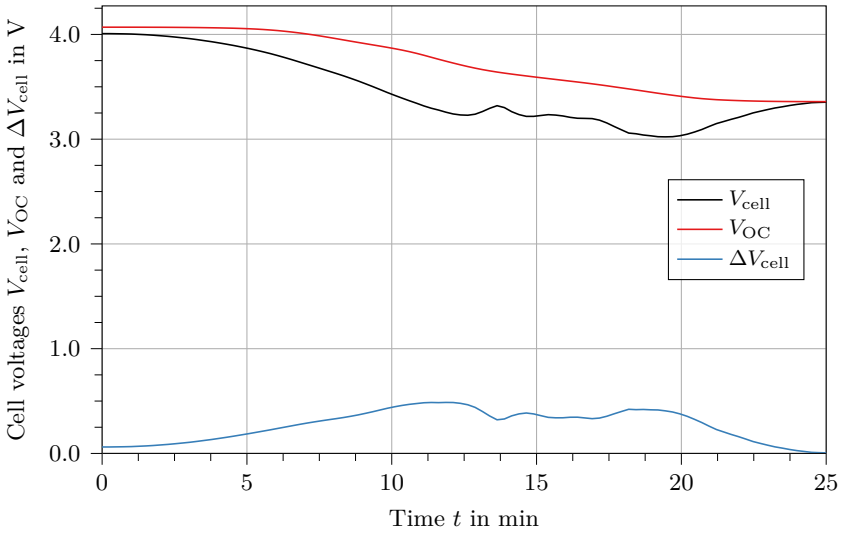

Figure 2.67: Open-circuit voltage, actual cell voltage, and voltage overpotential over time for the power profile given in Figure 2.63.

In the ideal case, discharge would occur at the open-circuit voltage. However, lower state of charge, high current draw, and low temperatures increase the overpotential, reducing usable voltage. Although higher temperatures mitigate this drop, they accelerate cell aging, which is typically undesirable.

2.6.2.2 State of Charge Evaluation

The cell's state of charge determines whether the battery pack can provide the required power for a given mission. To estimate the state of charge, the consumed energy is calculated using the Coulomb counting method [305–307], which integrates the current profile

as

$$E_{\text{cell}} = \int_0^t I_{\text{cell}}(t)\mathrm{d}t \tag{2.358}$$

This value is then used to calculate the state of charge as

$$\text{SOC} = \text{SOC}_{\text{init}} - \frac{E_{\text{cell}}}{E_{\text{cell,max}}} \tag{2.359}$$

taking into account an initial state of charge. The complementary depth of discharge (DOD) is defined as

$$\text{DOD} = 1 - \text{SOC}. \tag{2.360}$$

Figure 2.68 shows how higher discharge rates lead to a faster decrease in state of charge, and vice versa, for the profile given in Figure 2.63.

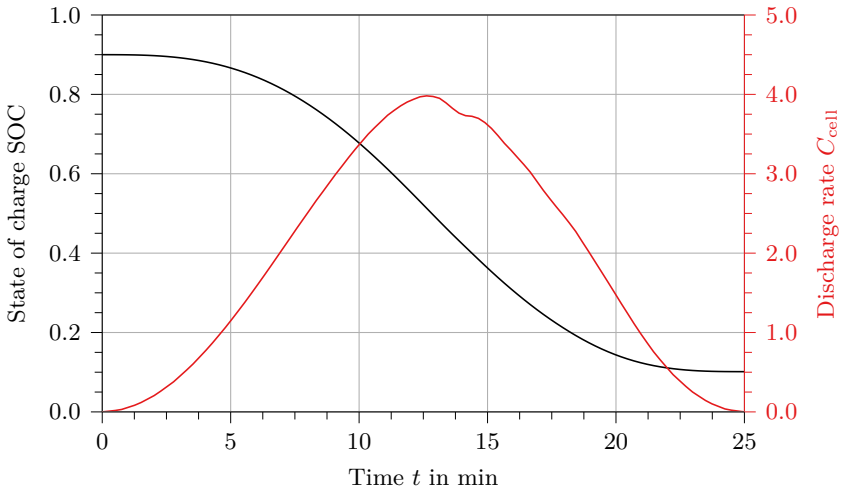

Figure 2.68: State of charge and discharge rate over time for the power profile given in Figure 2.63.

2.6.2.3 Electro-Thermal Model

As shown in Sections 2.6.2.1 and 2.6.2.2, the performance of a battery cell is strongly influenced by its temperature. Therefore, an electro-thermal model is developed to compute the transient temperature profile by accounting for internal heat generation and external cooling conditions.

Loss Sources in Battery Cells

According to [306, 308], the main sources of heat generation within battery cells can be described as

$$Q_{\text{cell,in}} = \Delta V_{\text{cell}}\, I_{\text{cell}} - \frac{T_{\text{cell}}\, \Delta S}{n\, F}\, I_{\text{cell}} \tag{2.361}$$

where ΔS is the entropy change, n the charge number of mobile ionic species and F the Faraday constant. The first term describes the irreversible heat power due to charge transfer processes, diffusion and migration, and Ohmic losses in both electrodes. The second term describes the reversible heat generation due to a change in reaction entropy. This term is often neglected but several researchers have shown that this effect should be considered in the thermal modelling process [306, 309]. The entropy change can be modelled as [308]

$$\Delta S = n\, F \left(\frac{\partial E_{\text{cell}}}{\partial T_{\text{cell}}} \right) \tag{2.362}$$

and substituted into Equation (2.361). Furthermore, heat generation due to enthalpy-of-mixing and phase changes, that is, heat associated with concentration gradients and phase transitions, is also present. However, their contributions are minor compared to the dominant mechanisms and are therefore neglected [309, 310].
In [306], entropy change values for different cell temperatures ranging from 0 to 40 °C are presented. Figure 2.69 shows that when the state of charge is below 30 %, the entropy

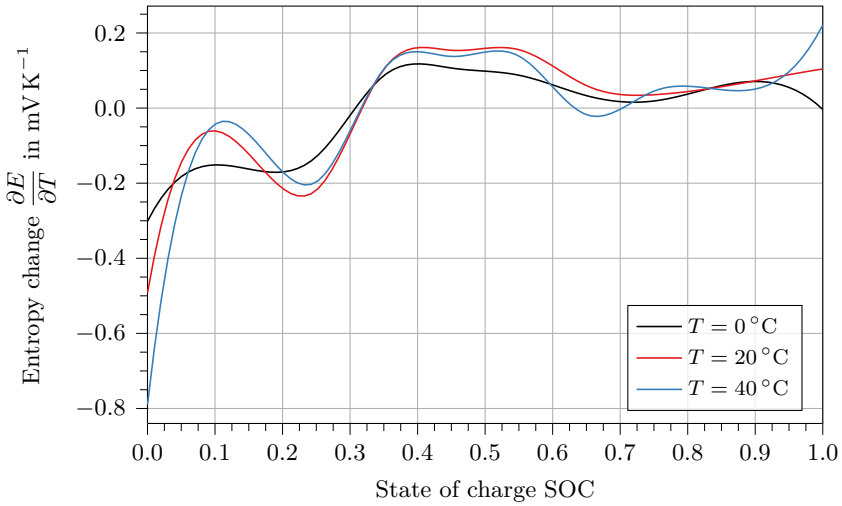

Figure 2.69: Entropy change versus state of charge for different cell temperatures ranging from $T_{\text{cell}} = 0-40\,°C$, adapted from [306]

change is positive, meaning the discharge reaction is endothermic and requires heat from the environment. As a result, the cell temperature decreases, partially compensating for irreversible losses. When the state of charge exceeds 30 %, the discharge reaction becomes exothermic and leads to a further increase in cell temperature.

Heat Dissipation From Battery Cells

The space between the cells in a battery pack can be utilised to provide convective heat transfer from the cell surface, with area A_{cell} and temperature T_{cell}, to the surroundings, as well as heat transfer via radiation. As outlined in Paragraph 2.1.6.3.2, the total dissipated heat from convection and radiation is given by

$$Q_{\text{cell,out}} = \alpha_{\text{cell}}\, A_{\text{cell}}\, (T_{\text{cell}} - T_{\text{amb}}) + \sigma_{\text{SB}}\, \varepsilon_{\text{cell}}\, A_{\text{cell}}\, (T_{\text{cell}}^4 - T_{\text{amb}}^4) \tag{2.363}$$

where α_{cell} is the convective heat transfer coefficient, σ_{SB} is the Stefan-Boltzmann constant, and $\varepsilon_{\text{cell}}$ is the surface emissivity of the cell. A wide range of research has been conducted on different cooling strategies such as air cooling [311–313], liquid cooling [314, 315], and more advanced methods including phase-change materials and internal heat pipes [308]. For air-cooled systems, Zhang et al. [316] reports heat transfer coefficients in the range $\alpha_{\text{cell}} = 10-25\,\text{W m}^{-2}\,\text{K}^{-1}$. These values are used directly, since the battery pack model does not provide details of the actual geometrical setup and thus no accuracy gain from a more detailed thermal model can be expected.

Heat Balance

Assuming a uniform cell temperature from core to surface, the heat balance equation is written as

$$m_{\text{cell}}\, c_{\text{p,cell}}\, \frac{\mathrm{d}T}{\mathrm{d}t} = Q_{\text{cell,in}} - Q_{\text{cell,out}} \tag{2.364}$$

where $c_{\text{p,cell}}$ is the specific heat capacity of the cell. Using all available data, the right-hand side of the equation can be determined as shown in Figure 2.70 for the profile given in

Figure 2.63.

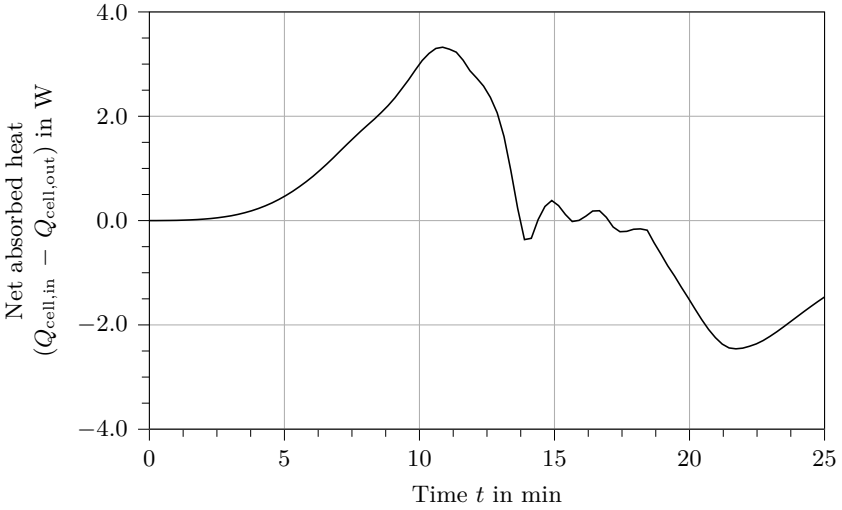

Figure 2.70: Net absorbed heat ($Q_{\mathrm{cell,in}} - Q_{\mathrm{cell,out}}$) of the cell over time for the power profile given in Figure 2.63.

Using Equations (2.361) and (2.363) and the data from Table 2.9, the temperature profile can be computed and is shown in Figure 2.71. It is noteworthy that when the battery is nearly fully charged and heated, the endothermic reaction kinetics help to limit the temperature rise to about 45 °C. If this effect were not taken into account, the cell temperature would be overestimated and the design might be considered infeasible.

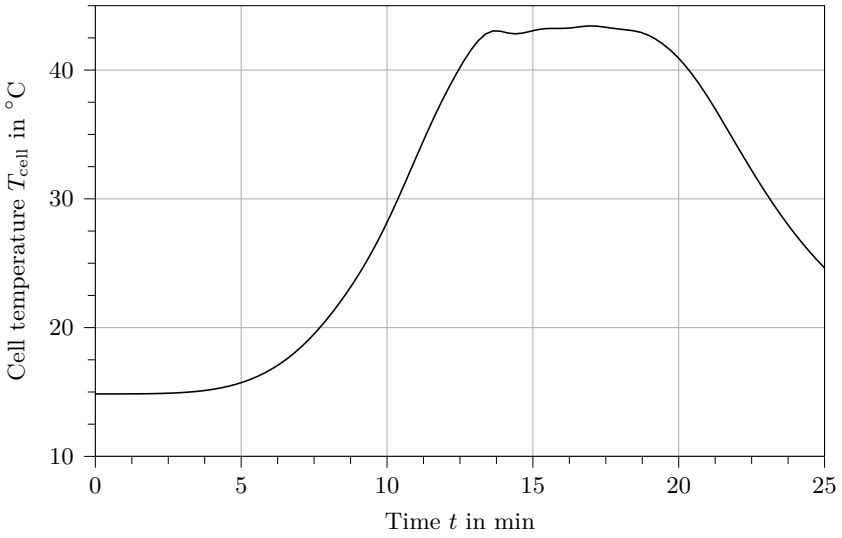

Figure 2.71: Cell temperature T_{cell} over time

Pack Performance

This allows for the determination of critical quantities such as the available battery voltage V_{Bat} and the corresponding current I_{Bat}, as illustrated in Figure 2.72.
As shown, the voltage drops from approximately 720 V to 540 V over time.

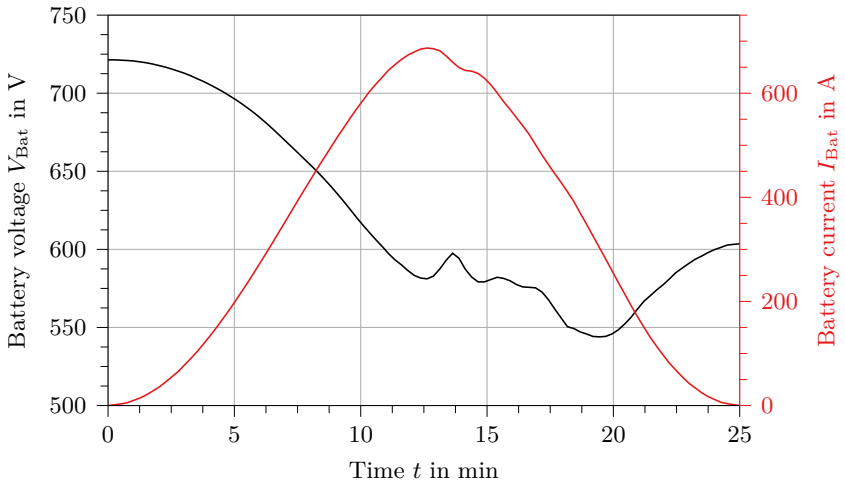

Figure 2.72: Battery voltage V_{Bat} and current I_{Bat} over time

2.6.3 Short Summary

A battery model has been developed that accounts for the cell arrangement and key operating parameters such as voltage, discharge rate, state of charge, and temperature. The model enables analysis at the pack level, which is essential for all- or hybrid-electric drivetrains. It allows for the determination of critical quantities such as the available battery voltage and current. The variation in voltage over time is critical in the design of power electronics, influencing the specification of semiconductor modules and insulation systems in both power distribution and electric machines.

3 Optimization Strategies

Electric drivetrain design involves multiple disciplines, as outlined in Chapter 2, and consequently presents a wide range of trade-offs that are of interest to the designer. To evaluate these effectively, optimization algorithms capable of addressing multiple objectives simultaneously are required. A variety of optimization algorithms have been proposed in the literature [317–322], but their results depends strongly on their suitability for the specific characteristics of the optimization problem.
The optimization process itself comprises the model to be optimized, the selected algorithm, and the visualization and interpretation of the resulting solutions. This chapter provides a literature-based overview of these aspects and compares different algorithms with respect to their applicability to electric drivetrain optimization.

3.1 Optimization Problems

Optimization is the process of determining the ideal set of controllable design variables for a model, subject to constraints [318]. In this context, variables are referred to as modifiable parameters, objective functions represent the performance indicators the optimization process seeks to optimize, and constraints define the conditions under which a solution is considered feasible [318, 321, 323].
Given these definitions, the most commonly used mathematical formulation of a nonlinear constrained optimization problem is [317, 321, 323]:

$$\min_{x} \quad F(x) \tag{3.1}$$

$$\text{subject to} \quad g_j(x) = 0 \qquad j = 1, \ldots, m_e \tag{3.2}$$

$$g_j(x) \leq 0 \qquad j = m_e, \ldots, m \tag{3.3}$$

$$x_{i_\mathrm{L}} \leq x_i \leq x_{i_\mathrm{U}} \qquad i = 1, \ldots, n, \tag{3.4}$$

where $x = (x_1, x_2, \ldots, x_n)$ are the n modifiable variables, bounded by their respective lower x_{i_L} and upper bounds x_{i_U}. The function $F(x)$ represents an arbitrary nonlinear single or multi-objective function, and g_j denotes the m equality and inequality constraints.
This section focuses on the classification of optimization problems, an experimental approach to address them, and the articulation of preferences in the case of multiple objectives.

3.1.1 Taxonomy

To select the most suitable and efficient optimization algorithm, the optimization problems must be classified, as a single algorithm is not capable of tackling all types. Several researchers have proposed classification schemes for this purpose [317, 318, 321]. Figure 3.1 provides an aggregated view of such a taxonomy.
This thesis will focus on deterministic functions, i.e., models that yield the same output for repeated evaluations with the same input, in contrast to stochastic problems, where inputs

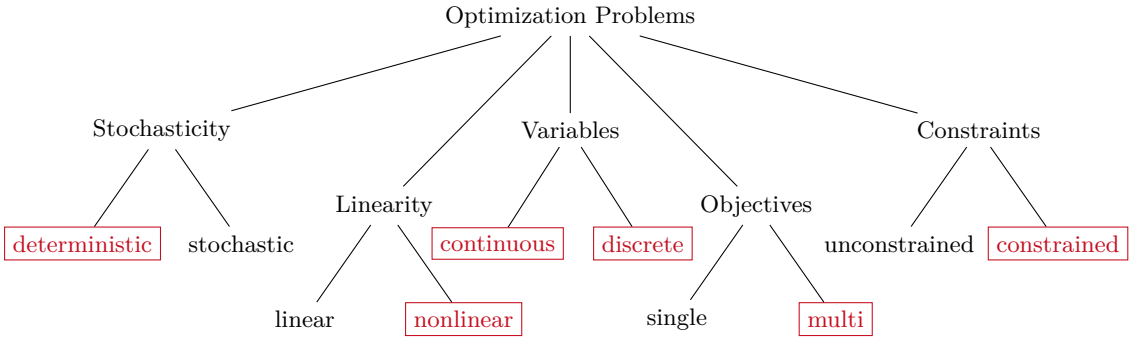

Figure 3.1: Taxonomy of optimization problems, based on [318]. Characteristics applying to the models in this thesis are marked in red.

are subject to uncertainty. For example, geometric inputs might be affected by manufacturing deviations [318]. The component models introduced in Chapter 2 are inherently nonlinear, and building entire systems from these components will further increase the nonlinearity.
Engineering design problems often involve mixed variables, i.e., both continuous and discrete ones. While the stack length of an electric machine is a continuous variable, discrete variables can be categorized as either integer or categorical. For example, the number of slots is an integer variable, while the magnet material is categorical. While single-objective problems are easier to tackle, multi-objective problems offer the possibility to analyze trade-offs between potentially conflicting objectives, such as mass and efficiency. The higher degree of information gained comes at a higher effort and necessitates the selection of a specific design from the trade-off curve. Engineering problems are also often subject to a larger number of constraints, arising from different technical disciplines, such as temperature limits for magnets.

3.1.2 Design of Experiments

Design of Experiments (DOE) is a set of techniques used to select the variable parameters such that the effects of changes in the objective space can be identified economically [322]. Design of experiments can be used to derive multiple solutions without the need for complex optimization procedures. This approach is simple and flexible; however, it cannot guarantee optimized solutions, nor can it derive information from other designs. Different methods are available, such as full factorial, fractional factorial, Box-Behnken, and Latin Hypercube sampling [322]. Among these, Latin Hypercube sampling attempts to choose the variables such that they are ideally orthogonally spaced within the n-dimensional variable space [322]. Design of experiments will be later used when different optimization algorithms are explained in Section 3.2.

3.1.3 Preference Articulation Methods

With two or more objectives, the selection of the most promising design point becomes a difficult issue, and a decision-making process is required. According to [324], preferences reflect decision processes with regard to the solution points in the objective space. These decisions can be made a priori, i.e., before the design space is viewed, thus anticipating the points in the criterion space. Another possibility is a posteriori preference articulation, where decisions are made with full knowledge of the objective space. In the following, one method of each type will be introduced.

Objective Weighting

Objective weighting, i.e., a linear scalarization of the objectives, is the most common a priori articulation method due to its simplicity and low computational complexity [325, 326]. The problem formulation can then be modified such that

$$\min_x \quad \sum_{i=1}^{n} w_i \, f_i(x) \tag{3.5}$$

$$\text{subject to} \quad g_j(x) = 0 \qquad j = 1, \ldots, m_e \tag{3.6}$$

$$g_j(x) \leq 0 \qquad j = m_e, \ldots, m \tag{3.7}$$

$$x_{i_\mathrm{L}} \leq x_i \leq x_{i_\mathrm{U}} \qquad i = 1, \ldots, n \tag{3.8}$$

$$\sum_i w_i = 1. \tag{3.9}$$

The weights w_i for each objective have to be determined prior to the optimization process and thus directly influence the outcome. The definition of the weights can be done in a subjective or objective way, and many methods exist [326]. A disadvantage is that a loss of information occurs, and the optimization has to be redone if the weighting is changed.

Pareto-Based Trade-Offs

The previously presented approach of weighting objectives is not able to cover trade-offs between opposing objectives, e.g., weight and efficiency. Thus, an a posteriori method of preference articulation is needed, which is used in this thesis. A common technique is Pareto-based optimization, named after Vilfredo Pareto [327]. By making the decision at the end of the optimization process, preferences can be changed without re-running the optimization itself. The problem formulation can then be modified such that

$$\min_x \quad f_1(x), f_2(x), \ldots, f_n(x) \tag{3.10}$$

$$\text{subject to} \quad g_j(x) = 0 \qquad j = 1, \ldots, m_e \tag{3.11}$$

$$g_j(x) \leq 0 \qquad j = m_e, \ldots, m \tag{3.12}$$

$$x_{i_\mathrm{L}} \leq x_i \leq x_{i_\mathrm{U}} \qquad i = 1, \ldots, n. \tag{3.13}$$

A Pareto-optimal solution P^*, also called a non-dominated solution, is defined as a solution in the objective space where one objective cannot be improved without compromising another one [327], e.g., lower weight is only possible at higher losses and lower efficiency, and vice versa. While this approach allows more insight into the problem, it comes at higher computational effort and difficult visualization. In Figure 3.2, the difference between the non-dominated Pareto front and the dominated set of solutions for a general bi-objective optimization problem is shown. This graph is used to further introduce the ideal and nadir points of a multi-objective Pareto front. While the ideal point

$$z^{\mathrm{id}} = \left(z_1^{\mathrm{id}}, z_2^{\mathrm{id}}, \ldots, z_n^{\mathrm{id}}\right) \tag{3.14}$$

is defined as the vector built by the best objective values within the Pareto front,

$$z_i^{\mathrm{id}} = \min_{x \in P^*} f_n(x), \tag{3.15}$$

the nadir point

$$z^{\mathrm{nad}} = \left(z_1^{\mathrm{nad}}, z_2^{\mathrm{nad}}, \ldots, z_n^{\mathrm{nad}}\right) \tag{3.16}$$

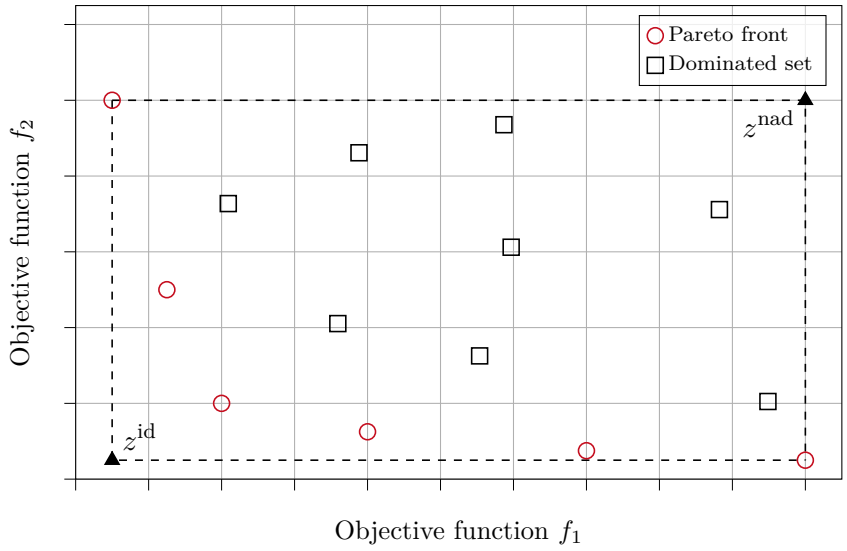

Figure 3.2: Pareto front, dominated solutions, nadir and ideal point of a general bi-objective optimization problem where both objective functions are minimized.

is similarly defined as the vector built by the worst objective values

$$z_i^{\text{nad}} = \max_{x \in P^*} f_n(x). \tag{3.17}$$

These definitions will be used to define performance metrics for a proper termination in Section 3.2.3.

3.2 Optimization Algorithms

The choice of optimization algorithm is as important as the problem definition itself. The following sections provide a classification of optimization algorithms and a closer examination of a specific class, namely Genetic Algorithms (GA).

3.2.1 Taxonomy

As with the taxonomy of optimization problems, various perspectives exist for classifying optimization algorithms [318, 321]. Figure 3.3 illustrates key aspects of this classification.

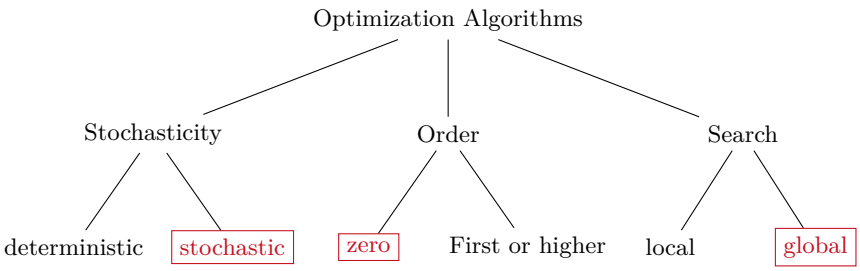

Figure 3.3: Taxonomy of optimization algorithms, based on [318]. Characteristics applicable to the algorithms used in this thesis are marked in red.

Regardless of whether the optimization model is deterministic or not, the algorithm itself may be deterministic or stochastic. Deterministic algorithms converge to the same solution

for identical inputs, whereas stochastic algorithms incorporate random processes, which is typical for most evolutionary algorithms [318].
The order of information refers to the type of information available at the optimization stage. In a zeroth-order model, only objective and constraint evaluations are accessible for given sets of design variables. Algorithms using only this information are known as gradient-free or derivative-free. If additional information such as gradients or curvature is available, gradient-based algorithms may be applied.
It is important to note that different optimisation approaches vary in their ability to identify local versus global optima. Gradient-based or scalarisation methods, such as the weighted sum approach, are prone to converging to local optima, particularly in non-convex or multimodal objective spaces. This limitation arises because the weighted sum reduces the problem to a single-objective formulation, which may constrain the search depending on the selected weight vector and the topology of the objective space [318].
In contrast, population-based algorithms such as the NSGA-II algorithm are designed for global exploration. They employ stochastic variation and selection across a diverse population, enabling the simultaneous investigation of multiple regions in the objective space. As a result, they are generally more effective in approximating the global Pareto front in multi-objective problems, which is of particular relevance to drivetrain system optimisation [318].

3.2.2 Genetic Algorithms

Considering the complexity of component modelling discussed in Chapter 2, as well as the classification of optimization problems in Section 3.1.1 and of algorithms in Section 3.2.1, Genetic Algorithms are chosen for optimization in this thesis. This choice is motivated by the aim of finding global optima and the impracticality of computing gradients for the component and system models.
Originally introduced by Holland [328] in 1975, genetic algorithms have become one of the most widely used optimization techniques in engineering. Genetic algorithms mimic biological evolution based on Darwin's principle of the survival of the fittest by introducing crossover and recombination, mutation, and selection into mathematical procedures.
The main advantages of genetic algorithms are their ability to efficiently solve multi-objective optimization problems that are non-linear, constrained, and include both continuous and discrete variables, as well as their suitability for parallelization, which enables exploration of the design space in multiple directions simultaneously. However, the choice of optimization parameters, such as population size, mutation and crossover rates, and termination criteria, can significantly affect convergence. Furthermore, unlike most gradient-based methods, the optimality of the resulting solutions cannot be formally proven [307].
In the following, three multi-objective evolutionary algorithms (MOEA) will be discussed in more detail. Their performance on a real-world problem will be evaluated in Section 3.3.1, using the implementation provided in *pymoo* [329].

NSGA-II Algorithm

In 2000, Deb et al. [330] proposed a fast elitist non-dominated sorting genetic algorithm (NSGA-II) specifically designed for multi-objective optimization problems. Algorithm 3.1 shows the pseudocode of the algorithm based on [319, 331].
Initially, a population is generated using the design of experiments introduced in Section 3.1.2, with an emphasis on Latin hypercube sampling to ensure diversity. The model's objectives and constraint values are evaluated, and individuals are ranked using non-dominated sorting based on Pareto dominance. Each individual's crowding distance is also calculated, providing a measure of how isolated a solution is from its neighbors in

Algorithm 3.1 Pseudocode of NSGA-II algorithm(adapted from [319, 331])

```
procedure NSGA-II(n_pop, n_gen, f_i(x))        ▷ n_pop individuals, n_gen generations, objective functions f_i(x)
    Initialize population using design of experiments
    Evaluate objective and constraint values for all individuals
    Perform non-dominated sorting to assign ranks
    Compute crowding distance for each front
    for j = 1 to n_gen do
        Create offspring population:
            Binary tournament selection based on rank and crowding distance
            Crossover and mutation to generate offspring
        Combine parent and offspring populations
        Perform non-dominated sorting on the combined population
        Compute crowding distance for each front
        Select next generation by choosing the best n_pop individuals
            Start from lowest-rank fronts and include individuals with highest crowding distance
    end for
end procedure
```

objective space.
The child population is then generated using binary tournament selection based on rank and crowding distance. Genetic operators such as crossover and mutation are applied to produce offspring [319, 330, 331]. During crossover, individuals exchange genetic material in a randomized but structured way to improve diversity. Mutation helps to avoid premature convergence and explore underrepresented regions of the design space [332].
In each generation, the parent and offspring populations are merged, and non-dominated sorting is applied to the combined set. The best n_{pop} individuals are then selected to form the next generation, prioritizing lower-rank fronts and maintaining diversity through crowding distance. These steps are repeated for n_{gen} generations or until a specified termination criterion is met.

U-NSGA-III Algorithm

The unified NSGA-III algorithm, as proposed by Seada and Deb [333], is an enhancement of the classical NSGA-III algorithm [334, 335]. The NSGA-III algorithm extends the NSGA-II algorithm by introducing reference directions in the objective space to better preserve diversity along the Pareto front [335]. However, its original implementation applies only weak selection pressure to non-dominated solutions in bi-objective problems. The U-NSGA-III algorithm addresses this limitation by incorporating niching-based tournament selection [333]. Algorithm 3.2 presents the pseudocode for the algorithm, based on [333].
The overall structure of the U-NSGA-III algorithm closely follows that of Algorithm 3.1. The key differences are highlighted above. The U-NSGA-III algorithm introduces a predefined set of reference directions, typically generated using the Das-Dennis approach [336], which ideally spans the entire Pareto front. In addition, niching-based tournament selection replaces the standard binary tournament. To enable this, objective vectors must be normalized and then associated with reference directions. A niche count is calculated for each direction, and individuals are selected to preserve diversity in the solution set [333]. Blank et al. [337] emphasize the importance of normalization methods that account for differing objective scales.

Algorithm 3.2 Pseudocode of U-NSGA-III (adapted from [319, 331])

procedure U-NSGA-III(n_{pop}, n_{gen}, Z_{dir}, $f_i(x)$) ▷ n_{pop} members evolved n_{gen} generations to solve $f_i(x)$ for a given set of reference directions Z_{dir}
    Initialize Population
    Generate random population of size n_{pop} by DOE
    Generate reference directions, e.g. Das-Dennis approach
    Evaluate objective and constraint values
    Assign rank based on Pareto dominance
    Generate child population
        Niching-based tournament selection
        Recombination and mutation
    for $j = 1$ to n_{gen} **do**
        for each parent and child in population **do**
            Assign rank based on Pareto dominance
            Normalize objectives and create reference set
            Associate each member with a reference direction
            Compute niche count of reference direction
            Loop (inside) by adding solutions to next generation starting from the first front until n_{pop} individuals are found
        end for
        Select feasible points on the lower front nearer to reference directions
        Create next generation
            Niching-based tournament selection
            Recombination and mutation
    end for
end procedure

AGE-MOEA Algorithm

Adaptive Geometry Estimation-based Multi-Objective Evolutionary Algorithm (AGE-MOEA) is another variation of the classical NSGA-II algorithm, designed to reduce the computational overhead of the NSGA-III algorithm while maintaining its benefits [338]. Algorithm 3.3 presents the pseudocode for the optimization algorithm based on [338].
The overall procedure of the AGE-MOEA algorithm is very similar to that of Algorithm 3.1, with the most significant changes highlighted in red. The major difference between the AGE-MOEA and NSGA-II algorithm is the use of a survival score instead of crowding distance. After normalizing the objectives, the geometry of the first front is estimated. This eliminates the need for predefined reference directions, as required in the NSGA-III algorithm methods. The survival score, which combines both diversity and proximity, is then used to select the mating pool. The computational cost of Pareto front estimation is lower compared to the U-NSGA-III algorithm [338].

3.2.3 Termination Criterion

In real engineering problems, a running metric measuring the improvement within the objective space from one to the next generation is needed, because the true Pareto front cannot be derived analytically. This metric must be able to cope with differently scaled objectives and ensure convergence and diversity of the calculated Pareto front. Blank and Deb [339] proposed such a running metric. During the convergence phase, which mostly happens within the early generations, the metric tracks the movement of the extreme points in the non-dominated set by measuring the distance from the old to the new nadir

Algorithm 3.3 Pseudocode of AGE-MOEA (adapted from [338])

```
procedure AGE-MOEA(n_pop, n_gen, Z_dir, f_i(x))        ▷ n_pop members evolved n_gen generations to solve f_i(x)
    Initialize Population
    Generate random population of size n_pop by DOE
    Evaluate objective and constraint values
    Assign rank based on Pareto dominance
    Generate child population
        Binary tournament selection
        Recombination and mutation
    for j = 1 to n_gen do
        for each parent and child in population do
            Assign rank based on Pareto dominance
            Normalize objectives
            Determine geometry of first front
            Calculate survival score based on diversity and proximity
            Loop (inside) by adding solutions to next generation starting from the first front until n_pop individuals are found
        end for
        Select feasible points on the lower front with highest survival score
        Create next generation
            Binary tournament selection
            Recombination and mutation
    end for
end procedure
```

and ideal point, respectively.
When the extreme points have settled, the algorithm enters the diversity phase. When the Pareto front is known, a multitude of performance metrics such as Generational Distance (GD) [340], Inverted Generational Distance (IGD) [341], or Hypervolume (HV) [320] exist. Inverted Generational Distance is defined as

$$\mathrm{IGD}(Q(t), P^*) = \frac{1}{|P^*|} \left(\min_{j=1}^{|Q(t)|} ||P_i^* - Q_j(t)|| \right) \tag{3.18}$$

and calculates the average distance from a solution in the true Pareto front P^* to the closest one in $Q(t)$ at generation t [339]. The computational complexity can be reduced by only taking the last and current front into account and defining the average improvement of the diversity of the Pareto front as

$$\varnothing_{\mathrm{t}} = \mathrm{IGD}\left(\bar{P}^t(t-1), \bar{P}^t(t)\right). \tag{3.19}$$

The termination criterion proposed by [339] is defined such that neither the maximum movement of the nadir and ideal point nor the maximum improvement of the diversity of the Pareto front, as measured by Equation (3.19), is above a certain threshold $\varepsilon_{\mathrm{opt}}$ within a sliding window of ω_{opt} generations.

3.3 Performance Comparison of Different Optimization Algorithms

In this section, a performance comparison of the three optimization algorithms introduced in Section 3.2 is performed by analyzing the optimization of a DC power cable, because it is a typical engineering task to select a proper cable for a given application. Considering only a single component instead of a whole drivetrain system as a first example reduces complexity and allows for a focus on the methods.

3.3.1 Problem Description

The model used to evaluate the performance of a single parametrization is taken from Section 2.4. The goal of the optimization is to minimize both the total mass m_{Cab} and the overall losses Q_{Cab} in a one-meter long cable made of copper as a conductor and Perfluoroalkoxy alkanes (PFA) as an insulation material. A DC current of 100 A at a DC voltage of 540 V is applied to the conductor, which is operated in free air at atmospheric pressure and an elevated temperature of 60 °C. These fixed parameters are summarized in Table 3.1.

Table 3.1: Fixed parameters of power cable optimization

	Description	Parameter	Value	Unit
General	Length	L_{Cab}	1	m
Conductor	Material		Copper	-
Insulation	Material		PFA	-
Ambient	Material		Air	
	Temperature	T_{amb}	70	°C
	Pressure	p_{amb}	101325	Pa
	Velocity	v_{amb}	0	$\mathrm{m\,s^{-1}}$
Operation	DC voltage	V_{DC}	540	V
	DC current	I_{DC}	150	A

The free variables in this optimization are the radius of the conductor r_{cond} and the thickness of the insulation t_{ins} which are allowed to vary between 0.5 – 25 mm and 0.05 – 5 mm, respectively. These two parameters trigger a change in the objectives as a change in them results in a variation of the volume and thus the mass of the cable, as well as a change in current density, which is directly linked to the losses within the conductor according to Equations (2.253) and (2.254). The variables are listed in Table 3.2.

Table 3.2: Variables of power cable optimization

	Description	Parameter	Range	Unit
Conductor	Radius	r_{cond}	0.5 – 25	mm
Insulation	Thickness	t_{ins}	0.05 – 5	mm

To ensure physically meaningful designs, two additional constraints are introduced in Table 3.3, which will divide possible solutions into feasible and non-feasible designs within the optimization process.
The temperature within the conductor is limited to 200 °C to avoid high DC resistance of the copper wire and match with the temperature rating of the insulating PFA. The safety

Table 3.3: Constraints of power cable optimization

	Description	Parameter	Value	Unit	Type
Conductor	Temperature	T_{cond}	200	°C	max
Insulation	Safety Factor	SF_{ins}	2	-	min

factor against an electrical breakdown has to be larger than two. Finally, the parameters of the optimization itself are defined in Table 3.4.

Table 3.4: Optimizer settings of power cable optimization

Description	Parameter	Value
Algorithm		NSGA-II, U-NSGA-III, AGE-MOEA
Population size	n_{Pop}	500
Number of offsprings	n_{Off}	500
Crossover rate	η_{c}	3
Mutation rate	η_{m}	3
Allowable average change	ϵ_{opt}	0.001
Sliding window	ω_{opt}	20
Max. number of generations	$n_{\mathrm{gen,max}}$	200

The three optimization algorithms outlined in Section 3.2 are investigated. A population size n_{pop} of 500 and an identically large number of offsprings n_{o} is chosen to guarantee a high possible diversity in the Pareto front at reasonable computational time. The rates for crossover η_{c} and η_{m} are both chosen to be three. A low number means that the two operators will allow the creation of offsprings which can be significantly diverse from their parents [342]. The allowable average change in the objective space $\varepsilon_{\mathrm{opt}}$ is limited to 0.001 using a sliding window of ω_{opt} evaluating the space change during the last 20 generations. This termination criterion should be reached at a maximum number of generations $n_{\mathrm{gen,max}}$ of 200; otherwise, it will be terminated.

3.3.2 Optimization Results and Discussion

This section presents the final results of the optimization described in Section 3.3.1 both in terms of absolute results and a statistical analysis. In total, the same optimization has been conducted with a different numbers parallelized cores ranging from one to 56 and repeated five times each thus resulting in a total of 35 similar runs. The task has been carried out on an Intel® Dual-Xeon® CPU E5-2690 v4 @ 2.60 GHz with a total of 28 physical cores.

3.3.2.1 Objective, Variable and Constraint Space

First, the absolute results of optimization with the three different algorithms are analyzed. This includes the visualization and discussion of the objective, variable and constraint space. Figures 3.4a to 3.4c show the objective space using NSGA-II, U-NSGA-III, and AGE-MOEA. In this case, the two objectives are visualized in a scatter plot showing the Pareto front of total mass of the cable m_{Cab} (f_1) against the total losses Q_{Cab} (f_2). Each feasible solution is assigned a specific color which is used to track the variables and constraints. The extreme points representing the most and lightweight design are highlighted as Design A and B, respectively.
As can be seen, all three algorithms converge to the same Pareto front in terms of extreme points A and B as well as the general shape of it. Each front is represented by 500 feasible design points, however the distribution of these points is not identical for all three algo-

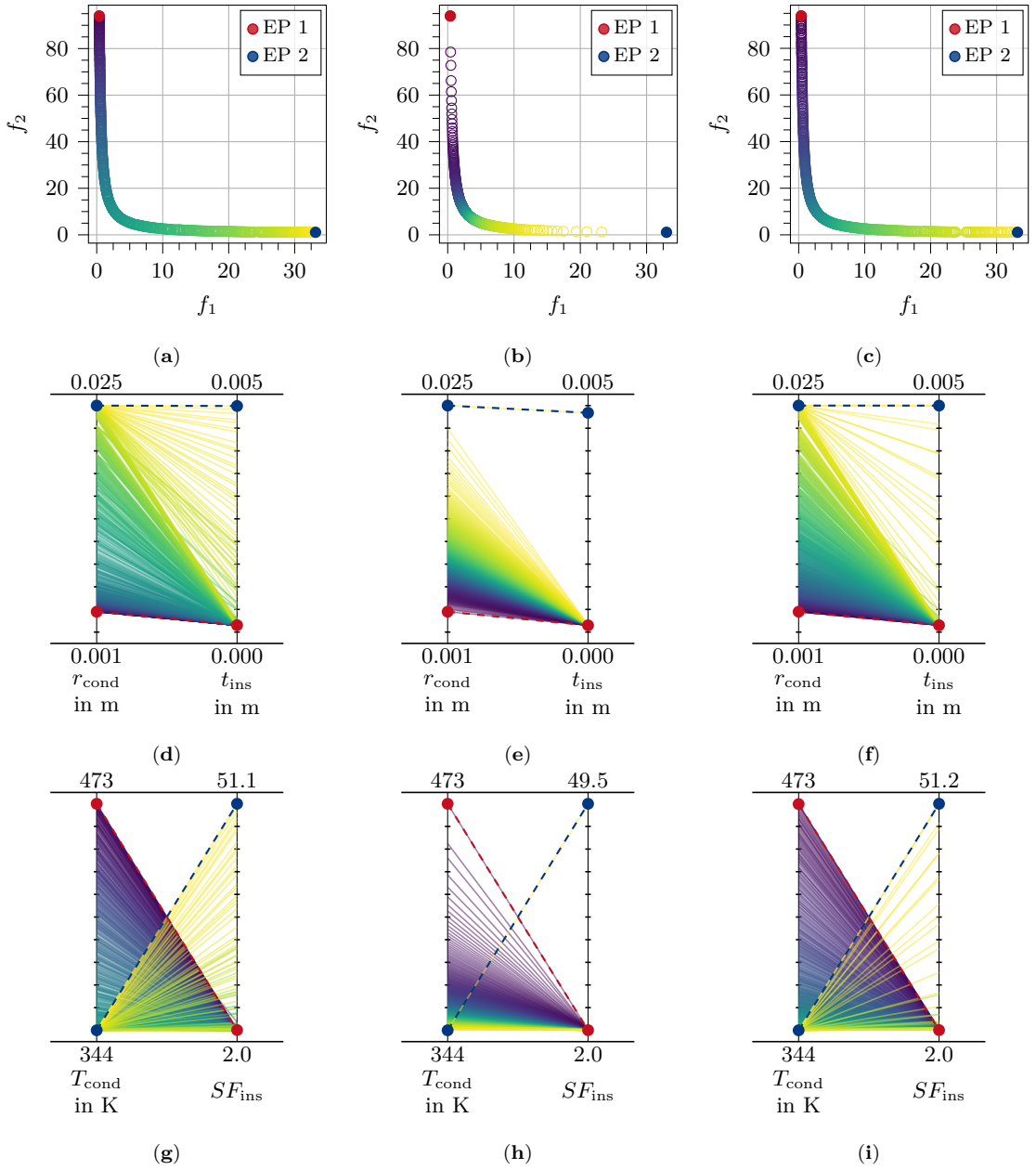

Figure 3.4: Final results for the optimization of a DC cable. (a) – (c) The two objectives are visualized in a scatter plot showing the total mass of the cable m_{Cab} in kg (f_1) versus the total losses Q_{Cab} in W (f_2) for the NSGA-II, the U-NSGA-III, and the AGE-MOEAa algorithm. Each solution is assigned a specific color which is used to track the variables and constraints. The extreme points are highlighted as EP 1 and EP 2; (d) – (f) The variable space, i.e., the behavior of the variables belonging to each design within the corresponding Pareto front, is visualized with parallel coordinate plots using the introduced color coding; (g) – (i) Similarly as for the variables, the constraint space is visualized with parallel coordinate plots.

rithms. Using the NSGA-II algorithm, Figure 3.4a shows a very homogenous distribution of points along the whole Pareto front. In contrast, Figure 3.4b clearly displays an accumulation of design points using the U-NSGA-III algorithm around the knee point of the front, while the area towards the extreme points is underrepresented. This behaviour is a direct result of using reference directions generated by the Das-Dennis approached as explained in Section 3.2.2. The only remedy would be to adapt those reference directions but the shape of the Pareto front is not always known a priori. When using the AGE-MOEA algorithm, then Figure 3.4c indicates a Pareto front similar to the one of the NSGA-II

algorithm but one can see a small interruption of the Pareto front around $f_1 = 25\,\mathrm{kg}$.
To further investigate the differences of the algorithms the variable and constraints space, i.e., the behaviour of the design variables and model results compared to the set constraints for the corresponding designs on the Pareto front, is visualized. This is done with so-called parallel coordinate plots. Parallel coordinate plots are extensively used to plot high-dimensional, multivariate data. Each variable or constraint is associate with a vertical axis. The axes are arranged in parallel and with the same distance from each other. Each line in the parallel coordinate plot corresponds with the data point from the Pareto front which has the same color coding. The position on the i-th axis corresponds to the i-th coordinate of the design point. This method enables to retrieve information about the correlation of two dimensions, e.g., positively and negatively correlating points, cluster or normal distributions [343, 344].
As has been seen in the previous Pareto plots, the objective space as visualized in Figures 3.4d to 3.4f is very similar for the different algorithms. The most lightweight, but also most inefficient design, represented by Design EP1, has a small conductor radius r_{cond} as well as a small insulation thickness, while a large conductor radius and thick insuulation is chosen for Design EP2 representing the most efficient, but also heaviest design. This correlates with the constraint spaces shown in Figures 3.4g to 3.4i indicating that the thicker the conductor radius the lower the conductor temperature T_{cond} and the thicker the insulation the higher the safety SF_{ins} against electrical breakdown. The constraint space explains that no design even more lightweight than Design EP1 can be found because it would require to further decrease both conductor radius and insulation thickness. Even though this would theoretically possible from the given variable range in Table 3.2 it would violate the constraints defined in Table 3.3 and thus result in an infeasible design.
Figures 3.4d and 3.4g show a homogeneous distribution within the variable and constraint space. The latter one even allows to separate the Pareto front into two clusters. Starting from Design EP2 with the highest allowable conductor radius and insulation thickness the latter one is constantly reduced to the allowable minimum, while keeping the former one constant. After that, insulation thickness is kept constant and the conductor radius is continuously decreased until Design EP1 is reached. The same behaviour can be spotted in Figures 3.4f and 3.4i for the AGE-MOEA algorithm, however the distribution near Design EP2 is not covered as uniformly as for the NSGA-II algorithm. The extreme points are however identical.
In contrast, Figures 3.4e and 3.4h show a different picture when the U-NSGA-III algorithm is used as optimization algorithm. Design EP2 exists and is close to the ones retrieved by the NSGA-II and AGE-MOEA algorithm but both the insulation thickness and the corresponding breakdown safety are lower. Furthermore, this method basically neglects the cluster with large insulation thicknesses.

3.3.2.2 Convergence Analysis

The convergence rates of the optimization process are exemplarily analyzed for the NSGA-II algorithm. Figure 3.5 shows the change of the ideal point Δz^{id}, nadir point Δz^{nad} and performance running metric $\varnothing_{\mathrm{t}}$ versus the number of generations n_{gen}. While the black bars show the actual change of the three different metrics, the red dashed line marks the allowable average change $\varepsilon_{\mathrm{opt}}$, which is set to 0.001.
It can be seen that the ideal point shown in Figure 3.5a and the running performance metric shown in Figure 3.5c both have settled below the allowable average change after 25 generations, while the change in the nadir point needs 44 generations until it is consistently below the allowable limit, as visible in Figure 3.5b. The optimization thus takes 64 generations to terminate due to the sliding window set to 20 generations.

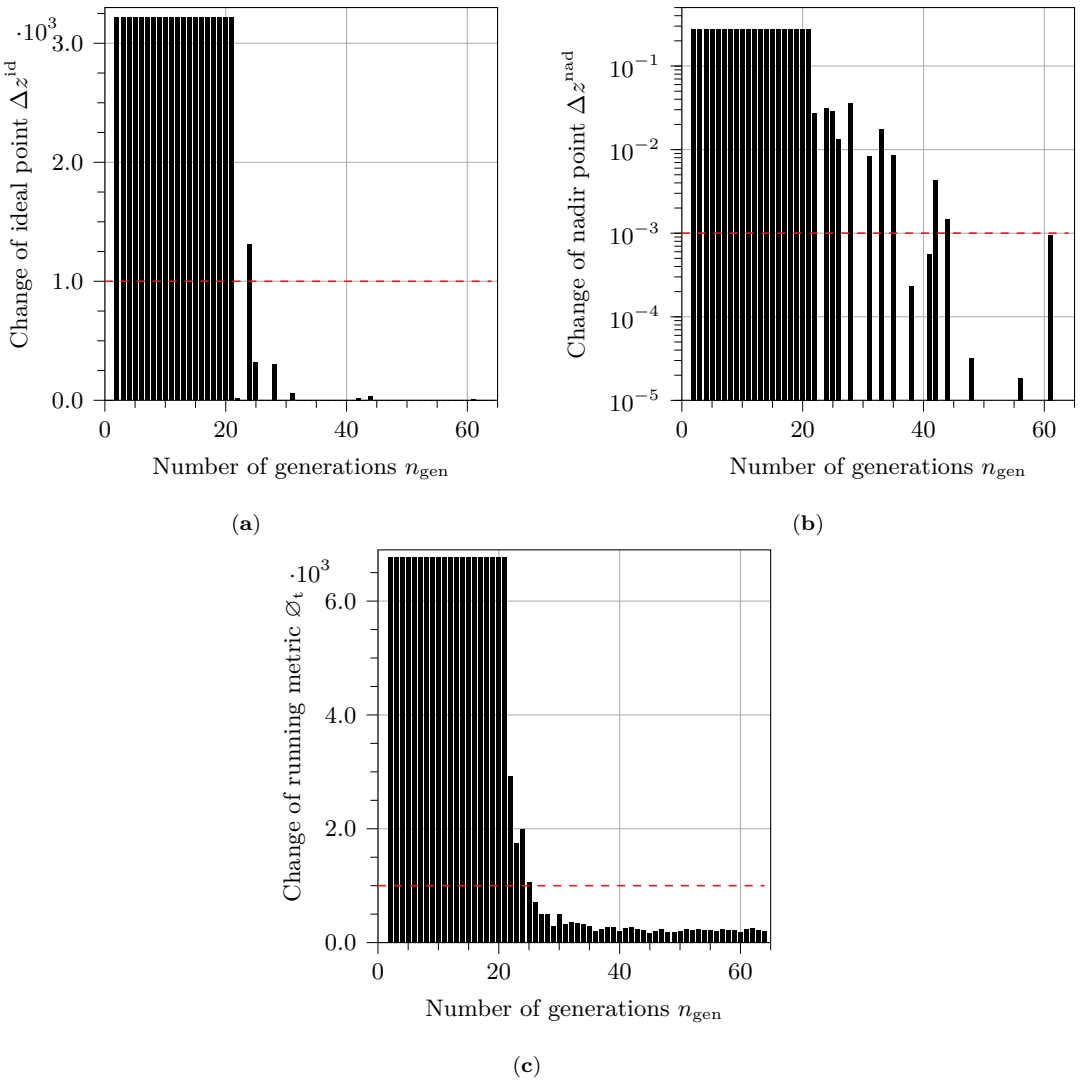

Figure 3.5: Convergence analysis for the cable optimization using NSGA-II. The red dashed line marks the allowable average change ε_{opt}. (a) Improvement of ideal point Δz^{id}; (b) Improvement of nadir point Δz^{nad}; (c) Improvement of running metric $\varnothing_t$

3.3.2.3 Statistical Analysis

Besides the differences in the quantitative results of the different optimization algorithms, a statistical analysis of them provides interesting insights. As stated in Section 3.3.2, the optimization has been repeated five times for different numbers of parallel processes for each algorithm. Figure 3.6 shows how many generations and how much computation time it takes to finish the optimization.

Figure 3.6a shows the averaged number of generations until termination n_{term} versus the number of parallel cores n_{CPU} for the three different optimization algorithms. The shaded area represents the standard deviation from the averaged values. As expected, there is no identifiable correlation between the number of parallel processes and the necessary number of generations until termination. The standard deviation is in the same range for the different algorithms. However, both the NSGA-II and the AGE-MOEAa algorithms terminate within 57.7 and 61.0 generations, while the U-NSGA-III algorithm takes 78.1 generations on average, making it the least efficient one. The averaged numbers are summarized in Table 3.5. The average execution time t_{exec} decreases inversely proportiona with the number of parallel processes, as shown in Figure 3.6b. However, an increase in overhead calculations to recombine the solutions can be seen. Increasing the number of

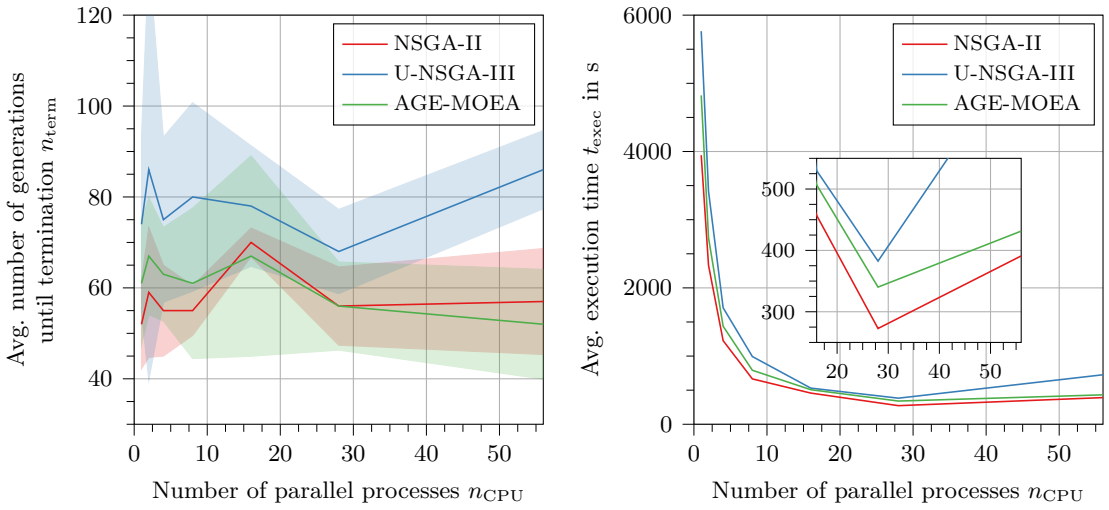

Figure 3.6: Analysis of parallelized execution of the optimization. (a) Averaged number of generations until termination n_{term} with a batch of five runs each for different optimization algorithms and number of parallel processors n_{CPU}; (b) Average time t_{exec} optimization takes to finish for different optimization algorithms and number of parallel processors n_{CPU}

Table 3.5: Statistical analysis of the convergence and execution time of different optimization algorithms

		Optimization algorithms			
Description	**Parameter**	**NSGA-II**	**U-NSGA-III**	**AGE-MOEA**	**Unit**
Average number of generations until termination	n_{term}	57.7	78.1	61.0	-
Average execution time	t_{exec}	272.72	382.52	340.2	s

processes from one to 28 for the NSGA-II algorithm results in a speedup of 14.5 times, indicating an overhead of 50 %. Consistently, the execution time is minimal for 28 parallel processes for all algorithms. This means the overhead increases significantly when hyperthreading is used in addition to the physical cores.

3.4 Short Summary

The previous sections demonstrate that for a representative engineering optimization problem, such as the optimization of a cable with respect to overall mass and losses, the NSGA-II algorithm is a simple, yet robust and reliable algorithm. It has been shown that the quality of the Pareto front is best for the NSGA-II algorithm, with a high diversity of solutions along the entire front, while AGE-MOEA reaches the same front, but the diversity at the extreme points is lower. The third algorithm, the U-NSGA-III algorithm, also reaches the same extreme points, but the Pareto front crowds along given reference directions, which are difficult to define when the objectives scale differently.
The NSGA-II algorithm also outperforms the other algorithms in the statistical analysis, requiring the lowest number of generations to terminate. Thus, it also has the lowest computation time when comparing the three options. Finally, it is beneficial to use all available physical cores of the computer to minimize average execution time and avoid hyperthreading, although the benefit of using a larger number of cores diminishes as the number of cores increases.

4 Drive Train Optimization of an All-Electric Vertical Take-Off and Landing Aircraft

Urban Air Mobility is envisioned to be one part of future mobility for intra- and intercity trips. Roland Berger [345] forecasts about 160 000 passenger drones by 2050 generating revenues worth about 80 billion euro, 90 % of them by airport shuttle and intercity services up to around 200 km of distance. The large potential revenues attracts both start-ups and major aero companies as well as investors resulting in more than 110 urban air mobility projects worldwide, with about ten of them listed on major stock exchanges, e.g., Archer Aviation Inc., Joby Aviation, Eve Air Mobility, Vertical Aerospace and Volocopter.
According to [345–348] the three main drivers for urban aviation are ultra-fast communication networks, autonomous flight technology and most importantly electric propulsion. Electric propulsion will offer several advantages compared to conventional, fossil fuel-driven powertrains. Electric drivetrains contain simpler components than gas turbines thus reducing production as well as maintenance cost. Furthermore, the increase in mass production of high-power battery cells for automotive reasons will lead to a drop of costs, an effect even amplified by electricity costs compared to kerosene. Environmental factors have to be valued as well. Electric propulsion allows travel without local emissions thus increasing the likelihood for acceptance of intra- and intercity services.
The main drawbacks of today's technology are the lower power densities of electric propulsion systems compared to gas turbines, and the still limited energy and power densities of battery cells relative to fossil fuels. As a result, only short-haul flights can currently be operated fully electrically.
During the design phase of an electric drivetrain for an aircraft application a strong focus will be to minimize weight and maximize operational efficiency to enable electric propulsion. This chapter will thus deal to deploy the component models described in Chapter 2 and utilize the optimization methods from Chapter 3 to evaluate different all-electric architectures of powertrains for a generic vertical take-off and landing concept.
A generalized version of Joby's S4 demonstrator vehicle serves as benchmark for all following investigations. This vehicle is deliberately chosen due to the availability of a range of data required to perform drivetrain analysis [349–351].
In this chapter the reference aircraft and mission are defined to ensure comparability of the drivetrain designs, and an overview of the all-electric drivetrain architectures will be presented. After that the chosen optimization setup and the boundary constraints are explained before the results of the comparative study of investigated topologies and variants will be presented and discussed. Finally, a more closer look on a chosen design proposal is taken.

4.1 Reference Aircraft and Mission

Meaningful drivetrain requirements are the basis for a fair comparison of possible drivetrains. These have to be derived from a conceptual aircraft, but as the focus of this work is on the electric drivetrain design the aircraft performance analysis is carried out on a high level of simplification.

Top Level Aircraft Requirements

Only a few top-level aircraft requirements are specified in Table 4.1 to avoid a detailed discussion of the aircraft itself. Urban air mobility requires short or negligible take-off distances, and thus the ability to take off and land vertically. This can be achieved through various types of lift arrangements, such as classical helicopter rotors, tilted wings, or tilted rotors. The latter arrangement is chosen for the reference aircraft as it is more efficient, as it can transition from hover or vertical climb to wing-borne flight [352], where the wing generates the majority of the required lift depending on its lift-to-drag ratio (L/D) in cruise conditions. The combination of distributed electric propulsion and tiltrotor design allows for both quiet operation and enhanced safety through redundancy.

Table 4.1: Top level aircraft requirements for a generic electric vertical take-off and landing vehicle for urban air mobility based on the Joby S4 production prototype [349–351]

Parameter	**Symbol**	**Value**		**Unit**
		Hover	Cruise	
Maximum Takeoff Weight (MTOW)	W_{TO}	2400		kg
Operating Empty Weight	W_{E}	1950		kg
Payload capacity	W_{P}	450		kg
Design range	R	150		km
Wingspan	L_{W}	12		m
Lift-to-drag ratio	L/D	-	12.6	-
Cruise speed	v_{cr}	-	70	$\mathrm{m\,s^{-1}}$
Climb speed	v_{v}	5.0	3.5	$\mathrm{m\,s^{-1}}$
Descent speed	v_{v}	-2.5	-5.0	$\mathrm{m\,s^{-1}}$

The maximum take-off weight of 2400 kg is well within the limit of 3175 kg defined by EASA's certification specification CS-VTOL [353], which is based on specification CS-27 [354]. The aircraft has a cruise speed v_{cr} of approximately $70\,\mathrm{m\,s^{-1}}$ ($240\,\mathrm{km\,h^{-1}}$), vertical climb and descent speeds v_{v} in the range of $-5.0 - 5.0\,\mathrm{m\,s^{-1}}$, and a lift-to-drag ratio L/D in cruise of 12.6. The aircraft is designed to operate at 1500 m altitude, achieving a design range of approximately 150 km.

Reference Electric Propulsion System Architecture

Figure 4.1 shows a schematic top view of the Joby S4 production prototype and a simplified architecture of the electric propulsion system (EPS). The aircraft has a streamlined fuselage designed for low drag and high efficiency. The aircraft features a high-wing, V-tail configuration with six tiltrotors mounted on the wings. These electric propellers tilt to enable vertical takeoff and landing while providing efficient forward flight in cruise mode. The tilt mechanism facilitates a smooth transition from hover to cruise, optimizing aerodynamic performance.

The aircraft employs a distributed electric propulsion system with six direct-drive electric propulsion units (EPUs) mounted on aerodynamically optimized pylons. Each electric propulsion unit consists of a high-performance electric motor, an inverter, and a liquid-cooled heat exchanger to ensure efficient thermal management. The direct-drive configuration eliminates the need for a gearbox, reducing mechanical complexity, improving reliability, and minimizing maintenance requirements.

The aircraft's energy storage system consists of lithium-ion battery modules integrated within the wing structure, optimizing weight distribution, structural integrity, and aerodynamic efficiency. The battery system is actively thermally managed to maintain stable performance under varying power demands. The batteries provide power to the six electric propulsion units, which are strategically positioned to enable efficient vertical take-off and landing operations and cruise flight. The liquid-cooled system ensures thermal stability during high-power operations, enhancing both performance and power density. The combination of distributed propulsion, integrated energy storage, and liquid cooling results in high redundancy, improved safety, and reduced acoustic signature [349, 351].

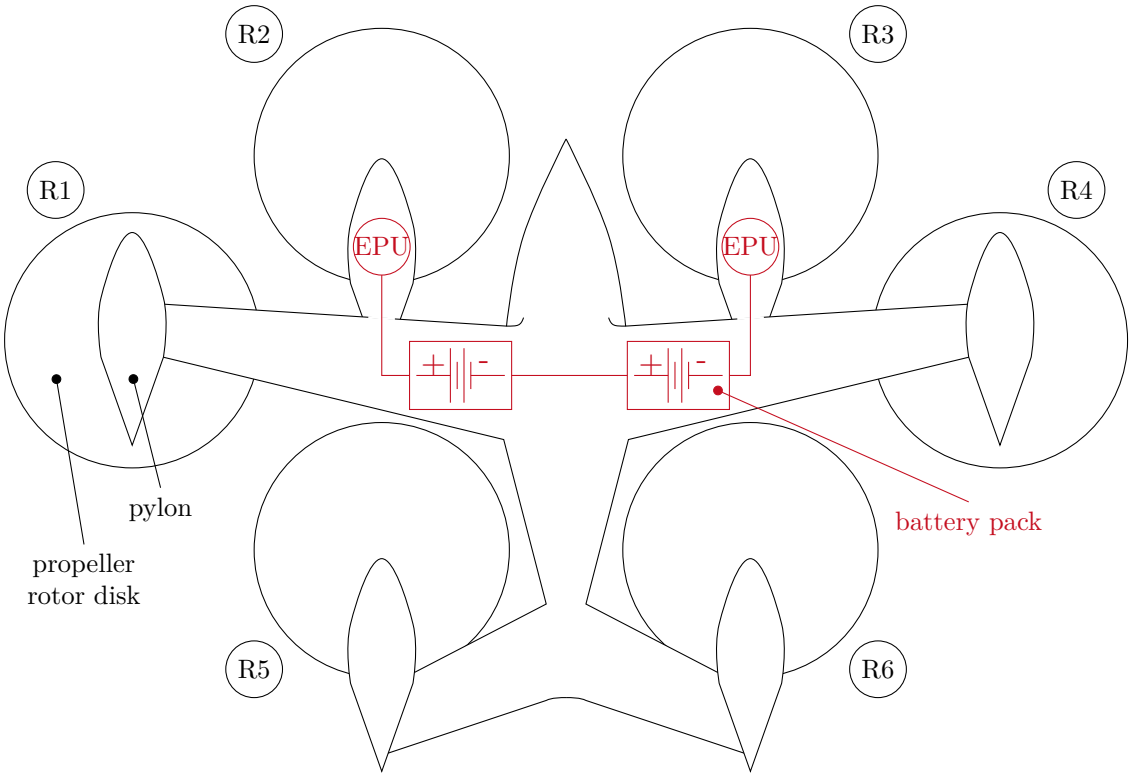

Figure 4.1: Schematic top view of the Joby S4 production prototype with a simplified layout of the electric propulsion system, consisting of six electric propulsion units and two interconnected battery packs (for better visibility, only two out of six propulsion units are shown). The propulsions units are mounted on pylons at the wingtips and mid-wing at each side of the fuselage to drive a propeller. The propeller rotor disks use an arbitrary numbering scheme R1 to R6.

To allow for the calculation of the required propeller shaft and overall battery power during mission analysis, efficiencies must be specified. The propeller efficiency η_{Prop} is assumed to be 0.65 for hover and 0.85 for cruise. The electric propulsion system efficiency, η_{EPS}, which describes the overall efficiency between the propeller shaft and the battery, is assumed to be 0.87 for hover and 0.93 for cruise. Table 4.2 summarizes the most important parameters of the electric propulsion system for mission analysis.

Table 4.2: Main parameters of electric propulsion system of Joby S4 production prototype [349–351]

Parameter	**Symbol**	**Value**		**Unit**
		Hover	Cruise	
Number of propellers	N_{Prop}	6		-
Propeller radius	r_{Prop}	1.45		m
Propeller efficiency	η_{Prop}	0.65	0.85	-
Electric propulsion system efficiency	η_{EPS}	0.87	0.93	-

Reference Mission and Flight Profile

The reference mission is characterized by the horizontal velocity v_h and vertical flight speed v_v, as illustrated in Figure 4.2a. The mission consists of five distinct segments. In the first segment, the aircraft performs a vertical hover climb with no horizontal movement to lift off the ground. It then transitions into a climb, during which the climb speed decreases linearly from $5\,\mathrm{m\,s^{-1}}$ to $2.5\,\mathrm{m\,s^{-1}}$, while the horizontal component increases linearly to $10\,\mathrm{m\,s^{-1}}$. Once this transition is complete, the aircraft reaches its operating altitude. The aircraft then executes a purely horizontal flight at a constant cruise speed to cover a given distance. Subsequently, the aircraft initiates its descent with a vertical velocity of $-5\,\mathrm{m\,s^{-1}}$ and gradually reduces its horizontal speed to zero. In the final phase, a controlled hover landing with a descent speed of $-2.5\,\mathrm{m\,s^{-1}}$ is performed.
These speed profiles are then integrated separately to derive the distance and altitude profiles, as shown in Figure 4.2b. Approximately 25 % of the total mission time is spent on vertical take-off and landing or transitional climb and descent. Furthermore, the traveled distance is primarily determined by the cruise time, as the other segments contribute minimally due to the low horizontal velocities.

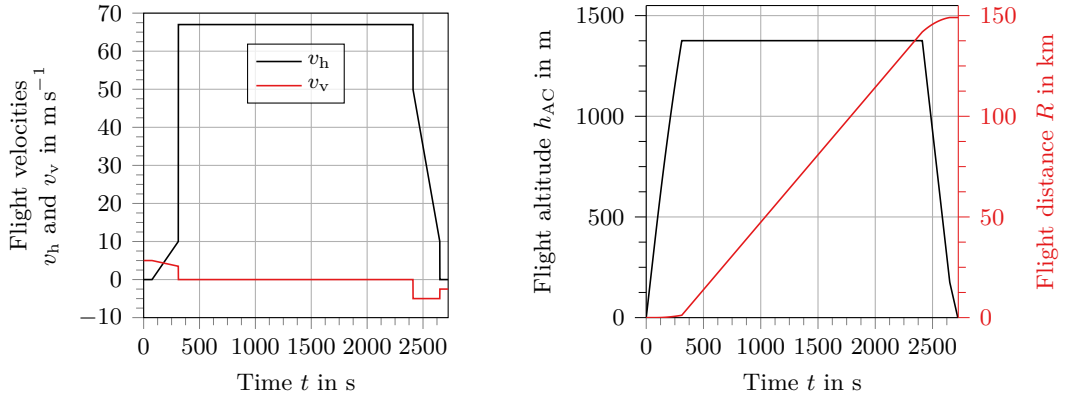

(**a**) Horizontal and vertical flight speeds

(**b**) Flight altitude and distance

Figure 4.2: Flight velocities and resulting altitude and range profile for aircraft similar to Joby's S4 production prototype defined in Table 4.1

Thrust Requirements

Every aircraft is subjected to three primary types of forces, as visualized in Figure 4.3. These forces can be classified into aerodynamic forces, including lift L_AC and drag D_AC; propulsive forces, represented by thrust T_AC; and the gravitational force, corresponding to the aircraft's weight G_AC, under steady-state, unaccelerated flight conditions [355, 356]. The equilibrium of forces along the flight direction and perpendicular to it is expressed as

$$T_\mathrm{AC} - D_\mathrm{AC} - \sin\alpha_\mathrm{AoA}\, G_\mathrm{AC} = 0 \tag{4.1}$$

$$L_\mathrm{AC} - \cos\alpha_\mathrm{AoA}\, G_\mathrm{AC} = 0 \tag{4.2}$$

which can be rearranged into a single equation to determine the required thrust

$$T_\mathrm{AC} = \mathrm{MTOW}\, g \left(\sin\alpha_\mathrm{AoA} + \frac{\cos\alpha_\mathrm{AoA}}{(L_\mathrm{AC}/D_\mathrm{AC})} \right) \tag{4.3}$$

where the lift-to-drag ratio is used to simplify the aerodynamic calculations.

Propeller Actuator Disk Theory

The primary flight regimes of the aircraft, i.e., climb, descent, and forward flight, can be modeled using actuator disk theory [357, 358]. The actuator disk theory assumes that

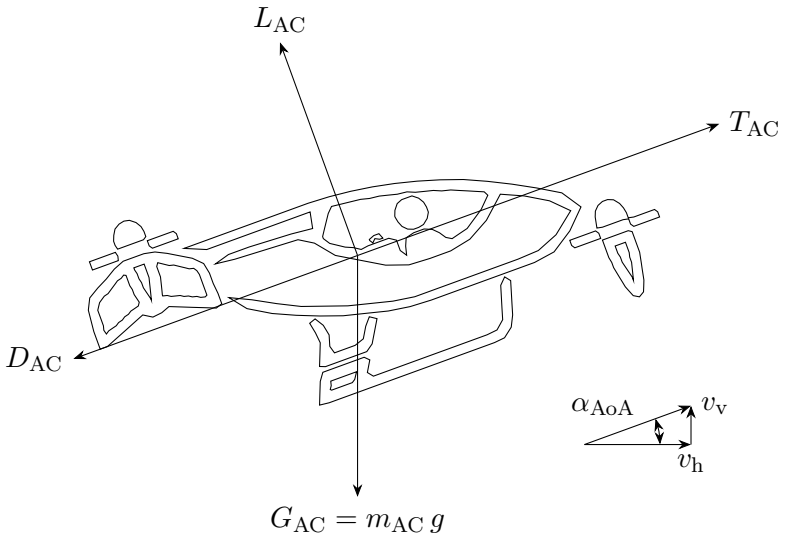

Figure 4.3: Schematic side view of a generic vertical take-off and landing vehicle, illustrating the four forces acting on the aircraft during steady-state, unaccelerated flight, as well as the horizontal velocity v_{h} and vertical velocity component v_{v}. The angle of attack α_{AoA} is exaggerated for clarity.

thrust is generated by an infinitely thin disk composed of an infinite number of blades, operating in incompressible airflow. This assumption holds for low Mach numbers [359]. The airflow is described using a one-dimensional stream tube, as shown in Figure 4.4.

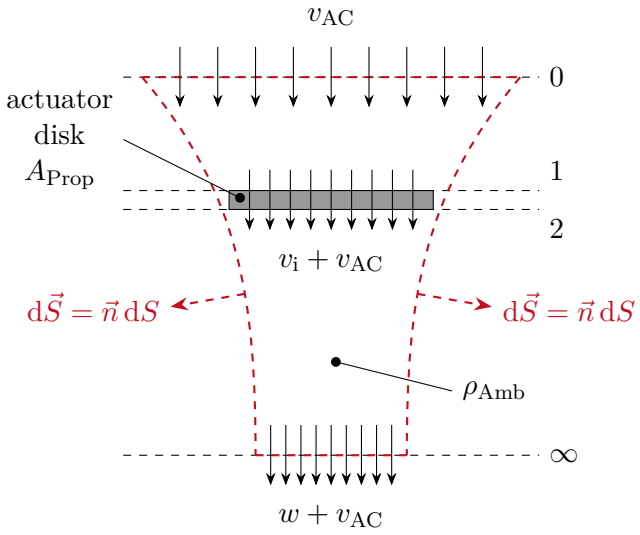

Figure 4.4: Schematic representation of different aerodynamic regions of an aircraft in vertical flight, used to derive the required thrust via actuator disk theory [357, 358].

When an aircraft moves with an airspeed v_{AC} in a given direction, a stream of air enters the control volume at section 0 with the same velocity. The propeller, represented by the actuator disk with an area A_{Prop}, induces an additional velocity v_{i} from section 1 to section 2 as it passes through the propeller. The airflow then exits the stream tube at section ∞ with a velocity of $w + v_{\mathrm{AC}}$. The induced velocity is derived by applying the conservation principles of mass, momentum, and energy. In the case of hovering flight, i.e., $v_{\mathrm{AC}} = 0$, this results in [357, 358]

$$v_{\mathrm{hov}} = v_{\mathrm{i}} = \sqrt{\frac{T_{\mathrm{AC}}}{2\,\rho_{\mathrm{Amb}}\,A_{\mathrm{Prop}}}}. \tag{4.4}$$

All other flight conditions are then described relative to the induced velocity during hov-

ering. Particular attention must be given to vertical descent conditions. Equation (4.5) describes the three possible states as

$$\frac{v_\mathrm{i}}{v_\mathrm{hov}} = \begin{cases} -\frac{x}{2} + \sqrt{\left(\frac{x}{2}\right)^2 + 1} & x \geq 0 \\ 0.974 - 1.125x - 1.372x^2 - 1.718x^3 - 0.655x^4 & -2 \leq x \leq 0 \\ -\frac{x}{2} - \sqrt{\left(\frac{x}{2}\right)^2 - 1} & x \leq 2 \end{cases} \tag{4.5}$$

where the climb velocity ratio x is defined as

$$x = \frac{v_\mathrm{AC}}{v_\mathrm{hov}}. \tag{4.6}$$

Equation (4.5) is visualized in Figure 4.5. As the climb velocity increases in the normal working state, the induced velocity decreases asymptotically toward zero. A similar trend occurs if the descent velocity increases in the windmill-brake state. The vortex ring state is characterized by unsteady flow, where both upward and downward velocities coexist. Thus, an approximation of the induced velocity is necessary, as momentum theory is not directly applicable [357, 358].

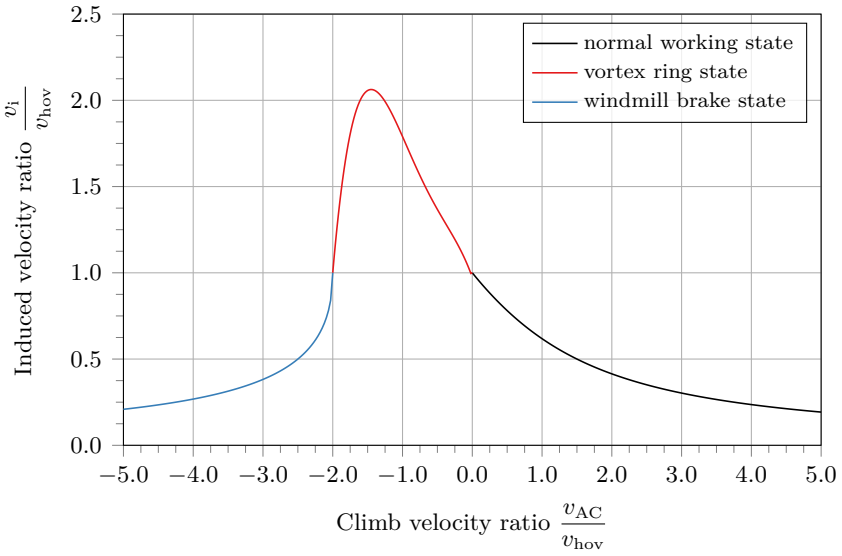

Figure 4.5: Induced velocity variation across the propeller disk for different flight conditions.

The total battery power can be determined as

$$P_\mathrm{Bat} = \frac{1}{\eta_\mathrm{Prop}\,\eta_\mathrm{EPS}}\, T_\mathrm{AC}\, \left(v_\mathrm{AC} + v_\mathrm{i}\right). \tag{4.7}$$

Figure 4.6 presents the required thrust and propeller shaft power for an aircraft defined in Table 4.1 following the mission profile outlined in Figure 4.2a.
Figure 4.6a illustrates that the thrust requirements in both climb and descent conditions are identical, as they are primarily governed by the aircraft's weight. During ascent, thrust continuously decreases due to the lift generated by the wing, which is influenced by the increasing horizontal velocity component and the decreasing air density at higher altitudes. In contrast, during horizontal flight, the required thrust is significantly lower and is directly proportional to the lift-to-drag ratio. When the aircraft transitions into descent while still maintaining horizontal velocity, the required thrust becomes negative, enabling potential

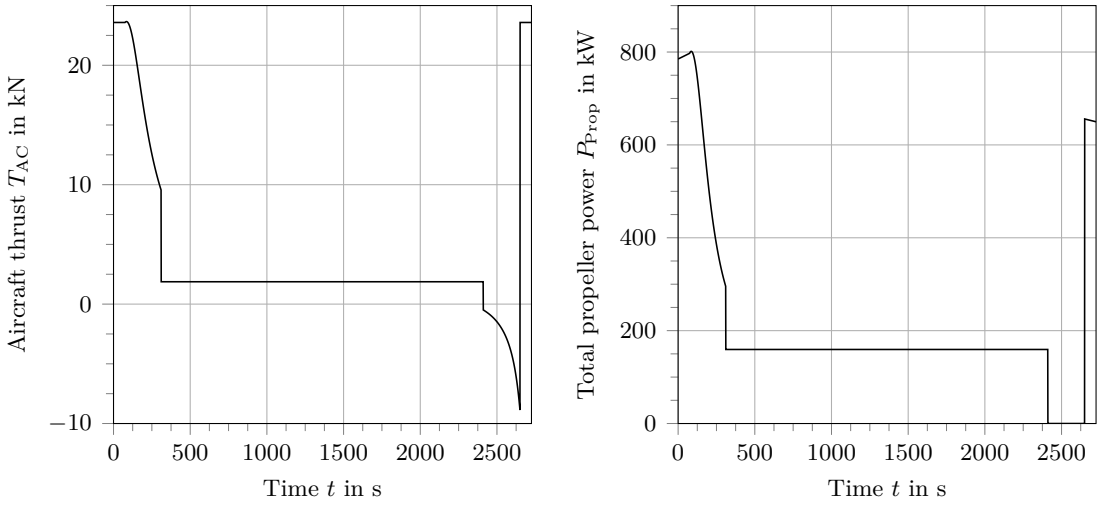

(**a**) Aircraft thrust

(**b**) Aircraft total propeller shaft power

Figure 4.6: Required thrust and total propeller shaft power of the aircraft as specified in Table 4.1 following the mission profile defined in Figure 4.2a.

recuperation, such as battery recharging. Once the aircraft enters hover descent, a sharp increase in required thrust is observed, reaching the take-off thrust level.
Overall the total propeller shaft power in Figure 4.6b shows a similar behaviour. While required thrust during hover ascent and descent is constant, the total propeller shaft power demand increases during steady climb due to the reduction in air density at higher altitudes. During descent, the behavior is reversed, with power requirements approximately 10 % lower than those in ascent. For horizontal flight, the power demand is approximately 20 % of the climb value. For simplicity, no recuperation is considered in this example, thus the power during gliding descent is set to zero.

4.2 Electric Propulsion Unit Performance Point Defintion for Different Aircraft Configurations

These power and thrust requirements serve as key parameters in the design process of the electric drivetrain components. The objective of the performance point definition is to determine the required power output that the electric propulsion system need to deliver during critical flight phases, especially during hover, to ensure that the system can meet the operational requirements of the aircraft for different aircraft configurations, i.e., different number of propellers N_{Prop} ranging from six to ten.

Total Peak Power Requirement

During hover, the aircraft must generate enough thrust to counteract its weight and maintain a stable position. Based on the mission analysis from Figure 4.6b, the power required at the end of the climb hover phase is approximately 800 kW. In addition to the nominal hover power, a control margin of approximately 10 % is added to account for dynamic conditions such as wind, variations in aircraft performance, and the need for maneuverability. This ensures that the aircraft has sufficient power reserve to maintain control under all expected flight conditions, especially during hover, where power demand can fluctuate due to changes in wind or control inputs.
Therefore, the selected performance point for the electric propulsion system is chosen as 900 kW of total peak power $P_{\mathrm{pk,tot}}$, which will serve as the main benchmark for the design

and performance assessment of the electric propulsion system. This value reflects the maximum power demand that the electric propulsion units must be capable of providing during hover to ensure stable flight and control margin.

Aircraft Configuration Assumptions and Parameters

In order to compare the aircraft with different numbers of propellers, the following assumptions are made. First, since the overall thrust required to maintain stable flight remains constant regardless of the number of propellers, it is assumed that the disk loading, defined as

$$D_{\mathrm{L}} = \frac{T_{\mathrm{AC}}}{N_{\mathrm{Prop}}\, A_{\mathrm{Prop}}} = \text{const.} \tag{4.8}$$

is constant. Disk loading refers to the ratio of the total thrust T_{AC} produced by the propellers to the total disk area A_{Prop} swept by the propellers. By maintaining a constant disk loading, the aircraft's aerodynamic performance is kept comparable between variants with different numbers of propellers. This assumption ensures that variations in the number of propellers do not affect the overall aerodynamic efficiency and power requirements. This assumption leads to a constant total disk area, which can be used to derive the radius of the propeller depending on the number of propellers

$$r_{\mathrm{Prop,2}} = \sqrt{\frac{N_{\mathrm{Prop,1}}}{N_{\mathrm{Prop,2}}}}\, r_{\mathrm{Prop,1}}, \tag{4.9}$$

where $r_{\mathrm{Prop,1}}$ and $r_{\mathrm{Prop,2}}$ represent the radii of the propellers in two different variants, and $N_{\mathrm{Prop,1}}$ and $N_{\mathrm{Prop,2}}$ represent the number of propellers in those variants.

Next, we assume that the propeller tip speed remains constant across all variants. The propeller tip speed is a critical parameter influencing the efficiency of the propeller and the noise generated during operation. A constant tip speed ensures that the aircraft maintains similar aerodynamic properties across the different variants, regardless of the number of propellers. Keeping tip speed constant prevents excessive noise generation and ensures compliance with efficiency constraints. This assumption results in the following relationship between the rotational speeds of the propellers

$$n_{\mathrm{Prop,2}} = \frac{r_{\mathrm{Prop,1}}}{r_{\mathrm{Prop,2}}}\, n_{\mathrm{Prop,1}}, \tag{4.10}$$

where $n_{\mathrm{Prop,1}}$ and $n_{\mathrm{Prop,2}}$ represent the rotational speeds of the propellers in the two variants.

The peak power of the electric propulsion units is an important factor in the overall design. It is based on a one rotor inoperative scenario, i.e., one arbitrary rotor fails. Due to the necessary balance of forces and moments exerted by the propellers on the aircraft, the propeller opposite to the failed one is shut down as well. This is a realistic scenario that ensures the electric propulsion unit is capable of withstanding the maximum power requirements during critical flight phases. Stoll and Bevirt [351] analyzed a number of different geometric arrangements of the propellers in case of six propellers, and concluded that in the optimal case the relationship for the peak power $P_{\mathrm{pk,EPU}}$ is given by

$$P_{\mathrm{pk,EPU}} = \frac{P_{\mathrm{pk,tot}}}{N_{\mathrm{Prop}} - 2} \tag{4.11}$$

where $P_{\mathrm{pk,tot}}$ is the total peak power required and N_{Prop} is the number of propellers. By considering a 30 % higher peak power rating than the continuous rating, we account for the transient power demands during hover or other critical flight phases. This ensures that the propulsion system remains reliable and capable of delivering sufficient power during

such demanding conditions.
In addition to the propulsion system, the propeller spinner's dimensions must also be considered as they determine the allowable dimensions of the electric propulsion unit. To prevent a degradation in propeller efficiency, the maximum area aspect ratio of the spinner AR_{Sp}, defined as the ratio of spinner area to propeller disk area, is limited to 5 %. This equals a maximum machine outer radius of approximately 20 % of the propeller radius. The area aspect ratio is a key factor influencing the aerodynamic efficiency of the propeller, and ensuring it remains below this threshold guarantees that the propeller operates efficiently across different variants [32]. The maximum spinner radius and thus outer radius of the electric propulsion unit, is defined as

$$r_{\mathrm{Sp}} = r_{\mathrm{EPU}} = \sqrt{AR_{\mathrm{Sp}}}\, r_{\mathrm{Prop}} \tag{4.12}$$

where r_{Sp} is the radius of the spinner and r_{EPU} the outer radius of the electric propulsion unit, e.g., the electric machine or the gearbox.
Lastly, as different numbers of propellers result in different power requirements, the average length of connection lines between the electric propulsion units and the batteries need to be considered, e.g., when assessing weight of the cabling or also tubing depending on the thermal management system layout. In the simplest case, one could assume that propellers are distributed evenly along the wingspan, which provides a reasonable approximation for most aircraft configurations. This ensures that the electrical system and associated components are distributed in a manner that avoids significant imbalance or excess weight in any particular area of the aircraft. The average length of a connection line can be expressed as

$$l_{\mathrm{avg}} = \frac{N_{\mathrm{Prop}}}{4\,(N_{\mathrm{Prop}} - 1)}\, L_{\mathrm{W}} \tag{4.13}$$

where L_{W} is the wingspan of the aircraft.
This assumption will be used, even though it is not fully accurate for aircraft like the Joby S4, where the distribution of propellers along the wingspan is not perfectly uniform, particularly when the number of propellers is small or intermediate. When the number of propellers increases to eight, two propellers are placed at the wingtip, which tends to increase the average wiring length compared to the six-propeller configuration, as more of the wiring must span the wingspan. In the case of ten propellers, the layout is expected to become more balanced, with a higher number of propellers placed near the fuselage and only one at the wingtip. As a result, the average wiring length for a ten-propeller configuration will likely approach the average length of the six-propeller configuration, albeit with slight variations due to the positioning of the additional propellers.
The performance point definition for three different aircraft configurations, with six, eight, and ten propellers, is summarized in Table 4.3.
While the required overall peak power remains constant at 900 kW for all configurations, the installed peak power decreases as the number of propellers increases. This is due to the fact that the electric propulsion unit peak power is determined based on a one rotor inoperative scenario. Specifically, the dimensioning electric propulsion unit continuous power decreases with values of 175 kW, 115 kW, and 85 kW for the six-, eight-, and ten-propeller configurations, respectively. Consequently, the installed overall peak power is 1350 kW for the six-, 1200 kW for the eight-, and 1125 kW for the ten-propeller configuration. These values will be used as inputs and constraints in the following investigations.
In comparison, Joby specified a peak power $P_{\mathrm{pk,EPU}}$ of 236 kW at a peak torque $T_{\mathrm{pk,EPU}}$ of 1800 N m and a continuous torque $T_{\mathrm{cont,EPU}}$ of 1380 N m for the electric propulsion unit of the six-propeller configuration. The torque specifications are nearly identical, while Joby's installed peak power $P_{\mathrm{pk,tot}}$ of 1416 kW is about 5 % higher than the calculated value of

Table 4.3: Performance point definition for three aircraft configurations with propeller count ranging from six to ten, based on assumptions presented in Section 4.2

Parameter	Symbol	Value			Unit
		Number of propellers N_{Prop}			
		6	8	10	
Propeller radius	r_{Prop}	1.45	1.26	1.12	m
Propeller rotational speed	n_{Prop}	1200	1600	2000	min^{-1}
Overall peak power required	$P_{\mathrm{pk,tot,req}}$		900		kW
Overall peak power installed	$P_{\mathrm{pk,tot}}$	1350	1200	1125	kW
EPU peak power	$P_{\mathrm{pk,EPU}}$	225	150	113	kW
EPU continuous power	$P_{\mathrm{cont,EPU}}$	175	115	85	kW
EPU peak torque	$T_{\mathrm{pk,EPU}}$	1790	1430	1280	N m
EPU continuous torque	$T_{\mathrm{cont,EPU}}$	1390	1100	970	N m
Available installation space	r_{Sp}	320	280	250	mm
Average length of connection lines	l_{avg}	7.20	6.90	6.60	m

1350 kW from Table 4.3, which could be due to additional safety margins or efficiency considerations. Similarly, the installed peak power $P_{\mathrm{pk,tot}}$ of 944 kW slightly exceeds the calculated value of 900 kW retrieved by the mission analysis for the one rotor inoperative scenario, indicating a conservative redundancy strategy. Overall, these minor deviations confirm that the assumptions made in this study provide a reasonable approximation of the actual system.
Furthermore, Joby specifies a target mass of approximately 28 kg per electric propulsion unit, totaling around 170 kg for the six-propeller configuration. However, the definition of this figure remains somewhat ambiguous. It is not explicitly stated which structural components are included, whether the mass of the thermal management system (e.g., heat exchangers, pump, and piping) is accounted for, or whether the value refers to a dry or operational (wet) condition. These aspects introduce uncertainties in the interpretation and comparability of the data and should be taken into account when assessing system-level mass implications. In addition, no detailed efficiency data are provided, which further limits comparability with the analysis presented in Section 4.5.

4.3 All-Electric Propulsion System Architecture Overview

This study investigates multiple electric propulsion unit architectures and configurations for aircraft with six, eight, and ten propellers, aiming to quantify the weight and efficiency impact of the electric propulsion system at the aircraft level. In all configurations, the battery is assumed to be a centrally located pack, directly connected to the electric propulsion units. Thus, only the archiecture of the electric propulsion units differ between the investigated variants. The baseline architecture and its variations are detailed below.

4.3.1 Baseline Configuration: Direct Liquid-Cooled Electric Machine and Inverter with Local Cooling System

4.3.1.1 System Description

The baseline electric propulsion unit architecture, as shown in Figure 4.7, features a direct liquid-cooled electric machine and a DC-AC inverter, both utilizing the same local

thermal management system. The inverter is battery-fed via a DC cable. Each unit operates independently, with the cooling systems of individual units not interconnected. This configuration ensures efficient heat dissipation while maintaining a compact and modular design.

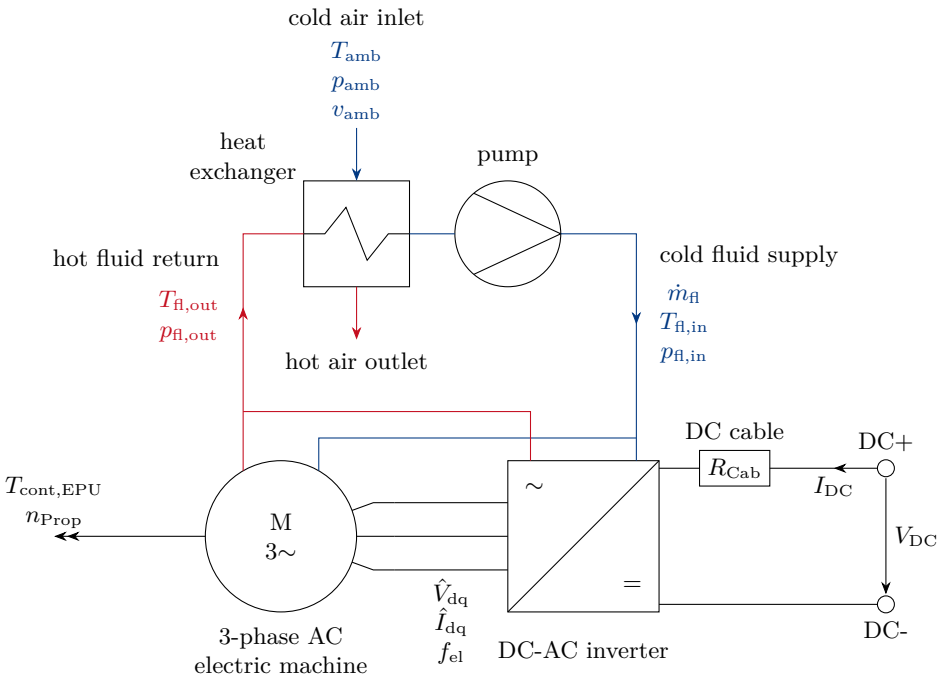

Figure 4.7: Schematic view of the baseline electric propulsion unit architecture featuring a direct liquid-cooled electric machine and inverter, and a common thermal management system. The global in- and outputs, as well as the most important exchange parameters, are listed.

The electric machine is a direct-drive, radial flux, in-runner, permanent magnet synchronous machine, eliminating the need for a gearbox and simplifying the drivetrain. The in-runner design positions the rotor inside the stator, offering advantages in mechanical stability and thermal management. The inverter employs a two-level topology using state-of-the-art silicon carbide modules and utilizes space vector modulation for optimal voltage utilization and reduced harmonic distortion. The system is optimized for thermal performance and reliable operation across various flight conditions.

Cooling System and Heat Dissipation Strategy

The cooling system plays a pivotal role in maintaining the thermal stability of the electric propulsion unit. The baseline configuration utilizes DowthermQ®, a synthetic heat transfer fluid known for its high thermal stability and low viscosity, making it suitable for high-power loads. This coolant is used across both the electric machine and inverter systems, simplifying the architecture by allowing both components to share the same thermal management system.

The electric machine employs direct slot cooling, where coolant flows through parallel channels embedded between the stator windings. This advanced cooling method provides significantly enhanced heat extraction compared to traditional jacket cooling, as it increases the surface area available for heat exchange. This localized cooling reduces the formation of hot spots and improves the machine's ability to maintain uniform temperature distribution, which is vital for optimizing continuous power ratings.

For the inverter, a similar liquid cooling approach is used. The semiconductor and capacitor modules are mounted onto a heatsink featuring rectangular fins, which are directly in contact with the same coolant. This ensures consistent thermal performance across both components, minimizing thermal losses and maintaining system efficiency.

The cooling loops of the electric machine and inverter are in parallel until the point where they merge before entering the liquid-air heat exchanger. The heat exchanger plays a crucial role in rejecting the accumulated heat to the ambient environment. Its effectiveness in transferring heat depends on its design, and the coolant's outlet temperature must not exceed the predefined inlet temperature to ensure the system operates within the desired thermal range.
A dedicated pump is located downstream of the heat exchanger to compensate for pressure losses in the system and ensure the coolant circulates through the entire loop. The pump must be selected based on the system's flow rate, pressure drop, and overall resistance to ensure the cooling fluid maintains sufficient velocity for optimal heat transfer.

System Integration and Component Placement
Efficient system integration plays a key role in maximizing power density and minimizing AC conduction losses and electromagnetic interference in the electric propulsion unit. In the baseline configuration, the inverter is positioned in close proximity to the electric machine to facilitate tight integration. This proximity not only reduces the length of high-frequency AC connections but also lowers stray inductance, which is critical for ensuring switching efficiency in the power electronics system. The compact integration helps reduce the overall system volume and enhances the system's reliability by minimizing the risk of faults in the electrical connections.

System Performance Considerations
The liquid-cooled architecture of the baseline configuration is primarily driven by the goal of achieving high power density while maintaining overall system efficiency. Liquid cooling allows for higher power density by enabling the dissipation of higher losses, which would otherwise exceed the thermal limits of air-cooled systems. This is particularly beneficial in aviation applications, where size and weight constraints demand highly compact and efficient powertrain solutions.
By increasing the thermal performance of critical components, the system can sustain high power outputs without excessive derating, ensuring consistent performance throughout the mission. The ability to operate at lower temperatures also reduces electrical resistance and mitigates thermal stress on components, which contributes to improved overall system reliability and longevity.
Despite the thermal advantages, the implementation of a liquid-based cooling system involves certain trade-offs. The addition of a liquid-based cooling system introduces extra mass due to the required heat exchanger, pump, and fluid circulation components. While this added weight must be carefully managed, it is partially offset by the increased power density of the electric machine and inverter, which can be designed for higher performance without exceeding thermal limits. Additionally, improved thermal control throughout the mission ensures that efficiency losses due to elevated temperatures are minimized, resulting in more stable and predictable powertrain operation.

Advantages and Design Trade-Offs
The baseline configuration offers a balanced approach between performance, efficiency, and system complexity. Direct liquid cooling provides superior cooling capability compared to air-cooled alternatives, allowing for higher power operation without the risk of thermal saturation. This is particularly important for sustained high-power flight phases, where effective heat dissipation ensures stable system behavior.
The modular nature of the local cooling system ensures that each propulsion unit remains thermally independent, simplifying system-level integration and reducing potential failure propagation between units. However, the inclusion of active cooling components introduces additional system complexity and requires careful optimization to ensure that the benefits in power density and thermal performance outweigh the mass and system integration

challenges.
Overall, the baseline configuration serves as a reference for evaluating alternative architectures. Variants for comparison include the use of direct air-cooling, the allowance for elevated temperature limits in the electric machine, the adoption of a global cooling system, and the inclusion of a geared drive system.
These variants, along with the baseline configuration, will undergo system optimization and be assessed regarding their impact on performance, efficiency, and power density, providing a comprehensive understanding of their respective benefits and trade-offs.

4.3.1.2 Optimization Setup

Building upon the system architecture described in Section 4.3.1, the optimization setup outlines the key parameters and strategies required for the optimization process. By varying specific input parameters, this analysis will explore the trade-offs between overall system mass and efficiency. The objective is to evaluate how different design choices affect the performance of the propulsion system while ensuring that predefined operational constraints are met.
The optimization setup involves defining both fixed and variable input parameters, establishing clear performance objectives, and incorporating various constraints related to system integration, weight, and thermal and mechanical limits. Material selection plays a critical role in determining the structural and thermal performance of key components. The following subsections detail the specific parameters, objectives, and constraints used in this optimization analysis.

Material Selection

In aerospace applications, the material selection for electric propulsion systems prioritizes high performance, focusing on low weight, high strength, and low losses to meet the stringent demands of aviation. For the electric machine, electromagnetic materials for laminations (Vacodur49 and Vacoflux48), magnets (NdFeB G54UH), and windings (copper) are selected for high magnetic induction, low losses, high temperature stability, and superior electrical and thermal conductivity. Steel (AISI4340) and aluminum are employed for structural components, such as the rotor shaft and stator frame, due to their excellent strength-to-weight ratio and ability to withstand high mechanical stresses. Insulation materials (Polyurethane and Myoflex) are chosen for their high dielectric strength combined with good thermal properties.
In the inverter, silicon carbide semiconductors are selected for high efficiency, and film capacitors made of polypropylene are chosen due to their high energy capacity. Aluminum is also used in the inverter housing and heat exchanger core, offering lightness and effective thermal management. The DC cable uses Aluminum conductors and thermally optimized Duralectric as insulation. For the heat exchanger, carbon fiber reinforced plastics are used in air ducts, providing strength while minimizing weight.
This selection balances high thermal and electrical performance with mechanical strength, ensuring efficiency and reliability in the highly demanding aerospace environment. An overview of the selected materials is given in Table 4.4.

Fixed Input Parameters

To maximize design flexibility, only a limited number of input parameters are fixed in the optimization process. These parameters are primarily related to fundamental system constraints that define the operating environment and boundary conditions.
The electric machine utilizes a Halbach array magnet arrangement with full pole coverage and operates at discrete fixed speeds corresponding to different propeller configurations. The inverter employs symmetrical space vector modulation and a constrained DC voltage range of $540 - 900\,\mathrm{V}$, with the upper limit determined by the voltage ratings of available

Table 4.4: Selected materials for the baseline electric propulsion unit components

	Component	Material
Electric Machine	Rotor Shaft	Steel AISI4340
	Rotor Yoke	Vacodur49 (150 µm)
	Magnets	NdFeB G54UH
	Sleeve	Carbon fiber reinforced plastics
	Slot Pipe	Carbon fiber reinforced plastics
	Stator Teeth and Yoke	Vacoflux48 (100 µm)
	Wire	Copper
	Wire Insulation	Polyurethane
	Phase Insulation	Myoflex
	Slot Insulation	Myoflex
	Stator Frame	Aluminum
Inverter	Semiconductors	Silicon Carbide (SiC)
	Capacitors	Polypropylene film capacitors
	Heat Sink	Aluminum
	Housing	Aluminum
DC cable	Conductor	Aluminum
	Insulation	Duralectric
HX	Core	Aluminum
	Air Ducts	Carbon fiber reinforced plastics
	Pipes	Aluminum

semiconductor modules. This voltage range is also applicable for the DC cable.
The ambient air conditions for all variants remain constant and do not vary, assuming ISA + 20 K, resulting in an ambient temperature of 35 °C and ambient pressure of 101 325 Pa. Furthermore, the available ambient air velocity v_{amb} is assumed to be $10\,\text{m}\,\text{s}^{-1}$, e.g., at the air duct inlets. This is reasonable for hover, where the flight velocity is likely lower when the inlets are placed downstream of the propellers.
For the liquid cooling cycle, the fluid inlet conditions (after the pump) are set to an inlet temperature $T_{\text{fl,in}}$ of 60 °C and an inlet pressure $p_{\text{fl,in}}$ of 200 000 Pa, providing sufficient temperature difference for both effective component cooling and heat dissipation to the ambient environment.
These fixed inputs establish a stable foundation for the optimization while allowing key design variables to be adjusted for optimal system performance. The defined values are summarized in Table 4.5.

Table 4.5: Fixed input parameters for the baseline electric propulsion unit

	Parameter	Symbol	Value	Unit
Electric Machine	Magnetization pattern		Halbach arrangement	-
	Pole coverage	α_{p}	1	-
	Number of phases	m_{ph}	3	-
	Rotational speed	n_{rot}	1200, 1600, 2000	min^{-1}
Inverter	Modulation method		Symmetrical SVM	-
	DC voltage	V_{DC}	540 – 900	V
DC Cable	DC voltage	V_{DC}	540 – 900	V
Pump	Mechanical efficiency	η_{mech}	0.65	-
	Electrical efficiency	η_{el}	0.95	-
	Outlet temperature	$T_{\text{fl,in}}$	60	°C
	Outlet pressure	$p_{\text{fl,in}}$	200000	Pa
Ambient	Temperature	T_{amb}	35	°C
	Pressure	p_{amb}	101325	Pa
	Velocity	v_{amb}	10	$\text{m}\,\text{s}^{-1}$

Design Input Variables

The optimization process considers a wide range of design input variables that directly influence system weight, efficiency, and key indicators such as manufacturability, reliability, and cost. These variables span the different components of the electric propulsion system and define the design space for optimization. Table 4.6 provides a complete list of all considered design input variables, their ranges, and their type, i.e., integer or real variables. In total, around 50 variables are considered, with more than ten of them being discrete parameters, making this a complex mixed-variable optimization problem. Due to the large number of variables, not every parameter is discussed individually.

Table 4.6: Variable input parameters for the baseline electric propulsion unit

	Parameter	Symbol	Range min	Range max	Unit	Type
Electric Machine	Shaft length	L_{stk}	25	100	mm	real
	Shaft inner radius	$r_{\mathrm{sh,i}}$	100	250	mm	real
	Rotor yoke thickness	t_{ry}	3	10	mm	real
	Magnet thickness	t_{mag}	2	15	mm	real
	Airgap thickness	g_{mech}	1	4	mm	real
	Tooth tip edge thickness	$t_{\mathrm{tt,e}}$	1	3	mm	real
	Relative tooth tip edge width	$\beta_{\mathrm{tt,e}}$	0.5	0.85	-	real
	Tooth tip center thickness	$t_{\mathrm{tt,c}}$	1	3	mm	real
	Relative tooth tip center width	$\beta_{\mathrm{tt,c}}$	0.5	0.85	-	real
	Slot depth	t_{sd}	5	60	mm	real
	Stator yoke thickness	t_{sy}	3	15	mm	real
	Pole pair number	p	30	70	-	int
	Slot number	Q_{s}	45	210	-	int
	Parallel winding paths	$n_{\mathrm{par,wdg}}$	1	70	-	int
	Winding turns	$N_{\mathrm{t,wdg}}$	1	100	-	int
	Wire insulation thickness	$t_{\mathrm{wire,ins}}$	10	200	µm	real
	Slot insulation thickness	$t_{\mathrm{slot,ins}}$	50	500	µm	real
	Phase insulation width ratio	$\beta_{\mathrm{ph,ins}}$	0.001	0.5	-	real
	q-axis current magnitude	$\hat{I}_q$	500	1300	A	real
	Coolant mass flow rate	$\dot{m}_{\mathrm{EM}}$	0.01	1	$\mathrm{kg\,s^{-1}}$	real
Inverter	Switching frequency ratio	$m_{\mathrm{c,sw}}$	8	50	-	int
	Semiconductor module index	i_{SC}	0	6	-	int
	Number of parallel semiconductors	$n_{\mathrm{SC,p}}$	1	5	-	int
	Gate driver module index	i_{GD}	0	4	-	int
	Bus bar conductor thickness	$t_{\mathrm{BB,cond}}$	1	10	mm	real
	Bus bar insulation thickness	$t_{\mathrm{BB,ins}}$	0.05	2	mm	real
	Number of fins on heatsink	N_{Fin}	1	200	-	int
	Fin width ratio	β_{Fin}	0.01	0.99	-	real
	Fin height	h_{Fin}	1	30	mm	real
	Coolant mass flow rate	$\dot{m}_{\mathrm{Inv}}$	0.01	1	$\mathrm{kg\,s^{-1}}$	real
DC Cable	conductor radius	r_{cond}	0.25	10	mm	real
	insulation thickness	t_{ins}	0.5	5	mm	real
HX	Number of passages	N_{P}	2	70	-	real
	Flow path length	$L_{\mathrm{FP,c/h}}$	10	400	mm	int
	Number of fins per pitch	$N_{\mathrm{fp,c/h}}$	2	150	-	int
	Number of offset fins	$N_{\mathrm{off,c/h}}$	2	150	-	real
	Fin height	$b_{\mathrm{Fin,c/h}}$	1	50	mm	real
	Fin thickness ratio	$\beta_{\mathrm{Fin,c/h}}$	0.01	0.99	-	real
	Air duct opening	$r_{\mathrm{in,c/h}}$	5	300	mm	real
	Air duct length	$l_{\mathrm{in,c/h}}$	50	300	mm	real
Pipe	inner radius	r_{pipe}	1	15	mm	real
	wall thickness	t_{pipe}	0.5	2	mm	real

The input variables can be broadly categorized into geometric parameters and operational parameters. Geometric parameters determine the physical dimensions of the components,

as well as their electromagnetic, structural, thermal, and thermodynamic properties. In the electric machine, these include rotor and stator dimensions such as shaft length, magnet thickness, and airgap thickness, as well as winding design parameters like slot depth and the number of winding turns. The cable geometry is defined by the conductor radius and the insulation thickness. The inverter geometry is shaped by semiconductor and capacitor packaging, as well as heat sink fin configuration. In the heat exchanger and piping, key parameters include passage design, fin arrangements, and duct geometry, which influence cooling effectiveness and overall system integration.
Operational parameters define the electrical and thermal working conditions of the components. From an electrical perspective, the q-axis current magnitude affects torque production and losses in the electric machine, while the switching frequency ratio influences power losses and controllability in the inverter. In both cases, the coolant mass flow rate impacts the thermal operating point, and consequently, the design of thermal management system components such as the heat exchanger and pump.
By adjusting these input variables within carefully defined limits, the optimization algorithm explores the most effective trade-offs between the defined objectives, which will be outlined in the next section.

Optimization Objectives

In aerospace applications, minimizing both overall system mass and losses is paramount to reducing energy consumption and maximizing range, while also ensuring overall aircraft feasibility. Additionally, lower weight allows for higher payload capacity, and improved powertrain efficiency reduces cooling requirements and enhances system reliability.
The objectives shown in Table 4.7 account for all components of the electric propulsion unit as defined in Section 4.3.1.1, including the masses of the electric machine, inverter, DC cables, and thermal management system. The primary sources of losses are copper and iron losses in the electric machine and semiconductor losses in the inverter, while losses from DC cables are considered but play a minor role.

Table 4.7: Optimization objectives for the baseline electric propulsion unit

Objective	Symbol	Unit	Type
Mass of electric propulsion unit	m_{EPU}	kg	min
Losses of electric propulsion unit	Q_{EPU}	kW	min

However, these objectives are inherently conflicting, forming a classical Pareto optimization problem. The optimization process must therefore balance these trade-offs to achieve a well-balanced design within the given constraints, which are explained in the next section.

Constraints

The optimization process is subject to over 60 constraints that govern the design space of the electric propulsion system. These constraints are categorized by discipline or subcomponent, as shown in Table 4.8. Due to their large number, not every constraint is detailed individually.
The most critical requirement is ensuring that the electric propulsion system delivers the required mechanical shaft power at a given propeller speed, as calculated in Table 4.3.
For the electric machine, approximately ten geometric constraints ensure compliance with manufacturing limits. A high modulation degree and power factor are beneficial for a lightweight inverter design, while limiting the short-circuit current ratio ensures that fault currents remain within nominal values, contributing to the machine's fault tolerance, including thermally. Flux densities in the iron lamination are constrained to prevent excessive losses, because saturation effects are not captured in the models described in Chapter 2. Thermodynamic constraints define allowable operating temperatures for materials, such

Table 4.8: Optimization constraints for the baseline electric propulsion unit

		Parameter	Symbol	Value	Unit	Type
Electric Machine		Shaft output power	P_{out}	175, 115, 85	kW	min
	Geometry	Shaft diameter ratio	$d_{\text{sh}}/l_{\text{sh}}$	0.3 – 7.0	-	minmax
		Shaft aspect ratio	$t_{\text{sh}}/d_{\text{sh}}$	0.01	-	min
		Magnet width	w_{mag}	5.0	mm	min
		Tooth tip width	t_{tte}	3.0	mm	min
		Tooth aspect ratio	$w_{\text{st,m}}/t_{\text{sd}}$	0.15 – 1.0	-	minmax
		Slot width	$w_{\text{sl,c}}$	3.0	mm	min
		Slot aspect ratio	$w_{\text{sl,m}}/t_{\text{sd}}$	0.15 – 1.0	-	minmax
		Stator yoke aspect ratio	$t_{\text{sy}}/d_{\text{sy}}$	0.01	-	min
		Frame aspect ratio	$t_{\text{fr}}/d_{\text{fr}}$	0.01	-	min
		Frame outer radius	$r_{\text{fr,o}}$	320, 280, 250	mm	max
	Electro-magnetic	Modulation degree	m_{a}	$2/\sqrt{3}$	-	max
		Power factor	$\cos\varphi_{\text{PF}}$	0.6	-	min
		Short circuit current ratio	K_{SC}	1.0	-	max
		Electric frequency	f_{el}	2000	Hz	max
		Rotor yoke flux density	B_{ry}	2.1	T	max
		Stator teeth flux density	B_{st}	2.0	T	max
		Stator yoke flux density	B_{sy}	2.0	T	max
	Thermo-dynamic	Magnet temperature	T_{mag}	100	°C	max
		Winding temperature	T_{wdg}	180	°C	max
		Iron lamination temperature	T_{iron}	150	°C	max
		Coolant outlet temperature	$T_{\text{fl,out}}$	150	°C	max
		Coolant velocity	v_{fl}	5.0	m s^{-1}	max
	Struc-tural	Magnet-yoke pressure	p_{sl}	1000	Pa	min
		Stress safety factor	$SF_{\text{sl},\sigma}$	1.5	-	min
		Torque safety factor	$SF_{\text{sl,T}}$	1.0	-	min
		Radial displacement	u_{rad}	0.5	-	max
	Insulation	Wire insulation safety factor	SF_{wire}	2.0	-	min
		Slot insulation safety factor	SF_{slot}	2.0	-	min
		Phase insulation safety factor	SF_{ph}	2.0	-	min
Inverter	**Semi-conductor**	Voltage utilization	$u_{\text{SC,V}}$	1.0	-	max
		Operating temperature	T_{SC}	150	°C	max
	Gate Driver	Voltage utilization	$u_{\text{GD,V}}$	1.0	-	max
		Switch-on voltage utilization	$u_{\text{GD,V,on}}$	1.0	-	max
		Switch-off voltage utilization	$u_{\text{GD,V,off}}$	1.0	-	max
		Average current utilization	$u_{\text{GD,I,avg}}$	1.0	-	max
		Peak current utilization	$u_{\text{GD,I,pk}}$	1.0	-	max
		Charge utilization	$u_{\text{GD,Qg}}$	1.0	-	max
	DC Link Capacitor	Voltage utilization	$u_{\text{Cap,V}}$	1.0	-	max
		Current utilization	$u_{\text{Cap,I}}$	1.0	-	max
		Relative voltage ripple	$\Delta V_{\text{Cap,rel}}$	0.05	-	max
		Operating temperature	T_{Cap}	85	°C	max
	Busbar	Current density	$J_{\text{BB,rms}}$	5.0	A mm^{-2}	max
		Insulation safety factor	$SF_{\text{BB,ins}}$	2.0	-	max
	Heat Sink	Fin thickness	t_{fin}	0.2	mm	min
		Fin spacing	s_{fin}	0.5	mm	min
		Coolant outlet temperature	$T_{\text{fl,out}}$	150	°C	max
		Coolant velocity	v_{fl}	5.0	m s^{-1}	max
DC Cable		Conductor temperature	T_{cond}	200	°C	max
		Insulation safety factor	SF_{cond}	2.0	-	min
HX	**Geometry**	Fin thickness	$t_{\text{fin,c/h}}$	0.2	mm	min
		Fin spacing	$s_{\text{fin,c/h}}$	0.4	mm	min
		Fin length	$l_{\text{fin,c/h}}$	2.0	mm	min
	Thermo-dynamic	Hot side outlet temperature	$T_{\text{out,h}}$	60	°C	max
		Hot side outlet pressure	$p_{\text{out,h}}$	101325	Pa	min
Pipe		Wall safety factor	SF_{mech}	5.0	-	min

as preventing magnet demagnetization, while insulation constraints ensure adequate protection against breakdowns. Structural constraints prevent rotor failures by limiting the stress in rotor components and ensuring that magnets remain attached to the rotor yoke. Additionally, a maximum allowable displacement of the rotor surface relative to the airgap prevents rotor blockage.
For the inverter, constraints are grouped by subcomponent, such as semiconductors, gate drivers, and capacitors are selected from real-world databases. Most constraints relate to maximum allowable utilization based on datasheet values, such as voltages and currents. Furthermore, temperature limits ensure safe operation, while excessive voltage ripple is mitigated through sufficient capacitance. For the DC cable, operating temperature and dielectric safety are key limitations.
The heat exchanger is subject to geometric constraints linked to manufacturability, such as fin thickness and spacing. The thermodynamic inlet conditions for the inverter depend on the coolant outlet temperatures and mass flow rates from both the electric machine and inverter, while the heat exchanger outlet temperature must not exceed the fluid inlet temperature, as defined in Table 4.5. The piping system is mechanically constrained by the pressure-induced stresses in the pipe walls.
The given set of variables, as defined in Table 4.6, spans a large design space used to identify Pareto-optimal designs for minimizing system mass and losses, as outlined in Table 4.7. The constraints from Table 4.8 ensure adherence to operational, geometric, thermodynamic, and manufacturability limits, thereby guaranteeing a feasible and reliable design. The results from this setup will be discussed in Section 4.5, where the trade-offs between system mass and efficiency will be analyzed in detail.

4.3.2 Investigated Variants

Building on the baseline configuration, four additional electric propulsion unit architectures and variants are investigated. Optimized designs will be compared against the baseline in Section 4.5.

4.3.2.1 Direct Air-Cooled Electric Machine and Inverter

This variant replaces liquid cooling with forced air cooling for both the electric machine and inverter, as shown in Figure 4.8. Heat dissipation is achieved through cooling fins integrated into the circumference of the stator housing, enhancing convective heat transfer to the surrounding airflow. Similarly, the inverter is equipped with a finned heatsink to facilitate efficient thermal dissipation. To ensure sufficient cooling performance, airflow is actively directed through dedicated ducts, guiding ambient air over both components before being exhausted from the system.
To account for the system-specific characteristics of the air-cooled configuration, all variables and constraints associated with liquid cooling components, i.e., heat exchangers, pumps, or piping, are omitted from the optimization setup. Instead, the electric machine employs annular air inlets and outlets to guide the airflow through an integrated fin structure within the stator frame, while the inverter uses a circular duct configuration for air intake and exhaust. The corresponding geometric and flow-related parameters are included in the optimization within defined bounds, as summarized in Table 4.9.
To ensure physically feasible and manufacturable designs, additional geometric constraints are imposed on the fin structure of the electric machine. These include minimum constraints on fin dimensions and spacing to ensure mechanical robustness and effective thermal performance. A summary of the applied constraints is provided in Table 4.10.
The primary motivation for this configuration is the simplification of the thermal manage-

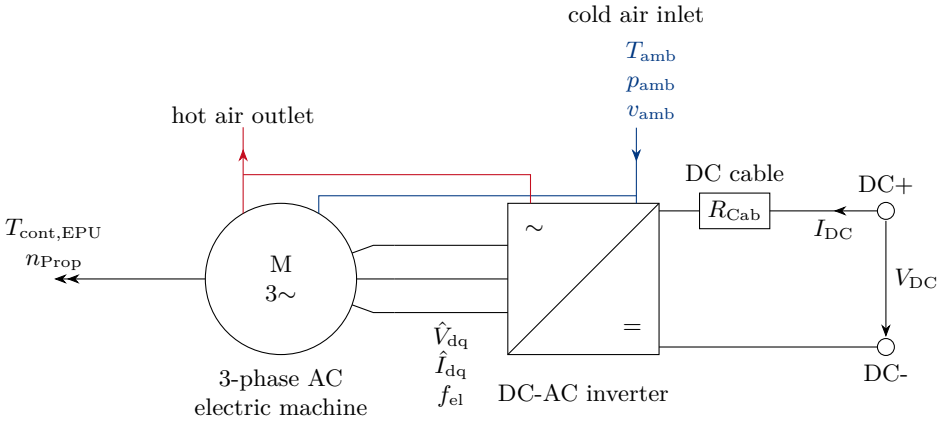

Figure 4.8: Schematic view of the electric propulsion unit architecture variant featuring a direct air-cooled electric machine and inverter. The global inputs and outputs, as well as the most important exchange parameters, are listed.

Table 4.9: Changes in variable input parameters for air-cooled electric propulsion unit variant

	Parameter	Symbol	Range min	Range max	Unit	Type
Electric Machine	Stator frame thickness	t_{fr}	4	150	mm	real
	Number of cooling fins	N_{Fin}	5	400	-	int
	Cooling channel width ratio	$\beta_{cc,w}$	0.02	0.98	-	real
	Cooling channel height ratio	$\beta_{cc,h}$	0.02	0.98	-	real
	Air duct opening height	$t_{in/out}$	1	250	mm	real
	Air duct length	$l_{in/out}$	50	250	mm	real
Inverter	Air duct opening	$r_{in/out}$	5	250	mm	real
	Air duct length	$l_{in/out}$	50	250	mm	real

Table 4.10: Changes in optimization constraints for air-cooled electric propulsion unit variant

		Parameter	Symbol	Value	Unit	Type
Electric Machine	**Geometry**	Frame base thickness	$t_{fr,b}$	1.5	mm	min
		Fin thickness	t_{fin}	1	mm	min
		Fin spacing	s_{fin}	1	mm	min
		Fin height	l_{fin}	1.0	mm	min

ment system. By eliminating liquid cooling components such as pumps and heat exchangers, system complexity is significantly reduced. This leads to fewer integration challenges, lower maintenance requirements, and improved reliability due to the absence of potential failure points associated with active cooling components, such as pump malfunctions or coolant leakage. Forced air-cooling systems are also inherently less susceptible to single-point failures, as they do not rely on active fluid circulation.
However, the main trade-off is the reduced cooling performance compared to liquid cooling. The achievable power density of the electric machine and inverter is likely lower, as forced air cooling is less effective at extracting heat from high-power components. This may necessitate larger cooling surfaces or a reduction in continuous power capability to prevent overheating, particularly during high-demand flight phases. Additionally, air cooling depends on external airflow conditions, i.e., performance can vary with altitude and ambient temperature. This necessitates careful design considerations to ensure thermal stability across all operating conditions.

4.3.2.2 Liquid-Cooled Electric Machine and Inverter with Elevated Temperature Limits

This variant retains the liquid cooling system of the baseline configuration but allows for higher operational temperature limits for the electric machine. By increasing the allowable magnet and winding temperatures, the thermal constraints on the machine are relaxed, enabling higher power densities while reducing the required cooling capacity.
To reflect these changes in the optimization process, the thermal constraint values for the electric machine are adjusted accordingly. An overview of the updated constraint parameters is provided in Table 4.11.

Table 4.11: Changes in optimization constraints for electric propulsion unit variant with elevated temperature limits of electric machine

		Parameter	Symbol	Value	Unit	Type
Electric Machine	**Thermodynamic**	Magnet temperature	T_{mag}	150	°C	max
		Winding temperature	T_{wdg}	200	°C	max

The primary motivation for this configuration is the potential to achieve further weight reductions and improved power density. Higher allowable temperatures enable the design of more compact and lightweight electric machines, as less active cooling is required to maintain thermal stability. Additionally, the reduced cooling demand allows for the downsizing of cooling system components such as heat exchangers and pumps, further decreasing overall system weight and complexity.
However, the main trade-off is the increased losses and reduction in efficiency. Operating at higher temperatures generally leads to increased resistive losses in the machine windings, potentially reducing overall system efficiency. Depending on the chosen machine design, higher inverter losses from increased electrical frequencies may also arise. These factors must be carefully balanced to ensure that the benefits of weight and cooling system reductions outweigh the penalties associated with increased losses.

4.3.2.3 Liquid-Cooled Electric Machine and Inverter with Central Cooling System

This variant modifies the baseline liquid-cooled configuration by replacing the local cooling loops with a centralized, global cooling system, as shown in Figure 4.9.
In this setup, all electric propulsion units on the aircraft are connected to a single shared cooling system that manages heat dissipation across the electric propulsion system. The centralized system consists of a common coolant circuit that circulates through each unit, extracting heat and rejecting it to the ambient environment via a centralized heat exchanger.
As the main change in this variant is the reconfiguration of the existing liquid-cooled system into a centralized, global cooling loop, there is no change to the optimization setup compared to the baseline configuration. The same parameters, constraints, and optimization boundaries are applied, with the primary focus on reconfiguring the cooling system to improve overall power density and efficiency. The temperature constraints from the previous section, as detailed in Table 4.11, also remain applicable in this variant.
The primary motivation for this configuration is the potential to optimize cooling system weight and efficiency at the aircraft level. By centralizing the cooling loop, the complexity of individual cooling systems within each electric propulsion unit is reduced. This can result in more compact and lightweight cooling components, as well as better utilization of available cooling capacity across all units. The global system also enables more efficient management of the overall thermal load, which can be beneficial in multi-motor configurations where heat dissipation demands vary across units.

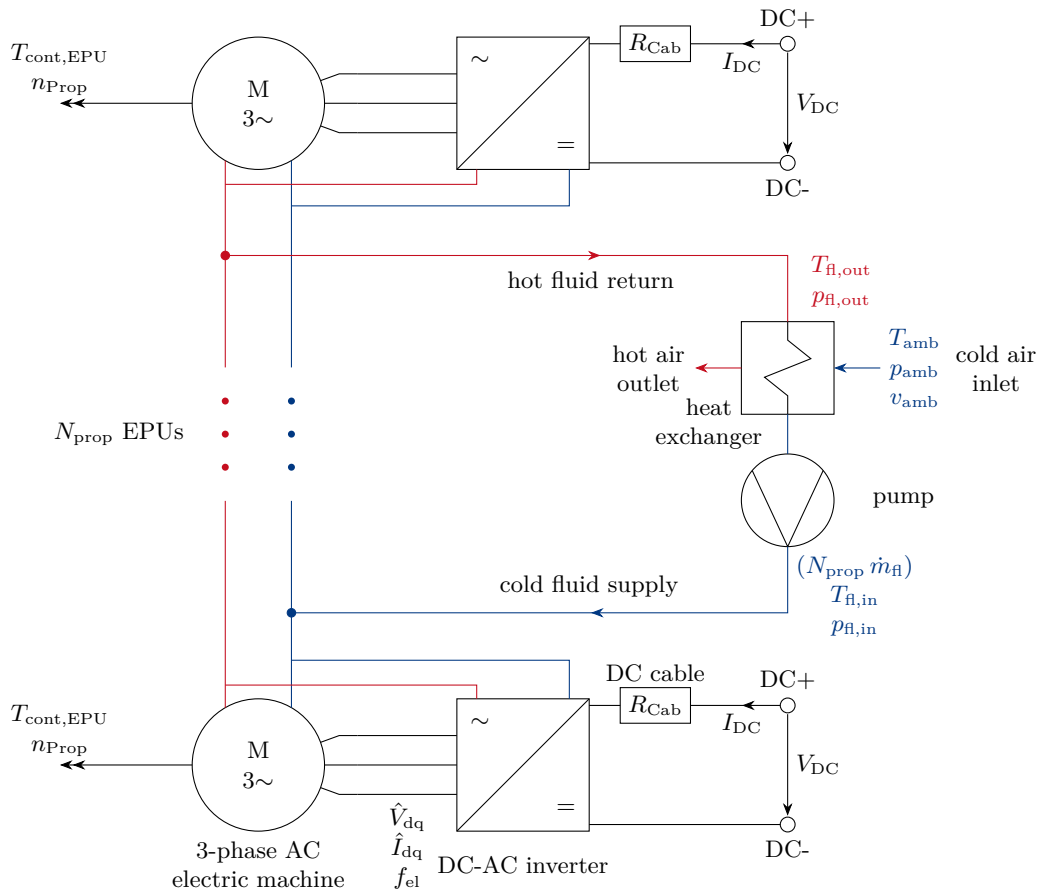

Figure 4.9: Schematic view of the electric propulsion unit architecture variant featuring a liquid-cooled electric machine and inverter with a central thermal management system. The global inputs and outputs, as well as the most important exchange parameters, are listed.

However, the main trade-off of a global cooling system is the increased complexity of coolant routing and integration across the entire aircraft. A shared cooling loop introduces additional challenges related to coolant distribution, system pressure management, and potential failure propagation. Furthermore, since individual units have less localized cooling control, system performance may vary under different flight conditions, particularly when some experience higher thermal loads than others. Additionally, maintenance complexity may increase due to the centralization of the cooling loop and its reliance on a single heat exchanger and pump system.

4.3.2.4 Liquid-Cooled, Geared Electric Machine and Inverter

This variant builds on the baseline liquid-cooled configuration but introduces a gearbox between the electric machine and the propeller shaft, as shown in Figure 4.10.
By increasing the rotational speed of the electric machine while reducing the torque requirement, the gearbox enables the use of a smaller, higher-speed motor with increased power density. This can potentially improve the efficiency of the electric machine while maintaining the required output torque at the propeller.
While the fixed inputs are primarily adjusted to account for the applied gear ratios, the key optimization changes for this variant are related to the machine's geometry. Specifically, adjustments are made to accommodate higher rotational speeds, which result in a smaller range of relevant pole-slot combinations due to the increased electrical base frequency. These changes are summarized in Tables 4.12 and 4.13.
The primary motivation for this configuration is the potential for weight reduction and im-

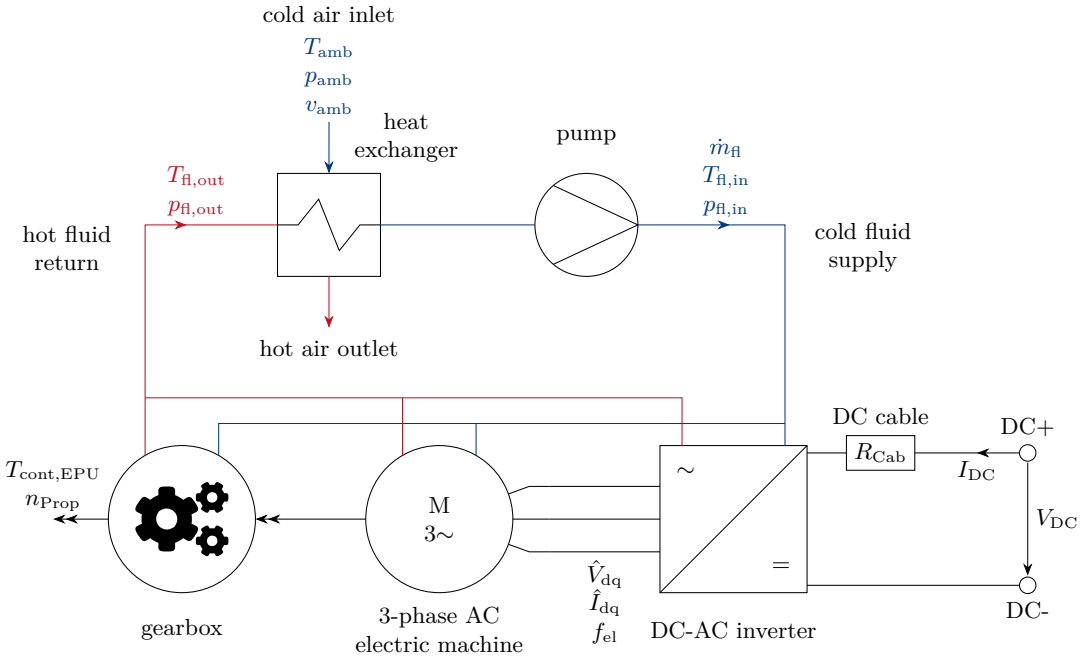

Figure 4.10: Schematic view of the electric propulsion unit architecture variant featuring a direct liquid-cooled gearbox, electric machine, and inverter. The global inputs and outputs, as well as the most important exchange parameters, are listed.

Table 4.12: Changes in fixed input parameters for geared electric propulsion unit variant

	Parameter	Symbol	Value	Unit
Gearbox	Total gear ratio	i_{GB}	5, 12	-

Table 4.13: Changes in variable input parameters for geared electric propulsion unit variant

	Parameter	Symbol	Range min	Range max	Unit	Type
Electric Machine	Shaft inner radius	$r_{sh,i}$	0	250	mm	real
	Pole pair number	p	2	12	-	int
	Slot number	Q_s	6	36	-	int
	Parallel winding paths	$n_{par,wdg}$	1	15	-	int

proved system efficiency. Higher rotational speeds allow for a more compact and lightweight motor design, reducing the mass of the electric machine while maintaining the same power output. Additionally, electric machines generally exhibit higher efficiency at increased speeds, which can contribute to overall energy savings. The introduction of a gearbox may also allow for better matching between the motor's optimal operating range and the aerodynamic requirements of the propeller.
However, the main trade-off is the added mechanical complexity and potential efficiency losses associated with the gearbox. While a well-designed gearbox can operate with high efficiency, it inevitably introduces additional frictional and mechanical losses. Furthermore, the gearbox represents an additional potential failure point, requiring periodic maintenance and lubrication. Noise and vibration control must also be addressed, particularly as gear meshing can introduce significant acoustic emissions and dynamic loads. Careful design and integration of the gearbox are essential to ensure that the overall benefits outweigh the drawbacks.

4.4 Derivation of Efficiency and Drag Penalty Factors

The multi-objective optimization of the various design variants results in Pareto fronts that illustrate the trade-offs between system mass and losses. However, these Pareto fronts do not provide a definitive "best" solution; rather, the optimal design is inherently dependent on specific use cases, mission requirements, and operational constraints. To facilitate the selection of the most suitable design from the Pareto front and to enable meaningful comparative analysis, a decision-making process is required. In this context, the weighted sum approach is widely used, as it combines multiple conflicting objectives into a single metric, enabling the identification of a single optimal solution.

4.4.1 Decision-Making Methods

Several methods for deriving weighting factors in multi-objective optimization are discussed in the literature:

1. **Normalization and Sensitivity Analysis:** In this method, both objectives are normalized (e.g., scaled to a $0-1$ range) to enable direct comparison, followed by sensitivity analysis to determine the relative importance of each objective. This technique provides insight into how each factor influences the overall system but does not directly provide a mechanism for deriving a weighting factor for optimization purposes. Sensitivity analysis identifies how changes in input variables affect the output, but it does not translate these effects into a single, optimized design. Thus, while useful for qualitative analysis, it is limited in that it does not provide a direct optimization framework. Additionally, the normalization process is highly sensitive to the selection of scaling parameters, which can introduce inconsistencies [360, 361].

2. **Analytic Hierarchy Process and Multi-Criteria Decision-Making:** Methods such as the Analytic Hierarchy Process or weighted scoring models are used to assign relative importance to each objective based on stakeholder preferences. These relative weights are then applied to combine multiple objectives into a single performance metric. Although the Analytic Hierarchy Process provides a structured approach for incorporating subjective judgment into the decision-making process, it introduces the risk of subjectivity and potential inconsistencies in the evaluation. Furthermore, the complexity of the method increases as more objectives and criteria are added, making it less suitable for purely technical optimization problems where objective metrics are well defined [362, 363].

3. **Conversion to Operational Equivalence via Penalty Factors:** A more direct and pragmatic approach is to express one objective as an equivalent increase of the second objective, e.g., expressing losses or decrease of efficiency as an equivalent increase in battery weight. In this method, a change in electric propulsion unit efficiency is translated into the additional battery mass required to meet mission performance. [364].

The primary motivation for selecting the conversion to operational equivalence via penalty factors is that it provides a clear, operationally meaningful translation of efficiency losses into a tangible, comparable design metric.
This approach is particularly relevant in aerospace design, where battery mass is a critical driver of overall system performance. By optimizing the battery system for a given mission

profile, a penalty factor can be derived that quantifies the impact of efficiency changes on battery weight. This method converts the bi-objective into a single-objective optimization problem and enables direct comparison of the different design variants described in Section 4.3 based on a common performance metric, i.e., weight, thereby facilitating the selection of the most appropriate design. Furthermore, this approach ensures that the derived penalty factor is not influenced by subjective preferences and instead reflects the true operational impact of efficiency losses.

4.4.2 Battery Optimization Setup and Results

Applying this approach, the battery is optimized for the mission profile given in Section 4.1, where the required battery capacity is determined by the energy consumption, which is a function of the overall drivetrain efficiency η_{EPS}, as shown in Equation (4.7).
As the battery model developed in Section 2.6 is relatively simple, the battery packs are fully described by the number of cells in series and parallel, as shown in Table 4.14.

Table 4.14: Variable input parameters for battery optimization

Parameter	**Symbol**	**Range**		**Unit**	**Type**
		min	**max**		
Cells in series	$n_{\mathrm{cell,s}}$	100	250	-	int
Cells in parallel	$n_{\mathrm{cell,p}}$	1	100	-	int

The battery is optimized for minimum mass and lowest operating temperature to reduce the required cooling capacity. The objectives are defined in Table 4.15.

Table 4.15: Optimization objectives for battery optimization

Objective	**Symbol**	**Unit**	**Type**
Mass of energy storage system	m_{ESS}	kg	min
Temperature of cells	T_{cell}	K	min

Feasible designs adhere to the constraints laid out in Table 4.16. On pack level, the DC voltage of the fully charged pack $V_{\mathrm{DC,max}}$ should not exceed 900 V to match the chosen semiconductor modules from Table 4.6. As per available battery specifications, the cells have a defined operating temperature range and shall not be discharged below a State-of-Charge of 20 % and a dynamic cell voltage of 2.5 V.

Table 4.16: Optimization constraints for battery optimization

	Parameter	**Symbol**	**Value**	**Unit**	**Type**
Pack	DC voltage (fully-charged)	$V_{\mathrm{DC,max}}$	900	V	max
Cell	Lower operating voltage	$V_{\mathrm{DC,min}}$	2.5	V	min
	State of Charge	$\mathrm{SOC}_{\mathrm{min}}$	0.2	-	min
	Operating temperature range	T_{Op}	0 – 60	°C	minmax

Three different cell types have been investigated, including an 18650 cell from Panasonic [300] and 21700 cells from Molicel [365] and Joby [349]. The resulting Pareto fronts are shown in Figure 4.11.
The results indicate that a reduction in battery mass generally leads to increased cell operating temperatures. However, even for the most lightweight designs, the maximum allowable temperature limit is not exceeded. Additionally, a larger cell form factor proves advantageous in terms of both weight and thermal performance. The weight advantage of

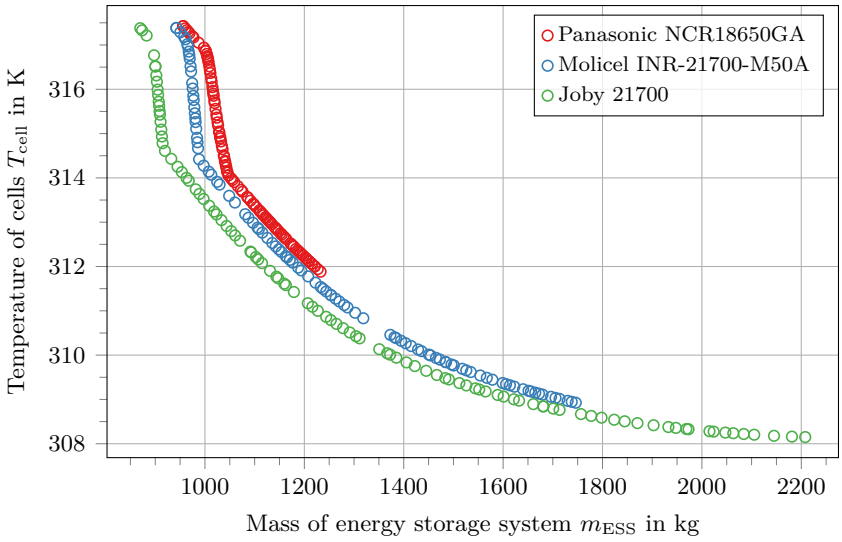

Figure 4.11: Pareto front of battery optimization for the mission profile from Section 4.1, comparing three different cell types at an exemplary electric propulsion system efficiency of $\eta_{\text{EPS}} = 90\,\%$

the Joby cell is particularly notable, with a mass difference of approximately 100 kg compared to the other cells in the most lightweight configuration. This weight difference can be attributed to factors such as higher specific energy, improved cell form factor, and reduced requirements for ancillary components. In particular, the Joby cell achieves a higher pack-level specific energy of approximately $235\,\text{W h kg}^{-1}$, primarily due to optimized cell packaging and reduced structural overhead [349]. This allows for fewer supporting components and results in a significantly lower total system mass compared to the other cell types.

Additionally, Figure 4.12 illustrates the variable and constraint space of the optimization using the Joby 21700 cells. It is evident that in order to minimize weight, the number of cells in series and parallel is selected such that both the upper allowable pack voltage when fully charged and the minimum cell voltage during operation are closely approached. The state-of-charge behavior indicates that the battery design is primarily power-limited rather than energy-limited, as the minimum allowable state of charge is not reached. Moreover, the thermal constraints are not active across the design space, suggesting that temperature limitations are not a concern for these configurations.

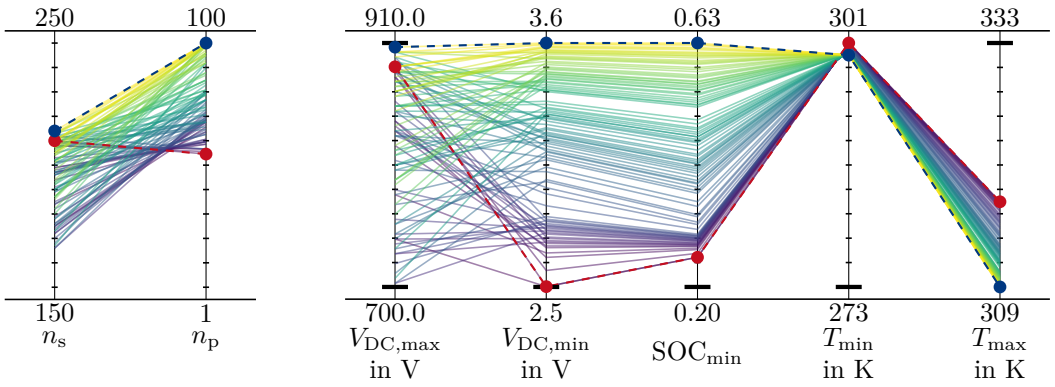

(**a**) Variable Space (**b**) Constraint Space

Figure 4.12: Variable and constraint space of the battery optimization using the Joby 21700 cell for the mission profile defined in Section 4.1, at a propulsion system efficiency of $\eta_{\text{EPS}} = 90\,\%$. Dashed lines indicate parameter and constraint values for the two extreme Pareto points: red for the minimum-mass and blue for the lowest-temperature design.

4.4.3 Penalty Factor Method

This procedure is then repeated for an electric propulsion system efficiency η_{EPS} ranging from 85 – 100 %. By comparing the most lightweight battery designs across different efficiency values, a penalty factor can be derived to quantify the incremental increase in battery mass associated with a 1 % drop in efficiency.
This method is justified because the most lightweight battery designs represent the minimum mass required to meet the mission's energy demands. Therefore, any reduction in drivetrain efficiency leads to a proportional increase in the required battery mass. As battery losses are already included in the mission energy calculation, the derived penalty factor inherently reflects the trade-off between drivetrain efficiency and battery mass. This relationship is illustrated in Figure 4.13.

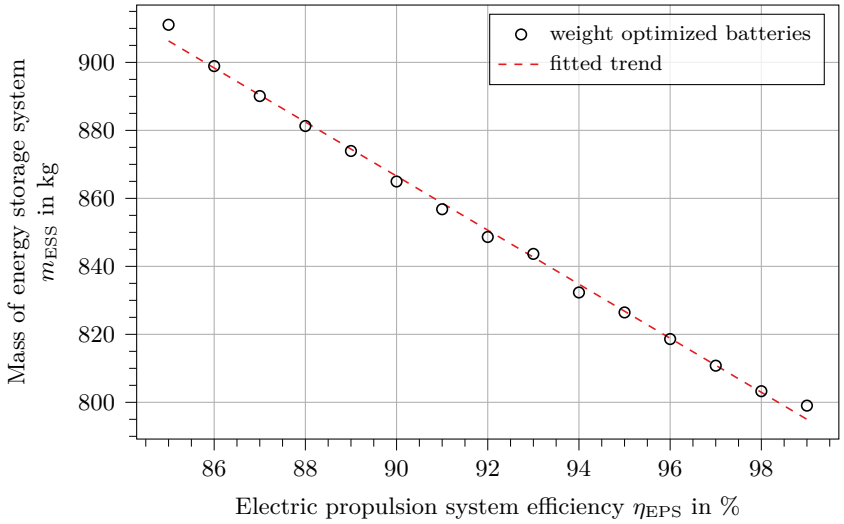

Figure 4.13: Mass of optimized battery design versus electric propulsion efficiency, obtained from individual optimization runs. The dashed line represents a linear fit to the data points.

It can be seen that the mass of the optimized battery designs follows a linear trend with respect to propulsion efficiency. The efficiency penalty factor is then derived by calculating the slope of this trend:

$$\frac{\Delta m_{\mathrm{ESS}}}{\Delta \eta_{\mathrm{EPS}}} \approx \frac{8.0\,\mathrm{kg}}{1\,\%} \tag{4.14}$$

On aircraft level, i.e., for each percent increase in propulsion efficiency, an additional 8.0 kg of battery mass is acceptable to maintain equivalent system performance. This efficiency penalty factor thus provides a unified metric for comparing different design variants in terms of both mass and efficiency.
The optimal design is the one that minimizes the sum of the actual weight and the weight equivalent of efficiency changes, as determined by the penalty factor.

$$\min \left(m_{\mathrm{EPU}} + \frac{Q_{\mathrm{EPU}}}{P_{\mathrm{cont,EPU}} + Q_{\mathrm{EPU}}} \frac{\Delta m_{\mathrm{ESS}}}{N_{\mathrm{EPU}}\,\Delta \eta_{\mathrm{EPS}}} \right) \tag{4.15}$$

Graphically, this corresponds to finding the tangency point between the Pareto front and a straight line with a slope equal to the penalty factor. This line represents a cost or weight function. An application example of this method can be found in Section 4.5.1.
As a byproduct, this method can also be extended to derive a drag penalty factor for vertical flight. This is particularly important for accounting for differences in thermal management systems, which may not be immediately apparent in terms of mass. These

differences, however, can significantly impact the overall design choice, especially when comparing air-cooled and liquid-cooled systems.
In vertical flight, where the propeller's induced velocity is the primary driver of power demand (as outlined in Equation (4.7)), the effect of drivetrain efficiency on the battery power requirement is similarly captured. In this case, additional drag raises the power demand and thus the battery requirements.
Due to the diminishing returns in the relationship between drivetrain efficiency and power demand, this correlation exhibits slight non-linearity. For example, increasing efficiency from 90 % to 91 % leads to a slightly larger reduction in power demand (approximately 1.2 %) rather than exactly 1 %. Despite this minor non-linearity, the error is minimal and acceptable for comparative purposes. This allows for a reliable drag penalty factor to be applied when comparing different designs.
In summary, the derived penalty factors offer a practical and unified metric to evaluate and compare various design variants, thereby supporting informed selection of optimal solutions from the Pareto fronts.

4.5 Comparative Study of Topologies and Variants of Distributed Electric Propulsion Systems

This section presents the results from the optimization studies described in Section 4.3 in a comparative manner. As a baseline configuration, the direct liquid-cooled machine and inverter with a local cooling system, introduced in Section 4.3.1, is used.
For the baseline variant, the process of selection the optimal design from the Pareto front for each configuration based on the penalty factor method introduced in Section 4.4 is exemplarily shown. This enables a consistent and operationally relevant comparison across different system architectures.
The comparison includes both specific metrics, such as power-to-weight ratio and efficiency, as well as absolute metrics, including mass and electrical losses. This dual perspective allows not only a fair assessment of each electric propulsion unit variant but also facilitates scalability and comparability of the electric propulsion system at the aircraft level, accounting for different numbers of propulsion units.

4.5.1 Liquid versus Air Cooling

To identify the optimal design from the results of the multi-objective optimization, the penalty factor method introduced in Section 4.4 is applied exemplarily to the baseline variant. Figure 4.14 shows the resulting Pareto fronts for the liquid-cooled direct-drive electric machine and inverter with a local cooling system, as described in Section 4.3.1, for different numbers of propellers. These results are derived from the optimization process based on the parameter sets defined in Tables 4.4 to 4.8. The Pareto front illustrates the trade-off between the electric propulsion unit mass m_{EPU} and losses Q_{EPU}, as outlined in Section 4.3.1.
As explained in Section 4.4.3, the optimal design point is found as the tangency point between the Pareto front and a straight line with a slope equal to the penalty factor, representing a cost function. This optimal design achieves the best trade-off between the two competing objectives, namely the mass and losses of the electric propulsion unit, from an operational perspective.
For the configuration with eight propellers, the lightest design is also the optimal one.

However, for the other two configurations, the Pareto front is steeper than the cost function defined by the penalty factor, shifting the optimal point away from the lowest-mass design. Additionally, since the penalty factor is defined globally at the aircraft level, the slope of the cost function increases with the number of propellers. However, due to the use of absolute values in this application, the difference is small and barely noticeable.

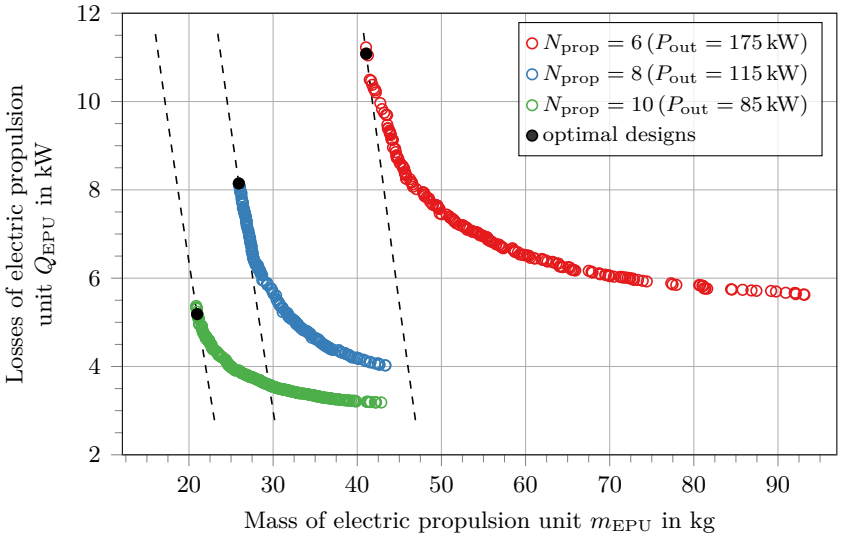

Figure 4.14: Pareto fronts illustrating the trade-off between mass m_{EPU} and losses Q_{EPU} of the electric propulsion unit for three different propeller configurations ($N_{\mathrm{Prop}} = 6-10$) in the baseline variant. This variant features a direct-drive, liquid-cooled electric machine and inverter with a local cooling system, as described in Section 4.3.1. The optimal designs are determined using the penalty factor method introduced in Section 4.4.3. Dashed lines visualize the cost functions associated with the penalty factor, with slight variations in slope corresponding to different propeller configurations.

The same method is subsequently applied to identify optimal designs for an alternative configuration using air-cooled electric machines and inverters, as introduced in Section 4.3.2.1. This enables a direct comparative analysis between the liquid- and air-cooled system variants. Key system-level metrics will be investigated for a varying number of propellers in the following. Figure 4.15 depicts the development of the specific power-to-weight ratio PTW_{EPU} and the efficiency η_{EPU} of a single electric propulsion unit as a function of the number of propellers N_{Prop} in the aircraft configuration.
For air-cooled propulsion units, the power-to-weight ratio increases linearly from approximately $2.9\,\mathrm{kW\,kg^{-1}}$ for the six-propeller to about $3.7\,\mathrm{kW\,kg^{-1}}$ for the ten-propeller configuration, corresponding to a 30 % increase in the power-to-weight ratio. The efficiency varies between approximately 95 % and 96 %, with the highest efficiency achieved for the eight-propeller configuration. This variation is primarily due to the thermal limitations imposed by the loss dissipation capacity of the system, including the allowable temperatures for the magnets, windings, and iron, which prevent more lightweight designs.
For liquid-cooled units, the power-to-weight ratio varies between $4.1\,\mathrm{kW\,kg^{-1}}$ for the ten-propeller and $4.4\,\mathrm{kW\,kg^{-1}}$ for the eight-propeller design. There is no clear benefit in terms of specific power density for increasing the number of propellers, due to the discrete design possibilities in terms of pole-slot combinations and the interdependency of electromagnetic and thermal constraints. The system efficiency varies between approximately 93.4 % and 94.2 %, with the highest efficiency achieved for the ten-propeller configuration. The main limiting factors are the same as for the air-cooled variant.
Figure 4.16 complements the analysis by presenting absolute figures for the system on aircraft level, i.e., total electric propulsion system mass m_{EPS} and losses Q_{EPS}. The mass includes the cumulated mass of the propulsion units plus the difference in battery mass

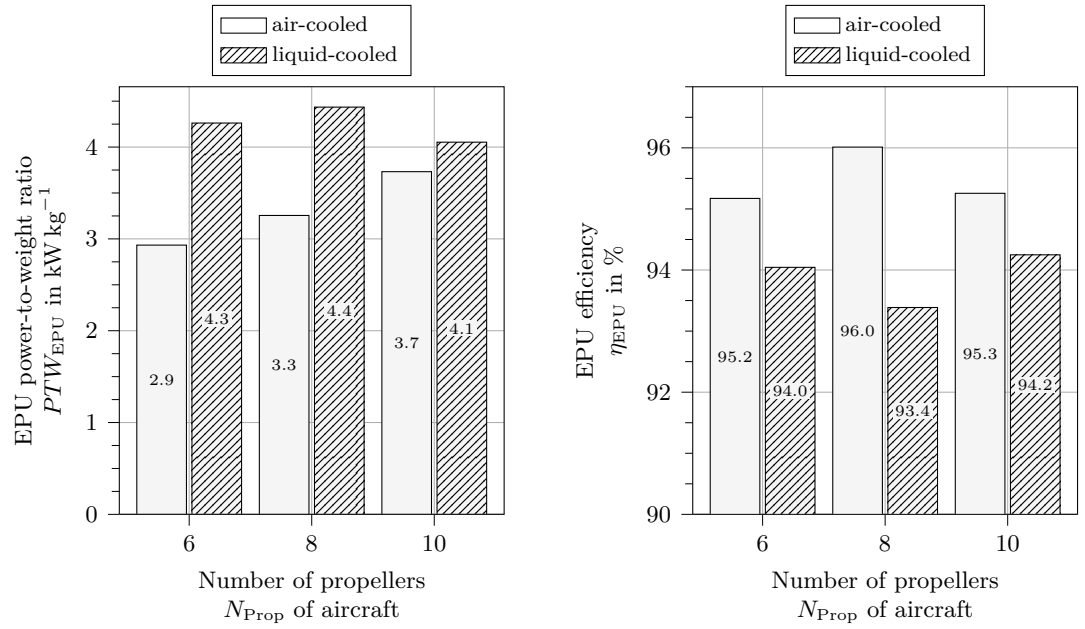

(**a**) Power-to-weight ratio

(**b**) Efficiency

Figure 4.15: Specific power-to-weight ratio PTW_{EPU} and efficiency η_{EPU} of electric propulsion unit for air-cooled and liquid-cooled configurations, as a function of the number of propellers N_{Prop}.

Δm_{ESS} due to the efficiency difference of the chosen designs, applied pairwise to the design with the lower efficiency.

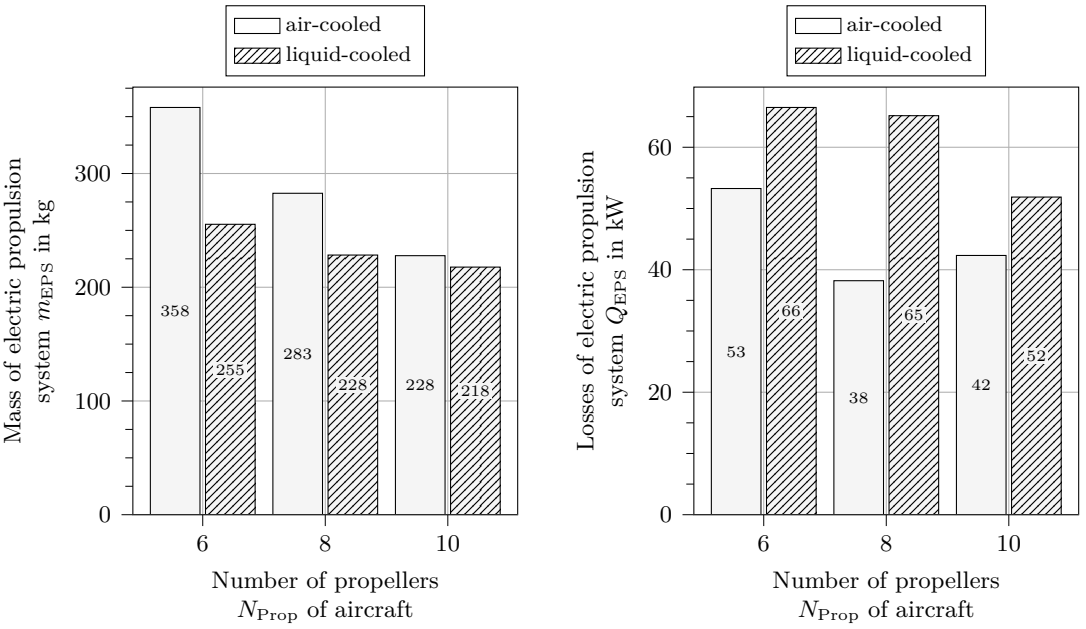

(**a**) Total mass

(**b**) Total losses

Figure 4.16: Mass m_{EPS} and losses Q_{EPS} of the electric propulsion system for air-cooled and liquid-cooled configurations, as a function of the number of propellers N_{Prop}.

For air-cooled systems, the total electric propulsion system mass decreases notably from 358 kg for the six-propeller to 228 kg for the ten-propeller configuration. Liquid-cooled configurations achieve significantly lower masses across all propeller counts, though the trend is less consistent and pronounced, with a reduction from 255 kg for the six-propeller to 218 kg for the eight- and ten-propeller configurations. For both variants, the reduction

in weight is largely due to the lower power requirements in the more propeller-intensive configurations, particularly due to the less demanding one rotor inoperative scenario as shown in Table 4.3.
Regarding total system losses, air-cooled systems exhibit a clear reduction from around 53 kW for the six-propeller down to 38 kW for the eight-propeller configuration, but increase again to around 42 kW if propeller count is increased to ten. Liquid-cooled configurations show higher losses overall between approximately 52 kW for the ten- and 66 kW for the six-propeller configuration, again reflecting the trade-off between improved specific power and reduced efficiency.
Overall, both figures illustrate the fundamental trade-offs between cooling strategy, efficiency, mass, and performance scalability as a function of propeller count. While liquid-cooled configurations offer higher system-specific power-to-weight ratios and enable lighter overall system masses, this comes at the cost of slightly lower system efficiencies and higher absolute system losses. The system power-to-weight ratio increases by 10 – 50 % for liquid-cooled systems compared to air-cooled systems, resulting in an aircraft-level weight reduction between 10 kg and 100 kg, depending on propeller count. The efficiency of liquid-cooled electric propulsion units is 1 – 2.5 % lower than for air-cooled systems, leading to increased electric propulsion system losses between 10 kW and 27 kW on aircraft level.
To explain this behaviour, a closer look is taken on the mass and loss contributions of the electric propulsion unit components for the selected propulsion units, as illustrated in Figure 4.17. Both variants show consistent weight and loss shares for the major components, with minor deviations.

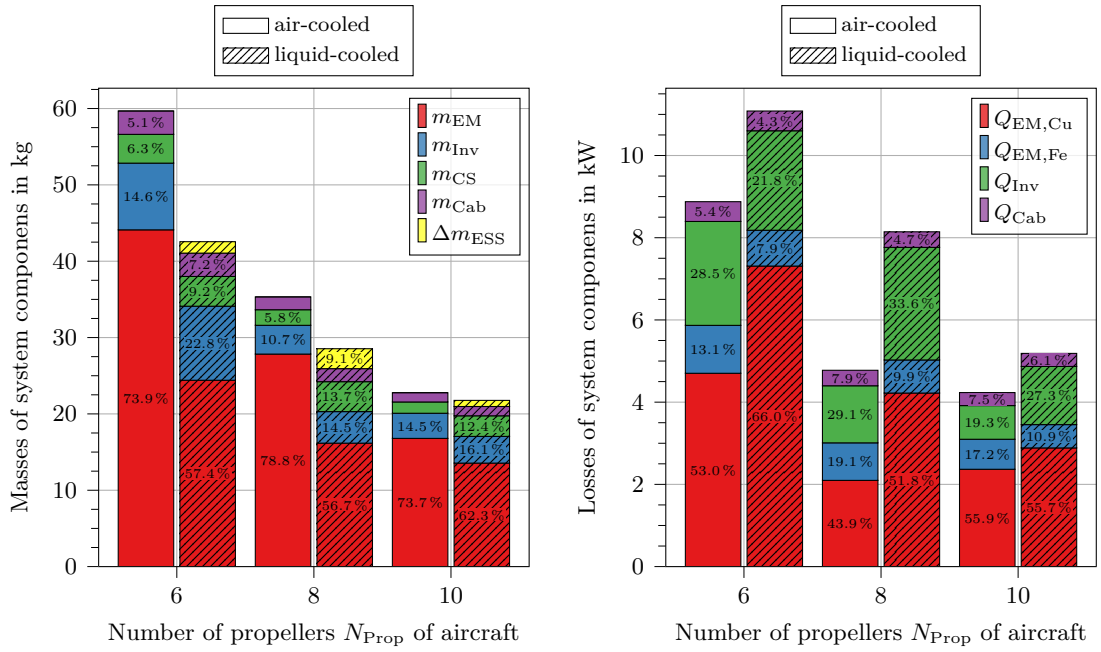

(**a**) Mass Breakdown

(**b**) Loss Breakdown

Figure 4.17: Mass and loss breakdown for the selected electric propulsion unit design, comparing air- and liquid-cooled variants, as a function of the number of propellers N_{Prop}. Percentage shares are shown only when the bar segment size permits; as a result, shares below approximately 5 % may not appear explicitly. The mass breakdown also includes the difference in battery mass Δm_{ESS} due to the efficiency difference of the chosen designs, applied pairwise to the design with the lower efficiency.

Figure 4.17a presents the mass breakdown for the key propulsion system components, namely the electric motor (m_{EM}), inverter (m_{Inv}), cooling system (m_{CS}), DC cabling (m_{Cab}), and difference in battery mass (Δm_{ESS}) due to the efficiency difference of the

chosen designs for various aircraft architectures with different numbers of propellers N_{Prop}. The figure differentiates between air-cooled and liquid-cooled systems using hatch patterns. The mass of the electric motor (m_{EM}) dominates across all configurations, consistently representing the largest fraction of the total system mass, with up to 80 %. Liquid-cooled variants allow for a reduction of electric motor mass between 3 – 20 kg per unit, while inverter, cooling system, and DC cabling masses remain fairly constant when comparing air- and liquid- cooled systems. Still, their relative contribution increases for liquid-cooled systems. As all liquid-cooled designs have lower efficiencies than the corresponding air-cooled ones, a penalty battery weight between 0.8 kg and 2.6 kg is added to the liquid-cooled variants for a fair comparison.

Figure 4.17b illustrates the breakdown of losses in key propulsion system components, namely the copper and iron losses of the electric motor ($Q_{\mathrm{EM,Cu}}$ and $Q_{\mathrm{EM,Fe}}$), inverter losses (Q_{Inv}), as well as the DC cable losses (Q_{Cab}) for various aircraft architectures with different numbers of propellers N_{Prop}.

Copper losses $Q_{\mathrm{EM,Cu}}$ not only dominate the total loss share, but also show an increase both in absolute and relative terms for liquid-cooled variants. Especially for the six- and eight-propeller configurations, copper losses increase by 2.0 – 2.5 kW, translating to a relative increase of around 10 – 15 %. On the other hand, iron losses $Q_{\mathrm{EM,Fe}}$ remain nearly constant and tend to slightly decrease in absolute terms, while their share reduces by as much as 40 – 50 %. For the inverter losses Q_{Inv}, the trends are not as consistent. While for the six-propeller configuration the absolute amount is nearly constant, and thus the share reduces by approximately 10 %, the losses nearly double for the other configurations. This increase is due to the higher electrical frequencies of the machines for these configurations. As the DC cables are cooled via natural convection, the absolut amount of losses Q_{Cab} is constant and their relative share decreases slightly.

Overall, this analysis clearly shows that the main driver of the increase in power density for liquid-cooled variants, as discussed in Figure 4.15, is attributed to the weight savings in the electric motor, which outweighs the absolute increase in the masses of the inverter and cooling system. However, the significant increase in copper losses within the motor is the primary driver of the system efficiency reduction.

As already discussed, air-cooled variants offer a simpler overall layout compared to liquid-cooled ones. Therefore, a further important aspect is the mass breakdown of the cooling system, as shown in Figure 4.18. It shows the individual contributions of the thermal management system for the electric motor ($m_{\mathrm{TMS,EM}}$) and inverter ($m_{\mathrm{TMS,Inv}}$), as well as the masses of the pipes (m_{Pipe}), the pump (m_{Pump}) and heat exchanger (m_{HX}), which are only relevant for the liquid-cooled configuration.

The mass of the cooling system in the liquid-cooled configuration increases with a higher number of propellers, which is due to the worse scaling of air-cooled solutions at higher power levels, as the efficiency of cooling fins is limited, particularly for inverters with restricted fin area and high loss densities. Conversely, the weight offset introduced by the pump and heat exchanger is more pronounced at lower power levels, i.e., higher propeller count. The weight of the pipes for variants with a local cooling system is negligible. Furthermore, a clear shift in the mass share allocation can be observed. The mass allocated to the thermal management system of the electric machine ($m_{\mathrm{TMS,EM}}$) becomes negligible (less than 2 %) for liquid-cooled variants, as it is reduced to the weight of the fluid within the cooling channels in the slots. The mass of the inverter thermal management system ($m_{\mathrm{TMS,Inv}}$) is significantly reduced for the six-propeller configuration but remains roughly constant for the other configurations due to the weight offset from the liquid and manifolds. Overall, the weight of the additional components such as pump and heat exchanger contributes to around 60 – 80 % of the cooling system mass.

As the liquid-cooled variant with a ten propeller configuration offers the best overall system

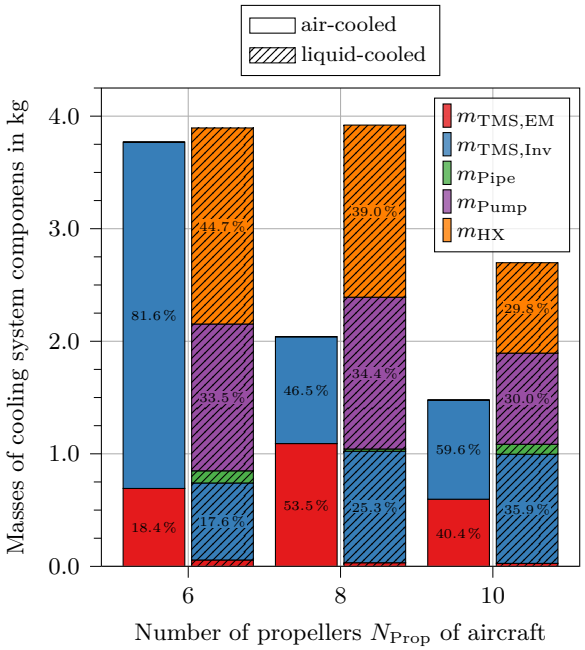

Figure 4.18: Mass breakdown of the cooling system for the selected electric propulsion unit design, comparing air- and liquid-cooled variants, as a function of the number of propellers N_{Prop}. Percentage shares are shown only when the bar segment size permits; as a result, shares below approximately 5 % may not appear explicitly.

performance so far, a few additional aspects will be considered, especially as the weight difference is less pronounced than expected. The key trade-off between electrical and thermal limitations will be investigated using stator winding current density J_{rms} and the magnet and winding temperatures (T_{mag} and T_{wdg}) as reference parameters. Figure 4.19 illustrates the behavior of these key trade-offs along the Pareto fronts for a ten propeller configuration, comparing air- and liquid-cooled variants and their optimal designs.
The behavior of stator slot current density serves as a strong indicator of the corresponding Pareto front and clearly highlights the trade-off between the electromagnetic and thermal domains. As shown in Figure 4.19a, more lightweight designs tend to require higher stator current densities to reduce mass in copper and stator iron. However, this results in increased losses and subsequently higher operating temperatures. Liquid-cooled configurations enable significantly higher current densities up to $18.6\,\mathrm{A\,mm^{-2}}$, compared to air-cooled ones, which are typically limited to around $14.7\,\mathrm{A\,mm^{-2}}$. Interestingly, the optimal points identified using the penalty factor method show only a minor deviation of about 2 kg in total system weight, a less pronounced effect than initially anticipated. A closer look at the thermal behavior (as illustrated in Figures 4.19b and 4.19c) reveals the underlying reasons: winding temperatures generally follow the current density trends, peaking around 160 °C in air-cooled and approximately 140 °C in liquid-cooled optimal designs, with observable jumps in the curves linked to discrete changes in pole-slot combinations. Importantly, some thermal margin remains, especially for the liquid-cooled system, before reaching the thermal limits defined in Table 4.8. However, magnet temperature emerges as the critical limiting factor, with both variants operating near the maximum allowable temperature of 100 °C across all Pareto-optimal designs. This constraint is more prominent and variable in air-cooled systems due to fluctuations in achievable air mass flow, whereas liquid-cooled designs offer greater control. These findings suggest that increasing the allowable temperature limits, particularly for the magnets, could substantially expand the feasible design space and enable even more lightweight solutions by supporting higher current densities.
Before the influence of higher temperature limits within the electric machine is investigated

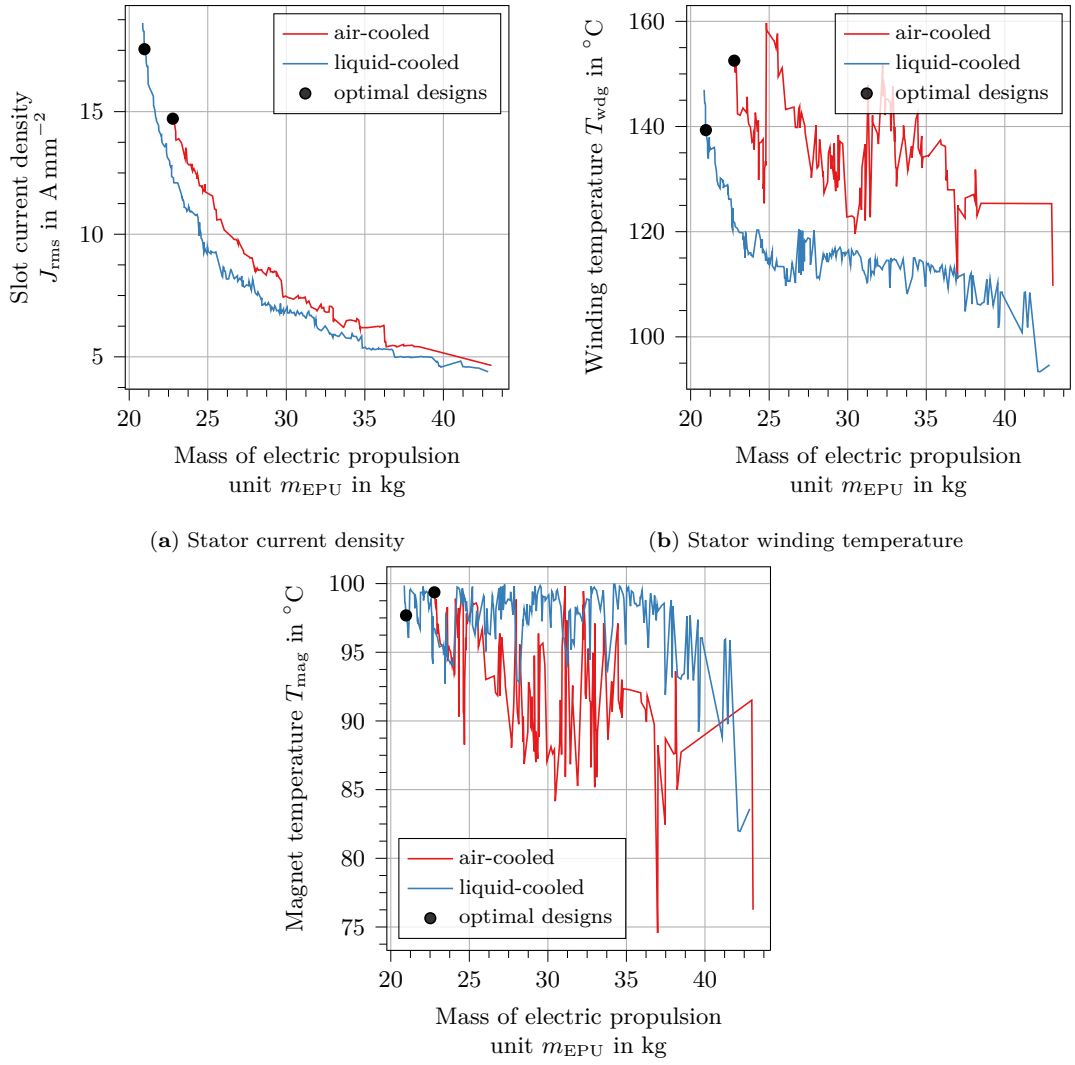

(**a**) Stator current density

(**b**) Stator winding temperature

(**c**) Magnet temperature

Figure 4.19: Behaviour of key trade-offs between electrical and thermal limitations along Pareto fronts for a ten propeller configuration, comparing air- and liquid cooled variants and their optimal designs

in Section 4.5.2, the key findings from the comparison of air- and liquid-cooled variants are presented. Liquid-cooled electric propulsion systems exhibit significantly higher power-to-weight ratios (PTW_{EPU} up to 4.5 kW kg^{-1}) and lower electric propulsion system mass (m_{EPS} reduced by up to 100 kg), particularly benefiting from a significant reduction in the electric machine's mass. However, this performance gain comes at the cost of lower efficiency, with η_{EPU} decreasing by up to 2.5 % and total losses (Q_{EPS}) increasing by up to 25 kW, primarily due to higher copper losses in the motor. While air-cooled systems offer simpler integration and higher efficiency, liquid cooling enables better scalability and lightweight design, particularly advantageous in configurations with more propellers. Nonetheless, thermal limitations, especially the magnet temperature, remain a critical factor in determining the optimal design.

4.5.2 Standard versus Elevated Machine Temperature Limits

Next, the baseline variant is compared with a liquid-cooled system with elevated machine temperature limits as outlined in Section 4.3.2.2, to investigate whether a performance gain as discussed in Section 4.5.1 can be achieved.
Figure 4.20 depicts the development of the specific power-to-weight ratio PTW_{EPU} and the efficiency η_{EPU} of a single electric propulsion unit as a function of the number of propellers N_{Prop} in the aircraft configuration.

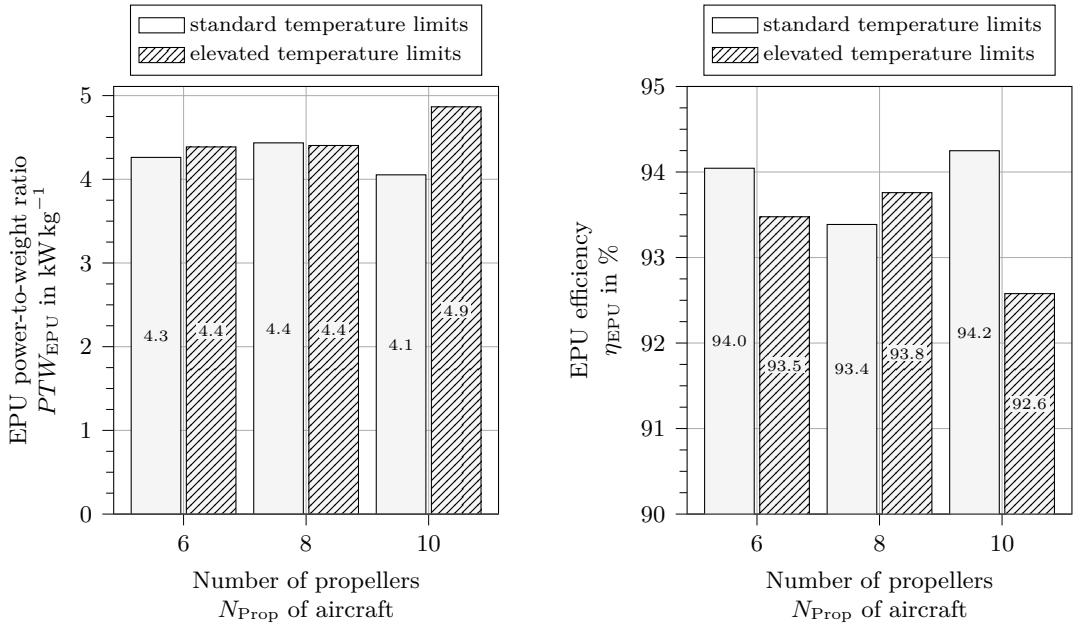

(**a**) Power-to-weight ratio

(**b**) Efficiency

Figure 4.20: Specific power-to-weight ratio PTW_{EPU} and efficiency η_{EPU} of electric propulsion unit for liquid cooled variant with standard and elevated machine temperture limits, as a function of the number of propellers N_{Prop}. Percentage shares are shown only when the bar segment size permits; as a result, shares below approximately 5 % may not appear explicitly.

For units with elevated machine temperature limits, the power-to-weight ratio varies between 4.4 kW kg^{-1} for the six- and eight-propeller and 4.9 kW kg^{-1} for the ten-propeller configuration. System efficiency changes between 92.6 % and 93.8 %, with the highest efficiency achieved for the eight-propeller configuration.
Compared to the baseline variant, increasing the allowable machine temperature limits enables similar or even higher power densities in the electric propulsion unit, particularly in the ten-propeller configuration, where the power-to-weight ratio increases by approximately 20 %. However, this gain in power density comes at the cost of reduced efficiency, with a decrease of around 0.5 % to 1.6 % relative to the baseline. Interestingly, in the eight-propeller configuration, a lower power density design is favored instead, which results in a modest efficiency improvement of approximately 0.4 %.
Figure 4.21 expands the analysis to the aircraft system level by presenting the total electric propulsion system mass m_{EPS} and corresponding losses Q_{EPS}. The mass accounts for the sum of propulsion unit weights and the battery mass offset Δm_{ESS} induced by differences in system efficiency, evaluated pairwise relative to the less efficient configuration.
For variants with elevated machine temperature limits, the total electric propulsion system mass decreases notably from 244 kg for the six-propeller to 188 kg for the ten-propeller configuration. Total electric propulsion system losses vary between 61 kW for the eight-propeller and 73 kW for the six-propeller configuration.

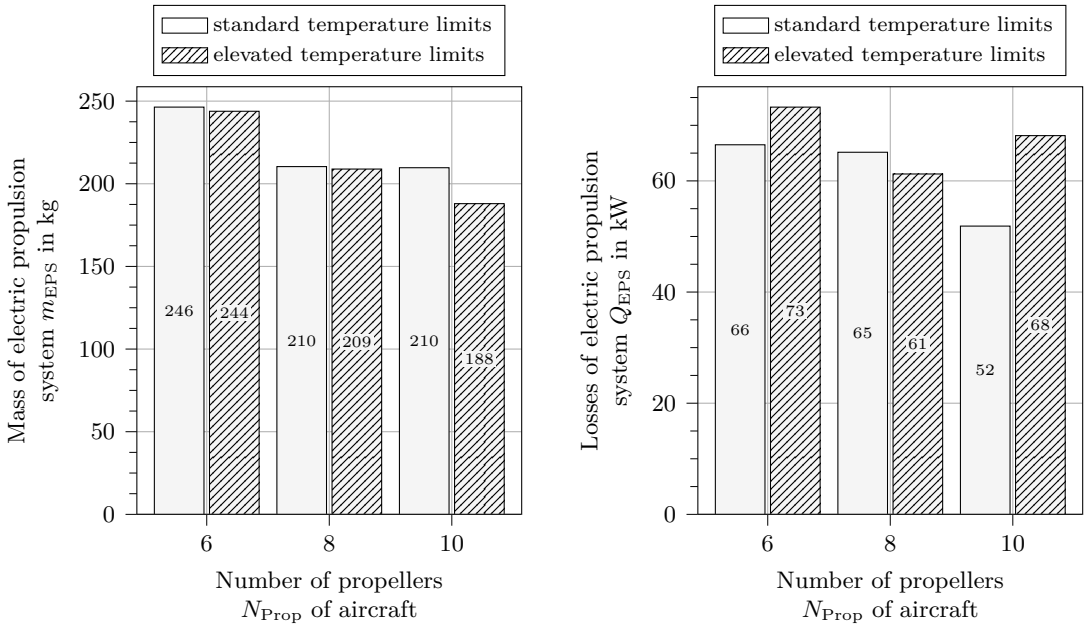

(**a**) Total mass

(**b**) Total losses

Figure 4.21: Mass m_{EPS} and losses Q_{EPS} of the electric propulsion system for liquid cooled variant with standard and elevated machine temperture limits, as a function of the number of propellers N_{Prop}.

Overall, this variant enables further reductions in electric propulsion system mass across all propeller configurations, with weight savings of up to 22 kg for the ten-propeller case. At the same time, system-level losses increase by up to 16 kW. While the six- and ten-propeller configurations follow the previously discussed trade-off between power density and efficiency, the eight-propeller case presents a notable deviation. Here, an electric propulsion unit with even lower power density than the baseline variant is selected, yet it resultsin a net system-level benefit. The associated gain in efficiency, and consequently the reduced battery mass penalty, outweighs the drawbacks of the lower specific power. This again highlights the necessity of integrated, physics-based component and system models to identify optimal configurations that may not emerge from isolated parameter comparisons.

To explain the impact of elevated temperature operation, a detailed breakdown of the mass and loss contributions of the electric propulsion unit components is shown in Figure 4.22. As with the cooling variants, both temperature limit variants display consistent trends across all considered architectures with varying degrees of impact depending on the number of propellers, except for the previously discussed anomaly of the eight-propeller configuration.

According to Figure 4.22a, the most significant effect of elevated temperature operation is observed in the mass of the electric motor m_{EM}, which decreases for the six- and ten-propeller configurations by 1.0 – 3.0 kg per unit due to relaxed thermal constraints. For the eight-propeller variant, however, an increase of 0.8 kg is observed. This corresponds to a relative mass reduction of up to 10 % compared to standard-temperature variants. Masses of the inverter (m_{Inv}), cabling (m_{Cab}), and cooling system components (m_{CS}) remain largely unchanged. Due to the reduction in overall system efficiency, battery mass penalties of up to 1.3 kg per system are added for the elevated temperature variants to ensure a fair comparison.

Figure 4.22b shows the corresponding breakdown of losses, highlighting the increase in copper losses $Q_{\mathrm{EM,Cu}}$ as the dominant effect. Copper losses rise by up to 1.6 kW, depending on the propeller count, which corresponds to a relative increase of 15 – 55 %. This is attributed to both the higher stator current density and the increase in winding resistance

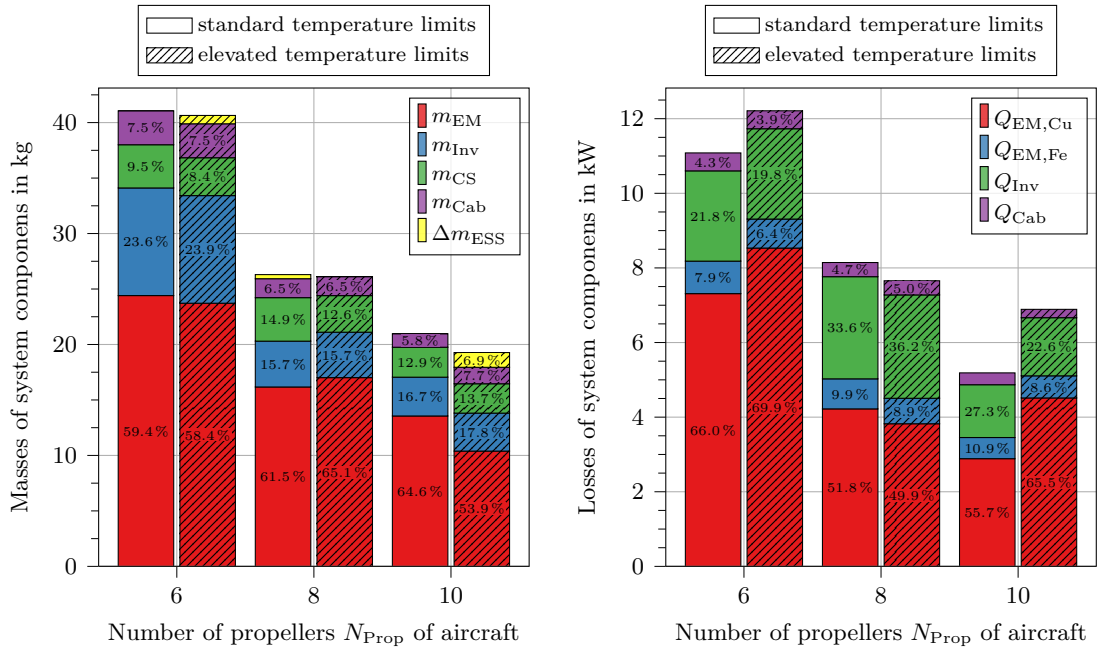

(**a**) Mass Breakdown

(**b**) Loss Breakdown

Figure 4.22: Mass and loss breakdown for the selected electric propulsion unit design, comparing standard and elevated component temperature limits, as a function of the number of propellers N_{Prop}. Percentage shares are shown only when the bar segment size permits; as a result, shares below approximately 5 % may not appear explicitly. Battery mass differences Δm_{ESS} are added to account for system efficiency changes.

at elevated operating temperatures.

Iron losses $Q_{\mathrm{EM,Fe}}$, being primarily dependent on frequency and flux density, remain nearly unchanged. For the ten-propeller configuration, a minor increase of 0.1 kW is observed, caused by higher electrical frequencies due to increased pole count. This also explains the corresponding rise in inverter losses Q_{Inv} by approximately 0.2 kW. Cable losses Q_{Cab} remain effectively constant, as neither current levels nor the thermal design constraints are altered.

Overall, elevated temperature operation enables improvements at the electric propulsion system level through moderate mass savings in the electric motor. Yet this effect becomes measurable only for the ten-propeller configuration, while the benefits for the remaining configurations are marginal.

As the ten-propeller configuration with elevated temperature limits again yields the best overall performance among the evaluated variants, a more detailed investigation of the governing design trade-offs is warranted. The same key parameters as in the previous comparison in Section 4.5.1 are examined. Figure 4.23 illustrates the evolution of these metrics along the Pareto fronts for the ten-propeller configuration, comparing standard and elevated temperature limits and their respective optimal designs.

With higher allowable temperature limits, the achievable stator current density J_{rms} reaches values up to 30 $\mathrm{A\,mm^{-2}}$, as shown in Figure 4.23a, enabling even more lightweight machine designs than in the baseline variant. Whereas the baseline design was clearly limited by the magnet temperature rather than the winding temperature, Figures 4.23b and 4.23c illustrate much improved thermal balancing in the elevated temperature case. The optimal design reaches a winding temperature T_{wdg} of approximately 190 °C and a magnet temperature T_{mag} of about 140 °C, both remaining roughly 10 K below the allowable limits defined in Table 4.11. While the winding temperature shows a roughly linear increase with decreasing mass, the magnet temperature remains relatively constant on average. However, both curves show significantly more fluctuation than in the baseline.

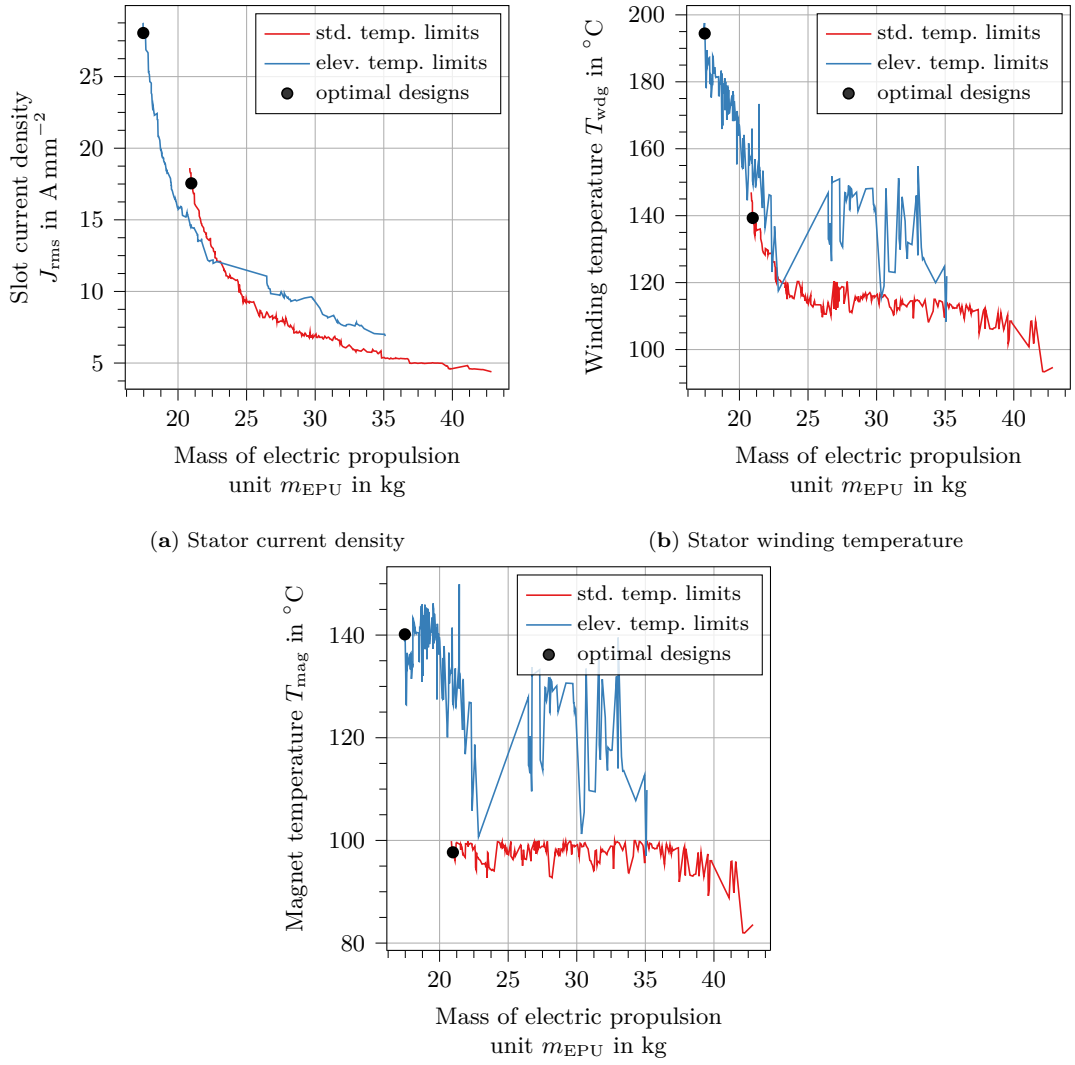

(**a**) Stator current density

(**b**) Stator winding temperature

(**c**) Magnet temperature

Figure 4.23: Behavior of key trade-offs between electrical and thermal limitations along Pareto fronts for the ten-propeller configuration, comparing standard and elevated component temperature limits.

In summary, elevated temperature operation offers tangible benefits for designs pushing thermal boundaries, primarily through higher J_{rms} and more compact motor geometries. Nevertheless, the extent of improvement remains configuration-dependent. While a notable mass reduction was achieved for the ten-propeller setup, other configurations exhibited limited or negligible gains.

In conclusion, the investigation of elevated temperature limits in liquid-cooled electric propulsion systems demonstrates advantages, particularly for the ten-propeller configuration. Elevated temperature operation facilitates higher power densities, reflected in an increased power-to-weight ratio PTW_{EPU} by approximately 20 %, and enables more compact motor designs. However, these benefits come at the cost of a slight reduction in efficiency, with η_{EPU} decreasing by up to 1.6 %. Additionally, the mass of the electric propulsion system m_{EPS} decreases notably in configurations with more propellers, offering potential weight savings of up to 20 kg, while total losses Q_{EPS} increase by up to 16 kW. The findings highlight the importance of balancing power density and efficiency for optimal system performance. Furthermore, the trade-offs vary significantly with different configurations, underlining the need for a detailed, physics-based approach to design optimization.

4.5.3 Local versus Central Cooling System

Another important design consideration is the layout of the cooling system. Therefore, the variant with a local cooling system from Section 4.3.2.2 is compared to an otherwise identical configuration using a central cooling system, as outlined in Section 4.3.2.3. This comparison investigates whether cooling system components, such as the pump and heat exchanger, scale favorably at the electric propulsion system level when centralized.
Figure 4.24 shows the specific power-to-weight ratio PTW_{EPU} and the efficiency η_{EPU} of a single electric propulsion unit as a function of the number of propellers N_{Prop} in the aircraft configuration.

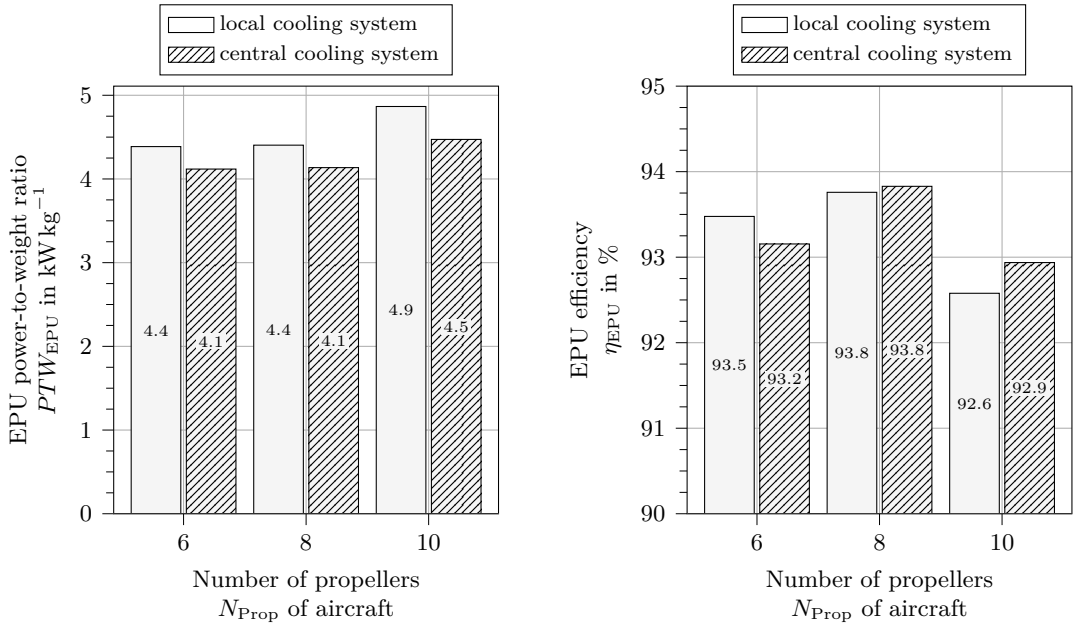

(**a**) Power-to-weight ratio

(**b**) Efficiency

Figure 4.24: Specific power-to-weight ratio PTW_{EPU} and efficiency η_{EPU} of electric propulsion unit for liquid cooled variants with local and central cooling system, as a function of the number of propellers N_{Prop}.

For variants with a local cooling system, the power-to-weight ratio ranges from 4.1 kW kg^{-1} for the six- and eight-propeller configurations to 4.5 kW kg^{-1} for the ten-propeller configuration. The corresponding efficiency varies between 92.9 % and 93.8 %, with the maximum efficiency observed in the eight-propeller configuration. Compared to the local cooling system variant, centralization results in a consistent reduction in power density of 0.3 – 0.4 kW kg^{-1}, while efficiency remains largely unaffected, varying by only 0.3 %.
Figure 4.25 extends the analysis to the system level by presenting the total electric propulsion system mass m_{EPS} and the corresponding total losses Q_{EPS}. For fair comparison, the mass of centralized cooling components, i.e., pump and heat exchanger, is distributed as a per-unit equivalent.
While the system mass for central cooling still decreases from 258 kg for the six- to 190 kg ten-propeller configuration, it remains higher by about 10 kg to 20 kg compared to the local cooling system variant. Total system losses are largely similar, with variations of only up to 4 kW.
These results indicate that, at the electric propulsion system level, central cooling offers no benefit in terms of weight or loss reduction. Moreover, this does not account for additional disadvantages such as increased failure propagation potential, reduced reliability, or performance sensitivity to operating conditions. The data also suggest that the pri-

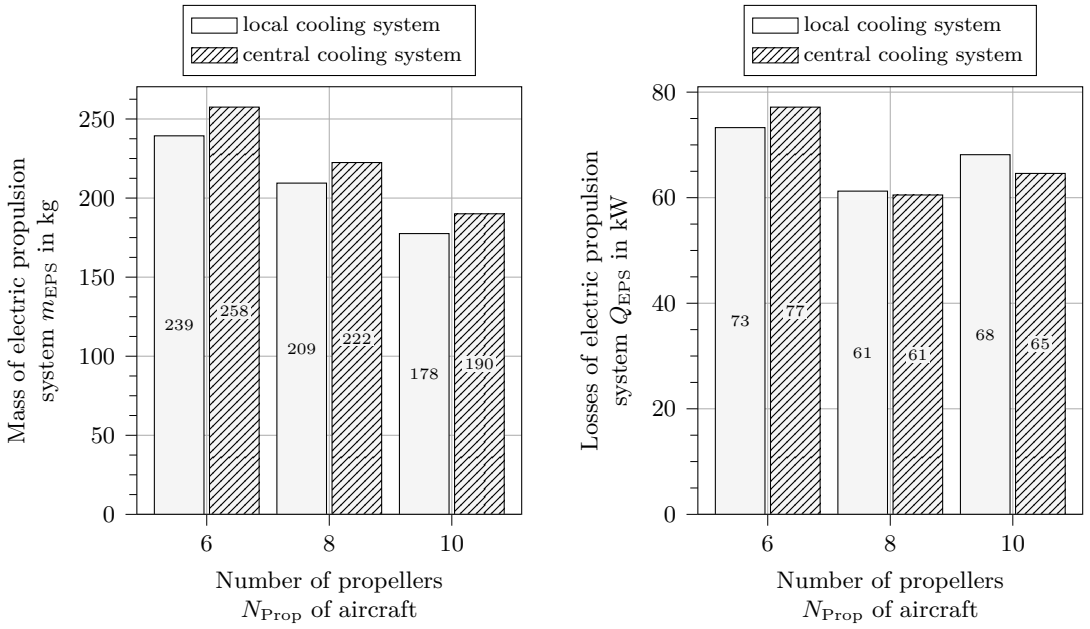

(**a**) Total mass

(**b**) Total losses

Figure 4.25: Mass m_{EPS} and losses Q_{EPS} of the electric propulsion system for liquid cooled variants with local and central cooling system, as a function of the number of propellers N_{Prop}.

mary differences between both variants lie in the cooling system design, rather than in the electrical components themselves.
This is confirmed in Figure 4.26, which provides a detailed breakdown of mass and loss contributions for the propulsion unit components.

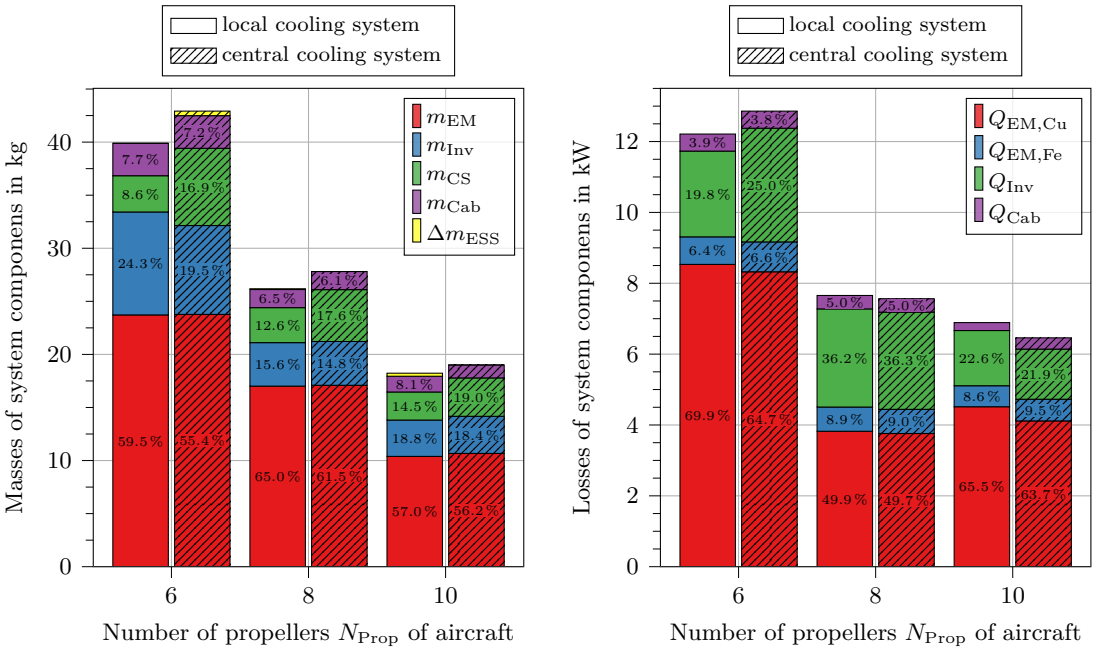

(**a**) Mass breakdown

(**b**) Loss breakdown

Figure 4.26: Mass and loss breakdown for the selected electric propulsion unit design, comparing liquid cooled variants with local and central cooling system, as a function of the number of propellers N_{Prop}. Percentage shares are shown only when the bar segment size permits; as a result, shares below approximately 5 % may not appear explicitly. Battery mass differences Δm_{ESS} are added to account for system efficiency changes.

As shown in Figure 4.26a, component masses for the electric machine, inverter, and DC cabling remain unchanged. Battery mass penalties are also negligible due to the nearly identical efficiency levels. The dominant factor contributing to the higher mass in the central cooling variant is the cooling system itself, which adds between 1.0 and 3.8 kg, corresponding to a relative increase of 40 % to 110 %. In the six-propeller case, the even higher proportional increase in cooling system mass results from the selection of a lighter but less efficient inverter, chosen to globally minimize propulsion system mass, as illustrated in Figure 4.26b. All other loss contributions remain unchanged.
To conclude the analysis of the centrally cooled variant, the mass breakdown of the cooling system is analyzed in Figure 4.27 to identify the main driver of the weight increase.

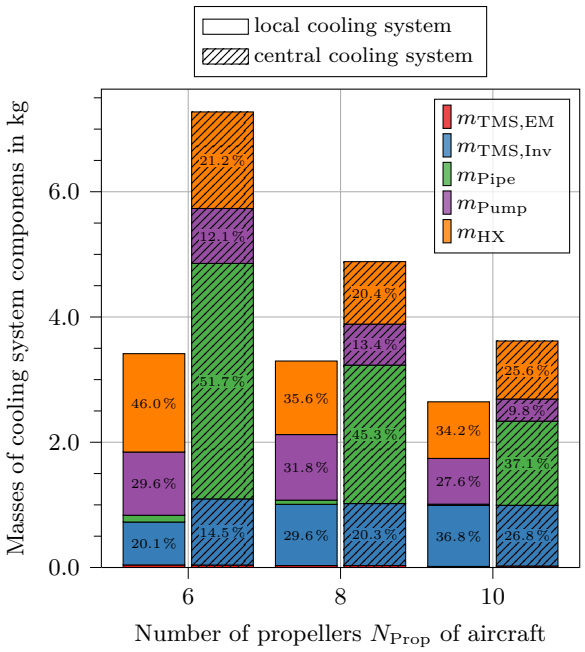

Figure 4.27: Mass breakdown of the cooling system for the selected electric propulsion unit design, comparing liquid cooled variants with local and central cooling system, as a function of the number of propellers N_{Prop}. Percentage shares are shown only when the bar segment size permits; as a result, shares below approximately 5 % may not appear explicitly.

It clearly shows that the mass increase of the central cooling system variant is primarily driven by the additional length of piping required to connect all cooling loops of the electric propulsion units with the central thermal management system, accounting for 40 – 50 % of the total cooling system mass. The effect decreases with higher number of propulsion units as the average piping length decreases as outlined in Section 4.2. In contrast, this share is negligible for the local cooling system variant. While the heat exchanger and the pump still contribute considerable mass fractions in both variants as anticipated in Section 4.3.2.3, both see a reduced share in the centralized setup, indicating economies of scale from using fewer, larger units.
In conclusion, central cooling systems offer no performance benefits in terms of efficiency or thermal losses, yet introduce significant mass penalties of up to 20 kg, primarily due to the additional piping required to interconnect the propulsion units. This added mass leads to a reduction in power-to-weight ratio PTW_{EPU} of up to 0.4 kW kg^{-1}, while efficiency differences remain negligible, below 0.3 %. Furthermore, central cooling systems may require at least two parallel flow paths to ensure redundancy in case of failure, further favoring local cooling architectures. Additional challenges, such as higher required pressure heads during flight maneuvers, were not considered in this analysis but would likely amplify the disadvantages of a centralized setup.

4.5.4 Direct versus Geared Drive

This section compares the performance of direct drive electric propulsion units with two geared drive variants: a single-stage gearbox represented by a gear ratio i_{GB} of five, and a two-stage gearbox with a gear ratio of twelve. The objective is to evaluate whether mechanical gearing can offer system-level advantages in terms of mass and efficiency. Since propulsion system efficiency influences energy storage requirements, each geared configuration is individually compared to an otherwise identical direct drive setup, ensuring consistent battery mass accounting.

4.5.4.1 Single-Stage Gearbox

Incorporating a single-stage gearbox allows the electric machine to operate at higher rotational speeds and lower torque levels, enabling the use of smaller, lighter machines with increased specific power. Figure 4.28 shows the specific power-to-weight ratio PTW_{EPU} and the efficiency η_{EPU} of a single electric propulsion unit as a function of the number of propellers N_{Prop} in the aircraft configuration.

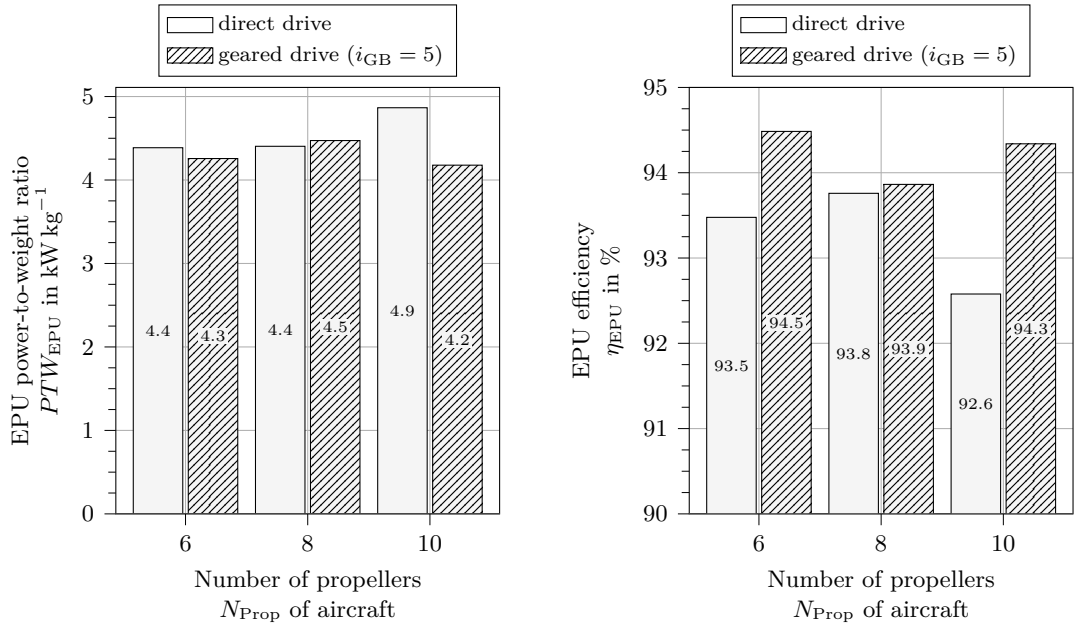

(**a**) Power-to-weight ratio

(**b**) Efficiency

Figure 4.28: Specific power-to-weight ratio PTW_{EPU} and efficiency η_{EPU} of the electric propulsion unit for direct and single-stage geared drive variants, as a function of the number of propellers N_{Prop}.

Notably, the optimal design point for each aircraft configuration differs from the expectations discussed in Section 4.3.2.4. The power-to-weight ratio of the electric propulsion unit decreases by 0.1 to 0.7 kW kg^{-1} for the six- and ten-propeller configurations, and only slightly increases by 0.1 kW kg^{-1} for the eight-propeller configuration compared to the direct drive variant. Meanwhile, efficiency improves by 0.1 % to 1.7 %.
This directly affects the system-level behavior, as shown in Figure 4.29, which presents the total electric propulsion system mass m_{EPS} and the corresponding total losses Q_{EPS}. Changes in power-to-weight ratio, combined with improved efficiency at the optimal design points, lead to a slight reduction in electric propulsion system mass of up to 5 kg when accounting for battery penalty mass in the eight-propeller configurations, while the six-propeller configuration is weight-neutral. For the ten-propeller configuration, however, the reduction in losses of around 17 kW is not sufficient to compensate for the decreased PTW_{EPU}, resulting in a 15 kg increase in system mass.

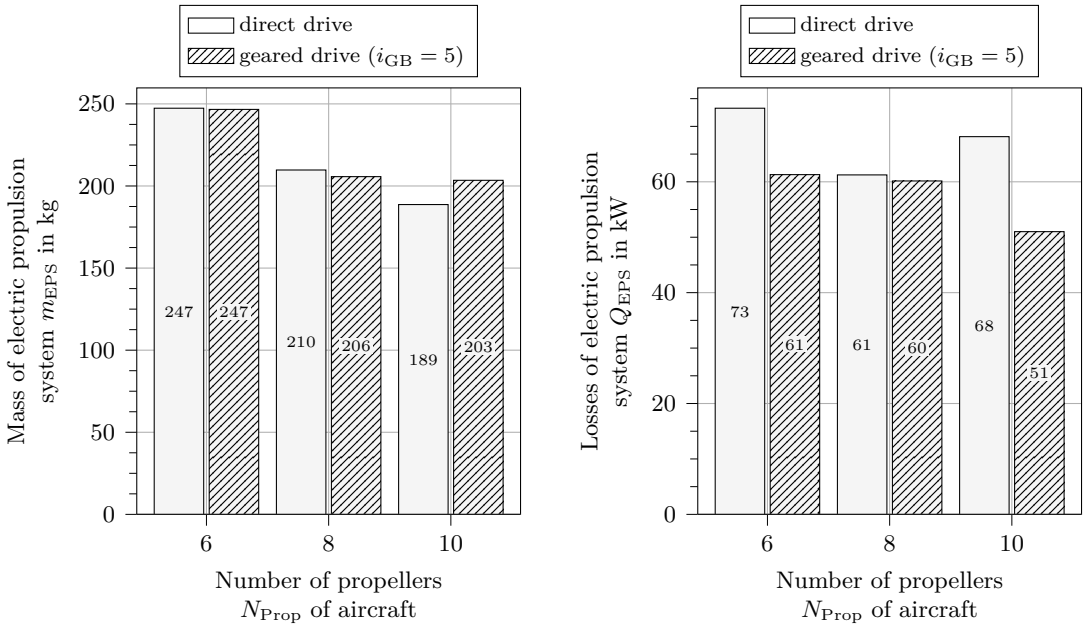

(**a**) Total mass (**b**) Total losses

Figure 4.29: Mass m_{EPS} and losses Q_{EPS} of the electric propulsion system for direct and single-stage geared drive variants, as a function of the number of propellers N_{Prop}.

A more detailed analysis is provided in Figure 4.30, which shows the breakdown of mass and losses among the propulsion unit components.

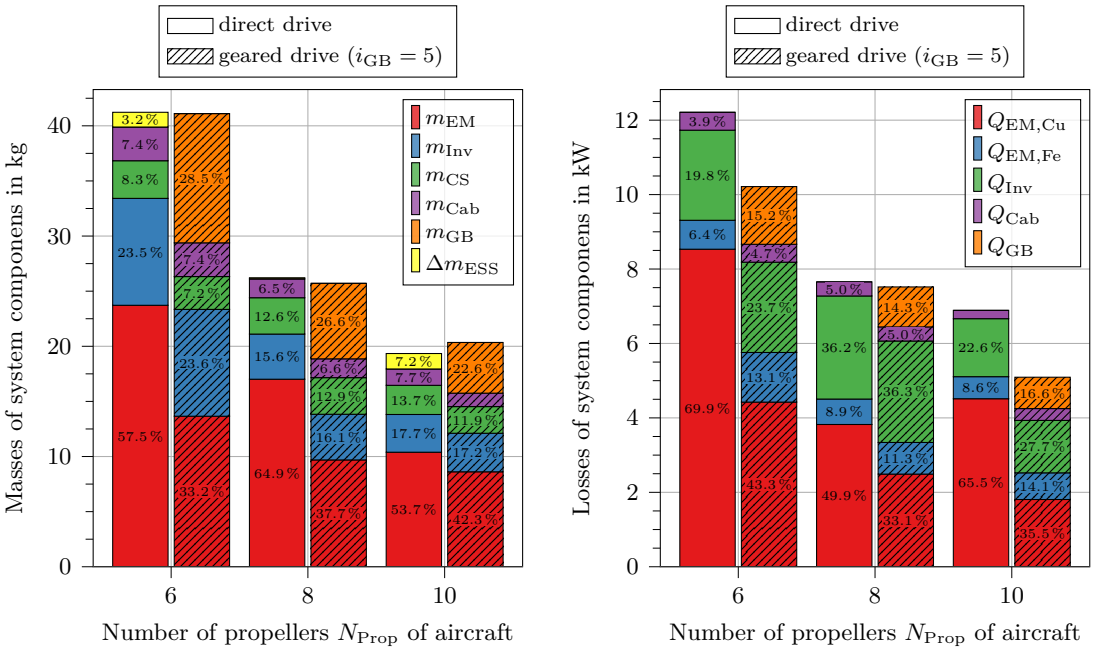

(**a**) Mass breakdown (**b**) Loss breakdown

Figure 4.30: Mass and loss breakdown for the selected electric propulsion unit design for direct and single-stage geared drive variants, as a function of the number of propellers N_{Prop}. Percentage shares are shown only when the bar segment size permits; as a result, shares below approximately 5 % may not appear explicitly. Battery mass differences Δm_{ESS} account for system efficiency changes.

As shown in Figure 4.30a, the primary mass change is caused by a significant relative reduction in electric machine mass of up to 45 %, alongside the introduction of the gearbox,

which accounts for approximately 20 – 30 % of the unit mass. This reduction results from the lower torque requirement due to the gear ratio, which reduces the amount of copper and iron needed in the machine. Consequently, as shown in Figure 4.30b, copper losses decrease by up to 55 %, while iron losses increase in both absolute and relative terms. Gearbox losses contribute roughly 15 % to total losses. Since overall power demands remain unchanged, the inverter and DC cabling masses and losses stay constant. Cooling system mass varies slightly due to minor efficiency differences.
To highlight key changes in governing design parameters, a closer examination is made of the ten-propeller configuration, as shown in Figure 4.31.

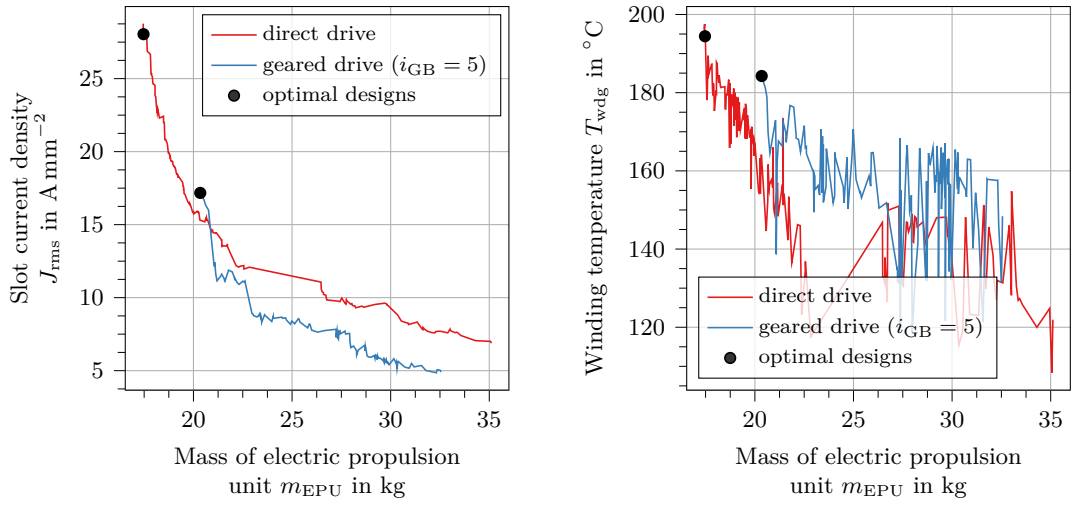

(**a**) Stator current density

(**b**) Stator winding temperature

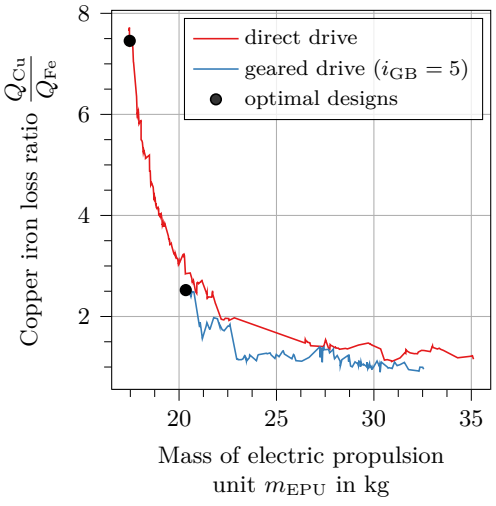

(**c**) Magnet temperature

Figure 4.31: Behavior of key trade-offs between electrical and thermal limitations along Pareto fronts for the ten-propeller configuration, comparing direct and single-stage geared drive variants.

Compared to direct drives, the stator slot current density of geared variants is clearly limited to much lower values (up to 17 A mm^{-2}), as shown in Figure 4.31a, while the winding temperature behavior remains similar between both variants, as shown in Figure 4.31b. This difference arises because geared variants are significantly more compact, which results in higher loss densities within the machine volume. As a result, the electric machine becomes harder to cool, limiting the achievable current densities. This effect is especially evident in high-speed drives and constrains the maximum power densities. It also influences the shape of Pareto-optimal designs. Figure 4.31c shows that for geared variants,

the ratio of copper to iron losses is significantly lower, which aligns with the breakdown presented in Figure 4.30b. The observed jumps in the curve are due to changes in pole-slot combinations.

4.5.4.2 Two-Stage Gearbox

For the two-stage gearbox variant, the mass and loss breakdown of the optimal design points in Figure 4.32 shows that both gearbox mass and losses increase further compared to the single-stage configuration. However, the corresponding mass reduction of the electric machine enabled by the lower torque requirement is less pronounced. Additionally, system losses increase slightly across all configurations, with a particularly notable rise in the eight-propeller setup. This stems primarily from the electric machine design, which, unlike in other configurations, is unable to achieve the same degree of loss reduction.
At the electric propulsion system level, this leads to a net mass increase of 20 kg to 65 kg for the eight- and ten-propeller configurations compared to their direct drive counterparts, while the six-propeller configuration remains roughly equivalent. These results clearly illustrate that at higher rotational speeds, structural limitations such as the need for thicker magnet retention sleeves and larger air gaps, begin to dominate the design trade-offs and negatively impact performance.

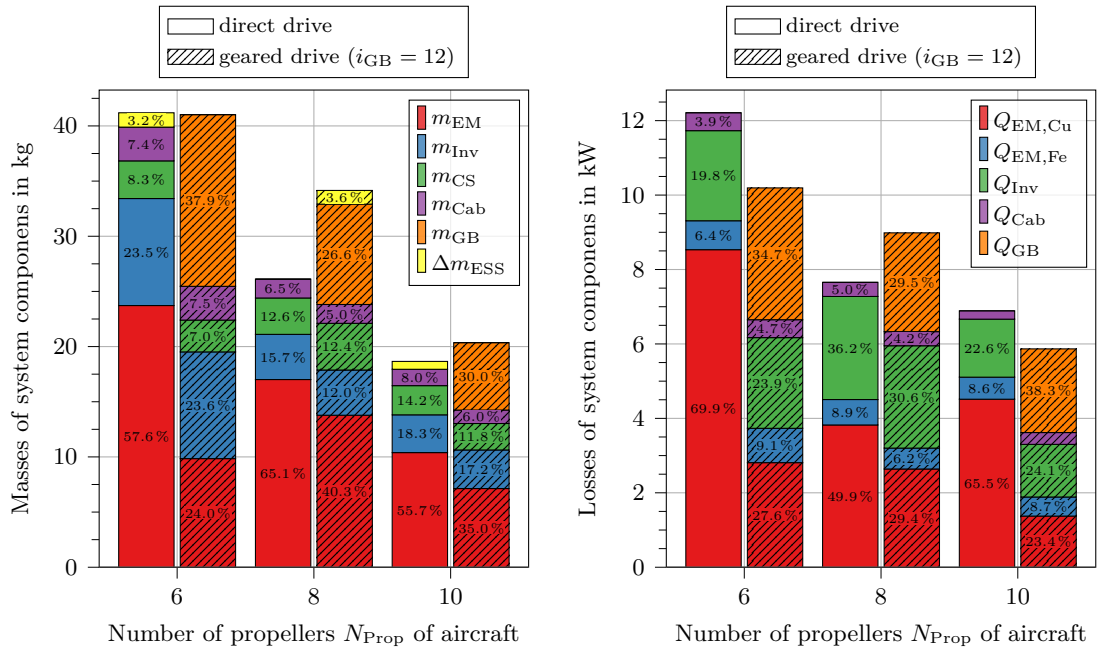

(**a**) Mass breakdown

(**b**) Loss breakdown

Figure 4.32: Mass and loss breakdown for the selected electric propulsion unit design for direct and two-stage geared drive variants, as a function of the number of propellers N_{Prop}. Percentage shares are shown only when the bar segment size permits; as a result, shares below approximately 5 % may not appear explicitly. Battery mass differences Δm_{ESS} account for system efficiency changes.

In conclusion, integrating a gearbox into a liquid-cooled electric propulsion system does not yield the anticipated gains in power-to-weight ratio. While minor mass savings of up to 5 kg can be achieved in certain configurations using a single-stage gearbox, these come with only modest efficiency improvements. For two-stage gearboxes, these effects are even reversed in some cases. Overall, the benefits are marginal and do not outweigh the associated downsides, such as increased engineering effort, greater failure propagation potential, and general reliability concerns. In the ten-propeller configuration, for example, the drop in power-to-weight ratio leads to a net increase in system mass despite reduced

losses.
Given the limited advantages and added complexity, the single-stage geared architecture is already less compelling than its direct-drive counterpart. When considering two-stage gearboxes, this conclusion becomes even clearer. Overall, the direct-driven ten-propeller configuration continues to be the most effective solution across all evaluated metrics.

4.5.5 Summary of Comparative Results

The preceding analysis compared multiple electric propulsion system architectures, as described in Section 4.3, with respect to their overall performance at the aircraft level. This comparison includes various cooling architectures, thermal limitations, and geared variants. To maintain a focus on architectural impacts, Figure 4.33 shows the mass of the electric propulsion system including only the relative battery mass differences resulting from efficiency losses, referenced against the air-cooled variant. This enables a fair comparison between architectures without obscuring architectural differences.

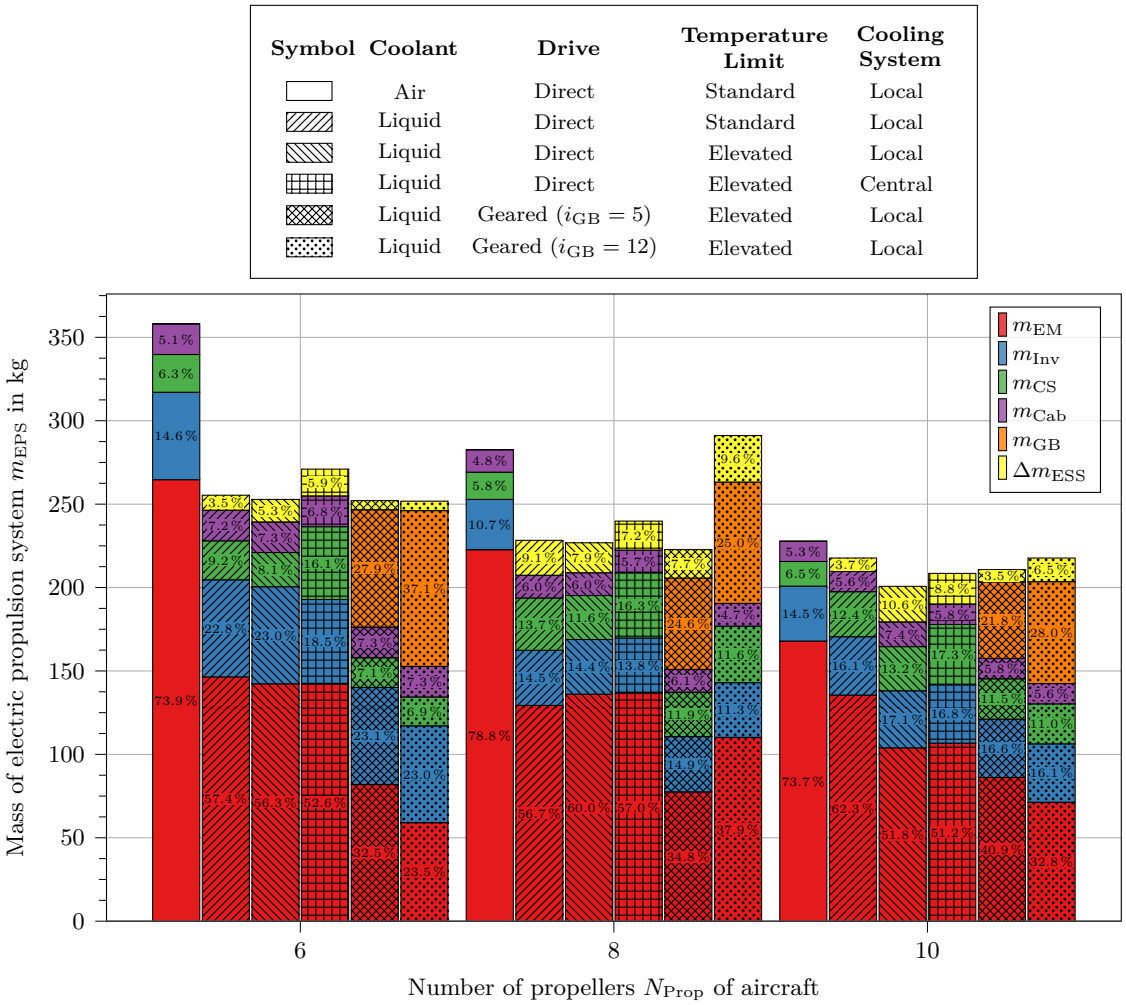

Figure 4.33: Comparison of the mass m_{EPS} of the electric propulsion system for all investigated variants, as a function of the number of propellers N_{Prop}. A battery penalty weight based on efficiency differences (relative to the air-cooled variant) is included. Absolute battery mass is excluded to focus the comparison on architectural impacts.

While the absolute battery mass clearly dominates the overall electric propulsion system mass m_{EPS}, architectural differences still lead to variations of up to 130 kg, correspond-

ing to approximately 10 – 15 % of the total system weight in some configurations. Even seemingly small savings can improve performance, reduce cooling complexity, integration effort, and system cost, thus remaining highly relevant for aircraft-level optimization.
Key findings include:

- The liquid-cooled, direct drive configuration with elevated machine temperature limits and a local cooling system consistently outperformed all other variants in terms of overall electric propulsion system mass, particularly in the ten-propeller configuration. The ability to operate at higher temperatures allowed for a reduction in machine size, which in turn reduced system-level mass without compromising thermal safety.

- Air-cooled variants, while simpler and requiring less complex cooling systems, showed significant limitations in thermal management. These systems necessitated larger electric machines and inverters to meet performance goals, as they were unable to efficiently dissipate heat. As a result, they exhibited higher system masses, despite demonstrating higher efficiency in some cases.

- For liquid-cooled, direct drive variants, local cooling systems outperformed central cooling systems. The additional complexity and mass introduced by the pipescompletely outweighed the advantages of lighter heat exchangers and pumps, further complicating concerns related to safety and reliability.

- The use of a gearbox allowed the electric machine to operate at higher speeds and lower torque levels, reducing the size of the machine and leading to comparable electric propulsion system weights to the direct drive variants. However, this benefit was minimal and was offset by the added complexity introduced by the gearbox, making the direct drive configuration the more attractive option in most cases.

Considering these findings, the liquid-cooled direct drive variant with elevated temperature limits and a local cooling system, particularly in the ten-propeller configuration, emerges as the most effective solution across all evaluated metrics. As outlined in Section 4.2, Joby's statement regarding the mass of a single electric propulsion unit lacks clarity, complicating direct comparison. Assuming that only the electric machine and inverter are included in their figure, the proposed design for the original six-propeller configuration has an estimated mass of approximately 200 kg, which is 30 kg more than Joby's reported value. For the eight- and ten-propeller configurations, the accumulated mass per unit is reduced to about 165 kg and 140 kg, respectively, corresponding to a reduction of 5 kg to 20 kg compared to Joby's figure. Given the uncertainties in Joby's reported figures and the inclusion of additional subsystems in the proposed design, the resulting propulsion unit masses can be considered well-aligned with realistic expectations for such systems.

4.6 Design Proposal

Among all investigated options, the liquid-cooled direct drive variant with elevated machine temperature limits and a local cooling system in the ten propeller configuration, as introduced in Section 4.3.2.2, proved to be the most effective solution overall, as demonstrated in Section 4.5. This configuration has therefore been selected for further detailed analysis.
The proposed electric propulsion system includes the electric machine, inverter, power cables, and the liquid cooling system. Numerical simulations have been carried out for the electric machine, capturing its electromagnetic, thermal, and structural behavior, as

well as for the inverter, considering its electro-thermal performance. These two components represent the most performance-sensitive parts of the system and were therefore prioritized for high-fidelity modeling. The detailed analysis can be found in Chapter B.
For the remaining subsystems, namely the power cables and the cooling infrastructure, no finite element or computational fluid dynamics simulations were conducted. Instead, these components are modeled using well-established analytical methods from electrical and thermal engineering literature, outlined in detail in Sections 2.4 and 2.5. This approach is justified by the high maturity and predictable behavior of these relatively simple components, which are typically designed using standardized calculation procedures or taken as components off the shelf, for example, the pump. Although this reduces the fidelity of the integrated model to some extent, it still provides a sufficiently accurate representation of system-level characteristics for comparative and preliminary design purposes.
The parameterization of the electric machine, inverter, power cables, and the cooling system, along with their key performance metrics, is presented in the following sections, providing justification for the selected parameter values.
Table 4.17 shows the parameterization of the electric machine for the selected system design proposal of a ten-propeller configuration, including the design bounds and the final optimal values used in the design.

Table 4.17: Parameterization of the electric machine for the selected system design proposal of a ten-propeller configuration, including design bounds and the final optimal values used in the design.

Parameter	**Symbol**	**Design Space**			**Unit**
		min	**optimal**	**max**	
Shaft length	L_{stk}	25	25.19	100	mm
Shaft inner radius	$r_{\mathrm{sh,i}}$	100	202.22	250	mm
Rotor yoke thickness	t_{ry}	3	3.01	10	mm
Magnet thickness	t_{mag}	2	5.06	15	mm
Airgap thickness	g_{mec}	1	1.00	4	mm
Tooth tip edge thickness	$t_{\mathrm{tt,e}}$	1	1.02	3	mm
Relative tooth tip edge width	$\beta_{\mathrm{tt,e}}$	0.5	0.81	0.85	-
Tooth tip center thickness	$t_{\mathrm{tt,c}}$	1	1.02	3	mm
Relative tooth tip center width	$\beta_{\mathrm{tt,c}}$	0.5	0.48	0.85	-
Slot depth	t_{sd}	5	10.87	60	mm
Stator yoke thickness	t_{sy}	3	3.25	15	mm
Pole pair number	p	30	42	70	-
Slot number	Q_{s}	45	108	210	-
Parallel winding paths	$n_{\mathrm{par,wdg}}$	1	12	70	-
Winding turns	$N_{\mathrm{t,wdg}}$	1	30	100	-
Wire insulation thickness	$t_{\mathrm{wire,ins}}$	10	17.96	200	µm
Slot insulation thickness	$t_{\mathrm{slot,ins}}$	50	190.30	500	µm
Phase insulation width ratio	$\beta_{\mathrm{ph,ins}}$	0.001	0.05	0.5	-
q-axis current magnitude	$\hat{I}_q$	250	390.44	1300	A
Coolant mass flow rate	$\dot{m}_{\mathrm{EM}}$	0.01	0.035	1	$\mathrm{kg\,s^{-1}}$

This parameter set results from a multi-objective optimization process that balances the electric propulsion system mass against electrical losses, and the selected design is based on the penalty factor method. As such, there is no simple, isolated rationale for the specific values chosen. Instead, the parameterization must be interpreted within the broader system context and the governing trade-offs of the design space.
To achieve high power density in a direct drive electric machine, pancake-like topologies are preferred. A high pole count increases the electrical frequency, enabling a thinner stator yoke and more compact core geometry. Additionally, a high slot number improves the quality of the back-EMF waveform and reduces harmonic content. However, further increases in these key parameters are limited by the resulting rise in electrical frequency, which leads to higher iron and inverter losses, as well as by geometrical and electromagnetic

constraints. The resulting dimensions of the magnets, teeth, and slots already approach the manufacturing limits defined in Table 4.8, while both the stator yoke thickness and stack length are at the lower bounds of the design space. As a result, further increases in the radial dimension do not yield additional improvements in power density. The relative width of the tooth balances the available space for both the teeth and the slot.
The magnet and airgap thicknesses are also critical to this balance. Thicker magnets improve flux density and reduce the risk of demagnetization, supporting higher torque output and efficiency, but at the cost of increased material use and rotor inertia. The selected magnet thickness represents a trade-off between magnetic performance and mass. The airgap thickness, meanwhile, strongly affects magnetic coupling and power factor. A smaller airgap enhances flux linkage, which not only increases torque density but also improves the power factor by reducing the share of reactive current in the machine. Nevertheless, the airgap cannot be minimized indefinitely due to mechanical tolerances, manufacturing precision, and rotor dynamic stability. Consequently, both magnet and airgap dimensions are selected near the lower feasible bounds to maximize performance without compromising robustness.
The winding configuration is driven by the objective to minimize copper losses while ensuring compatibility with the inverter and slot geometry. The highest feasible number of parallel winding paths is selected for this machine design, which reduces the current per conductor and thus significantly lowers copper losses. At the same time, a high number of turns per phase is chosen to increase the induced voltage, improving the inverter's modulation index and enabling more efficient use of the DC link voltage. This elevated voltage level allows the required shaft output power to be achieved with lower current, further reducing ohmic losses. However, the increased number of turns reduces the available slot area for active copper due to longer conductor lengths and additional insulation requirements. While the thicknesses of wire and slot insulation are defined by voltage safety margins to prevent electrical breakdown, their cumulative effect, combined with the high turn count, reduces the copper fill factor. This constraint increases current density, which partially offsets the gains in efficiency. The resulting winding design reflects an optimized trade-off between electromagnetic performance, thermal behavior, and electrical insulation requirements.
Table 4.18 summarizes the key performance characteristics of the electric machine design resulting from the parameterization detailed in Table 4.17.

Table 4.18: Performance characteristics of the electric machine for the selected system design proposal of a ten-propeller configuration.

Parameter	**Symbol**	**Value**	**Unit**
Machine diameter	d_{EM}	471	mm
Machine length	l_{EM}	65	mm
Shaft speed	n_{EM}	2000	min^{-1}
Output continuous torque	$T_{\mathrm{cont,EM}}$	405.98	N m
Output continuous power	$P_{\mathrm{cont,EM}}$	85.03	kW
Peak back-EMF (phase)	$\hat{e}_{\mathrm{ph}}$	146.20	V
d-axis inductance	L_{d}	47.66	µH
q-axis inductance	L_{q}	47.66	µH
Power factor	$\cos\varphi$	0.68	-
Flux density in stator tooth	$B_{\mathrm{st,max}}$	1.94	T
Flux density in stator yoke	$B_{\mathrm{sy,max}}$	1.91	T
Iron losses	$Q_{\mathrm{EM,Fe}}$	592.56	W
Copper winding losses	$Q_{\mathrm{EM,Cu}}$	4514.92	W
Magnet temperature	T_{mag}	139.84	°C
Winding average temperature	$T_{\mathrm{wdg,avg}}$	175.36	°C
Winding max. temperature	$T_{\mathrm{wdg,max}}$	192.62	°C

The resulting electric machine achieves the required output power and torque at the defined shaft speed, confirming the feasibility of the proposed direct drive configuration. Furthermore, all other constraints set in Tables 4.8 and 4.11 are respected. The power factor is optimized within the limits imposed by the short-circuit current ratio, balancing efficient inverter utilization and system stability.
The peak flux densities in both the stator teeth and yoke are close to the material saturation limits, ensuring effective use of the magnetic material without excessive core loss. Copper and iron losses remain within acceptable ranges for thermal management and overall efficiency. The magnet temperature is well below the demagnetization threshold, while both the average and peak temperatures of the windings remain below the maximum insulation class limits, indicating that the liquid cooling system is adequately sized to maintain safe operating conditions under continuous load.
Next, the inverter is discussed in more detail. Table 4.19 presents the parameterization of the DC-AC inverter for the selected system design proposal with a ten-propeller configuration, including the design bounds and the final optimal values used in the design.

Table 4.19: Parameterization of the DC-AC inverter for the selected system design proposal of a ten-propeller configuration, including design bounds and the final optimal values used in the design.

Parameter	**Symbol**	**Design Space**			**Unit**
		min	**optimal**	**max**	
Switching frequency ratio	$m_{\mathrm{c,sw}}$	8	10	50	-
Semiconductor module index	i_{SC}	0	3 (Semikron SK200MB120CR03TE2)	6	-
Number of parallel semiconductors	$n_{\mathrm{SC,p}}$	1	2	5	-
Gate driver module index	i_{GD}	0	2 (Semikron SKYPER 42 R)	4	-
DC Link capacitor module index	i_{DCCap}	0	289 (Vishay MKP1848H62070+P*)	344	-
Number of capacitors in series	$n_{\mathrm{DCCap,s}}$	1	1	3	-
Number of capacitors in parallel	$n_{\mathrm{DCCap,p}}$	1	10	15	-
Input bus bar conductor thickness	$t_{\mathrm{BB,in,cond}}$	0.2	0.41	5	mm
Input bus bar insulation thickness	$t_{\mathrm{BB,in,ins}}$	0.05	0.32	2	mm
Output bus bar conductor thickness	$t_{\mathrm{BB,out,cond}}$	0.2	1.97	5	mm
Output bus bar insulation thickness	$t_{\mathrm{BB,out,ins}}$	0.05	0.28	2	mm
Number of fins on heatsink	N_{Fin}	1	97	200	-
Fin width ratio	β_{Fin}	0.01	0.29	0.99	-
Fin height	h_{fin}	1	1.00	30	mm
Coolant mass flow rate	$\dot{m}_{\mathrm{Inv}}$	0.01	0.015	1	$\mathrm{kg\,s^{-1}}$

The inverter employs two Semikron SK200MB120CR03TE2 silicon-carbide modules in parallel, along with the matching SKYPER 42 R gate driver, to carry the current required to achieve the specified output power. The DC-Link capacitor is formed by a bank of ten parallelized Vishay MKP1848H62070+P* polypropylene film capacitors. The busbar dimensions are chosen primarily based on current and voltage ratings to avoid excessive heating and ensure insulation integrity. The selected heatsink configuration maximizes the available surface area to allow for efficient thermal dissipation.
Table 4.20 summarizes the key performance characteristics of the DC-AC inverter resulting from the parameterization shown in Table 4.19.
As shown, the inverter delivers approximately 91 kV A to meet the power demand of the electric machine, while the DC-link capacitor maintains a voltage ripple well below the limits specified in Table 4.8, while operating at a moderate switching frequency of 14 kHz for SiC modules. The gate driver and capacitor losses are minor contributors to the overall heat generation, with the primary losses originating in the transistors due to the high output current. The transistor and diode junction operating temperatures are also well below the temperature limits specified in Table 4.8.

Table 4.20: Performance characteristics of the DC-AC inverter for the selected system design proposal of a ten-propeller configuration. Includes absolute and relative comparison between analytical model predictions and numerical simulation results.

Parameter	Symbol	Unit	Value
Inverter dimensions (L x W x H)	-	250 x 250 x 100	mm
DC Link voltage range	V_{DC}	540 – 900	V
Output line-line voltage	$\hat{V}_{\mathrm{AC,LL}}$	274	V
Output line current	$\hat{I}_{\mathrm{AC,LL}}$	395	A
Output line current	$\hat{I}_{\mathrm{AC,LL}}$	91	kV A
Switching frequency	f_{sw}	14	kHz
DC Link voltage ripple	$\Delta V_{\mathrm{Cap,rel}}$	0.04	-
Transistor conduction losses	$Q_{\mathrm{con,T}}$	80.75	W
Transistor switch-on losses	$Q_{\mathrm{sw,on,T}}$	10.04	W
Transistor switch-off losses	$Q_{\mathrm{sw,off,T}}$	6.84	W
Diode conduction losses	$Q_{\mathrm{con,D}}$	26.59	W
Diode switch-off losses	$Q_{\mathrm{sw,off,D}}$	8.08	W
Total semiconductor losses	Q_{SC}	1587.55	W
Transistor junction temperature	$T_{\mathrm{j,T}}$	139.89	°C
Diode junction temperature	$T_{\mathrm{j,D}}$	139.89	°C

Now, the cooling system consisting of the heat exchanger, fluid pipes, and the pump is presented. Table 4.21 shows the parameterization of the system.

Table 4.21: Parameterization of the cooling system for the selected system design proposal of a ten-propeller configuration, including design bounds and the final optimal values used in the design.

	Parameter	Symbol	Design Space			Unit
			min	optimal	max	
Heat Exchanger	Number of passages	N_{P}	2	10	70	-
	Flow path length hot side	$L_{\mathrm{FP,h}}$	10	256.06	400	mm
	Number of fins per pitch on hot side	$N_{\mathrm{fp,h}}$	2	39	150	-
	Number of offset fins on hot side	$N_{\mathrm{off,h}}$	2	128	150	-
	Fin height on hot side	$b_{\mathrm{Fin,h}}$	1	1.012	50	mm
	Fin thickness ratio on hot side	$\beta_{\mathrm{Fin,h}}$	0.01	0.334	0.99	-
	Flow path length cold side	$L_{\mathrm{FP,c}}$	10	23.56	400	mm
	Number of fins per pitch on cold side	$N_{\mathrm{fp,c}}$	2	102	150	-
	Number of offset fins on cold side	$N_{\mathrm{off,c}}$	2	11	150	-
	Fin height on cold side	$b_{\mathrm{Fin,c}}$	1	19.39	50	mm
	Fin thickness ratio on cold side	$\beta_{\mathrm{Fin,c}}$	0.01	0.334	0.99	-
	Air duct inlet opening	r_{in}	5	117.59	300	mm
	Air duct inlet length	l_{in}	50	54.22	300	mm
	Air duct outlet opening	r_{out}	5	159.25	300	mm
	Air duct outlet length	l_{out}	50	56.54	300	mm
Pipe	inner radius	r_{pipe}	1	2.03	15	mm
	wall thickness	t_{pipe}	0.5	0.86	2	mm

The parameters of the heat exchanger are selected to minimize the overall weight of the cooling system while ensuring sufficient thermal performance to dissipate the combined losses of the electric machine and the inverter to the ambient. On the cold air side, the flow path is relatively short, with air channels of approximately 2 mm by 20 mm cross-section, ensuring that the pressure drop remains within the available pressure budget. On the hot, liquid side, the flow path is roughly ten times longer, and the channel cross-section is significantly smaller, around 0.4 mm by 1.0 mm, to maximize the heat transfer surface area. The pipe dimensions are chosen to support the required fluid mass flow without introducing risks of water hammer or structural issues.
Table 4.22 summarizes the key performance characteristics of the cooling system.
The heat exchanger is highly compact while still capable of effectively dissipating system losses to the environment. The resulting temperature rise of the cold air remains moderate,

Table 4.22: Performance characteristics of the cooling system for the selected system design proposal of a ten-propeller configuration. Includes absolute and relative comparison between analytical model predictions and numerical simulation results.

	Parameter	Symbol	Value	Unit
Heat Exchanger	Dimensions (L x W x H)	-	256 x 25 x 235	mm
	Heat dissipation capacity	Q_{HX}	7000	W
	Number of transfer units	NTU	1.59	-
	Effectiveness	ϵ_{HX}	0.75	-
	Thermal conductance	$U\,A$	150.75	$\mathrm{W\,K^{-1}}$
	Temperature increase on cold side	ΔT_{c}	14.47	K
	Temperature decrease on hot side	ΔT_{h}	74.21	K
	Pressure loss on cold side	Δp_{c}	128.90	Pa
	Pressure loss on hot side	Δp_{h}	21.78	kPa
Pump	Volumetric flow	$\dot{V}_{\mathrm{Pump}}$	4.78	$\mathrm{L\,min^{-1}}$
	Pressure head	H_{Pump}	73.60	kPa

and the pressure drop on the liquid side is kept low. The selected pump is capable of delivering the total required fluid flow and compensating for the pressure losses across the entire system. A suitable aerospace-grade electric pump that can meet these performance targets within the defined weight budget would be, for instance, a Cascon Series-100 pump. Finally, the parameterization of the DC cable is presented in Table 4.23, and its corresponding performance metrics are summarized in Table 4.24.

Table 4.23: Parameterization of the DC cable for the selected system design proposal of a ten-propeller configuration, including design bounds and the final optimal values used in the design.

Parameter	Symbol	Design Space			Unit
		min	optimal	max	
conductor radius	r_{cond}	0.25	3.33	10	mm
insulation thickness	t_{ins}	0.5	0.50	5	mm

Table 4.24: Performance characteristics of the DC cable for the selected system design proposal of a ten-propeller configuration. Includes absolute and relative comparison between analytical model predictions and numerical simulation results.

Parameter	Symbol	Value	Unit
DC voltage range	V_{DC}	540 – 900	V
Ampacity	I_{DC}	175	A

To transport the current required to deliver the necessary output shaft power for propeller operation while staying within the thermal limitations specified in Table 4.8, a cable with a cross-sectional area of approximately $35\,\mathrm{mm}^2$ is required. An example of a suitable solution is the Glenair Turboflex 961-151, size AWG 4.
In summary, the proposed design successfully integrates high-performance subsystems to deliver an optimized propulsion system for the aircraft and its mission, as specified in Section 4.1. For the most critical subsystems, the numerical verification shows good agreement (see Chapter B), thereby demonstrating the effectiveness of the analytical models.

4.7 Short Summary

This chapter presented a comprehensive methodology for the drive train optimization of an all-electric vertical take-off and landing aircraft. Beginning with the definition of the reference aircraft and mission, a detailed performance point analysis was conducted

to determine the electrical power unit requirements for various flight conditions. Based on these requirements, several all-electric propulsion system architectures were developed for a range of propeller configurations, starting from a baseline configuration featuring a liquid-cooled electric machine and inverter with a local cooling system. Additional system variants were introduced as alternatives to the baseline configuration, including air-cooled options, designs with elevated temperature limits, centralized cooling systems, and geared drive concepts.

A multi-criteria optimization approach was applied to each variant, aiming to minimize both the overall weight and the losses of the electric propulsion units. To enable consistent comparison across architectures and propeller configurations, a penalty factor method was introduced to account for efficiency losses and drag penalties.

The chapter also included a detailed comparative study of the propulsion system variants, evaluating trade-offs between cooling methods, thermal limits, cooling system architectures, and mechanical configurations such as direct versus geared drive.

Based on the insights gained from this analysis, the liquid-cooled direct-drive variant with elevated machine temperature limits and a local cooling system in the ten-propeller configuration was identified as the most effective overall solution. Consequently, a design proposal was presented that demonstrates a well-integrated and optimized propulsion system tailored to the specific demands of an electric vertical take-off and landing aircraft.

5 Summary, Conclusion and Outlook

Despite ongoing improvements in the efficiency of conventional gas turbine engines, the continuous growth of global air travel has led to a steady increase in absolute CO_2 emissions from civil aviation. In light of this, the development of cleaner alternatives has become an urgent priority. One particularly promising path is the use of electric propulsion systems, especially given recent advancements in battery cell power and energy density, alongside broader trends in the electrification of aircraft systems.

Historically, the development of airframes and propulsion systems has been carried out somewhat independently, with limited cross-disciplinary integration in the early design phases. However, the challenges associated with electric aviation, particularly the strict mass constraints and their impact on operational and economic feasibility, require a more integrated and system-level approach.

In the early stages of electric aircraft development, many airframers relied heavily on simplified metrics such as component power-to-weight ratios or standalone subsystem efficiencies to assess and compare potential propulsion solutions. While these metrics offer initial guidance, there is growing consensus that they are insufficient to capture the complex interactions between components and their influence on overall aircraft performance. To address this, a modular, physics-based framework has been created in the scope of this thesis to bridge the gap between generic metrics and detailed 3D, numerically evaluated designs. It allows for the evaluation and sizing of electric propulsion architectures based on consistent and realistic physical models of individual components, combining relevant disciplines and being coupled to describe a full system. While the models remain largely analytical in nature to support fast execution and early-stage design space exploration, they go significantly beyond empirical or black-box approaches by capturing key behaviors and constraints of electric drivetrains at a meaningful level of detail, offering both a much more realistic picture and a meaningful starting point for more detailed design activities. A set of models, including key subsystems such as electric machines, power electronics, gearboxes, cables, cooling systems (including heat sinks, heat exchangers, pipes, and pumps), and battery packs has been subsequently developed in Chapter 2 according to the approach described above. This chapter provides a solid foundation for the subsequent exploration of system-level integration and design space optimization.

After that, various optimization algorithms have been tested on a simple component of the electric propulsion system, i.e., a DC cable, in Chapter 3 to determine their suitability and effectiveness in the context of the modular framework developed in the thesis, before applying them to more complex architectures. Among the algorithms tested, NSGA-II emerged as the most effective choice. This algorithm provides good convergence, well-spaced Pareto fronts in the objective space, and can handle both real and discrete parameters, as well as a large set of constraints.

In Chapter 4, the framework was applied to optimize the electric propulsion system of an electric vertical take-off and landing vehicle, similar to Joby's S4 aircraft. The process began by defining the reference aircraft and mission, followed by a performance point analysis to determine the electrical power unit requirements for various flight conditions. Several propulsion system architectures were developed, starting with a baseline configuration featuring a liquid-cooled electric machine and inverter with a local cooling system.

Additional variants included air-cooled options, designs with elevated temperature limits, centralized cooling systems, and geared drive concepts. A multi-criteria optimization approach was applied to minimize both weight and losses of the propulsion units, incorporating a penalty factor method to account for efficiency losses and drag penalties.
A comparative study of the propulsion system variants was conducted, evaluating trade-offs between cooling methods, thermal limits, and mechanical configurations. The liquid-cooled direct-drive variant with elevated temperature limits and a local cooling system in the ten-propeller configuration emerged as the most effective solution, leading to a design proposal tailored to the aircraft's specific demands.
The key conclusions of this thesis are as follows:

1. **Holistic Physics-Based Framework Bridges Gap Between Conceptual and Detailed Design Phases:** This thesis presents a novel modular framework that advances electric propulsion system design by embedding physics-based principles directly into early-stage evaluation processes. Unlike conventional approaches that compromise between simplified empirical correlations and resource-intensive detailed simulations, this framework strategically implements first-principles modeling with targeted fidelity to capture critical thermal-electrical interdependencies, mechanical constraints, and component interactions without finite element overhead. By explicitly modeling how component-level decisions propagate through the entire system, the approach reveals architectural opportunities and constraints that remain hidden in traditional siloed analyses. This holistic perspective bridges the methodological gap between conceptual design and detailed engineering, enabling designers to identify system-level synergies that are particularly valuable for novel aircraft configurations where propulsion integration is critical to overall viability.

2. **Multi-Criteria Optimization Methodology Enables Systematic Architecture Evaluation:** This thesis establishes a systematic multi-objective methodology for evaluating different electric propulsion architectures under realistic constraints. Through comparative analysis of optimization algorithms, the NSGA-II algorithm emerges as most effective for navigating the complex trade space between system mass and power losses. A penalty factor method has been developed to account for efficiency reductions and aerodynamic drag, enabling the selection of a specific design point. The developed approach supports objective comparison across architectural concepts, providing quantitative assessment of their relative merits within specific operational contexts and establishing a consistent framework for architecture-level decision making that applies across various electric aircraft categories.

3. **Configuration Analysis Identifies Optimal Propulsion Solution for Vertical Take-Off and Landing Aircraft:** This thesis delivers concrete design guidance for electric vertical take-off and landing aircraft through comprehensive trade-off analysis of multiple propulsion configurations. By applying the developed framework to a representative use case, summarized in Section 4.5.5 similar to Joby's S4 demonstrator, the research systematically evaluates different propeller configurations, cooling strategies, thermal limits, and mechanical arrangements. The analysis reveals that a liquid-cooled direct-drive system with elevated temperature limits and a local cooling system in a ten-propeller configuration offers the most favorable performance characteristics for the studied mission profile, demonstrating how integrated analysis can translate theoretical advantages into actionable architectural recommendations.

As the aviation industry continues to push towards more sustainable and environmentally friendly solutions, electric propulsion systems hold a significant promise. However, realizing their full potential will require more than incremental improvements in individual

components. A truly, vertically integrated approach that considers both the electric system components and their interactions as well as the aircraft design from the outset will be crucial in overcoming the mass and operational efficiency challenges inherent to electric aviation.

While this thesis presents a robust and extensible framework for the optimization of electric aircraft propulsion systems, several promising directions remain for future development.

First, the fidelity of component models could be further improved on the domain level. For example, in the electromagnetic domain, integrating coupled subdomain formulations or magnetic equivalent circuit models would enable more accurate representation of nonlinear effects such as magnetic saturation and localized losses. In a similar way, refining thermal and fluidic models would allow for better assessment of cooling performance under transient conditions or across specific mission profiles.

Expanding the framework's library to include a broader range of component variants and topologies, such as axial or transversal flux machines and multi-level inverter designs, would allow exploration of more advanced and tailored propulsion architectures. In addition, incorporating new technologies such as fuel cells or gas turbines would make it possible to model and optimize hybrid-electric and turbo-electric propulsion systems, which are especially relevant for aircraft with longer range requirements.

At the same time, economic and environmental aspects are becoming increasingly important in propulsion system design. The integration of cost models covering production, operation, and full lifecycle considerations, as well as sustainability metrics like carbon emissions and environmental material impact, would support more comprehensive trade-off analyses that go beyond purely technical performance indicators.

To strengthen the connection between propulsion and the aircraft as a whole, a logical next step would be the integration of the developed framework into multidisciplinary aircraft design environments such as SUAVE [366]. This would enable simultaneous optimization of both airframe and propulsion system, leading to better alignment of mission requirements and design performance from the very beginning of the development process.

Finally, the use of machine learning and artificial intelligence offers a promising path to improve both computational efficiency and model flexibility. Techniques such as surrogate modeling can approximate complex physics-based simulations, while surrogate-assisted optimization enables the exploration of large and intricate design spaces more quickly. These approaches can significantly reduce computational effort while still preserving a high level of accuracy.

Taken together, these avenues demonstrate that the proposed framework can serve not only as a valuable tool for early-stage analysis, but also as a foundation for next-generation design environments that support integrated, sustainable, and economically viable solutions in electric aircraft propulsion.

A Temperature Nodes and Resistances of Lumped Parameter Thermal Networks of Electric Machines

This appendix provides additional information on the lumped parameter thermal networks discussed in Section 2.1.6.4.

A.1 Temperature Nodes

Table A.1 lists all temperature nodes used in the developed thermal networks. For the spatial location of these nodes, refer to Figure 2.19.

Table A.1: Temperature Nodes in Lumped Parameter Thermal Network

Node	Temperature	Description
0	T_0	Temperature of ambient environment
1	T_1	Temperature of active housing part
2	T_2	Temperature of housing overhang (front)
3	T_3	Temperature of housing front surface
4	T_4	Temperature of front endcap
5	T_5	Temperature of housing overhang (rear)
6	T_6	Temperature of housing rear surface
7	T_7	Temperature of rear endcap
8	T_8	Temperature of stator lamination (stator yoke back iron)
9	T_9	Temperature of stator bore (inner surface)
10	T_{10}	Temperature of rotor surface
11	T_{11}	Temperature of magnet centre point
12	T_{12}	Temperature of rotor yoke lamination
13	T_{13}	Temperature of shaft centre
14	T_{14}	Temperature of shaft front
15	T_{15}	Temperature of shaft rear
16	T_{16}	Temperature of shaft overhang (front)
17	T_{17}	Temperature of shaft overhang (rear)
18	T_{18}	Temperature of end space (front)
19	T_{19}	Temperature of end space (rear)
20	T_{20}	Temperature of stator sleeve
21	T_{21}	Temperature of rotor banding
22	T_{22}	Temperature of bearing (front)
23	T_{23}	Temperature of bearing (rear)
24	T_{24}	Temperature of rotor lamination (front)
25	T_{25}	Temperature of rotor lamination (rear)
26	T_{26}	Temperature of magnet (front)
27	T_{27}	Temperature of magnet (rear)
28	T_{28}	Temperature of end winding outer (front) - bottom coil (C1)
29	T_{29}	Temperature of end winding end (front) - bottom coil (C1)

Continued on next page

Table A.1: Temperature Nodes in Lumped Parameter Thermal Network (continued)

Node	Temperature	Description
30	T_{30}	Temperature of end winding front (front) - bottom coil (C1)
31	T_{31}	Temperature of end winding rear (front) - bottom coil (C1)
32	T_{32}	Temperature of end winding (front average) - bottom coil (C1)
33	T_{33}	Temperature of end winding outer (rear) - bottom coil (C1)
34	T_{34}	Temperature of end winding end (rear) - bottom coil (C1)
35	T_{35}	Temperature of end winding front (rear) - bottom coil (C1)
36	T_{36}	Temperature of end winding rear (rear) - bottom coil (C1)
37	T_{37}	Temperature of end winding (rear average) - bottom coil (C1)
38	T_{38}	Temperature of wedge - bottom coil (C1)
39	T_{39}	Temperature of slot centre - bottom coil (C1)
40	T_{40}	Temperature of liner - bottom coil (C1)
41	T_{41}	Temperature of liner yoke - bottom coil (C1)
42	T_{42}	Temperature of winding (front) - bottom coil (C1)
43	T_{43}	Temperature of winding (rear) - bottom coil (C1)
44	T_{44}	Temperature of winding (average) - bottom coil (C1)
45	T_{45}	Temperature of stator tooth - bottom coil (C1)
46	T_{46}	Temperature of end winding outer (front) - top coil (C2)
47	T_{47}	Temperature of end winding inner (front) - top coil (C2)
48	T_{48}	Temperature of end winding end (front) - top coil (C2)
49	T_{49}	Temperature of end winding front (front) - top coil (C2)
50	T_{50}	Temperature of end winding rear (front) - top coil (C2)
51	T_{51}	Temperature of end winding (front average) - top coil (C2)
52	T_{52}	Temperature of end winding outer (rear) - top coil (C2)
53	T_{53}	Temperature of end winding inner (rear) - top coil (C2)
54	T_{54}	Temperature of end winding end (rear) - top coil (C2)
55	T_{55}	Temperature of end winding front (rear) - top coil (C2)
56	T_{56}	Temperature of end winding rear (rear) - top coil (C2)
57	T_{57}	Temperature of end winding (rear average) - top coil (C2)
58	T_{58}	Temperature of slot centre - top coil (C2)
59	T_{59}	Temperature of liner - top coil (C2)
60	T_{60}	Temperature of winding inner centre - top coil (C2)
61	T_{61}	Temperature of winding (front) - top coil (C2)
62	T_{62}	Temperature of winding (rear) - top coil (C2)
63	T_{63}	Temperature of winding (average) - top coil (C2)
64	T_{64}	Temperature of stator tooth - top coil (C2)
65	T_{65}	Temperature of fluid inlet
66	T_{66}	Temperature of fluid in cooling channel

A.2 Thermal Resistances

Table A.2 lists all thermal resistances between temperature nodes that are relevant for both the jacket- and slot-cooled machine variants, as shown in Figure 2.19.

Table A.2: Common thermal resistances in Lumped Parameter Thermal Network

Nodes	Resistance	Description
0-1	R_{0-1}	Thermal resistance between ambient environment and active housing part
0-2	R_{0-2}	Thermal resistance between ambient environment and housing overhang (front)
0-4	R_{0-4}	Thermal resistance between ambient environment and front endcap
0-5	R_{0-5}	Thermal resistance between ambient environment and housing overhang (rear)
0-7	R_{0-7}	Thermal resistance between ambient environment and rear endcap
0-14	R_{0-14}	Thermal resistance between ambient environment and shaft front
0-15	R_{0-15}	Thermal resistance between ambient environment and shaft rear

Continued on next page

Table A.2: Common thermal resistances in Lumped Parameter Thermal Network (continued)

Nodes	Resistance	Description
1-2	R_{1-2}	Thermal resistance between active housing part and housing overhang (front)
1-5	R_{1-5}	Thermal resistance between active housing part and housing overhang (rear)
1-8	R_{1-8}	Thermal resistance between active housing part and stator lamination (stator yoke back iron)
2-3	R_{2-3}	Thermal resistance between housing overhang (front) and housing front surface
2-18	R_{2-18}	Thermal resistance between housing overhang (front) and end space (front)
3-4	R_{3-4}	Thermal resistance between housing front surface and front endcap
4-18	R_{4-18}	Thermal resistance between front endcap and end space (front)
4-22	R_{4-22}	Thermal resistance between front endcap and bearing (front)
5-6	R_{5-6}	Thermal resistance between housing overhang (rear) and housing rear surface
5-19	R_{5-19}	Thermal resistance between housing overhang (rear) and end space (rear)
6-7	R_{6-7}	Thermal resistance between housing rear surface and rear endcap
7-19	R_{7-19}	Thermal resistance between rear endcap and end space (rear)
7-23	R_{7-23}	Thermal resistance between rear endcap and bearing (rear)
8-39	R_{8-39}	Thermal resistance between stator lamination (stator yoke back iron) and slot centre - bottom coil (C1)
8-41	R_{8-41}	Thermal resistance between stator lamination (stator yoke back iron) and liner yoke - bottom coil (C1)
8-45	R_{8-45}	Thermal resistance between stator lamination (stator yoke back iron) and stator tooth - bottom coil (C1)
9-20	R_{9-20}	Thermal resistance between stator bore (inner surface) and stator sleeve
9-38	R_{9-38}	Thermal resistance between stator bore (inner surface) and wedge - bottom coil (C1)
9-64	R_{9-64}	Thermal resistance between stator bore (inner surface) and stator tooth - top coil (C2)
10-20	R_{10-20}	Thermal resistance between rotor surface and stator sleeve
10-21	R_{10-21}	Thermal resistance between rotor surface and rotor banding
11-12	R_{11-12}	Thermal resistance between magnet centre point and rotor yoke lamination
11-21	R_{11-21}	Thermal resistance between magnet centre point and rotor banding
11-26	R_{11-26}	Thermal resistance between magnet centre point and magnet (front)
11-27	R_{11-27}	Thermal resistance between magnet centre point and magnet (rear)
12-13	R_{12-13}	Thermal resistance between rotor yoke lamination and shaft centre
12-24	R_{12-24}	Thermal resistance between rotor yoke lamination and rotor lamination (front)
12-25	R_{12-25}	Thermal resistance between rotor yoke lamination and rotor lamination (rear)
13-16	R_{13-16}	Thermal resistance between shaft centre and shaft overhang (front)
13-17	R_{13-17}	Thermal resistance between shaft centre and shaft overhang (rear)
14-16	R_{14-16}	Thermal resistance between shaft front and shaft overhang (front)
14-22	R_{14-22}	Thermal resistance between shaft front and bearing (front)
15-17	R_{15-17}	Thermal resistance between shaft rear and shaft overhang (rear)
15-23	R_{15-23}	Thermal resistance between shaft rear and bearing (rear)
16-18	R_{16-18}	Thermal resistance between shaft overhang (front) and end space (front)
17-19	R_{17-19}	Thermal resistance between shaft overhang (rear) and end space (rear)
18-22	R_{18-22}	Thermal resistance between end space (front) and bearing (front)
18-24	R_{18-24}	Thermal resistance between end space (front) and rotor lamination (front)
18-26	R_{18-26}	Thermal resistance between end space (front) and magnet (front)
18-28	R_{18-28}	Thermal resistance between end space (front) and end winding outer (front) - bottom coil (C1)
18-30	R_{18-30}	Thermal resistance between end space (front) and end winding front (front) - bottom coil (C1)
18-47	R_{18-47}	Thermal resistance between end space (front) and end winding inner (front) - top coil (C2)
18-49	R_{18-49}	Thermal resistance between end space (front) and end winding front (front) - top coil (C2)
18-65	R_{18-65}	Thermal resistance between end space (front) and fluid inlet
18-66	R_{18-66}	Thermal resistance between end space (front) and fluid in cooling channel
19-23	R_{19-23}	Thermal resistance between end space (rear) and bearing (rear)
19-25	R_{19-25}	Thermal resistance between end space (rear) and rotor lamination (rear)
19-27	R_{19-27}	Thermal resistance between end space (rear) and magnet (rear)

Continued on next page

Table A.2: Common thermal resistances in Lumped Parameter Thermal Network (continued)

Nodes	Resistance	Description
19-33	R_{19-33}	Thermal resistance between end space (rear) and end winding outer (rear) - bottom coil (C1)
19-36	R_{19-36}	Thermal resistance between end space (rear) and end winding rear (rear) - bottom coil (C1)
19-53	R_{19-53}	Thermal resistance between end space (rear) and end winding inner (rear) - top coil (C2)
19-56	R_{19-56}	Thermal resistance between end space (rear) and end winding rear (rear) - top coil (C2)
19-66	R_{19-66}	Thermal resistance between end space (rear) and fluid in cooling channel
28-32	R_{28-32}	Thermal resistance between end winding outer (front) - bottom coil (C1) and end winding (front average) - bottom coil (C1)
28-46	R_{28-46}	Thermal resistance between end winding outer (front) - bottom coil (C1) and end winding outer (front) - top coil (C2)
29-32	R_{29-32}	Thermal resistance between end winding end (front) - bottom coil (C1) and end winding (front average) - bottom coil (C1)
29-42	R_{29-42}	Thermal resistance between end winding end (front) - bottom coil (C1) and winding (front) - bottom coil (C1)
30-31	R_{30-31}	Thermal resistance between end winding front (front) - bottom coil (C1) and end winding rear (front) - bottom coil (C1)
30-32	R_{30-32}	Thermal resistance between end winding front (front) - bottom coil (C1) and end winding (front average) - bottom coil (C1)
31-32	R_{31-32}	Thermal resistance between end winding rear (front) - bottom coil (C1) and end winding (front average) - bottom coil (C1)
32-42	R_{32-42}	Thermal resistance between end winding (front average) - bottom coil (C1) and winding (front) - bottom coil (C1)
32-46	R_{32-46}	Thermal resistance between end winding (front average) - bottom coil (C1) and end winding outer (front) - top coil (C2)
33-37	R_{33-37}	Thermal resistance between end winding outer (rear) - bottom coil (C1) and end winding (rear average) - bottom coil (C1)
33-52	R_{33-52}	Thermal resistance between end winding outer (rear) - bottom coil (C1) and end winding outer (rear) - top coil (C2)
34-37	R_{34-37}	Thermal resistance between end winding end (rear) - bottom coil (C1) and end winding (rear average) - bottom coil (C1)
34-43	R_{34-43}	Thermal resistance between end winding end (rear) - bottom coil (C1) and winding (rear) - bottom coil (C1)
35-36	R_{35-36}	Thermal resistance between end winding front (rear) - bottom coil (C1) and end winding rear (rear) - bottom coil (C1)
35-37	R_{35-37}	Thermal resistance between end winding front (rear) - bottom coil (C1) and end winding (rear average) - bottom coil (C1)
36-37	R_{36-37}	Thermal resistance between end winding rear (rear) - bottom coil (C1) and end winding (rear average) - bottom coil (C1)
37-43	R_{37-43}	Thermal resistance between end winding (rear average) - bottom coil (C1) and winding (rear) - bottom coil (C1)
37-52	R_{37-52}	Thermal resistance between end winding (rear average) - bottom coil (C1) and end winding outer (rear) - top coil (C2)
38-60	R_{38-60}	Thermal resistance between wedge - bottom coil (C1) and winding inner centre - top coil (C2)
38-63	R_{38-63}	Thermal resistance between wedge - bottom coil (C1) and winding (average) - top coil (C2)
39-40	R_{39-40}	Thermal resistance between slot centre - bottom coil (C1) and liner - bottom coil (C1)
39-44	R_{39-44}	Thermal resistance between slot centre - bottom coil (C1) and winding (average) - bottom coil (C1)
39-66	R_{39-66}	Thermal resistance between slot centre - bottom coil (C1) and fluid in cooling channel
40-44	R_{40-44}	Thermal resistance between liner - bottom coil (C1) and winding (average) - bottom coil (C1)
40-45	R_{40-45}	Thermal resistance between liner - bottom coil (C1) and stator tooth - bottom coil (C1)

Continued on next page

Table A.2: Common thermal resistances in Lumped Parameter Thermal Network (continued)

Nodes	Resistance	Description
41-44	R_{41-44}	Thermal resistance between liner yoke - bottom coil (C1) and winding (average) - bottom coil (C1)
41-60	R_{41-60}	Thermal resistance between liner yoke - bottom coil (C1) and winding inner centre - top coil (C2)
42-43	R_{42-43}	Thermal resistance between winding (front) - bottom coil (C1) and winding (rear) - bottom coil (C1)
42-44	R_{42-44}	Thermal resistance between winding (front) - bottom coil (C1) and winding (average) - bottom coil (C1)
43-44	R_{43-44}	Thermal resistance between winding (rear) - bottom coil (C1) and winding (average) - bottom coil (C1)
44-60	R_{44-60}	Thermal resistance between winding (average) - bottom coil (C1) and winding inner centre - top coil (C2)
45-64	R_{45-64}	Thermal resistance between stator tooth - bottom coil (C1) and stator tooth - top coil (C2)
46-47	R_{46-47}	Thermal resistance between end winding outer (front) - top coil (C2) and end winding inner (front) - top coil (C2)
46-51	R_{46-51}	Thermal resistance between end winding outer (front) - top coil (C2) and end winding (front average) - top coil (C2)
47-51	R_{47-51}	Thermal resistance between end winding inner (front) - top coil (C2) and end winding (front average) - top coil (C2)
48-51	R_{48-51}	Thermal resistance between end winding end (front) - top coil (C2) and end winding (front average) - top coil (C2)
48-61	R_{48-61}	Thermal resistance between end winding end (front) - top coil (C2) and winding (front) - top coil (C2)
49-50	R_{49-50}	Thermal resistance between end winding front (front) - top coil (C2) and end winding rear (front) - top coil (C2)
49-51	R_{49-51}	Thermal resistance between end winding front (front) - top coil (C2) and end winding (front average) - top coil (C2)
50-51	R_{50-51}	Thermal resistance between end winding rear (front) - top coil (C2) and end winding (front average) - top coil (C2)
51-61	R_{51-61}	Thermal resistance between end winding (front average) - top coil (C2) and winding (front) - top coil (C2)
52-53	R_{52-53}	Thermal resistance between end winding outer (rear) - top coil (C2) and end winding inner (rear) - top coil (C2)
52-57	R_{52-57}	Thermal resistance between end winding outer (rear) - top coil (C2) and end winding (rear average) - top coil (C2)
53-57	R_{53-57}	Thermal resistance between end winding inner (rear) - top coil (C2) and end winding (rear average) - top coil (C2)
54-57	R_{54-57}	Thermal resistance between end winding end (rear) - top coil (C2) and end winding (rear average) - top coil (C2)
54-62	R_{54-62}	Thermal resistance between end winding end (rear) - top coil (C2) and winding (rear) - top coil (C2)
55-56	R_{55-56}	Thermal resistance between end winding front (rear) - top coil (C2) and end winding rear (rear) - top coil (C2)
55-57	R_{55-57}	Thermal resistance between end winding front (rear) - top coil (C2) and end winding (rear average) - top coil (C2)
56-57	R_{56-57}	Thermal resistance between end winding rear (rear) - top coil (C2) and end winding (rear average) - top coil (C2)
57-62	R_{57-62}	Thermal resistance between end winding (rear average) - top coil (C2) and winding (rear) - top coil (C2)
58-59	R_{58-59}	Thermal resistance between slot centre - top coil (C2) and liner - top coil (C2)
58-63	R_{58-63}	Thermal resistance between slot centre - top coil (C2) and winding (average) - top coil (C2)
58-66	R_{58-66}	Thermal resistance between slot centre - top coil (C2) and fluid in cooling channel
59-63	R_{59-63}	Thermal resistance between liner - top coil (C2) and winding (average) - top coil (C2)
59-64	R_{59-64}	Thermal resistance between liner - top coil (C2) and stator tooth - top coil (C2)

Continued on next page

Table A.2: Common thermal resistances in Lumped Parameter Thermal Network (continued)

Nodes	Resistance	Description
60-63	R_{60-63}	Thermal resistance between winding inner centre - top coil (C2) and winding (average) - top coil (C2)
61-62	R_{61-62}	Thermal resistance between winding (front) - top coil (C2) and winding (rear) - top coil (C2)
61-63	R_{61-63}	Thermal resistance between winding (front) - top coil (C2) and winding (average) - top coil (C2)
62-63	R_{62-63}	Thermal resistance between winding (rear) - top coil (C2) and winding (average) - top coil (C2)

In addition, Table A.3 lists the resistances required exclusively for the jacket-cooled variant, while Table A.4 applies to slot-cooled topologies. These tables correspond to the network extensions shown in Figure 2.20.

Table A.3: Additional thermal resistances in Lumped Parameter Thermal Network for jacket cooled machines

Nodes	Resistance	Description
1-66	R_{1-66}	Thermal resistance between active housing part and fluid in cooling channel
2-66	R_{2-66}	Thermal resistance between housing overhang (front) and fluid in cooling channel
5-66	R_{5-66}	Thermal resistance between housing overhang (rear) and fluid in cooling channel
65-66	R_{65-66}	Thermal resistance between fluid inlet and fluid in cooling channel

Table A.4: Additional thermal resistances in Lumped Parameter Thermal Network for slot cooled machines

Nodes	Resistance	Description
18-65	R_{18-65}	Thermal resistance between end space (front) and fluid inlet
18-66	R_{18-66}	Thermal resistance between end space (front) and fluid in cooling channel
19-66	R_{19-66}	Thermal resistance between end space (rear) and fluid in cooling channel
39-66	R_{39-66}	Thermal resistance between slot centre - bottom coil (C1) and fluid in cooling channel
58-66	R_{58-66}	Thermal resistance between slot centre - top coil (C2) and fluid in cooling channel

B Finite Element Verification of the Design Proposal

This appendix presents the finite element verification of the electric machine and DC-AC inverter designs proposed in Section 4.6. The objective is to assess the accuracy and robustness of the proposed analytical models by comparing their performance predictions against numerical reference results obtained through finite element simulations. The verification covers the electromagnetic, thermal, and structural behaviour of the electric machine, as well as the electro-thermal performance of the inverter.

B.1 Verification of Electric Machine

Table B.1 summarizes the key performance characteristics of the electric machine design resulting from the parameterization detailed in Table 4.17. The listed values include both analytical results from the proposed electromagnetic subdomain model and the lumped parameter thermal network and numerical results obtained through finite element analysis using Ansys Motor-CAD®.

Table B.1: Performance characteristics of the electric machine for the selected system design proposal of a ten-propeller configuration. Includes absolute and relative comparison between analytical model predictions and finite element simulation results.

Parameter	**Symbol**	**Unit**	**Value**		**Error**
			analytical	**FE**	
Machine diameter	d_{EM}	mm	471		-
Machine length	l_{EM}	mm	65		-
Shaft speed	n_{EM}	min^{-1}	2000		-
Output continuous torque	$T_{\mathrm{cont,EM}}$	N m	405.98	385.75	4.98 %
Output continuous power	$P_{\mathrm{cont,EM}}$	kW	85.03	80.79	4.98 %
Peak back-EMF (phase)	$\hat{e}_{\mathrm{ph}}$	V	146.20	137.28	6.10 %
d-axis inductance	L_{d}	µH	47.66	47.05	1.29 %
q-axis inductance	L_{q}	µH	47.66	51.00	−7.01 %
Power factor	$\cos\varphi_{\mathrm{PF}}$	-	0.68	0.64	6.16 %
Flux density in stator tooth	$B_{\mathrm{st,max}}$	T	1.94	1.81	6.66 %
Flux density in stator yoke	$B_{\mathrm{sy,max}}$	T	1.91	2.06	−7.89 %
Iron losses	$Q_{\mathrm{EM,Fe}}$	W	592.56	575.52	2.87 %
Copper winding losses	$Q_{\mathrm{EM,Cu}}$	W	4514.92	4576.42	−1.36 %
Magnet temperature	T_{mag}	°C	139.84	139.93	−0.07 %
Winding average temperature	$T_{\mathrm{wdg,avg}}$	°C	175.36	175.91	0.30 %
Winding max. temperature	$T_{\mathrm{wdg,max}}$	°C	192.62	193.32	−0.36 %

The deviations between the analytical and numerical results of the electromagnetic properties are generally small, typically well within 10 %, and can be attributed to the idealized assumptions inherent in the subdomain model. This model presumes linear magnetic material behavior, simplified slot and magnet geometries, and idealized winding distributions. As a result, it introduces slight over- or underestimations in parameters such as torque, flux density, and back-EMF. Notably, local saturation effects are not accounted for, which contributes to discrepancies particularly in regions with high flux concentration, such as

the stator yoke and teeth.
A closer look into the electromagnetics of the design supports this reasoning. Figure B.1 compares the analytical and numerical results of the radial and tangential airgap flux density, stator tooth flux density and the vector potential in the slot at the stator yoke surface, which is used to calculate the stator yoke flux density.

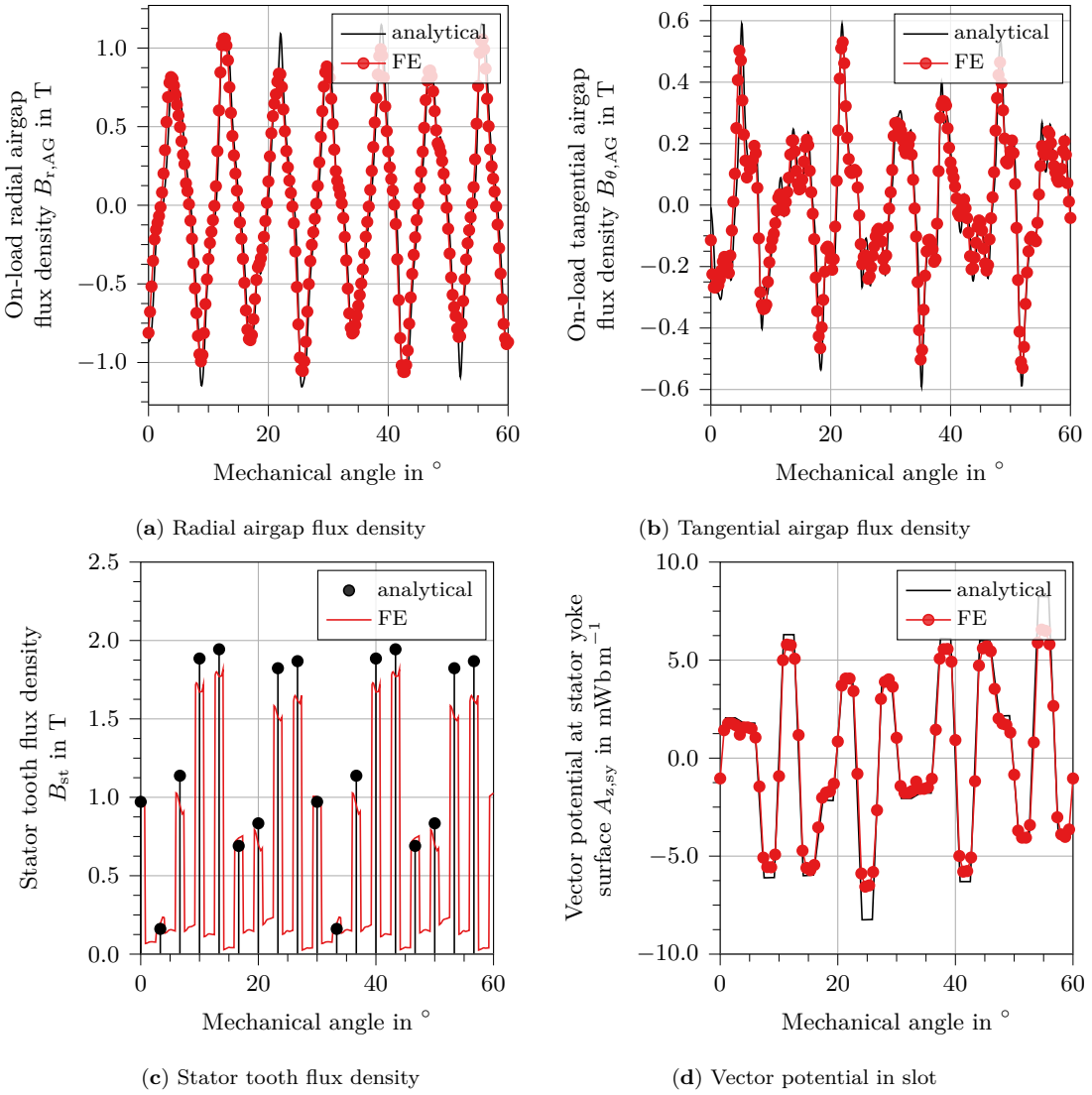

(**a**) Radial airgap flux density

(**b**) Tangential airgap flux density

(**c**) Stator tooth flux density

(**d**) Vector potential in slot

Figure B.1: Overview of the electromagnetic characteristics of the proposed electric machine design, comparing analytical and numerical results, including radial and tangential airgap flux densities, stator tooth flux density, and the vector potential in the slot, which is used to calculate the stator yoke flux density.

The radial and tangential airgap flux densities in Figures B.1a and B.1b show very good agreement in overall shape and peak positions. However, some peak values deviate by up to 20 %. These differences can be attributed to the analytical method's overestimation of torque and back-EMF, as these are calculated using the Maxwell stress tensor.
The vector potential at the stator yoke surface in Figure B.1d is overestimated in the analytical model. However, finite element results indicate even higher flux densities at this location, suggesting the influence of saturation effects that are not accounted for in the analytical model.
The flux densities in the stator teeth in Figure B.1c also show a good match between the analytical and numerical results. However, the analytical values tend to be slightly higher, which indicates an underestimation of leakage flux in the analytical model. This

underestimation would result in a higher flux density in the stator teeth compared to the finite element results.
The deviations in back-EMF and inductances due to saturation and leakage effects directly contribute to the error in the calculation of the power factor.
The deviations in stator tooth and yoke flux densities are also the primary drivers of the error in the iron loss calculation. Due to the opposing tendencies of over- and underestimation, the resulting iron losses remain only slightly off. For the copper losses, the small discrepancy arises from differences in the calculated end-winding length. Nevertheless, the overall errors are minimal. This, in turn, positively impacts the accuracy of the thermal analysis. As shown in Figure B.2, the relative error in temperature prediction remains well below 1 % for all nodes of the lumped parameter thermal network.

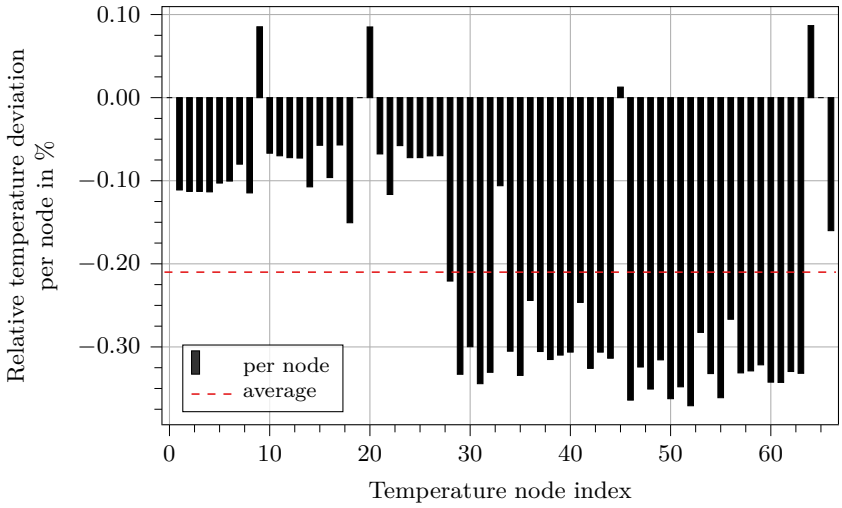

Figure B.2: Relative and average temperature deviation across the lumped parameter thermal network for the proposed electric machine design, comparing analytical and numerical results.

Despite these deviations, the electric machine model demonstrates sufficient accuracy for optimization tasks, providing an excellent balance between predictive fidelity and computational efficiency.

B.2 Verification of DC-AC Inverter

Table B.2 summarizes the key performance characteristics of the DC-AC inverter resulting from the parameterization shown in Table 4.19. The listed values include both analytical results from the proposed electro-thermal model and numerical results obtained using finite element simulations via Semikron's online tool SemiSel™.
As shown, the inverter delivers approximately 91 kV A to meet the power demand of the electric machine, while the DC-link capacitor maintains a voltage ripple well below the limits specified in Table 4.8. The numerical evaluation reveals that conduction losses of the transistor and diode are overestimated by around 10 %, leading to a similar deviation in the total semiconductor losses. Transistor switch-off losses are underestimated by more than 15 %, although their absolute values remain low. Other switching losses, including switch-on and reverse recovery, show very good agreement between the analytical and numerical results. These deviations can primarily be attributed to the digitalization of datasheet values and, in the case of conduction losses, to the estimation of on-state resistance via differentiation of the forward output characteristic. This method is sensitive to steep slopes, which can introduce notable errors in resistance and loss calculations.

Table B.2: Performance characteristics of the DC-AC inverter for the selected system design proposal of a ten-propeller configuration. Includes absolute and relative comparison between analytical model predictions and numerical simulation results.

Parameter	**Symbol**	**Unit**	**Value**		**Error**
			analytical	**FE**	
Inverter dimensions (L x W x H)	-	mm	250 x 250 x 100		-
DC Link voltage range	V_{DC}	volt	540 – 900		-
Output line-line voltage	$\hat{V}_{\mathrm{AC,LL}}$	V	274		-
Output line current	$\hat{I}_{\mathrm{AC,LL}}$	A	395		-
Output line current	$\hat{I}_{\mathrm{AC,LL}}$	kV A	91		-
Switching frequency	f_{sw}	kHz	14		-
DC Link voltage ripple	$\Delta V_{\mathrm{Cap,rel}}$	-	0.04		-
Transistor conduction losses	$Q_{\mathrm{con,T}}$	W	80.75	73.66	9.63 %
Transistor switch-on losses	$Q_{\mathrm{sw,on,T}}$	W	10.04	9.87	1.72 %
Transistor switch-off losses	$Q_{\mathrm{sw,off,T}}$	W	6.84	8.18	−16.38 %
Diode conduction losses	$Q_{\mathrm{con,D}}$	W	26.59	24.10	10.33 %
Diode switch-off losses	$Q_{\mathrm{sw,on,D}}$	W	8.08	7.75	4.25 %
Total semiconductor losses	Q_{SC}	W	1587.55	1428.51	11.13 %
Transistor junction temperature	$T_{\mathrm{j,T}}$	°C	139.89	139.46	0.31 %
Diode junction temperature	$T_{\mathrm{j,D}}$	°C	139.89	139.46	0.31 %

Despite these discrepancies, the calculated junction temperatures of both the transistor and diode closely match the numerical reference. Overall, the agreement between analytical and numerical evaluation is sufficiently accurate for use in early-stage design and optimization.

Abbreviations

2L	Two-Level
3LNPC	Three-Level Neutral Point Clamped
3LTNPC	Three-Level T-Type Neutral Point Clamped
AC	Alternating Current
AGE-MOEA	Adaptive Geometry Estimation-based Multi-Objective Evolutionary Algorithm
AGMA	American Gear Manufacturers Association
AoA	Angle of Attack
ASTM	American Society for Testing and Materials
AWG	American Wire Gauge
CCM	Continuous Conduction Mode
CO_2	Carbon Dioxide
CS	Certification Specification
DC	Direct Current
DCM	Discontinuous Conduction Mode
DFT	Discrete Fourier Transform
DOD	Depth of Discharge
DOE	Design of Experiments
EASA	European Union Aviation Safety Agency
EM	Electric Machine
EMF	Electromotive Force
EPDS	Electric Power Distribution System
EPS	Electric Propulsion System
EPU	Electric Propulsion Unit
ESS	Energy Storage System
FE	Finite Element
FIT	Failures In Time
GB	Gearbox
GD	Generational Distance
H_2O	Water
HV	Hypervolume
HX	Heat Exchanger
IEA	International Energy Agency
IEC	International Electrotechnical Commission
IGBT	Insulated Gate Bipolar Transistor
IGD	Inverted Generational Distance
ISA	International Standard Atmosphere
ISO	International Organization for Standardization
LC	Inductor-Capacitor
LPTN	Lumped Parameter Thermal Network
MICADO	Multidisciplinary Integrated Conceptual Aircraft Design and Optimization
MMF	Magnetomotive Force
MOSFET	Metal-Oxide-Semiconductor Field-Effect Transistor

MOEA	Multi-Objective Evolutionary Algorithm
MTOW	Maximum Takeoff Weight
NASA	National Aeronautics and Space Administration
NO_x	Nitrogen Oxide
NSGA-II	Non-dominated Sorting Genetic Algorithm II
NSGA-III	Non-dominated Sorting Genetic Algorithm III
NTU	Number of Transfer Units
OSF	Offset Strip Fin
PFA	Perfluoroalkoxy alkanes
PMSM	Permanent Magnet Synchronous Machine
PWM	Pulse Width Modulation
RMS	Root Mean Square
RPK	Revenue Passenger Kilometer
SiC	Silicon Carbide
SOC	State of Charge
SO_x	Sulphur Oxide
SUAVE	Stanford University Aerospace Vehicle Environment
SVM	Space Vector Modulation
TLAR	Top Level Aircraft Requirements
U-NSGA-III	Unified Non-dominated Sorting Genetic Algorithm III
VTOL	Vertical Take-Off and Landing
WDT	Winding Distribution Table

List of Symbols

Constants

Symbol	Unit	Description
μ_0	$\mathrm{H\,m^{-1}}$	Magnetic permeability of vacuum
π	-	Circle constant, ratio of circumference to diameter
σ_{SB}	$\mathrm{W\,m^{-2}\,K^{-4}}$	Stefan-Boltzmann constant
e	-	Euler number
g	$\mathrm{m\,s^{-2}}$	Gravitational acceleration

Greek Symbols

Symbol	Unit	Description
α_{AoA}	rad	Angle of attack
α_{Cab}	$\mathrm{W\,m^{-2}\,K^{-1}}$	Convective heat transfer coefficient for cable
α_{cell}	$\mathrm{W\,m^{-2}\,K^{-1}}$	Convective heat transfer coefficient for cell
α_{conv}	$\mathrm{W\,m^{-2}\,K^{-1}}$	Convective heat transfer coefficient
$\alpha_{\mathrm{E,D}}$	$\mathrm{K^{-1}}$	Temperature coefficient for diode switching losses
$\alpha_{\mathrm{E,T}}$	$\mathrm{K^{-1}}$	Temperature coefficient for transistor switching losses
α_{k}	-	Inclination of discretized trapezoidal layer
α_{p}	-	Magnet pole width to pole pitch ratio
α_{rad}	$\mathrm{W\,m^{-2}\,K^{-1}}$	Radiation heat transfer coefficient
$\alpha_{r_{\mathrm{on,T}}}$	$\mathrm{\Omega\,K^{-1}}$	Temperature coefficient of transistor on-state resistance
α_{T}	$\mathrm{K^{-1}}$	Thermal expansion coefficient
α_{tot}	$\mathrm{W\,m^{-2}\,K^{-1}}$	Total heat transfer coefficient
$\alpha_{V_{\mathrm{CE,0}}}$	$\mathrm{V\,K^{-1}}$	Temperature coefficient of transistor threshold voltage
β	$\mathrm{K^{-1}}$	Thermal expansion coefficient
$\beta_{\mathrm{cc,h}}$	-	Cooling channel height ratio
$\beta_{\mathrm{cc,w}}$	-	Cooling channel width ratio
β_{Fin}	-	Fin width ratio
$\beta_{\mathrm{Fin,c}}$	-	Fin thickness ratio on cold side
$\beta_{\mathrm{Fin,h}}$	-	Fin thickness ratio on hot side
β_{HX}	$\mathrm{m^{-1}}$	Surface area density of heat exchanger
$\beta_{\mathrm{ph,ins}}$	-	Phase insulation width ratio
$\beta_{\mathrm{sy,i}}$	-	Stator tooth width to slot pitch ratio
$\beta_{\mathrm{tt,c}}$	-	Tooth tip center to slot pitch ratio
$\beta_{\mathrm{tt,e}}$	-	Tooth tip edge to slot pitch ratio
Δh_{k}	m	Radial height of discretized layer
Δh_{sg}	m	Height parameter for slot geometry

$\Delta I_{\mathrm{DC,L}}$	A	Harmonic content of inverter input current
ΔI_{L}	A	Current ripple in inductor
Δm_{ESS}	kg	Change in energy storage system mass
Δp	Pa	Pressure drop
Δp_{c}	Pa	Pressure drop on cold side
Δp_{h}	kPa	Pressure drop on hot side
ΔS	$\mathrm{J\,mol^{-1}\,K^{-1}}$	Entropy change
Δs_{k}	m	Edge length of discretized layer
ΔT	K	Temperature difference
ΔT_{c}	K	Temperature increase on cold side
ΔT_{h}	K	Temperature increase on hot side
δ	m	Interference
$\underline{\delta}$	m	Interference vector
Δh_{k}	m	Radial height of discretized layer
Δh_{sg}	m	Height parameter for slot geometry
$\Delta I_{\mathrm{DC,L}}$	A	Harmonic content of inverter input current
ΔI_{L}	A	Current ripple in inductor
Δm_{ESS}	kg	Change in energy storage system mass
Δp	Pa	Pressure drop
Δp_{c}	Pa	Pressure drop on cold side
Δp_{h}	kPa	Pressure drop on hot side
$\underline{\delta}_{\mathrm{Q}}$	m	Interference due to thermal loads
$\underline{\delta}_{\mathrm{rot}}$	m	Interference due to rotation
ΔS	$\mathrm{J\,mol^{-1}\,K^{-1}}$	Entropy change
Δs_{k}	m	Edge length of discretized layer
$\underline{\delta}_{\mathrm{stat}}$	m	Interference due to static pressure
ΔT	K	Temperature difference
ΔT_{c}	K	Temperature increase on cold side
ΔT_{h}	K	Temperature decrease on hot side
ΔV_{cell}	V	Cell overpotential
$\Delta V_{\mathrm{cell,corr}}$	V	Overpotential correction factor
$\Delta V_{\mathrm{Cap,rel}}$	-	Relative voltage ripple of capacitor
ΔV_{in}	V	Input voltage
ΔV_{out}	V	Output voltage
$\Delta V_{\mathrm{pp,DC}}$	V	Peak-to-peak voltage ripple
Δz^{id}	-	Change in ideal point
Δz^{nad}	-	Change in nadir point
$\Delta \eta_{\mathrm{EPS}}$	-	Change in electric propulsion system efficiency
δ_{skin}	m	Skin penetration depth
ΔV_{cell}	V	Cell overpotential
$\Delta V_{\mathrm{cell,corr}}$	V	Overpotential correction factor
$\Delta V_{\mathrm{Cap,rel}}$	-	Relative voltage ripple of capacitor
ΔV_{in}	V	Input voltage
ΔV_{out}	V	Output voltage
$\Delta V_{\mathrm{pp,DC}}$	V	Peak-to-peak voltage ripple
Δz^{id}	-	Change in ideal point
Δz^{nad}	-	Change in nadir point
$\Delta \eta_{\mathrm{EPS}}$	-	Change in electric propulsion system efficiency
δ	m	Interference
$\underline{\delta}$	m	Interference vector
$\underline{\delta}_{\mathrm{Q}}$	m	Interference due to thermal loads

$\underline{\delta}_{\mathrm{rot}}$	m	Interference due to rotation
δ_{skin}	m	Skin penetration depth
$\underline{\delta}_{\mathrm{stat}}$	m	Interference due to static pressure
ϵ	-	Ratio of loss source area to base surface area
ϵ_{rad}	-	Radial strain
ϵ_{tan}	-	Tangential strain
ε	-	Emissivity
$\varepsilon_{\mathrm{cell}}$	-	Cell emissivity
$\varepsilon_{\mathrm{eff}}$	-	Effective emissivity factor
$\varepsilon_{\mathrm{HX}}$	-	Heat exchanger effectiveness
$\varepsilon_{\mathrm{opt}}$	-	Allowable average change in objective space
ε_{r}	$\mathrm{V\,m^{-1}}$	Dielectric strength
η_{c}	-	Crossover rate
$\eta_{\mathrm{comp,i}}$	-	Efficiency of component i
η_{el}	-	Electrical efficiency
η_{EM}	-	Efficiency of electric machine
η_{EPS}	-	Total efficiency of electric propulsion system
η_{EPU}	-	Efficiency of electric propulsion unit
η_{fin}	-	Fin surface efficiency
η_{GB}	-	Total gearbox efficiency
η_{m}	-	Mutation rate
η_{mech}	-	Mechanical efficiency
η_{o}	-	Overall fin surface efficiency
η_{Prop}	-	Propeller efficiency
$\eta_{\mathrm{st,i}}$	-	Efficiency of individual gearbox stage
λ	$\mathrm{W\,m^{-1}\,K^{-1}}$	Thermal conductivity
λ_{ax}	$\mathrm{W\,m^{-1}\,K^{-1}}$	Axial thermal conductivity
λ_{cond}	$\mathrm{W\,m^{-1}\,K^{-1}}$	Thermal conductivity of conductor
λ_{FIT}	FIT	Failure In Time rate
$\lambda_{\mathrm{impreg}}$	$\mathrm{W\,m^{-1}\,K^{-1}}$	Thermal conductivity of impregnation material
λ_{ins}	$\mathrm{W\,m^{-1}\,K^{-1}}$	Thermal conductivity of insulation
λ_{rad}	$\mathrm{W\,m^{-1}\,K^{-1}}$	Radial thermal conductivity
λ_{sep}	$\mathrm{W\,m^{-1}\,K^{-1}}$	Thermal conductivity of separator
λ_{tan}	$\mathrm{W\,m^{-1}\,K^{-1}}$	Tangential thermal conductivity
$\lambda_{\mathrm{wire,ins}}$	$\mathrm{W\,m^{-1}\,K^{-1}}$	Thermal conductivity of wire insulation
μ	Pa s	Dynamic viscosity
μ_{eff}	-	Effective relative permeability
μ_{r}	-	Relative permeability
ν	-	Harmonic order
ν	$\mathrm{m^2\,s^{-1}}$	Kinematic viscosity
ν_{rt}	-	Poisson's ratio in tangential direction due to radial stress
ν_{tr}	-	Poisson's ratio in radial direction due to tangential stress
ω	$\mathrm{rad\,s^{-1}}$	Angular velocity
ω_{el}	$\mathrm{rad\,s^{-1}}$	Electrical angular speed
ω_{nom}	$\mathrm{rad\,s^{-1}}$	Nominal angular velocity
ω_{opt}	-	Sliding window for optimization
Φ	Wb	Magnetic flux per turn
Φ_{m}	Wb	Main flux
Φ_{σ}	Wb	Leakage flux
$\Phi_{\mathrm{st,i}}$	Wb	Flux entering the i-th tooth
φ	-	Coefficient for non-circular form of rectangular slots

φ_I	rad	Current angle relative to direct axis
φ_PF	rad	Power factor angle
φ_U	rad	Voltage angle relative to direct axis
Ψ_B	-	Bilitzky's geometrical coefficient
Ψ_i	Wb	Flux linkage of a single coil side in i-th slot
Ψ_m	Wb	Main flux-linkage
Ψ_ph	Wb	Flux linkage per phase
Ψ_σ	Wb	Leakage flux-linkage
ρ	$\mathrm{kg\,m^{-3}}$	Density
ρ_Amb	$\mathrm{kg\,m^{-3}}$	Ambient air density
ρ_cond	$\mathrm{kg\,m^{-3}}$	Density of conductor material
ρ_el	$\Omega\,\mathrm{m}$	Electrical resistivity
ρ_i	$\mathrm{kg\,m^{-3}}$	Fluid density at inlet
ρ_ins	$\mathrm{kg\,m^{-3}}$	Density of insulation material
ρ_m	$\mathrm{kg\,m^{-3}}$	Mean density
ρ_o	$\mathrm{kg\,m^{-3}}$	Fluid density at outlet
σ	-	Porosity
σ_el	$\mathrm{S\,m^{-1}}$	Electrical conductivity of conductor material
σ_HX	-	Porosity of heat exchanger surface
σ_rad	Pa	Radial stress
σ_tan	Pa	Tangential stress
σ_vMises	Pa	Von Mises equivalent stress
$\sigma_{\mathrm{y},i}$	Pa	Yield strength of the i-th layer
$\tau_{\mathrm{avg},i}$	Pa	Average shear stress in the i-th section
τ_c	-	Coil pitch parameter
τ_p	rad	Pole pitch
τ_s	rad	Slot pitch
$\boldsymbol{\Theta}$	K	Temperature vector
$\Theta_\mathrm{u/v/w}$	A	Ampere-turns per slot for each phase
θ	rad	Angular coordinate
θ_0	rad	Initial angular position
θ_i	rad	Angular position of i-th slot
θ_in	rad	Inner angle of cylinder segment
θ_m	rad	Angular span of magnet
θ_out	rad	Outer angle of cylinder segment
$\theta_\mathrm{sy,i}$	rad	Angular width of inner stator yoke
$\theta_\mathrm{tt,c}$	rad	Angular width of tooth tip center
$\theta_\mathrm{tt,e}$	rad	Angular width of tooth tip edge
ξ	-	Row shift parameter for WDT
ξ_a	-	Geometrical factor for slot permeance
ζ	-	Pressure loss coefficient

Latin Symbols

Symbol	Unit	Description
A	$\mathrm{m^2}$	Surface or cross-sectional area
A_bb	$\mathrm{m^2}$	Bus bar cross-sectional area

A_c	m^2	Free-flow cross-sectional area
A_cond	m^2	Cross-sectional area of conductor
A_cube	m^2	Cross-sectional area of the entire cuboid
A_f	m^2	Total fin area
A_fr	m^2	Frontal area
A_ft	-	Fin-to-total area ratio
A_h	$\mathrm{Wb\,m^{-1}}$	Homogeneous solution of magnetic vector potential
A_impreg	m^2	Cross-sectional area of impregnation material
A_p	m^2	Total primary area
A_p	$\mathrm{Wb\,m^{-1}}$	Particular solution of magnetic vector potential
A_slot	m^2	Slot area
A_t	m^2	Total heat transfer area
A_w	m^2	Wall area
$A_\mathrm{wire,ins}$	m^2	Cross-sectional area of wire insulation
A_z	$\mathrm{Wb\,m^{-1}}$	Magnetic vector potential in z-direction
b	m	Width or spacing
b_fin	m	Plate spacing
b_oa	rad	Slot opening width
b_sa	rad	Slot width
$B_\mathrm{1r,AR}$	T	Radial flux density component due to armature reaction
$B_\mathrm{1\theta,AR}$	T	Tangential flux density component due to armature reaction
$B_\mathrm{2r,NL}$	T	Radial flux density component at no load
$B_\mathrm{2\theta,NL}$	T	Tangential flux density component at no load
B_ind	T	Magnetic field in inductor
B_r	T	Radial component of magnetic flux density
$B_\mathrm{r,AG}$	T	Radial component of airgap flux density
B_ry	T	Flux density in rotor yoke
$B_\mathrm{st,i}$	T	Flux density in i-th stator tooth
$B_\mathrm{sy,i}$	T	Flux density in stator yoke at i-th position
B_θ	T	Tangential component of magnetic flux density
$B_\mathrm{\theta,AG}$	T	Tangential component of airgap flux density
C_DC	F	DC link capacitance
C_i	F	Input capacitor of DC-DC converter
C_o	F	Output capacitor of DC-DC converter
$C_{\nu,i}$	-	In-phase component of EMF phasor
d_h	m	Hydraulic diameter
D_D	-	Diode duty cycle
$D_\mathrm{D,CCM}$	-	Diode duty cycle in continuous conduction mode
$D_\mathrm{D,DCM}$	-	Diode duty cycle in discontinuous conduction mode
D_T	-	Transistor duty cycle
$D_\mathrm{T,CCM}$	-	Transistor duty cycle in continuous conduction mode
$D_\mathrm{T,DCM}$	-	Transistor duty cycle in discontinuous conduction mode
e_ph	V	Back electromotive force per phase
E_conv	J	Energy stored in conventional sources (e.g., kerosene)
E_elec	J	Energy stored electrically
$E_\mathrm{off,T}$	J	Switch-off energy of transistor
$E_\mathrm{on,T}$	J	Switch-on energy loss of transistor
E_rad	Pa	Radial Young's modulus
$E_\mathrm{rr,D}$	J	Reverse recovery energy of diode
E_tan	Pa	Tangential Young's modulus
E_tot	J	Total energy stored

f_c	-	Friction coefficient
f_el	Hz	Fundamental electrical frequency
f_o	-	Overshoot factor
f_sw	Hz	Switching frequency
f_t	-	Total overshoot factor
f_w	-	Factor accounting for non-uniform voltage distribution in winding
G_mag	m	Magnetic airgap
g_mech	m	Mechanical airgap
Gr	-	Grashof number
H_E	-	Degree of energy hybridization
H_P	-	Degree of power hybridization
H_r	$\mathrm{A\,m^{-1}}$	Radial component of magnetic field intensity
H_θ	$\mathrm{A\,m^{-1}}$	Tangential component of magnetic field intensity
h	m	Altitude (height) above sea level
h	$\mathrm{W\,m^{-2}\,K^{-1}}$	Heat transfer coefficient
h_cc	m	Height of cooling channel
h_cond	m	Height of conductor
h_cube	m	Height of cuboid element
$I_\mathrm{AC,Ph,pk}$	A	Peak phase current of AC system
I_C	A	Collector current
$I_\mathrm{C,avg}$	A	Average DC link capacitor current
$I_\mathrm{C,in,RMS}$	A	RMS current through input capacitor
$I_\mathrm{C,out,RMS}$	A	RMS current through output capacitor
$I_\mathrm{C,rms}$	A	RMS current ripple of DC link capacitor
$I_\mathrm{DC,L,avg}$	A	Average inverter input current
$I_\mathrm{DC,L,rms}$	A	RMS inverter input current
$I_\mathrm{G,avg}$	A	Average gate current
$I_\mathrm{G,pk}$	A	Peak gate current
I_in	A	Input current of DC-DC converter
I_L	A	Inductor current
$I_\mathrm{L,avg}$	A	Average inductor current
$I_\mathrm{L,max}$	A	Maximum inductor current
$I_\mathrm{L,min}$	A	Minimum inductor current
$I_\mathrm{L,RMS}$	A	RMS inductor current
I_out	A	Output current of DC-DC converter
I_ref	A	Reference current
I_RMS	A	RMS current
I_s	A	Stator/inverter output phase current
i_C	A	DC link capacitor current
i_d	A	Current on direct axis
$i_\mathrm{DC,L}$	A	Inverter input current
$i_\mathrm{DC,L,avg}$	A	Average inverter input current related to pulse period
$i_\mathrm{DC,L,rms}$	A	RMS value of inverter input current
$i_\mathrm{DC,S}$	A	Source current
i_GB	-	Gearbox ratio
i_q	A	Current on quadrature axis
i_st	-	Gear ratio per stage
$i_\mathrm{st,max}$	-	Maximum allowable gear ratio per stage
i_u	A	Instantaneous current in phase u
i_v	A	Inverter output current in phase v

i_w	A	Inverter output current in phase w
$J_\mathrm{bb,rms}$	$\mathrm{A\,m^{-2}}$	Current density in bus bar cross section
J_z	$\mathrm{A\,m^{-2}}$	Current density in z-direction
J_{i0}	$\mathrm{A\,m^{-2}}$	DC component of current density in the i-th slot
J_{in}	$\mathrm{A\,m^{-2}}$	n-th harmonic of current density in the i-th slot
K_eddy	-	Eddy current loss coefficient
K_GB	-	Gearbox correlation factor
K_hyst	-	Hysteresis loss coefficient
$K_\mathrm{I,D}$	-	Current exponent for diode switching losses
$K_\mathrm{I,T}$	-	Current exponent for transistor switching losses
$K_\mathrm{V,D}$	-	Voltage exponent for diode switching losses
$K_\mathrm{V,T}$	-	Voltage exponent for transistor switching losses
k_AC	-	AC loss increase factor
k_cond	-	Conductor fill factor
k_mount	-	Additional mounting-related mass factor
k_sf	-	Staple factor of iron sheets
k_slot	-	Slot fill factor
k_w	-	Winding factor
k_w1	-	Fundamental winding factor
$k_{\mathrm{d},\nu}$	-	Distribution factor for ν-th harmonic
$k_{\mathrm{p},\nu}$	-	Pitch factor for ν-th harmonic
$k_{\mathrm{w},\nu}$	-	Winding factor for ν-th harmonic
L	H	Inductance
L_b	H	Boost inductance
L_Cab	m	Cable length
L_char	m	Characteristic length scale
L_crit	m	Critical cable length
L_ew	H	End winding leakage inductance
L_m	H	Magnetizing inductance
L_mm	H	Mutual magnetizing inductance
L_ms	H	Self magnetizing inductance
L_s	H	Synchronous inductance
L_slot	H	Slot leakage inductance
L_stk	m	Stack length of electric machine
L_tt	H	Tooth tip leakage inductance
L_σ	H	Leakage inductance
$L_{\sigma\mathrm{ph}}$	H	Phase leakage inductance
L_δ	H	Air gap leakage inductance
l_ax	m	Axial length
l_EM	m	Total machine length
l_fin	m	Fin length
l_path	m	Path length for heat conduction
M_r	$\mathrm{A\,m^{-1}}$	Radial component of magnetization vector
M_rck	$\mathrm{A\,m^{-1}}$	Cosine component of radial magnetization
M_rk	$\mathrm{A\,m^{-1}}$	Magnitude of k-th harmonic of radial magnetization
M_rsk	$\mathrm{A\,m^{-1}}$	Sine component of radial magnetization
M_θ	$\mathrm{A\,m^{-1}}$	Tangential component of magnetization vector
$M_{\theta\mathrm{ck}}$	$\mathrm{A\,m^{-1}}$	Cosine component of tangential magnetization
$M_{\theta\mathrm{k}}$	$\mathrm{A\,m^{-1}}$	Magnitude of k-th harmonic of tangential magnetization
$M_{\theta\mathrm{sk}}$	$\mathrm{A\,m^{-1}}$	Sine component of tangential magnetization
m_a	-	Modulation degree

$m_{\mathrm{a,max}}$	-	Maximum modulation degee
m_{Cab}	kg	Total mass of cable
$m_{\mathrm{comp,i}}$	kg	Mass of i-th component
m_{cond}	kg	Mass of conductor
m_{EPS}	kg	Total mass of electric propulsion system
m_{f}	-	Frequency ratio
m_{Fe}	kg	Mass of iron core
m_{GB}	kg	Mass of gearbox
m_{ins}	kg	Mass of insulation
m_{ph}	-	Number of phases
$m_{\mathrm{st,i}}$	kg	Mass of i-th gearbox stage
m_{strand}	-	Stranding factor
N_{c}	-	Number of coils
N_{Fin}	-	Number of fins
N_{st}	-	Number of gearbox stages
N_{t}	-	Number of turns
N_{t1}, N_{t2}	-	Number of turns in first/second layer
N_{ts}	-	Number of turns per slot
n_{EM}	min^{-1}	Rotational speed of electric machine
n_{es}	-	Number of empty slots (dead coils)
n_{g}	-	Number of wound coils per phase in periodic segment
n_{Inv}	-	Number of inverter levels
$n_{\mathrm{lay,wdg}}$	-	Number of winding layers
n_{o}	-	Number of simultaneous switching events
n_{par}	-	Number of parallel paths
n_{Prop}	min^{-1}	Rotational speed of propeller
n_{wc}	-	Number of wound coils per phase
$n_{\mathrm{wdg,lay}}$	-	Number of winding layers per slot
Nu	-	Nusselt number
Nu_{L}	-	Nusselt number for laminar flow
Nu_{T}	-	Nusselt number for turbulent flow
P	W	Power
P^*	-	Pareto-optimal solution set
P_{Bat}	W	Battery power
$P_{\mathrm{comp,i}}$	W	Power requirement of i-th component
$P_{\mathrm{cont,EM}}$	W	Output continuous power
$P_{\mathrm{cont,EPU}}$	W	Continuous power of EPU
$P_{\mathrm{cont,EPU}}$	W	EPU continuous power
P_{conv}	W	Propulsive power provided by conventional gas turbines
P_{elec}	W	Total electric propulsive power installed
P_{GD}	W	Gate driver output power
P_{in}	W	Input power
P_{out}	W	Shaft output power
$P_{\mathrm{pk,EPU}}$	W	EPU peak power
$P_{\mathrm{pk,tot}}$	W	Total peak power
$P_{\mathrm{pk,tot,req}}$	W	Overall peak power required
$P_{\mathrm{Prop,mech}}$	W	Mechanical shaft power delivered to propeller
$P_{\mathrm{st,i}}$	W	Input power of i-th gearbox stage
P_{tot}	W	Total installed propulsive power
p	-	Number of pole pairs
p	Pa	Pressure

p_{amb}	Pa	Ambient pressure
p_{c}	Pa	Contact pressure
p_{eddy}	$\mathrm{W\,kg^{-1}}$	Specific eddy current loss
p_{fin}	m	Fin pitch
$p_{\mathrm{fl,in}}$	Pa	Fluid inlet pressure
$p_{\mathrm{fl,out}}$	Pa	Fluid outlet pressure
p_{hyst}	$\mathrm{W\,kg^{-1}}$	Specific hysteresis loss
p_{in}	Pa	Inner pressure
p_{int}	Pa	Internal pressure
p_{min}	Pa	Minimum pressure
p_{out}	Pa	Outer pressure
$p_{\mathrm{out,h}}$	Pa	Hot side outlet pressure
p_{sl}	Pa	Magnet-yoke pressure
Pr	-	Prandtl number
$PTW_{\mathrm{comp,i}}$	$\mathrm{kW\,kg^{-1}}$	Power-to-weight ratio of i-th component
PTW_{EPU}	$\mathrm{kW\,kg^{-1}}$	Power-to-weight ratio of electric propulsion unit
Q	W	Heat flow, power loss
Q_{Cab}	W	DC cable losses
Q_{Cap}	W	Capacitor losses
$Q_{\mathrm{cell,in}}$	W	Heat generation in cell
$Q_{\mathrm{cell,out}}$	W	Heat dissipation from cell
$Q_{\mathrm{ch,rad}}$	W	Radiation from U-shaped channel
$Q_{\mathrm{con,D}}$	W	Conduction losses in diode
$Q_{\mathrm{con,T}}$	W	Conduction losses in transistor
Q_{Cu}	W	Copper loss
$Q_{\mathrm{EM,Cu}}$	W	Copper losses of electric motor
$Q_{\mathrm{EM,Fe}}$	W	Iron losses of electric motor
Q_{EPU}	W	Losses of electric propulsion unit
Q_{EPS}	W	Losses of electric propulsion system
Q_{Fe}	W	Iron loss
Q_{Fe}	$\mathrm{W\,kg^{-1}}$	Specific iron loss
Q_{G}	C	Gate charge
Q_{HX}	W	Heat dissipation capacity
Q_{Inv}	W	Inverter losses
Q_{S}	-	Number of stator slots
Q_{SC}	W	Total semiconductor losses
$Q_{\mathrm{sw,D}}$	W	Switching losses in diode
$Q_{\mathrm{sw,off,D}}$	W	Switch-off losses in diode
$Q_{\mathrm{sw,off,T}}$	W	Switch-off losses in transistor
$Q_{\mathrm{sw,on,T}}$	W	Switch-on losses in transistor
$Q_{\mathrm{sw,T}}$	W	Switching losses in transistor
$Q_{\mathrm{con,T}}$	W	Transistor conduction losses
$Q_{\mathrm{sw,on,T}}$	W	Transistor switch-off losses
$Q_{\mathrm{sw,on,T}}$	W	Transistor switch-on losses
$Q_{\mathrm{tot,D}}$	W	Total power loss in diode
$Q_{\mathrm{tot,T}}$	W	Total power loss in transistor
$Q_{\mathrm{tot,rad}}$	W	Total radiative heat transfer
q	-	Number of slots per pole and phase
R^2	-	Coefficient of determination (goodness of fit)
R_{AC}	Ω	AC resistance
$R_{\mathrm{cseg,rad}}$	$\mathrm{K\,W^{-1}}$	Thermal resistance of cylinder segment in radial direction

R_{DC}	Ω	DC resistance
R_{ESR}	Ω	Equivalent series resistance of capacitor
R_{G}	Ω	External gate resistance
$R_{\mathrm{G,int}}$	Ω	Internal gate resistance
R_{th}	$\mathrm{K\,W^{-1}}$	Thermal resistance
$R_{\mathrm{th,b}}$	$\mathrm{K\,W^{-1}}$	Thermal resistance of base
$R_{\mathrm{th,ca}}$	$\mathrm{K\,W^{-1}}$	Case-to-ambient thermal resistance
$R_{\mathrm{th,cc}}$	$\mathrm{K\,W^{-1}}$	Core-to-case thermal resistance
$R_{\mathrm{th,cs}}$	$\mathrm{K\,W^{-1}}$	Thermal resistance from case to sink
$R_{\mathrm{th,fa}}$	$\mathrm{K\,W^{-1}}$	Thermal resistance fin to ambient
$R_{\mathrm{th,jc,D}}$	$\mathrm{K\,W^{-1}}$	Thermal resistance from junction to case for diode
$R_{\mathrm{th,jc,T}}$	$\mathrm{K\,W^{-1}}$	Thermal resistance from junction to case for transistor
$R_{\mathrm{th,sa}}$	$\mathrm{K\,W^{-1}}$	Thermal resistance from sink to ambient
$R_{\mathrm{th,sep}}$	$\mathrm{K\,W^{-1}}$	Thermal wall resistance
$R_{\mathrm{th,sp}}$	$\mathrm{K\,W^{-1}}$	Heat spreading resistance
r	-	Reflection factor
r_{bend}	m	Bend radius
r_{cell}	m	Cell radius
r_{cond}	m	Conductor radius
$r_{\mathrm{cond,o}}$	m	Outer conductor radius
r_{EM}	m	Total machine radius
r_{EPU}	m	EPU outer radius
$r_{\mathrm{fr,o}}$	m	Frame outer radius
r_{h}	m	Hydraulic radius
r_{in}	m	Inner radius
$r_{\mathrm{in,c/h}}$	m	Air duct opening on cold/hot side
$r_{\mathrm{ins,i}}$	m	Inner insulation radius
$r_{\mathrm{ins,o}}$	m	Outer insulation radius
r_{m}	m	Mean radius of toroidal inductor
$r_{\mathrm{m,i}}$	m	Inner radius of magnet
$r_{\mathrm{m,o}}$	m	Outer radius of magnet
r_{out}	m	Outer radius
$r_{\mathrm{out,c/h}}$	m	Air duct outlet opening on cold/hot side
r_{pipe}	m	Pipe inner radius
$r_{\mathrm{pp,DC}}$	-	Normalized voltage ripple amplitude
$r_{\mathrm{pp,max}}$	-	Maximum normalized peak-to-peak voltage ripple amplitude
r_{Prop}	m	Propeller radius
$r_{\mathrm{sh,i}}$	m	Inner radius of shaft
$r_{\mathrm{sh,o}}$	m	Outer shaft radius
$r_{\mathrm{sl,o}}$	m	Outer slot radius
r_{Sp}	m	Spinner radius
$r_{\mathrm{st,i}}$	m	Inner radius of stator tooth
$r_{\mathrm{sy,i}}$	m	Inner radius of stator yoke
$r_{\mathrm{sy,o}}$	m	Outer stator yoke radius
$r_{\mathrm{tt,c}}$	m	Radius at tooth tip center
$r_{\mathrm{tt,e}}$	m	Radius at tooth tip edge
Ra	-	Rayleigh number
Re	-	Reynolds number
Re_{ax}	-	Axial Reynolds number
Re_{eff}	-	Effective Reynolds number
S_{Φ}	-	Source term in transport equation

s_{fin}	m	Fin spacing
$s_{\text{fin,c/h}}$	m	Fin spacing on cold/hot side
$SF_{\text{BB,ins}}$	-	Insulation safety factor
SF_{cond}	-	Insulation safety factor
SF_{ins}	-	Insulation safety factor
SF_{ins}	-	Safety factor for insulation
SF_{mech}	-	Wall safety factor
SF_{ph}	-	Phase insulation safety factor
SF_{slot}	-	Slot insulation safety factor
$SF_{\text{sl},\sigma}$	-	Stress safety factor
$SF_{\text{sl,T}}$	-	Torque safety factor
SF_{wire}	-	Wire insulation safety factor
SOC	-	State of charge
SOC_{init}	-	Initial state of charge
t	s	Time
T	K	Temperature
Ta	-	Taylor number
t_{bb}	m	Bus bar conductor thickness
$t_{\text{BB,cond}}$	m	Bus bar conductor thickness
$t_{\text{BB,in,cond}}$	m	Input bus bar conductor thickness
$t_{\text{BB,in,ins}}$	m	Input bus bar insulation thickness
$t_{\text{BB,ins}}$	m	Bus bar insulation thickness
$t_{\text{BB,out,cond}}$	m	Output bus bar conductor thickness
$t_{\text{BB,out,ins}}$	m	Output bus bar insulation thickness
t_{bp}	m	Baseplate thickness
t_{c}	m	Core thickness of toroidal inductor
$t_{\text{c,Inv}}$	m	Wall thickness of inverter casing
t_{end}	m	End plate thickness
t_{exec}	s	Execution time
t_{fin}	m	Fin thickness
$t_{\text{fin,c/h}}$	m	Fin thickness on cold/hot side
t_{fr}	m	Stator frame thickness
$t_{\text{fr,b}}$	m	Frame base thickness
$t_{\text{in/out}}$	m	Air duct opening height
t_{ins}	m	Insulation thickness
$t_{\text{ins,bb}}$	m	Insulation thickness of bus bar
t_{mag}	m	Magnet thickness
t_{pipe}	m	Pipe wall thickness
t_{pp}	s	Time for peak-to-peak voltage
t_{r}	s	Signal rise time
t_{ry}	m	Thickness of rotor yoke
t_{sd}	m	Slot depth
t_{sep}	m	Separation distance
t_{sh}	m	Thickness of shaft
t_{sl}	m	Thickness of sleeve
$t_{\text{slot,ins}}$	m	Thickness of slot insulation
t_{sp}	m	Thickness of slot pipe
t_{sy}	m	Thickness of stator yoke
$t_{\text{tt,c}}$	m	Thickness of tooth tip center
$t_{\text{tt,e}}$	m	Thickness of tooth tip edge
t_{wdg}	-	Machine periodicity

$t_{\mathrm{wire,ins}}$	m	Thickness of wire insulation
T_{AC}	N	Aircraft thrust
T_{amb}	K	Ambient temperature
T_{b}	K	Base temperature
T_{c}	K	Case temperature
$T_{\mathrm{c,Cap}}$	K	Core temperature of capacitor
T_{Cap}	K	Operating temperature of capacitor
T_{cell}	K	Cell temperature
T_{cond}	K	Conductor temperature
$T_{\mathrm{cond,o}}$	K	Outer conductor temperature
$T_{\mathrm{cont,EM}}$	N m	Output continuous torque
$T_{\mathrm{cont,EPU}}$	N m	EPU continuous torque
T_{EM}	N m	Torque of electric machine
T_{fin}	K	Fin surface temperature
$T_{\mathrm{fl,in}}$	K	Fluid inlet temperature
$T_{\mathrm{fl,out}}$	K	Fluid outlet temperature
$T_{\mathrm{in,c}}$	K	Cold side inlet temperature
$T_{\mathrm{in,h}}$	K	Hot side inlet temperature
$T_{\mathrm{ins,i}}$	K	Inner insulation temperature
$T_{\mathrm{ins,o}}$	K	Outer insulation temperature
T_{iron}	K	Iron lamination temperature
$T_{\mathrm{j,D}}$	K	Junction temperature of diode
$T_{\mathrm{j,T}}$	K	Junction temperature of transistor
T_{m}	K	Mean temperature
T_{mag}	K	Magnet temperature
T_{max}	K	Maximum temperature
T_{Op}	K	Operating temperature
$T_{\mathrm{out,c}}$	K	Cold side outlet temperature
$T_{\mathrm{out,h}}$	K	Hot side outlet temperature
$T_{\mathrm{pk,EPU}}$	N m	EPU peak torque
T_{Prop}	N m	Propeller torque
T_{ref}	K	Reference temperature
T_{s}	K	Heat sink temperature
T_{SC}	K	Operating temperature
T_{sw}	s	Switching period
T_{w}	K	Wall temperature
T_{wdg}	K	Winding temperature
$T_{\mathrm{wdg,avg}}$	K	Winding average temperature
$T_{\mathrm{wdg,max}}$	K	Winding maximum temperature
u	m	Displacement
UA	$\mathrm{W\,K^{-1}}$	Thermal conductance
$u_{\mathrm{Cap,I}}$	-	Current utilization of capacitor
$u_{\mathrm{Cap,V}}$	-	Voltage utilization of capacitor
u_{d}	V	Voltage on direct axis
$u_{\mathrm{GD,I,avg}}$	-	Average current utilization of gate driver
$u_{\mathrm{GD,I,pk}}$	-	Peak current utilization of gate driver
$u_{\mathrm{GD,Qg}}$	-	Charge utilization of gate driver
$u_{\mathrm{GD,V}}$	-	Voltage utilization of gate driver
$u_{\mathrm{GD,V,off}}$	-	Switch-off voltage utilization of gate driver
$u_{\mathrm{GD,V,on}}$	-	Switch-on voltage utilization of gate driver
u_{q}	V	Voltage on quadrature axis

u_{rad}	m	Radial displacement
$u_{\mathrm{SC,V}}$	-	Voltage utilization of semiconductor
v	$\mathrm{m\,s^{-1}}$	Velocity
V	$\mathrm{m^3}$	Volume
v_{AC}	$\mathrm{m\,s^{-1}}$	Aircraft velocity
V_{acc}	V	Acceptance test voltage
v_{amb}	$\mathrm{m\,s^{-1}}$	Ambient air velocity
v_{ax}	$\mathrm{m\,s^{-1}}$	Axial flow velocity
V_{b}	V	Breakdown voltage
V_{Bat}	V	Battery voltage
v_{c}	V	Carrier signal voltage
V_{CE}	V	Collector-emitter voltage
$V_{\mathrm{CE,0}}$	V	Threshold voltage of transistor
$V_{\mathrm{CE,sat}}$	V	Collector-emitter saturation voltage
V_{cell}	V	Cell voltage
$V_{\mathrm{cell,nom}}$	V	Nominal cell voltage
V_{CES}	V	Maximum collector-emitter voltage (blocking voltage)
V_{com}	V	Commutating voltage
V_{cond}	$\mathrm{m^3}$	Conductor volume
v_{cr}	$\mathrm{m\,s^{-1}}$	Cruise speed
V_{DC}	V	DC voltage
$V_{\mathrm{DC,avg}}$	V	DC average voltage component
$V_{\mathrm{DC,max}}$	V	DC voltage (fully-charged)
$V_{\mathrm{DC,min}}$	V	Lower operating voltage
v_{eff}	$\mathrm{m\,s^{-1}}$	Effective velocity
V_{F}	V	Forward voltage
$V_{\mathrm{F,0}}$	V	Threshold voltage of diode
v_{fl}	$\mathrm{m\,s^{-1}}$	Coolant velocity
$V_{\mathrm{G,off}}$	V	Turn-off gate voltage
$V_{\mathrm{G,on}}$	V	Turn-on gate voltage
V_{GE}	V	Gate-emitter voltage
v_{h}	$\mathrm{m\,s^{-1}}$	Horizontal velocity
v_{hov}	$\mathrm{m\,s^{-1}}$	Hover induced velocity
v_{i}	$\mathrm{m\,s^{-1}}$	Induced velocity
V_{in}	V	Input voltage of DC-DC converter
V_{L}	V	Inductor voltage
V_{o}	V	Total overshoot voltage
V_{OC}	V	Open-circuit voltage
V_{out}	V	Output voltage of DC-DC converter
v_{p}	$\mathrm{m\,s^{-1}}$	Wave propagation velocity
v_{rad}	$\mathrm{m\,s^{-1}}$	Rotational airgap velocity
V_{r}	V	Rated insulation voltage
v_{ref}	V	Reference voltage
V_{ref}	V	Reference voltage
V_{s}	V	Switching voltage
v_{sn}	V	Neutral point voltage
V_{type}	V	Type test voltage
v_{u}	V	Output voltage of phase u
v_{un}	V	Pole voltage of phase v
$v_{\mathrm{un,1}}$	V	Fundamental component of pole voltage of phase u
v_{us}	V	Phase voltage of phase v

v_v	$\mathrm{m\,s^{-1}}$	Vertical velocity
v_v	V	Output voltage of phase v
v_vn	V	Pole voltage of phase v
v_vs	V	Phase voltage of phase v
v_w	V	Output voltage of phase w
v_wn	V	Pole voltage of phase w
v_ws	V	Phase voltage of phase w
v_xn	V	Generic pole voltage
$\hat{V}_\mathrm{1,ph}$	V	Amplitude of fundamental phase voltage
$\hat{V}_\mathrm{AC,LL}$	V	Output line-line voltage
$\hat{V}\|1,ph\|$	V	Amplitude of fundamental phase voltage
$\dot{V}_\mathrm{Pump}$	$\mathrm{L\,min^{-1}}$	Volumetric flow
w	m	Width
W_E	kg	Operating empty weight
W_P	kg	Payload capacity
W_TO	kg	Maximum takeoff weight
w_bb	m	Bus bar terminal width
w_cc	m	Width of cooling channel
w_cond	m	Width of conductor
w_cube	m	Width of cuboid element
w_HS	m	Heat sink width
w_HX	m	Heat exchanger width
$w_\mathrm{m,k}$	m	Mean width of discretized layer
w_mag	m	Magnet width
$w_\mathrm{sl,c}$	m	Width of slot center
$w_\mathrm{sl,m}$	m	Mean width of slot width
w_st	m	Width of stator tooth
$w_\mathrm{st,m}$	m	Mean width of stator tooth
w_sy	m	Width of stator yoke
$w_\mathrm{sy,i}$	m	Width of stator yoke at inner radius
W_u, W_v, W_uv	J	Magnetic energies
x_i	-	Individual design variable
$x_{i\|L\|}$	-	Lower bound of design variable i
$x_{i\|U\|}$	-	Upper bound of design variable i
y_p	-	Coil throw/pitch
z	-	Allowable utilization ratio of blocking voltage
z^{id}	-	Ideal point vector
z_i^{id}	-	Ideal point for objective i
z^{nad}	-	Nadir point vector
z_i^{nad}	-	Nadir point for objective i
Z_dir	-	Reference directions

List of Figures

List of Tables

Bibliography

[1] Lee, D. S., Fahey, D. W., Skowron, A., Allen, M. R., Burkhardt, U., Chen, Q., Doherty, S. J., Freeman, S., Forster, P. M., Fuglestvedt, J., Gettelman, A., de León, R. R., Lim, L. L., Lund, M. T., Millar, R. J., Owen, B., Penner, J. E., Pitari, G., Prather, M. J., Sausen, R., and Wilcox, L. J., "The Contribution of Global Aviation to Anthropogenic Climate Forcing for 2000 to 2018," *Atmospheric environment (Oxford, England : 1994)*, Vol. 244, 2021, pp. 1–29. doi: 10.1016/j.atmosenv.2020.117834.

[2] International Civil Aviation Organization, "Effects of Novel Coronavirus (COVID-19) on Civil Aviation: Economic Impact Analysis," Montréal, Canada, 2021. https://www.icao.int/sustainability/Documents/COVID-19/ICAO%20COVID%202021%2004%2008%20Economic%20Impact%20TH%20Toru.pdf, Last accessed: September 26, 2025.

[3] International Energy Agency, "Greenhouse Gas Emissions from Energy," Paris, France, 2025. https://www.iea.org/data-and-statistics/data-product/greenhouse-gas-emissions-from-energy, Last accessed: September 26, 2025.

[4] Graver, B., Rutherford, D., and Zheng, S., "CO_2 Emissions from Commercial Avaition: 2013, 2018, and 2019," The International Council on Clean Transportation, Washington, DC, USA, 2019. https://theicct.org/sites/default/files/publications/CO2-commercial-aviation-oct2020.pdf, Last accessed: September 26, 2025.

[5] Bergero, C., Gosnell, G., Gielen, D., Kang, S., Bazilian, M., and Davis, S. J., "Pathways to Net-Zero Emissions from Aviation," *Nature Sustainability*, Vol. 6, No. 4, 2023, pp. 404–414. doi: 10.1038/s41893-022-01046-9.

[6] Penner, J. E., Lister, D. H., Griggs, D. J., Dokken, D. J., and McFarland, M., *Aviation and the Global Atmosphere: A Special Report of the Intergovernmental Panel on Climate Change*, Cambridge University Press, UK, 1999.

[7] Derwent, R., Collins, W., Johnson, C., and Stevenson, D., "Global Ozone Concentrations and Regional Air Quality," *Environmental Science & Technology*, Vol. 36, No. 19, 2002, pp. 379A–382A. doi: 10.1021/es022419q.

[8] Airbus S.A.S., "Global Market Forecast: Cities, Airports and Aircraft 2019 - 2038," Blangac Cedex, France, 2019. https://www.airbus.com/sites/g/files/jlcbta136/files/2021-09/GMF-2019-2038-Airbus-Commercial-Aircraft-book.pdf, Last accessed: September 26, 2025.

[9] International Energy Agency, "Energy Technology Perspectives 2020," IEA Publications, Paris, France, 2020. https://iea.blob.core.windows.net/assets/7f8aed40-89af-4348-be19-c8a67df0b9ea/Energy_Technology_Perspectives_2020_PDF.pdf, Last accessed: September 26, 2025.

[10] Nolte, P., Apffelstaedt, A., Gollnick, V., and Rötger, T., "Quantitative Assessment of Technology Impact on Aviation Fuel Efficiency," *Air Transport and Operation Symposium*, 2012, pp. 1–19. doi: 10.3233/978-1-61499-119-9-514.

[11] Follen, G. J., Del Rosario, R., Wahls, R., and Madavan, N., "NASA's Fundamental Aeronautics Subsonic Fixed Wing Project: Generation N+3 Technology Portfolio," *SAE Technical Paper Series*, SAE International, Warrendale, PA, USA, 2011, pp. 1–14. doi: 10.4271/2011-01-2521.

[12] Guynn, M. D., Berton, J. J., Tong, M. J., and Haller, W. J., "Advanced Single-Aisle Transport Propulsion Design Options Revisited," *Aviation Technology, Integration, and Operations Conference*, American Institute of Aeronautics and Astronautics, Los Angeles, CA, USA, 2013, pp. 1–17. doi: 10.2514/6.2013-4330.

[13] International Civil Aviation Organization, "Technology Standards," Montréal, Canada, 2011. https://www.icao.int/environmental-protection/Pages/technology-standards.aspx, Last accessed: September 26, 2025.

[14] International Civil Aviation Organization, "Resolution A39-3: Consolidated Statement of Continuing ICAO Policies and Practices Related to Environmental Protection – Global Market-Based Measure (MBM) Scheme," Montréal, Canada, 2016. https://www.icao.int/environmental-protection/Documents/Resolution_A39_3.pdf, Last accessed: September 26, 2025.

[15] Air Transport Action Group, "Aviation: Benefit Beyond Borders," Geneva, Switzerland, 2018. https://atag.org/media/lggnx00h/abbb18_full-report_web-2.pdf, Last accessed: September 26, 2025.

[16] European Commission: Directorate-General for Mobility and Transport and Directorate-General for Research and Innovation, "Flightpath 2050: Europe's Vision for Aviation: Report of the High Level Group," Publications Office of the European Union, Luxembourg, 2012. doi: 10.2777/15458.

[17] Air Transport Action Group, "Beginner's Guide to Sustainable Aviation Fuel," Geneva, Switzerland, 2017. https://aviationbenefits.org/media/168027/atag-beginners-guide-to-saf-edition-2023.pdf, Last accessed: September 26, 2025.

[18] Capaz, R. S., Guida, E., Seabra, J. E. A., Osseweijer, P., and Posada, J. A., "Mitigating Carbon Emissions Through Sustainable Aviation Fuels: Costs and Potential," *Biofuels, Bioproducts and Biorefining*, Vol. 15, No. 2, 2021, pp. 502–524. doi: 10.1002/bbb.2168.

[19] O'Malley, J., Pavlenko, N., and Searle, S., "Estimating Sustainable Aviation Fuel Feedstock Availability to Meet Growing European Union Demand," The International Council on Clean Transportation, Washington, DC, USA, 2021. https://theicct.org/wp-content/uploads/2021/06/Sustainable-aviation-fuel-feedstock-eu-mar2021.pdf, Last accessed: September 26, 2025.

[20] Thomson, R., Weichenhain, U., Sachdeva, N., and Kaufmann, M., "Hydrogen: A Future Fuel for Aviation?" Roland Berger GmbH, Munich, Germany, 2020. www.rolandberger.com/publications/publication_pdf/roland_berger_hydrogen_the_future_fuel_for_aviation.pdf, Last accessed: September 26, 2025.

[21] Brelje, B. J., and Martins, J. R. R. A., "Electric, Hybrid, and Turboelectric Fixed-Wing Aircraft: A Review of Concepts, Models, and Design Approaches," *Progress in Aerospace Sciences*, Vol. 104, 2019, pp. 1–19. doi: 10.1016/j.paerosci.2018.06.004.

[22] Voskuijl, M., van Bogaert, J., and Rao, A. G., "Analysis and Design of Hybrid Electric Regional Turboprop Aircraft," *CEAS Aeronautical Journal*, Vol. 9, No. 1, 2018, pp. 15–25. doi: 10.1007/s13272-017-0272-1.

[23] Nazari-Heris, M., and Mohammadi-Ivatloo, B., "Application of Robust Optimization Method to Power System Problems," *Classical and Recent Aspects of Power System Optimization*, Elsevier, 2018, pp. 19–32. doi: 10.1016/B978-0-12-812441-3.00002-1.

[24] International Energy Agency, "Global EV Outlook 2020: Entering the Decade of Electric Drive?" IEA Publications, Paris, France, 2020. https://iea.blob.core.windows.net/assets/af46e012-18c2-44d6-becd-bad21fa844fd/Global_EV_Outlook_2020.pdf, Last accessed: September 26, 2025.

[25] Sinnett, M., "787 No-Bleed Systems: Saving Fuel and Enhancing Operational Efficiencies," *Aero Quartely*, Vol. 10, No. 28, 2007, pp. 6–11.

[26] Zaporozhets, O., Isaienko, V., and Synylo, K., "Trends on Current and Forecasted Aircraft Hybrid Electric Architectures and Their Impact on Environment," *Energy*, Vol. 45, No. 211, 2020, pp. 1–11. doi: 10.1016/j.energy.2020.118814.

[27] Brown, G., "Weights and Efficiencies of Electric Components of a Turboelectric Aircraft Propulsion System," *49th AIAA Aerospace Sciences Meeting Including the New Horizons Forum and Aerospace Exposition*, American Institute of Aeronautics and Astronautics, Orlando, FL, USA, 2011, pp. 1–18. doi: 10.2514/6.2011-225.

[28] Biser, S., Wortmann, G., Ruppert, S., Filipenko, M., Noe, M., and Boll, M., "Predesign Considerations for the DC Link Voltage Level of the CENTRELINE Fuselage Fan Drive Unit," *Aerospace*, Vol. 6, No. 12, 2019. doi: 10.3390/aerospace6120126.

[29] Filipenko, M., Biser, S., Boll, M., Corduan, M., Noe, M., and Rostek, P., "Comparative Analysis and Optimization of Technical and Weight Parameters of Turbo-Electric Propulsion Systems," *Aerospace*, Vol. 7, No. 8, 2020. doi: 10.3390/aerospace7080107.

[30] Felder, J., Kim, H. D., and Brown, G., "Turboelectric Distributed Propulsion Engine Cycle Analysis for Hybrid-Wing-Body Aircraft," *47th AIAA Aerospace Sciences Meeting Including The New Horizons Forum and Aerospace Exposition*, American Institute of Aeronautics and Astronautics, Orlando, FL, USA, 2009, pp. 1–25. doi: 10.2514/6.2009-1132.

[31] Welstead, J., and Felder, J. L., "Conceptual Design of a Single-Aisle Turboelectric Commercial Transport with Fuselage Boundary Layer Ingestion," *54th AIAA Aerospace Sciences Meeting*, American Institute of Aeronautics and Astronautics, San Diego, CA, USA, 2016, pp. 1–17. doi: 10.2514/6.2016-1027.

[32] Biser, S., Atanasov, G., Hepperle, M., Filipenko, M., Keller, D., Vechtel, D., Boll, M., Kastner, N., and Noe, M., "Design Space Exploration Study and Optimization of a Distributed Turbo-Electric Propulsion System for a Regional Passenger Aircraft," *AIAA Propulsion and Energy 2020 Forum*, American Institute of Aeronautics and Astronautics, Reston, Virginia, USA, 2020, pp. 1–27. doi: 10.2514/6.2020-3592.

[33] Pornet, C., Vratny, P. C., Schmidt, M., and Isikveren, A. T., "Conceptual Studies of Future Hybrid-Electric Regional Aircraft," *Conference Proceedings of the 22nd International Symposium on Air Breathing Engines 2015*, American Institute of Aeronautics and Astronautics, Phoenix, AZ, USA, 2015, pp. 1–20. doi: 2374.UC/745830.

[34] Luongo, C. A., Masson, P. J., Nam, T., Mavris, D., Kim, H. D., Brown, G. V., Waters, M., and Hall, D., "Next Generation More-Electric Aircraft: A Potential Application for HTS Superconductors," *IEEE Transactions on Applied Superconductivity*, Vol. 19, No. 3, 2009, pp. 1055–1068. doi: 10.1109/TASC.2009.2019021.

[35] Gray, J. S., Mader, C. A., Kenway, G. K., and Martins, J. R. R. A., "Approach to Modeling Boundary Layer Ingestion Using a Fully Coupled Propulsion-RANS Model," *58th AIAA/ASCE/AHS/ASC Structures, Structural Dynamics, and Materials Conference*, American Institute of Aeronautics and Astronautics, Grapevine, TX, USA, 2017, pp. 1–16. doi: 10.2514/6.2017-1753.

[36] Isikveren, A. T., Seitz, A., Bijewitz, J., Mirzoyan, A., Isyanov, A., Grenon, R., Atinault, O., Godard, J.-L., and Stückl, S., "Distributed Propulsion and Ultra-High By-Pass Rotor Study at Aircraft Level," *The Aeronautical Journal*, Vol. 119, No. 1221, 2015, pp. 1327–1376. doi: 10.1017/S0001924000011295.

[37] Vratny, P. C., "Conceptual Design Methods of Electric Power Architectures for Hybrid Energy Aircraft," Ph.D. thesis, TU Munich, Munich, Germany, 2018.

[38] Stückl, S., "Methods for the Design and Evaluation of Future Aircraft Concepts Utilizing Electric Propulsion Systems," Ph.D. thesis, TU Munich, Munich, Germany, 2016.

[39] Isikveren, A. T., Seitz, A., Vratny, P. C., and Pornet, C., "Conceptual Studies of Universally-Electric Systems Architectures Suitable for Transport Aircraft," *61. Deutscher Luft- Und Raumfahrtkongress 2012*, Deutsche Gesellschaft für Luft- und Raumfahrt - Lilienthal-Oberth e.V, Berlin, Germany, 2012, pp. 1–16.

[40] Lorenz, L., Seitz, A., Kuhn, H., and Sizmann, A., "Hybrid Power Trains for Future Mobility," *62. Deutscher Luft- Und Raumfahrtkongress 2013*, Deutsche Gesellschaft für Luft- und Raumfahrt - Lilienthal-Oberth e.V, Stuttgart, Germany, 2013, pp. 1–17.

[41] Baumann, B. M., Washington, G., Glenn, B. C., and Rizzoni, G., "Mechatronic Design and Control of Hybrid Electric Vehicles," *IEEE/ASME Transactions on Mechatronics*, Vol. 5, No. 1, 2000, pp. 58–72. doi: 10.1109/3516.828590.

[42] Isikveren, A. T., "Method of Quadrant-Based Algorithmic Nomographs for Hybrid/-Electric Aircraft Predesign," *Journal of Aircraft*, Vol. 55, No. 1, 2018, pp. 396–405. doi: 10.2514/1.C034355.

[43] Vertical Flight Society, "Sikorsky HEX 2-Rotor Tiltwing (Technology Demonstrator)," 2024. https://evtol.news/sikorsky-hex-2-rotor, Last accessed: September 26, 2025.

[44] European Union Aviation Safety Agency, "EASA Certifies Electric Aircraft, First Type Certification for Fully Electric Plane World-Wide," 2020. https://www.easa.europa.eu/en/newsroom-and-events/press-releases/easa-certifies-electric-aircraft-first-type-certification-fully, Last accessed: September 26, 2025.

[45] Eviation Aircraft Inc., "Eviation's Alice Achieves Milestone with First Flight of All-Electric Aircraft," 2020. https://www.eviation.com/Press%20Release/eviations-alice-achieves-milestone-with-first-flight-of-all-electric-aircraft/, Last accessed: September 26, 2025.

[46] Garret-Glaser, B., "First Flight of MagniX eCaravan Showcases Maturity of Electric Aviation," Aviation Today, 2020. https://www.aviationtoday.com/2020/05/29/historic-flight-of-magnixs-ecaravan-showcases-maturity-of-electric-aviation/, Last accessed: September 26, 2025.

[47] Villamizar, H., "Sector Analysis: The State of EVTOL Innovators," Airways Magazine, 2025. https://www.airwaysmag.com/new-post/the-state-of-evtol-innovators, Last accessed: September 26, 2025.

[48] Sahoo, S., Zhao, X., and Kyprianidis, K., "A Review of Concepts, Benefits, and Challenges for Future Electrical Propulsion-Based Aircraft," *Aerospace*, Vol. 7, No. 4, 2020. doi: 10.3390/aerospace7040044.

[49] Stückl, S., van Toor, J., and Lobentanzer, H., "Voltair - The All Electric Propulsion Concept Platform: A Vision for Atomospheric Friendly Flight," *28th Congress of the Aeronautical Sciences*, International Council of the Aeronautical Sciences, Brisbane, Australia, 2012, pp. 1–11.

[50] Cinar, G., Emeneth, M., and Mavris, D. N., "A Methodology for Sizing and Analysis of Electric Propulsion Subsystems for Unmanned Aerial Vehicles," *54th AIAA Aerospace Sciences Meeting*, American Institute of Aeronautics and Astronautics, San Diego, CA, USA, 2016, pp. 1–11. doi: 10.2514/6.2016-0216.

[51] Hepperle, M., "Electric Flight: Potential and Limitations," *Energy Efficient Technologies and Concepts of Operation*, NATO STO-MP-AVT-209, Neuilly-sur-Seine Cedex, France, 2012, pp. 1–30.

[52] van Bogaert, J., "Assessment of Potential Fuel Saving Benefits of Hybrid-Electric Regional Aircraft," Master's thesis, TU Delft, Delft, The Netherlands, 2015.

[53] Pornet, C., Gologan, C., Vratny, P. C., Seitz, A., Schmitz, O., Isikveren, A. T., and Hornung, M., "Methodology for Sizing and Performance Assessment of Hybrid Energy Aircraft," *Journal of Aircraft*, Vol. 52, No. 1, 2015, pp. 341–352. doi: 10.2514/1.C032716.

[54] Finger, D. F., de Vries, R., Vos, R., Braun, C., and Bil, C., "A Comparison of Hybrid-Electric Aircraft Sizing Methods," *AIAA Scitech 2020 Forum*, American Institute of Aeronautics and Astronautics, Orlando, FL, USA, 2020, pp. 1–31. doi: 10.2514/6.2020-1006.

[55] de Vries, R., Brown, M. T., and Vos, R., "A Preliminary Sizing Method for Hybrid-Electric Aircraft Including Aero-Propulsive Interaction Effects," *2018 Aviation Technology, Integration, and Operations Conference*, American Institute of Aeronautics and Astronautics, Atlanta, GA, USA, 2018, pp. 1–29. doi: 10.2514/6.2018-4228.

[56] Choi, T., Soban, D., and Mavris, D., "Creation of a Design Framework for All-Electric Aircraft Propulsion Architectures," *3rd International Energy Conversion Engineering Conference*, American Institute of Aeronautics and Astronautics, San Francisco, CA, USA, 2005, pp. 1–11. doi: 10.2514/6.2005-5549.

[57] Cinar, G., Mavris, D. N., Emeneth, M., Schneegans, A., and Fefermann, Y., "Development of Parametric Power Generation and Distribution Subsystem Models at the Conceptual Aircraft Design Stage," *55th AIAA Aerospace Sciences Meeting*, American Institute of Aeronautics and Astronautics, Grapevine, TX, USA, 2017, pp. 1–18. doi: 10.2514/6.2017-1182.

[58] Cinar, G., Mavris, D. N., Emeneth, M., Schneegans, A., Riediger, C., Fefermann, Y., and Isikveren, A., "Sizing, Integration and Performance Evaluation of Hybrid Electric Propulsion Subsystem Architectures," *55th AIAA Aerospace Sciences Meeting*, American Institute of Aeronautics and Astronautics, Grapevine, TX, USA, 2017, pp. 1–18. doi: 10.2514/6.2017-1183.

[59] Pesce, T., and Lienkamp, M., "Definition And Optimization Of The Drive Train Topology For Electric Vehicles," *World Electric Vehicle Journal*, Vol. 5, No. 1, 2012, pp. 24–35. doi: 10.3390/wevj5010024.

[60] Mester, V., Gillon, F., and Brochet, P., "Optimal Design of Electric Vehicles Drive Train," *COMPEL - The International Journal for Computation and Mathematics in Electrical and Electronic Engineering*, Vol. 24, No. 3, 2005, pp. 967–983. doi: 10.1108/03321640510598274.

[61] Aigner, B., Nollmann, M., and Stumpf, E., "Design of a Hybrid Electric Propulsion System within a Preliminary Aircraft Design Software Environment," *67. Deutscher Luft- Und Raumfahrtkongress*, Deutsche Gesellschaft für Luft- und Raumfahrt - Lilienthal-Oberth e.V, Bonn, Germany, 2018, pp. 1–14. doi: 10.25967/480153.

[62] Schültke, F., Aigner, B., Effing, T., Strathoff, P., and Stumpf, E., "MICADO: Overview of Recent Developments within the Conceptual Aircraft Design and Optimization Environment," *69. Deutscher Luft- Und Raumfahrtkongress*, Deutsche Gesellschaft für Luft- und Raumfahrt - Lilienthal-Oberth e.V, Bonn, Germany, 2020, pp. 1–15. doi: 10.25967/530093.

[63] Aigner, B., Strathoff, P., and Stumpf, E., "MICADO: Recent Developments of Models for Design and Evaluation of Electric Aircraft Propulsion Systems," *69. Deutscher Luft- Und Raumfahrtkongress*, Deutsche Gesellschaft für Luft- und Raumfahrt - Lilienthal-Oberth e.V, Bonn, Germany, 2020, pp. 1–10. doi: 10.25967/530051.

[64] Vratny, P. C., Gologan, C., Pornet, C., Isikveren, A. T., and Hornung, M., "Battery Pack Modeling Methods for Universally Electric Aircraft," *4th CEAS Air & Space Conference*, Council of European Aerospace Societies, Linköping, Sweden, 2013, pp. 1–11.

[65] Vratny, P. C., Kuhn, H., and Hornung, M., "Influences of Voltage Variations on Electric Power Architectures for Hybrid Electric Aircraft," *CEAS Aeronautical Journal*, Vol. 8, No. 1, 2017, pp. 31–43. doi: 10.1007/s13272-016-0218-z.

[66] Holdstock, T., and Bryant, M., "Electric Drivetrain Architecture Optimisation for Autonomous Vehicles Based on Representative Cycles," *17th International CTI Symposium Automotive Transmissions*, Springer Vieweg, Berlin, Germany, 2018, pp. 1–11.

[67] Hadbi, D., Retière, N., Roboam, X., Sareni, B., and Wurtz, F., "Comparison Between System Design Optimization Strategies for More Electric Aircraft Network," *International Journal of Applied Electromagnetics and Mechanics*, Vol. 53, No. 2, 2017, pp. 289–305. doi: 10.3233/JAE-140174.

[68] Graessler, I., and Hentze, J., "The New V-Model of VDI 2206 and Its Validation," *at – Automatisierungstechnik*, Vol. 68, No. 5, 2020, pp. 312–324. doi: 10.1515/auto-2020-0015.

[69] Verein Deutscher Ingenieure/Verband der Elektrotechnik, "VDI/VDE 2206:2021-11 Development of Mechatronic and Cyber-Physical Systems," Düsseldorf, Germany, 2004.

[70] Cao, W., Mecrow, B. C., Atkinson, G. J., Bennett, J. W., and Atkinson, D. J., "Overview of Electric Motor Technologies Used for More Electric Aircraft (MEA)," *IEEE Transactions on Industrial Electronics*, Vol. 59, No. 9, 2012, pp. 3523–3531. doi: 10.1109/TIE.2011.2165453.

[71] Jack, A. G., Mecrow, B. C., and Haylock, J., "A Comparative Study of Permanent Magnet and Switched Reluctance Motors for High Performance Fault Tolerant Applications," *IAS '95. Conference Record of the 1995 IEEE Industry Applications Conference Thirtieth IAS Annual Meeting*, IEEE, Orlando, FL, USA, 1995, pp. 734–740. doi: 10.1109/IAS.1995.530372.

[72] Guo, H., Xu, J., and Kuang, X., "A Novel Fault Tolerant Permanent Magnet Synchronous Motor With Improved Optimal Torque Control for Aerospace Application," *Chinese Journal of Aeronautics*, Vol. 28, No. 2, 2015, pp. 535–544. doi: 10.1016/j.cja.2015.01.008.

[73] Estima, J. O., and Cardoso, A. J. M., "A Fault-Tolerant Permanent Magnet Synchronous Motor Drive With Integrated Voltage Source Inverter Open-Circuit Faults Diagnosis," *Proceedings of the 2011 14th European Conference on Power Electronics and Applications*, IEEE, Birmingham, UK, 2011, pp. 1–10.

[74] Cheong, B., "Advanced Modelling and Evolutionary Multiobjective Optimization of Motor Drive for Aerospace Applications," Ph.D. thesis, University of Nottingham, Nottingham, 2019.

[75] Rodríguez, A. L., Gómez, D. J., Villar, I., López-de-Heredia, A., and Etxeberria-Otadui, I., "Improved Analytical Multiphysical Modeling of a Surface PMSM," *2014 International Conference on Electrical Machines (ICEM)*, IEEE, Berlin, Germany, 2014, pp. 1224–1230. doi: 10.1109/ICELMACH.2014.6960338.

[76] IEC 60034-18-41:2014, "Rotating Electrical Machines - Part 18-41: Partial Discharge Free Electrical Insulation Systems (Type I) Used in Rotating Electrical Machines Fed From Voltage Converters - Qualification and Quality Control Tests," 2014.

[77] Park, R. H., "Two-Reaction Theory of Synchronous Machines," *Transactions of the American Institute of Electrical Engineers*, Vol. 48, No. 3, 1929, pp. 716–727. doi: 10.1109/T-AIEE.1929.5055275.

[78] Caruso, M., Di Tommaso, A., Marignetti, F., Miceli, R., and Ricco Galluzzo, G., "A General Mathematical Formulation for Winding Layout Arrangement of Electrical Machines," *Energies*, Vol. 11, No. 2, 2018, pp. 1–24. doi: 10.3390/en11020446.

[79] Di Tommaso, A. O., Genduso, F., and Miceli, R., "A Software for the Evaluation of Winding Factor Harmonic Distribution in High Efficiency Electrical Motors and Generators," *2013 Eighth International Conference and Exhibition on Ecological Vehicles and Renewable Energies (EVER)*, IEEE, Monte Carlo, Monaco, 2013, pp. 1–6. doi: 10.1109/EVER.2013.6521571.

[80] Di Tommaso, A. O., Genduso, F., Miceli, R., and Spataro, C., "Assisted Software Design of a Wide Variety of Windings in Rotating Electrical Machinery," *2014 Ninth International Conference on Ecological Vehicles and Renewable Energies (EVER)*, IEEE, Monte Carlo, Monaco, 2014, pp. 1–6. doi: 10.1109/EVER.2014.6844095.

[81] Libert, F., and Soulard, J., "Investigation on Pole-Slot Combinations for Permanent-Magnet Machines with Concentrated Windings," *2004 International Conference on Electrical Machines (ICEM)*, ICEM, Cracow, Poland, 2004, pp. 1–6.

[82] Sequenz, H., *Die Wicklungen elektrischer Maschinen: Erster Band: Wechselstrom-Ankerwicklungen*, 1st ed., Springer Wien, Wien, 1950.

[83] Sequenz, H., *Die Wicklungen elektrischer Maschinen: Zweiter Band: Wendewicklungen*, 1st ed., Springer Wien, Wien, 1952.

[84] Richter, R., *Elektrische Maschinen*, 5th ed., Springer Berlin Heidelberg, Berlin, Heidelberg, 1950. doi: 10.1007/978-3-642-86545-9.

[85] Magnussen, F., and Sadarangani, C., "Winding Factors and Joule Losses of Permanent Magnet Machines with Concentrated Windings," *IEEE International Electric Machines and Drives Conference*, IEEE, Madison, WI, USA, 2003, pp. 333–339. doi: 10.1109/IEMDC.2003.1211284.

[86] Farshadnia, M., Dutta, R., Fletcher, J. E., Ahsanullah, K., Rahman, M. F., and Lovatt, H. C., "Analysis of MMF and Back-EMF Waveforms for Fractional-Slot Concentrated-Wound Permanent Magnet Machines," *2014 International Conference on Electrical Machines (ICEM)*, IEEE, Berlin, Germany, 2014, pp. 1976–1982. doi: 10.1109/ICELMACH.2014.6960455.

[87] Wu, L. J., Zhu, Z. Q., Staton, D., Popescu, M., and Hawkins, D., "An Improved Subdomain Model for Predicting Magnetic Field of Surface-Mounted Permanent Magnet Machines Accounting for Tooth-Tips," *IEEE Transactions on Magnetics*, Vol. 47, No. 6, 2011, pp. 1693–1704. doi: 10.1109/TMAG.2011.2116031.

[88] Wu, L. J., Zhu, Z. Q., Staton, D., Popescu, M., and Hawkins, D., "Subdomain Model for Predicting Armature Reaction Field of Surface-Mounted Permanent-Magnet Machines Accounting for Tooth-Tips," *IEEE Transactions on Magnetics*, Vol. 47, No. 4, 2011, pp. 812–822. doi: 10.1109/TMAG.2011.2104969.

[89] Zhu, Z. Q., Howe, D., Bolte, E., and Ackermann, B., "Instantaneous Magnetic Field Distribution In Brushless Permanent Magnet DC Motors. I. Open-Circuit Field," *IEEE Transactions on Magnetics*, Vol. 29, No. 1, 1993, pp. 124–135. doi: 10.1109/20.195557.

[90] Zhu, Z. Q., and Howe, D., "Instantaneous Magnetic Field Distribution In Brushless Permanent Magnet DC Motors. II. Armature-Reaction Field," *IEEE Transactions on Magnetics*, Vol. 29, No. 1, 1993, pp. 136–142. doi: 10.1109/20.195558.

[91] Zhu, Z. Q., and Howe, D., "Instantaneous Magnetic Field Distribution In Brushless Permanent Magnet DC Motors. III. Effect Of Stator Slotting," *IEEE Transactions on Magnetics*, Vol. 29, No. 1, 1993, pp. 143–151. doi: 10.1109/20.195559.

[92] Zhu, Z. Q., and Howe, D., "Instantaneous Magnetic Field Distribution In Brushless Permanent Magnet DC Motors. IV. Magnetic Field On Load," *IEEE Transactions on Magnetics*, Vol. 29, No. 1, 1993, pp. 152–158. doi: 10.1109/20.195560.

[93] Zhu, Z. Q., Howe, D., and Chan, C. C., "Improved Analytical Model For Predicting The Magnetic Field Distribution In Brushless Permanent-Magnet Machines," *IEEE Transactions on Magnetics*, Vol. 38, No. 1, 2002, pp. 229–238. doi: 10.1109/20.990112.

[94] Zarko, D., Ban, D., and Lipo, T. A., "Analytical Calculation Of Magnetic Field Distribution In The Slotted Air Gap Of A Surface Permanent-Magnet Motor Using Complex Relative Air-Gap Permeance," *IEEE Transactions on Magnetics*, Vol. 42, No. 7, 2006, pp. 1828–1837. doi: 10.1109/TMAG.2006.874594.

[95] Zarko, D., Ban, D., and Lipo, T. A., "Analytical Solution For Electromagnetic Torque In Surface Permanent-Magnet Motors Using Conformal Mapping," *IEEE*

Transactions on Magnetics, Vol. 45, No. 7, 2009, pp. 2943–2954. doi: 10.1109/T-MAG.2009.2014689.

[96] Dubas, F., and Espanet, C., "Analytical Solution of the Magnetic Field in Permanent-Magnet Motors Taking Into Account Slotting Effect: No-Load Vector Potential and Flux Density Calculation," *IEEE Transactions on Magnetics*, Vol. 45, No. 5, 2009, pp. 2097–2109. doi: 10.1109/TMAG.2009.2013245.

[97] Zhu, Z. Q., Wu, L. J., and Xia, Z. P., "An Accurate Subdomain Model for Magnetic Field Computation in Slotted Surface-Mounted Permanent-Magnet Machines," *IEEE Transactions on Magnetics*, Vol. 46, No. 4, 2010, pp. 1100–1115. doi: 10.1109/TMAG.2009.2038153.

[98] Shen, Y., "Novel Permanent Magnet Brushless Machines Having Segmented Halbach Array," Ph.D. thesis, The University of Sheffield, Sheffield, UK, 2012.

[99] Shen, Y., Liu, G. Y., Xia, Z. P., and Zhu, Z. Q., "Determination of Maximum Electromagnetic Torque in PM Brushless Machines Having Two-Segment Halbach Array," *IEEE Transactions on Industrial Electronics*, Vol. 61, No. 2, 2014, pp. 718–729. doi: 10.1109/TIE.2013.2254101.

[100] Lenz, E., "Ueber die Bestimmung der Richtung der durch elektrodynamische Vertheilung erregten galvanischen Ströme," *Annalen der Physik und Chemie*, Vol. 107, No. 31, 1834, pp. 483–494. doi: 10.1002/andp.18341073103.

[101] Faraday, M., *On the Induction of Electric Currents. On the Evolution of Electricity from Magnetism. On a New Electrical Condition of Matter. On Arago's Magnetic Phenomena*, The Royal Society, 1832. doi: 10.5479/sil.389404.39088006367056.

[102] Mallek, M., Tang, Y., Lee, J., Wassar, T., Franchek, M. A., and Pickett, J., "An Analytical Subdomain Model of Torque Dense Halbach Array Motors," *Energies*, Vol. 11, No. 12, 2018, p. 3254. doi: 10.3390/en11123254.

[103] Shin, K.-H., Cho, H.-W., Lee, S.-H., and Choi, J.-Y., "Armature Reaction Field and Inductance Calculations for a Permanent Magnet Linear Synchronous Machine Based on Subdomain Model," *IEEE Transactions on Magnetics*, Vol. 53, No. 6, 2017, pp. 1–4. doi: 10.1109/TMAG.2017.2665661.

[104] Pyrhönen, J., Jokinen, T., and Hrabovcová, V., *Design of Rotating Electrical Machines*, John Wiley & Sons, Ltd., Chichester, UK, 2008. doi: 10.1002/9780470740095.

[105] Tian, Z., Zhang, C., and Zhang, S., "Analytical Calculation of Magnetic Field Distribution and Stator Iron Losses for Surface-Mounted Permanent Magnet Synchronous Machines," *Energies*, Vol. 10, No. 3, 2017, p. 320. doi: 10.3390/en10030320.

[106] Ramakrishnan, K., Romanazzi, P., Zarko, D., Mastinu, G., A. Howey, D., and Miotto, A., "Improved Analytical Model of an Outer Rotor Surface Permanent Magnet Machine for Efficiency Calculation with Thermal Effect," *SAE International Journal of Alternative Powertrains*, Vol. 6, No. 1, 2017, pp. 34–46. doi: 10.4271/2017-01-0185.

[107] Madariaga, C., Jara, W., Tapia, J. A., Pyrhonen, J., Lindh, P., and Riedemann, J. A., "Closed-Form Solution for the Slot Leakage Inductance of Tooth-Coil-Winding Permanent Magnet Machines," *IEEE Transactions on Energy Conversion*, Vol. 34, No. 3, 2019, pp. 1572–1580. doi: 10.1109/TEC.2019.2908053.

[108] Laksar, J., "Improved Calculation of the Slot Leakage Inductance of Different Slot Shapes," *Electrical Engineering*, Vol. 102, No. 3, 2020, pp. 1129–1139. doi: 10.1007/s00202-019-00910-w.

[109] Cavagnino, A., "Accuracy-Enhanced Algorithms for the Slot Leakage Inductance Computation of Double-Layer Windings," *IEEE Transactions on Industry Applications*, Vol. 53, No. 5, 2017, pp. 4422–4430. doi: 10.1109/TIA.2017.2712687.

[110] Nachouane, A. B., Abdelli, A., Friedrich, G., and Vivier, S., "Estimation of Windage Losses inside Very Narrow Air Gaps of High Speed Electrical Machines Without an Internal Ventilation Using CFD Methods," *2016 XXII International Conference on Electrical Machines (ICEM)*, IEEE, Lausanne, Switzerland, 2016, pp. 2704–2710. doi: 10.1109/ICELMACH.2016.7732904.

[111] Sirimanna, S., Balachandran, T., and Haran, K., "A Review on Magnet Loss Analysis, Validation, Design Considerations, and Reduction Strategies in Permanent Magnet Synchronous Motors," *Energies*, Vol. 15, No. 17, 2022, p. 6116. doi: 10.3390/en15176116.

[112] Ionel, D. M., Popescu, M., McGilp, M. I., Miller, T. J. E., Dellinger, S. J., and Heideman, R. J., "Computation of Core Losses in Electrical Machines Using Improved Models for Laminated Steel," *IEEE Transactions on Industry Applications*, Vol. 43, No. 6, 2007, pp. 1554–1564. doi: 10.1109/TIA.2007.908159.

[113] Qiu, J., and Zhou, M., "Analytical Solution for Interference Fit for Multi-Layer Thick-Walled Cylinders and the Application in Crankshaft Bearing Design," *Applied Sciences*, Vol. 6, No. 6, 2016, p. 167. doi: 10.3390/app6060167.

[114] Vullo, V., *Circular Cylinders and Pressure Vessels: Stress Analysis and Design*, Springer Series in Solid and Structural Mechanics, Vol. 3, Springer International Publishing, Cham, Switzerland, 2014.

[115] Chen, L., and Zhu, C., "Strength Analysis for Surface-Mounted Permanent Magnet Rotor in High-Speed Motor," *TELKOMNIKA Indonesian Journal of Electrical Engineering*, Vol. 12, No. 10, 2014, pp. 7131–7142. doi: 10.11591/ijeecs.v12.i10.pp7131-7142.

[116] Chen, L., Zhu, C., Zhong, Z., Liu, B., and Wan, A., "Rotor Strength Analysis for High-Speed Segmented Surface-Mounted Permanent Magnet Synchronous Machines," *IET Electric Power Applications*, Vol. 12, No. 7, 2018, pp. 979–990. doi: 10.1049/iet-epa.2017.0686.

[117] Cheng, W., Deng, Z., Xiao, L., Zhong, B., and Zhang, B., "Strength Analytical Solution to Ultra-High-Speed Permanent Magnet Rotor Considering Temperature Gradient and Segmental Permanent Magnet Effect," *Advances in Mechanical Engineering*, Vol. 11, No. 4, 2019, pp. 1–12. doi: 10.1177/1687814019842034.

[118] Versteeg, H. K., and Malalasekera, W., *An Introduction to Computational Fluid Dynamics: The Finite Volume Method*, 2nd ed., Pearson Education Limited, Harlow, UK, 2007.

[119] Langeheinecke, K., Kaufmann, A., and Thieleke, G., *Thermodynamik für Ingenieure*, Springer Vieweg Wiesbaden, Wiesbaden, Germany, 2017.

[120] Nerg, J., Rilla, M., and Pyrhonen, J., "Thermal Analysis of Radial-Flux Electrical Machines With a High Power Density," *IEEE Transactions on Industrial Electronics*, Vol. 55, No. 10, 2008, pp. 3543–3554. doi: 10.1109/TIE.2008.927403.

[121] Kylander, G., "Thermal Modelling of Small Cage Induction Motors," Ph.D. thesis, Chalmers Universisty of Technology, Gothenburg, Sweden, 1995.

[122] Andersson, B., "Lumped Parameter Thermal Modelling of Electric Machines: Analysis of an Interior Permanent Magnet Synchronous Machine for Vehicle Applications," Master's thesis, Chalmers Universisty of Technology, Gothenburg, Sweden, 2013.

[123] Boglietti, A., Cavagnino, A., Staton, D., Shanel, M., Mueller, M., and Mejuto, C., "Evolution and Modern Approaches for Thermal Analysis of Electrical Machines," *IEEE Transactions on Industrial Electronics*, Vol. 56, No. 3, 2009, pp. 871–882. doi: 10.1109/TIE.2008.2011622.

[124] Liu, Z. J., Howe, D., Mellor, P. H., and Jenkins, M. K., "Thermal Analysis of Permanent Magnet Machines," *1993 Sixth International Conference on Electrical Machines and Drives (Conf. Publ. No. 376)*, IET, Oxford, UK, 1993, pp. 359–364.

[125] Stephan, P., Kabelac, S., Kind, M., Mewes, D., Schaber, K., and Wetzel, T., *VDI-Wärmeatlas*, 11$^{\text{th}}$ ed., Springer Vieweg, Berlin, Heidelberg, Germany, 2019.

[126] Wrobel, R., and Mellor, P. H., "A General Cuboidal Element for Three-Dimensional Thermal Modelling," *IEEE Transactions on Magnetics*, Vol. 46, No. 8, 2010, pp. 3197–3200. doi: 10.1109/TMAG.2010.2043928.

[127] Jaritz, M., Hillers, A., and Biela, J., "General Analytical Model for the Thermal Resistance of Windings Made of Solid or Litz Wire," *IEEE Transactions on Power Electronics*, Vol. 34, No. 1, 2019, pp. 668–684. doi: 10.1109/TPEL.2018.2817126.

[128] Hashin, Z., and Shtrikman, S., "A Variational Approach to the Theory of the Effective Magnetic Permeability of Multiphase Materials," *J. Appl. Phys.*, Vol. 33, No. 10, 1962, pp. 3125–3131. doi: 10.1063/1.1728579.

[129] Simpson, N., Wrobel, R., and Mellor, P. H., "Estimation of Equivalent Thermal Parameters of Impregnated Electrical Windings," *IEEE Transactions on Industry Applications*, Vol. 49, No. 6, 2013, pp. 2505–2515. doi: 10.1109/TIA.2013.2263271.

[130] Kurte, F., "Modell-Entwicklung zur Beschreibung der Wärmeleitfähigkeit von verpressten Litzen zur Optimierung von Wicklungen elektrischer Maschinen," Master's thesis, Friedrich-Alexander Universität, Erlangen, 2019.

[131] Soderberg, C. R., "Steady Flow of Heat in Large Turbine-Generators," *Transactions of the American Institute of Electrical Engineers*, Vol. 50, No. 2, 1931, pp. 782–798.

[132] Churchill, S. W., and Chu, H. H. S., "Correlating Equations for Laminar and Turbulent Free Convection from a Vertical Plate," *International Journal of Heat and Mass Transfer*, Vol. 18, No. 11, 1975, pp. 1323–1329. doi: 10.1016/0017-9310(75)90243-4.

[133] Staton, D., Boglietti, A., and Cavagnino, A., "Solving the More Difficult Aspects of Electric Motor Thermal Analysis in Small and Medium Size Industrial Induction Motors," *IEEE Transactions on Energy Conversion*, Vol. 20, No. 3, 2005, pp. 620–628. doi: 10.1109/TEC.2005.847979.

[134] Gnielinski, V., "Berechnung mittlerer Wärme- und Stoffübergangskoeffizienten an laminar und turbulent überströmten Einzelkörpern mit Hilfe einer einheitlichen Gleichung," *Forsch. Ing. Wes*, Vol. 41, 1975. doi: 10.1007/BF02560793.

[135] Chong, Y. C., "Thermal Analysis and Air Flow Modelling of Electrical Machines," Ph.D. thesis, University of Edinburgh, Edinburgh, UK, 2015.

[136] Kaye, J., and Elgar, E. C., "Modes of Adiabatic and Diabatic Fluid Flow in an Annulus With an Inner Rotating Cylinder," *Journal of Fluids Engineering*, Vol. 80, No. 3, 1958, pp. 753–763. doi: 10.1115/1.4012502.

[137] Rybiński, W., and Mikielewicz, J., "Analytical Solutions of Heat Transfer for Laminar Flow in Rectangular Channels," *Archives of Thermodynamics*, Vol. 35, No. 4, 2014, pp. 29–42. doi: 10.2478/aoter-2014-0031.

[138] Lee, P.-S., and Garimella, S. V., "Thermally Developing Flow and Heat Transfer in Rectangular Microchannels of Different Aspect Ratios," *International Journal of Heat and Mass Transfer*, Vol. 49, No. 17-18, 2006, pp. 3060–3067. doi: 10.1016/j.ijheatmasstransfer.2006.02.011.

[139] Schubert, E., "Schubert, E. Wärmeübergangszahlen an Wickelköpfen und Lagerschilden geschlossener Asynchronmaschinen," *Elektrie*, Vol. 22, No. 4, 1968, pp. 16–162.

[140] Motor Design Ltd., "Motor-CAD 2023R1 Manual," 2022.

[141] Hemmati, R., Wu, F., and El-Refaie, A., "Survey of Insulation Systems in Electrical Machines," *2019 IEEE International Electric Machines & Drives Conference (IEMDC)*, IEEE, San Diego, CA, USA, 2019, pp. 2069–2076. doi: 10.1109/IEMDC.2019.8785099.

[142] Stone, G. C., Boulter, E. A., Culbert, I., and Dhirani, H., *Electrical Insulation for Rotating Machines: Design, Evaluation, Aging, Testing, and Repair*, 2nd ed., IEEE Press Series on Power Engineering, John Wiley & Sons, Inc., Hoboken, NJ, USA, 2014.

[143] Siddique, A., Yadava, G. S., and Singh, B., "A Review of Stator Fault Monitoring Techniques of Induction Motors," *IEEE Transactions on Energy Conversion*, Vol. 20, No. 1, 2005, pp. 106–114. doi: 10.1109/TEC.2004.837304.

[144] Faiz, J., Nejadi–Koti, H., and Valipour, Z., "Comprehensive Review on Inter–Turn Fault Indexes in Permanent Magnet Motors," *IET Electric Power Applications*, Vol. 11, No. 1, 2017, pp. 142–156. doi: 10.1049/iet-epa.2016.0196.

[145] Morshuis, P. H. F., "Degradation of Solid Dielectrics Due to Internal Partial Discharge: Some Thoughts on Progress Made and Where To Go Now," *IEEE Transactions on Dielectrics and Electrical Insulation*, Vol. 12, No. 5, 2005, pp. 905–913. doi: 10.1109/TDEI.2005.1522185.

[146] Esfahani, A. N., Shahabi, S., and Kordi, B., "Partial Discharge Detection and Identification At Low Air Pressure in Noisy Environment," *High Voltage*, Vol. 6, 2021, pp. 850–860. doi: 10.1049/hve2.12101.

[147] Paschen, F., "Ueber die zum Funkenübergang in Luft, Wasserstoff und Kohlensäure bei verschiedenen Drucken erforderliche Potentialdifferenz," *Annalen der Physik und Chemie*, Vol. 273, No. 5, 1889, pp. 69–96. doi: 10.1002/andp.18892730505.

[148] Yin, W., "Failure Mechanism of Winding Insulations in Inverter-Fed Motors," *IEEE Electrical Insulation Magazine*, Vol. 13, No. 6, 1997, pp. 18–23. doi: 10.1109/57.637150.

[149] Kandev, N., Castelan, P., Lebey, T., Amyot, N., and Hudon, C., "Testing of Low-Voltage Motor Turn Insulation Intended for Pulse-Width Modulated Applications," *IEEE Transactions on Dielectrics and Electrical Insulation*, Vol. 7, No. 6, 2000, pp. 783–789. doi: 10.1109/94.891989.

[150] Moghadam, D. E., Speck, J., Grossmann, S., and Stahl, J., "Parameters Affecting The Turn Insulation Lifetime and Durability," *IEEE Transactions on Dielectrics and Electrical Insulation*, Vol. 25, No. 2, 2018, pp. 516–523. doi: 10.1109/T-DEI.2017.006905.

[151] Montanari, G. C., Seri, P., and Negri, F., "Partial Discharge and Aging Phenomena in Insulation Systems of Rotating Machines Fed by Power Electronics," *2017 International Symposium on Electrical Insulating Materials (ISEIM)*, IEEE, Toyohashi, Japan, 2017, pp. 167–170. doi: 10.23919/ISEIM.2017.8088714.

[152] Daoudi, K., and Boudi, E. M., "Genetic Algorithm Approach for Spur Gears Design Optimization," *2018 International Conference on Electronics, Control, Optimization and Computer Science (ICECOCS)*, IEEE, Kenitra, Morocco, 2018, pp. 1–5. doi: 10.1109/ICECOCS.2018.8610520.

[153] Aziz, E.-S., and Chassapis, C., "An Intelligent System for Spur Gear Design and Analysis," *Volume 2A: 27th Design Automation Conference*, American Society of Mechanical Engineers, Pittsburgh, PA, USA, 2001, pp. 277–286. doi: 10.1115/DETC2001/DAC-21037.

[154] Qin, Z., Wu, Y.-T., and Lyu, S.-K., "A Review of Recent Advances in Design Optimization of Gearbox," *International Journal of Precision Engineering and Manufacturing*, Vol. 19, No. 11, 2018, pp. 1753–1762. doi: 10.1007/s12541-018-0203-z.

[155] Radzevich, S. P., *Dudley's Handbook of Practical Gear Design and Manufacture*, CRC Press, Boca Raton, FL, USA, 2012.

[156] Niemann, G., Winter, H., Höhn, B.-R., and Stahl, K., *Maschinenelemente 1: Konstruktion und Berechnung von Verbindungen, Lagern, Wellen*, Springer Vieweg, Berlin, Heidelberg, 2019.

[157] Niemann, G., and Winter, H., *Maschinenelemente: Band 2: Getriebe allgemein, Zahnradgetriebe – Grundlagen, Stirnradgetriebe*, 2nd ed., Springer Vieweg, Berlin, Heidelberg, Germany, 2003.

[158] ISO 6336-1:2019, "Calculation of Load Capacity of Spur and Helical Gears – Part 1: Basic Principles, Introduction and General Influence Factors," International Standardization Organization, Geneva, Switzerland, 2019.

[159] ISO 6336-2:2019, "Calculation of Load Capacity of Spur and Helical Gears – Part 2: Calculation of Surface Durability (Pitting)," International Standardization Organization, Geneva, Switzerland, 2019.

[160] ISO 6336-3:2019, "Calculation of Load Capacity of Spur and Helical Gears – Part 3: Calculation of Tooth Bending Strength," International Standardization Organization, Geneva, Switzerland, 2019.

[161] ISO 6336-4:2019, "Calculation of Load Capacity of Spur and Helical Gears – Part 4: Calculation of Tooth Flank Fracture Load Capacity," International Standardization Organization, Geneva, Switzerland, 2019.

[162] ANSI/AGMA 2001-D04, "Fundamental Rating Factors and Calculation Methods for Involute Spur and Helical Gear Teeth," American Gear Manufacturer Association, Alexandria, VA, USA, 2010.

[163] Gologlu, C., and Zeyveli, M., "A Genetic Approach to Automate Preliminary Design of Gear Drives," *Computers & Industrial Engineering*, Vol. 57, No. 3, 2009, pp. 1043–1051. doi: 10.1016/j.cie.2009.04.006.

[164] Penčić, M., Čavić, M., Rackov, M., and Borovac, B. A., "Optimization of Planetary Gear Trains with Spur, Helical and Double Helical Gears," *Conference Proceedings of the 8th International Scientific and Expert Conference*, Trnava, Slovakia, 2016, pp. 29–34.

[165] Tripathi, V. K., and Chauhan, H. M., "Multi Objective Optimization of Planetary Gear Train," *Simulated Evolution and Learning*, Lecture Notes in Computer Science, Vol. 6457, edited by K. Deb, A. Bhattacharya, N. Chakraborti, P. Chakroborty, S. Das, J. Dutta, S. K. Gupta, A. Jain, V. Aggarwal, J. Branke, S. J. Louis, and K. C. Tan, Springer, Berlin, Heidelberg, Germany, 2010, pp. 578–582.

[166] Mendi, F., Başkal, T., Boran, K., and Boran, F. E., "Optimization of Module, Shaft Diameter and Rolling Bearing for Spur Gear Through Genetic Algorithm," *Expert Systems with Applications*, Vol. 37, No. 12, 2010, pp. 8058–8064. doi: 10.1016/j.eswa.2010.05.082.

[167] Maputi, E. S., and Arora, R., "Design Optimization of a Three-Stage Transmission Using Advanced Optimization Techniques," *International Journal for Simulation and Multidisciplinary Design Optimization*, Vol. 10, 2019, p. A8. doi: 10.1051/smdo/2019009.

[168] Deb, K., and Jain, S., "Multi-Speed Gearbox Design Using Multi-Objective Evolutionary Algorithms," *Journal of Mechanical Design*, Vol. 125, No. 3, 2003, pp. 609–619. doi: 10.1115/1.1596242.

[169] Chong, T. H., Bae, In., and Park, G.-J., "A New and Generalized Methodology to Design Multi-Stage Gear Drives by Integrating The Dimensional and the Configuration Design Process," *Mechanism and Machine Theory*, Vol. 37, No. 3, 2002, pp. 295–310. doi: 10.1016/S0094-114X(01)00078-7.

[170] Bae, I., Chong, T. H., and Kubo, A., "Development and Application of an Automatic Design System for Multi-Stage Gear Drives," *Volume 4: 9th International Power Transmission and Gearing Conference, Parts A and B*, ASMEDC, Chicago, IL, USA, 2003, pp. 605–614. doi: 10.1115/DETC2003/PTG-48078.

[171] Bartlett, H. L., Lawson, B. E., and Goldfarb, M., "On the Design of Power Gear Trains: Insight Regarding Number of Stages and Their Respective Ratios," *PloS one*, Vol. 13, No. 6, 2018. doi: 10.1371/journal.pone.0198048.

[172] Brown, G. V., Kascak, A. F., Ebihara, B., Johnson, D., Choi, B., Siebert, M., and Buccieri, C., "NASA Glenn Research Center Program in High Power Density Motors for Aeropropulsion," National Aeronautics and Space Administration, Cleveland, OH, USA, 2005. https://ntrs.nasa.gov/api/citations/20060003628/downloads/20060003628.pdf, Last accessed: September 26, 2025.

[173] Zakrzewski, A., "Analytical and Model Based Design of Gearboxes for Hybrid-Electric Short-Range Aircraft," Master's thesis, Universität Stutgart, Stuttgart, Germany, 2019.

[174] Anderson, N. E., Loewenthal, S. H., and Black, J. D., "An Analytical Method to Predict Efficiency of Aircraft Gearboxes," *Journal of Mechanisms, Transmissions, and Automation in Design*, Vol. 108, No. 3, 1986, pp. 424–432. doi: 10.1115/1.3258750.

[175] Otten, T., Becker, R., Reitenbach, S., Schaber, R., and Engler, A., "Development and Application of a Predesign Tool for Aero Engine Power Gearboxes," *24th International Society of Air-Breathing Engines Conference*, Vol. 2, Canberrra, Australia, 2019, pp. 791–804. https://elib.dlr.de/129589/1/ISABE_2019-24136_FINAL.pdf.

[176] Rashid, M. H., *Power Electronics Handbook: Devices, Circuits, and Applications*, 4th ed., Person India, Noida, India, 2018.

[177] Mohan, N., Undeland, T. M., and Robbins, W. P., *Power Electronics: Converters, Applications, and Design*, 3rd ed., Wiley, Hoboken, NJ, USA, 2003.

[178] Rockett, A., *The Materials Science of Semiconductors*, Springer, New York, NY, USA, 2008.

[179] Wintrich, A., Nicolai, U., Tursky, W., and Reimann, T., *Application Manual Power Semiconductors*, 2nd ed., SEMIKRON International GmbH, Nuremberg, Germany, 2015.

[180] Deboy, G., Treu, M., Haeberlen, O., and Neumayr, D., "Si, SiC and GaN Power Devices: An Unbiased View on Key Performance Indicators," *2016 IEEE International Electron Devices Meeting (IEDM)*, IEEE, San Francisco, CA, USA, 2016, pp. 1–24. doi: 10.1109/IEDM.2016.7838458.

[181] Habetler, T. G., Naik, R., and Nondahl, T. A., "Design and Implementation of An Inverter Output LC Filter Used For Dv/Dt Reduction," *IEEE Transactions on Power Electronics*, Vol. 17, No. 3, 2002, pp. 327–331. doi: 10.1109/TPEL.2002.1004240.

[182] Steinke, J. K., Stulz, C. A., and Pohjalainen, P. A., "Use Of A LC Filter To Achieve a Motor Friendly Performance of the PWM Voltage Source Inverter," *1997 IEEE International Electric Machines and Drives Conference Record*, IEEE, Milwaukee, WI, USA, 1997, pp. TA2/4.1–TA2/4.3. doi: 10.1109/IEMDC.1997.604203.

[183] Krug, D., "Vergleichende Untersuchungen von Mehrpunkt-Schaltungstopologien mit zentralem Gleich- spannungszwischenkreis für Mittelspannungsanwendungen," Ph.D. thesis, TU Dresden, Dresden, Germany, 2016.

[184] Schweizer, M., Friedli, T., and Kolar, J. W., "Comparative Evaluation of Advanced Three-Phase Three-Level Inverter/Converter Topologies Against Two-Level Systems," *IEEE Transactions on Industrial Electronics*, Vol. 60, No. 12, 2013, pp. 5515–5527. doi: 10.1109/TIE.2012.2233698.

[185] Krug, D., Bernet, S., Fazel, S. S., Jalili, K., and Malinowski, M., "Comparison of 2.3-kV Medium-Voltage Multilevel Converters for Industrial Medium-Voltage Drives," *IEEE Transactions on Industrial Electronics*, Vol. 54, No. 6, 2007, pp. 2979–2992.

[186] Nabae, A., Takahashi, I., and Akagi, H., "A New Neutral-Point-Clamped PWM Inverter," *IEEE Transactions on Industry Applications*, Vol. IA-17, No. 5, 1981, pp. 518–523. doi: 10.1109/TIA.1981.4503992.

[187] Teichmann, R., and Bernet, S., "A Comparison of Three-Level Converters Versus Two-Level Converters for Low-Voltage Drives, Traction, and Utility Applications," *IEEE Transactions on Industry Applications*, Vol. 41, No. 3, 2005, pp. 855–865. doi: 10.1109/TIA.2005.847285.

[188] Yuratich, M. A., Abusara, M. A., Sharkh, S. M., and Orfanoudakis, G. I., "Loss Comparison of Two and Three-Level Inverter Topologies," *5th IET International Conference on Power Electronics, Machines and Drives (PEMD 2010)*, IET, Brighton, UK, 2010, p. 143. doi: 10.1049/cp.2010.0172.

[189] Rabl, I., "3L NPC, TNPC & ANPC Topology: Application Note AN-11-001," Semikron Danfoss International, Nuremberg, Germany, 2025. https://assets.danfoss.com/documents/latest/468748/AB501636827467en-000301.pdf, Last accessed: September 26, 2025.

[190] Backlund, B., Rahimo, M., Klaka, S., and Siefken, J., "Topologies, Voltage Ratings and State of the Art High Power Semiconductor Devices For Medium Voltage Wind Energy Conversion," *2009 IEEE Power Electronics and Machines in Wind Applications*, IEEE, Lincoln, NE, USA, 2009, pp. 1–6. doi: 10.1109/PEMWA.2009.5208365.

[191] Schröder, D., and Böcker, J., *Elektrische Antriebe: Regelung von Antriebssystemen*, 5th ed., Springer Vieweg, Berlin, Heidelberg, Germany, 2021.

[192] Kim, S.-H., *Electric Motor Control. DC, AC, and BLDC Motors*, Elsevier, Amsterdam, The Netherlands, 2017.

[193] Holmes, D. G., and Lipo, T. A., *Pulse Width Modulation for Power Converters: Principles and Practice*, Wiley-IEEE Press, Hoboken, NJ, USA, 2003.

[194] Williams, B., Li, P., Adam, G., and Holliday, D., "Comparative Study of Modulation Techniques for Two-Level Voltage Source Inverters," *Renewable Energy and Sustainable Development*, Vol. 2, No. 1, 2016, pp. 6–11. doi: 10.21622/RESD.2016.02.1.006.

[195] Blaabjerg, F., Kaźmierkowski, M. P., and Krishnan, R., *Control in Power Electronics: Selected Problems*, Academic Press, Cambridge, MA, USA, 2002.

[196] Gaballah, M. M., "Design and Implementation of Space Vector PWM Inverter Based on a Low Cost Microcontroller," *Arab J Sci Eng*, Vol. 38, No. 11, 2013, pp. 3059–3070. doi: 10.1007/s13369-012-0464-2.

[197] van der Broeck, H. W., Skudelny, H.-C., and Stanke, G. V., "Analysis and Realization of a Pulsewidth Modulator Based on Voltage Space Vectors," *IEEE Transactions on Industry Applications*, Vol. 24, No. 1, 1988, pp. 142–150. doi: 10.1109/28.87265.

[198] Zhou, K., and Wang, D., "Relationship Between Space-Vector Modulation and Three-Phase Carrier-Based PWM: A Comprehensive Analysis," *IEEE Transactions on Industrial Electronics*, Vol. 49, No. 1, 2002, pp. 186–196. doi: 10.1109/41.982262.

[199] Kabza, H., Schulze, H.-J., Gerstenmaier, Y., Voss, P., Schmid, J. W. W., Pfirsch, F., and Platzoder, K., "Cosmic Radiation as a Cause For Power Device Failure and Possible Countermeasures," *Proceedings of the 6th International Symposium on Power Semiconductor Devices and Ics*, IEEE, Davos, Switzerland, 1994, pp. 9–12. doi: 10.1109/ISPSD.1994.583620.

[200] Felgemacher, C., Araujo, S. V., Zacharias, P., Nesemann, K., and Gruber, A., "Cosmic Radiation Ruggedness of Si and SiC Power Semiconductors," *2016 28th International Symposium on Power Semiconductor Devices and ICs (ISPSD)*, IEEE, Prague, Czech Republic, 2016, pp. 51–54. doi: 10.1109/ISPSD.2016.7520775.

[201] Tsyplakov, E., "Failure Rates of IGBT Modules Due to Cosmic Rays: Application Note 5SYA 2042-09," ABB Power Grids Switzerland Ltd., Lenzburg, Switzerland, 2019.

[202] Scheuermann, U., and Schilling, U., "Cosmic Ray Failures of Power Modules: The Diode Makes the Difference," *Proceedings of the Conference for Power Conversion and Intelligent Motion (PCIM)*, VDE, Nuremberg, Germany, 2015, pp. 494–501.

[203] Schilling, U., "Cosmic Ray Failures in Power Electronics: Application Note AN 17-003," Semikron Danfoss International, Nuremberg, Germany, 2008. https://assets.danfoss.com/documents/latest/465381/AB501641368473en-000201.pdf, Last accessed: September 26, 2025.

[204] Semikron Danfoss International, "Datasheet SEMiX151GB12E4s," Nuremberg, Germany, 2013. https://assets.danfoss.com/documents/latest/420826/AI498150581385en-000101.pdf, Last accessed: September 26, 2025.

[205] Kashihara, Y., and Itoh, J., "Performance Evaluation among Four Types of Five-Level Topologies Using Pareto Front Curves," *2013 IEEE Energy Conversion Congress and Exposition*, IEEE, Denver, CO, USA, 2013, pp. 1296–1303. doi: 10.1109/ECCE.2013.6646854.

[206] Kim, T.-J., Kang, D.-W., Lee, Y.-H., and Hyun, D.-S., "The Analysis of Conduction and Switching Losses in Multi-Level Inverter System," *2001 IEEE 32nd Annual Power Electronics Specialists Conference (IEEE Cat. No.01CH37230)*, IEEE, Vancouver, BC, Canada, 2001, pp. 1363–1368. doi: 10.1109/PESC.2001.954310.

[207] Rastogi, Y., "Design and Testing of a 3-Phase Voltage Source Inverter for Mild Hybrid Vehicle Application," Master's thesis, Chalmers Universisty of Technology, Gothenburg, Sweden, 2018.

[208] Reimers, J., Dorn-Gomba, L., Mak, C., and Emadi, A., "Automotive Traction Inverters: Current Status and Future Trends," *IEEE Transactions on Vehicular Technology*, Vol. 68, No. 4, 2019, pp. 3337–3350. doi: 10.1109/TVT.2019.2897899.

[209] Hermwille, M., "IGBT Driver Calculation: Application Note AN-7004," Semikron Danfoss International, Nuremberg, Germany, 2007. https://shop.semikron-danfoss.com/out/pictures/wysiwigpro/AN-7004_IGBT_Driver_Calculation_rev00.pdf, Last accessed: September 26, 2025.

[210] Kolar, J. W., and Round, S. D., "Analytical Calculation of the RMS Current Stress on the DC-Link Capacitor of Voltage-PWM Converter Systems," *IEE Proceedings - Electric Power Applications*, Vol. 153, No. 4, 2006, pp. 535–543. doi: 10.1049/ip-epa:20050458.

[211] Winkelnkemper, M., "Reduzierung von Zwischenkreiskapazitäten in Frequenzumrichtern für Niederspannungsantriebe," Ph.D. thesis, Technische Universität Berlin, Berlin, 2005.

[212] Gopalakrishnan, K. S., Janakiraman, S., Das, S., and Narayanan, G., "Analytical Evaluation of DC Capacitor RMS Current and Voltage Ripple in Neutral-Point Clamped Inverters," *Sādhanā*, Vol. 42, No. 6, 2017, pp. 827–839. doi: 10.1007/s12046-017-0668-y.

[213] Vujacic, M., Hammami, M., Srndovic, M., and Grandi, G., "Analysis of DC-Link Voltage Switching Ripple in Three-Phase PWM Inverters," *Energies*, Vol. 11, No. 2, 2018, p. 471. doi: 10.3390/en11020471.

[214] Hammami, M., Rizzoli, G., Mandrioli, R., and Grandi, G., "Capacitors Voltage Switching Ripple in Three-Phase Three-Level Neutral Point Clamped Inverters with

Self-Balancing Carrier-Based Modulation," *Energies*, Vol. 11, No. 12, 2018, pp. 1–20. doi: 10.3390/en11123244.

[215] Carneiro, H., "Calculating and Interpreting Power Dissipation for Polypropylene Film DC-Link Capacitors," Vishay Intertechnology Inc., 2017. https://www.vishay.com/docs/26071/calcinterppowdisspolypfilmdcl.pdf, Last accessed: September 26, 2025.

[216] Wen, H., Xiao, W., Wen, X., and Armstrong, P., "Analysis and Evaluation of DC-Link Capacitors for High-Power-Density Electric Vehicle Drive Systems," *IEEE Transactions on Vehicular Technology*, Vol. 61, No. 7, 2012, pp. 2950–2964. doi: 10.1109/TVT.2012.2206082.

[217] Wang, H., and Blaabjerg, F., "Reliability of Capacitors for DC-Link Applications in Power Electronic Converters: An Overview," *IEEE Transactions on Industry Applications*, Vol. 50, No. 5, 2014, pp. 3569–3578. doi: 10.1109/TIA.2014.2308357.

[218] Ugur, M., and Keysan, O., "DC Link Capacitor Optimization for Integrated Modular Motor Drives," *2017 IEEE 26th International Symposium on Industrial Electronics (ISIE)*, IEEE, Edinburgh, UK, 2017, pp. 263–270. doi: 10.1109/ISIE.2017.8001258.

[219] Waffler, S., "Hochkompakter bidirektionaler DC-DC-Wandler für Hybridfahrzeuge," Ph.D. thesis, ETH Zurich, Zurich, Switzerland, 2013.

[220] Christen, D., "Analysis and Performance Evaluation of Converter Systems for EV-Ultra-Fast Charging Stations with Integrated Grid Storage," Ph.D. thesis, ETH Zurich, Zurich, Switzerland, 2017.

[221] Kyocera AVX Corp., "Medium Power Film Capacitors," Fountain Inn, SC, USA, 2019. https://catalogs.kyocera-avx.com/MediumPowerFilm.pdf, Last accessed: September 26, 2025.

[222] Vishay Intertechnology, Inc., "Metallized Polypropylene DC-Link Film Capacitor," Malvern, PA, USA, 2022. https://www.vishay.com/docs/28164/mkp1848dcl.pdf.

[223] CDE Cornell Dubilier, "Type 947D Polypropylene, High Energy Density, DC Link Capacitors: High Current, High Capacitance for Inverter Applications," New Bedford, MA, USA, 2012. https://www.cde.com/resources/catalogs/947D.pdf, Last accessed: September 26, 2025.

[224] Callegaro, A. D., Guo, J., Eull, M., Danen, B., Gibson, J., Preindl, M., Bilgin, B., and Emadi, A., "Bus Bar Design for High-Power Inverters," *IEEE Transactions on Power Electronics*, Vol. 33, No. 3, 2018, pp. 2354–2367. doi: 10.1109/TPEL.2017.2691668.

[225] Nordelöf, A., Alatalo, M., and Söderman, M. L., "A Scalable Life Cycle Inventory of an Automotive Power Electronic Inverter Unit: Part I: Design and Composition," *The International Journal of Life Cycle Assessment*, Vol. 24, No. 1, 2019, pp. 78–92. doi: 10.1007/s11367-018-1503-3.

[226] Cho, I.-S., Han, Y.-S., Lee, S.-J., and Lee, B.-J., "Study on the Heat Dissipation Behavior of Diecast Mg Inverter Housing for Eco-Friendly Hybrid Vehicles," *Journal of Korea Foundry Society*, Vol. 38, No. 3, 2018, pp. 60–65. doi: 10.7777/jkfs.2018.38.3.60.

[227] Lai, J.-S., and Nelson, D. J., "Energy Management Power Converters in Hybrid Electric and Fuel Cell Vehicles," *Proceedings of the IEEE*, Vol. 95, No. 4, 2007, pp. 766–777. doi: 10.1109/JPROC.2006.890122.

[228] Kumar, L., and Jain, S., "Electric Propulsion System for Electric Vehicular Technology: A Review," *Renewable and Sustainable Energy Reviews*, Vol. 29, 2014, pp. 924–940. doi: 10.1016/j.rser.2013.09.014.

[229] Raghavendra, K. V. G., Zeb, K., Muthusamy, A., Krishna, T. N. V., Kumar, S. V. S. V. P., Kim, D.-H., Kim, M.-S., Cho, H.-G., and Kim, H.-G., "A Comprehensive Review of DC–DC Converter Topologies and Modulation Strategies with Recent Advances in Solar Photovoltaic Systems," *Electronics*, Vol. 9, No. 1, 2020, p. 31. doi: 10.3390/electronics9010031.

[230] Wu, X., Wang, J., Zhang, Y., Du, J., Liu, Z., and Chen, Y., "Review of DC-DC Converter Topologies Based on Impedance Network with Wide Input Voltage Range and High Gain for Fuel Cell Vehicles," *Automotive Innovation*, Vol. 4, No. 4, 2021, pp. 351–372. doi: 10.1007/s42154-021-00163-z.

[231] Rogers, E., "Understanding Boost Power Stages in Switchmode Power Supplies," Dallas, TX, USA, 1999. https://www.ti.com.cn/cn/lit/an/slva061/slva061.pdf, Last accessed: September 26, 2025.

[232] Kim, J.-I., Weon, D.-H., Jeon, J.-H., Mohammadi, S., and Katehi, L., "Design of Toroidal Inductors Using Stressed Metal Technology," *IEEE MTT-S International Microwave Symposium Digest, 2005*, IEEE, Long Beach, CA, USA, 2005, pp. 705–708. doi: 10.1109/MWSYM.2005.1516706.

[233] McLyman, T., *Transformer and Inductor Design Handbook*, 4$^{\text{th}}$ ed., CRC Press, Boca Raton, FL, USA, 2011.

[234] Valchev, V. C., and van den Bossche, A., *Inductors and Transformers for Power Electronics*, CRC Press, Boca Raton, FL, USA, 2018.

[235] Dearborn, S., "Power Management in Portable Applications: Understanding the Buck Switchmode Power Converter," Chandler, AZ, USA, 2015. https://ww1.microchip.com/downloads/aemDocuments/documents/APID/ApplicationNotes/ApplicationNotes/00793a.pdf, Last accessed: September 26, 2025.

[236] Thue, W. A., *Electrical Power Cable Engineering*, 3$^{\text{rd}}$ ed., CRC Press, Boca Raton, FL, USA, 2012.

[237] Glenair, Inc., "TurboFlex Series 96: Ultra Flexible, Ultra Durable Power Distribution Cable," Glendale, CA, USA, 2019. https://www.glenair.com/catalogs/turboflex.pdf, Last accessed: September 26, 2025.

[238] ASTM International, "Specification for Concentric-Lay-Stranded Copper Conductors, Hard, Medium-Hard, or Soft," ASTM International, West Conshohocken, PA, USA, 2017. doi: 10.10.1520/B0008-23.

[239] ASTM International, "Specification for Concentric-Lay-Stranded Aluminum 1350 Conductors," ASTM International, West Conshohocken, PA, USA, 2016. doi: 10.1520/B0231_B0231M-23.

[240] Neher, J. H., and McGrath, M. H., "The Calculation of the Temperature Rise and Load Capability of Cable Systems," *Transactions of the American Institute of Electrical Engineers. Part III: Power Apparatus and Systems*, Vol. 76, No. 3, 1957, pp. 752–764. doi: 10.1109/AIEEPAS.1957.4499653.

[241] Ilgevičius, A., "Analytical and Numerical Analysis and Simulation of Heat Transfer in Electrical Conductors and Fuses," Ph.D. thesis, Universität der Bundeswehr, Munich, Germany, 2004.

[242] Simons, D. M., "Cable Geometry and the Calculation of Current-Carrying Capacity," *Transactions of the American Institute of Electrical Engineers*, Vol. XLII, 1923, pp. 600–620. doi: 10.1109/T-AIEE.1923.5060901.

[243] Sarajcev, I., Majstrovic, M., and Medic, I., "Calculation Of Losses In Electric Power Cables As The Base For Cable Temperature Analysis," *WIT Transactions on Engineering Sciences*, Vol. 27, 2000, pp. 529–537.

[244] IEC 60287-1-1:2006, "Electric Cables - Calculation of the Current Rating - Part 1-1: Current Rating Equations (100 % Load Factor) and Calculation of Losses - General," 2006.

[245] Pryer, D. W., and Gale, P. F., "Cables," *Electrical Engineer's Reference Book*, Newnes, London, UK, 2003, pp. 31.1–31.44. doi: 10.1016/B978-075064637-6/50031-9.

[246] Riba, J.-R., "Analysis of Formulas to Calculate the AC Resistance of Different Conductors' Configurations," *Electric Power Systems Research*, Vol. 127, 2015, pp. 93–100. doi: 10.1016/j.epsr.2015.05.023.

[247] Vandelac, J. P., and Ziogas, P., "A Novel Approach for Minimizing High Frequency Transformer Copper Losses," *1987 IEEE Power Electronics Specialists Conference*, IEEE, Blacksburg, VA, USA, 1987, pp. 355–367. doi: 10.1109/PESC.1987.7077203.

[248] Dowell, P. L., "Effects of Eddy Currents in Transformer Windings," *Proceedings of the Institution of Electrical Engineers*, Vol. 113, No. 8, 1966, p. 1387. doi: 10.1049/piee.1966.0236.

[249] Roßkopf, A., Bär, E., and Joffe, C., "Influence of Inner Skin- and Proximity Effects on Conduction in Litz Wires," *IEEE Transactions on Power Electronics*, Vol. 29, No. 10, 2014, pp. 5454–5461. doi: 10.1109/TPEL.2013.2293847.

[250] Sullivan, C. R., and Zhang, R. Y., "Simplified Design Method for Litz Wire," *2014 IEEE Applied Power Electronics Conference and Exposition - APEC 2014*, IEEE, Fort Worth, TX, USA, 2014, pp. 2667–2674. doi: 10.1109/APEC.2014.6803681.

[251] Ferreira, J. A., "Improved Analytical Modeling of Conductive Losses in Magnetic Components," *IEEE Transactions on Power Electronics*, Vol. 9, No. 1, 1994, pp. 127–131. doi: 10.1109/63.285503.

[252] Ilgevičius, A., and Liess, H. D., "Thermal Analysis of Electrical Wires by Finite Volume Method," *Elektronika ir Elektrotechnika*, Vol. 46, No. 4, 2003, pp. 87–92.

[253] Glenair, Inc., "Series 970 PowerTrip Connectors," Glendale, CA, USA, 2013. https://cdn.glenair.com/catalogs/powertrip-connectors.pdf, Last accessed: September 26, 2025.

[254] Kays, W. M., and London, A. L., *Compact Heat Exchangers*, 3rd ed., Krieger Publishing, Malabar, FL, USA, 1998.

[255] Sekulic, D. P., "Compact Heat Exchangers," *Handbook of Thermal Science and Engineering*, Springer, Cham, Switzerland, 2018, pp. 1501–1520.

[256] Shah, R. K., and Sekulic, D. P., *Fundamentals of Heat Exchanger Design*, John Wiley & Sons, Inc., Hoboken, NJ, USA, 2003.

[257] Hesselgreaves, J. E., Law, R., and Reay, D. A., *Compact Heat Exchangers: Selection, Design and Operation*, 2nd ed., Butterworth-Heinemann, Amsterdam, The Netherlands, 2017.

[258] Manglik, R. M., and Bergles, A. E., "Heat Transfer and Pressure Drop Correlations for the Rectangular Offset Strip Fin Compact Heat Exchanger," *Experimental Thermal and Fluid Science*, Vol. 10, No. 2, 1995, pp. 171–180. doi: 10.1016/0894-1777(94)00096-Q.

[259] Gardner, K. A., "Efficiency of Extended Surface," *ASME Trans*, Vol. 67, No. 8, 1945, pp. 621–631. doi: 10.1115/1.4018343.

[260] Elenbaas, W., "The Dissipation of Heat by Free Convection of Spheres and Horizontal Cylinders," *Physica*, Vol. 9, No. 3, 1942, pp. 285–296. doi: 10.1016/S0031-8914(42)90111-3.

[261] Bilitzky, A., "The Effect of Geometry on Heat Transfer by Free Convection from a Fin Array," Master's thesis, Ben-Gurion University of the Negev, Beer Sheva, Israel, 1986.

[262] van de Pol, D. W., and Tierney, J. K., "Free Convection Nusselt Number for Vertical U-Shaped Channels," *Journal of Heat Transfer*, Vol. 95, No. 4, 1973, pp. 542–543. doi: 10.1115/1.3450106.

[263] Welling, J. R., and Wooldridge, C. B., "Free Convection Heat Transfer Coefficients From Rectangular Vertical Fins," *Journal of Heat Transfer*, Vol. 87, No. 4, 1965, pp. 439–444. doi: 10.1115/1.3689135.

[264] Churchill, S. W., and Usagi, R., "A General Expression for the Correlation of Rates of Transfer and Other Phenomena," *AIChE Journal*, Vol. 18, No. 6, 1972, pp. 1121–1128. doi: 10.1002/aic.690180606.

[265] Teertstra, P., Yovanovich, M. M., Culham, J. R., and Lemczyk, T., "Analytical Forced Convection Modeling of Plate Fin Heat Sinks," *Fifteenth Annual IEEE Semiconductor Thermal Measurement and Management Symposium (Cat. No.99CH36306)*, IEEE, San Diego, CA, USA, 1999, pp. 34–41. doi: 10.1109/STHERM.1999.762426.

[266] Naidu, S. V., Rao, V. D., Rao, B. G., Sombabu, A., and Sreenivasulu, B., "Natural Convection Heat Transfer From Fin Arrays: Experimental and Theoretical Study on Effect of Inclination of Base on Heat Transfer," *Journal of Engineering and Applied Sciences*, Vol. 5, No. 9, 2010, pp. 7–15.

[267] Shabany, Y., "Radiation Heat Transfer from Plate-Fin Heat Sinks," *2008 Twenty-Fourth Annual IEEE Semionductor Thermal Measurement and Management Symposium*, IEEE, San Jose, CA, USA, 2008, pp. 132–136. doi: 10.1109/STHERM.2008.4509379.

[268] Yu, S.-H., Jang, D., and Lee, K.-S., "Effect of Radiation in a Radial Heat Sink Under Natural Convection," *International Journal of Heat and Mass Transfer*, Vol. 55, No. 1-3, 2012, pp. 505–509. doi: 10.1016/j.ijheatmasstransfer.2011.09.026.

[269] Turkyilmazoglu, M., "Efficiency of the Longitudinal Fins of Trapezoidal Profile in Motion," *Journal of Heat Transfer*, Vol. 139, No. 9, 2017. doi: 10.1115/1.4036328.

[270] Yovanovich, M. M., Culham, J. R., and Teertstra, P., "Analytical Modeling of Spreading Resistance in Flux Tubes, Half Spaces, and Compound Disks," *IEEE Transactions on Components, Packaging, and Manufacturing Technology: Part A*, Vol. 21, No. 1, 1998, pp. 168–176. doi: 10.1109/95.679046.

[271] Yovanovich, M. M., Muzychka, Y. S., and Culham, J. R., "Spreading Resistance of Isoflux Rectangles and Strips on Compound Flux Channels," *Journal of Thermophysics and Heat Transfer*, Vol. 13, No. 4, 1999, pp. 495–500. doi: 10.2514/2.6467.

[272] Muzychka, Y. S., Culham, J. R., and Yovanovich, M. M., "Thermal Spreading Resistance of Eccentric Heat Sources on Rectangular Flux Channels," *Journal of Electronic Packaging*, Vol. 125, No. 2, 2003, pp. 178–185. doi: 10.1115/1.1568125.

[273] Khan, W. A., Culham, J. R., and Yovanovich, M. M., "Optimization of Microchannel Heat Sinks Using Entropy Generation Minimization Method," *IEEE Transactions on Components and Packaging Technologies*, Vol. 32, No. 2, 2009, pp. 243–251. doi: 10.1109/TCAPT.2009.2022586.

[274] Lee, S., "Optimum Design and Selection of Heat Sinks," *IEEE Transactions on Components, Packaging, and Manufacturing Technology: Part A*, Vol. 18, No. 4, 1995, pp. 812–817. doi: 10.1109/95.477468.

[275] Culham, J. R., and Muzychka, Y. S., "Optimization of Plate Fin Heat Sinks Using Entropy Generation Minimization," *IEEE Transactions on Components and Packaging Technologies*, Vol. 24, No. 2, 2001, pp. 159–165. doi: 10.1109/6144.926378.

[276] Lindstedt, M., and Karvinen, R., "Optimization of Plate Fin Arrays with Laminar and Turbulent Forced Convection," *Journal of Physics: Conference Series*, Vol. 395, 2012, pp. 1–8. doi: 10.1088/1742-6596/395/1/012059.

[277] Muzychka, Y., and Yovanovich, M. M., "Modeling Friction Factors in Non-Circular Ducts for Developing Laminar Flow," *2nd AIAA, Theoretical Fluid Mechanics Meeting*, American Institute of Aeronautics and Astronautics, Albuquerque, NM, USA, 1998, pp. 1–12. doi: 10.2514/6.1998-2492.

[278] Cascon Inc., "Series 100: High Reliability Fuel and Coolant Pumps," Yarmouth, ME, USA, 2021. https://www.casconpump.com/product/series-300-100-hi-rel-fuel-and-coolant-pump/, Last accessed: September 26, 2025.

[279] Rista, C., "Consolidation of Broad Spectrum HEL Cooling Pump Designs into Discrete Product Families," Destin, FL, USA, 2019. https://www.barber-nichols.com/wp-content/uploads/2019/11/Consolidation-of-Broad-Spectrum-HEL-Cooling-Pump-Designs-into-Discrete-Product-Families.pdf, Last accessed: September 26, 2025.

[280] Parker Hannifin Corporation, "Engine-Driven Pumps," Kalamazoo, MI, USA, 2009. https://www.parker.com/content/dam/Parker-com/Literature/Hydraulic-Systems-Division/HSD-literature-files/HSD-OTS-Aircraft-Engine-Driven-Pumps.pdf, Last accessed: September 26, 2025.

[281] Woodward Inc., "Brushless DC Motor," Fort Collins, CO, USA, 2021. https://www.woodward.com/products/wp-content/uploads/sites/3/2024/08/WD-100-06398_-.pdf, Last accessed: September 26, 2025.

[282] Weisbach, J. L., *Lehrbuch der Ingenieur-und Maschinen-Mechanik*, Vieweg und Sohn, Braunschweig, Germany, 1865.

[283] Darcy, H., *Recherches Experimentales Relatives au Mouvement de L'Eau dans les Tuyaux*, Mallet-Bachelier, Paris, France, 1857.

[284] Hagen, G., "Ueber die Bewegung des Wassers in engen cylindrischen Röhren," *Annalen der Physik und Chemie*, Vol. 122, No. 3, 1839, pp. 423–442. doi: 10.1002/andp.18391220304.

[285] Poiseuille, J. L. M., "Recherches experimentales sur Ie mouvement des liquides dans les tubes de tres-petits diametres," *Memoires presentes par divers savants a i'Academie Royale des Sciences de l'Institut de France*, Vol. IX, Imprímerie Royale, Paris, France, 1846, pp. 433–544.

[286] Colebrook, C. F., and White, C. M., "Experiments with Fluid Friction in Roughened Pipes," *Proceedings of the Royal Society of London. Series A - Mathematical and Physical Sciences*, Vol. 161, No. 906, 1937, pp. 367–381. doi: 10.1098/rspa.1937.0150.

[287] Colebrook, C. F., "Turbulent Flow in Pipes, with Particular Reference to the Transition Region Between the Smooth and Rough Pipe Laws," *Journal of the Institution of Civil Engineers*, Vol. 11, No. 4, 1939, pp. 133–156. doi: 10.1680/ijoti.1939.13150.

[288] de Almeida Minhoni, R. T., Pereira, F. F. S., Da Silva, T. B. G., Castro, E. R., and Saad, J. C. C., "The Performance of Explicit Formulas for Determining the Darcy-Weisbach Friction Factor," *Engenharia Agrícola*, Vol. 40, No. 2, 2020, pp. 258–265. doi: 10.1590/1809-4430-Eng.Agric.v40n2p258-265/2020.

[289] Vatankhah, A. R., "Approximate Analytical Solutions for the Colebrook Equation," *Journal of Hydraulic Engineering*, Vol. 144, No. 5, 2018, pp. 1–8. doi: 10.1061/(ASCE)HY.1943-7900.0001454.

[290] Perry, R. H., and Green, D. W., *Perry's Chemical Engineers' Handbook*, 8$^{\text{th}}$ ed., McGraw-Hill, New York, NY, USA, 2008.

[291] Spedding, P. L., Benard, E., and Mcnally, G. M., "Fluid Flow through 90 Degree Bends," *Developments in Chemical Engineering and Mineral Processing*, Vol. 12, No. 1-2, 2004, pp. 107–128. doi: 10.1002/apj.5500120109.

[292] White, C. M., "Streamline Flow through Curved Pipes," *Proceedings of the Royal Society of London. Series A - Mathematical and Physical Sciences*, Vol. 123, No. 792, 1929, pp. 645–663. doi: 10.1098/rspa.1929.0089.

[293] Itō, H., "Friction Factors for Turbulent Flow in Curved Pipes," *Journal of Basic Engineering*, Vol. 81, No. 2, 1959, pp. 123–132. doi: 10.1115/1.4008390.

[294] Linse, C., and Kuhn, R., "Design of High-Voltage Battery Packs for Electric Vehicles," *Advances in Battery Technologies for Electric Vehicles*, edited by B. Scrosati, J. Garche, and W. Tillmetz, Woodhead Publishing, Cambridge, UK, 2015, pp. 245–263.

[295] Xue, N., Du, W., Greszler, T. A., Shyy, W., and Martins, J. R., "Design of a Lithium-Ion Battery Pack for PHEV Using a Hybrid Optimization Method," *Applied Energy*, Vol. 115, 2014, pp. 591–602. doi: 10.1016/j.apenergy.2013.10.044.

[296] Dubarry, M., Vuillaume, N., and Liaw, B. Y., "From Single Cell Model to Battery Pack Simulation for Li-Ion Batteries," *Journal of Power Sources*, Vol. 186, No. 2, 2009, pp. 500–507. doi: 10.1016/j.jpowsour.2008.10.051.

[297] Liu, Y., Sun, Q., Li, W., Adair, K. R., Li, J., and Sun, X., "A Comprehensive Review on Recent Progress in Aluminum–Air Batteries," *Green Energy & Environment*, Vol. 2, No. 3, 2017, pp. 246–277. doi: 10.1016/j.gee.2017.06.006.

[298] Huber, C., and Kuhn, R., "Thermal Management of Batteries for Electric Vehicles," *Advances in Battery Technologies for Electric Vehicles*, edited by B. Scrosati, J. Garche, and W. Tillmetz, Woodhead Publishing, Cambridge, UK, 2015, pp. 327–358.

[299] Gu, W. B., Wang, C. Y., and Liaw, B. Y., "The Use of Computer Simulation in the Evaluation of Electric Vehicle Batteries," *Journal of Power Sources*, Vol. 75, No. 1, 1998, pp. 151–161. doi: 10.1016/S0378-7753(98)00119-0.

[300] Panasonic Corp., "Specifications for NCR18650GA," 2022. https://www.orbtronic.com/content/Datasheet-specs-Sanyo-Panasonic-NCR18650GA-3500mah.pdf, Last accessed: September 26, 2025.

[301] Pampel, F., Pischinger, S., and Teuber, M., "A Systematic Comparison of the Packing Density of Battery Cell-to-Pack Concepts at Different Degrees of Implementation," *Results in Engineering*, Vol. 13, 2022, pp. 1–3. doi: 10.1016/j.rineng.2021.100310.

[302] Löbberding, H., Wessel, S., Offermanns, C., Kehrer, M., Rother, J., Heimes, H., and Kampker, A., "From Cell to Battery System in BEVs: Analysis of System Packing Efficiency and Cell Types," *World Electric Vehicle Journal*, Vol. 11, No. 4, 2020, pp. 1–15. doi: 10.3390/wevj11040077.

[303] Ogura, K., and Kolhe, M. L., "Battery Technologies for Electric Vehicles," *Electric Vehicles: Prospects and Challenges*, edited by T. Muneer, K. L. Mohan, and A. Doyle, Elsevier, Amsterdam, The Netherlands, 2017, pp. 139–167.

[304] Saha, B., and Goebel, K., "Modeling Li-Ion Battery Capacity Depletion in a Particle Filtering Framework," *Proceedings of Annual Conference of the PHM Society*, Vol. 1, 2009, pp. 1–10.

[305] Kim, U. S., Yi, J., Shin, C. B., Han, T., and Park, S., "Modelling the Thermal Behaviour of a Lithium-Ion Battery During Charge," *Journal of Power Sources*, Vol. 196, No. 11, 2011, pp. 5115–5121. doi: 10.1016/j.jpowsour.2011.01.103.

[306] Shadman Rad, M., Danilov, D. L., Baghalha, M., Kazemeini, M., and Notten, P., "Adaptive Thermal Modeling of Li-Ion Batteries," *Electrochimica Acta*, Vol. 102, 2013, pp. 183–195. doi: 10.1016/j.electacta.2013.03.167.

[307] Yang, Z., Patil, D., and Fahimi, B., "Electrothermal Modeling of Lithium-Ion Batteries for Electric Vehicles," *IEEE Transactions on Vehicular Technology*, Vol. 68, No. 1, 2019, pp. 170–179. doi: 10.1109/TVT.2018.2880138.

[308] Raijmakers, L. H. J., Danilov, D. L., Eichel, R.-A., and Notten, P. H. L., "A Review on Various Temperature-Indication Methods for Li-Ion Batteries," *Applied Energy*, Vol. 240, 2019, pp. 918–945. doi: 10.1016/j.apenergy.2019.02.078.

[309] Thomas, K. E., and Newman, J., "Thermal Modeling of Porous Insertion Electrodes," *Journal of The Electrochemical Society*, Vol. 150, No. 2, 2003, pp. A176–A192. doi: 10.1149/1.1531194.

[310] Forgez, C., Vinh Do, D., Friedrich, G., Morcrette, M., and Delacourt, C., "Thermal Modeling of a Cylindrical $LiFePO_4$/Graphite Lithium-Ion Battery," *Journal of Power Sources*, Vol. 195, No. 9, 2010, pp. 2961–2968. doi: 10.1016/j.jpowsour.2009.10.105.

[311] Fan, L., Khodadadi, J. M., and Pesaran, A. A., "A Parametric Study on Thermal Management of an Air-Cooled Lithium-Ion Battery Module for Plug-In Hybrid Electric Vehicles," *Journal of Power Sources*, Vol. 238, 2013, pp. 301–312. doi: 10.1016/j.jpowsour.2013.03.050.

[312] Park, H., "A Design of Air Flow Configuration for Cooling Lithium Ion Battery in Hybrid Electric Vehicles," *Journal of Power Sources*, Vol. 239, 2013, pp. 30–36. doi: 10.1016/j.jpowsour.2013.03.102.

[313] Wang, T., Tseng, K. J., Zhao, J., and Wei, Z., "Thermal Investigation of Lithium-Ion Battery Module with Different Cell Arrangement Structures and Forced Air-Cooling Strategies," *Applied Energy*, Vol. 134, 2014, pp. 229–238. doi: 10.1016/j.apenergy.2014.08.013.

[314] Kim, G.-H., Gonder, J., Lustbader, J., and Pesaran, A., "Thermal Management of Batteries in Advanced Vehicles Using Phase-Change Materials," *World Electric Vehicle Journal*, Vol. 2, No. 2, 2008, pp. 134–147. doi: 10.3390/wevj2020134.

[315] Tong, W., Somasundaram, K., Birgersson, E., Mujumdar, A. S., and Yap, C., "Numerical Investigation of Water Cooling for a Lithium-Ion Bipolar Battery Pack," *International Journal of Thermal Sciences*, Vol. 94, 2015, pp. 259–269. doi: 10.1016/j.ijthermalsci.2015.03.005.

[316] Zhang, H., Cao, D., and Du, H. (eds.), *Modeling, Dynamics and Control of Electrified Vehicles*, Woodhead Publishing, Cambridge, UK, 2018.

[317] Boyd, S., and Vandenberghe, L., *Convex Optimization*, Cambridge University Press, Cambridge, UK, 2013.

[318] Martins, J. R. R. A., and Ning, A., *Engineering Design Optimization*, Cambridge University Press, Cambridge, UK, 2022.

[319] Coello Coello, C. A., Lamont, G. B., and van Veldhuizen, D. A., *Evolutionary Algorithms for Solving Multi-Objective Problems*, 2nd ed., Springer, Boston, MA, USA, 2007.

[320] Zitzler, E., and Thiele, L., "Multiobjective Optimization Using Evolutionary Algorithms – A Comparative Case Study," *Parallel Problem Solving from Nature – PPSN V*, Lecture Notes in Computer Science, Vol. 1498, edited by G. Goos, J. Hartmanis, J. van Leeuwen, A. E. Eiben, T. Bäck, M. Schoenauer, and H.-P. Schwefel, Springer, Berlin, Heidelberg, Germany, 1998, pp. 292–301.

[321] Nocedal, J., and Wright, S. J., *Numerical Optimization*, 2nd ed., Springer Series in Operations Research and Financial Engineering, Springer, New York, NY, USA, 2006.

[322] Cavazzuti, M., *Optimization Methods*, Springer, Berlin, Heidelberg, Germany, 2013.

[323] Perez, R. E., Jansen, P. W., and Martins, J. R. R. A., "pyOpt: A Python-Based Object-Oriented Framework for Nonlinear Constrained Optimization," *Structural and Multidisciplinary Optimization*, Vol. 45, No. 1, 2012, pp. 101–118. doi: 10.1007/s00158-011-0666-3.

[324] Marler, R. T., and Arora, J. S., "Survey of Multi-Objective Optimization Methods for Engineering," *Structural and Multidisciplinary Optimization*, Vol. 26, No. 6, 2004, pp. 369–395. doi: 10.1007/s00158-003-0368-6.

[325] Odu, G. O., "Weighting Methods for Multi-Criteria Decision Making Technique," *Journal of Applied Sciences and Environmental Management*, Vol. 23, No. 8, 2019, p. 1449. doi: 10.4314/jasem.v23i8.7.

[326] Zardari, N. H., Ahmed, K., Shirazi, S. M., and Yusop, Z. B., *Weighting Methods and Their Effects on Multi-Criteria Decision Making Model Outcomes in Water Resources Management*, Springer, Cham, Switzerland, 2015.

[327] Pareto, V. (ed.), *Manual of Political Economy: A Critical and Variorum Edition*, Oxford University Press, Oxford, 2014.

[328] Holland, J. H., *Adaptation in Natural and Artificial Systems: An Introductory Analysis with Applications to Biology, Control, and Artificial Intelligence*, Complex Adaptive Systems, MIT Press, Cambridge, MA, USA, 1992.

[329] Blank, J., and Deb, K., "Pymoo: Multi-Objective Optimization in Python," *IEEE Access*, Vol. 8, 2020, pp. 89497–89509. doi: 10.1109/ACCESS.2020.2990567.

[330] Deb, K., Agrawal, S., Pratap, A., and Meyarivan, T., "A Fast Elitist Non-Dominated Sorting Genetic Algorithm for Multi-Objective Optimization: NSGA-II," *Parallel Problem Solving from Nature PPSN VI*, Lecture Notes in Computer Science, Vol. 1917, edited by G. Goos, J. Hartmanis, J. van Leeuwen, M. Schoenauer, K. Deb, G. Rudolph, X. Yao, E. Lutton, J. J. Merelo, and H.-P. Schwefel, Springer, Berlin, Heidelberg, Germany, 2000, pp. 849–858.

[331] Assunção, W. K. G., Colanzi, T. E., Vergilio, S. R., and Pozo, A. T. R., "Generating Integration Test Orders for Aspect Oriented Software with Multi-Objective Algorithms," *Revista de Informática Teórica e Aplicada*, Vol. 20, No. 2, 2013, p. 301. doi: 10.22456/2175-2745.25720.

[332] Srinivas, M., and Patnaik, L. M., "Adaptive Probabilities of Crossover and Mutation in Genetic Algorithms," *IEEE Transactions on Systems, Man, and Cybernetics*, Vol. 24, No. 4, 1994, pp. 656–667. doi: 10.1109/21.286385.

[333] Seada, H., and Deb, K., "A Unified Evolutionary Optimization Procedure for Single, Multiple, and Many Objectives," *IEEE Transactions on Evolutionary Computation*, Vol. 20, No. 3, 2016, pp. 358–369. doi: 10.1109/TEVC.2015.2459718.

[334] Jain, H., and Deb, K., "An Evolutionary Many-Objective Optimization Algorithm Using Reference-Point Based Nondominated Sorting Approach, Part II: Handling Constraints and Extending to an Adaptive Approach," *IEEE Transactions on Evolutionary Computation*, Vol. 18, No. 4, 2014, pp. 602–622. doi: 10.1109/TEVC.2013.2281534.

[335] Deb, K., and Jain, H., "An Evolutionary Many-Objective Optimization Algorithm Using Reference-Point-Based Nondominated Sorting Approach, Part I: Solving Problems With Box Constraints," *IEEE Transactions on Evolutionary Computation*, Vol. 18, No. 4, 2014, pp. 577–601. doi: 10.1109/TEVC.2013.2281535.

[336] Das, I., and Dennis, J. E., "Normal-Boundary Intersection: A New Method for Generating the Pareto Surface in Nonlinear Multicriteria Optimization Problems," *SIAM Journal on Optimization*, Vol. 8, No. 3, 1998, pp. 631–657. doi: 10.1137/S1052623496307510.

[337] Blank, J., Deb, K., and Roy, P. C., "Investigating the Normalization Procedure of NSGA-III," *Evolutionary Multi-Criterion Optimization*, Lecture Notes in Computer Science, Vol. 11411, edited by K. Deb, E. Goodman, C. A. C. Coello, K. Klamroth, K. Miettinen, S. Mostaghim, and P. Reed, Springer, Cham, Switzerland, 2019, pp. 229–240.

[338] Panichella, A., "An Adaptive Evolutionary Algorithm Based on Non-Euclidean Geometry for Many-Objective Optimization," *Proceedings of the Genetic and Evolutionary Computation Conference*, edited by M. López-Ibáñez, A. Auger, and T. Stützle, ACM, New York, NY, USA, 2019, pp. 595–603. doi: 10.1145/3321707.3321839.

[339] Blank, J., and Deb, K., "A Running Performance Metric and Termination Criterion for Evaluating Evolutionary Multi- and Many-Objective Optimization Algorithms," *2020 IEEE Congress on Evolutionary Computation (CEC)*, IEEE, Glasgow, UK, 2020, pp. 1–8. doi: 10.1109/CEC48606.2020.9185546.

[340] van Veldhuizen, D. A., "Multiobjective Evolutionary Algorithms: Classifications, Analyses, and New Innovations," Ph.D. thesis, Air Force Institute of Technology, Ohio, OH, USA, 1999.

[341] Coello Coello, C. A., and Reyes Sierra, M., "A Study of the Parallelization of a Coevolutionary Multi-Objective Evolutionary Algorithm," *MICAI 2004: Advances in Artificial Intelligence*, Lecture Notes in Computer Science, Vol. 2972, edited by G. Goos, J. Hartmanis, J. van Leeuwen, R. Monroy, G. Arroyo-Figueroa, L. E. Sucar, and H. Sossa, Springer, Berlin, Heidelberg, Germany, 2004, pp. 688–697.

[342] Deb, K., and Agrawal, R. B., "Simulated Binary Crossover for Continuous Search Space," *Complex Systems*, Vol. 9, No. 2, 1995, pp. 115–148.

[343] Inselberg, A., "The Plane with Parallel Coordinates," *The Visual Computer*, Vol. 1, No. 2, 1985, pp. 69–91. doi: 10.1007/BF01898350.

[344] Inselberg, A., *Parallel Coordinates: Visual Multidimensional Geometry and Its Applications*, Springer, New York, NY, USA, 2009.

[345] Hader, M., Baur, S., Kopera, S., Schönberg, T., and Hasenberg, J.-P., "Urban Air Mobility: USD 90 Billion of Potential: How to Capture a Share of the Passenger Drone Market," Roland Berger GmbH, Munich, Germany, 2020. https://www.google.com/url?sa=t&source=web&rct=j&opi=89978449&url=https://www.rolandberger.com/publications/publication_pdf/roland_berger_urban_air_mobility_1.pdf&ved=2ahUKEwjnue_4rpaNAxVinf0HHX1VHkwQFnoECBYQAQ&usg=AOvVaw33Vw6XP_UH_KFDOpVxiDoM, Last accessed: September 26, 2025.

[346] Baur, S., Schickram, S., Homulenko, A., Martinez, N., and Dyskin, A., "Urban Air Mobility: The Rise of a New Mode of Transportation," Roland Berger GmbH, Munich, Germany, 2018. https://www.google.com/url?sa=t&source=web&rct=j&opi=89978449&url=https://www.rolandberger.com/publications/publication_pdf/Roland_Berger_Urban_Air_Mobility.pdf&ved=2ahUKEwjP_bmXr5aNAxVwk_0HHdw7OOAQFnoECAkQAQ&usg=AOvVaw2XnmYUqMTprldIq6_4Mo-M, Last accessed: September 26, 2025.

[347] Rothfeld, R., Straubinger, A., Fu, M., Al Haddad, C., and Antoniou, C., "Urban Air Mobility," *Demand for Emerging Transportation Systems*, Elsevier, Amsterdam, The Netherlands, 2020, pp. 267–284.

[348] Straubinger, A., Rothfeld, R., Shamiyeh, M., Büchter, K.-D., Kaiser, J., and Plötner, K. O., "An Overview of Current Research and Developments in Urban Air Mobility: Setting the Scene for UAM Introduction," *Journal of Air Transport Management*, Vol. 87, 2020, p. 101852. doi: 10.1016/j.jairtraman.2020.101852.

[349] Vertical Flight Society, "Joby Aviation S4 (Production Prototype)," 2024. https://evtol.news/joby-aviation-s4-production-prototype, Last accessed: September 26, 2025.

[350] Lim, S. K. Y., "Comprehensive Multi-Disciplinary Design of an Electric Vertical Take-Off and Landing Aircraft," Ph.D. thesis, Nanyang Technological University, Singapore, 2024.

[351] Stoll, A., and Bevirt, J., "Development Of eVTOL Aircraft For Urban Air Mobility At Joby Aviation," *Proceedings of the Vertical Flight Society 78th Annual Forum*, The Vertical Flight Society, Fort Worth, TX, USA, 2022, pp. 1–11. doi: 10.4050/F-0078-2022-17528.

[352] Bertram, O., "UAM Vehicle Design with Emphasis on Electric Powertrain Architectures," *AIAA SCITECH 2022 Forum*, American Institute of Aeronautics and Astronautics, San Diego, CA, USA, 2022, pp. 1–26. doi: 10.2514/6.2022-1995.

[353] European Union Aviation Safety Agency, "Special Condition Vertical Take-Off and Landing (VTOL) Aircraft," European Union Aviation Safety Agency, Cologne, Germany, 2019.

[354] European Union Aviation Safety Agency, "Certification Specification, Acceptable Means of Compliance and Guidance Material for Small Rotorcraft (CS-27)," European Union Aviation Safety Agency, Cologne, Germany, 2021.

[355] McClamroch, N. H., *Steady Aircraft Flight and Performance*, Princeton University Press, Princeton, NJ, USA, 2011.

[356] Nicolai, L. M., and Carichner, G. E., *Fundamentals of Aircraft and Airship Design, Volume 1: Aircraft Design*, AIAA Educaction, Reston, VA, USA, 2010.

[357] Rotaru, C., and Todorov, M., "Helicopter Flight Physics," *Flight Physics - Models, Techniques and Technologies*, edited by K. Volkov, InTech, London, UK, 2018, pp. 19–46.

[358] Bittner, W., *Flugmechanik der Hubschrauber*, Springer, Berlin, Heidelberg, Germany, 2009.

[359] Leishman, J. G., *Principles of Helicopter Aerodynamics*, 2nd ed., Cambridge Aerospace Series, Cambridge University Press, Cambridge, UK, 2006.

[360] Zitzler, E., Deb, K., and Thiele, L., "Comparison of Multiobjective Evolutionary Algorithms: Empirical Results," *Evolutionary Computation*, Vol. 8, No. 2, 2000, pp. 173–195. doi: 10.1162/106365600568202.

[361] Deb, K., *Multi-Objective Optimization Using Evolutionary Algorithms*, Wiley-Interscience Series in Systems and Optimization, Wiley, Hoboken, NJ, USA, 2001.

[362] Saaty, T. L., and Vargas, L. G., *Models, Methods, Concepts & Applications of the Analytic Hierarchy Process*, International Series in Operations Research & Management Science, Vol. 175, Springer, New York, NY, USA, 2012.

[363] Belton, V., *Multiple Criteria Decision Analysis: An Integrated Approach*, Springer, New York, NY, USA, 2002.

[364] Anderson, A. D., Renner, N. J., Wang, Y., Lee, D., Agrawal, S., Sirimanna, S., Haran, K., Banerjee, A., Starr, M. J., and Felder, J. L., "System Weight Comparison of Electric Machine Topologies for Electric Aircraft Propulsion," *2018 AIAA/IEEE Electric Aircraft Technologies Symposium*, American Institute of Aeronautics and Astronautics, Cincinnati, OH, USA, 2018, pp. 1–16. doi: 10.2514/6.2018-4983.

[365] E-One Moli Energy Corporation, "Product Data Sheet Model INR-21700-M50A," 2017. https://www.molicel.com/wp-content/uploads/INR21700M50A-V3-80097.pdf, Last accessed: September 26, 2025.

[366] Botero, E. M., Wendorff, A., MacDonald, T., Variyar, A., Vegh, J., Lukaczyk, T. W., Alonso, J. J., Orra, T. H., and Ilario Da Silva, C., "SUAVE: An Open-Source Environment for Conceptual Vehicle Design and Optimization," *54th AIAA Aerospace Sciences Meeting*, American Institute of Aeronautics and Astronautics, San Diego, CA, USA, 2016, pp. 1–16. doi: 10.2514/6.2016-1275.